Bioengineering and biotechnology approaches in cardiovascular regenerative medicine, volume II

Edited by
Jianyi Zhang, Zhen Ma, Vahid Serpooshan,
Yuji Nakada and Keiichi Fukuda

About Frontiers

Frontiers is more than just an open access publisher of scholarly articles: it is a pioneering approach to the world of academia, radically improving the way scholarly research is managed. The grand vision of Frontiers is a world where all people have an equal opportunity to seek, share and generate knowledge. Frontiers provides immediate and permanent online open access to all its publications, but this alone is not enough to realize our grand goals.

Frontiers journal series

The Frontiers journal series is a multi-tier and interdisciplinary set of open-access, online journals, promising a paradigm shift from the current review, selection and dissemination processes in academic publishing. All Frontiers journals are driven by researchers for researchers; therefore, they constitute a service to the scholarly community. At the same time, the *Frontiers journal series* operates on a revolutionary invention, the tiered publishing system, initially addressing specific communities of scholars, and gradually climbing up to broader public understanding, thus serving the interests of the lay society, too.

Dedication to quality

Each Frontiers article is a landmark of the highest quality, thanks to genuinely collaborative interactions between authors and review editors, who include some of the world's best academicians. Research must be certified by peers before entering a stream of knowledge that may eventually reach the public – and shape society; therefore, Frontiers only applies the most rigorous and unbiased reviews. Frontiers revolutionizes research publishing by freely delivering the most outstanding research, evaluated with no bias from both the academic and social point of view. By applying the most advanced information technologies, Frontiers is catapulting scholarly publishing into a new generation.

What are Frontiers Research Topics?

Frontiers Research Topics are very popular trademarks of the *Frontiers journals series*: they are collections of at least ten articles, all centered on a particular subject. With their unique mix of varied contributions from Original Research to Review Articles, Frontiers Research Topics unify the most influential researchers, the latest key findings and historical advances in a hot research area.

Find out more on how to host your own Frontiers Research Topic or contribute to one as an author by contacting the Frontiers editorial office: frontiersin.org/about/contact

Bioengineering and biotechnology approaches in cardiovascular regenerative medicine, volume II

Topic editors

Jianyi Zhang — University of Alabama at Birmingham, United States
Zhen Ma — Syracuse University, United States
Vahid Serpooshan — Emory University, United States
Yuji Nakada — University of Alabama at Birmingham, United States
Keiichi Fukuda — Keio University, Japan

Table of
contents

Frontiers | Frontiers in Bioengineering and Biotechnology

Editorial: Bioengineering and biotechnology approaches in cardiovascular regenerative medicine, volume II

Mehdi Salar Amoli[1], Zhen Ma[2,3], Yuji Nakada[4], Keiichi Fukuda[5], Jianyi Zhang[4,6]* and Vahid Serpooshan[1,7,8]*

[1]Wallace H. Coulter Department of Biomedical Engineering, Emory University School of Medicine and Georgia Institute of Technology, Atlanta, GA, United States, [2]Department of Biomedical and Chemical Engineering, Syracuse University, Syracuse, NY, United States, [3]BioInspired Syracuse Institute for Material and Living Systems, Syracuse University, Syracuse, NY, United States, [4]Department of Biomedical Engineering, School of Medicine and School of Engineering, University of Alabama at Birmingham, Birmingham, AL, United States, [5]Department of Cardiology, Keio University School of Medicine, Tokyo, Japan, [6]Department of Medicine, School of Medicine, University of Alabama at Birmingham, Birmingham, AL, United States, [7]Department of Pediatrics, Emory University School of Medicine, Atlanta, GA, United States, [8]Children's Healthcare of Atlanta, Atlanta, GA, United States

Editorial on the Research Topic
Bioengineering and biotechnology approaches in cardiovascular regenerative medicine, volume II

Recent advances in the treatment of cardiovascular diseases (CVDs) have come a long way towards addressing these complications and have significantly improved patient survival and quality of life. However, CVDs remain the leading cause of mortality and morbidity worldwide (Roth et al., 2020). This is partly due to the limited ability of mammalian heart tissue to regenerate itself after injuries (Kikuchi and Poss, 2012). Thus, significant research effort has been dedicated to understanding the underlying mechanisms of cardiac regeneration and developing strategies to enhance these processes. Among various techniques, cardiovascular tissue engineering and biofabrication strategies, aiming at creation of functional tissue analogues, have shown great promise. Given the critical importance of such efforts, this Research Topic presents several outstanding studies on the advancement and implementation of bioengineering and biotechnology principles in cardiovascular regenerative medicine.

The efforts to regenerate cardiac tissue requires integration of a range of disciplines, including basic biology of heart regeneration, cellular mechanisms governing cell proliferation and differentiation, plus advanced tissue engineering techniques, such as 3D organoid systems and biomaterials. Aiming to understand the mechanisms governing proliferative capacity of cardiomyocytes (CMs), Nguyen et al. employed single nucleus RNA sequencing to determine the parameters affecting CM cell cycle activation, resulting in a higher proliferative capacity of CMs in a pig model of myocardial infarction (MI) (Nguyen et al.). Different groups of molecules were identified to contribute to CM proliferation, paving the way for further studies including in human subjects. In a different study, this

group also used single-cell RNA sequencing to examine another aspect of myocardial regeneration, the coronary vasculature. The single-nucleus RNA sequencing results demonstrated that only one subpopulation of endothelial cells (ECs) showed increased proliferation in response to the MI, while other EC population underwent endothelial-to-mesenchymal (EndMT) transition in the regenerating pig hearts. The latter EC population could be further examined in future studies as a potential new target to enhance heart regeneration.

A paramount factor to consider in devising cardiac regenerative strategies is the source of cardiac cells, such as CMs and cardiac fibroblasts. To date, induced pluripotent stem cell (iPSC)-derived CMs are increasingly employed in a variety of cardiovascular tissue engineering efforts. Wang et al., examined the impact of somatic-cell lineage of iPSCs on their CM differentiation by comparing the iPSCs derived from cardiac (atrial and ventricular fibroblasts) and non-cardiac (skin, kidney, and peripheral blood) lineage cells (Wang et al.). The cardiac origin iPSCs showed no significant differences in CM differentiation yield, and the resulting CMs exhibited consistent expression of pluripotency genes and electrophysiological function. However, these features altered significantly when comparing cardiac versus non-cardiac originated iPSC-CMs, signifying the importance of the iPSC origin in cardiac regenerative therapies. Another study focusing on the importance of cell origin, by Floy et al., investigated the differences between valve interstitial fibroblasts and left ventricular cardiac fibroblasts (LVCFBs) (Floy et al.). Transcriptomic analysis demonstrated a range of genes that differed in their expression among the two groups, suggesting LVCFBs to be more susceptible to conversion to myofibroblasts. Subsequent analyses of calcification and ECM synthesis demonstrated critical differences between the 2 cells, highlighting the importance of cell selection for regenerative strategies.

In parallel to the rapidly growing applications of iPSC-CMs *in vivo* regenerative therapies, these cells offer an unprecedented opportunity for the creation of robust *in vitro* models to study cardiac homeostasis and diseases. In a study by Shi et al., an *in vitro* iPSC-CM model was employed to gain a deeper insight into the cardiac muscle mechanobiology by examining the assembly and maturation of costameres, a structural-functional component of striated muscle cell, and their impact on myofibrillogenesis (Shi et al.). It was shown that the formation of costameres and myofibrils took place in an alternating fashion. The presence of pre-costameres affected myofibrilla formation, which in turn led to maturation of costameres. It was also shown that costamer maturation was impacted by contractile power of CMs, highlighting the importance of the extracellular matrix (ECM) mechanical properties, such as stiffness, on cardiac physiological functions. Stem cell-based *in vitro* platforms have also found increasing applications in disease modeling. Wang et al., reviewed recent efforts on establishing stem cell-based models of human fibrosis which engages a wide spectrum of organs, including the cardiovascular system (Wang et al.). This article provides a comprehensive and updated summary of different strategies that have been developed and utilized for accurate modeling of fibrotic pathologies.

In addition to the different cell sources, the bioengineering technologies applied can also have a significant impact on the success of cardiac regenerative therapies. Organoid technology, for instance, has found numerous applications in the field, as they provide a three-dimensional (3D) cellular microenvironment, replicating certain structural and functionalities of the native heart tissue. However, certain aspects of the organoid/spheroid systems, such as vascularization, pose challenges towards accurate representation of the cardiovascular tissues. Liang et al., reported the significance of Wnt signaling modulation as a method to develop vascularized cardiac organoids containing CMs and ECs (Liang et al.). Treatment with a range of small molecules, enabling codifferentiation of PSCs into CMs and cardiac ECs resulted in formation of vascularized organoids that can serve as a model for drug toxicity analyses. Similarly, aiming to generate an accurate replicate of cardiac tissue, Kahn-Krell et al., presented a facile approach to generate spheroids containing four major iPSC-derived cardiac cell types, including CMs, ECs, smooth muscle cells, and cardiac fibroblasts (Kahn-Krell et al.). These spheroids, created via a 3D suspension culture method, expressed major functional cardiac markers, and further established a robust *in vitro* platform for further research in cardiac regeneration. Considering the importance of vascularization in organoid development aimed at regeneration of complex tissues, LaMontagne et al., reviewed strategies to vascularize cortical organoids (LaMontagne et al.). One promising technique incorporates ECs along with signaling molecules into the organoids to induce vessel formation. Fusion of vascular spheroids with cortical organoids, and codifferentiation of different cell types are other robust strategies. Replication of native ECM cues, such as mechanical properties or proteins like collagen, is also known to impact angiogenesis. Further, bioreactors that enable dynamic flow surrounding the spheroids are also suggested as a method to enhance vascularization. These approaches could be applied to the cardiac regeneration field enhancing the ability of developed spheroids in recapitulating the native tissue structures.

Over the past 2 decades, a variety of bioengineering methods have been employed to amplify the regenerative capacity of endogenous or exogenous CMs. A study by Xiao et al., reviewed different approaches employed for enhancing the therapeutic impact of CMs derived from pluripotent stem cells (Xiao et al.). These strategies, including pre-treatment of cells with biomolecules such as growth factors, modifying the gene expression profile to enhance proliferative capacity of CMs, and co-transplantation with other cell types such as ECs or mesenchymal stem cells can have a significant impact on the outcome of cardiac tissue engineering strategies. In addition to the cellular methods described above, biomaterial-based strategies are a major area of research in cardiac regenerative strategies. Guo et al., described current advances in hemostatic biomaterials, including naturally derived biomaterials like protein- or polysaccharide-based materials, or inorganic biomaterials, such as zeolite and kaolin (Guo et al.). Description of hemostatic biomaterial mechanism of action, including physical, chemical, and physiological mechanisms, and further suggestions on design of these biomaterials demonstrate a clear path for future research.

Among biomaterial-based cardiac tissue engineering methods, decellularized ECM (dECM) strategies have gained increasing attention both for basic science research, as well as translational applications. Lopera Higuita et al., used decellularized bovine vein ECM as scaffolds for development of vascular grafts (Lopera Higuita

et al.). Using an antigen removal processing method, they circumvented some key disadvantages of other decellularization techniques, maintaining the structure and composition of the natural ECM. The team demonstrated superior EC proliferation and migration on the scaffolds due to maintenance of basement membrane proteins. In another dECM-based approach, Guo et al., evaluated the functional impairment of tissue-engineered blood vessels (TEBVs) due to the inflammatory response (Guo et al.). Decellularized carotid arteries of female pigs were coated with anti-CD34 antibody functionalized heparin-collagen. The team demonstrated the effect of intravenous transplantation of regulatory T cells in inhibition of intimal hyperplasia. Adverse remodeling of vascular grafts is the focus of another study in this Research Topic, by Tan et al., where a wide range of strategies are suggested to prevent such processes (Tan et al.). These include cell-based strategies, such as iPSC incorporation, or biomaterial-based strategies, such as scaffold functionalization.

In addition to the applications exemplified above, 3D scaffold systems are also increasingly used for delivery of biomolecules/drugs to enhance tissue regeneration. Clayton et al., developed plasma polymerized nanoparticles and demonstrated their use for delivery of platelet derived growth factors to cardiac cells both *in vitro* and *in vivo* (Clayton et al.). The nanoparticles did not pose any adverse effect on viability or contractile function of CMs, while maintained the functionality of conjugated growth factors. This method for direct delivery of growth factors can boost the regenerative capacity of various tissue engineered implants in the future.

In summary, the unprecedented advances in the 21st century, in the fields of cardiovascular bioengineering and regenerative medicine have enabled development of robust platforms for both *in vitro* disease modeling and drug screening, as well a variety of clinical therapies. Some key future directions and grand challenges at the interface of engineering and cardiovascular medicine include personalized and precision medicine, cell and genome engineering, and the design and development of smart biomedical devices.

Author contributions

MS: Data curation, Methodology, Resources, Writing–original draft, Writing–review and editing. ZM: Supervision, Writing–review and editing. YN: Writing–review and editing. KF: Writing–review and editing. JZ: Resources, Supervision, Writing–review and editing. VS: Conceptualization, Data curation, Funding acquisition, Methodology, Resources, Supervision, Writing–original draft, Writing–review and editing.

Conflict of interest

The authors declare that the research was conducted in the absence of any commercial or financial relationships that could be construed as a potential conflict of interest.

The author(s) declared that they were an editorial board member of Frontiers, at the time of submission. This had no impact on the peer review process and the final decision.

Publisher's note

References

Kikuchi, K., and Poss, K. D. (2012). Cardiac regenerative capacity and mechanisms. *Annu. Rev. Cell Dev. Biol.* 28, 719–741. doi:10.1146/annurev-cellbio-101011-155739

Roth, G. A., Mensah, G. A., Johnson, C. O., Addolorato, G., Ammirati, E., Baddour, L. M., et al. (2020). Global burden of cardiovascular diseases and risk factors, 1990-2019: update from the GBD 2019 study. *J. Am. Coll. Cardiol.* 76, 2982–3021. doi:10.1016/j.jacc.2020.11.010

Cardiomyocyte Cell-Cycle Regulation in Neonatal Large Mammals: Single Nucleus RNA-Sequencing Data Analysis *via* an Artificial-Intelligence–Based Pipeline

Thanh Nguyen[1†], Yuhua Wei[1†], Yuji Nakada[1], Yang Zhou[1] and Jianyi Zhang[1,2]*

[1]Department of Biomedical Engineering, University of Alabama at Birmingham, Birmingham, AL, United States, [2]Cardiovascular Diseases, Department of Medicine, University of Alabama at Birmingham, Birmingham, AL, United States

Adult mammalian cardiomyocytes have very limited capacity to proliferate and repair the myocardial infarction. However, when apical resection (AR) was performed in pig hearts on postnatal day (P) 1 (AR_{P1}) and acute myocardial infarction (MI) was induced on P28 (MI_{P28}), the animals recovered with no evidence of myocardial scarring or decline in contractile performance. Furthermore, the repair process appeared to be driven by cardiomyocyte proliferation, but the regulatory molecules that govern the AR_{P1}-induced enhancement of myocardial recovery remain unclear. Single-nucleus RNA sequencing (snRNA-seq) data collected from fetal pig hearts and the hearts of pigs that underwent AR_{P1}, MI_{P28}, both AR_{P1} and MI, or neither myocardial injury were evaluated *via* autoencoder, cluster analysis, sparse learning, and semisupervised learning. Ten clusters of cardiomyocytes (CM1–CM10) were identified across all experimental groups and time points. CM1 was only observed in AR_{P1} hearts on P28 and was enriched for the expression of T-box transcription factors 5 and 20 (TBX5 and TBX20, respectively), Erb-B2 receptor tyrosine kinase 4 (ERBB4), and G Protein-Coupled Receptor Kinase 5 (GRK5), as well as genes associated with the proliferation and growth of cardiac muscle. CM1 cardiomyocytes also highly expressed genes for glycolysis while lowly expressed genes for adrenergic signaling, which suggested that CM1 were immature cardiomyocytes. Thus, we have identified a cluster of cardiomyocytes, CM1, in neonatal pig hearts that appeared to be generated in response to AR injury on P1 and may have been primed for activation of CM cell-cycle activation and proliferation by the upregulation of TBX5, TBX20, ERBB4, and GRK5.

Keywords: single-nucleus RNA-sequencing, heart, infarct, cardiomyocytes, cell cycle, autoencoder

INTRODUCTION

Mammalian cardiomyocytes exit the cell cycle during the perinatal period and lose the ability to proliferate; thus, the hearts of mammals are unable to repair the damage caused by myocardial injury that occurs more than 2 days after birth (Porrello et al., 2011; Lam and Sadek, 2018; Ye et al., 2018; Zhu et al., 2018). However, when apical resection (AR) was performed in pig hearts on postnatal day (P) 1 (AR_{P1}), and acute myocardial infarction (MI) was induced on P28 (MI_{P28}), the animals completely recovered with no evidence of myocardial scarring or decline in contractile performance

by P56, whereas the hearts of animals that underwent MI on P28 without previous AR injury displayed significant fibrosis and declines in contractile activity (Zhao et al., 2020). Furthermore, the repair process appeared to be driven by the proliferation of cardiomyocytes, and comparative analyses of bulk and single-nuclei RNA sequencing (snRNA-seq) data from the hearts of animals that underwent AR_{P1} only, MI_{P28} only, or both AR_{P1} and MI_{P28} ($AR_{P1}MI_{P28}$), as well as uninjured (CTL) and fetal pig hearts, suggested that signaling pathways associated with cell-cycle activity, glycolytic metabolism, and declines in DNA damage were upregulated in the cardiomyocytes of $AR_{P1}MI_{P28}$ hearts (Zhang et al., 2020; Zhao et al., 2020; Nakada et al., 2022). Also, in our previous study using snRNA-seq data (Nakada et al., 2022), we found a novel cardiomyocyte subpopulation marked by coupregulation of Nebulin (NEB) and Pyruvate Kinase M1/2 (PKM), which uniquely appeared in regenerative $AR_{P1}MI_{P28}$ heart on postnatal day P35. On the other hand, how AR_{P1} cardiomyocytes differed from CTL ones such that they responded differently following MI_{P28} injury was not thoroughly examined. For the studies presented in this report, we collected more snRNA-seq data from the cardiac tissues of additional animals and then analyzed our expanded dataset with an artificial-intelligence–based pipeline for deeper understanding on which regulatory molecules and signaling pathways contributed to the AR_{P1}-associated enhancement of myocardial regeneration, and which cardiomyocyte subsets highly utilizes these regulators. We expanded the snRNA-seq dataset by obtaining a new MI_{P28}-only group on postnatal days P30, P35, and P42 and more AR_{P1}-MI_{P28} pigs at P30, P35, and P42. In addition, an artificial-intelligence technique was developed and applied for high-dimensional snRNA-seq data using a much smaller number of dimensions (Wang et al., 2016) and consequently improved snRNA-seq data clustering findings.

RESULTS

Autoencoding and Cluster Analysis Identified 10 Cardiomyocyte Populations in the Hearts of Fetal, AR_{P1}, MI_{P28}, and $AR_{P1}MI_{P28}$ Animals

Our complete dataset encompassed the results from snRNA-seq analyses of myocardial tissues in animals that underwent AR_{P1} only and were sacrificed on P28 and P56 (AR_{P1}-P28 and ARP1-P56, respectively); animals that underwent MI_{P28} only and were sacrificed on P30, P35, P42, and P56 (MI_{P28}-P30, -P35, -P42, and -P56, respectively); animals that underwent both AR_{P1} and MI_{P28} and were sacrificed on P30, P35, P42, and P56 ($AR_{P1}MI_{P28}$-P30, -P35, -P42, and -P56, respectively); CTL animals that were sacrificed on P1, P28, and P56 (CTL-P1, -P28, and -P56, respectively); and embryos obtained on embryonic day 80 (Fetal) (**Supplementary Table S1**). Tissues were collected from the border zone of infarction or the corresponding region of non-infarcted hearts, and nuclei with <500 or >25,000 unique molecular identifiers (UMIs), or with >25% mitochondrial UMIs were excluded from subsequent analyses. A total of

283,421 nuclei from 41 hearts were included in our analyses; 1,786 (median) genes and 31,736 (median) UMIs were captured per nucleus (**Supplementary Table S2**), and 129,991 of the nuclei were from cardiomyocytes. Data were aligned and normalized with the Seurat v.4 toolkit (Hao et al., 2021), and then embedded with an autoencoder before clustering and visualization *via* Uniform Manifold Approximation and Projection (UMAP) (McInnes et al., 2018; Meehan, 2021); this deep-learning–based method has outperformed other state-of-the-art approaches for unsupervised cluster analysis (Yang et al., 2019).

When data for all cell types were analyzed (**Supplementary Figure S1**), most of the clusters contained cells from multiple injury groups and time points, indicating that the results were not influenced by between-batch variation or sampling error, and each cluster was composed primarily of a single cell type (cardiomyocytes, smooth muscle cells, endothelial cells, fibroblasts, immune cells, or skeletal muscle–like cells. The skeletal muscle–like cluster uniquely expressed exclusive-skeletal-markers myosin light chain 3 (MYL3) (Hailstones and Gunning, 1990) and Myosin light chain kinase 2 (MYLK2) (Stull et al., 2011); meanwhile, it expresses cardiac Actin Alpha Cardiac Muscle 1 (ACTC1) and Myosin Heavy Chain 7 (MYH7). Cardiac muscle populations expressing both cardiomyocyte and skeletal muscle markers were reported in Clément et al. (1999). Also, the cardiac/skeletal muscle–like cluster upregulated both Nebulin (NEB) and Pyruvate Kinase M1/2 (PKM), which were consistent with the PKM+/NEB + cardiomyocyte subpopulation in our previous report (Nakada et al., 2022). Cardiomyocytes were distributed into 10 clusters (CM1–CM10) (**Figures 1A, B**), each of which was associated with a set of explicitly expressed marker genes (**Figure 1C**, **Supplementary Tables S3–S4**).

Cardiomyocytes in the CM1 cluster were found almost exclusively in AR_{P1}-P28 hearts, where they comprised 62.91% of the total cardiomyocyte population (**Figure 1D**). The CM2 cluster included a substantial proportion of cardiomyocytes from CTL (22.53%) and AR_{P1} (25.11%) hearts at P28, as well as $AR_{P1}MI_{P28}$ hearts at P30 (31.77%) and P35 (21.17%). CM3 cardiomyocytes were present only in CTL-P56 hearts, where they comprised just 2.63% of all cardiomyocytes and expressed elevated levels of genes associated with cell differentiation. Small numbers of CM4 cardiomyocytes, which expressed high levels of collagen [Collagen Type V Alpha 2 Chain (COL5A2) and Collagen Type III Alpha 1 Chain (COL3A1)] and genes that regulate the pluripotency of stem cells, including APC (Kielman et al., 2002), PIK3CA (Jeong et al., 2017), MAPK1 (Lu et al., 2008), and JARID2 (Landeira et al., 2010) (**Supplementary Figure S2A**), were present in all hearts. Cardiomyocytes from CM5 were only in CTL-P56 hearts and explicitly expressed genes that drive cardiomyocyte maturation, such as Ankyrin Repeat And SOCS Box Containing 18 (ASB18), Yip1 Domain Family Member 7 (YIPF7), Creatine Kinase, M-Type (CKM), and Creatine Kinase, Mitochondrial 2 (CKMT2) (Uosaki et al., 2015; Guo and Pu, 2020). CM6 included the majority (57.16%–69.69%) of cardiomyocytes from all injury groups (AR_{P1}, MI_{P28}, and $AR_{P1}MI_{P28}$) on P56 and was enriched for
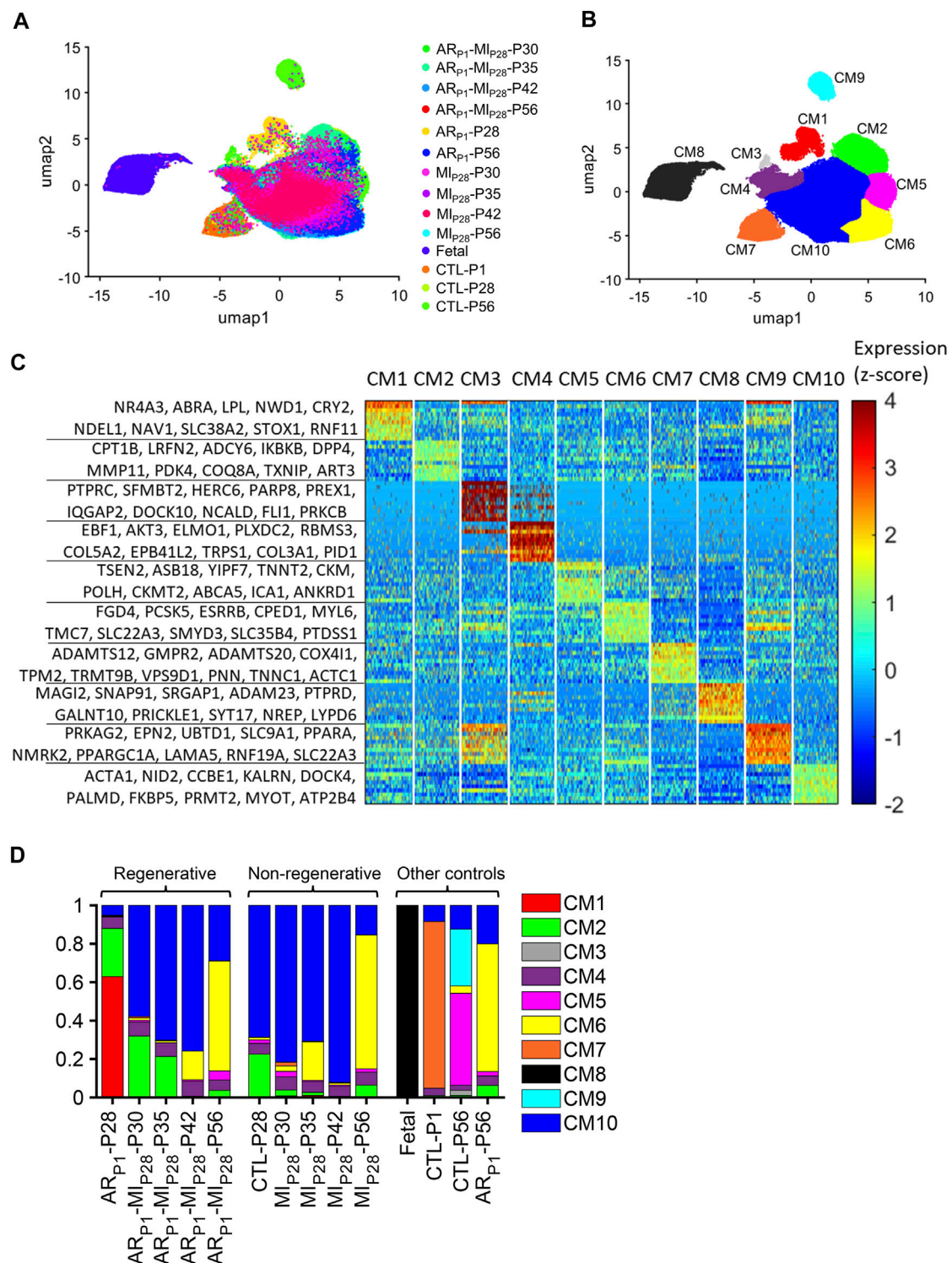
FIGURE 1 | Cluster analysis identified 10 populations of cardiomyocytes in Fetal, CTL, AR_{P1}, MI_{P28}, and $AR_{P1}MI_{P28}$ hearts. **(A,B)** Cardiomyocyte snRNA-seq data were reduced to 10 dimensions with an autoencoder, processed *via* cluster analysis, visualized *via* UMAP, and displayed according to **(A)** experimental group and time point and **(B)** cluster (CM1–CM10). **(C)** The expression of genes that were explicitly associated with each cluster is displayed as a heat map. **(D)** The proportion of cardiomyocytes from each cluster is displayed for each experimental group and time point.
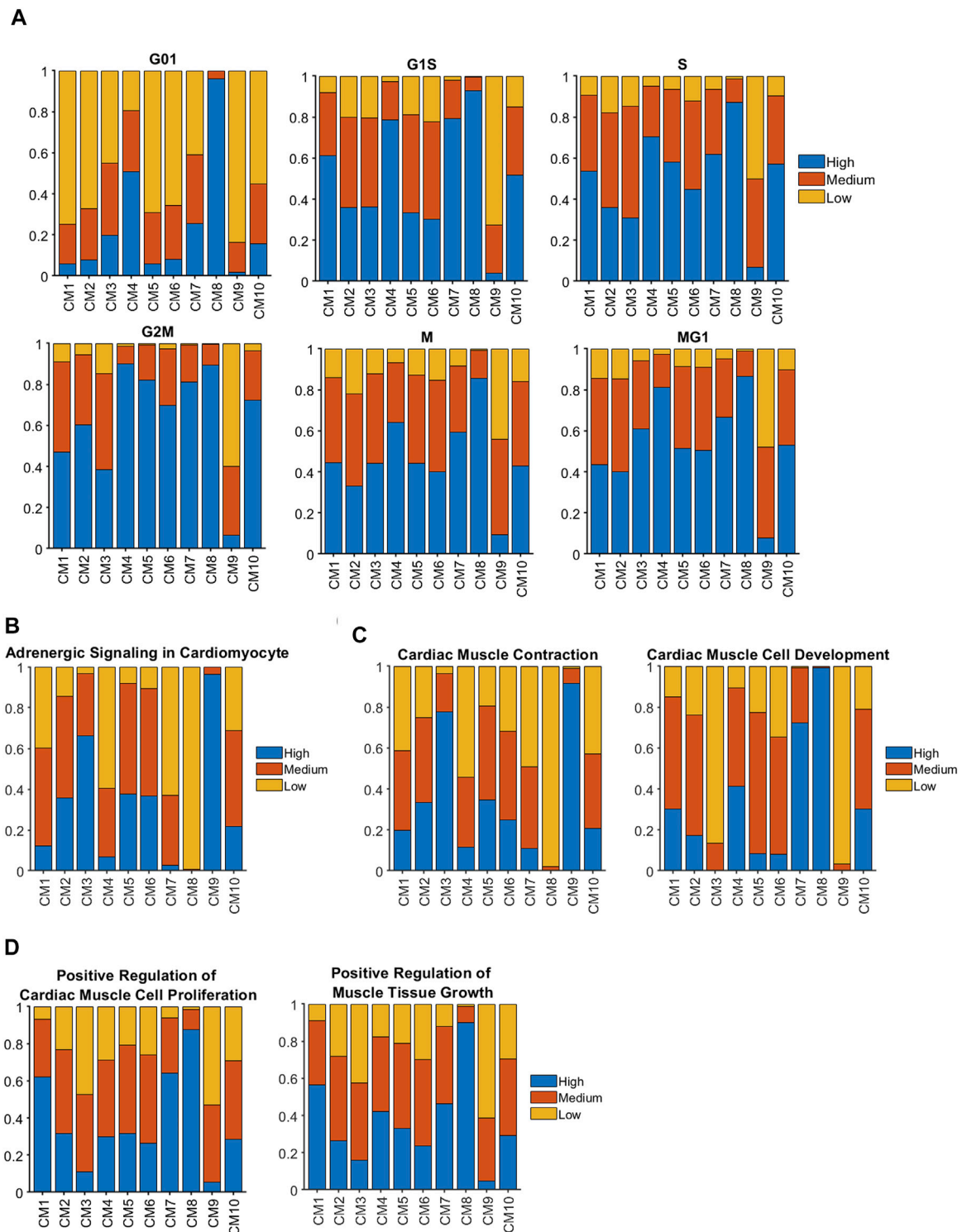
FIGURE 2 | Genes that contribute to cell-cycle activity and muscle growth tended to be more highly expressed in clusters associated with regenerating hearts than in CTL hearts at P28 and afterward. Sparse analysis was conducted for the expression of genes associated with **(A)** the cell-cycle, **(B)** adrenergic signaling, **(C)** the contractile activity and development of cardiac muscle, and **(D)** cardiac-muscle cell proliferation and muscular growth; then, the proportion of cardiomyocytes with high, medium, or low levels of expression was calculated for each cluster.

the expression of Z-disc and insulin-signaling genes. CM7 encompassed most (86.75%) of the cardiomyocytes in CTL-P1 hearts and was associated with elevated levels of genes that participate in the morphogenesis of cardiac muscle and myofibril assembly. The CM8 cluster included nearly all (99.69%) of the cardiomyocytes in fetal hearts, none of those from any other group or time point, and was enriched for genes that contribute to embryonic development. CM9 cardiomyocytes were present only in CTL-P56 hearts, where they comprised 29.51% of all cardiomyocytes, and expressed high levels of genes associated with the Z-disc, focal-adhesion, and other structural components of muscle cells. Finally, cardiomyocytes from the CM10 cluster were found in all nonfetal groups at all time points and included the majority (57.85%–92.16%) of cardiomyocytes in MI_{P28} and $AR_{P1}MI_{P28}$ hearts from P30-P42. The pairwise similarities among these clusters were presented in **Supplementary Figure S3**.

AR_{P1} and MI_{P28}, Both Alone and in Combination, Promoted Cardiomyocyte Cell-Cycle Activity for Approximately Two Weeks After Myocardial Infarction Induction

Sparse modeling (Bi et al., 2003; Huang et al., 2010; Chkifa et al., 2015; Zhang et al., 2014) enables researchers to extract relevant data from datasets that contain a large number of variables that do not contribute to the property being studied. When sparse modeling was used to evaluate the expression of cell-cycle genes in our cardiomyocyte snRNA-seq dataset (**Supplementary Figure S4**), our results are consistent with our previous report in (Nakada et al., 2022). Briefly, the proportion of high-cell-cycle in each phase of the cell cycle was the greatest in Fetal and CTL-P1 hearts. Also, these proportions in CTL-P1 hearts were higher than in hearts from any other postnatal group, which is consistent with the perinatal occurrence of cardiomyocyte cell-cycle arrest. However, cycling cardiomyocytes were much more common in AR_{P1} hearts at P28, and in both MI_{P28} and $AR_{P1}MI_{P28}$ hearts from P30-P42, than in CTL hearts at P28 or P56. Cell-cycle activity was also significantly more common in cardiomyocytes from $AR_{P1}MI_{P28}$ hearts than from MI_{P28} hearts on P35 (G1S: $p = 1.06 \times 10^{-58}$; S: $p = 9.67 \times 10^{-12}$; G2M: $p = 7.44 \times 10^{-66}$; M: $p = 4.11 \times 10^{-7}$) but not on P42, which suggests that AR on P1 promoted cardiomyocyte proliferation for approximately 1 week after MI induction on P28. Notably, this period of AR_{P1}-enhanced proliferation coincided with a greater proportion of CM2 cardiomyocytes in $AR_{P1}MI_{P28}$ hearts.

AR_{P1}-P28 Hearts Contained a Cluster of Cardiomyocytes With a Latent Capacity for Myocardial Proliferation and Growth

When cell-cycle gene expression was evaluated for cardiomyocyte (CM1) clusters (**Figure 2A**), cycling activity tended to be highest in CM8 and lowest in CM9, which is consistent with our observation that these two clusters were almost exclusively associated with Fetal and CTL-P56 hearts, respectively. The proportion of cycling cells was also elevated among CM4

cardiomyocytes, which express high levels of pluripotency-maintenance genes (Mouse Genome Informatics, 2022) (**Supplementary Figure S2B**) and consequently, appear to have some progenitor-cell–like properties. However, CM1 cardiomyocytes, which were found only in AR_{P1} hearts at P28, were not especially more proliferative than CM9 (primarily in CTL-P56); for example, G2M (Mouse Genome Informatics, 2021a) [odds ratio (OR) = 2.66, $p = 3.38 \times 10^{-76}$] and MG1 (Cui et al., 2020) (OR = 1.45, $p = 1.59 \times 10^{-21}$) cells were less common in CM1 than in CM10, which comprised the bulk of cardiomyocytes in both MI_{P28} and $AR_{P1}MI_{P28}$ hearts during the 2 weeks after MI induction. Nevertheless, analyses of adrenergic signaling (KEGG: Adrenergic signaling in cardiomyocytes, 2021) (**Figure 2B**), cardiac-muscle contraction (Mouse Genome Informatics, 2021b), and cardiac-muscle–cell development (Gene Ontology: Cardiac Muscle Cell Development, 2021) (**Figure 2C**) indicated that CM1 cardiomyocytes were functionally immature, while genes associated with the proliferation (Mouse Genome Informatics, 2021c) (OR = 5.61, $p < 10^{-60}$) and growth (Mouse Genome Informatics, 2021d) (OR = 4.35, $p < 10^{-60}$) of cardiac muscle (**Figure 2D**) were more highly expressed in CM1 than in CM10. Collectively, these observations suggest that although CM1 cardiomyocytes themselves did not display exceptionally high levels of cell-cycle activity, they were still immature and might retain a latent capacity for proliferation that could have been reactivated by MI induction on P28.

CM1 Cardiomyocytes Express Elevated Levels of T-Box Transcription Factors 5 and 20 (TBX5 and TBX20), Erb-B2 Receptor Tyrosine Kinase 4, and G Protein-Coupled Receptor Kinase 5

CM1 cardiomyocytes were enriched for expression of the regulatory molecules TBX5 ($p = 8.65 \times 10^{-184}$), TBX20 ($p = 2.97 \times 10^{-225}$), and Erb-B2 receptor tyrosine kinase 4 (ERBB4) ($p = 4.86 \times 10^{-186}$) (**Figure 3A**). Notably, these three genes were also coupregulated in the clusters that were exclusively associated with Fetal hearts (CM8) and with CTL hearts on P1 (CM7), and previous reports have shown that disruptions of TBX5 (Misra et al., 2014; Maitra et al., 2009), TBX20 (Xiang et al., 2016; Chakraborty and Yutzey, 2012), or ERBB4 (Bersell et al., 2009) activity reduce cardiomyocyte proliferation in fetal and neonatal mouse hearts. Furthermore, the expression of G protein-coupled receptor kinase 5 (GRK5), which is associated with cardiac hypertrophy (Gold et al., 2012; Traynham et al., 2015), was upregulated in CM1 cardiomyocytes. Thus, we queried the TRRUSTv2 (Han et al., 2018) and STRING v11.5 (Szklarczyk et al., 2021) databases to identify the genes that are targeted by or interact with these four molecules, and then used the database for annotation, visualization, and integrated discovery (DAVID) bioinformatics resources (Huang et al., 2009) with the Gene Ontology Annotation (GOA) (Huntley et al., 2015), Kyoto Encyclopedia of Genes and Genomes (KEGG) (Kanehisa et al., 2017), and Reactome (Jassal et al., 2020) databases to characterize the network (**Figure 3B**) of biological processes and signaling pathways that may have been upregulated in CM1
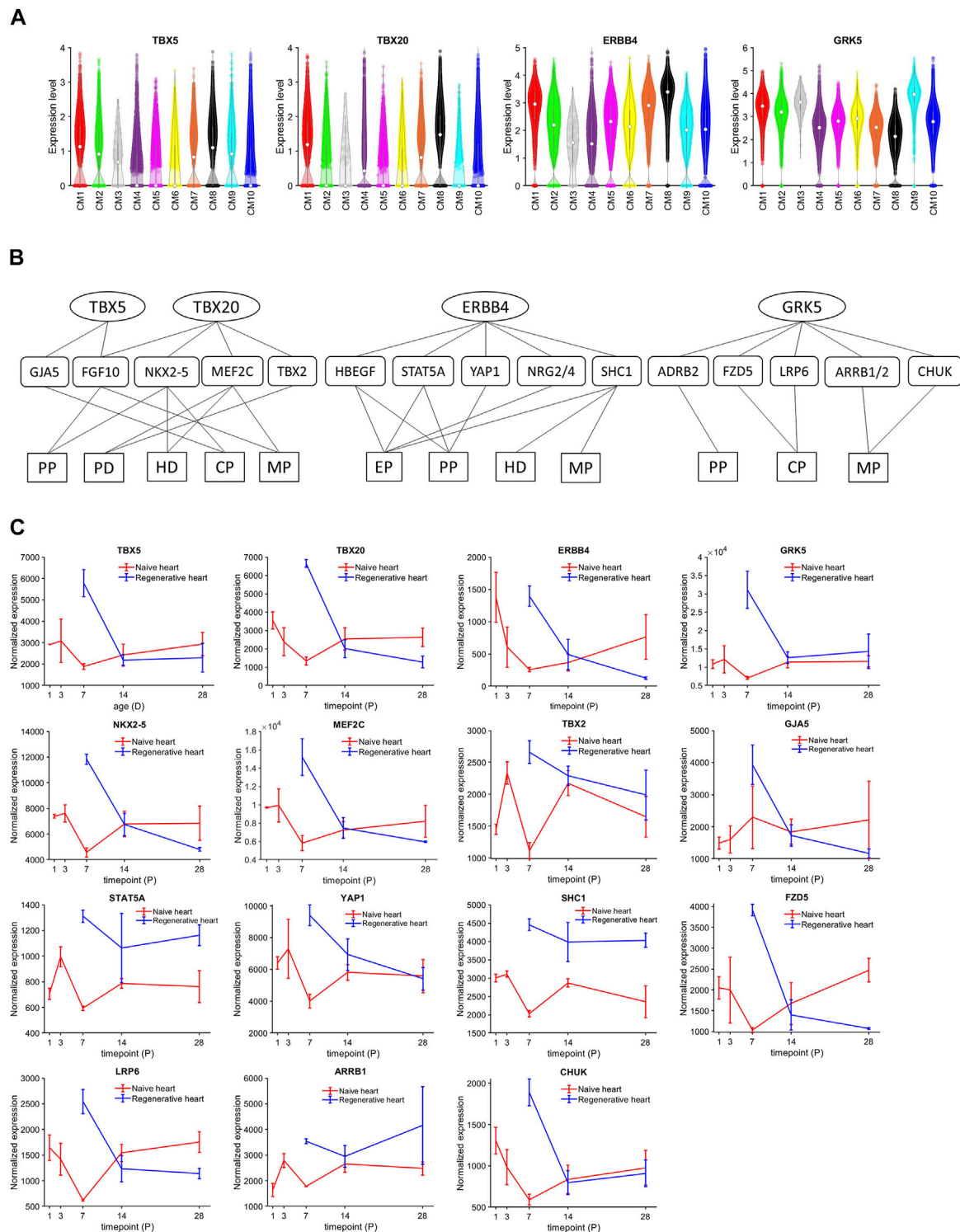
FIGURE 3 | TBX5, TBX20, ERBB4, and GRK5 were consistently upregulated in CM1, CM7, and CM8 cardiomyocytes. **(A)** The abundance of TBX5, TBX20, ERBB4, and GRK5 RNA transcripts was measured in cardiomyocytes from each cluster and displayed in a violin plot. The expression was normalized according to the Seurat pipeline: the expression matrix was scaled by the ScaleData function with vars. to. regress set to nUMI and nGenes; then, the scaled expression was log-normalized. **(B)** The network of genes, cellular processes, and signaling pathways regulated by TBX5, TBX20, ERBB4, and GRK5 was evaluated with DAVID bioinformatics resources. Targeted genes were identified in the TRRUST v2 (TBX5 and TBX20) and STRING v11.5 (ERBB4 and GRK5) databases and functional/pathway data were obtained from the GOA, KEGG, and Reactome databases. PP, positive regulation of cell proliferation; PD, positive regulation of cardiac muscle cell differentiation; CP, canonical Wnt signaling pathway; MP, MAPK signaling pathway; Ep, ErbB signaling pathway. **(C)** The bulk RNAseq expressions of TBX5, TBX20, ERBB4, GRK5, NKX2-5, MEF2C, TBX2, GJA5, STAT5A, YAP1, SHC1, FZD5, LRP5, ARRB1, and CHUK in regenerative and naïve pig heart. The transcript counts were normalized using DeSeq2 pipeline.
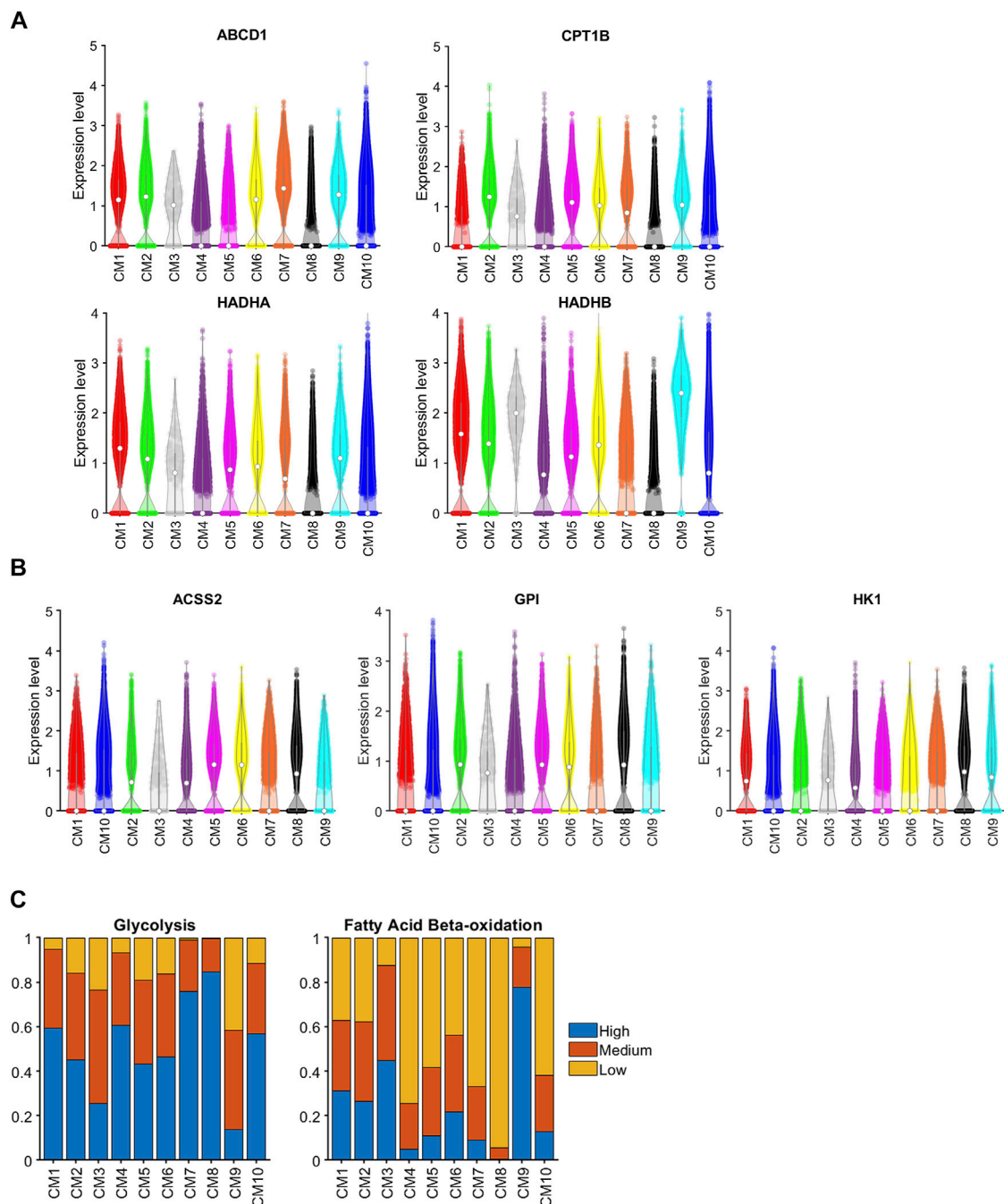
FIGURE 4 | Genes associated with both glycolysis and βFAOX were upregulated in CM1 and CM2. The abundance of RNA transcripts for genes that contribute to **(A)** glycolysis (ABCD1, CPT1B, HADHA, and HADHB) and **(B)** βFAOX (ACSS2, GPI, and HK1) was measured in cardiomyocytes from each cluster and displayed in a violin plot. The expression was normalized according to the Seurat pipeline: the expression matrix was scaled by the ScaleData function with vars.to.regress set to nUMI and nGenes; then, the scaled expression was log-normalized. **(C)** Sparse analysis was conducted for the expression of glycolysis and βFAOX genes, and the proportion of cardiomyocytes with high, medium, or low levels of expression was calculated for each cluster.

cardiomyocytes. Collectively, our results identified increases in processes of cell proliferation (Mouse Genomic Informatics, 2021a) and cardiac-muscle–cell differentiation (Mouse Genome Informatics, 2021c), as well as in ErbB (Zhu et al., 2010), MAPK (Liu and Zhong, 2017), and canonical Wnt (Kwon

et al., 2007) signaling (**Supplementary Tables S5, S6**). Intermediate molecules in the network included: 1) Fibroblast Growth Factor 10 (FGF10), which is activated by both TBX5 and TBX20, phosphorylates Forkhead Box O3 (FOXO3), and downregulates the cell-cycle inhibitor p27 (Rochais et al.,

2014); 2) Gap Junction Protein Alpha 5 (GJA5), which is activated by TBX5 and contributes to the differentiation of induced-pluripotent stem cells into cardiomyocytes, endothelial cells, and other cardiac cell types (Paik et al., 2018); 3) Myocyte Enhancer Factor 2C (MEF2C) and NK2 Homeobox 5 (NKX2-5), which are upregulated by TBX20 and cooperatively participate in the embryonic development of mouse hearts (Vincentz et al., 2008; Materna et al., 2019); 4) the Hippo pathway effector Yes-associated Protein 1 (YAP1), which is activated by ERBB4 and regulates the cell cycle by interacting with transcription factors of the Transcriptional Enhanced Associate Domain (TEAD) family (Zhao et al., 2008; Yuan et al., 2020); and 5) Beta-2 Adrenergic Receptor (ADRB2), as well as downstream components of the canonical Wnt signaling pathway (Chen et al., 2009), which may reactivate proliferation in mature cardiomyocytes (Fan et al., 2018). Notably, bulk-RNA seq data (Zhang et al., 2020) cross-checking also showed the overexpression of TBX5, TBX20, ERBB4, GRK5, NKX2-5, MEF2C, TBX2, GJA5, STAT5A, YAP1, SHC1, FZD5, LRP6, ARRB1, and CHUK among regenerative hearts (**Figure 3C**). Here, these regenerative-hearts expressions on postnatal day 7 (P7) were even higher than they are in naïve-hearts P1 and P3.

CM1 and CM2 Cardiomyocytes Were Enriched for the Expression of Genes That Contribute to Both Glycolysis and β Fatty Acid Oxidation

As cardiomyocytes mature, the primary mechanism for ATP generation switches from glycolysis to beta fatty acid oxidation (β-FAOX) (Lopaschuk and Jaswal, 2010), which is consistent with our observation that glycolysis genes [Acyl-CoA Synthetase Short Chain Family Member 2 (ACSS2), Glucose-6-Phosphate Isomerase (GPI), and Hexokinase 1 (HK1) (Glycolysis, 2021)] were highly expressed in the CM8 cluster (i.e., fetal cardiomyocytes) but not in CM9 (i.e., the CTL-P56–exclusive cluster), while genes involved in β-FAOX [ATP Binding Cassette Subfamily D Member 1 (ABCD1) (van Roermund et al., 2011), Carnitine Palmitoyltransferase 1B (CPT1B) (Angelini et al., 2021), and Hydroxyacyl-CoA Dehydrogenase Trifunctional Multienzyme Complex Subunits Alpha (Miklas et al., 2019) and Beta (Sekine et al., 2021) (HADHA and HADHB, respectively)] were downregulated in CM8 and upregulated in CM9 (**Figures 4A, B**). Sparse-model analysis indicated that glycolysis (Glycolysis, 2021) was the dominant metabolic pathway in most other cardiomyocyte clusters. Compared to CM9 (primarily CTL-P56 cardiomyocytes), glycolysis markers were upregulated in CM1 (OR = 9.21, $p < 10^{-60}$), CM2 (OR = 5.23, $p < 10^{-60}$), and CM10 (OR = 8.28, $p10^{-60}$), yet did not reach the CM7 (CTL-P1 exclusive) and CM8 (Fetal exclusive) level. In addition, compared to CM8, β-FAOX markers were upregulated in CM1 (OR = 128.77, $p < 10^{-60}$), CM2 (OR = 102.75, $p < 10^{-60}$), and in CM10 (OR = 41.68, $p < 10^{-60}$), yet did not reach CM9 level, (**Figure 4C**). β-FAOX upregulation in CM10 was significantly less than in CM1 and CM2. Notably, the CM2 and CM10 clusters comprised most (~90% or more) of the cardiomyocytes in $AR_{P1}MI_{P28}$ hearts during the first week after MI induction, and DAVID analysis indicated that the

metabolism of CM2 but not CM10, cardiomyocytes was also supported by increases in insulin (KEGG: Insulin signaling pathway, 2021) and glucagon (KEGG: Insulin signaling pathway, 2021) signaling. Nevertheless, assessments of cell-cycle activity in the CM2 and CM10 clusters were similar (**Figure 3A**), so whether CM2 cardiomyocytes have a unique role in the AR_{P1}-induced enhancement of myocardial repair and regeneration remains unclear.

The Fate of CM1 Cardiomyocytes After Myocardial Infarction on P28 May Have Been Regulated by Protein Kinase AMP-Activated Noncatalytic Subunit Gamma 2, Nuclear Receptor Subfamily 4 Group a Member 3, and Activating Transcription Factor 3

Because cardiomyocytes in the CM1 cluster appeared to retain some latent capacity for proliferation and were present almost exclusively in AR_{P1} hearts at P28, whereas the CM2 and CM10 clusters collectively encompassed most of the cardiomyocytes in $AR_{P1}MI_{P28}$ hearts at P30 and P35 and were more similar to CM1 than other $AR_{P1}MI_{P28}$ clusters (**Supplementary Figure S3**), we used a semisupervised machine-learning technique to investigate whether the induction of MI in hearts that had recovered from previous AR surgery could have triggered the transformation of CM1 cardiomyocytes into CM2 and CM10 cardiomyocytes. snRNA-seq data for each cardiomyocyte in the CM1 cluster were compared to data for CM2 and CM10 cardiomyocytes from $AR_{P1}MI_{P28}$ hearts on P30; then, the CM1 cardiomyocytes were distributed by semisupervised machine-learning into two subpopulations: CM1a or CM1b, which more closely resembled cardiomyocytes from the CM2 or CM10 clusters. (**Figure 5A**). Transcription factors that were differentially expressed between the CM1a and CM1b subpopulations (**Figure 5B**, **Supplementary Table S7**) included protein kinase AMP-activated noncatalytic subunit gamma 2 (PRKAG2), nuclear receptor subfamily 4 group a member 3 (NR4A3), and activating transcription factor 3 (ATF3), which were also more highly expressed in CM2 than in CM10 cardiomyocytes, and the expression of all three genes declined in ARP1MIP28 hearts after P35, which coincided with the disappearance of CM2 cardiomyocytes. Notably, PRKAG2 regulates both glycolysis and fatty acid oxidation (Hinson et al., 2016), which were uniquely coupregulated in CM1 and CM2 cardiomyocytes, and both NR4A3 and ATF3 appear to be cardioprotective: NR4A3 was associated with improvements in infarct size and cardiac function, as well as declines in inflammation when overexpressed in infarcted mouse hearts (Jiang et al., 2019), and measures of cardiac fibrosis, hypertrophy, and function, as well as glucose tolerance, were worse in mice carrying a cardiac-specific ATF3-knockout mutation than in wild type mice when the animals were fed a high-fat diet (Kalfon et al., 2017). There are 38.15% CM1 (**Figure 5C**) cells co-expressing PRKAG2, NR4A3, and ATF3. Then, multiplying the percentage of PRKAG2 + NR4A3 + ATF3 + CM1 cells by the proportion of CM1 cells (38.15%) in
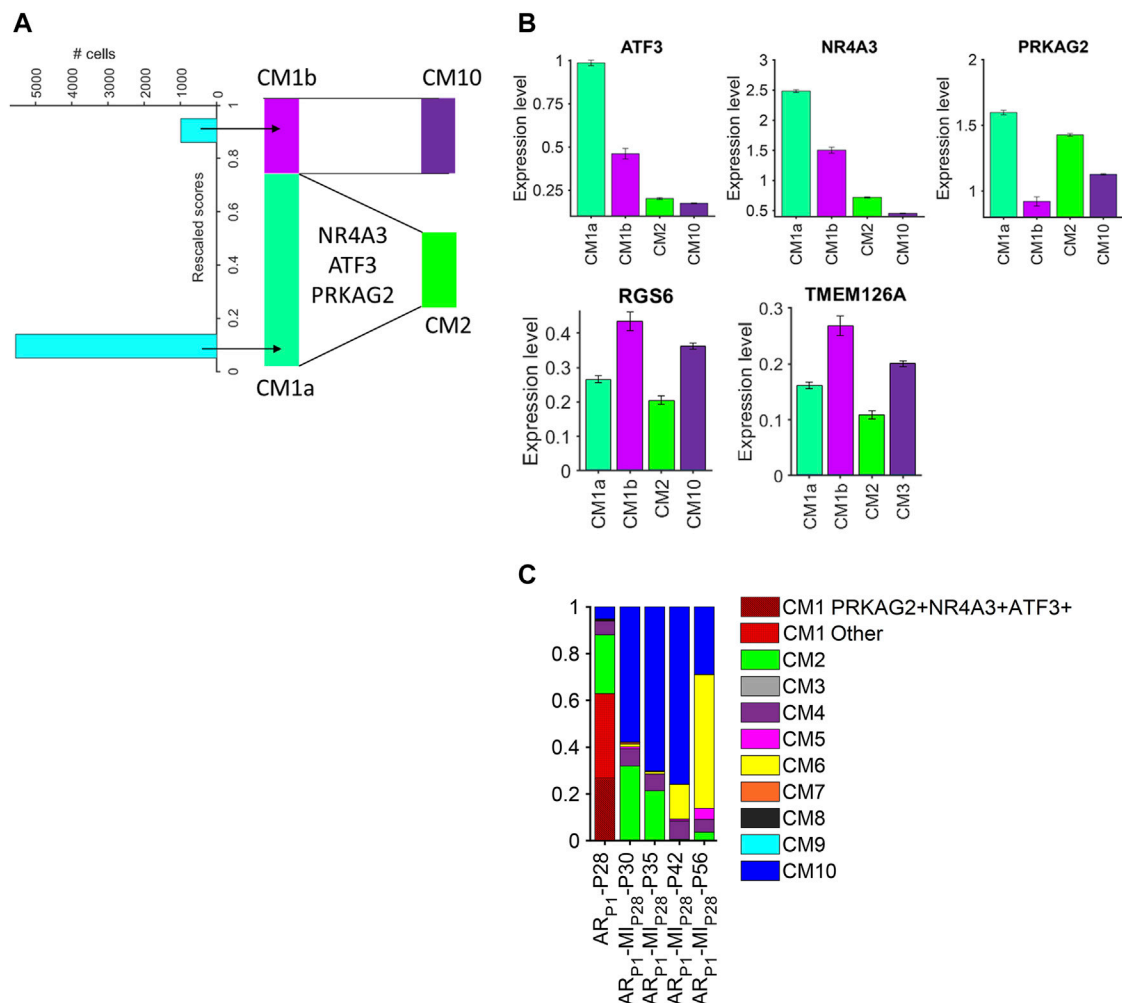
FIGURE 5 | Cardiomyocytes in the CM1 cluster could be partitioned into CM2- and CM10-like subpopulations. **(A)** snRNA-seq data for CM1 cardiomyocytes in AR$_{P1}$-P28 hearts and for CM2 and CM10 cardiomyocytes in AR$_{P1}$MI$_{P28}$-P30 hearts were evaluated with a semisupervised learning model to calculate a rescaled score for each CM1 cardiomyocyte. Cardiomyocytes with rescaled scores approaching 0 were designated CM1a (CM2-like) and cardiomyocytes with rescaled scores approaching 1 were designated CM1b (CM10-like). **(B)** The abundance of ATF3, NR4A3, PRKAG2, RGS6, and TMEM126A RNA transcripts was measured in CM1a, CM1b, CM2, and CM10 cardiomyocytes. **(C)** The proportion of PRKAG2+NR4A3+ATF3+ cardiomyocytes in CM1 (AR$_{P1}$-P28), in comparison with CM2 proportions.

ARP1P28 cardiomyocytes (62.91%) yields 24.00%. This PRKAG2 + NR4A3 + ATF3 + percentage is similar to CM2 percentage in ARP1MIP28P30 and ARP1MIP28P35. Collectively, these observations suggest that CM1 may be composed of the mix-transition states. Also, PRKAG2, NR4A3, and ATF3 may function as molecular switches that trigger the transformation of CM1 cardiomyocytes into CM2 cardiomyocytes. Meanwhile, from the same analysis, transformation from CM1 into CM10 cardiomyocytes may associate with the expressions of RGS6 and TMEM126A, which consistently upregulated in CM1b and CM10.

CM1 Markers ERBB4 and GRK5 Are Highly Expressed in Regenerative Hearts

The roles of TBX5 (Maitra et al., 2009; Misra et al., 2014), TBX20 (Chakraborty and Yutzey, 2012; Xiang et al., 2016), and ERBB4

(Bersell et al., 2009) in cardiomyocyte proliferation had been reported in previous independent studies; therefore, we focused on validating ERBB4 and GRK5, which localize on the cell surface, protein expression in our pig tissue. The western blotting of ERBB4 and GRK5 showed increased protein levels in AR$_{P1}$-P28, which is consistent with our snRNA-seq data (**Figure 6**). Western blotting measures the protein expression in the whole tissue, including cardiomyocytes and noncardiomyocytes; therefore, we performed further immunofluorescence validation (cardiomyocyte-specific).

We are interested in investigating the specific expression of GRK5 during heart regeneration as existing GRK5 studies (Martini et al., 2008; Islam et al., 2013; Traynham et al., 2016; de Lucia et al., 2022) have not found the role of GRK5 in cardiomyocyte proliferation. Therefore, additional immunofluorescence analysis (**Figure 7**) was performed to

FIGURE 6 | Western blotting confirming ERBB4 and GRK5 expression. The expression in each sample was scaled according to GAAPDH level to ensure equal loading. **(A)** Representative Western Blotting image in each group. Each row presents a protein, in order: ERBB4, and GRK5. Each column presents a sample, in order: Fetal (3 samples), CTL-P28 (3 samples), and AR_{P1}-P28 (3 samples). **(B)** Bar chart comparing the average expression among groups. Here, the value for each sample is represented in a circle dot. The horizontal lines and stars (*) represent nonparametric statistical comparisons between two groups. *p-value < 0.05.

show the GRK5 expression in cardiomyocytes undergoing the regenerative or non-regenerative process. We found that GRK5 expression increases ($p = 0.03$) 7 days after MIP28 injury in the control (CTL-P28 and MI_{P28}-P35) group. But the increased GRK5 level in the control group is still less than its level in AR_{P1}-P28 samples ($p = 0.03$). This result is consistent with snRNA-seq analysis, where GRK5 expression is the most elevated in CM1 (exclusively for AR_{P1}-P28) among the injured-heart cardiomyocytes. Surprisingly, immunofluorescence analysis shows that GRK5 is also highly expressed in the Fetal group, where cardiomyocytes are expected to actively proliferate.

DISCUSSION

Although the proliferative capacity of mammalian cardiomyocytes is extremely limited, the meager amount of myocardial regeneration that occurs after MI in the adult heart appears to require the presence of cycling cardiomyocytes (Laflamme and Murry, 2011). A number of studies have shown that mammalian cardiomyocytes remain proliferative for only a few days after birth (Porrello et al., 2011; Lam and Sadek, 2018; Ye et al., 2018; Zhu et al., 2018) but when AR surgery was performed in pigs on P1, cardiomyocytes proliferated in response to MI injury that occurred on P28, and the animals fully recovered with little or no evidence of contractile dysfunction or myocardial scarring (Zhao et al., 2020). The snRNA-seq analyses presented here build upon these previous observations by showing that the proportion of cycling cardiomyocytes increased in response to either AR_{P1} or MI_{P28}, and in animals that underwent both surgical procedures, AR_{P1} appeared to further upregulate cardiomyocyte cell-cycle activity for 1 week after MI induction.

Cluster analysis of our snRNA-seq data indicated that cardiomyocytes in the hearts of Fetal pigs, CTL (uninjured) neonatal pigs, and neonatal pigs that underwent AR_{P1}, MI_{P28}, or both ($AR_{P1}MI_{P28}$) can collectively be grouped into 10 different subpopulations (CM1–CM10), and that the abundance of each cluster varied depending on the injury group and time-point analyzed. Cell-cycle gene expression tended to be highest in CM8, which is consistent with our observation that this cluster comprised >99% of the cardiomyocytes in fetal hearts but was absent in all other groups, and cell cycle activity was greater in CM1–7 and CM10 than in CM9, which was almost exclusively associated with CTL-P56 hearts. Notably, the CM1 cluster comprised >60% of the cardiomyocytes in AR_{P1}-P28 hearts but was absent in all other groups, including CTL-P28 hearts, which suggests that CM1 cardiomyocytes may have a prominent role in the AR_{P1}-induced enhancement of myocardial regeneration. As in **Figure 1B**, CM1 is very separated from CM8 (representing fetal cardiomyocytes) and CM7 (representing neonatal day 1 cardiomyocyte). Therefore, CM1 is more likely associated with the later postnatal period regeneration rather than the neonatal period. In addition, we hypothesize that CM1 responds to the second myocardial infarction injury on the postnatal day 28 (MI_{P28}) by transiting to CM2 or CM10. This response may change the transcription profile of CM1 cardiomyocytes; therefore, the analysis may not represent this "CM1—the same cluster" in AR_{P1}-MI_{P28}-P30 and AR_{P1}-MI_{P28}-P30. Therefore, we performed semi-supervised learning to find which regulators might determine the transition from CM1 into CM2 or CM10. Interestingly, proliferative regulators, TBX5 and GRK5 continued expressing highly in CM2. Different from our previous publication (Nakada et al., 2022), which only detected six cardiomyocyte subpopulations, the newly added data, and AI-based pipeline enabled significantly deeper analysis, resulting in ten subpopulations. Beyond reconfirming the PKM2+/NEB + subpopulation as in (Nakada et al., 2022), this work characterized four cardiomyocyte subpopulations in injured-
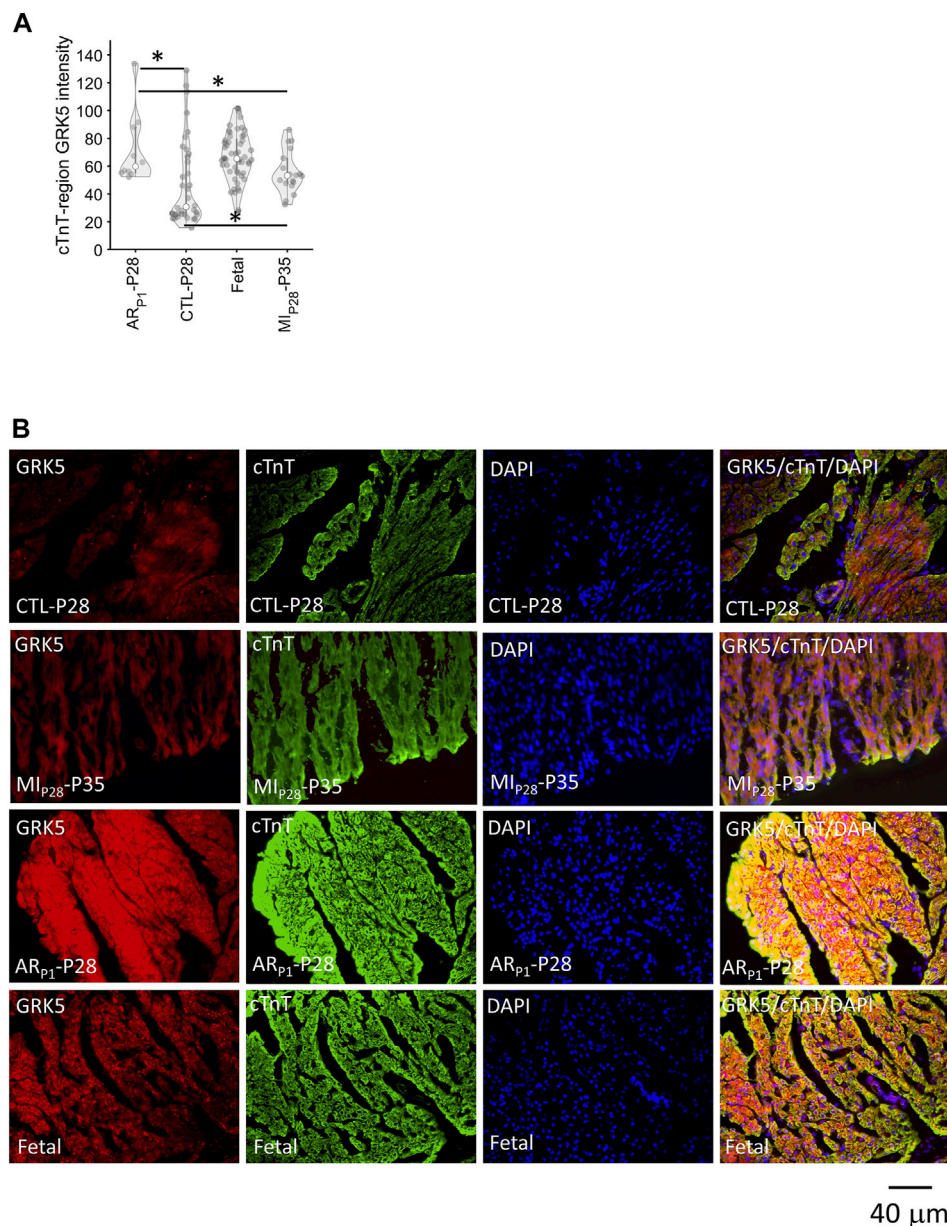
FIGURE 7 | Immunofluorescence analysis confirming GRK5 expression in cardiomyocytes. Here, the expression of GRK5 was represented by the average GRK5 red-channel value (light intensity) that is overlapped with cardiac troponin (cTnT) blue-channel (foreground), which was calculated after adjusting GRK5 red-channel background. DAPI (blue) indicates nuclei. **(A)** Violinplot of GRK5 intensity in 118 staining images. Here, the horizontal bar and the star (*) indicate nonparametric Wilcoxon's rank sum test between two sample groups. *p-value < 0.05. **(B)** Representative images of GRK5/cTnT/DAPI in each group.

heart cardiomyocytes (CM1, CM2, CM10, and CM6). Furthermore, transitions among these subpopulations (CM1, CM2, and CM10) were investigated, which had not been examined in our previous work (Nakada et al., 2022).

Cell-cycle activity was not substantially greater in CM1 cardiomyocytes than in cardiomyocytes from any other cluster except CM9. However, TBX5, TBX20, ERBB4, and GRK5, which have been linked to the proliferation of fetal and neonatal cardiomyocytes [TBX5 (Misra et al., 2014; Maitra et al., 2009), TBX20 (Xiang et al., 2016; Chakraborty and Yutzey, 2012),

ERBB4 (Bersell et al., 2009)] and cardiac hypertrophy [GRK5 (Gold et al., 2012; Traynham et al., 2015)], were upregulated in the CM1 cluster, as well as in Fetal cardiomyocytes. Bioinformatics analysis (**Figure 3B**) showed that TBX5 and TBX20 transcription factors amplified the expression of positive regulation of cell proliferation, cardiac muscle cell differentiation, canonical Wnt signaling pathway, and MAPK signaling pathway makers. Furthermore, ERBB4 and GRK5, which are surface receptor proteins, may activate ERBB, canonical Wnt, and MAPK signaling pathways at downstream.

Thus, AR on P1 may have primed cardiomyocytes for cell-cycle reactivation by maintaining the signaling mechanisms associated with these four molecules through at least P28. TBX5 and GRK5 were also highly expressed in CM2 cardiomyocytes, which comprised ~20% of cardiomyocytes in AR_{P1}-P28 hearts and a substantially greater proportion of cardiomyocytes in $AR_{P1}MI_{P28}$ than in MI_{P28} hearts during the first week after MI induction. This 7-day window coincided with the period when cycling cardiomyocytes were significantly more common in $AR_{P1}MI_{P28}$ hearts, and although we did not observe differences between cardiomyocyte clusters, injury groups, or time-points in the expression of downstream effectors of these signaling pathways, the results from bulk RNA sequencing assessments suggested that MI induction on P1 upregulated the expression of two molecules identified in our network analysis, MEF2C and NKX2-5, as well as TBX5 (Zhang et al., 2020). CM1 and CM2 cardiomyocytes also displayed substantial evidence of both glycolytic and βFAOX metabolism, while most of the other cardiomyocytes (i.e., CM10 and CM4) in $AR_{P1}MI_{P28}$ and MI_{P28} hearts on P30 and P35 relied primarily on glycolysis for energy production, but whether TBX5 or GRK5 activate βFAOX in neonatal cardiomyocytes, and if so, whether βFAOX upregulation improves the regenerative response to myocardial injury, has yet to be investigated.

The TBX5+/TBX20+/ERBB4+/GRK5+ cardiomyocyte subpopulation (CM1) and its markers were not detected in our previous report (Nakada et al., 2022). This subpopulation was detected in this study by adding new snRNA-seq data and applying the artificial-intelligence techniques. Pipelines to analyze snRNA-seq data include unsupervised clustering (Kiselev et al., 2019), which means the technical result depends on the data being used. Given the same data, it is known that different pipelines can lead to different results (Vieth et al., 2019). Therefore, whether the novel CM1 subpopulation appeared in this study primarily due to adding new data or using a different pipeline is yet to be investigated. From the computational perspective, compared to the Seurat-based pipeline (Hao et al., 2021) used in (Nakada et al., 2022), the artificial-intelligence-based pipeline gives the dimensional reduction advantage. Before clustering, artificial intelligence (autoencoder) reduced the high-dimensional snRNA-seq data into 10 dimensions; meanwhile, Seurat, applying Principal Component Analysis still reduced into 2,000 dimensions. Notably, both of them use the same principle to compute lower-number dimensions: when using the lower-number dimensions to reconstruct the data, the difference between the reconstructed data and original high-dimensional data is minimized. In computing, given the similar optimization criteria, using a lower number of dimensions is better to "curse of dimensionality" issue (Trunk, 1979): the calculation is much less accurate if too many data dimensions are used.

As support of our finding, the roles of TBX5, TBX20, and ERBB4 in promoting cardiomyocyte proliferation had been reported in other studies. In addition, we confirmed the evaluated protein levels of ERBB4 and GRK5 in regenerative heart tissue. Therefore, immunofluorescence analysis was performed to quantify GRK5 expression within cardiomyocytes, where we confirmed the signal intensity of the cTnT region/GRK5 in AR_{P1}-P28 and Fetal groups were higher. Overall, our results suggest that GRK5 may contribute to cardiomyocyte proliferation, whose mechanisms are yet to be further confirmed in future studies.

In conclusion, the results presented here identified a cluster of cardiomyocytes, CM1, in neonatal pig hearts that appeared to be generated in response to AR injury on P1, which in turn, results in CMs cell-cycle activation, and has improved recovery from subsequent AMI on P28. Although CM1 cardiomyocytes did not appear to be substantially more proliferative than cardiomyocytes from other clusters that were present in injured and uninjured hearts through P42, they may have been primed for cell-cycle reactivation by the upregulation of regulatory molecules that contribute to cardiomyocyte proliferation (TBX5, TBX20, and ERBB4) and cardiac hypertrophy (GRK5). Collectively, these observations support future investigations of the roles of these four regulatory molecules in cardiomyocyte proliferation and myocardial repair.

MATERIALS AND METHODS

Animals

All experimental protocols were approved by The Institutional Animal Care and Use Committee (IACUC) of the University of Alabama, Birmingham, and performed in accordance with the National Institutes of Health Guide for the Care and Use of Laboratory Animals (NIH publication No 85-23). Pigs were purchased from Prestage Farm, Inc. (West Point, MS) and cared for as described previously (Zhao et al., 2020). Pigs were housed in an incubator at ~85°F with room air through P14 and then transferred to the normal room and grown under regular pig feeding and ~72°F temperature. Animals were fed bovine colostrum every 4 h for the first 2 days of life, a 1:1 mixture of colostrum: sow's milk on day 3 of life, and sow's milk thereafter. Supplemental iron was provided on day 7.

Aapical Resection and Myocardial Infarction–Induction Surgery

Pigs were anesthetized with isoflurane and placed on a heating pad in a dorsal recumbent position; then, a median sternotomy was performed to expose the heart. AR was performed on P1 by removing 4–5 mm of tissue from the ventricular apex, and MI was induced on P28 by permanently occluding the left-anterior descending coronary artery with a suture; then, the sternum was reapproximated, and the chest was closed in layers, and the air was evacuated from the mediastinum.

Nuclei Isolation

Tissues were cut while submerged in cold phosphate-buffered saline (PBS) or UW solution, washed to remove blood, and transferred into 1 ml lysis buffer (10 mM Tris-HCl, 10 mM NaCl, 3 mM $MgCl_2$, 0.1% Nonidet™ P40 Substitute, and 50 U/ml RNase inhibitor in DEPC-treated water), cut into smaller pieces, and aspirated with the lysis buffer into a 50-ml tube; then, 10 ml of lysis buffer was added,

the tissues were ground for 20–30 s, and more lysis buffer was added. The mixture was placed on ice for 10 min, filtered with 100-μm and 70-μm strainers, and centrifuged for 5 min at 700 rcf and 4°C; then, the supernatant was removed, and the pellet was resuspended in 10 ml nuclei wash and resuspension buffer [1 × PBS, 1.0% bovine serum albumin (BSA), and 50 U/ml RNase inhibitor]. The suspension was passed through a 40-μm strainer, and the nuclei were centrifuged again for 5 min at 700 rcf and 4°C; then, the supernatant was removed, the pellet was resuspended in 1 ml nuclei wash, and resuspension buffer and the nuclei were centrifuged a third time for 5 min at 700 rcf and 4°C. The supernatant was removed; then, the pellet was resuspended in 5 ml sucrose cushion buffer I (2.7 ml Nuclei PURE 2M Sucrose Cushion Solution and 300 μl Nuclei PURE Sucrose Cushion Buffer) and mixed with 10 ml sucrose buffer. The mixture was layered over 5 ml of sucrose cushion buffer in a second Eppendorf tube and then centrifuged for 60 min at 13,000 g and 4°C. All but 100 μl of the supernatant was removed, the nuclei were resuspended in nuclei wash and resuspension buffer, and the solution was passed through a 40-μm strainer; then, the nuclei concentration was determined with a cell counter or hemocytometer and adjusted to 1,000 nuclei/μl. The nuclei were placed on ice, stained with propidium iodide for 5 min, and then immediately processed *via* the 10× Genomics® Single-Cell Protocol.

Pre-Processing of snRNA-Seq Data

Sample demultiplexing, barcode processing, and gene counting were performed with Cell Ranger Single-Cell Software v.3.10 (https://support.10xgenomics.com/single-cell-gene expression/ software). Reads were aligned to the Sscrofa11.1 pre-mRNA reference genome (Pig, 2021), and the pre-mRNA portion of the reference genome was extracted for single-nuclei UMI mapping with Cell Ranger mkref pre-mRNA. Only confidently mapped reads with valid barcodes and UMIs were used to generate the gene-barcode matrix. Cross-sample integration and quality-control were performed with the Seurat R package. Doublets were identified by using Seurat's standard pipeline (https://satijalab.org/seurat/v3.2/pbmc3k_tutorial.html), and barcodes were removed if they had fewer than 500 UMIs, more than 30,000 UMIs, or >5% mitochondrial UMIs. Nuclei were removed if they had <200 detected genes or if >25% of the transcripts were from mitochondrial genes. Mitochondrial genes and other transcript identifiers were removed without mapping to the official gene symbols from later analyses. Data were normalized as directed in the online Seurat tutorial (https:// satijalab.org/seurat/v3.2/pbmc3k_tutorial.html); total expression was multiplied by a factor of 10,000 and then log-transformed. Variations in the number of genes and UMIs detected per cell were accommodated by normalizing the scaled expression matrix *via* the ScaleData function with vars. to. regress set to nUMI and nGenes. Normalization returned two gene-cell matrices: the first was in log scale, and the second was the adjusted gene-cell count.

Autoencoder

An autoencoder (Kramer, 1991) is a deep-neural-network artificial-intelligence technique used to synthesize (Sheikh et al., 2021), denoise (Eraslan et al., 2019), or translate (Cho et al., 2014) data. A data-synthesis autoencoder has at least three layers: an input layer, which consists of the original high-dimensional dataset, a central embedded layer with fewer dimensions (typically 10–20), and a synthetic output layer whose dimensionality is equivalent to the input layer. The autoencoding procedure is performed by encoding the input layer into the embedded layer, decoding the embedded layer into the output layer, and then evaluating the extent of similarity between the input and output layers. When the output layer matches the input layer with maximum fidelity, the embedded layer is considered an accurate low-dimensional representation of the input data. Notably, the immense datasets generated *via* single-cell and single-nucleus genomic analyses can require a prohibitively large amount of computer memory, so a number of recent studies (Wang and Gu, 2018; Eraslan et al., 2019; Tran et al., 2021) have reduced the dimensionality of the input data before the autoencoding procedure is initiated. However, the transcriptional heterogeneity of cardiac cells is exceptionally high (Nahrendorf and Swirski, 2013; Vidal et al., 2019; Tsedeke et al., 2021) and likely to be exacerbated by the physiological changes that occur in response to AR surgery and MI induction. Thus, since any attempt to reduce the dimensionality of the input data before autoencoding could mask this complexity, the input layer used for the studies reported here included the complete list of 14,753 genes (i.e., 14,753 dimensions) with at least 1,000 UMIs in our dataset.

Autoencoding was performed in Matlab (trainAutoencoder, 2021) with self-built models; the architecture of the autoencoder was restricted to three layers, and the embedded layer contained 10 dimensions (**Supplementary Figure S5**). Optimization was achieved by minimizing the function

$$E = \frac{1}{N} \sum_{i}^{N} \sum_{j}^{N} \left(x_i - y_j \right)^2 + 0.001 ||W||^2 + Q, \qquad (1)$$

where N denotes the number of data points, x_i denotes an arbitrary input data point, y_j denotes an arbitrary synthetic data point, $||W||^2$ represents the regularization of autoencoder weights, and Q represents the sparsity parameters (trainAutoencoder, 2021).

Data Visualization and Clustering

After autoencoding, the embedded data was reduced from 10 to 2 dimensions *via* Uniform Manifold Approximation (UMAP) toolkit (McInnes et al., 2018; Meehan, 2021), and clustering was performed with the UMAP toolkit density-based clustering (dbscan) algorithm (McInnes et al., 2018; Meehan, 2021; Ester et al., 1996; dbscan, 2021); the 30th-distance graph (minpts, or n_neighbors = 30) was plotted, and epsilon (or min_dist) was set to 0.3 (Meehan, 2021). Cardiomyocytes were identified *via* expression of the cardiomyocyte-specific markers ACTC1 and MYH7 (**Supplementary Note S1**); then, the cardiomyocyte data was extracted, and the autoencoding, visualization (UMAP), and clustering (dbscan) procedures were repeated. The assignment of cardiomyocyte clusters (CM1–CM10) was based on visualization and the distribution

of cardiomyocytes in each subgroup (**Supplementary Note S2**), and marker genes for each cluster were identified according to the following criteria: 1) a cluster *p*-value [Fisher's Exact test (Fisher, 1922)] of less than 10^{-6}, 2) expression by at least 50% of cells in the cluster, and 3) mean abundance at least 1.3-fold greater among cells in the cluster than in the total cardiomyocyte population.

Algorithm Quality Analysis

After being clustered UMAP toolkit (McInnes et al., 2018; Meehan, 2021), the snRNA-seq clusters were validated and manually adjusted (if needed) by the cell-groups' localization in each sample group. In **Supplementary Figure S6**, the cell-landscape in each group revealed specific regions that were significantly enriched by or were exclusive for AR_{P_1}-P28, AR_{P_1}-MI_{P28}-P30/P35, injured P56, Fetal, CTL-P1, and CTL-P56 cardiomyocytes. There were regions mapped to CM1, CM2, CM6, CM8, CM7, and CM5/CM9, respectively (**Supplementary Figure S7B**). This result explained and justified our clustering parameter settings. This strategy was also used in other single-cell analyses, such as in (Cui et al., 2020).

In addition to the (minpts = 30, epsilon = 0.3) parameter, combination was manually examined according to the instruction in (DBSCAN, 2022). Briefly, for each cell-point, the distances between the point and 30 other nearest points were calculated; then, among these 30 distances, the largest distance was selected as "30th nearest distance." Repeating this process for all cell-points, the list of "30th nearest distances" for all cell-points between 0.1 and 1.2 was obtained, as displayed on the *y*-axis of **Supplementary Figure S7A**. At any threshold *t* on the *y*-axis, the number of cell-points *m* having "30th nearest distances" < *t* was counted, and the (*m*, *t*) dot was drawn in **Supplementary Figure S7A**. Repeating the (*m*, *t*) process as t increased from 0.1 to 1.2 and connecting these (*m*, *t*) dots, the "30th nearest distance curve" was completed as shown in **Supplementary Figure S7A**. On "30th nearest distance curve," "the elbow" (*m*, *t*) point corresponds to $t \approx 0.3$. This result further justified our decision to use the parameter combination (minpts = 30, epsilon = 0.3).

On the other hand, we manually examined the clustering result when slightly changing minpts = 25, 30, and 35, and epsilon = 0.25, 0.3, and 0.35 with the Matlab UMAP toolkit (Meehan, 2021). Changing these parameters may yield different numbers of clusters. However, using the cell groups localization to manually merge the smaller clusters, we reconstructed a nearly identical cluster landscape to what was obtained using (minpts = 30, epsilon = 0.3) parameter combination. This result justified the robustness of the cluster algorithm and toolkit.

We also justified the criteria by the number of marker genes and their percentage over the entire pig genome, which consists of 25,800 genes. **Table 1** shows that the number of genes passing two criteria (to qualify as cluster markers) is always less than 2% of the genome. Furthermore, we combined the marker genes from all 10 CM clusters, yielding 1,069 marker genes. Then, for the gene, we counted in how many CM clusters such that the gene was a marker. There were 636 genes (59.50%) that were markers of only one CM cluster; 312 genes (29.19%) that were markers of two CM clusters; 98 genes (9.17%) that were markers of three clusters; 21 genes (1.96%) that were markers of four clusters; and only 2 genes (0.19%) that were markers of five clusters. There were no genes that were markers of six or more clusters. Therefore, the criteria to select cluster markers ensured that the markers were very specific for the cluster.

DAVID Functional Annotation

Cluster-specific markers were analyzed with the DAVID functional annotation tool (Huang et al., 2009). Only terms present in the manually annotated Gene Ontology (Huntley et al., 2015), KEGG (Kanehisa et al., 2017), and Reactome (Jassal et al., 2020) categories were selected. To avoid false discoveries caused by multi-hypothesis testing, the selected results were required to have $p < 0.01$ or Benjamini-adjusted (Li and Barber, 2019) $p < 0.05$.

Sparse Modeling

Because the markers selected *via* our DAVID functional analysis were restricted to those present in manually annotated databases, complementary analyses were conducted without the selected markers *via* Sparse modeling. Briefly, for each cell expression data vector **x**, the sparse model estimates a score *y* from the linear formula

$$y = \mathbf{w}\mathbf{x} + b. \tag{2}$$

Only genes known to be associated with the ontology or pathway being evaluated were considered [e.g., G2M scores were calculated using only genes with known G2M ontology (Mouse Genome Informatics, 2021a)], and higher *y* implied that the cell was more likely to undergo the corresponding process. Sparse analysis also requires predefined "positive" ($y = 1$) and "negative" ($y = -1$) cell groups (**Table 2**); thus, cell-cycle gene scores (for example) were calculated with Fetal and CTL-P56 cardiomyocytes as the positive and negative groups, respectively, because Fetal cardiomyocytes are highly proliferative, whereas CTL-P56 cardiomyocytes have exited the cell cycle.

The **w** and *b* (bias) parameters of **Eq. 1** were computed by minimizing

$$\frac{1}{2}|\mathbf{w}| + C\sum_{\forall i} \epsilon_i. \tag{3}$$

Subject to

$$\begin{cases} y_i\left(\mathbf{w}\mathbf{x}_i + b\right) + \epsilon_i \geq 1 \\ \epsilon_i \geq 0 \end{cases} \forall i, \tag{4}$$

where *i* denotes an arbitrary "positive" or "negative" cell and the "margins" of the model are defined by $\mathbf{w}\mathbf{x} + b = 1$ and $\mathbf{w}\mathbf{x} + b = -1$. A good model will have a very high percentage (e.g., 90%) of cells with $\epsilon_i = 0$.

Scores were computed for all cells; then, cells with $y > 1$ (from **Eq. 2**) were categorized "high," cells with $y < -1$ were categorized "low," and cells with $-1 \leq y \leq 1$ were categorized "middle." Thus, a "high" G2M categorization (for example) indicated that the cell was more Fetal- than CTL-P56–like and, consequently, more likely to execute the G2M phase transition. Significance was evaluated by calculating the OR and *p*-value [Fisher's Exact

TABLE 1 | Number and proportion of genes passing the cluster marker criteria: expressing in more than 50% of the cluster cell and having at least 1.3-fold abundance.

Cardiomyocyte (CM) cluster	Criterion 1: genes expressed in more than 50% of the cluster cell		Criterion 2: expression is 1.3-fold higher (than other clusters)		Criterion 1 and Criterion 2	
	#Genes	%Genome (%)	#Genes	%Genome (%)	#Genes	%Genome (%)
CM1	881	3.40	2,263	8.74	126	0.49
CM2	964	3.73	1,221	4.72	74	0.29
CM3	1,541	5.95	5,610	21.68	419	1.62
CM4	1,435	5.54	9,670	37.36	274	1.06
CM5	1,090	4.21	1,935	7.48	109	0.42
CM6	1,073	4.15	1,209	4.67	89	0.34
CM7	862	3.33	4,438	17.15	102	0.39
CM8	807	3.12	6,544	25.29	206	0.80
CM9	855	3.30	1,277	4.93	241	0.93
CM10	912	3.52	1,391	5.38	8	0.03

TABLE 2 | Positive and negative cell groups for Sparse analysis.

Analysis	Positive cell group	Negative cell group
Cell cycle phases (Cui et al., 2020) (G01, G1S, S, G2M, M, and MG1)	Fetal cardiomyocytes	Naïve-P56 cardiomyocytes
Cardiomyocyte adrenergic signaling (KEGG: Adrenergic signaling in cardiomyocytes, 2021)	CM9*	CM8*
Cardiac muscle contraction (Mouse Genome Informatics, 2021b)	CM9	CM8
Cardiac muscle cell development (Gene Ontology: Cardiac Muscle Cell Development, 2021)	CM8	CM9
Positive regulation of cardiac muscle cell proliferation (Mouse Genome Informatics, 2021c)	CM8	CM9
Positive regulation of cardiac muscle tissue growth (Mouse Genome Informatics, 2021d)	CM8	CM9
Glycolysis (Glycolysis, 2021)	CM8	CM9
Beta fatty acid oxidation (Mouse Genomic Informatics, 2021b)	CM9	CM8

The CM8 and CM9 clusters were exclusively associated with cardiomyocytes from Fetal and CTL-P56 hearts, respectively.

Test (Fisher, 1922)] for the proportion of "high" cells in each group, and $p < 10^{-6}$ was considered significant.

Network Analysis for TBX5, TBX20, ERBB4, and GRK5

Genes targeted by TBX5 and TBX20 were identified in the TRRUST v2 database (Han et al., 2018), and genes that function downstream of ERBB4 and GRK5 were identified in the STRING v11.5 (Szklarczyk et al., 2021) database. Identified genes were combined into a single set and analyzed *via* DAVID (Huang et al., 2009).

Semisupervised Learning Analysis

The semisupervised learning model was built with the Matlab "fitsemiself" function (Matlab, 2021); CM2 cardiomyocytes from $AR_{P1}MI_{P28}$-P30 hearts were used as the class 1 cells, and CM10 cardiomyocytes from $AR_{P1}MI_{P28}$-P30 hearts were used as the class 2 cells. For each CM1 cardiomyocyte from AR_{P1}-P28 hearts, the model calculated a rescaled score between 0 and 1; cells with scores approaching 0 or 1 were categorized an CM1a (i.e., CM2-like) or CM1b (i.e., CM10-like), respectively.

Cardiomyocyte Pairwise Cluster Similarity Analysis

The similarity between two cardiomyocyte clusters, denoted as CM*x* and CM*y*, was calculated by averaging 1,000 similarity

scores between 1,000 randomly selected cells in CM*x* and 1,000 randomly selected cells in CM*y*. The cell-cell similarity was computed using the following equation

$$\sqrt{\sum_{j=1}^{m} \left(sign(x_j) - sign(y_j)\right)^2}. \quad (5)$$

Here, x, y represents the gene expression of a randomly selected cell in CM*x* and CM*y*, correspondingly, *m* is the number of genes, and *j* represents the gene index. The "sign" function converts the expression into the binary (0 or 1) format, whereas $x(i) = 1$ means the *i*th gene expresses in cell *x*, while $x(i) = 0$ means the *i*th gene does not express in cell *x*.

Bulk-RNA Sequencing Analysis

The regenerative pig heart bulk-RNA sequencing data was obtained from the Gene Expression Omnibus database, accession number GSE144883, and processed according to (Zhang et al., 2020). Briefly, the paired-end fastq files were trimmed using TrimGalore (Krueger, 2019), then mapped to Ensembl Sscrofa11.1 pre-mRNA reference pig genome (Pig, 2021) using STAR v.2.5.2 (Dobin et al., 2013), then the transcripts for each gene (raw expression) were counted using HtSeq v.0.6.1 (Anders et al., 2015). Then, the raw expression matrix was normalized using Deseq2 (Love et al., 2014). Expressions between 3 regenerative hearts, which underwent

myocardial infraction on postnatal day 1, and 3 naïve hearts were compared, and error-bar plotted.

Western Blotting

The Western blotting protocol, which quantified protein expression of ERBB4, GRK5, and GAPDH was completed according to our previous publication (Zhang et al., 2020). Tissues were lysed in PIPA Lysis and Extraction Buffer (Thermo Scientific, 89,901) with Halt™ Protease and phosphatase Single-Use Inhibitor Cocktail (Thermo Scientific, 78,442); then, the lysates were denatured at 95°C for 6°min, separated in a 4%–20% precast gel (Bio-rad, 4568093), and transferred onto a PVDF membrane (Bio-rad, 1704156). The membrane was incubated with 5% nonfat dry milk (Bio-rad, 1706404) for 30 min, with primary antibodies at 4°C overnight, and then with horseradish-peroxidase (HRP)–conjugated secondary antibodies for 30 min. Protein bands were detected with the chemiluminescent HRP substrate (Millipore, WBKLS0500) in a ChemiDocTM Imaging System (Bio-rad).

We performed western blotting in three Fetal, AR_{P1}-P28, and three CTL-P28 samples. In each sample, protein expression was scaled according to GAPDH to confirm equal loading. Then, statistical comparison and testing were performed using the nonparametric test, according to (Zhao et al., 2021), due to the small sample size. A p-value < 0.05 indicates statistical significance.

Histology

The immunofluorescence analyses were conducted similar to our previous work in Nakada et al. (2022). Hearts were cut into transverse blocks (thickness: 1 cm), and myocardium from the anterior-apical zone (AAZ) were either snap-frozen with liquid nitrogen or processed with 10% formalin fixation and dehydration with 10%- 30% sucrose overnight. Samples were cut into transverse sections (thickness: 10 μm) and stained with antibodies against GRK5 (1:100, rabbit polyclonal, Invitrogen, PA5-106484) and cardiac troponin T (1:50, mouse monoclonal, R&D System, MAB 1874) overnight was followed by blocking in Ultravision Protein Block (Epredia, TA125PBQ) for 7 min. For each group, at least 10 sections of border zone myocardium were analyzed, and a total of 118 images from subendomyocardium, and subepimyocardium were counted. Anti-rabbit and anti-mouse secondary antibodies conjugated to Alexa Fluor 555 and 488 were used for visualization by microscopy. DAPI was used for nuclei staining.

To quantify the GRK5 light intensity at the cardiac troponin T area, the following image processing pipeline was performed (**Supplementary Figure S8**). First, each staining image (including GRK5 and cTnT) was represented in Matlab by the Red-Green-Blue channel matrices. Here, in the red-channel matrix, the number between 0 (totally no red) and 255 (maximum red) represents the red color intensity, so does in the green-channel and blue-channel. Then, image segmentation was performed in the cTnT image green channel: green >10 implied the "foreground" (with cTnT) areas, while green <10 implied the "background" (**Supplementary Figure S8B**). Then, the "segmented" image

was mapped to the GRK5 red channel, where this channel was adjusted by subtracting with the background red channel baseline (**Supplementary Figure S8C**). GRK5 intensity was calculated by the mean of the foreground red-channel (adjusted) number, which was between 0 and 255. Since only the overlap between GRK5 (red) and cTnT (green) areas was used in GRK5 intensity calculation, this approach was better to quantify GRK5 in cardiomyocytes. Then, statistical comparison among the groups was completed using nonparametric Wilcoxon's Rank sum test. A p-value < 0.05 indicates statistical significance.

The background red channel baseline was determined in each GRK5 image based on the distribution (histogram) of the background red channel numbers. Manually investigating all 118 images, we noted three background scenarios. First, when the background numbers follow a power-law distribution, where most of the numbers were around 0 and much fewer nonzero backgrounds, the baseline was set to 0, implying no background adjustment was needed. Second, when the background number appeared to be in a homogeneous distribution, which was either normal, uniform, or power-law, the baseline was set to be the average of the background number. Third, when the background numbers formed two or more distributions, we separated these distributions and set the baseline to be the average of the largest (most right) distribution.

DATA AVAILABILITY STATEMENT

The datasets presented in this study can be found in online repositories. The names of the repository/repositories and accession number(s) can be found below: https://www.ncbi.nlm.nih.gov/geo/, GSE185289.

ETHICS STATEMENT

The animal study was reviewed and all experimental protocol were approved by The Institutional Animal Care and Use Committee (IACUC) of the University of Alabama, Birmingham, and performed in accordance with the National Institutes of Health Guide for the Care and Use of Laboratory Animals (NIH publication No 85-23).

AUTHOR CONTRIBUTIONS

TN, YW, YN, YZ, and JZ conducted the experiments and analyzed the data. TN, YW, YN, YZ, and JZ designed the study and wrote the manuscript.

FUNDING

ACKNOWLEDGMENTS

SUPPLEMENTARY MATERIAL

The Supplementary Material for this article can be found online at: https://www.frontiersin.org/articles/10.3389/fbioe.2022.914450/full#supplementary-material

Supplementary Figure S1 | Cluster analysis identified six different cell types in hearts from Fetal, CTL, ARP1, MIP28, and ARP1MIP28 animals. snRNA-seq data for all cells from each experimental group and time point were processed via cluster analysis and visualized *via* UMAP. **(A)** Results are displayed for each experimental group and time point. **(B)** Results are displayed for each of six different cell types (cardiomyocytes, fibroblasts, immune cells, smooth muscle cells, endothelial cells, and cardiomyocyte/skeletal-like muscle cells). **(C)** The expression of cell-type–specific genes that were explicitly associated with each cluster is displayed as a heat map (cardiomyocytes: myosin heavy chain 7 [MYH7], Actin Alpha Cardiac Muscle 1 [ACTC1]; fibroblasts: Collagen Type I Alpha 1 [COL1A1], Collagen Type I Alpha 2 [COL1A2]; immune cells: Bridging Integrator 2 [BIN2], gamma-interferon-inducible lysosomal thiol reductase [IFI30]; smooth-muscle cells: Actin Alpha 2 [ACTA2], Myosin Heavy Chain 11 [MYH11]; endothelial cells: Platelet And Endothelial Cell Adhesion Molecule 1 [PECAM1], Kinase Insert Domain Receptor [KDR]; skeletal-muscle cells: Myosin Light Chain Kinase 2 [MYLK2], Nebulin [NEB]).

Supplementary Figure S2 | Upregulation of pluripotent genes in CM4 cardiomyocyte. **(A)** Regulators in KEGG signaling pathways regulating pluripotency of stem cells, including AKT Serine/Threonine Kinase 3 [AKT3], Janus Kinase 1 [JAK1], Janus Kinase 2 [JAK2], Jumonji And AT-Rich Interaction Domain Containing 2 [JARID2], Mitogen-Activated Protein Kinase 1 [MAPK1], Phosphatidylinositol-4,5-Bisphosphate 3-Kinase Catalytic Subunit Alpha [PIK3CA], Signal Transducer And Activator Of Transcription 3 [STAT3], and Zinc Finger Homeobox 3 [ZFHX3]. **(B)** Genes responsible for stem cell population maintenance according to Gene Ontology annotation, including APC Regulator Of WNT Signaling Pathway [APC], AT-Rich Interaction Domain 1A [ARID1A], DEAD-Box Helicase 6 [DDX6], Forkhead Box O1 [FOXO1], Nuclear Receptor Coactivator 3 [NCOA3], Recombination Signal Binding Protein For Immunoglobulin Kappa J Region [RBPJ], SWI/SNF Related, Matrix Associated, Actin Dependent Regulator Of Chromatin, Subfamily A, Member 2 [SMARCA2], SWI/SNF Related, Matrix Associated, Actin Dependent Regulator Of Chromatin Subfamily C Member 1 [SMARCC1], SS18 Subunit Of BAF Chromatin Remodeling Complex [SS18], and Transcription Factor 7 Like 2 [TCF7L2]. The expression was normalized according to the Seurat pipeline: the expression matrix was scaled by the ScaleData function with

vars.to.regress set to nUMI and nGenes; then, the scaled expression was log-normalized.

Supplementary Figure S3 | Pairwise similarity among cardiomyocyte CM1-CM10 clusters. The cluster similarity was calculated by averaging 1000 cell-cell similarity scores, whereas the cells were randomly selected in each cluster. The left-side bar maps the color to the similarity score, where more red implies a higher degree of similarity.

Supplementary Figure S4 | Cardiomyocyte cell-cycle gene expression tended to be greater in ARP1, MIP28, and ARP1MIP28 hearts from P30-P42 than in CTL hearts on P28. Sparse analysis was conducted for the expression of genes associated with the G01, G1S, S, G2M, M, and MG1 phases of the cell cycle, and the proportion of cardiomyocytes with high levels of expression was calculated for each experimental group and time point.

Supplementary Figure S5 | Schematic representation of the autoencoder model. The autoencoder constructed for the analyses presented here consisted of an input layer, a central embedded layer, and an output layer. The input layer included 14,753 genes and was alternately encoded into a 10-dimensional embedded layer and then decoded into a synthetic output layer comprising the same genes present in the input layer. The accuracy of the embedded layer was optimized by minimizing the indicated function.

Supplementary Figure S6 | Cell localization in each sample group's cardiomyocyte. Here, the umap plots for all cells were drawn, and the cells were colored based on: whether the cell belongs to a specific sample group (red) or the cell belongs to other sample groups. The order, from left to right and from top to bottom, is: CTL-P28, ARP1-P28, MIP28-P30, ARP1-MIP28-P30, MIP28-P35, ARP1-MIP28-P35, MIP28-P42, ARP1-MIP28-P42, MIP28-P56, ARP1-MIP28-P56, Fetal, CTL-P1, CTL-P56, and ARP1-P56.

Supplementary Figure S7 | Algorithm-quality analysis confirming that the parameter combination (minpts = 30, epsilon = 0.3) in UMAP toolkit is robust. **(A)** The 30th-nearest-distance plot show that the "elbow" point, which determine the optimal epsilon parameter (according to [92]) is approximately 0.3. **(B)** The preserved cluster landscape draw by slightly changing the parameters: minpts = 25, 30, 35, and epsilon = 0.25, 0.3, 0.35.

Supplementary Figure S8 | Summary of Immunofluorescence image processing. **(A)** The staining images (red: GRK5, green: cardiac troponin cTnT) were represented in red(R)/green(G)/blue(B) channel matrices. **(B)** Image segmentation was performed on the blue channel, which divided the image into the background (no cTnT, black) and foreground (with cTnT, white). **(C)** The red channel background distribution was plotted to determine a background baseline. This distribution had three scenarios. Top: near-zero distribution, the baseline (indicated by the dashed line) = 0; middle: one distribution form, the baseline = average of red channel background; bottom: the two or more distributions appeared, then the baseline = average of the largest (most right) distribution. **(D)** the red channel (GRK5) was adjusted by subtracting this channel from the background baseline.

REFERENCES

Anders, S., Pyl, P. T., and Huber, W. (2015). HTSeq--a Python Framework to Work with High-Throughput Sequencing Data. *Bioinformatics* 31, 166–169. doi:10.1093/bioinformatics/btu638

Angelini, A., Saha, P. K., Jain, A., Jung, S. Y., Mynatt, R. L., Pi, X., et al. (2021). PHDs/CPT1B/VDAC1 axis Regulates Long-Chain Fatty Acid Oxidation in Cardiomyocytes. *Cell Rep.* 37, 109767. doi:10.1016/j.celrep.2021.109767

Bersell, K., Arab, S., Haring, B., and Kühn, B. (2009). Neuregulin1/ErbB4 Signaling Induces Cardiomyocyte Proliferation and Repair of Heart Injury. *Cell* 138, 257–270. doi:10.1016/j.cell.2009.04.060

Bi, J., Bennett, K., Embrechts, M., Breneman, C., and Song, M. (2003). Dimensionality Reduction via Sparse Support Vector Machines. *J. Mach. Learn. Res.* 3, 1229–1243.

Chakraborty, S., and Yutzey, K. E. (2012). Tbx20 Regulation of Cardiac Cell Proliferation and Lineage Specialization during Embryonic and Fetal Development *In Vivo*. *Dev. Biol.* 363, 234–246. doi:10.1016/j.ydbio.2011.12.034

Chen, M., Philipp, M., Wang, J., Premont, R. T., Garrison, T. R., Caron, M. G., et al. (2009). G Protein-Coupled Receptor Kinases Phosphorylate LRP6 in the Wnt Pathway. *J. Biol. Chem.* 284, 35040–35048. doi:10.1074/jbc.m109.047456

Chkifa, A., Cohen, A., and Schwab, C. (2015). Breaking the Curse of Dimensionality in Sparse Polynomial Approximation of Parametric PDEs. *J. de Mathématiques Pures Appliquées* 103, 400–428. doi:10.1016/j.matpur.2014.04.009

Cho, K., Van Merriënboer, B., Bahdanau, D., and Bengio, Y. (2014). On the Properties of Neural Machine Translation: Encoder-Decoder Approaches. *arXiv Prepr. arXiv* 1409, 1259.

Clément, S., Chaponnier, C., and Gabbiani, G. (1999). A Subpopulation of Cardiomyocytes Expressing Alpha-Skeletal Actin Is Identified by a Specific Polyclonal Antibody. *Circ. Res.* 85, e51–8. doi:10.1161/01.res.85.10.e51

Cui, M., Wang, Z., Chen, K., Shah, A. M., Tan, W., Duan, L., et al. (2020). Dynamic Transcriptional Responses to Injury of Regenerative and Non-regenerative Cardiomyocytes Revealed by Single-Nucleus RNA Sequencing. *Dev. Cell* 53, 102–116. doi:10.1016/j.devcel.2020.02.019

dbscan (2021). *Dbscan*. Natick, Massachusetts: MathWorks, Inc. https://www.mathworks.com/help/stats/dbscan.html

DBSCAN (2022). *Introduction to DBSCAN*. Natick, Massachusetts: Mathworks, Inc. https://www.mathworks.com/help/stats/dbscan-clustering.html

de Lucia, C., Grisanti, L. A., Borghetti, G., Piedepalumbo, M., Ibetti, J., Lucchese, A. M., et al. (2022). G Protein-Coupled Receptor Kinase 5 (GRK5) Contributes to

Impaired Cardiac Function and Immune Cell Recruitment in Post-ischemic Heart Failure. *Cardiovasc Res.* 118, 169–183. doi:10.1093/cvr/cvab044

Dobin, A., Davis, C. A., Schlesinger, F., Drenkow, J., Zaleski, C., Jha, S., et al. (2013). STAR: Ultrafast Universal RNA-Seq Aligner. *Bioinformatics* 29, 15–21. doi:10. 1093/bioinformatics/bts635

Eraslan, G., Simon, L. M., Mircea, M., Mueller, N. S., and Theis, F. J. (2019). Single-cell RNA-Seq Denoising Using a Deep Count Autoencoder. *Nat. Commun.* 10, 390. doi:10.1038/s41467-018-07931-2

Ester, M., Kriegel, H.-P., Sander, J., and Xu, X. (1996). A Density-Based Algorithm for Discovering Clusters in Large Spatial Databases with Noise. KDD'96. *Proc. Second Int. Conf. Knowl. Discov. Data Min.*, 226–231.

Fan, Y., Ho, B. X., Pang, J. K. S., Pek, N. M. Q., Hor, J. H., Ng, S.-Y., et al. (2018). Wnt/β-catenin-mediated Signaling Re-activates Proliferation of Matured Cardiomyocytes. *Stem Cell Res. Ther.* 9, 338. doi:10.1186/s13287-018-1086-8

Fisher, R. A. (1922). On the Interpretation of χ 2 from Contingency Tables, and the Calculation of P. *J. R. Stat. Soc.* 85, 87–94. doi:10.2307/2340521

Gene Ontology: Cardiac Muscle Cell Development (2021). *Gene Ontology: Cardiac Muscle Cell Development.* http://www.informatics.jax.org/vocab/gene_ontology/GO:0055013

Glycolysis.(2021). *Gluconeogenesis - Sus scrofa Pig.* https://www.genome.jp/kegg-bin/show_pathway?ssc00010

Gold, J. I., Gao, E., Shang, X., Premont, R. T., and Koch, W. J. (2012). Determining the Absolute Requirement of G Protein-Coupled Receptor Kinase 5 for Pathological Cardiac Hypertrophy. *Circ. Res.* 111, 1048–1053. doi:10.1161/circresaha.112.273367

Guo, Y., and Pu, W. T. (2020). Cardiomyocyte Maturation. *Circ. Res.* 126, 1086–1106. doi:10.1161/circresaha.119.315862

Hailstones, D. L., and Gunning, P. W. (1990). Characterization of Human Myosin Light Chains 1sa and 3nm: Implications for Isoform Evolution and Function. *Mol. Cell Biol.* 10, 1095–1104. doi:10.1128/mcb.10.3.1095-1104.1990

Han, H., Cho, J.-W., Lee, S., Yun, A., Kim, H., Bae, D., et al. (2018). TRRUST V2: an Expanded Reference Database of Human and Mouse Transcriptional Regulatory Interactions. *Nucleic Acids Res.* 46, D380–D386. doi:10.1093/nar/gkx1013

Hao, Y., Hao, S., Andersen-Nissen, E., Mauck, W. M., 3rd, Zheng, S., Butler, A., et al. (2021). Integrated Analysis of Multimodal Single-Cell Data. *Cell* 184, 3573–3587. doi:10.1016/j.cell.2021.04.048

Hinson, J. T., Chopra, A., Lowe, A., Sheng, C. C., Gupta, R. M., Kuppusamy, R., et al. (2016). Integrative Analysis of PRKAG2 Cardiomyopathy iPS and Microtissue Models Identifies AMPK as a Regulator of Metabolism, Survival, and Fibrosis. *Cell Rep.* 17, 3292–3304. doi:10.1016/j.celrep.2016.11.066

Huang, D. W., Sherman, B. T., and Lempicki, R. A. (2009). Systematic and Integrative Analysis of Large Gene Lists Using DAVID Bioinformatics Resources. *Nat. Protoc.* 4, 44–57. doi:10.1038/nprot.2008.211

Huang, K., Zheng, D., Sun, J., Hotta, Y., Fujimoto, K., and Naoi, S. (2010). Sparse Learning for Support Vector Classification. *Pattern Recognit. Lett.* 31, 1944–1951. doi:10.1016/j.patrec.2010.06.017

Huntley, R. P., Sawford, T., Mutowo-Meullenet, P., Shypitsyna, A., Bonilla, C., Martin, M. J., et al. (2015). The GOA Database: Gene Ontology Annotation Updates for 2015. *Nucleic Acids Res.* 43, D1057–D1063. doi:10.1093/nar/gku1113

Islam, K. N., Bae, J.-W., Gao, E., and Koch, W. J. (2013). Regulation of Nuclear Factor κB (NF-Kb) in the Nucleus of Cardiomyocytes by G Protein-Coupled Receptor Kinase 5 (GRK5). *J. Biol. Chem.* 288, 35683–35689. doi:10.1074/jbc.m113.529347

Jassal, B., Matthews, L., Viteri, G., Gong, C., Lorente, P., Fabregat, A., et al. (2020). The Reactome Pathway Knowledgebase. *Nucleic Acids Res.* 48, D498–D503. doi:10.1093/nar/gkz1031

Jeong, H.-C., Park, S.-J., Choi, J.-J., Go, Y.-H., Hong, S.-K., Kwon, O.-S., et al. (2017). PRMT8 Controls the Pluripotency and Mesodermal Fate of Human Embryonic Stem Cells by Enhancing the PI3K/AKT/SOX2 Axis. *Stem Cells* 35, 2037–2049. doi:10.1002/stem.2642

Jiang, Y., Feng, Y.-P., Tang, L.-X., Yan, Y.-L., and Bai, J.-W. (2019). The Protective Role of NR4A3 in Acute Myocardial Infarction by Suppressing Inflammatory Responses via JAK2-Stat3/nf-Kb Pathway. *Biochem. Biophysical Res. Commun.* 517, 697–702. doi:10.1016/j.bbrc.2019.07.116

Kalfon, R., Koren, L., Aviram, S., Schwartz, O., Hai, T., and Aronheim, A. (2017). ATF3 Expression in Cardiomyocytes Preserves Homeostasis in the Heart and Controls Peripheral Glucose Tolerance. *Cardiovasc Res.* 113, 134–146. doi:10.1093/cvr/cvw228

Kanehisa, M., Furumichi, M., Tanabe, M., Sato, Y., and Morishima, K. (2017). KEGG: New Perspectives on Genomes, Pathways, Diseases and Drugs. *Nucleic Acids Res.* 45, D353–D361. doi:10.1093/nar/gkw1092

KEGG: Adrenergic signaling in cardiomyocytes (2021). *KEGG: Adrenergic Signaling in Cardiomyocytes.* https://www.genome.jp/entry/pathway+hsa04261

KEGG: Insulin signaling pathway (2021). *KEGG: Insulin Signaling Pathway.* https://www.genome.jp/entry/pathway+hsa04910

Kielman, M. F., Rindapää, M., Gaspar, C., van Poppel, N., Breukel, C., van Leeuwen, S., et al. (2002). Apc Modulates Embryonic Stem-Cell Differentiation by Controlling the Dosage of β-catenin Signaling. *Nat. Genet.* 32, 594–605. doi:10.1038/ng1045

Kiselev, V. Y., Andrews, T. S., and Hemberg, M. (2019). Challenges in Unsupervised Clustering of Single-Cell RNA-Seq Data. *Nat. Rev. Genet.* 20, 273–282. doi:10.1038/s41576-018-0088-9

Kramer, M. A. (1991). Nonlinear Principal Component Analysis Using Autoassociative Neural Networks. *AIChE J.* 37, 233–243. doi:10.1002/aic.690370209

Krueger, F. (2019). *Trim Galore.* Cambridge, United Kingdom: Babraham Bioinformatics. https://www.bioinformatics.babraham.ac.uk/projects/trim_galore/

Kwon, C., Arnold, J., Hsiao, E. C., Taketo, M. M., Conklin, B. R., and Srivastava, D. (2007). Canonical Wnt Signaling Is a Positive Regulator of Mammalian Cardiac Progenitors. *Proc. Natl. Acad. Sci. U.S.A.* 104, 10894–10899. doi:10.1073/pnas.0704044104

Laflamme, M. A., and Murry, C. E. (2011). Heart Regeneration. *Nature* 473, 326–335. doi:10.1038/nature10147

Lam, N. T., and Sadek, H. A. (2018). Neonatal Heart Regeneration. *Circulation* 138, 412–423. doi:10.1161/circulationaha.118.033648

Landeira, D., Sauer, S., Poot, R., Dvorkina, M., Mazzarella, L., Jørgensen, H. F., et al. (2010). Jarid2 Is a PRC2 Component in Embryonic Stem Cells Required for Multi-Lineage Differentiation and Recruitment of PRC1 and RNA Polymerase II to Developmental Regulators. *Nat. Cell Biol.* 12, 618–624. doi:10.1038/ncb2065

Li, A., and Barber, R. F. (2019). Multiple Testing with the Structure-adaptive Benjamini-Hochberg Algorithm. *J. R. Stat. Soc. B* 81, 45–74. doi:10.1111/rssb.12298

Liu, P., and Zhong, T. P. (2017). MAPK/ERK Signalling Is Required for Zebrafish Cardiac Regeneration. *Biotechnol. Lett.* 39, 1069–1077. doi:10.1007/s10529-017-2327-0

Lopaschuk, G. D., and Jaswal, J. S. (2010). Energy Metabolic Phenotype of the Cardiomyocyte during Development, Differentiation, and Postnatal Maturation. *J. Cardiovasc Pharmacol.* 56, 130–140. doi:10.1097/fjc.0b013e3181e74a14

Love, M. I., Huber, W., and Anders, S. (2014). Moderated Estimation of Fold Change and Dispersion for RNA-Seq Data with DESeq2. *Genome Biol.* 15, 550. doi:10.1186/s13059-014-0550-8

Lu, C.-W., Yabuuchi, A., Chen, L., Viswanathan, S., Kim, K., and Daley, G. Q. (2008). Ras-MAPK Signaling Promotes Trophectoderm Formation from Embryonic Stem Cells and Mouse Embryos. *Nat. Genet.* 40, 921–926. doi:10.1038/ng.173

Maitra, M., Schluterman, M. K., Nichols, H. A., Richardson, J. A., Lo, C. W., Srivastava, D., et al. (2009). Interaction of Gata4 and Gata6 with Tbx5 Is Critical for Normal Cardiac Development. *Dev. Biol.* 326, 368–377. doi:10.1016/j.ydbio.2008.11.004

Martini, J. S., Raake, P., Vinge, L. E., DeGeorge, B. R., Jr., Chuprun, J. K., Harris, D. M., et al. (2008). Uncovering G Protein-Coupled Receptor Kinase-5 as a Histone Deacetylase Kinase in the Nucleus of Cardiomyocytes. *Proc. Natl. Acad. Sci. U.S.A.* 105, 12457–12462. doi:10.1073/pnas.0803153105

Materna, S. C., Sinha, T., Barnes, R. M., Lammerts van Bueren, K., and Black, B. L. (2019). Cardiovascular Development and Survival Require Mef2c Function in the Myocardial but Not the Endothelial Lineage. *Dev. Biol.* 445, 170–177. doi:10. 1016/j.ydbio.2018.12.002

Matlab (2021). *Fitsemiself.* Natick, Massachusetts: Mathworks, Inc. https://www. mathworks.com/help/stats/fitsemiself.html

McInnes, L., Healy, J., and Melville, J. (2018). UMAP: Uniform Manifold Approximation and Projection for Dimension Reduction. *arXiv Prepr. arXiv* 1802, 03426.

Meehan, S. (2021). Uniform Manifold Approximation and Projection (UMAP). *Comput. Biol.* 6.

Miklas, J. W., Clark, E., Levy, S., Detraux, D., Leonard, A., Beussman, K., et al. (2019). TFPa/HADHA Is Required for Fatty Acid Beta-Oxidation and Cardiolipin Re-modeling in Human Cardiomyocytes. *Nat. Commun.* 10, 4671. doi:10.1038/s41467-019-12482-1

Misra, C., Chang, S.-W., Basu, M., Huang, N., and Garg, V. (2014). Disruption of Myocardial Gata4 and Tbx5 Results in Defects in Cardiomyocyte Proliferation and Atrioventricular Septation. *Hum. Mol. Genet.* 23, 5025–5035. doi:10.1093/hmg/ddu215

Mouse Genome Informatics (2021). *Gene Ontolog Annotations: G2/M Transition of Mitotic Cell Cycles.*

Mouse Genome Informatics (2021). *Gene Ontology Annotations: Cardiac Muscle Contraction.*

Mouse Genome Informatics (2021). *Gene Ontology Annotations: Positive Regulation of Cardiac Muscle Cell Proliferation*.

Mouse Genome Informatics (2021). *Gene Ontology Annotations: Positive Regulation of Cardiac Muscle Tissue Growth*.

Mouse Genome Informatics (2022). *GO:0019827 Stem Cell Population Maintenance*.

Mouse Genomic Informatics (2021). *Gene Ontology Annotations: Positive Regulation of Cell Population Proliferation*.

Mouse Genomic Informatics (2021). *Gene Ontology: Annotations: Fatty Acid Beta-Oxidation*.

Nahrendorf, M., and Swirski, F. K. (2013). Monocyte and Macrophage Heterogeneity in the Heart. *Circ. Res.* 112, 1624–1633. doi:10.1161/circresaha.113.300890

Nakada, Y., Zhou, Y., Gong, W., Zhang, E. Y., Skie, E., Nguyen, T., et al. (2022). Single Nucleus Transcriptomics: Apical Resection in Newborn Pigs Extends the Time-Window of Cardiomyocyte Proliferation and Myocardial Regeneration. *Circulation* 145 (23), 1744–1747.

Paik, D. T., Tian, L., Lee, J., Sayed, N., Chen, I. Y., Rhee, S., et al. (2018). Large-Scale Single-Cell RNA-Seq Reveals Molecular Signatures of Heterogeneous Populations of Human Induced Pluripotent Stem Cell-Derived Endothelial Cells. *Circ. Res.* 123, 443–450. doi:10.1161/circresaha.118.312913

Pig (Sscrofa11.1) (2021). *Pig assembly and gene annotation*. Ensembl.

Porrello, E. R., Mahmoud, A. I., Simpson, E., Hill, J. A., Richardson, J. A., Olson, E. N., et al. (2011). Transient Regenerative Potential of the Neonatal Mouse Heart. *Science* 331, 1078–1080. doi:10.1126/science.1200708

Rochais, F., Sturny, R., Chao, C.-M., Mesbah, K., Bennett, M., Mohun, T. J., et al. (2014). FGF10 Promotes Regional Foetal Cardiomyocyte Proliferation and Adult Cardiomyocyte Cell-Cycle Re-entry. *Cardiovasc Res.* 104, 432–442. doi:10.1093/cvr/cvu232

Sekine, Y., Yamamoto, K., Kurata, M., Honda, A., Onishi, I., Kinowaki, Y., et al. (2021). HADHB, a Fatty Acid Beta-Oxidation Enzyme, Is a Potential Prognostic Predictor in Malignant Lymphoma. *Pathology* 54, 286–293.

Sheikh, T. S., Khan, A., Fahim, M., and Ahmad, M. (2021). *International Conference on Analysis of Images, Social Networks and Texts*. Springer, 270–281.

Stull, J. T., Kamm, K. E., and Vandenboom, R. (2011). Myosin Light Chain Kinase and the Role of Myosin Light Chain Phosphorylation in Skeletal Muscle. *Archives Biochem. Biophysics* 510, 120–128. doi:10.1016/j.abb.2011.01.017

Szklarczyk, D., Gable, A. L., Nastou, K. C., Lyon, D., Kirsch, R., Pyysalo, S., et al. (2021). The STRING Database in 2021: Customizable Protein-Protein Networks, and Functional Characterization of User-Uploaded Gene/measurement Sets. *Nucleic Acids Res.* 49, D605–D612. doi:10.1093/nar/gkaa1074

trainAutoencoder (2021). *trainAutoencoder*. Natick, Massachusetts: Mathworks, Inc.

Tran, D., Nguyen, H., Tran, B., La Vecchia, C., Luu, H. N., and Nguyen, T. (2021). Fast and Precise Single-Cell Data Analysis Using a Hierarchical Autoencoder. *Nat. Commun.* 12, 1029. doi:10.1038/s41467-021-21312-2

Traynham, C. J., Cannavo, A., Zhou, Y., Vouga, A. G., Woodall, B. P., Hullmann, J., et al. (2015). Differential Role of G Protein-Coupled Receptor Kinase 5 in Physiological versus Pathological Cardiac Hypertrophy. *Circ. Res.* 117, 1001–1012. doi:10.1161/circresaha.115.306961

Traynham, C. J., Hullmann, J., and Koch, W. J. (2016). "Canonical and Non-canonical Actions of GRK5 in the Heart". *J. Mol. Cell. Cardiol.* 92, 196–202. doi:10.1016/j.yjmcc.2016.01.027

Trunk, G. V. (1979). A Problem of Dimensionality: A Simple Example. *IEEE Trans. Pattern Anal. Mach. Intell.* PAMI-1, 306–307. doi:10.1109/tpami.1979.4766926

Tsedeke, A. T., Allanki, S., Gentile, A., Jimenez-Amilburu, V., Rasouli, S. J., Guenther, S., et al. (2021). Cardiomyocyte Heterogeneity during Zebrafish Development and Regeneration. *Dev. Biol.* 476, 259–271. doi:10.1016/j.ydbio.2021.03.014

Uosaki, H., Cahan, P., Lee, D. I., Wang, S., Miyamoto, M., Fernandez, L., et al. (2015). Transcriptional Landscape of Cardiomyocyte Maturation. *Cell Rep.* 13, 1705–1716. doi:10.1016/j.celrep.2015.10.032

van Roermund, C. W. T., Visser, W. F., Ijlst, L., Waterham, H. R., and Wanders, R. J. A. (2011). Differential Substrate Specificities of Human ABCD1 and ABCD2 in Peroxisomal Fatty Acid β-oxidation. *Biochimica Biophysica Acta (BBA) - Mol. Cell Biol. Lipids* 1811, 148–152. doi:10.1016/j.bbalip.2010.11.010

Vidal, R., Wagner, J. U. G., Braeuning, C., Fischer, C., Patrick, R., Tombor, L., et al. (2019). Transcriptional Heterogeneity of Fibroblasts Is a Hallmark of the Aging Heart. *JCI Insight* 4. doi:10.1172/jci.insight.131092

Vieth, B., Parekh, S., Ziegenhain, C., Enard, W., and Hellmann, I. (2019). A Systematic Evaluation of Single Cell RNA-Seq Analysis Pipelines. *Nat. Commun.* 10, 4667. doi:10.1038/s41467-019-12266-7

Vincentz, J. W., Barnes, R. M., Firulli, B. A., Conway, S. J., and Firulli, A. B. (2008). Cooperative Interaction ofNkx2.5andMef2ctranscription Factors during Heart Development. *Dev. Dyn.* 237, 3809–3819. doi:10.1002/dvdy.21803

Wang, D., and Gu, J. (2018). VASC: Dimension Reduction and Visualization of Single-Cell RNA-Seq Data by Deep Variational Autoencoder. *Genomics, Proteomics Bioinforma.* 16, 320–331. doi:10.1016/j.gpb.2018.08.003

Wang, Y., Yao, H., and Zhao, S. (2016). Auto-encoder Based Dimensionality Reduction. *Neurocomputing* 184, 232–242. doi:10.1016/j.neucom.2015.08.104

Xiang, F.-l., Guo, M., and Yutzey, K. E. (2016). Overexpression of Tbx20 in Adult Cardiomyocytes Promotes Proliferation and Improves Cardiac Function after Myocardial Infarction. *Circulation* 133, 1081–1092. doi:10.1161/circulationaha.115.019357

Yang, X., Deng, C., Zheng, F., Yan, J., and Liu, W. (2019). Deep Spectral Clustering Using Dual Autoencoder Network. Proceedings of the IEEE/CVF Conference on Computer Vision and Pattern Recognition 4066-4075. IEEE.

Ye, L., D'Agostino, G., Loo, S. J., Wang, C. X., Su, L. P., Tan, S. H., et al. (2018). Early Regenerative Capacity in the Porcine Heart. *Circulation* 138, 2798–2808. doi:10.1161/circulationaha.117.031542

Yuan, Y., Park, J., Feng, A., Awasthi, P., Wang, Z., Chen, Q., et al. (2020). YAP1/TAZ-TEAD Transcriptional Networks Maintain Skin Homeostasis by Regulating Cell Proliferation and Limiting KLF4 Activity. *Nat. Commun.* 11, 1472. doi:10.1038/s41467-020-15301-0

Zhang, E., Nguyen, T., Zhao, M., Dang, S. D. H., Chen, J. Y., Bian, W., et al. (2020). Identifying the Key Regulators that Promote Cell-Cycle Activity in the Hearts of Early Neonatal Pigs after Myocardial Injury. *PLoS One* 15, e0232963. doi:10.1371/journal.pone.0232963

Zhang, Y., Zhou, G., Jin, J., Zhao, Q., Wang, X., and Cichocki, A. (2014). Aggregation of Sparse Linear Discriminant Analyses for Event-Related Potential Classification in Brain-Computer Interface. *Int. J. Neur. Syst.* 24, 1450003. doi:10.1142/s0129065714500038

Zhao, B., Ye, X., Yu, J., Li, L., Li, W., Li, S., et al. (2008). TEAD Mediates YAP-dependent Gene Induction and Growth Control. *Genes Dev.* 22, 1962–1971. doi:10.1101/gad.1664408

Zhao, M., Nakada, Y., Wei, Y., Bian, W., Chu, Y., Borovjagin, A. V., et al. (2021). Cyclin D2 Overexpression Enhances the Efficacy of Human Induced Pluripotent Stem Cell-Derived Cardiomyocytes for Myocardial Repair in a Swine Model of Myocardial Infarction. *Circulation* 144, 210–228. doi:10.1161/circulationaha.120.049497

Zhao, M., Zhang, E., Wei, Y., Zhou, Y., Walcott, G. P., and Zhang, J. (2020). Apical Resection Prolongs the Cell Cycle Activity and Promotes Myocardial Regeneration after Left Ventricular Injury in Neonatal Pig. *Circulation* 142, 913–916. doi:10.1161/circulationaha.119.044619

Zhu, W.-Z., Xie, Y., Moyes, K. W., Gold, J. D., Askari, B., and Laflamme, M. A. (2010). Neuregulin/ErbB Signaling Regulates Cardiac Subtype Specification in Differentiating Human Embryonic Stem Cells. *Circ. Res.* 107, 776–786. doi:10.1161/circresaha.110.223917

Zhu, W., Zhang, E., Zhao, M., Chong, Z., Fan, C., Tang, Y., et al. (2018). Regenerative Potential of Neonatal Porcine Hearts. *Circulation* 138, 2809–2816. doi:10.1161/circulationaha.118.034886

A three-dimensional culture system for generating cardiac spheroids composed of cardiomyocytes, endothelial cells, smooth-muscle cells, and cardiac fibroblasts derived from human induced-pluripotent stem cells

Asher Kahn-Krell[1], Danielle Pretorius[1], Bijay Guragain[1], Xi Lou[1], Yuhua Wei[1], Jianhua Zhang[2,3], Aijun Qiao[1], Yuji Nakada[1], Timothy J. Kamp[2,3,4], Lei Ye[1] and Jianyi Zhang[1,5]*

[1]Department of Biomedical Engineering, School of Medicine and School of Engineering, University of Alabama at Birmingham, Birmingham, AL, United States, [2]Department of Medicine, School of Medicine and Public Health, University of Wisconsin-Madison, Madison, WI, United States, [3]Stem Cell and Regenerative Medicine Center, University of Wisconsin-Madison, Madison, WI, United States, [4]Department of Cell and Regenerative Biology, School of Medicine and Public Health, University of Wisconsin-Madison, Madison, WI, United States, [5]Department of Medicine/Cardiovascular Diseases, University of Alabama at Birmingham, Birmingham, AL, United States

Cardiomyocytes (CMs), endothelial cells (ECs), smooth-muscle cells (SMCs), and cardiac fibroblasts (CFs) differentiated from human induced-pluripotent stem cells (hiPSCs) are the fundamental components of cell-based regenerative myocardial therapy and can be used as *in-vitro* models for mechanistic studies and drug testing. However, newly differentiated hiPSC-CMs tend to more closely resemble fetal CMs than the mature CMs of adult hearts, and current techniques for improving CM maturation can be both complex and labor-intensive. Thus, the production of CMs for commercial and industrial applications will require more elementary methods for promoting CM maturity. CMs tend to develop a more mature phenotype when cultured as spheroids in a three-dimensional (3D) environment, rather than as two-dimensional monolayers, and the activity of ECs, SMCs, and CFs promote both CM maturation and electrical activity. Here, we introduce a simple and reproducible 3D-culture−based process for generating spheroids containing all four cardiac-cell types (i.e., cardiac spheroids) that is compatible with a wide range of applications and research equipment. Subsequent experiments demonstrated that the inclusion of vascular cells and CFs was associated with an increase in spheroid size, a decline in apoptosis, an improvement in sarcomere maturation and a change in CM bioenergetics.

Introduction

The development of efficient protocols for differentiating human induced-pluripotent stem cells (hiPSCs) into cardiomyocytes (CMs), endothelial cells (ECs), smooth-muscle cells (SMCs), and cardiac fibroblasts (CFs) (Adams et al., 2013; Liu et al., 2016; Palpant et al., 2017; Zhu et al., 2017; Kwong et al., 2019; Zhang et al., 2019; Kahn-Krell et al., 2021) has led to the establishment of an array of utilizations in the field of cardiac regeneration. Although early proposed applications focused on direct injections (Menasché et al., 2001; Laflamme et al., 2007; Sanganalmath and Bolli, 2013; Ye et al., 2014) and the transplantation of engineered cardiac tissues (Schaefer et al., 2017; Shadrin et al., 2017; Gao et al., 2018) and sheets (Ishigami et al., 2018; Bayrak and Gümüşderelioğlu, 2019; Tsuruyama et al., 2019) to resupply cardiomyocytes, lost to injuries such as myocardial infarction (MI), the uses of these cardiac surrogates have expanded to include *in-vitro* modeling of myocardial disease (Long et al., 2018; Giacomelli et al., 2021), drug screening (Mathur et al., 2015; Huebsch et al., 2016; Mills et al., 2017), and exosome production (Liu et al., 2017). A wide range of formats has been explored to fulfill the needs of each potential application including patches (Schaefer et al., 2017; Shadrin et al., 2017; Gao et al., 2018), sheets (Ishigami et al., 2018; Bayrak and Gümüşderelioğlu, 2019; Tsuruyama et al., 2019), spheres (Fischer et al., 2018; Chang et al., 2020), wires (Jackman et al., 2016; Sun and Nunes, 2016), and decellularized tissues (Das et al., 2019; Alexanian et al., 2020; Hochman-Mendez et al., 2020). The utilization of these products and the needs of each use play a key role in the ideal option for each situation. However, there is a crucial need to establish tools for multiple applications related to MI and heart failure that can be easily reproduced and scaled (Zhang et al., 2021a).

Although current differentiation techniques can produce beating hiPSC-derived CMs in as little as 9 days (Lian et al., 2012; Zhang et al., 2012), the biomolecular (Cao et al., 2008; Synnergren et al., 2008; Xu et al., 2009; Synnergren et al., 2010), electrical (Caspi et al., 2009; Kim et al., 2010; Lee et al., 2011), and mechanical (Binah et al., 2007; Zhang et al., 2021b) properties of these newly differentiated cells tend to resemble those of fetal CMs, rather than the mature CMs of adult hearts (Robertson et al., 2013). Electrical stimulation (Chan et al., 2013; Richards et al., 2016; Ruan et al., 2016; LaBarge et al., 2019a) and mechanical stretching (Lux et al., 2016; Ruan et al., 2016; Zhang et al., 2017; LaBarge et al., 2019a) have been used to increase the maturity of engineered

cardiac tissue but are difficult to apply until after the tissue is manufactured. Thus, the production of CMs for commercial and industrial applications will require more elementary methods for promoting CM maturation (Zhang et al., 2021a), such as manipulating the conditions of hiPSC-CM culture (Haishuang Lin et al., 2017; Parikh et al., 2017; Jackman et al., 2018; Selvaraj et al., 2019).

Another method to increase complexity and functionality of cardiac tissue models is to use additional cell types that more accurately recreate the myocardial environment. When cultured in a three-dimensional (3D) environment, rather than as two-dimensional monolayers, CMs coalesce into spheroids (Fischer et al., 2018; Chang et al., 2020) and tend to develop a more mature phenotype (Jha et al., 2016; Sacchetto et al., 2020; Kai-Li Wang et al., 2021). ECs and SMCs also promote CM maturation (Pinto et al., 2016; Ayoubi et al., 2017; Giacomelli et al., 2017; Zhu et al., 2017; Kwong et al., 2019) while facilitating oxygen and nutrient delivery, which improves cell survival (Garzoni et al., 2009; Zhang et al., 2021a; Pretorius et al., 2021), and CFs contribute to myocardial development both by producing components of the extracellular matrix (ECM) and by forming gap junctions with CMs to support electronic signal transduction (Zhang et al., 2019; Beauchamp et al., 2020; Giacomelli et al., 2020; Li et al., 2020; Pretorius et al., 2021). A range of ratios between these different cell types have been explored in previous studies but a relationship of CM:EC:SMC:CF of 4:2:1:1 is predominantly used (Gao et al., 2018; Arai et al., 2020; Beauchamp et al., 2020; Daly et al., 2021; Pretorius et al., 2021) as it roughly recapitulates the relationships found in native myocardium of myocytes predominating with endothelial cells compromising the greatest non-myocyte population (Banerjee et al., 2007; Pinto et al., 2016).

Along with the functionality and maturity requirements for broad cardiac tissue surrogate application two important biomanufacturing considerations are system format and scalability. A uniform shape, size, and culture condition that can function in a range of uses would allow for centralized production (Abbasalizadeh et al., 2017; Adil and Schaffer, 2017; Li et al., 2017; Tomov et al., 2019). Spherical spheroids cultured in suspension provide a format that is broadly compatible with existing research equipment, is highly movable, and can function as a building block for larger construct needs (Mattapally et al., 2018; LaBarge et al., 2019a; LaBarge et al., 2019b; Kim et al., 2020; Daly et al., 2021; Polonchuk et al., 2021). Additionally, using previously established CM spheroid production processes combined with whole spheroid

fusion, a scalable spheroid biomanufacturing platform can be established that does not require dissociation (Beauchamp et al., 2015; Bin Lin et al., 2017; Miwa et al., 2020; Kahn-Krell et al., 2021).

For the experiments described in this report, we differentiated hiPSCs into CMs, ECs, SMCs, and CFs and then combined the differentiated cells in a 3D culture environment, where they formed spheroids containing all four cardiac-cell types (i.e., cardiac microtissues). Subsequent analyses suggested that the inclusion of vascular cells and CFs increased spheroid size, reduced cellular apoptosis, and tended to promote sarcomere maturation and CM energy production. This process, with the potential to be scaled, advances on previous cardiac spheroid models (Giacomelli et al., 2017; Voges et al., 2017; Lee et al., 2019b; Helms et al., 2019; Keung et al., 2019; Beauchamp et al., 2020; Buono et al., 2020; Giacomelli et al., 2020; Israeli et al., 2020; Kupfer et al., 2020; Thomas et al., 2021) by producing large diameter tissues with cells from a single iPSC line, no exogenous matrix, and a reproducible product.

Materials and methods

hiPSC culture and expansion

All cells used in the study were differentiated from human induced pluripotent stem cell (hiPSC) line LZ-hiPSC5 which was reprogramed from human cardiac fibroblasts as described previously (Zhang et al., 2014). hiPSCs were cultured on 6-well plates in mTeSR Plus (STEMCELL Technologies) for 3 days, detached with gentle cell dissociation reagent (GCDR) (STEMCELL Technologies), resuspended in 40 ml TeSR E8 3D seed media (STEMCELL Technologies) supplemented with 10 µM Y27632 at a density of 1.5×10^5 cells/mL, and then cultured in a 125 ml Erlenmeyer flask on a Belly Dancer orbital shaker (IBI Scientific) at a speed of 4.75. On each of the following 2 days, 1.2 ml of feed medium was added to the flask, and after an additional day, half of the culture volume was replaced with fresh seed medium. After 4 days of culture on the orbital shaker, aggregates were dissociated with GCDR for 8 min, broken into smaller cell clumps via pipetting through a 37-µm reversible strainer (STEMCELL Technologies), and then diluted to a density of 1.5×10^5 cells/mL. Cells were cultured as previously described (Kahn-Krell et al., 2021) for four more days before differentiation was initiated.

CM differentiation

Cardiomyocyte (CM) differentiation was performed as described previously (Kahn-Krell et al., 2021). Briefly,

differentiation was initiated on differentiation day (dD) 0 by replacing the culture media with RPMI 1640 supplemented with $1 \times$ B27 without insulin (RPMI/B27−), 6 µM CHIR99021, and 10 µM Y-27632 at a density of 1.5×10^6 cells/mL. On dD1, the media was replaced with a 1.2-fold volume of RPMI/B27−, 1 µM CHIR99021, and 10 µM Y-27632, and the cells were cultured for two more days. On dD3, 70% of the culture media was replaced with RPMI/B27− supplemented with 10 µM IWR-1-endo; on dD5, the media was changed to RPMI/B27−; and on dD7, the media was changed to RPMI1640 supplemented with B27 with insulin (RPMI/B27+) in a volume equivalent to the volume used on dD0. Metabolic purification of the differentiated CMs was initiated on dD9 by changing the media to RPMI1640 without glucose supplemented with B27+ and 0.12% (w/w) sodium DL-lactate (Millipore Sigma). Three days later (on dD12), the purification media was replaced with RPMI/B27+, and the medium was refreshed every 5 days until spheroid assembly. Spheroid assembly was performed no more than 30 days after differentiation was initiated and as close to dD12 as possible.

EC differentiation

Endothelial-cell (EC) differentiation of hiPSCs was performed in monolayers of cultured hiPSCs with the STEMdiff Endothelial Differentiation Kit (STEMCELL Technologies) as directed by the manufacturer's instructions. Briefly, hiPSCs were seeded into mTeSR Plus (STEMCELL Technologies) in a 6 well plate at a density of 5.0×10^4 per well and then on dD1 and dD2, the medium was changed to 3 ml STEMdiff Mesoderm Induction Medium (STEMCELL Technologies). The medium was replaced with 4 ml of STEMdiff Endothelial Induction Medium (STEMCELL Technologies) on dD3 and refreshed on dD5. On dD7, the cells were dissociated with ACCUTASE (Corning), transferred into a fibronectin-coated T75 flask, and cultured in EGM-2 MV (Lonza) supplemented with SB431542 (Fischer Scientific) until 100% confluent. Purification was performed by dissociating the cells, resuspending them in cold Dulbecco phosphate-buffered saline (DPBS) with 2% fetal bovine serum (FBS) at a density of 1×10^6 cells/100 µL, and then collecting cells that expressed both CD31 and CD144 via flow cytometry on a BD FACS Aria II instrument; 100-µL samples were labeled by incubating them with 5 µL of AlexaFluor-conjugated CD31 and 20 µL of phycoerythrin-conjugated CD144 antibodies for 45 min on ice and then washed in DPBS.

SMC differentiation

hiPSCs were treated via the EC differentiation protocol through dD7 and then differentiated into smooth-muscle cells

(SMCs) as described previously (Yang et al., 2016). Briefly, the cells were cultured until 80% confluent, and then the media was changed to high-glucose DMEM supplemented with 5% FBS, 5 ng/ml platelet-derived growth factor beta (PDGF-β), and 2.5 ng/ml transforming growth factor beta (TGFβ). The media was changed every 3 days for 9 days and then replaced with SmGM-2.

Cardiac fibroblast differentiation

When hiPSCs reached 100% confluency the medium was changed to RPMI/B27–insulin supplemented with 12 μM CHIR99021 (Tocris) for 24 h, RPMI/B27–insulin for 24 h, and then cardiac fibroblast differentiation basal (CFBM) medium (DMEM, high glucose with HAS, linoleic acid, lecithin, ascorbic acid, GlutaMAX, hydrocortisone hemisuccinate, rh insulin) supplemented with 75 ng/ml bFGF (WiCell Research Institute) for 18 days; the CFBM/bFGF medium was changed every other day.

CM, EC, SMC, and CF purity assessments

Cells were dissociated, washed in DPBS, fixed with 4% paraformaldehyde (PFA) for 15 min, washed three times, permeabilized with 0.1% Triton-X in DPBS, and blocked with 4% bovine serum albumin (BSA) and 4% FBS in DPBS for 30 min each; then, the cells were incubated with lineage-specific antibodies (Supplemental Table S1) for 1 h and analyzed on an Attune NxT flow cytometer (Thermo Fisher Scientific).

Spheroid fabrication and culture

A 2 ml sample of CM spheroids were treated with CM dissociation media (CMDM) (STEMCELL Technologies) for 15 min at 37°C with periodic mixing then counted to determine culture density. ECs, SMCs, and CFs were dissociated from monolayer cultures and 5.0×10^6, 2.5×10^6, and 2.5×10^6 of each respectively were combined and resuspended in 1 ml of spheroid media (OM) (Supplemental Table S3). Based on cell counts 1.0×10^7 total CMs were collected as whole spheroids in a 50 ml conical tube and the media was replaced with 19 ml OM. After addition of the other cell types the contents were mixed well and 200 μL was transferred to each well of a 96-Well, Nunclon Sphera-Treated, U-Shaped-Bottom Microplate (Thermo Fisher Scientific) to produce 96 spheroids. The media was refreshed every 2 days for 7 days, and then the spheroids were transferred to 6-well Ultra-Low Attachment Microplates (Corning), with no more than 16 spheroids per well. Plates were maintained on a belly dancer shaker (IBI Scientific) at speed of 4.75, and the media was exchanged every 4–7 days.

Spheroid size measurements

Spheroids were photographed with an Olympus CKX53 microscope at ×4 magnification, and spheroid diameters were determined with a modified ImageJ macro (Ivanov et al., 2014) as indicated in the Supplemental Information.

Quantitative polymerase chain reaction (qPCR)

RNA was extracted with TRIZOL (Thermo Fisher) and purified on Direct-zol RNA Miniprep Plus (Zymo Research) columns as directed by the manufacturer's protocol. Reverse transcription was performed with Superscript IV VILO Master Mix (Invitrogen), and samples were diluted to 5 ng/μL. Each qPCR reaction was performed with 5 ng of cDNA, 0.5 μM primers (Supplemental Table S2), and PowerUp SYBR Green Master Mix (Applied Biosystems), and analysis was conducted on a QuantStudio Real-Time PCR Machine (Applied Biosystems). Results for each CT value were normalized to intrinsic glyceraldehyde phosphate dehydrogenase (GAPDH) abundance and to the CT value determined on the first day after spheroid assembly for each batch of spheroids. Data was collected from four independent batches of spheroids for each gene.

Western blotting

Spheroids were digested in 100 μL RIPA Buffer (Sigma-Aldrich); then, protein lysates were collected, mixed with ×1 Halt proteinase inhibitor cocktail mix (Thermo Scientific), and sonicated twice in 3-s intervals at 50% power. Sample concentrations were determined via Pierce BCA Protein Assay (Thermo Scientific), and then samples containing ×4 Laemmli Sample Buffer (Bio-Rad), 2 Mercaptoethanol (Bio-Rad), and 7.5 μg protein were run on an Expressplus PAGE 4–20% Gel (GenScript) at 200 V for 30 min. Proteins were transferred to nitrocellulose membranes with a Trans-Blot Turbo Transfer System (Bio-Rad); then, the membranes were blocked in 5% Blotting Grade Blocker Non Fat Dry Milk (Bio-Rad) for 30 min and stained with primary and secondary antibodies (Supplemental Table S1) for 1 h each. Blots were incubated for 5 min in Pierce SuperSignal West Pico PLUS Chemiluminescent Substrate (Thermo Scientific) and imaged with the ChemiDoc Touch Imaging System (Biorad). Protein bands were quantified with Image Lab Software (Bio-Rad);

FIGURE 1
Experimental design. **(A)** hiPSCs were differentiated into CMs, ECs, SMCs, and CFs via established methods. **(B)** Spheroids containing all four cell types (C4 spheroids) were produced by combining a 4:2:1:1 ratio of CMs, ECs, SMCs, and CFs in 96-well U plates and allowing the cells to fuse for 7 days; then, **(C)** the spheroids were transferred to 6-well plates and **(D)** cultured with shaking for to 60 days. **(E)** Procedures for spheroid manufacture and experimental analyses are displayed on a timeline.

results for each sample were normalized to intrinsic beta actin abundance and to measurements made on the first day after spheroid assembly for each batch of spheroids. Data was collected from four independent batches of spheroids for each protein.

Spheroid preservation and sectioning

Spheroids were fixed in 4% formaldehyde (Pierce) for 15 min, placed in 30% sucrose at 4°C overnight, and then then embedded in Tissue-Plus O.C.T Compound (Fisher Scientific) for histological analysis. Blocks were cut into 10-μm sections, mounted on charged glass microscope slides (Globe Scientific) and then stored at −20°C.

Masson-trichrome staining

Slides containing sections obtained at 100-μm intervals (i.e., every 10th section) were fixed in Bouin's Solution at 55°C for 1 h and then treated with Weigerts iron hematoxylin working solution for 10 min, with Biebrich scarlet-acid fuchsin for 5 min, with phosphomolybdic acid-phosphotungstic acid for 5 min, with aniline blue solution for 5 min, and with 1% acetic acid for 1 min; then, the sections were dehydrated in 95% alcohol for 2 min, cleared with 2 changes of xylene, and mounted with permount and coverslips overnight. Sections were imaged with a ×10 objective on an Olympus B×51 Fluorescence Microscope; when multiple fields of view were required for a single section, the images were stitched together with Photoshop software.

Apoptosis

The spheroid core was identified by determining which Masson-trichrome–stained sections had the greatest surface area; then, sections from the core were stained using the *In Situ* Cell Death Detection Kit, TMR red (Sigma) according to

FIGURE 2

Size and histological assessments. **(A)** C4 spheroids were generated from the indicated CM population sizes (0.6×10^5 black; 0.8×10^5 purple; 1.0×10^5 pink; , 1.2×10^5 orange; , 1.4×10^5 yellow), and spheroid diameters were measured on D7 and D30; results were displayed as box-whisker plots. **(B)** C4 spheroids were cut into 10-µm sections, and the sections were stained via terminal deoxynucleotidyl transferase dUTP nick end labeling (TUNEL); then, apoptosis was quantified as the percentage of TUNEL-positive cells in 4 spheroids/group. **(C)** Images of C1, C3, and C4 spheroids

(Continued)

FIGURE 2
generated from an initial population of 1×10^5 CMs were obtained each day from D0−D7 (bar = 500 µM). **(D)** Spheroid diameters of all 3 groups (C1 black; C3 yellow; C4 blue) were measured on D7, D30, and D60; results are displayed as violin plots. **(E)** Spheroids were cut into 10-µm sections and stained with Masson-trichrome; representative images are displayed for every 10th sequential section from a C4 spheroid on D60 (bar = 500 µM). **(F)** Representative images are displayed for the centermost sections from C1, C3, and C4 spheroids at the indicated time points (bar = 500 µM for the first three columns, and bar = 100 µM for the far-right column); muscle fibers appear red and collagen fibers appear blue. (*$p < 0.05$, **$p < 0.01$, ***$p < 0.001$; n > 30 per group; p-values determined as mean $\pm$ SEM).

the manufacturers protocol. Briefly, sections were fixed in 4% PFA for 15 min, permeabilized in 0.1% Triton X-100 and 0.1% sodium citrate for 2 min on ice, incubated with TUNEL reaction mixture and 4′, 6-diamidino-2-phenylindole (DAPI) for 1 h at 37°C, mounted in VECTASHIELD hardset Antifade Mounting Medium, and visualized via confocal laser scanning (Olympus FV3000 confocal microscope). Sections were evaluated for at least two spheroids in each of four batches, and positively stained cells or the size of stained regions were quantified with a modified ImageJ macro (Ivanov et al., 2014) as indicated in the Supplemental Information.

Immunostaining and apoptosis detection

The spheroid core was identified by determining which Masson-trichrome–stained sections had the greatest surface area; then, sections from the core were fixed in 4% PFA for 15 min, blocked, permeabilized in 10% donkey serum, 10% Tween20, 3% BSA, and 0.05% Triton-X for 30 min, incubated with primary antibodies (Supplemental Table S1) at room temperature for 45 min, washed with PBS (3 washes, 5 min per wash), incubated with DAPI and fluorescent secondary antibodies at room temperature for 45 min, mounted in VECTASHIELD hardset Antifade Mounting Medium, and visualized via confocal laser scanning (Olympus FV3000 confocal microscope). Sections were evaluated for at least two spheroids in each of four batches, and positively stained cells or the size of stained regions were quantified with a modified ImageJ macro (Ivanov et al., 2014) as indicated in the Supplemental Information.

ATP, NAD, and NADH quantification

ATP content was measured using a luminescent ATP detection Assay kit (ab113849; Abcam) following the manufacturer's protocol. The amount of ATP was normalized to the total protein content, which was determined using a protein assay (23227, ThermoFisher). The data was presented as nanomoles per milligram protein. Total NAD+ and NADH levels were measured by colorimetric kit (ab65348; Abcam) according to manufacturer's instruction. cAMP level was measured by Direct cAMP Enzyme-linked Immunosorbent Assay (ELISA) using a direct cAMP ELISA kit (ADI-900-066A, Enzo Life Sciences) following the manufacturer's instructions. Tissue cAMP level was normalized to the total protein content and presented as picomole per milligram protein.

Microelectrode array (MEA)

CytoView MEA 24 well plates (Axion Biosystems) were precoated with 3 µg/ml fibronectin and incubated at 37°C for 1 h. Whole spheroids (1 per well) or CMs collected from dissociated spheroids were added to each well of the MEA plate. Isolated CMs were obtained by treating spheroids with CMDM and periodic pipetting for 30 min at 37°C, selected with the EasySep Human PSC-Derived Cardiomyocyte Enrichment Kit (StemCell), and resuspended at a concentration of 1.2×10^7 cells/mL in CM support media (CMSM) (StemCell Technologies); 5 µL of resuspended CMs were added to each well. Whole spheroids were analyzed 24–48 h after plating, and CMs were analyzed 7 days after plating. Field potential and contractility measurements were collected on a Maestro Edge apparatus (Axion Biosystems) and analyzed by using the Cardiac Module in Axion Navigator software. Action potential durations (APDs) were determined using the LEAP assay and characterized using the Cardiac Analysis Tool.

Transmission electron microscopy (TEM)

Spheroids were transferred onto a fibronectin-coated (1 µg/ml), 0.4-µm pore Transwell Polycarbonate Membrane and cultured for 3 days; then, the membranes were fixed in 2.5% glutaraldehyde solution for 1 h at 4°C and delivered to the UAB High-Resolution Imaging Facility. Sample blocks were sectioned along the width of the transwells with a diamond knife, and samples were mounted and viewed with a Tecnai Spirit T12 Transmission Electron Microscope. At least 4 images were collected for each spheroid, and sarcomere lengths and widths were determined for all sarcomeres in an image by using the line-measure tool in ImageJ software. Sarcomere lengths were determined as the distance from z-line to z-line and widths were determined as the distance from one end to the other of a continuous z-line.
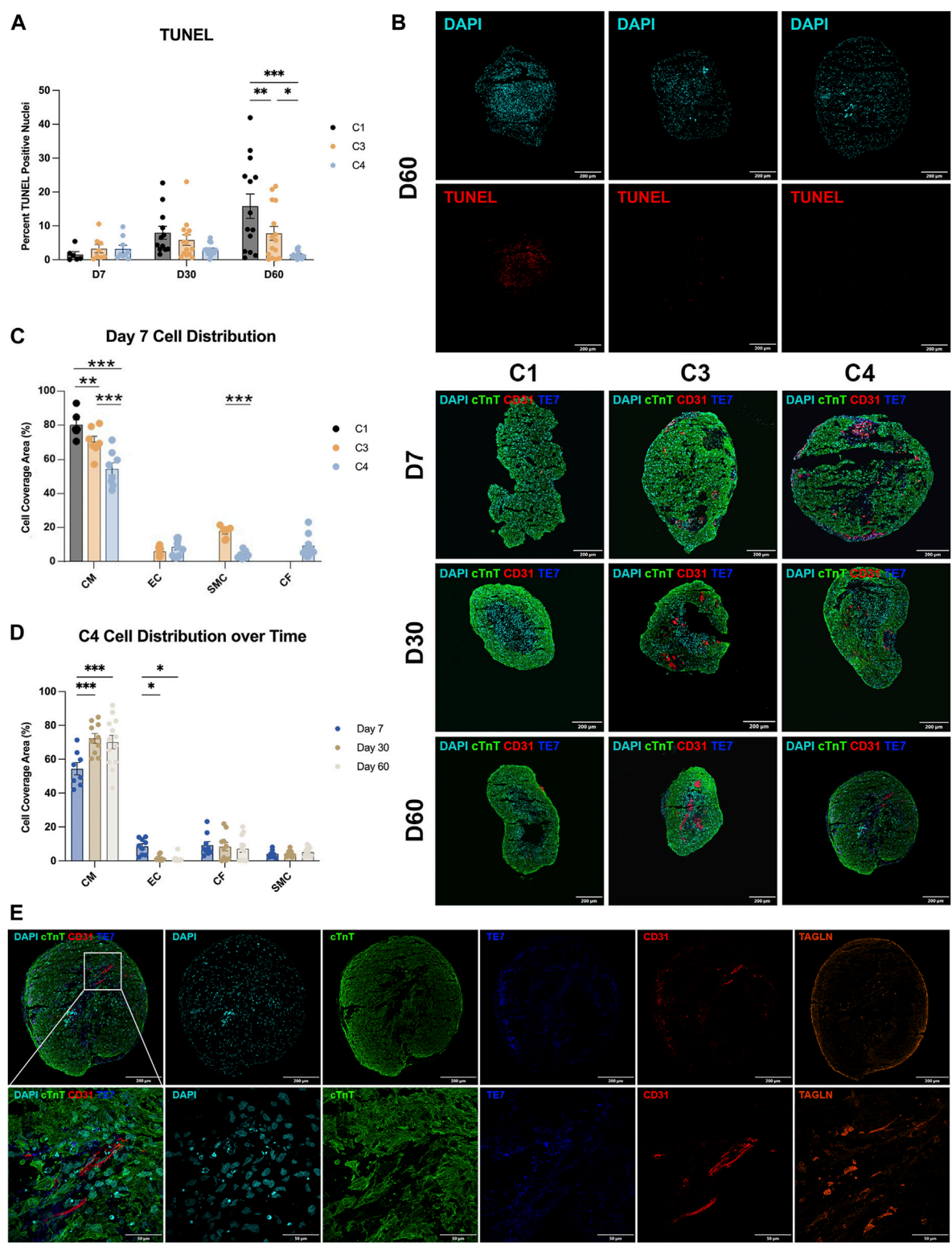
FIGURE 3

Apoptosis and cell-occupancy measurements. **(A)** C1, C3, and C4 spheroids were collected at the indicated time points and cut into 10-µm sections; then, the surface areas of every 10th section were measured, and the centermost section (i.e., the one with the largest surface area) was TUNEL-stained. Nuclei were counterstained with DAPI, and apoptosis was quantified as the percentage of TUNEL-positive cells. Representative images are displayed for the centermost sections from each group on D60. **(B)** Centermost sections were stained with cTnT, CD31, and TE-7

(*Continued*)

FIGURE 3
antibodies to visualize CMs, ECs, and CFs, respectively, and nuclei were counterstained with DAPI; representative images are displayed for each group on D7, D30, and D60. **(C,D)** CM, EC, and CF occupancy were quantified as the percentage of total surface area that was positive for expression of the corresponding marker protein and summarized **(C)** for C1, C3, and C4 on D7 and **(D)** for C4 on D7, D30, and D60. **(E)** Representative sections from a C4 spheroid on D60 are displayed at high magnification to demonstrate the presence of elongated ECs. (*$p < 0.05$, **$p < 0.01$, ***$p < 0.001$; n > 6 per group).

Statistical analysis

Data are presented as mean ± SEM, as box-and-whisker plots, or as violin plots, and significance was evaluated via the Student's t-test or analysis of variance (ANOVA). Analyses were performed with GraphPad Prism8 software (GraphPad Prism, RRID:SCR_002798), and $p < 0.05$ was considered significant.

Results

The inclusion of hiPSC-ECs, -SMCs, and CFs in CM spheroids increased spheroid size and improved cell viability

hiPSCs were differentiated into CMs, ECs, SMCs, and CFs via published protocols or the use of commercially available kits (Yang et al., 2016; Zhang et al., 2019; Kahn-Krell et al., 2021), and flow-cytometry analyses with lineage-specific antibodies [CMs: cardiac troponin T (cTnT), ECs: CD144 and CD31, SMCs: smooth-muscle actin (SMA), CFs: TE-7] confirmed that the purity of each differentiated cell population exceeded 95% (Supplementary Figures S1–S4). Spheroids containing CMs alone (C1) and spheroids containing a 4:2:1 ratio of CMs, ECs, and SMCs (C3) or a 4:2:1:1 ratio of CMs, ECs, SMCs, and CFs (C4) were produced by culturing the indicated proportions of cell types in low-attachment 96-well U plates for 1 week to promote aggregation and fusion (Figures 1A,B), and then in low-attachment 6-well plates on an orbital shaker for the remainder of the culture period (Figures 1C,D). D0 was defined as the day the spheroids/spheroids were initially assembled, and samples were obtained after one (D1), seven (D7), 14 (D14), 30 (D30), and 60 (D60) days of culture for characterization (Figure 1E); synchronized beating was observed in all constructs throughout the culture period. Size optimization studies determined that the mean diameter of C4 spheroids on D30 was larger (though not significantly) when the spheroids were generated from 1.0×10^5 seeded CMs (~801 μm) than from other initial CM population sizes (698–791 μm) (Figure 2A), with no significant increase in the proportion of apoptotic cells (Figure 2B). Thus, all spheroids and spheroids produced for subsequent experiments were constructed with 1.0×10^5 CMs.

C4 spheroids coalesced into a largely spherical shape within 3–4 days of seeding, while the architecture of the C3 spheroids and (especially) C1 spheroids remained irregular through at least D7 (Figure 2C). C4 spheroid diameters were also significantly smaller on D7 (C1: 1,198 ± 38.2 μm; C3: 1,016 ± 21.1 μm; C4: 964 ± 12.6 μm, $p < 0.001$ versus C1 and C3), but the trend was reversed on D30 (C1: 719 ± 11.9 μm; C3: 714 ± 10.4 μm; C4: 804 ± 13.9 μm, $p < 0.001$ versus C1 and C3) and D60 (C1: 676 ± 14.7 μm; C3: 678 ± 8.8 μm; C4: 730 ± 11.7 μm, $p < 0.01$ versus C1, $p < 0.05$ versus C3), when C4 spheroids were significantly larger than the other two constructs (Figure 2D). These differences may be accounted for by proliferation of non-myocytes in the C3 and C4 groups however, over time all groups showed trends of decreasing diameter and further immunostaining (Figure 3) did not show significant increases in ECs, SMCs, or CFs. Observations in Masson-trichrome stained sequential sections (Figure 2E) suggested that the density of muscle cells and fibers increased from D7 to D60 in all constructs, but only C3 and C4 spheroids displayed evidence of collagen formation (Figure 2F), which is consistent with the absence of ECM-producing ECs, SMCs, or CFs (Lee et al., 2019a; Strikoudis et al., 2019) in C1 spheroids. Furthermore, although assessments of apoptosis (TUNEL staining) did not differ significantly among groups on D7, apoptotic cells became increasingly common in C1 spheroids and (to a lesser extent) C3 spheroids during the culture period, while the proportion of apoptotic cells in C4 spheroids remained stable through at least D60, when apoptotic cells were significantly less common in C4 spheroids than in the other two constructs and in C3 spheroids than in C1 spheroids (Figure 3A). Apoptotic cells also tended to be located toward the center of C1 spheroids, which suggests that the vascular cells and CFs present in C4 spheroids facilitated access of the culture medium to the spheroid interior. These findings are consistent with previous work supporting the crucial role that non-myocytes play in promoting CM survival particularly where nutrient and oxygen diffusion is limited through release of paracrine factors (Ye et al., 2014; Hodgkinson et al., 2016; Giacomelli et al., 2017; Giacomelli et al., 2020; Munarin et al., 2020; Pretorius et al., 2021).

hiPSC-CMs occupied a progressively larger proportion of C4 spheroids over time

The distribution of cell types during the culture period was evaluated in sections stained for the expression of cTnT, CD31, and the fibroblast marker TE-7 (Figure 3B), as well as with SMC marker transgelin (TAGLIN). On D7, the proportion of cTnT-
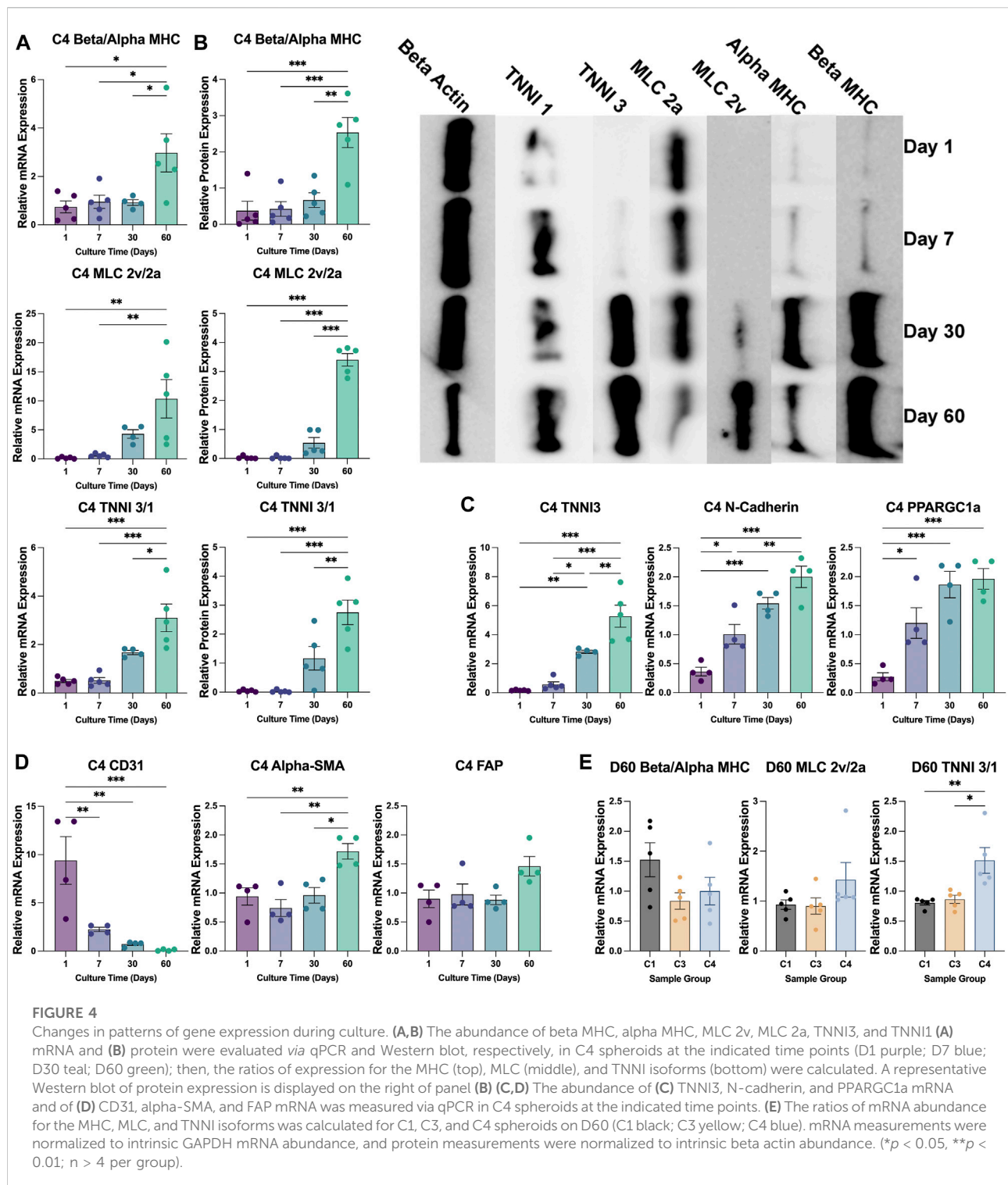
FIGURE 4

Changes in patterns of gene expression during culture. **(A,B)** The abundance of beta MHC, alpha MHC, MLC 2v, MLC 2a, TNNI3, and TNNI1 **(A)** mRNA and **(B)** protein were evaluated *via* qPCR and Western blot, respectively, in C4 spheroids at the indicated time points (D1 purple; D7 blue; D30 teal; D60 green); then, the ratios of expression for the MHC (top), MLC (middle), and TNNI isoforms (bottom) were calculated. A representative Western blot of protein expression is displayed on the right of panel **(B) (C,D)** The abundance of **(C)** TNNI3, N-cadherin, and PPARGC1a mRNA and of **(D)** CD31, alpha-SMA, and FAP mRNA was measured via qPCR in C4 spheroids at the indicated time points. **(E)** The ratios of mRNA abundance for the MHC, MLC, and TNNI isoforms was calculated for C1, C3, and C4 spheroids on D60 (C1 black; C3 yellow; C4 blue). mRNA measurements were normalized to intrinsic GAPDH mRNA abundance, and protein measurements were normalized to intrinsic beta actin abundance. (*$p < 0.05$, **$p < 0.01$; n > 4 per group).

positive surface area (i.e., CM occupancy) was significantly lower in C4 spheroids than in the other two constructs, and in C3 spheroids than in C1 spheroids (Figure 3C), which is consistent with the initial composition of cell types used during spheroid construction. In C4 spheroids, CM occupancy

increased from D7 to D30, while EC occupancy declined over the same period (Figure 3D), perhaps because the ECs grew from centrally located clumps on D7 into elongated structures that permeated the entire spheroid on D30 and D60 (Figure 3E). CM and EC occupancy remained largely stable in C4 spheroids from
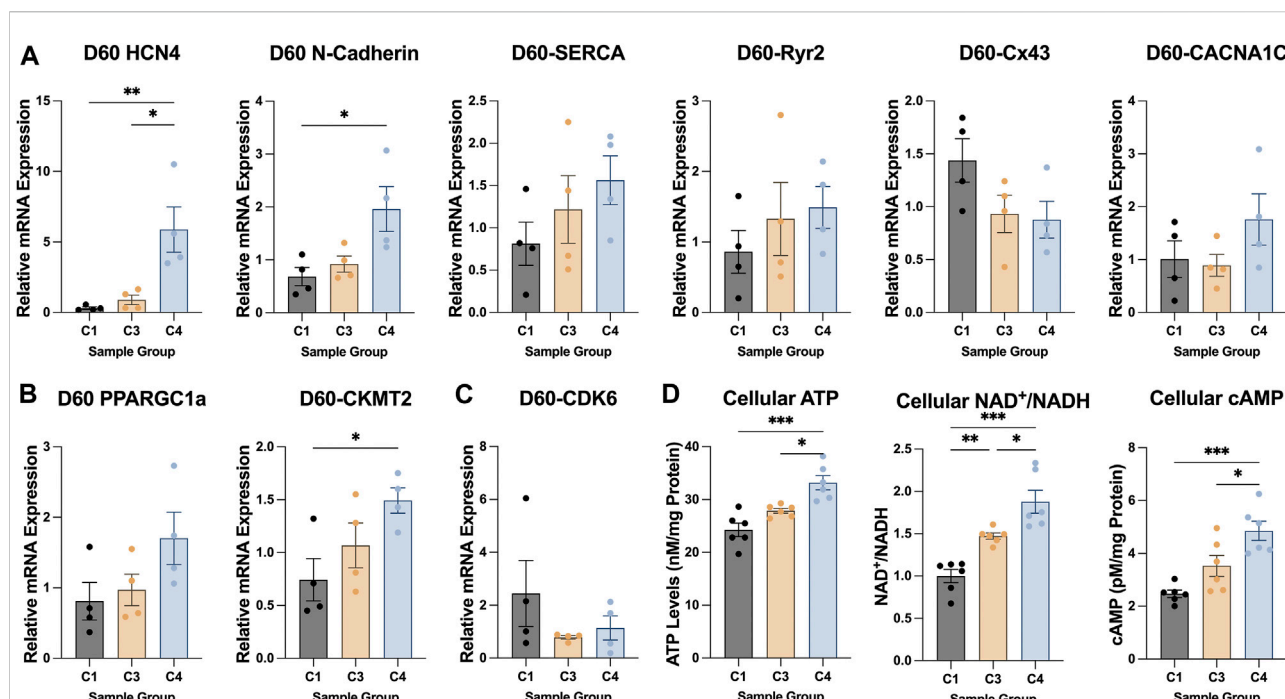
FIGURE 5
Patterns of metabolic, electrical, and cell-cycle gene expression in C1, C3, and C4 spheroids. The magnitude of expression for genes that contribute to CM **(A)** electrical conduction (HCN4, N-cadherin, SERCA, Ryr2, Cx43, CACNA1C), **(B)** metabolism (PPARGC1a, CKMT2), and **(C)** cell-cycle activity (CDK6) was evaluated in C1, C3, and C4 spheroids on D60 (C1 black; C3 yellow; C4 blue) via qPCR; measurements were normalized to intrinsic GAPDH mRNA abundance. **(D)** ATP abundance, the NAD/NADH ratio, and cellular cAMP was evaluated in C1, C3, and C4 spheroids on D60 (C1 black; C3 yellow; C4 blue) via luminescent ATP detection assay, colorimetric assay, and direct cAMP ELISA respectively (*$p < 0.05$, **$p < 0.01$; n > 4 per group).

D30 to D60, while SMC and CF occupancy did not change significantly throughout the 60-day culture period. Although some restructuring occurred, immunofluorescent imaging studies illustrated sparse and non-uniform distribution of non-myocytes throughout the time course suggesting that even small amounts of these cells can provide the necessary benefit to CM survival. Low levels of CD31 expression were also observed in C1 spheroids, and both C3 spheroids and C1 spheroids contained a very small number of TE-7–positive cells, perhaps because growth factors present in the culture medium (e.g., VEGF, FGF) induced EC- and CF-like phenotypes in hiPSC-derived cells that were not fully differentiated before the constructs were assembled.

hiPSC-CMs in C4 spheroids matured during the culture period

CM maturation and ventricular specification is associated with increases in the ratios of expression for beta versus alpha myosin heavy chain (beta:alpha MHC), ventricular versus atrial myosin light-chain 2 (MLC 2v:2a), and cardiac (type 3) versus slow-skeletal (type 1) troponin I (TNNI 3:1) (Guo and Pu, 2020; Karbassi et al., 2020).

When calculated from measurements of either mRNA (Figure 4A) or protein (Figure 4B) abundance, each of the three ratios increased significantly in C4 spheroids throughout the culture period, including from D30 to D60 for all except the ratio of MLC 2v:2a mRNA, and the abundance of structural (TNNI3), electromechanical (N-cadherin), and metabolic [peroxisome proliferator-activated receptor gamma coactivator 1-alpha (PPARGC1a)] markers for CM maturation significantly increased through at least D30 (Figure 4C). Alpha-SMA expression also increased significantly throughout the culture period, while CD31 expression significantly declined, and the expression of fibroblast activating protein (FAP) was largely unchanged (Figure 4D). Collectively, these observations indicate that the maturation and modification of both CMs and vascular cells continues for at least 2 months in cultured C4 spheroids.

The inclusion of hiPSC-ECs, -SMCs, and CFs increased sarcomere maturation and CM energy production in cardiac spheroids

The TNNI 3:1 mRNA ratio was also significantly higher in C4 spheroids than in C3 spheroids or C1 spheroids on D60,

FIGURE 6
TEM assessments of the ultrastructure of C1, C3, and C4 spheroids. **(A)** Whole C1, C3, and C4 spheroids on day 60 were sectioned and imaged via TEM (bar = 2 µM for the top row, and bar = 1 µM for the bottom row); ZL: Z-line, ML: M-line, MT: mitochondria, GJ: gap junction, N: nucleus. **(B)** Sarcomere lengths were calculated by measuring the distance between adjacent Z-lines. **(C)** Sarcomere widths were measured as the length of each uninterrupted Z-line. (*$p < 0.05$, **$p < 0.01$, ***$p < 0.001$; n > 5 spheroids per group).

but the ratios of beta:alpha MHC and MLC 2v:2a mRNA did not differ significantly among the three groups (Figure 4E). mRNA levels on D60 for a panel of genes that participate in CM electrical conduction [hyperpolarization activated cyclic nucleotide gated potassium channel 4 (HCN4), N-cadherin, sarcoplasmic/endoplasmic reticulum calcium ATPase (SERCA), ryanodine receptor 2 (Ryr2), connexin 43 (Cx43), calcium voltage-gated channel subunit alpha 1C (CACNA1C); Figure 5A] and metabolism [PPARGC1a, creatine kinase, mitochondrial 2 (CKMT2); Figure 5B] also tended to be more highly expressed in C4 spheroids; however, the only differences that reached statistical significance were for CKMT2 and N-cadherin, which were significantly greater in C4 spheroids than in C1 spheroids, and for HCN4, which was significantly greater in C4 spheroids than in either of the other two groups. These expression level differences observed on day 60 were found to be mostly absent when the same genes we examined on day 7 after formation (Supplementary Figure S5). Notably, mRNA levels for both Cx43 and the cell-cycle regulatory molecule cyclin-dependent kinase 6 (CDK6) (Figure 5C) appeared to be lower in C4 spheroids than in C1 spheroids, but not significantly, while ATP levels, the ratio of NAD:NADH, and cAMP levels were significantly greater in C4 spheroids than in

C1 spheroids (Figure 5D). Furthermore, observations in transmission electron microscopy (TEM) images collected on D60 confirmed that all three spheroid constructs contained Z-lines and gap junctions, but more complex structures, such as M-lines, I-bands, and A-bands, were observed only in C3 and C4 spheroids. This was notably a qualitative improvement from images collected on spheroids at D30 (Supplementary Figure S6). Contractile fibers also appeared to be more organized, and mitochondria better aligned, in C4 spheroids (Figure 6A), and both sarcomere lengths (Figure 6B) and widths (Figure 6C) were significantly greater in C4 spheroids than C1 spheroids. Thus, the inclusion of ECs, SMCs, and CFs in cardiac spheroids tended to promote sarcomere maturation and CM energy production.

Field-potential duration and conduction velocity were greater in CMs from C4 spheroids than from C1 spheroids

MEA assessments conducted on D30 of whole spheroids (Figure 7A) indicated that the electromechanical properties of all three constructs were generally similar: spike amplitude measurements were significantly greater in C4 spheroids than
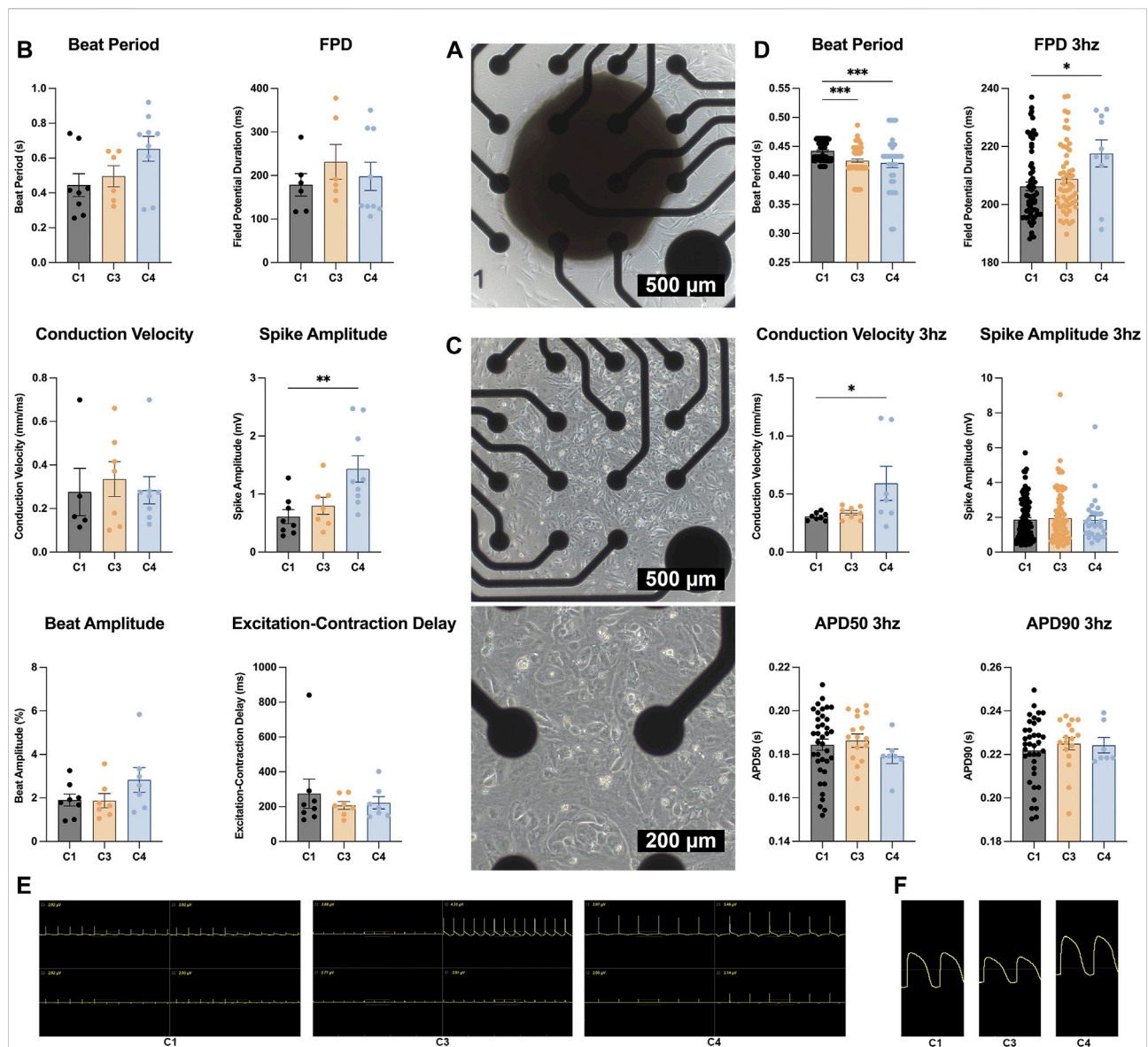
FIGURE 7
MEA assessments. **(A)** Whole C1, C3, and C4 spheroids (C1 black; C3 yellow; C4 blue) were attached to a 4 × 4 MEA; then, field potentials and impedance were measured and used to calculate **(B)** beat period, spike amplitude, field potential duration (FPD), conduction velocity, beat amplitude, and excitation. **(C)** C1, C3, and C4 spheroids (C1 black; C3 yellow; C4 blue) were dissociated on D30; then, CMs were collected and plated on the MEA electrodes. Field potentials and impedance were measured with and without pacing at 3 hz (330 ms or 180 bpm) and used to calculate **(D)** beat period, spike amplitude, FPD, conduction velocity, and the action potential duration until 50 and 90% recovery (APD50 and APD90), respectively. **(E)** MEA field potential traces for C1, C3, and C4 whole organoids only showing the 4 electrodes that were used for analysis. **(F)** MEA field potential traces of dissociated C1, C3, and C4 organoids after undergoing LEAP induction (*$p < 0.05$, **$p < 0.01$, ***$p < 0.001$; n > 6 per group).

in C1 spheroids, but variations among groups in beat period, beat amplitude, field-potential duration, conduction velocity, and excitation-contraction delay were small and not significant (Figure 7B). However, when CMs were isolated from the constructs (Figure 7C), beat period was significantly shorter for CMs from C3 or C4 spheroids (i.e., C3 or C4 CMs) than from C1 spheroids (C1 CMs), and field-potential durations were significantly longer in C4 than in C1 CMs when the cells were paced at 3 hz (Figure 7D). Conduction velocities were also significantly greater in C4 than C1 CMs during pacing, likely because the variability among measurements in C4 CMs was exceptionally high, while measurements of spike amplitudes and action-potential durations were similar in CMs from all three constructs.

TABLE 1 Data collected from MEA analysis of whole and dissociated spheroids.

Format	Group	Beat period (s)	Spike amplitude (mV)	FPD (ms)	Conduction velocity (cm/s)	Beat amplitude (%)	ECD (ms)	APD50 (ms)	APD90 (ms)
Whole Spheroid	C1	0.45 ± 0.07	0.61 ± 0.12	179 ± 26	27.6 ± 10.9	1.90 ± 0.27	275 ± 83		
	C3	0.50 ± 0.06	0.80 ± 0.15	231 ± 40	33.6 ± 8.0	1.88 ± 0.33	207 ± 22		
	C4	0.65 ± 0.07	1.43 ± 0.23	198 ± 32	28.5 ± 6.3	2.83 ± 0.57	222 ± 35		
Isolated CMs (Paced at 3 Hz)	C1	0.44 ± 0.01	1.87 ± 0.12	206 ± 2	30.7 ± 1.1	2.02 ± 0.13	142 ± 3	184 ± 3	222 ± 2
	C3	0.43 ± 0.01	1.95 ± 0.15	209 ± 2	34.0 ± 1.9	2.10 ± 0.19	144 ± 3	186 ± 3	225 ± 3
	C4	0.42 ± 0.01	1.85 ± 0.24	218 ± 5	59.3 ± 14.7	1.74 ± 0.17	146 ± 3	179 ± 3	224 ± 4

Discussion

The biological properties and activity of cells in the human heart are reproduced with greater fidelity by cardiac spheroids than by other *in-vitro* cell-culture systems. Thus, spheroids tend to provide a more accurate platform for modeling cardiac disease or drug development, and the individual cell populations present in cardiac spheroids may be more suitable for tissue engineering and other therapeutic applications. Here, we show that spheroids composed of hiPSC-derived CMs, ECs, SMCs, and CFs can be readily assembled and cultured for up to 60 days in solution; that C4 spheroids were significantly larger than C1 spheroids or C3 spheroids; and that the inclusion of vascular cells and CFs tended to promote sarcomere maturation and CM energy production. Furthermore, whereas apoptotic cells became increasingly common from D7 to D60 in C1 spheroids and C3 spheroids, the proportion in C4 spheroids remained stable throughout the culture period, which suggests that C4 spheroids are sufficiently durable for long-term studies. Notably, all four cardiac-cell types were differentiated from the same line of hiPSCs and, consequently, had the same genetic background, and the ratio of CMs, ECs, SMCs, and CFs (4:2:1:1) in C4 spheroids roughly followed the distribution trends found in human myocardium (Banerjee et al., 2007; Pinto et al., 2016; Gao et al., 2018; Arai et al., 2020; Beauchamp et al., 2020; Daly et al., 2021; Pretorius et al., 2021), but whether this ratio also produces the most native-like cardiac-cell phenotypes in cultured spheroids has yet to be conclusively demonstrated. The present study illustrates that additional optimization of this seeding ratio may be necessary to account for cell loss and restructuring that occurs and techniques for determining the composition in the fully matured tissue may be necessary. Additionally, the ideal ratio for different applications may vary depending on the region or state of myocardium that is being modeled.

The suspension culture system used in this report is broadly compatible with existing research equipment, and quality control checkpoints can be incorporated to maximize reproducibility; thus, our protocol can be readily adapted for a wide range of applications (Mattapally et al., 2018; LaBarge et al., 2019a; LaBarge et al., 2019b; Kim et al., 2020; Daly et al., 2021; Polonchuk et al., 2021) and production facilities (Abbasalizadeh et al., 2017; Adil and Schaffer, 2017; Li et al., 2017; Tomov et al., 2019). Furthermore, techniques for promoting spheroid fusion (Kim et al., 2018; Mattapally et al., 2018) and for the use of spheroids in 3D bioprinting (Duan, 2016; Maiullari et al., 2018; Aguilar et al., 2019; Alonzo et al., 2019; LaBarge et al., 2019b; Qasim et al., 2019; Lu Wang et al., 2021) have already been established, so the spheroids generated via this protocol could serve as building blocks for even larger and more sophisticated cardiac-tissue constructs, and because ECM production occurred spontaneously in C4 spheroids, exogenously administered ECM components may be unnecessary. However, only ~50 spheroids per batch were produced in this study, and several of the steps were performed manually, so additional automation will be necessary to maximize productivity on an industrial scale.

The wide application of cardiac spheroid systems has led many groups to develop a range of models for both *in vitro* and *in vivo* uses. The microtissues in the present study achieved a greater overall diameter (500–1000 µm) than were previously produced (50–400 µm) with maintained cellular complexity and viability (Beauchamp et al., 2020; Giacomelli et al., 2020; Giacomelli et al., 2021). Although decreased central necrosis was observed in the C4 spheroids, the large diameter and fusion process raises concerns for nutrient and oxygen diffusion (Langan et al., 2016) which will require further assessment in future studies. The use of bioreactor culture environment rather than static culture may provide partial mitigation. Spheroids were also shown to maintain beating and viability over a 60 days period which provides greater longitudinal analysis than the single time points at 28, 20, 15, 30, and 12 days used by others (Ravenscroft et al., 2016; Giacomelli et al., 2017; Israeli et al., 2020; Polonchuk et al., 2021; Thomas et al., 2021). Finally, the protocol of fusing the multiple cell types into larger cardiac spheroids described here uses 96 well plates, a widely used format, and doesn't require CM dissociation, a challenging and labor intensive step, while still maintaining consistent ratios of cell

types. This is in comparison to complicated fabrication processes involving complete CM dissociation, hanging drop methods, agarose mold production, and additional centrifugation steps (Nugraha et al., 2019; Buono et al., 2020; Kupfer et al., 2020; Giacomelli et al., 2021; Thomas et al., 2021) and high variability due to spontaneous differentiation compared with the combination of purified cell types (Hoang et al., 2018; Schulze et al., 2019; Israeli et al., 2020) found in other studies.

Although the current study showed improvements in key biomolecular and functional markers a limitation in the data was the lack of functional cardiac metrics at each time point. Particularly, the lack of electromechanical testing at D60 when other biomarkers appeared to show the greatest improvement leaves a gap in maturation characterization. Future iterations of the cardiac spheroid model should consider incorporating data from both early and late time points for all analyses to provide greater longitudinal understanding. Additionally, the media composition chosen was based on previous work with cardiac cell coculture (Giacomelli et al., 2017; Gao et al., 2018; Noor et al., 2019; Pretorius et al., 2021) but was not optimized or fully defined. The use of FBS, although routine, has previously been shown to lead to dedifferentiation of ECs (Kaupisch et al., 2012; Sriram et al., 2015) and an alternative media formulation may be considered for future model iterations that is cGMP compliant (Zimmermann, 2020).

In conclusion, the experiments in this report demonstrate that C4 spheroids composed of four different hiPSC-derived cell populations (CMs, ECs, SMCs, and CFs) can be efficiently manufactured via a 3D suspension culture that is compatible with a wide range of applications and research equipment. Measures of spheroid size and cell viability were significantly greater in C4 spheroids than in spheroids lacking CFs after 60 days of culture, and the inclusion of vascular cells and CFs tended to promote sarcomere maturation and CM energy production. Future work will continue to investigate methods for improving CM maturity and spheroid yield while incorporating automated processes that are suitable for large-scale production facilities (Table 1).

Data availability statement

The raw data supporting the conclusion of this article will be made available by the authors, without undue reservation.

Author contributions

AK-K developed the fabrication protocol, designed the experiments, performed histology and imaging, sample preparation, and wrote the manuscript. DP assisted in experimental design, collected TEM images, and completed manuscript edits. BG performed cell culture and sample analysis. XL assisted in experimental design and performed cell culture. YW assisted in experimental design and performed cell culture. JhZ differentiated and characterized the CFs. AQ collected data on bioenergetics. YN and TK assisted in experimental design and manuscript edits. LY helped with manuscript preparation and revisions. JyZ provided project leadership, funding acquisition, method development and manuscript revisions.

Conflict of interest

The authors declare that the research was conducted in the absence of any commercial or financial relationships that could be construed as a potential conflict of interest.

Publisher's note

All claims expressed in this article are solely those of the authors and do not necessarily represent those of their affiliated organizations, or those of the publisher, the editors and the reviewers. Any product that may be evaluated in this article, or claim that may be made by its manufacturer, is not guaranteed or endorsed by the publisher.

Supplementary material

The Supplementary Material for this article can be found online at: https://www.frontiersin.org/articles/10.3389/fbioe.2022.908848/full#supplementary-material

References

Abbasalizadeh, S., Pakzad, M., Cabral, J., and Baharvand, H. (2017). Allogeneic cell therapy manufacturing: Process development technologies and facility design options. *Expert Opin. Biol. Ther.* 17 (10), 1201–1219. doi:10.1080/14712598.2017.1354982

Adams, W. J., Zhang, Y., Cloutier, J., Kuchimanchi, P., Newton, G., Sehrawat, S., et al. (2013). Functional vascular endothelium derived from human induced pluripotent stem cells. *Stem Cell Rep.* 1 (2), 105–113. doi:10.1016/j.stemcr.2013.06.007

Adil, M. M., and Schaffer, D. V. (2017). Expansion of human pluripotent stem cells. *Curr. Opin. Chem. Eng.* 15, 24–35. doi:10.1016/j.coche.2016.11.002

Aguilar, I. N., Smith, L. J., Olivos, D. J., Chu, T.-M. G., Kacena, M. A., Wagner, D. R., et al. (2019). Scaffold-free bioprinting of mesenchymal stem cells with the regenova printer: Optimization of printing parameters. *Bioprinting* 15, e00048. doi:10.1016/j.bprint.2019.e00048

Alexanian, R. A., Mahapatra, K., Lang, D., Vaidyanathan, R., Markandeya, Y. S., Gill, R. K., et al. (2020). Induced cardiac progenitor cells repopulate decellularized mouse heart scaffolds and differentiate to generate cardiac tissue. *Biochimica Biophysica Acta (BBA) - Mol. Cell Res.* 1867 (3), 118559. doi:10.1016/j.bbamcr.2019.118559

Alonzo, M., AnilKumar, S., Roman, B., Tasnim, N., and Joddar, B. (2019). 3D bioprinting of cardiac tissue and cardiac stem cell therapy. *Transl. Res.* 211, 64–83. doi:10.1016/j.trsl.2019.04.004

Arai, K., Murata, D., Takao, S., Nakamura, A., Itoh, M., Kitsuka, T., et al. (2020). Drug response analysis for scaffold-free cardiac constructs fabricated using bio-3D printer. *Sci. Rep.* 10 (1), 8972. doi:10.1038/s41598-020-65681-y

Ayoubi, S., Sheikh, S. P., and Eskildsen, T. V. (2017). Human induced pluripotent stem cell-derived vascular smooth muscle cells: Differentiation and therapeutic potential. *Cardiovasc. Res.* 113 (11), 1282–1293. doi:10.1093/cvr/cvx125

Banerjee, I., Fuseler, J. W., Price, R. L., Borg, T. K., and Baudino, T. A. (2007). Determination of cell types and numbers during cardiac development in the neonatal and adult rat and mouse. *Am. J. Physiology-Heart Circulatory Physiology* 293 (3), H1883–H1891. doi:10.1152/ajpheart.00514.2007

Bayrak, G. K., and Gümüşderelioğlu, M. (2019). Construction of cardiomyoblast sheets for cardiac tissue repair: Comparison of three different approaches. *Cytotechnology* 71 (4), 819–833. doi:10.1007/s10616-019-00325-2

Beauchamp, P., Jackson, C. B., Ozhathil, L. C., Agarkova, I., Galindo, C. L., Sawyer, D. B., et al. (2020). 3D Co-culture of hiPSC-derived cardiomyocytes with cardiac fibroblasts improves tissue-like features of cardiac spheroids. *Front. Mol. Biosci.* 7, 14. doi:10.3389/fmolb.2020.00014

Beauchamp, P., Moritz, W., Kelm, J. M., Ullrich, N. D., Agarkova, I., Anson, B. D., et al. (2015). Development and characterization of a scaffold-free 3D spheroid model of induced pluripotent stem cell-derived human cardiomyocytes. *Tissue Eng. Part C. Methods* 21 (8), 852–861. doi:10.1089/ten.tec.2014.0376

Bin Lin, B., Lin, X., Stachel, M., Wang, E., Luo, Y., Lader, J., et al. (2017). Culture in glucose-depleted medium supplemented with fatty acid and 3, 3', 5-Triiodo-l-Thyronine facilitates purification and maturation of human pluripotent stem cell-derived cardiomyocytes. *Front. Endocrinol.* 8, 253. doi:10.3389/fendo.2017.00253

Binah, O., Dolnikov, K., Sadan, O., Shilkrut, M., Zeevi-Levin, N., Amit, M., et al. (2007). Functional and developmental properties of human embryonic stem cells–derived cardiomyocytes. *J. Electrocardiol.* 40 (6), S192–S196. doi:10.1016/j.jelectrocard.2007.05.035

Buono, M. F., Boehmer, L. v., Strang, J., Hoerstrup, S. P., Emmert, M. Y., Nugraha, B., et al. (2020). Human cardiac organoids for modeling genetic cardiomyopathy. *Cells* 9 (7), 1733. doi:10.3390/cells9071733

Cao, F., Wagner, R. A., Wilson, K. D., Xie, X., Fu, J.-D., Drukker, M., et al. (2008). Transcriptional and functional profiling of human embryonic stem cell-derived cardiomyocytes. *PLoS ONE* 3 (10), e3474. doi:10.1371/journal.pone.0003474

Caspi, O., Itzhaki, I., Kehat, I., Gepstein, A., Arbel, G., Huber, I., et al. (2009). *In vitro* electrophysiological drug testing using human embryonic stem cell derived cardiomyocytes. *Stem Cells Dev.* 18 (1), 161–172. doi:10.1089/scd.2007.0280

Chan, Y.-C., Ting, S., Lee, Y.-K., Ng, K.-M., Zhang, J., Chen, Z., et al. (2013). Electrical stimulation promotes maturation of cardiomyocytes derived from human embryonic stem cells. *J. Cardiovasc. Transl. Res.* 6 (6), 989–999. doi:10.1007/s12265-013-9510-z

Chang, S., Finklea, F., Williams, B., Hammons, H., Hodge, A., Scott, S., et al. (2020). Emulsion-based encapsulation of pluripotent stem cells in hydrogel microspheres for cardiac differentiation. *Biotechnol. Prog.* 36 (4), e2986. doi:10.1002/btpr.2986

Daly, A. C., Davidson, M. D., and Burdick, J. A. (2021). 3D bioprinting of high cell-density heterogeneous tissue models through spheroid fusion within self-healing hydrogels. *Nat. Commun.* 12 (1), 753. doi:10.1038/s41467-021-21029-2

Das, S., Kim, S.-W., Choi, Y.-J., Lee, S., Lee, S.-H., Kong, J.-S., et al. (2019). Decellularized extracellular matrix bioinks and the external stimuli to enhance cardiac tissue development *in vitro*. *Acta Biomater.* 95, 188–200. Acta Biomater 70 2018. doi:10.1016/j.actbio.2019.04.026

Duan, B. (2016). State-of-the-Art review of 3D bioprinting for cardiovascular tissue engineering. *Ann. Biomed. Eng.* 45 (1), 195–209. doi:10.1007/s10439-016-1607-5

Fischer, B., Meier, A., Dehne, A., Salhotra, A., Tran, T. A., Neumann, S., et al. (2018). A complete workflow for the differentiation and the dissociation of hiPSC-derived cardiospheres. *Stem Cell Res.* 32, 65–72. doi:10.1016/j.scr.2018.08.015

Gao, L., Gregorich, Z. R., Zhu, W., Mattapally, S., Oduk, Y., Lou, X., et al. (2018). Large cardiac muscle patches engineered from human induced-pluripotent stem cell–derived cardiac cells improve recovery from myocardial infarction in swine. *Circulation* 137 (16), 1712–1730. doi:10.1161/circulationaha.117.030785

Garzoni, L. R., Rossi, M. I. D., Barros, A. P. D. N. d., Guarani, V., Keramidas, M., Balottin, L. B. L., et al. (2009). Dissecting coronary angiogenesis: 3D co-culture of cardiomyocytes with endothelial or mesenchymal cells. *Exp. Cell Res.* 315 (19), 3406–3418. doi:10.1016/j.yexcr.2009.09.016

Giacomelli, E., Bellin, M., Sala, L., Meer, B. J. v., Tertoolen, L. G. J., Orlova, V. V., et al. (2017). Three-dimensional cardiac microtissues composed of cardiomyocytes and endothelial cells co-differentiated from human pluripotent stem cells. *Dev. Camb. Engl.* 144 (6), 1008–1017. doi:10.1242/dev.143438

Giacomelli, E., Meraviglia, V., Campostrini, G., Cochrane, A., Cao, X., Helden, R. W. J. v., et al. (2020). Human-iPSC-Derived cardiac stromal cells enhance maturation in 3D cardiac microtissues and reveal non-cardiomyocyte contributions to heart disease. *Cell Stem Cell* 26 (6), 862–879.e11. e811. doi:10.1016/j.stem.2020.05.004

Giacomelli, E., Sala, L., Oostwaard, D. W.-v., and Bellin, M. (2021). Cardiac microtissues from human pluripotent stem cells recapitulate the phenotype of long-QT syndrome. *Biochem. Biophysical Res. Commun.* 572, 118–124. doi:10.1016/j.bbrc.2021.07.068

Guo, Y., and Pu, W. T. (2020). Cardiomyocyte maturation. *Circ. Res.* 126 (8), 1086–1106. doi:10.1161/circresaha.119.315862

Haishuang Lin, H., Li, Q., and Lei, Y. (2017). Three-dimensional tissues using human pluripotent stem cell spheroids as biofabrication building blocks. *Biofabrication* 9 (2), 025007. doi:10.1088/1758-5090/aa663b

Helms, H. R., Jarrell, D. K., and Jacot, J. G. (2019). Generation of cardiac organoids using cardiomyocytes, endothelial cells, epicardial cells, and cardiac fibroblasts derived from human induced pluripotent stem cells. *FASEB J.* 33 (S1), lb170. doi:10.1096/fasebj.2019.33.1_supplement.lb170

Hoang, P., Wang, J., Conklin, B. R., Healy, K. E., and Ma, Z. (2018). Generation of spatial-patterned early-developing cardiac organoids using human pluripotent stem cells. *Nat. Protoc.* 13 (4), 723–737. doi:10.1038/nprot.2018.006

Hochman-Mendez, C., Campos, D. B. P. d., Pinto, R. S., Mendes, B. J. d. S., Rocha, G. M., Monnerat, G., et al. (2020). Tissue-engineered human embryonic stem cell-containing cardiac patches: Evaluating recellularization of decellularized matrix. *J. Tissue Eng.* 11, 204173142092148. doi:10.1177/2041731420921482

Hodgkinson, C. P., Bareja, A., Gomez, J. A., and Dzau, V. J. (2016). Emerging concepts in paracrine mechanisms in regenerative cardiovascular medicine and biology. *Circ. Res.* 118 (1), 95–107. doi:10.1161/circresaha.115.305373

Huebsch, N., Loskill, P., Deveshwar, N., Spencer, C. I., Judge, L. M., Mandegar, M. A., et al. (2016). Miniaturized iPS-cell-derived cardiac muscles for physiologically relevant drug response analyses. *Sci. Rep.* 6 (1), 24726. doi:10.1038/srep24726

Ishigami, M., Masumoto, H., Ikuno, T., Aoki, T., Kawatou, M., Minakata, K., et al. (2018). Human iPS cell-derived cardiac tissue sheets for functional restoration of infarcted porcine hearts. *PLoS ONE* 13 (8), e0201650. doi:10.1371/journal.pone.0201650

Israeli, Y., Gabalski, M., Ball, K., Wasserman, A., Zou, J., Ni, G., et al. (2020). *Generation of heart organoids modeling early human cardiac development under defined conditions*. Laurel Hollow: bioRxiv. doi:10.1101/2020.06.25.171611

Ivanov, D. P., Parker, T. L., Walker, D. A., Alexander, C., Ashford, M. B., Gellert, P. R., et al. (2014). Multiplexing spheroid volume, resazurin and acid phosphatase viability assays for high-throughput screening of tumour spheroids and stem cell neurospheres. *PLoS ONE* 9 (8), e103817. doi:10.1371/journal.pone.0103817

Jackman, C. P., Carlson, A. L., and Bursac, N. (2016). Dynamic culture yields engineered myocardium with near-adult functional output. *Biomaterials* 111, 66–79. Circ. Res. 109 2011. doi:10.1016/j.biomaterials.2016.09.024

Jackman, C., Li, H., and Bursac, N. (2018). Long-term contractile activity and thyroid hormone supplementation produce engineered rat myocardium with adult-like structure and function. *Acta Biomater.* 78, 98–110. Current opinion in chemical engineering 7 2015). doi:10.1016/j.actbio.2018.08.003

Jha, R., Wu, Q., Singh, M., Preininger, M. K., Han, P., Ding, G., et al. (2016). Simulated microgravity and 3D culture enhance induction, viability, proliferation and differentiation of cardiac progenitors from human pluripotent stem cells. *Sci. Rep.* 6 (1), 30956. doi:10.1038/srep30956

Kahn-Krell, A., Pretorius, D., Ou, J., Fast, V. G., Litovsky, S., Berry, J., et al. (2021). Bioreactor suspension culture: Differentiation and production of cardiomyocyte spheroids from human induced pluripotent stem cells. *Front. Bioeng. Biotechnol.* 9, 674260. doi:10.3389/fbioe.2021.674260

Kai-Li Wang, K.-L., Xue, Q., Xu, X.-H., Hu, F., and Shao, H. (2021). Recent progress in induced pluripotent stem cell-derived 3D cultures for cardiac regeneration. *Cell Tissue Res.* 384 (2), 231–240. doi:10.1007/s00441-021-03414-x

Karbassi, E., Fenix, A., Marchiano, S., Muraoka, N., Nakamura, K., Yang, X., et al. (2020). Cardiomyocyte maturation: Advances in knowledge and implications for regenerative medicine. *Nat. Rev. Cardiol.* 17 (6), 341–359. doi:10.1038/s41569-019-0331-x

Kaupisch, A., Kennedy, L., Stelmanis, V., Tye, B., Kane, N. M., Mountford, J. C., et al. (2012). Derivation of vascular endothelial cells from human embryonic stem cells under GMP-compliant conditions: Towards clinical studies in ischaemic disease. *J. Cardiovasc. Transl. Res.* 5 (5), 605–617. doi:10.1007/s12265-012-9379-2

Keung, W., Chan, P. K. W., Backeris, P. C., Lee, E. K., Wong, N., Wong, A. O. T., et al. (2019). Human cardiac ventricular-like organoid chambers and tissue strips from pluripotent stem cells as a two-tiered assay for inotropic responses. *Clin. Pharmacol. Ther.* 106 (2), 402–414. doi:10.1002/cpt.1385

Kim, C., Majdi, M., Xia, P., Wei, K. A., Talantova, M., Spiering, S., et al. (2010). Non-cardiomyocytes influence the electrophysiological maturation of human embryonic stem cell-derived cardiomyocytes during differentiation. *Stem Cells Dev.* 19 (6), 783–795. doi:10.1089/scd.2009.0349

Kim, T. Y., Kofron, C. M., King, M. E., Markes, A. R., Okundaye, A. O., Qu, Z., et al. (2018). Directed fusion of cardiac spheroids into larger heterocellular microtissues enables investigation of cardiac action potential propagation via cardiac fibroblasts. *PLoS ONE* 13 (5), e0196714. doi:10.1371/journal.pone.0196714

Kim, S. j., Kim, E. M., Yamamoto, M., Park, H., and Shin, H. (2020). Engineering multi-cellular spheroids for tissue engineering and regenerative medicine. *Adv. Healthc. Mat.* 9 (23), 2000608. doi:10.1002/adhm.202000608

Kupfer, M. E., Lin, W.-H., Ravikumar, V., Qiu, K., Wang, L., Gao, L., et al. (2020). *In situ* expansion, differentiation, and electromechanical coupling of human cardiac muscle in a 3D bioprinted, chambered organoid. *Circ. Res.* 127 (2), 207–224. doi:10.1161/circresaha.119.316155

Kwong, G., Marquez, H. A., Yang, C., Wong, J. Y., and Kotton, D. N. (2019). Generation of a purified iPSC-derived smooth muscle-like population for cell sheet engineering. *Stem Cell Rep.* 13 (3), 499–514. doi:10.1016/j.stemcr.2019.07.014

LaBarge, W., Mattappally, S., Kannappan, R., Fast, V. G., Pretorius, D., Berry, J. L., et al. (2019a). Maturation of three-dimensional, hiPSC-derived cardiomyocyte spheroids utilizing cyclic, uniaxial stretch and electrical stimulation. *PLoS ONE* 14 (7), e0219442. doi:10.1371/journal.pone.0219442

LaBarge, W., Morales, A., Pretorius, D., Kahn-Krell, A. M., Kannappan, R., Zhang, J., et al. (2019b). Scaffold-Free bioprinter utilizing layer-by-layer printing of cellular spheroids. *Micromachines* 10 (9), 570. doi:10.3390/mi10090570

Laflamme, M. A., Chen, K. Y., Naumova, A. V., Muskheli, V., Fugate, J. A., Dupras, S. K., et al. (2007). Cardiomyocytes derived from human embryonic stem cells in pro-survival factors enhance function of infarcted rat hearts. *Nat. Biotechnol.* 25 (9), 1015–1024. doi:10.1038/nbt1327

Langan, L. M., Dodd, N. J., Owen, S. F., Purcell, W. M., Jackson, S. K., Jha, A. N., et al. (2016). Direct measurements of oxygen gradients in spheroid culture system using electron parametric resonance oximetry. *PLoS One* 11 (2), e0149492. doi:10.1371/journal.pone.0149492

Lee, Y.-K., Ng, K.-M., Lai, W.-H., Chan, Y.-C., Lau, Y.-M., Lian, Q., et al. (2011). Calcium homeostasis in human induced pluripotent stem cell-derived cardiomyocytes. *Stem Cell Rev. Rep.* 7 (4), 976–986. doi:10.1007/s12015-011-9273-3

Lee, A., Hudson, A. R., Shiwarski, D. J., Tashman, J. W., Hinton, T. J., Yerneni, S., et al. (2019a). 3D bioprinting of collagen to rebuild components of the human heart. *Science* 365 (6452), 482–487. doi:10.1126/science.aav9051

Lee, M.-O., Jung, K. B., Jo, S.-J., Hyun, S.-A., Moon, K.-S., Seo, J.-W., et al. (2019b). Modelling cardiac fibrosis using three-dimensional cardiac microtissues derived from human embryonic stem cells. *J. Biol. Eng.* 13 (1), 15. doi:10.1186/s13036-019-0139-6

Li, Y., Li, L., Chen, Z.-N., Gao, G., Yao, R., Sun, W., et al. (2017). Engineering-derived approaches for iPSC preparation, expansion, differentiation and applications. *Biofabrication* 9 (3), 032001. doi:10.1088/1758-5090/aa7e9a

Li, Y., Song, D., Mao, L., Abraham, D. M., and Bursac, N. (2020). Lack of Thy1 defines a pathogenic fraction of cardiac fibroblasts in heart failure. *Biomaterials* 236, 119824. doi:10.1016/j.biomaterials.2020.119824

Lian, X., Hsiao, C., Wilson, G., Zhu, K., Hazeltine, L. B., Azarin, S. M., et al. (2012). Robust cardiomyocyte differentiation from human pluripotent stem cells via temporal modulation of canonical Wnt signaling. *Proc. Natl. Acad. Sci. U. S. A.* 109 (27), E1848–E1857. doi:10.1073/pnas.1200250109

Liu, X., Qi, J., Xu, X., Zeisberg, M., Guan, K., Zeisberg, E. M., et al. (2016). Differentiation of functional endothelial cells from human induced pluripotent stem cells: A novel, highly efficient and cost effective method. *Differentiation* 92 (4), 225–236. doi:10.1016/j.diff.2016.05.004

Liu, L., Jin, X., Hu, C.-F., Li, R., Zhou, Z. e., Shen, C.-X., et al. (2017). Exosomes derived from mesenchymal stem cells rescue myocardial ischaemia/reperfusion injury by inducing cardiomyocyte autophagy via AMPK and akt pathways. *Cell. Physiol. biochem.* 43 (1), 52–68. doi:10.1159/000480317

Long, C., Li, H., Tiburcy, M., Rodriguez-Caycedo, C., Kyrychenko, V., Zhou, H., et al. (2018). Correction of diverse muscular dystrophy mutations in human engineered heart muscle by single-site genome editing. *Sci. Adv.* 4 (1), eaap9004. doi:10.1126/sciadv.aap9004

Lu Wang, L., Serpooshan, V., and Zhang, J. (2021). Engineering human cardiac muscle patch constructs for prevention of post-infarction LV remodeling. *Front. Cardiovasc. Med.* 8, 621781. doi:10.3389/fcvm.2021.621781

Lux, M., Andrée, B., Horvath, T., Nosko, A., Manikowski, D., Hilfiker-Kleiner, D., et al. (2016). *In vitro* maturation of large-scale cardiac patches based on a perfusable starter matrix by cyclic mechanical stimulation. *Acta Biomater.* 30, 177–187. doi:10.1016/j.actbio.2015.11.006

Maiullari, F., Costantini, M., Milan, M., Pace, V., Chirivì, M., Maiullari, S., et al. (2018). A multi-cellular 3D bioprinting approach for vascularized heart tissue engineering based on HUVECs and iPSC-derived cardiomyocytes. *Sci. Rep.* 8 (1), 13532. doi:10.1038/s41598-018-31848-x

Mathur, A., Loskill, P., Shao, K., Huebsch, N., Hong, S., Marcus, S. G., et al. (2015). Human iPSC-based cardiac microphysiological system for drug screening applications. *Sci. Rep.* 5 (1), 8883. doi:10.1038/srep08883

Mattapally, S., Zhu, W., Fast, V. G., Gao, L., Worley, C., Kannappan, R., et al. (2018). Spheroids of cardiomyocytes derived from human-induced pluripotent stem cells improve recovery from myocardial injury in mice. *Am. J. Physiology-Heart Circulatory Physiology* 315 (2), H327–H339. doi:10.1152/ajpheart.00688.2017

Menasché, P., Hagège, A. A., Scorsin, M., Pouzet, B., Desnos, M., Duboc, D., et al. (2001). Myoblast transplantation for heart failure. *Lancet* 357 (9252), 279–280. doi:10.1016/s0140-6736(00)03617-5

Mills, R. J., Titmarsh, D. M., Koenig, X., Parker, B. L., Ryall, J. G., Quaife-Ryan, G. A., et al. (2017). Functional screening in human cardiac organoids reveals a metabolic mechanism for cardiomyocyte cell cycle arrest. *Proc. Natl. Acad. Sci. U. S. A.* 114 (40), E8372–E8381. doi:10.1073/pnas.1707316114

Miwa, T., Idiris, A., and Kumagai, H. (2020). A novel cardiac differentiation method of a large number and uniformly-sized spheroids using microfabricated culture vessels. *Regen. Ther.* 15, 18–26. doi:10.1016/j.reth.2020.04.008

Munarin, F., Kant, R. J., Rupert, C. E., Khoo, A., and Coulombe, K. L. K. (2020). Engineered human myocardium with local release of angiogenic proteins improves vascularization and cardiac function in injured rat hearts. *Biomaterials* 251, 120033. doi:10.1016/j.biomaterials.2020.120033

Noor, N., Shapira, A., Edri, R., Gal, I., Wertheim, L., Dvir, T., et al. (2019). 3D printing of personalized thick and perfusable cardiac patches and hearts. *Adv. Sci. (Weinh).* 6 (11), 1900344. doi:10.1002/advs.201900344

Nugraha, B., Buono, M. F., Boehmer, L., Hoerstrup, S. P., and Emmert, M. Y. (2019). Human cardiac organoids for disease modeling. *Clin. Pharmacol. Ther.* 105 (1), 79–85. doi:10.1002/cpt.1286

Palpant, N. J., Pabon, L., Friedman, C. E., Roberts, M., Hadland, B., Zaunbrecher, R. J., et al. (2017). Generating high-purity cardiac and endothelial derivatives from patterned mesoderm using human pluripotent stem cells. *Nat. Protoc.* 12 (1), 15–31. doi:10.1038/nprot.2016.153

Parikh, S. S., Blackwell, D. J., Gomez-Hurtado, N., Frisk, M., Wang, L., Kim, K., et al. (2017). Thyroid and glucocorticoid hormones promote functional T-tubule development in human-induced pluripotent stem cell–derived cardiomyocytes. *Circ. Res.* 121 (12), 1323–1330. doi:10.1161/circresaha.117.311920

Pinto, A. R., Ilinykh, A., Ivey, M. J., Kuwabara, J. T., D'Antoni, M. L., Debuque, R., et al. (2016). Revisiting cardiac cellular composition. *Circ. Res.* 118 (3), 400–409. doi:10.1161/circresaha.115.307778

Polonchuk, L., Surija, L., Lee, M. H., Sharma, P., Ming, C. L. C., Richter, F., et al. (2021). Towards engineering heart tissues from bioprinted cardiac spheroids. *Biofabrication* 13 (4), 045009. doi:10.1088/1758-5090/ac14ca

Pretorius, D., Kahn-Krell, A. M., Lou, X., Fast, V. G., Berry, J. L., Kamp, T. J., et al. (2021). Layer-by-layer fabrication of large and thick human cardiac muscle patch constructs with superior electrophysiological properties. *Front. Cell Dev. Biol.* 9, 670504. doi:10.3389/fcell.2021.670504

Qasim, M., Haq, F., Kang, M.-H., and Kim, J.-H. (2019). 3D printing approaches for cardiac tissue engineering and role of immune modulation in tissue regeneration. *Int. J. Nanomedicine* 14, 1311–1333. doi:10.2147/ijn.s189587

Ravenscroft, S. M., Pointon, A., Williams, A. W., Cross, M. J., and Sidaway, J. E. (2016). Cardiac non-myocyte cells show enhanced pharmacological function suggestive of contractile maturity in stem cell derived cardiomyocyte microtissues. *Toxicol. Sci.* 152 (1), 99–112. doi:10.1093/toxsci/kfw069

Richards, D. J., Tan, Y., Coyle, R., Li, Y., Xu, R., Yeung, N., et al. (2016). Nanowires and electrical stimulation synergistically improve functions of hiPSC cardiac spheroids. *Nano Lett.* 16 (7), 4670–4678. doi:10.1021/acs.nanolett.6b02093

Robertson, C., Tran, D. D., and George, S. C. (2013). Concise review: Maturation phases of human pluripotent stem cell-derived cardiomyocytes. *STEM CELLS* 31 (5), 829–837. doi:10.1002/stem.1331

Ruan, J.-L., Tulloch, N. L., Razumova, M. V., Saiget, M., Muskheli, V., Pabon, L., et al. (2016). Mechanical stress conditioning and electrical stimulation promote contractility and force maturation of induced pluripotent stem cell-derived human cardiac tissue. *Circulation* 134 (20), 1557–1567. doi:10.1161/circulationaha.114.014998

Sacchetto, C., Vitiello, L., Windt, L. J. d., Rampazzo, A., and Calore, M. (2020). Modeling cardiovascular diseases with hiPSC-derived cardiomyocytes in 2D and 3D cultures. *Int. J. Mol. Sci.* 21 (9), 3404. doi:10.3390/ijms21093404

Sanganalmath, S. K., and Bolli, R. (2013). Cell therapy for heart failure. *Circ. Res.* 113 (6), 810–834. doi:10.1161/circresaha.113.300219

Schaefer, J. A., Guzman, P. A., Riemenschneider, S. B., Kamp, T. J., and Tranquillo, R. T. (2017). A cardiac patch from aligned microvessel and cardiomyocyte patches. *J. Tissue Eng. Regen. Med.* 12 (2), 546–556. doi:10.1002/term.2568

Schulze, M. L., Lemoine, M. D., Fischer, A. W., Scherschel, K., David, R., Riecken, K., et al. (2019). Dissecting hiPSC-CM pacemaker function in a cardiac organoid model. *Biomaterials* 206, 133–145. doi:10.1016/j.biomaterials.2019.03.023

Selvaraj, S., Mondragon-Gonzalez, R., Xu, B., Magli, A., Kim, H., Lainé, J., et al. (2019). Screening identifies small molecules that enhance the maturation of human pluripotent stem cell-derived myotubes. *eLife* 8, e47970. doi:10.7554/elife.47970

Shadrin, I. Y., Allen, B. W., Qian, Y., Jackman, C. P., Carlson, A. L., Juhas, M. E., et al. (2017). Cardiopatch platform enables maturation and scale-up of human pluripotent stem cell-derived engineered heart tissues. *Nat. Commun.* 8 (1), 1825. doi:10.1038/s41467-017-01946-x

Sriram, G., Tan, J. Y., Islam, I., Rufaihah, A. J., and Cao, T. (2015). Efficient differentiation of human embryonic stem cells to arterial and venous endothelial cells under feeder- and serum-free conditions. *Stem Cell Res. Ther.* 6 (1), 261. doi:10.1186/s13287-015-0260-5

Strikoudis, A., Cieślak, A., Loffredo, L., Chen, Y.-W., Patel, N., Saqi, A., et al. (2019). Modeling of fibrotic Lung disease using 3D organoids derived from human pluripotent stem cells. *Cell Rep.* 27 (12), 3709–3723.e5. doi:10.1016/j.celrep.2019.05.077

Sun, X., and Nunes, S. S. (2016). Biowire platform for maturation of human pluripotent stem cell-derived cardiomyocytes. *Methods* 101, 21–26. doi:10.1016/j.ymeth.2015.11.005

Synnergren, J., Åkesson, K., Dahlenborg, K., Vidarsson, H., Améen, C., Steel, D., et al. (2008). Molecular signature of cardiomyocyte clusters derived from human embryonic stem cells. *STEM CELLS* 26 (7), 1831–1840. doi:10.1634/stemcells.2007-1033

Synnergren, J., Heins, N., Brolén, G., Eriksson, G., Lindahl, A., Hyllner, J., et al. (2010). Transcriptional profiling of human embryonic stem cells differentiating to definitive and primitive endoderm and further toward the hepatic lineage. *Stem Cells Dev.* 19 (7), 961–978. doi:10.1089/scd.2009.0220

Thomas, D., Kim, H., Lopez, N., and Wu, J. C. (2021). Fabrication of 3D cardiac microtissue arrays using human iPSC-derived cardiomyocytes, cardiac fibroblasts, and endothelial cells. *J. Vis. Exp.* 169 (169). doi:10.3791/61879

Tomov, M. L., Gil, C. J., Cetnar, A., Theus, A. S., Lima, B. J., Nish, J. E., et al. (2019). Engineering functional cardiac tissues for regenerative medicine applications. *Curr. Cardiol. Rep.* 21 (9), 105. doi:10.1007/s11886-019-1178-9

Tsuruyama, S., Matsuura, K., Sakaguchi, K., and Shimizu, T. (2019). Pulsatile tubular cardiac tissues fabricated by wrapping human iPS cells-derived cardiomyocyte sheets. *Regen. Ther.* 11, 297–305. doi:10.1016/j.reth.2019.09.001

Voges, H. K., Mills, R. J., Elliott, D. A., Parton, R. G., Porrello, E. R., Hudson, J. E., et al. (2017). Development of a human cardiac organoid injury model reveals innate regenerative potential. *Development* 144 (6), 1118–1127. doi:10.1242/dev.143966

Xu, X. Q., Soo, S. Y., Sun, W., and Zweigerdt, R. (2009). Global expression profile of highly enriched cardiomyocytes derived from human embryonic stem cells. *STEM CELLS* 27 (9), 2163–2174. doi:10.1002/stem.166

Yang, L., Geng, Z., Nickel, T., Johnson, C., Gao, L., Dutton, J., et al. (2016). Differentiation of human induced-pluripotent stem cells into smooth-muscle cells: Two novel protocols. *PLoS ONE* 11 (1), e0147155. doi:10.1371/journal.pone.0147155

Ye, L., Chang, Y.-H., Xiong, Q., Zhang, P., Zhang, L., Somasundaram, P., et al. (2014). Cardiac repair in a porcine model of acute myocardial infarction with human induced pluripotent stem cell-derived cardiovascular cells. *Cell Stem Cell* 15 (6), 750–761. doi:10.1016/j.stem.2014.11.009

Zhang, J., Klos, M., Wilson, G. F., Herman, A. M., Lian, X., Raval, K. K., et al. (2012). Extracellular matrix promotes highly efficient cardiac differentiation of human pluripotent stem cells: The matrix sandwich method. *Circ. Res.* 111 (9), 1125–1136. doi:10.1161/CIRCRESAHA.112.273144

Zhang, L., Guo, J., Zhang, P., Xiong, Q., Wu, S. C., Xia, L., et al. (2014). Derivation and high engraftment of patient-specific cardiomyocyte sheet using induced pluripotent stem cells generated from adult cardiac fibroblast. *Circ. Heart Fail.* 8 (1), 156–166. doi:10.1161/circheartfailure.114.001317

Zhang, W., Kong, C. W., Tong, M. H., Chooi, W. H., Huang, N., Li, R. A., et al. (2017). Maturation of human embryonic stem cell-derived cardiomyocytes (hESC-CMs) in 3D collagen matrix: Effects of niche cell supplementation and mechanical stimulation. *Acta Biomater.* 49, 204–217. doi:10.1016/j.actbio.2016.11.058

Zhang, J., Tao, R., Campbell, K. F., Carvalho, J. L., Ruiz, E. C., Kim, G. C., et al. (2019). Functional cardiac fibroblasts derived from human pluripotent stem cells via second heart field progenitors. *Nat. Commun.* 10 (1), 2238. doi:10.1038/s41467-019-09831-5

Zhang, J., Bolli, R., Garry, D. J., Marbán, E., Menasché, P., Zimmermann, W.-H., et al. (2021a). Basic and translational research in cardiac repair and regeneration. *J. Am. Coll. Cardiol.* 78 (21), 2092–2105. doi:10.1016/j.jacc.2021.09.019

Zhang, J. Z., Zhao, S. R., Tu, C., Pang, P., Zhang, M., Wu, J. C., et al. (2021b). Protocol to measure contraction, calcium, and action potential in human-induced pluripotent stem cell-derived cardiomyocytes. *Star. Protoc.* 2 (4), 100859. doi:10.1016/j.xpro.2021.100859

Zhu, W., Gao, L., and Zhang, J. (2017). Pluripotent stem cell derived cardiac cells for myocardial repair. *J. Vis. Exp.* 120, 55142. doi:10.3791/55142

Zimmermann, W.-H. (2020). Tissue engineered heart repair from preclinical models to first-in-patient studies. *Curr. Opin. Physiology* 14, 70–77. doi:10.1016/j.cophys.2020.02.001

The Inhibitory Effect of Regulatory T Cells on the Intimal Hyperplasia of Tissue-Engineered Blood Vessels in Diabetic Pigs

Fengjie Guo[1], Zhipeng Ren[2], Dongxu Liu[3], Linghui Wang[2], Xiaobin Hou[2]* and Wen Chen[3]*

[1]Outpatient Department, The 8th Medical Center, Chinese PLA General Hospital, Beijing, China, [2]Department of Thoracic Surgery, The First Medical Center, Chinese PLA General Hospital, Beijing, China, [3]Department of Pathology, The 8th Medical Center, Chinese PLA General Hospital, Beijing, China

Severe inflammatory response and functional impairment of endothelial progenitor cells (EPCs) often lead to the implantation failure of EPC-captured tissue-engineered blood vessels (TEBVs) in diabetes. Regulatory T cells (Treg cells) are the most important inhibitory immune cells, but their effects in angiogenesis remain undefined, and the differences in the microenvironment may be an important reason. Here, we constructed a TEBV coated with an anti-CD34 antibody-functionalized heparin-collagen multilayer (anti-CD34 antibody-modified TEBV) using layer-by-layer self-assembly. Then, TEBVs were implanted into diabetic pigs. All TEBVs remained unobstructed 60 days after implantation, although varying degrees of intimal hyperplasia were detectable. Severe intimal hyperplasia was observed in the control group and peripheral injection of Treg cells group. Intravenous injection of Treg cells significantly inhibited intimal hyperplasia, inflammation, and cell apoptosis. Moreover, intravenous injection increased the proportion of circulating EPCs, while peripheral injection did not have these effects and reduced microvessel density around the TEBV. Interestingly, many Nestin^{+} cells could be detected in TEBVs, most of which were fusiform, showing the characteristics of smooth-muscle cells. Treg cell intravenous transplantation markedly reduced the number of Nestin^{+} cells in the TEBV. In conclusion, Treg cells inhibited the intimal hyperplasia of TEBVs in diabetic pigs by promoting EPC mobilization, anti-inflammatory action, and cellular protection.

Keywords: regulatory T cell, diabetes, tissue-engineered blood vessel, endothelial progenitor cell, intimal hyperplasia

INTRODUCTION

In recent years, the incidence and mortality of cardiovascular and cerebrovascular diseases have increased year by year, leading to a significant increase in the clinical demand for tissue-engineered blood vessels (TEBVs) (Song et al., 2018). Endothelial progenitor cells (EPCs) were first reported in the late 20th century and specifically express CD34, CD133, VEGFR-2 (KDR), and CD144 (Afshari et al., 2020; Naserian et al., 2020; Xing et al., 2020; Nouri Barkestani et al., 2021). Many scientists constructed EPC-captured TEBVs using CD34 or CD133 antibodies, and animal experiments showed that these TEBVs can achieve rapid endothelialization (Rotmans et al., 2005). However, most patients who need TEBV implantation clinically have underlying diseases such as diabetes. Our

previous study showed that the long-term patency rate of EPC-captured TEBV in diabetic rats was very low, which may be due to various reasons (Chen et al., 2015b). High glucose reduced the number and function of homing EPCs and induced the pathological proliferation of vascular smooth muscle cells (Chen et al., 2015a). Therefore, it is of great clinical significance to improve the patency rate of TEBV in diabetes mellitus.

TEBV implantation inevitably activates the recipient's immune system, and excessive inflammatory response can impair homing EPC function. The occurrence and development of diabetes mellitus are closely related to chronic inflammation and abnormal immune regulation (Halim and Halim, 2019). High glucose can cause excessive activation of the inflammatory response, further damage migrating endothelial cells and homing EPCs, and may cause implantation failure of EPC-captured TEBV (Petrelli et al., 2012). Regulatory T cells (Treg cells) are the primary inhibitory immune cells that can down-regulate an overactive immune response by secreting immunosuppressive molecules or by direct cellular contact (Kawada, 2018). In diabetic patients, Treg cell numbers were significantly decreased, while Th1 cell proliferation and interferon-γ concentrations were increased, leading to excessive inflammatory responses (Qin et al., 2021; Zhou et al., 2021). We speculate that Treg cell transplantation may be an effective method to improve the patency of TEBV in diabetes mellitus.

The interaction between Treg cells and angiogenesis was considered to be "a dark double track" (Gasparri et al., 2013). Some studies have found that Treg cells are an important source of VEGF in cancer, and the elimination of Treg cells can significantly reduce the production of VEGF. However, other studies have shown that Treg cells inhibit angiogenesis in ischemic tissue by reducing T cell and macrophage infiltration (Zouggari et al., 2009). Many studies have also reported the association between Treg cells and EPCs, and the proportion of Treg cells in peripheral blood is positively correlated with the proportion of early EPCs (Choi et al., 2018). These results suggest that the microenvironment may be an important factor affecting the regulation of angiogenesis by Treg cells. After TEBV implantation, the peripheral blood circulating in the TEBV contains sufficient oxygen and nutrients, while the damaged tissues around TEBV are relatively ischemic and hypoxia, so it can be used as an important model to study the relationship between Treg cells and angiogenesis. Our preliminary results showed that the vascular wall thickness of mice, rats, and rabbits was very thin, and oxygen and nutrients can permeate the whole layer of TEBV. In this study, we constructed a diabetic pig model to study the effect of Treg cells on EPC-captured TEBV in diabetes and to explore the relationship between Treg cells and angiogenesis.

MATERIALS AND METHODS

Construction of an Anti-CD34 Antibody-Modified TEBV

The carotid arteries of female Landrace pigs weighing about 60 kg were used. The blood was repeatedly rinsed with normal saline, and the surrounding fat and connective tissue were removed. The blood vessels were placed in 0.5% trypsin (Hyclone) and incubated at 37° for 12 h. After washing with normal saline three times, the vessels were placed in 0.5% TritonX-100 hypotonic solution (0.01 mol/L TrIS-HCl), shaken, and washed for 24 h. The vessels were then placed in 0.5% TritonX-100 hypertonic solution (1.5 mol/L KCL solution), shaken, and washed for 24 h. After full washing of normal saline, an acellular vascular scaffold was obtained.

We constructed TEBV coated with an anti-CD34 antibody functionalized heparin-collagen multilayer (anti-CD34 antibody modified TEBV) using layer-by-layer self-assembly. The acellular vascular scaffold was immersed in 3 mg/ml PEI solution (Sigma) for 2 h. After washing with PBS three times, immersing vascular scaffold in 1 mg/ml heparin solution (negative charge) for 15 min. After washing with ABS buffer three times, the vascular scaffold was immersed in 1 mg/ml collagen solution (positive charge) for 15 min. Heparin solution and collagen solution were alternately treated 10 times to obtain a vascular scaffold coated with a heparin-collagen multilayer. After washing with ABS buffer three times, the vascular scaffold was placed in 0.25% glutaraldehyde for 2 h and washed with PBS 3 times. Then placing it in 60 ug/mL anti-CD34 antibody solution (Abcam) and incubated for 12 h under dark conditions. After washing with PBS three times, anti-CD34 antibody modified TEBV was obtained.

Hemolytic Test

The experiment was divided into five groups: negative control group (0.9% NaCl solution), positive control group (Double distilled water), matrix group (Acellular vascular matrix), Hep-Col group (TEBV scaffold after coating 10 layers), and CD34 group (anti-CD34 antibody modified TEBV). 4 ml of anticoagulant peripheral blood from pigs was collected and then diluted with 0.9% NaCl solution in a ratio of 4:5. Then diluted blood was added to each group, followed by a 37-degree water bath for 1 h, and centrifugation at 1500 g for 5 min. Add the supernatant to the 96-well plate, and test the absorbance of each group (OD: 570 nm).

Cell Culture

Treg cells were isolated from peripheral blood of pig receptors using EasySep™ CD4+CD127lowCD25+ Treg sorting kit (Novobiotec) and cultured in RPMI1640 containing 10% fetal bovine serum (Hyclone). Treg cells were further expanded to 3×10^9 with the Treg Expansion Kit (Novobiotec). Isolation and culture of EPCs were performed using the method previously reported. In short, peripheral blood from diabetic patients was collected and mononuclear cells were isolated using lymphocyte separation fluid (Tianjin Haoyang Biological Manufacture Co., Ltd). Isolated mononuclear cells were cultured in an EGM-2 complete medium (Lonza) containing 15% fetal bovine serum. After 48h, unattached cells were removed, and the attached cells continued selective culture.

Animal Experiment

All animal experiments were performed in accordance with the regulations on animal experiments of Chinese PLA General Hospital (Beijing, China) and were approved by the Ethics Committee of Chinese PLA General Hospital (NO:

309201803051058). Referring to previous reports (Lewczuk et al., 2018; Pierzynowska et al., 2020), we used streptozotocin (Sigma) injection to construct a diabetic pig model. After fasting for 16 h, pigs weighing about 60 kg were anesthetized with ketamine (35 mg/kg) and diazepam (1.5 mg/kg), and streptozotocin (150 mg/kg) injected *via* ear vein. Fasting blood glucose was measured 1, 2, 3, and 7 days after administration. Fasting blood glucose > 7 mmol for 7 consecutive days was considered the successful establishment of the diabetes model.

After anesthesia, the common carotid artery was carefully separated after routine disinfection. The proximal and distal ends were blocked with arterial clamps. After the carotid artery was severed, anti-CD34 antibody modified TEBV (about 2.5 cm in length) was anastomosed. Stop the bleeding carefully and close the skin layer by layer. Aspirin enteric-coated tablets (0.1 g/day, orally) and low molecular weight heparin calcium injection (5, 000IU/day, subcutaneously) were given postoperatively. The experiment was divided into four groups: scaffold group (implanting vascular scaffold coated with heparin-collagen multilayer), control group (implanting anti-CD34 antibody modified TEBV), peripheral injection group (Treg cells were injected around TEBV after implantation of anti-CD34 antibody modified TEBV) and intravenous injection group (Treg cells were injected *via* ear vein after implantation of anti-CD34 antibody modified TEBV). There were 8 animals in each group.

Specimen Sampling and Histological Staining

After 60 days of implantation, animals in each group were anesthetized. The implanted TEBVs were collected and fixed in 10% paraformaldehyde for 24 h. After paraffin sections, some sections were stained with hematoxylin and eosin (H&E, Sigma) and some were immunohistochemistry. In short, paraffin sections were routinely dewaxed to water, treated with 3% H_2O_2 for 5 min, and then sealed with sheep serum working solution for 5min anti-CD31, SM-actin, ki-67, CD68, LCA, CD4, CD8, CD20, CD56, CD38 primary antibodies (All purchased from Abcam) were added and incubated overnight at 4°. After washing with PBS 3 times, a biotin-labeled secondary antibody was added and incubated at 37° for 30 min, then washed with PBS 3 times. Streptomycin working solution labeled with horseradish enzyme was added and washed with PBS 3 times, and the color was displayed for 10 min. Rinse thoroughly with running water, redye with hematoxylin, and seal sheet. Both Nestin$^+$ cells and CD90$^+$ cells showed stem cell characteristics and had the potential to differentiate into endothelial cells or smooth muscle cells after implantation of bioartificial blood vessels (Kirkton et al., 2019). Therefore, we further detected the number of Nestin$^+$ cells and CD90$^+$ cells in the implanted TEBVs by immunohistochemistry. Under high power field (HPF), 10 fields were randomly selected to count positive staining cells in each section, and then the average value was calculated.

TUNEL Staining

The slices were treated with 3% H_2O_2 for 10 min and added with 0.1% Triton X-100 for 2 min. After washing with PBS 3 times, the reaction mixture (Roche) was added and incubated at 37° for 60 min. After that, DAPI (Sigma) was added to stain the nuclei and seal the sheet after washing with PBS 3 times.

Flow Cytometry

Peripheral blood of each group was collected 7 days after TEBV implantation. Mononuclear cells were isolated by a lymphocyte separation medium. After washing with PBS 3 times, the fluorescent-dye conjuncted antibodies of CD34, VEGFR-2, ICAM-1, VCAM-1, and E-selection (All purchased from BD) were added and incubated in dark for 15min. After washing with PBS 3 times, the proportion of EPCs and mean fluorescence intensity (MFI) of ICAM-1, VCAM-1, and E-selection was detected by flow cytometry (BD FACSCanto flow cytometer). Plasma was also collected and the concentrations of VEGF and SDF-1 were detected by ELISA (Huijia). The operation was carried out strictly in accordance with ELISA kit instructions.

Co-Culture Experiment

A Transwell chamber was used for the cell co-culture experiment, Treg cells were added into the upper chamber, and mononuclear cells isolated from peripheral blood of diabetic patients were added into the lower chamber. The experiment was divided into 6 groups: diabetes group (untreated mononuclear cells), Treg cell group (Treg cells were co-cultured with mononuclear cells), IL-10 Neu group (Treg cells were co-cultured with mononuclear cells and IL-10 neutralizing antibody were added), TGF-β Neu group (Treg cells were co-cultured with mononuclear cells and TGF-β neutralizing antibody were added), HLA-G Neu group (Treg cells were co-cultured with mononuclear cells and HLA-G neutralizing antibody were added), and CTLA-4 Neu group (Treg cells were co-cultured with mononuclear cells and CTLA-4 neutralizing antibody were added). After co-culture for 48 h, cells of each group were collected. After washing with PBS 3 times, CD34-PE and VEGFR-2-APC (All purchased from BD) were added and incubated in dark for 15min. After washing with PBS 3 times, the proportion of EPCs was detected by flow cytometry.

We further conducted the co-culture experiment of Treg cells and EPCs. After 48 h of co-culture, Treg cells in the upper chamber were removed. After continued culture for 48 h, the supernatant was collected and the concentrations of VEGF and SDF-1 were detected by ELISA. The operation was carried out strictly in accordance with ELISA kit instructions.

EPCs of each group were collected after 1 week. After washing with PBS 3 times, CD31-PE (BD) was added and incubated for 15 min. After washing with PBS 3 times, the proportion of CD31$^+$cells were detected by flow cytometry.

Statistical Evaluation

Data are presented as mean ± SEM. GraphPad Software 5.0 was used for all statistical calculations. To ascertain the significance of differences, we performed ANOVA and Bonferroni post hoc test. A value of $p < 0.05$ was considered statistically significant.

RESULTS

Characteristics of the Anti-CD34 Antibody-Modified Tissue-Engineered Blood Vessel

H&E staining and transmission electron microscopy showed that the TEBV scaffold was basically composed of fibrous tissue,
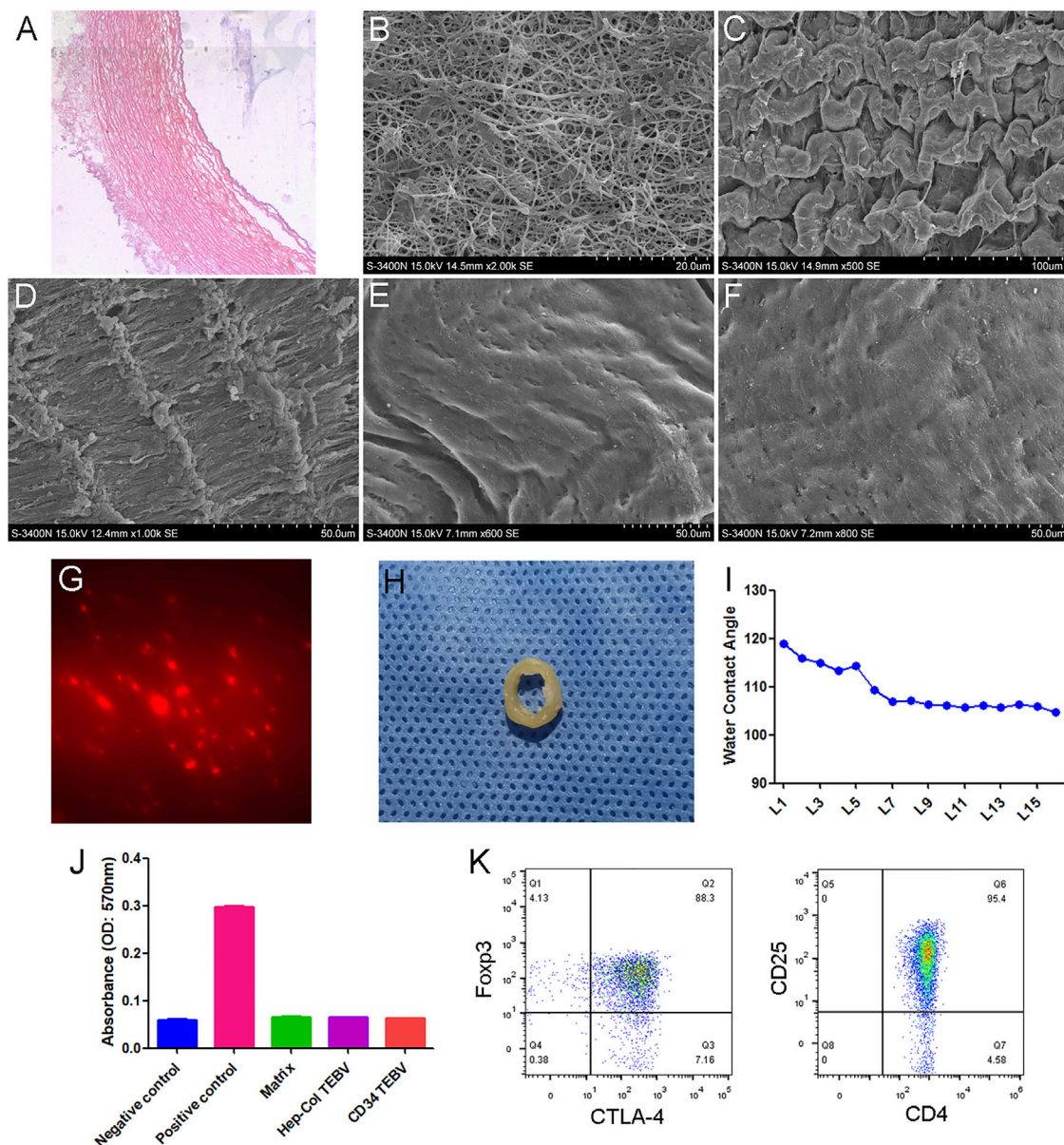
FIGURE 1 | Characteristics of anti-CD34 antibody modified TEBV. **(A)** H&E staining of TEBV acellular scaffold. **(B)** Transmission electron microscopy images. Scanning electron microscope showing the surface of TEBV scaffold before coating **(C)** and after coating 2 layers **(D)**, 5 layers **(E)**, and 10 layers **(F)**. **(G)** Red fluorescence (CD34-PE) could be observed on the surface of TEBV after 2 h of washing with normal saline. **(H)** The general picture of anti-CD34 antibody modified TEBV. **(I)** Water Contact Angle test results showed that the contact angle decreased with the increase of coating layers. The contact angle did not change significantly after 7 layers of coating. **(J)** *In vitro* hemolysis experiments showed that coating of collagen, heparin and CD34 antibody had no significant effect on the hemolysis of the acellular vascular matrix. **(K)** Flow cytometry results showed that more than 90% of the expanded cells expressed both CD4 and CD25. Foxp3 and CTLA-4 were also highly expressed.

without any cells (**Figures 1A,B**). A scanning electron microscope showed that the surface of the TEBV scaffold was flatter and smoother with the increase of coating layers (**Figures 1C–F**). **Figure 1G** showed that red fluorescence (CD34-PE) could be observed on the surface of TEBV after 2 h of washing with normal saline. Water Contact Angle test results showed that the contact angle decreased with the increase of coating layers. The contact angle did not change

significantly after 7 layers of coating (**Figure 1I**). *In vitro* hemolysis experiments showed that the coating of collagen, heparin and CD34 antibody had no significant effect on the hemolysis of the acellular vascular matrix (**Figure 1J**). Treg cells were sorted and expanded *in vitro*. Flow cytometry results showed that more than 90% of the expanded cells expressed both CD4 and CD25, and more than 85% expressed both Foxp3 and CTLA-4 (**Figure 1K**).

FIGURE 2 | Treg cell transplantation inhibited intimal hyperplasia of anti-CD34 antibody modified TEBV in diabetes mellitus. **(A)** H and E staining, all TEBV were not completely blocked at 60 days after implantation. **(B)** The thickness of intimal hyperplasia in the intravenous injection group was smaller than that in the control group and peripheral injection group. **(C)** Immunohistochemistry was used to detect the expression of CD31, SM-actin, and ki-67. An intact endothelial cell layer was observed in the intravenous injection group. **(D)** Ki-67 proliferation index in the intravenous injection group was smaller than that in the control group and peripheral injection group. *$p < 0.05$ ($n = 8$) versus Control group. #$p < 0.05$ ($n = 8$) versus Peripheral injection group. Values are mean ± SD.

Treg cell transplantation inhibited intimal hyperplasia of anti-CD34 antibody modified TEBV in diabetes mellitus.

At 60 days after implantation, all TEBV samples were not completely blocked, mainly due to the heparin coating and anticoagulant therapy. The inner surface of TEBV in the scaffold group was mainly composed of thrombus and organized thrombus, and severe damage and degradation of the TEBV matrix were observed. If further degradation *in vivo*, TEBVs rupture, and massive bleeding may occur. Different degrees of intimal hyperplasia were observed in the control group, peripheral injection group, and intravenous injection group, which did not have continuity with the normal smooth muscle layer in the TEBV scaffold, suggesting that smooth muscle cells in the intimal hyperplasia may be mainly derived from the differentiation of peripheral blood stem cells. The thickness of intimal hyperplasia in the peripheral injection group was smaller than that in the control group, but there was no statistical difference in the ki-67 proliferation index. The thickness of intimal hyperplasia was the smallest in the intravenous injection group, and an intact endothelial cell layer was observed. **Figure 2**.

Treg cell transplantation reduced the inflammatory response associated with TEBV implantation in diabetes mellitus.

Immunohistochemistry was used to label the number of lymphocytes and macrophages, and the density of microvessels. A large number of macrophages and lymphocytes were observed in the scaffold group, which may be an important reason for the rapid degradation of vascular matrix materials. Compared with the control group, the number of macrophages and CD31+ microvessel density around TEBV decreased by 30.53% and 70.18% in the peripheral injection group, respectively, while the number of lymphocytes did not differ statistically between the two groups. Compared with the control group, there was no significant change in CD31+ microvessel density around TEBV in the intravenous injection group, while the number of lymphocytes and macrophages was significantly reduced. **Figures 3A–D**.

Peripheral blood of each group was collected 7 days after TEBV implantation, and the proportion of EPCs and the expression of pro-inflammatory molecules were detected. Flow cytometry showed no statistical difference in the proportion of peripheral blood EPCs and the expression of ICAM-1, VCAM-1, and E-selectin between the scaffold group, control group, and peripheral injection group. ELISA results showed that there were no significant differences in plasma VEGF and SDF-1
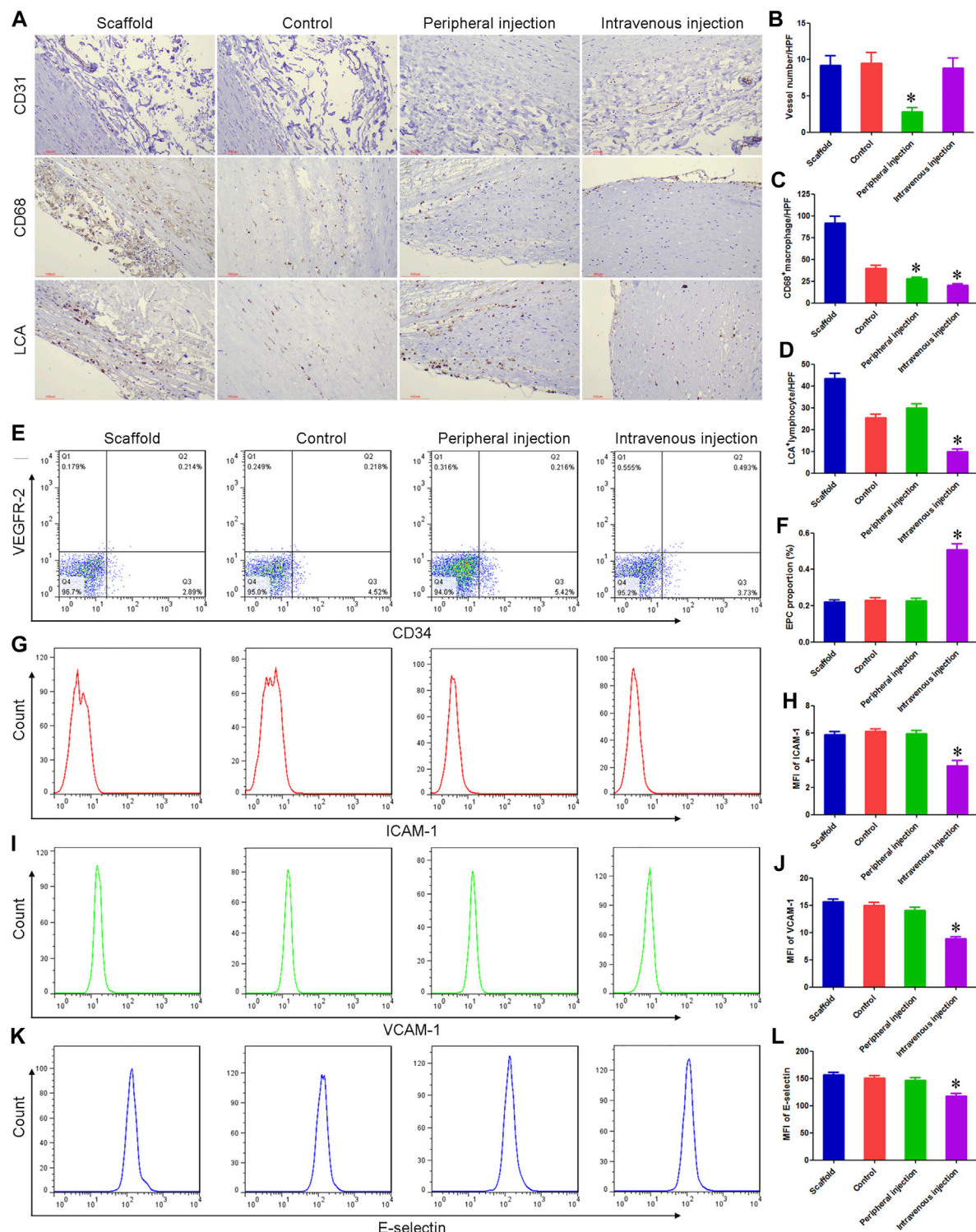
FIGURE 3 | Treg cell transplantation reduced the inflammatory response associated with TEBV implantation in diabetes mellitus. **(A)** Immunohistochemistry was used to detect the expression of CD31, CD68, and lymphocyte common antigen (LCA). **(B–D)** Compared with the control group, the number of macrophages (CD68^{+}) and microvessel density (CD31^{+}) around TEBV decreased in the peripheral injection group, respectively, while the number of lymphocytes (LCA^{+}) did not differ statistically between the two groups. Compared with the control group, there was no significant change in CD31^{+} microvessel density around TEBV in the intravenous injection group, while the number of lymphocytes and macrophages was significantly reduced. **(E)** Flow cytometry was used to detect the proportion of EPCs in peripheral blood. **(F)** Compared with the control group and peripheral injection group, the proportion of EPCs was significantly increased in the intravenous injection group. **(G,I,K)** Flow cytometry was used to detect the expression of ICAM-1, VCAM-1, and e-selectin on EPCs. **(H,J,L)** Compared with the control group and peripheral injection group, the expression of ICAM-1, VCAM-1, and e-selectin was significantly decreased in the intravenous injection group. $*p < 0.05$ ($n = 8$) versus Control group. Values are mean ± SD.

FIGURE 4 | Treg cells intravenous transplantation reduced the number of apoptotic cells and Nestin + cells in anti-CD34 antibody modified TEBV. **(A)** TUNEL staining was used to detect cell apoptosis. **(B)** Immunohistochemistry was used to detect the number of Nestin$^+$ cells and CD90$^+$ cells. **(C)** Compared with the control group and peripheral injection group, the number of apoptotic cells was significantly decreased in the intravenous injection group. **(D)** Immunohistochemical results showed that many Nestin$^+$ cells could be detected in both the control group and peripheral injection group, most of which were fusiform, showing the characteristics of smooth muscle cells. Compared with the control group and peripheral group, the number of Nestin$^+$ cells were reduced by 78.51% and 77.92% in the intravenous injection group, respectively. **(E)** There was no statistical difference in the number of CD90$^+$ cells among the four groups. $*p < 0.05$ ($n = 8$) versus Control group. $^\#p < 0.05$ ($n = 8$) versus Peripheral injection group. Values are mean ± SD.

concentrations among the three groups. Compared with the control group, the proportion of EPCs and the concentration of VEGF and SDF-1 were significantly increased in the intravenous injection group, while the expression of ICAM-1, VCAM-1, and e-selectin was significantly decreased. These results suggest that Treg cells can inhibit angiogenesis in the ischemic microenvironment (around TEBV), possibly by inhibiting the vascularization process initiated by an inflammatory response. On the other hand, Treg cells can promote angiogenesis and rapid endothelialization in nutrient and oxygen-rich sites (in TEBV) by enhancing mobilization and paracrine of EPCs and decreasing the expression of pro-inflammatory molecules. **Figures 3E–3L** and **Supplementary Figures S1, S2**.

We further detected the number of different lymphocyte subsets in TEBV. Immunohistochemical results showed that there was no statistical difference in the number of CD4$^+$T cells, CD8$^+$T cells, B cells, plasma cells, and NK cells

FIGURE 5 | Effect of Treg cells on EPCs function in diabetic patients. **(A,B)** Flow cytometry was used to detect the proportion of EPCs and CD31^{+}cells. **(C)** Compared with the diabetes group, the proportion of EPC in the Treg cell group increased markedly. IL-10 neutralization could inhibit this effect on Treg cells. **(D)** There was no statistical difference in the proportion of CD31^{+} endothelial cells among all groups. **(E,F)** Compared with the diabetes group, the concentration of VEGF and SDF-1 in the EPC supernatant of the Treg cell group increased by 4.75 and 5.13 times, respectively. IL-10 neutralization can inhibit these effects of Treg cells. *$p < 0.05$ ($n = 6$) versus Diabetes group. #$p < 0.05$ ($n = 6$) versus Treg cell group. Values are mean ± SD.

between the scaffold group, control group, and peripheral injection group. Compared with the control group, the number of CD8^{+}T cells was significantly reduced in the intravenous injection group, while there were no significant differences in CD4^{+}T cells, B cells, plasma cells, and NK cells. These results suggest that CD8^{+}T cells may play a more important role after TEBV implantation **Supplementary Figure S3**.

Treg cell transplantation inhibited cell apoptosis in anti-CD34 antibody-modified TEBV.

TUNEL staining results showed that the percentage of apoptotic cells in the control group and peripheral injection group was 27.83% and 17.17%, respectively, and the difference was statistically significant. The percentage of apoptotic cells in the intravenous injection group was 6.58%, and the differences were statistically significant compared with the control group and peripheral injection group. **Figures 4A,C**.
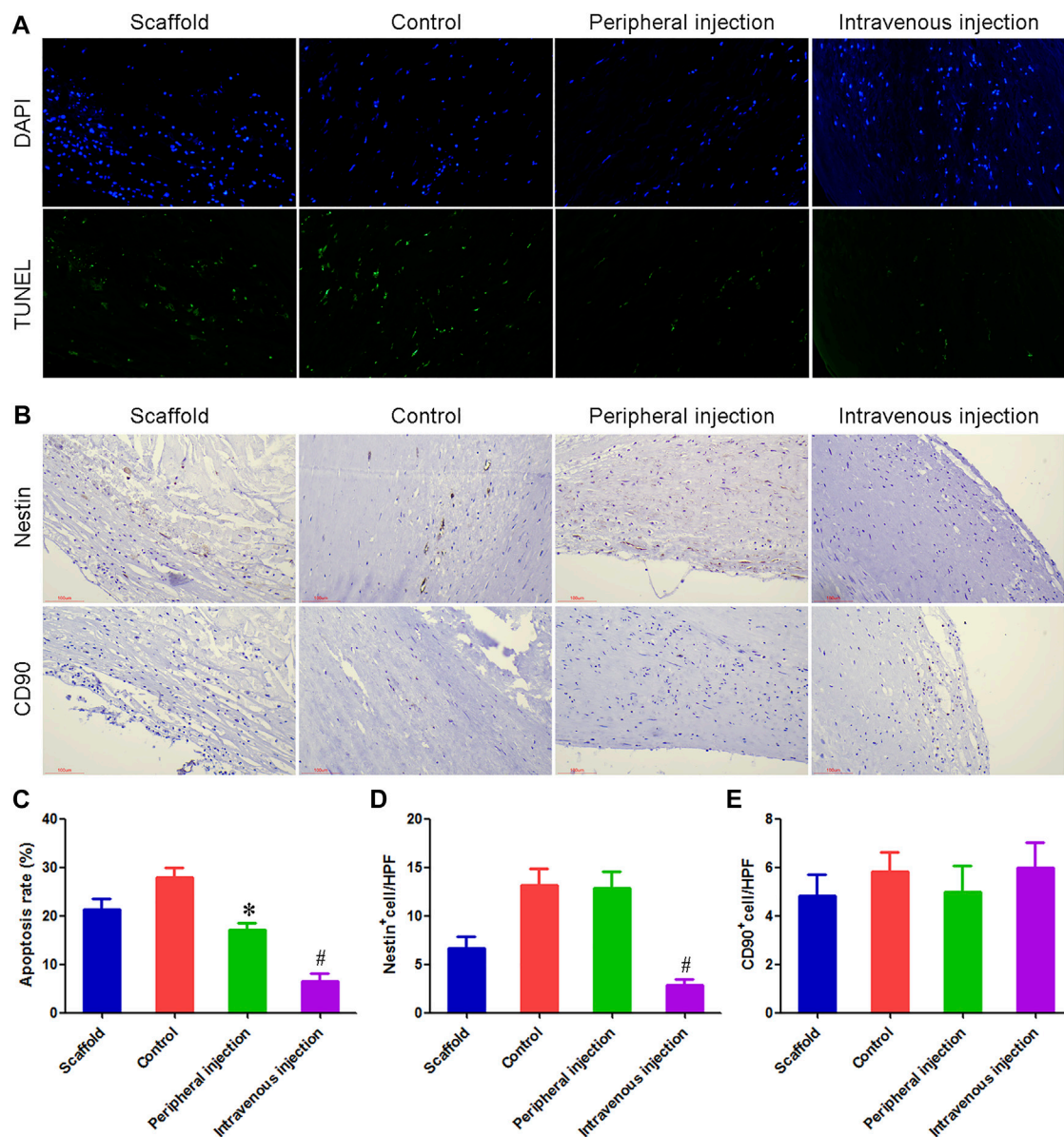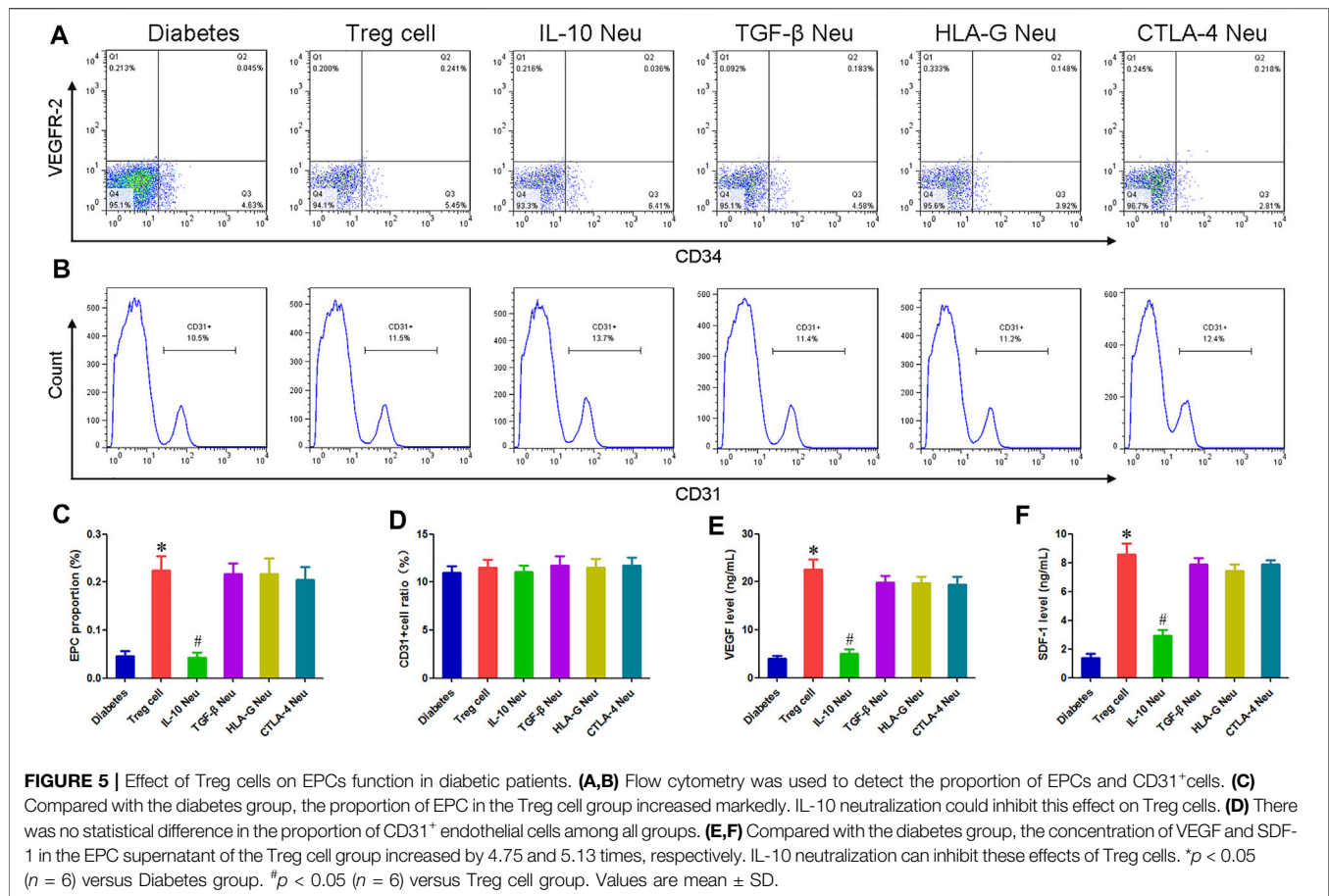
Treg cells intravenous transplantation reduced the number of Nestin^{+} cells in anti-CD34 antibody modified TEBV.

Immunohistochemical results showed that many Nestin^{+} cells could be detected in both the control group and peripheral injection group, most of which were fusiform, showing the characteristics of smooth muscle cells. This result indicated that in diabetes, Nestin^{+} cells mainly differentiated into vascular smooth muscle cells and promoted the occurrence of

intimal hyperplasia. Compared with the control group and peripheral group, Nestin^{+} cells were reduced by 78.51% and 77.92% in the intravenous injection group, respectively. There was no statistical difference in the number of CD90^{+} cells among the four groups. **Figures 4B,D,E**.

Effect of Treg cells on EPCs function in diabetic patients.

Compared with the diabetes group, the proportion of EPC in the Treg cell group increased markedly, indicating that Treg cells can promote the proliferation of EPC in diabetes mellitus. IL-10 neutralization could inhibit this effect of Treg cells, and the EPC proportion in the IL-10 Neu group was reduced by 80.89% compared with the Treg cell group. The neutralization of TGF-β, CTLA-4, and HLA-G had no significant effect. **Figures 5A,C**.

Compared with the diabetes group, the concentration of VEGF and SDF-1 in the EPC supernatant of the Treg cell group increased by 4.75 and 5.13 times, respectively. IL-10 neutralization can inhibit these effects of Treg cells, and the concentration of VEGF and SDF-1 in the IL-10 Neu group decreased by 77.73% and 65.63%, respectively, compared with the Treg cell group. The neutralization of TGF-β, CTLA-4, and HLA-G had no significant effect. **Figures 5E,F**.

After 1 week of co-culture, we detected the proportion of CD31^{+} endothelial cells. Flow cytometry results showed that there was no statistical difference in the proportion of CD31^{+}

endothelial cells among all groups, indicating that Treg cells had no significant effect on the differentiation of EPCs. **Figures 5B,D**.

DISCUSSION

EPC captured TEBV is considered the development direction of the new generation of TEBV, which can maintain a good patency effect in animal experiments (Hao et al., 2020). However, many patients with cardiovascular and cerebrovascular diseases are often accompanied by basic diseases such as diabetes. The microenvironment of high glucose and high oxidative stress damages the function of homing EPCs and promotes the pathological proliferation of vascular smooth muscle cells, leading to the implantation failure of TEBV (Chen et al., 2018). Our previous study showed that the patency rate of EPC-captured TEBV was very low in diabetic rats. In this study, we constructed a diabetic pig model and found that all implanted TEBVs were not completely blocked, mainly due to heparin coating and anticoagulant therapy. However, 60 days after implantation, intimal hyperplasia occurred in the control TEBV, while intravenous injection of Treg cells significantly inhibited intimal hyperplasia. Immunohistochemical results showed that the number of macrophages, CD8^{+}T cells, and apoptotic cells were significantly reduced in the intravenous injection group. Interestingly, our study also showed that Treg cells decreased the number of Nestin^{+} cells in TEBV. Clinical results showed that Nestin^{+} cells and CD90^{+} cells simultaneously expressed CD44, CD73, and CD140a, and had the potential to differentiate into endothelial cells or smooth muscle cells after implantation of bioartificial blood vessels (Kirkton et al., 2019). Our results indicated that in diabetes, Nestin^{+} cells mainly differentiated into vascular smooth muscle cells and promoted the occurrence of intimal hyperplasia.

Successful implantation of biomaterials *in vivo* is closely related to the inflammatory response. Low intensity inflammatory response can induce homing of EPCs and initiate the vascularization process of biomaterials (Garg et al., 2008). However, the over-activation of inflammatory response in diabetes mellitus will further damage the function of homing EPCs and inhibit angiogenesis in biomaterials. At present, the correlation between Treg cells and angiogenesis is highly controversial. Some studies have found that Treg cells can inhibit angiogenesis in ischemic tissues, anti-CD25 treatment, and subsequent Treg deletion were significantly enhanced postischemic neovasculplasmin (Zouggari et al., 2009). But other studies found that Treg cells were the main source of VEGF, which can induce angiogenesis. After TEBV implantation, the peripheral blood circulating in the lumen contains sufficient oxygen and nutrients, while the damaged tissues around TEBV are relatively ischemic and hypoxia, so it can be used as an important model to study the relationship between Treg cells and angiogenesis. In order to sufficiently isolate the exchange of matter between the

inside and outside of the TEBV, we transplanted TEBV into a pig model. The results showed that intravenous injection of Treg cells could promote long-term patency of TEBV and inhibit intimal hyperplasia, while Treg cells used around TEBV had no significant effect, and microvessel density around TEBV was significantly reduced. After implantation *in vivo*, the surrounding tissues of TEBV are a relatively ischemic and anoxic microenvironment, and inflammatory cells in the blood arrive at a very late time and are difficult to survive. Treg cells further inhibited the activation and function of inflammatory cells, thus weakening angiogenesis.

Treg cells exert immunosuppressive function mainly through two mechanisms. Treg cells highly express HLA-G and CTLA-4, which can inhibit the proliferation and activation of immune cells through direct contact or exosome (Hao et al., 2007; Zhang et al., 2018; Rana and Biswas, 2020). Treg cells can also secrete IL-10 and TGF-β, indirectly exerting biological functions (Song et al., 2021; Tagkareli et al., 2022). Clinical studies have shown that Treg cells are positively correlated with early EPCs, but the specific mechanism is unclear. Our results showed that intravenous injection of Treg cells after TEBV implantation could improve the proportion of EPCs and the concentration of VEGF in peripheral blood. *In vitro* experiments further confirmed that IL-10 mediated the angiogenic function of Treg cells. EPCs also highly produce IL-10, TGF-β, and HLA-G, these cytokines in EPCs will be the potential pathways in immune regulation (Naserian, 2020). Recent articles demonstrated that TNFR1 and Tie-2 can be used as the important markers for tissue-engineered materials related to inflammation detection (Nouri Barkestani et al., 2021). Some studies have shown that an important target of IL-10 action is STAT3, which promotes the expression and secretion of VEGF and SDF-1 (Wang et al., 2015; Shirakawa et al., 2018). Therefore, we believe that Treg cells in the ischemic tissues (around the TEBV) mainly block the initiation of vascularization by inhibiting the infiltration and function of inflammatory cells, while Treg cells in the tissue with abundant blood circulation (in the TEBV) mainly promote the mobilization of EPCs and the secretion of angiogenic factors through the IL-10 pathway.

In conclusion, Intravenous transplantation of Treg cells can delay the occurrence of intimal hyperplasia in diabetic pigs by promoting EPCs mobilization, anti-inflammatory action, and cellular protection. We also found that the correlation between Treg cells and angiogenesis was mainly closely related to the microenvironment. Our study provides a new target for the clinical transformation of TEBV and provides new theoretical support for understanding the correlation between inflammation and angiogenesis.

DATA AVAILABILITY STATEMENT

The original contributions presented in the study are included in the article/**Supplementary Material**; further inquiries can be directed to the corresponding authors.

ETHICS STATEMENT

The animal study was reviewed and approved by the Animal Ethics Committee of the Chinese PLA General Hospital.

AUTHOR CONTRIBUTIONS

XH and WC conceived and designed the study. FG, ZR, DL, and LW performed the experiments. FG and WC wrote the manuscript and prepared data, figures, and tables. DL and LW provided constructive advice on the experiments and manuscript. All the authors commented on the previous versions of this manuscript. All authors read and approved the final manuscript.

SUPPLEMENTARY MATERIAL

The Supplementary Material for this article can be found online at: https://www.frontiersin.org/articles/10.3389/fbioe.2022.929867/full#supplementary-material

REFERENCES

Afshari, A., Shamdani, S., Uzan, G., Naserian, S., and Azarpira, N. (2020). Different Approaches for Transformation of Mesenchymal Stem Cells into Hepatocyte-like Cells. *Stem Cell Res. Ther.* 11, 54. doi:10.1186/s13287-020-1555-8

Chen, W., Yang, M., Bai, J., Li, X., Kong, X., Gao, Y., et al. (2018). Exosome-Modified Tissue Engineered Blood Vessel for Endothelial Progenitor Cell Capture and Targeted siRNA Delivery. *Macromol. Biosci.* 18. doi:10.1002/mabi.201700242

Chen, W., Wu, Y., Li, L., Yang, M., Shen, L., Liu, G., et al. (2015a). Adenosine Accelerates the Healing of Diabetic Ischemic Ulcers by Improving Autophagy of Endothelial Progenitor Cells Grown on a Biomaterial. *Sci. Rep.* 5, 11594. doi:10.1038/srep11594

Chen, W., Zeng, W., Sun, J., Yang, M., Li, L., Zhou, J., et al. (2015b). Construction of an Aptamer-SiRNA Chimera-Modified Tissue-Engineered Blood Vessel for Cell-type-specific Capture and Delivery. *ACS Nano* 9, 6069–6076. doi:10.1021/acsnano.5b01203

Choi, D.-H., Chmura, S. A., Ramachandran, V., Dionis-Petersen, K. Y., Kobayashi, Y., Nishi, T., et al. (2018). The Ratio of Circulating Regulatory Cluster of Differentiation 4 T Cells to Endothelial Progenitor Cells Predicts Clinically Significant Acute Rejection after Heart Transplantation. *J. Heart Lung Transplant.* 37, 496–502. doi:10.1016/j.healun.2017.10.012

Garg, R., Tellez, A., Alviar, C., Granada, J., Kleiman, N. S., and Lev, E. I. (2008). The Effect of Percutaneous Coronary Intervention on Inflammatory Response and Endothelial Progenitor Cell Recruitment. *Cathet. Cardiovasc. Interv.* 72, 205–209. doi:10.1002/ccd.21611

Gasparri, M. L., Bellati, F., Napoletano, C., Panici, P. B., and Nuti, M. (2013). Interaction between Treg Cells and Angiogenesis: a Dark Double Track. *Int. J. Cancer* 132, 2469. doi:10.1002/ijc.27920

Halim, M., and Halim, A. (2019). The Effects of Inflammation, Aging and Oxidative Stress on the Pathogenesis of Diabetes Mellitus (Type 2 Diabetes). *Diabetes & Metabolic Syndrome Clin. Res. Rev.* 13, 1165–1172. doi:10.1016/j.dsx.2019.01.040

Hao, D., Fan, Y., Xiao, W., Liu, R., Pivetti, C., Walimbe, T., et al. (2020). Rapid Endothelialization of Small Diameter Vascular Grafts by a Bioactive Integrin-Binding Ligand Specifically Targeting Endothelial Progenitor Cells and Endothelial Cells. *Acta Biomater.* 108, 178–193. doi:10.1016/j.actbio.2020.03.005

Hao, S., Liu, Y., Yuan, J., Zhang, X., He, T., Wu, X., et al. (2007). Novel Exosome-Targeted CD4+T Cell Vaccine Counteracting CD4+25+Regulatory T Cell-Mediated Immune Suppression and Stimulating Efficient Central Memory CD8+CTL Responses. *J. Immunol.* 179, 2731–2740. doi:10.4049/jimmunol.179.5.2731

Kawada, T. (2018). Regulatory T Cells, Natural Killer Cells, and Obesity in Patients with Gestational Diabetes Mellitus. *Am. J. Reprod. Immunol.* 79, e12831. doi:10.1111/aji.12831

Kirkton, R. D., Santiago-Maysonet, M., Lawson, J. H., Tente, W. E., Dahl, S. L. M., Niklason, L. E., et al. (2019). Bioengineered Human Acellular Vessels Recellularize and Evolve into Living Blood Vessels after Human Implantation. *Sci. Transl. Med.* 11. doi:10.1126/scitranslmed.aau6934

Lewczuk, B., Prusik, M., Ziółkowska, N., Dąbrowski, M., Martniuk, K., Hanuszewska, M., et al. (2018). Effects of Streptozotocin-Induced Diabetes on the Pineal Gland in the Domestic Pig. *Int. J. Mol. Sci.* 19. doi:10.3390/ijms19103077

Naserian, S., Abdelgawad, M. E., Afshar Bakshloo, M., Ha, G., Arouche, N., Cohen, J. L., et al. (2020). The TNF/TNFR2 Signaling Pathway Is a Key Regulatory Factor in Endothelial Progenitor Cell Immunosuppressive Effect. *Cell Commun. Signal* 18, 94. doi:10.1186/s12964-020-00564-3

Nouri Barkestani, M., Shamdani, S., Afshar Bakshloo, M., Arouche, N., Bambai, B., Uzan, G., et al. (2021). TNFα Priming through its Interaction with TNFR2 Enhances Endothelial Progenitor Cell Immunosuppressive Effect: New Hope for Their Widespread Clinical Application. *Cell Commun. Signal* 19, 1. doi:10.1186/s12964-020-00683-x

Petrelli, A., Di Fenza, R., Carvello, M., Gatti, F., Secchi, A., and Fiorina, P. (2012). Strategies to Reverse Endothelial Progenitor Cell Dysfunction in Diabetes. *Exp. Diabetes Res.* 2012, 471823. doi:10.1155/2012/471823

Pierzynowska, K., Oredsson, S., and Pierzynowski, S. (2020). Amylase-Dependent Regulation of Glucose Metabolism and Insulin/Glucagon Secretion in the Streptozotocin-Induced Diabetic Pig Model and in a Rat Pancreatic Beta-Cell Line, BRIN-BD11. *J. Diabetes Res.* 2020, 2148740. doi:10.1155/2020/2148740

Qin, W., Sun, L., Dong, M., An, G., Zhang, K., Zhang, C., et al. (2021). Regulatory T Cells and Diabetes Mellitus. *Hum. Gene Ther.* 32, 875–881. doi:10.1089/hum.2021.024

Rana, J., and Biswas, M. (2020). Regulatory T Cell Therapy: Current and Future Design Perspectives. *Cell. Immunol.* 356, 104193. doi:10.1016/j.cellimm.2020.104193

Rotmans, J. I., Heyligers, J. M. M., Verhagen, H. J. M., Velema, E., Nagtegaal, M. M., De Kleijn, D. P. V., et al. (2005). *In Vivo* cell Seeding with Anti-CD34 Antibodies Successfully Accelerates Endothelialization but Stimulates Intimal Hyperplasia in Porcine Arteriovenous Expanded Polytetrafluoroethylene Grafts. *Circulation* 112, 12–18. doi:10.1161/circulationaha.104.504407

Shirakawa, K., Endo, J., Kataoka, M., Katsumata, Y., Yoshida, N., Yamamoto, T., et al. (2018). IL (Interleukin)-10-STAT3-Galectin-3 Axis Is Essential for Osteopontin-Producing Reparative Macrophage Polarization after Myocardial Infarction. *Circulation* 138, 2021–2035. doi:10.1161/circulationaha.118.035047

Song, H.-H. G., Rumma, R. T., Ozaki, C. K., Edelman, E. R., and Chen, C. S. (2018). Vascular Tissue Engineering: Progress, Challenges, and Clinical Promise. *Cell Stem Cell* 22, 340–354. doi:10.1016/j.stem.2018.02.009

Song, L., Wang, S., Fang, T., Qiu, X., Wang, X., Zhou, X., et al. (2021). Changes in Peripheral Blood Regulatory T Cells and IL-6 and IL-10 Levels Predict Response of Pediatric Medulloblastoma and Germ Cell Tumors with Residual or Disseminated Disease to Craniospinal Irradiation. *Int. J. Radiat. Oncology*Biology*Physics* 111, 479–490. doi:10.1016/j.ijrobp.2021.04.041

Tagkareli, S., Salagianni, M., Galani, I. E., Manioudaki, M., Pavlos, E., Thanopoulou, K., et al. (2022). CD103 Integrin Identifies a High IL-10-producing FoxP3 + Regulatory T-cell Population Suppressing Allergic Airway Inflammation. *Allergy* 77, 1150–1164. doi:10.1111/all.15144

Wang, Y., Chen, Q., Zhang, Z., Jiang, F., Meng, X., and Yan, H. (2015). Interleukin-10 Overexpression Improves the Function of Endothelial Progenitor Cells Stimulated with TNF-α through the Activation of the STAT3 Signaling Pathway. *Int. J. Mol. Med.* 35, 471–477. doi:10.3892/ijmm.2014.2034

Xing, Z., Zhao, C., Liu, H., and Fan, Y. (2020). Endothelial Progenitor Cell-Derived Extracellular Vesicles: A Novel Candidate for Regenerative Medicine and Disease Treatment. *Adv. Healthc. Mater* 9, e2000255. doi:10.1002/adhm.202000255

Zhang, B., Yeo, R. W. Y., Lai, R. C., Sim, E. W. K., Chin, K. C., and Lim, S. K. (2018). Mesenchymal Stromal Cell Exosome-Enhanced Regulatory T-Cell Production through an Antigen-Presenting Cell-Mediated Pathway. *Cytotherapy* 20, 687–696. doi:10.1016/j.jcyt.2018.02.372

Zhou, L., He, X., Cai, P., Li, T., Peng, R., Dang, J., et al. (2021). Induced Regulatory T Cells Suppress Tc1 Cells through TGF-β Signaling to Ameliorate STZ-Induced Type 1 Diabetes Mellitus. *Cell Mol. Immunol.* 18, 698–710. doi:10.1038/s41423-020-00623-2

Zouggari, Y., Ait-Oufella, H., Waeckel, L., Vilar, J., Loinard, C., Cochain, C., et al. (2009). Regulatory T Cells Modulate Postischemic Neovascularization. *Circulation* 120, 1415–1425. doi:10.1161/circulationaha.109.875583

Basement Membrane of Tissue Engineered Extracellular Matrix Scaffolds Modulates Rapid Human Endothelial Cell Recellularization and Promote Quiescent Behavior After Monolayer Formation

Manuela Lopera Higuita, Nicholas A. Shortreed, Surendra Dasari and Leigh G. Griffiths *

Mayo Clinic, Rochester, MN, United States

Off-the-shelf small diameter vascular grafts are an attractive alternative to eliminate the shortcomings of autologous tissues for vascular grafting. Bovine saphenous vein (SV) extracellular matrix (ECM) scaffolds are potentially ideal small diameter vascular grafts, due to their inherent architecture and signaling molecules capable of driving repopulating cell behavior and regeneration. However, harnessing this potential is predicated on the ability of the scaffold generation technique to maintain the delicate structure, composition, and associated functions of native vascular ECM. Previous de-cellularization methods have been uniformly demonstrated to disrupt the delicate basement membrane components of native vascular ECM. The antigen removal (AR) tissue processing method utilizes the protein chemistry principle of differential solubility to achieve a step-wise removal of antigens with similar physiochemical properties. Briefly, the cellular components of SV are permeabilized and the actomyosin crossbridges are relaxed, followed by lipophilic antigen removal, sarcomeric disassembly, hydrophilic antigen removal, nuclease digestion, and washout. Here, we demonstrate that bovine SV ECM scaffolds generated using the novel AR approach results in the retention of native basement membrane protein structure, composition (e.g., Collagen IV and laminin), and associated cell modulatory function. Presence of basement membrane proteins in AR vascular ECM scaffolds increases the rate of endothelial cell monolayer formation by enhancing cell migration and proliferation. Following monolayer formation, basement membrane proteins promote appropriate formation of adherence junction and apicobasal polarization, increasing the secretion of nitric oxide, and driving repopulating endothelial cells toward a quiescent phenotype. We conclude that the presence of an intact native vascular basement membrane in the AR SV ECM scaffolds modulates human endothelial cell quiescent monolayer formation which is essential for vessel homeostasis.

Keywords: extracellular matrix, tissue engineering, cardiovascular diseases, small diameter vessels, cell behavior

1 INTRODUCTION

Diseases of small diameter blood vessels (i.e., < 6 mm) such as coronary artery diseases and peripheral vascular diseases affect over 25 million people in the United States (Fryar et al., 2012; Benjamin et al., 2019). While a wide array of treatments have been evaluated, the use of autologous tissues for vascular bypass remains the standard of care for small diameter vessel diseases, with over 4.2 million people undergoing vascular grafting every year (Slovut and Lipsitz, 2012; Alexander and Smith, 2016). However, lack of suitable autologous grafts due to pre-existing vascular diseases deprive approximately one-third of patients from receiving life-saving vascular grafting (Hillis et al., 2011; Popovic et al., 2013; Taggart, 2013; de Vries et al., 2016; McKavanagh et al., 2017; Tranbaugh et al., 2017). Additionally, for patients with suitable vasculature, autologous tissue harvesting results in increased morbidity and potential for donor site complications (Hillis et al., 2012). The development of an off-the-shelf small diameter vascular graft has the potential to overcome the challenges associated with autologous vessel harvest, providing a solution with sufficient length and unlimited availability applicable for the treatment of vascular diseases in all patients.

Acellular extracellular matrix (ECM) scaffolds derived from xenogeneic vascular tissue have the potential to serve as an ideal source for off-the-shelf vascular grafts. For vascular tissues, in addition to providing structural support, the ECM contains growth factors, proteases, cytokines, proteoglycans, collagens, laminin, fibronectin fibrils, and other biologically active molecules, each of which have the potential to influence repopulating endothelial cell proliferation, differentiation, migration, and apoptosis (Faulk et al., 2014a). The effects of individual native ECM proteins, particularly vascular basement membrane components, have been extensively researched and shown to modulate advantageous endothelial cell behaviors, with the potential to mediate rapid monolayer formation and drive endothelial cells toward a quiescent phenotype (Morrissey and Sherwood, 2015). Laminin for instance, has been demonstrated to mediate human endothelial cell differentiation into capillary-like structures, while collagen IV (Col IV) has been demonstrated to influence endothelial cell adhesion and migration (Xing et al., 2021). While independent individual effects of important basement membrane proteins on endothelial cell behavior have been documented by previous *in vitro* studies, such single molecule studies fail to recapitulate the structural organization and compositional complexity of native vascular basement membranes. Determining the combined effect of these complex ECM factors on endothelial cell behavior in intact ECM scaffolds has not been possible due to the inability of de-cellularization methods to retain native ECM protein structure, composition, and function (Crapo et al., 2011). In particular, disruption of delicate endothelial basement membrane components (e.g., collagen IV, laminin) is very common with de-cellularization approaches, regardless of specific chemicals employed (Faulk et al., 2014b). Additionally, the disruption of ECM proteins caused by tissue processing methods have further implications, as modified ECM proteins have the potential to negatively modulate endothelial cell behavior and lead to cellular dysfunction possibly causing inflammatory syndromes, intimal hyperplasia, thrombosis (Huang and Greenspan, 2012; Lee et al., 2014).

The purpose of this article is to determine the combined effect of ECM basement membrane factors on the endothelial cell behavior by utilizing antigen-removed ECM vascular scaffolds. Antigen removal (AR), unlike the common de-cellularization technique, is a tissue processing method shown to retain the composition and function of ECM proteins, while significantly reducing the antigenic content from xenogeneic tissues (Dalgliesh et al., 2018; Lopera Higuita and Griffiths, 2020a). Specifically, when applied to a small diameter bovine saphenous vein (SV, <3.5 mm diameter), AR tissue processing resulted in the elimination of 98.5% of the tissue antigenic components while retaining the predominant structural, functional, and compositional characteristics of the ECM (Lopera Higuita and Griffiths, 2020a). The retention of the ECM proteins was determined by the extensive characterization of antigen- removed ECM scaffolds in the previous work, where the mechanical properties of the acellular scaffold and the content of elastin, desmosine, collagen, and pyridinaline were all retained compared to untreated tissues (Lopera Higuita and Griffiths, 2020a).

Furthermore, retention of important endothelial basement membrane proteins by the AR tissue processing method suggests that AR-SV scaffolds are an ideal testing material to determine the drivers of endothelial behavior in native ECM. The anisotropic organization of SV (i.e., luminal surface of the vessel, which is lined with basement membrane proteins (BM) and abluminal surface of the vessel, which is mainly composed of loose structural non-basement membrane proteins (e.g., collagen I) (NBM)) allows for the comparison of endothelial cell response in the presence versus absence of basement membrane components, in otherwise identical scaffolds (i.e., processed *via* the same tissue processing method). We hypothesize the presence of basement membrane proteins in the lumen side of the AR-SV vascular graft (i.e., BM side seeding) will: 1) increase the rate at which seeded endothelial cells form a monolayer and 2) drive the quiescence cell behavior once a confluent monolayer is formed, when compared to the endothelial cell response in the absence of such proteins (i.e., NBM side seeding).

2 MATERIALS AND METHODS

All chemicals were purchased from Sigma-Aldrich (St. Louis, MO) unless otherwise stated. All experiments were performed with n = 6 replicates per group, unless otherwise stated.

2.1 Tissue Harvest

Fresh bovine saphenous veins (SV) were harvested and processed as previously stated (Lopera Higuita et al., 2021).

2.2 Antigen Removal

All ECM scaffold generation steps were performed in 4 ml of solution at RT, 150 rpm, and changed twice daily, unless otherwise stated. Previously frozen SV were thawed, planarized by incising the vessel longitudinally and cut into discs using 14 mm biopsy punches, unless otherwise stated. All chemicals were added to a base buffer solution (0.5 mM Pefabloc, 1% v/v antibiotic antimycotic solution (AAS) in 10 mM Tris–HCl (pH 8.0). Antigen removal (AR) samples (scaffolds) underwent sarcomeric

relaxation (3% amidosulfobetaine-16 (ASB-16), 120 mM potassium chloride (KCl), 4 mM $MgCl_2$, 4 mM EDTA, 5.88 mM Na-ATP, 10 mM 2,3 Butanedione monoxime (BDM), 0.5 mM Pefabloc, and 1% AAS in 10 mM Tris–HCl, pH 7.6) twice for 30 min each. Relaxed veins were incubated in a lipophilic protein solubilization solution (3% ASB-16 in 100 mM dithiothreitol (DTT), 2 mM $MgCl_2$, and 600 mM KCl, in the base buffer) for 48 h. AR-scaffolds underwent sarcomeric disassembly by washing in the base buffer twice for 15 min, followed by incubation in 50 nM Latranculin B (Cayman Chemical, Ann Arbor, MI) in the base buffer for 2 h; washed again with the base buffer twice for 15 min and incubated for 2 h in 0.6 M KCl in the base buffer; washed a final time with the base buffer twice for 15 min and incubated 2 h in 1 M potassium iodine (KI) in base buffer, followed by overnight incubation in the base buffer alone. The KCl and KI steps were repeated the next day, followed by overnight incubation in the base buffer. Scaffolds were then placed in the lipophilic protein solubilization solution for 48 h, followed by 24 h incubation in the hydrophilic protein removal solution (100 mM dithiothreitol (DTT), 2 mM $MgCl_2$ and 600 mM KCl, in base buffer). Subsequently, scaffolds underwent 24 h of nuclease digestion (10 Kunitz units/mL DNase I, 15 Kunitz units/mL RNase A, 0.5 mM Pefabloc, 1% AAS, 0.15 M NaCl, 5 mM $MgCl_2–6H_2O$ in 10 mM Tris–HCl, pH 7.6) and 96 h of washout in the base buffer at 4°C (**Supplementary Figure S1**).

2.3 EC Recellularization

Human aortic endothelial cells (hAECs), GFP-labeled hAECs (GFP-hAECs), human umbilical vein cells (HUVECs), and GFP-labeled HUVECS (GFP-HUVECs, all cells from Angio-Proteomie, Boston, MA) were expanded to P4, unless otherwise stated, in a T-25 flask coated with quick coating solution (Angio-Proteomie) at 37°C, 5% CO_2. Cells were cultured in 7 ml of the endothelial cell growth medium (Lonza, Allendale, NJ) with the solution changed at 24 h after thawing once every 3 days. Cells were lifted using Accutase® solution, hAECs were re-seeded on scaffolds at a cell seeding density of 450 cells/mm^2 and HUVECs were re-seeded at a cell density of 600 cells/mm^2, unless stated otherwise and cultured under the same conditions. Before cell seeding, all the scaffolds were incubated in 1% AAS in endothelial cell media overnight.

2.4 Endothelial Cell Migration Plus Proliferation Assay

Endothelial cell migration and proliferation assay was performed by seeding hAECs as a 3.5 mm disc of cells in the center of 1 × 1 cm square scaffolds in 24-well plates. Scaffolds were generated using 6 ml of the corresponding AR solutions. Scaffolds were sutured on to high temperature foam to allow the cell-seeded scaffolds to float in an inverted orientation (i.e., cell-seeded side of the scaffold facing the bottom of the plate) on top of the culture media. The high temperature foam also resisted the effect of cell traction or scaffold recoil on the scaffold during culture, thereby keeping the scaffolds planarized throughout the experiment. Additionally, these culture conditions allowed for inverted microscopy imaging of GFP-labeled cells at multiple time points without disrupting the scaffolds or seeded cells. A 3.5 mm diameter glass cylinder was used to seed GFP-hAECs

in a circular shape in the center of the scaffold. Cells were allowed to adhere for 6 h in 50 µL of cell culture media. Following adhesion, the glass cylinder was removed, 500 µL of cell media was added, and cells were monitored using inverted microscopy (Nikon Eclipse Ts2R, Minato City, Tokyo, Japan) at days 1, 4, 8, 12, 16, and 20, with the culture media being changed every other days. To obtain images of the entire scaffolds, 20–30 images were taken from each scaffold at 4 x and arranged using the microscope stitch function. The combined effect of hAEC migration and proliferation was estimated using the non-directional mean migratory distance. This was calculated by measuring the total area covered by cells, fitting a circle of equivalent area, and extracting its radius using MATLAB (MATLAB®, The MathWorks, Inc., Natick, MA).

2.5 Endothelial Cell Migration Assay (Proliferation Inhibited With Mytomiocin)

For the endothelial cell migration assay, 1 × 1 cm scaffolds were generated using 6 ml of the corresponding AR solutions. Scaffolds were sutured on to high temperature foam and the cell culture was undertaken in 24-well plates. A glass cylinder 3.5 mm in diameter was used to seed the GFP-hAECs in a circular shape. The cells were allowed to adhere for 6 h in 50 µL of the cell media. After adhesion, the cells were unconfined and treated with 1 µg/ml of proliferator inhibitor (Mitomycin C) in 300 µL of the media for 48 h. Following 48 h of incubation, cell were imaged using inverted microscopy (Nikon Eclipse Ts2R, Minato City, Tokyo, Japan) at days 3, 6, and 10 post seeding. Migration was determined by the mean migratory distance obtained as described in **Section 2.4**.

2.6 Endothelial Cell Proliferation Assay (*via* FUCCI Staining)

For the endothelial cell proliferation assay, 1 × 1 cm scaffolds were generated using 6 ml of the corresponding AR solutions. The scaffolds were sutured on to high temperature foam, to avoid scaffold recoil, and the cell culture was undertaken in 24-well plates. The hAEC cells were transfected using the Premo FUCCI Cell Cycle Sensor (ThermoFisher Scientific, Waltham, MA) following the manufacturer's protocols. Briefly, early passage (P2) hAECs were seeded on to six well tissue culture plastic coated with a quick coating solution (Angio-Proteomie) at a 50% confluency rate, in 3 ml of media and allowed to adhere overnight. After cell adhesion, hAECs were treated with 120 particles per cell (PPC) of Premo FUCCI in 500 µL of the cell media overnight. After transfection, cells were detached and seeded onto scaffolds using a 12 mm internal diameter stainless steel cylinder at a density of 250 cell/mm^2 (i.e., ~50% confluency) in 500 µL of the media and allowed to adhere overnight. After 12 h of post-seeding, the proliferating cells were counted using inverted microscopy (Nikon Eclipse Ts2R, Minato City, Tokyo, Japan).

2.7 Histology

Sample sections were stained with Hematoxylin and Eosin (H&E), Verhoeff van Gieson staining (VVG), and Picro–Sirius Red (PSR). Collagen birefringence was measured from PSR slides using polarized light and the percentage area of collagen polarization

was calculated. For immunofluorescence staining of adherence junctions and cell polarization, antigen retrieval was performed *via* a heat-mediated sodium citrate buffer (10 mM Sodium citrate, 0.05% Tween 20, pH 6.0) and non-specific binding was blocked. For adherence junction staining, slides were incubated in rabbit anti–VE cadherin and mouse anti-β-catenin primary antibodies (11 μg/ml, 5 μg/ml respectively, Abcam, Cambridge, MA). For cell polarization, slides were incubated with mouse anti-podocalyxin (PODXL) and rabbit anti-collagen IV antibody (1:100, 1:200, respectively, Abcam). Fluorescent anti-mouse secondary antibody (1:200, Abcam) tagged with Alexa Fluor 546, anti-rabbit secondary antibody tagged with Alexa Fluor 647 (1:200, Abcam), and DAPI (ProLongTM Gold antifade reagent with DAPI, Invitrogen) were used for visualization.

For bovine laminin and collagen IV staining, sections were deparaffinized and antigen retrieval was performed *via* proteinase K (DAKO, Carpinteria, CA) at room temperature. Bovine laminin was stained using a rabbit anti-laminin antibody (1:20, Invitrogen, Carlsbad, CA). Collagen IV was stained using a rabbit anti-collagen IV antibody (1:200, Abcam). The fluorescent anti-rabbit secondary antibody tagged with Alexa Fluor 647 (1:200, Abcam) and DAPI (ProLongTM Gold antifade reagent with DAPI, Invitrogen) was used for visualization. For all stains, the slides were imaged using a Nikon Eclipse E600 microscope (Nikon, Minato City, Tokyo, Japan) and digital images were collected.

2.8 Human Laminin Production by Seeded Human Cells

For human laminin quantification, scaffolds seeded with hAECs at 100% confluency were fixed in 10% buffered formalin at day 4, embedded in paraffin, and 4 μm sections mounted on glass slides. Sections were de-paraffinized and antigen retrieval was performed *via* proteinase K (DAKO). Samples were stained using the rabbit anti-laminin antibody (1:200, Abcam). The fluorescent anti-rabbit secondary antibody tagged with Alexa Fluor 647 (1:200, Abcam) and DAPI (ProLongTM Gold antifade reagent with DAPI, Invitrogen) was used for visualization. Slides were imaged using a Nikon Eclipse E600 microscope (Nikon, Minato City, Tokyo, Japan) and the digital images were collected. Human laminin intensity per cell was measured for all cells in n = 6 scaffolds *via* NIS-Elements software (Nikon, Tokyo, Japan).

2.9 Endothelial Cell Activation/Quiescence Assessment by RNA-Sequencing

For cell activation/quiescence assessment by RNA-sequencing, hAECs were seeded at 100% confluency onto the basement membrane side of AR scaffolds (area of 1.9 cm^2) or seeded directly into the wells of a tissue culture plate (area of 1.9 cm^2—24-well plate). All cells were seeded at the same initial time point, after 6 h the cells seeded onto tissue culture plastic were treated overnight with either 1 μM simvastatin, 5 ng/ml TNFα, or left untreated (Control). After an overnight treatment or incubation, RNA was extracted *via* a Qiagen RNeasy mini kit, according to the manufacturer's directions. Total RNA concentration and quality were determined using Qubit fluorometry (Invitrogen). Sequencing

libraries were prepared using the Illumina TruSeq® RNA Stranded Kit (Illumina, San Diego, CA) following the manufacturer's instructions. The concentration and purity of the prepared libraries were checked using the Agilent TapeStation D1000 (Agilent Technologies, Santa Clara, CA). Libraries were sequenced at up to eight samples per lane following Illumina's standard protocol using the Illumina cBot and HiSeq 3,000/4000 PE Cluster Kit (Illumina, San Diego, CA). The flow cells were sequenced as 100 × 2 paired end reads on an Illumina HiSeq 4,000 using the HiSeq Control Software HD 3.4.0.38 collection software (Illumina, San Diego, CA). Base-calling was performed using Illumina's RTA version 2.7.7 (Illumina, San Diego, CA).

2.10 Bioinformatics Analysis of RNA-Seq Data

Raw read data were processed using a previously published MAPR-Seq pipeline and generate gene-wise read count data (Kalari et al., 2014). In brief, the sequencing data were quality controlled using the FASTQC software. Read data were aligned against the human reference genome (GRCh38) using a STAR aligner (Dobin et al., 2013). Gene expression counts were obtained using HTSeq software configured to use RefSeq human transcriptome (version 78) as the reference transcriptome (Anders et al., 2015). Gene-wise read counts observed in each sample were processed using the edgeR software for obtaining differentially expressed genes between any two experimental groups (Robinson et al., 2010). The software was configured to remove any genes with <100 counts in all samples across both groups. Read count data for the remaining genes were normalized using trimmed means of the M-values method. Gene-wise differential expression between the groups was tested using a generalized linear model configured to use negative binomial distribution. Differential expression *p*-values were corrected using the Benjamini–Hochberg method. Genes with an adjusted *p*-value <0.05 and an absolute log2 fold change ≥2.0 were considered as significantly differentially expressed and considered for further analyses.

Differential expression data of each pair-wise comparison were subjected to pathway analyses using two different methods. First, we computed the rank value of each gene using -1*log2 (*p*-value)*sign (fold change). The (gene, rank) pairs of each pair-wise comparison were subjected to gene set enrichment analyses using the PreRanked method encoded in the GSEA software, which was configured to use KEGG, REACTOME, HALLMARK, and BIOCARTA gene set databases for testing the pathway enrichment. Independently, genes that were statistically, significantly, and differentially expressed were utilized for the pathway analysis using the Webgestalt software (Liao et al., 2019). Gene sets or pathways with an adjusted *p*-value of <0.05 were considered to be statistically significant.

Z-scores for each gene were calculated and then subsequently plotted in a heatmap *via* the web-based program Heatmapper (Babicki et al., 2016). Hierarchial clustering was performed for each heatmap based on average linkage measurements.
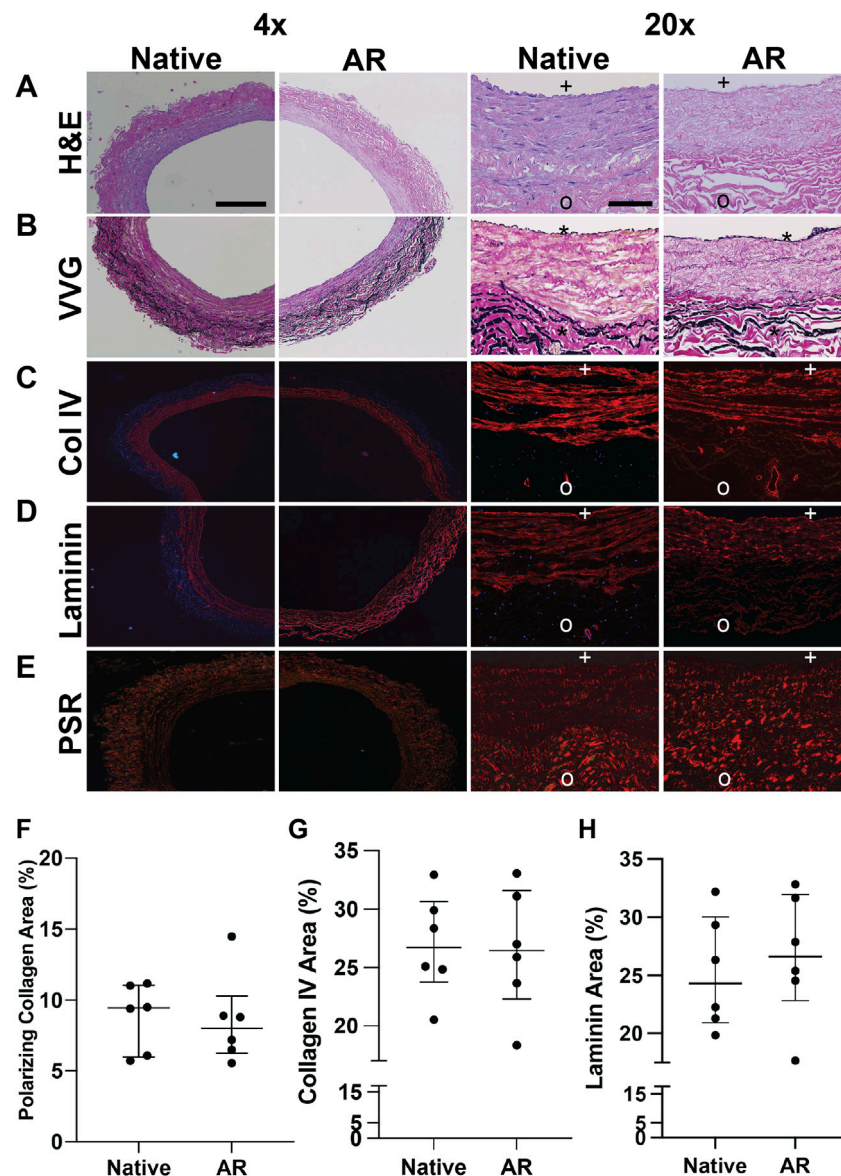
FIGURE 1 | Macromolecular structure and content retention in AR–SV ECM scaffolds. Basement membrane proteins are present in the basement membrane side (BM) of the vessel (marked with +), and are completely absent in the non-basement membrane (NBM) side (marked with o). H&E images of SV segments demonstrate complete acellularity of AR-scaffolds, while preserving the native collagen content and organization **(A)**. Elastin content and organization assessed *via* Verhoeff van Geison staining (VVG) demonstrate the retention of native SV internal (*) and external elastic laminae in AR-scaffolds **(B)**. Content and organization of basement membrane proteins (Col IV **(C)** and laminin **(D)**) in the basement membrane side of AR-SV ECM scaffolds were unchanged when compared to native tissue. Collagen alignment (PSR and polarized light) and immunofluorescence staining demonstrates the capability of AR tissue processing method of retaining the native SV collagen macromolecular structure and organization **(E)** as assessed by percent birefringence using PSR polarized light **(F)**, percent collagen IV **(G)**, and laminin **(H)**. 4 x images scale bar 200 μm. 20 x images scale bar 50 μm.

An independent unsupervised t-distributed stochastic neighbor embedding (t-SNE) analysis was performed by ranking the entire gene expression dataset by decreasing the order of their expression coefficient of variation metric. Top ranking 1,000 genes were utilized for the t-SNE analysis. A list of (gene, eigenvalues) associated with the first two principal components (PCs) were extracted for further analysis. All gene expression analyses were performed using R statistical programming language (version 4.1).

2.11 Statistical Analysis

All data were analyzed for outliers using the ROUT method with Q = 1%. Migration plus proliferation data were analyzed using repeated measure 2-way ANOVA with Geisser-Greenhouse and Sidak correction. Migration-only data were analyzed using repeated measure 3-way ANOVA with the Geisser-Greenhouse and Tukey correction. All other data were analyzed with the Mann–Whitney test. All data are expressed as median ±
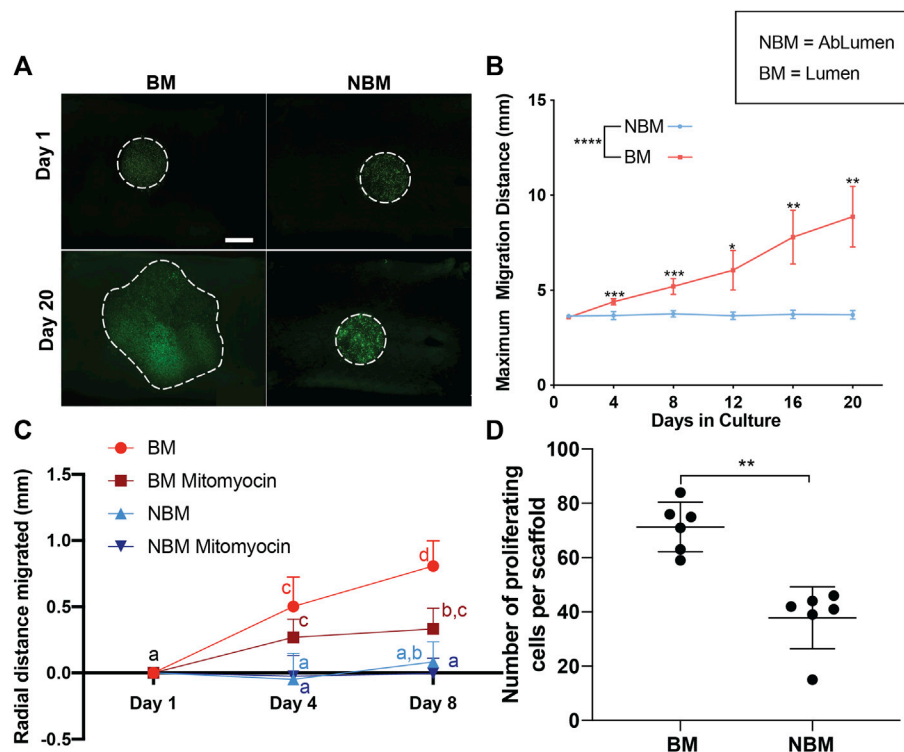
FIGURE 2 | Effects of the presence (BM) versus the absence (NBM) of basement membrane proteins on human aortic endothelial cell (hAECs) migration and proliferation. Inverted microscopy images of GFP-labeled hAECs demonstrate that cells seeded on the BM surface cover a larger surface area than those seeded on the non-basement membrane protein (NBM) surface following 20 days in culture **(A)**. Dashed lines for Day 1 images indicate the initial seeding location of the cells. Dashed lines on Day 20 images indicate the final location of the cells. Due to the uneven surface of the scaffolds and the imaging method (stitch function in microscope Nikon Eclipse Ts2R), different values of cell brightness and focus are present in the images. A quantitative analysis of cell migration distance shows a significant increase in the maximal migration distance for cells seeded on the BM surface versus the NBM surface at all post-seeding timepoints **(B)**. Analysis of cell migration only (i.e., proliferation inhibited with mitomycin) shows a significant difference in the maximal radial distance migrated by treated-hAECs seeded on the BM surface (BM mitomyocin) when compared to treated-hAECs seeded on the NBM surface (NBM mitomyocin) at all timepoints **(C)**. Groups not connected by the same lower case letter are significantly different. Maximal migratory distance following 9 days of culture was reduced by the addition of mitomycin for cells seeded on the BM surface, but not for those seeded on the NBM surface **(D)** Assessment of proliferation only (i.e., FUCCI staining) demonstrated a significantly higher number of proliferating hAECs on the BM surface when compared to the cells in the NBM surface **(D)**. Scale bar A, 5,000 µm * = $p < 0.05$, ** = $p < 0.01$, *** = $p < 0.001$.

interquartile range (IQR). Statistical significance is defined at $p < 0.05$.

3 RESULTS

3.1 Antigen Removal Preserves Native Saphenous Veins Composition and Basement Membrane Integrity

Preservation of the native SV structural (e.g., Col I) and basement membrane proteins (e.g., Laminin, Col IV) organization, content, and macromolecular integrity in AR-SV ECM scaffolds was assessed using histology, polarized light microscopy, and immunofluorescence. H&E stained sections demonstrate that AR scaffolds are completely acellular, while native ECM morphology is well preserved both in the luminal and abluminal regions (**Figure 1A**).

VVG-stained sections demonstrate the preservation of native SV elastin and collagen content in AR scaffolds. Elastin fibril organization is preserved, as evidenced by the intact internal and external elastic laminae in AR scaffolds (**Figure 1B**). Immunofluorescent staining of basement membrane proteins (i.e., Col IV and laminin) demonstrated the retention of native basement membrane component content and organization on the luminal surface of AR-scaffolds (**Figures 1C,D**). Collagen polarization of PSR-stained sections under polarized light demonstrated the retention of native SV collagen birefringence in AR scaffolds (**Figure 1E**). Quantification of the collagen birefringence [7.99% (6.24–10.3)] area (**Figure 1F**), collagen IV [26.46% (22.33–31.6)] area (**Figure 1G**), and laminin [26.63% (22.8–31.95) area (**Figure 1H**) remained unchanged when compared to the native SV (collagen birefringence: 9.46% [5.98–11.07] area, $p > 0.999$, collagen IV: 26.73% [23.78–30.66] area, $p > 0.999$, laminin: 26.34% [21.8–30.76], $p > 0.999$).
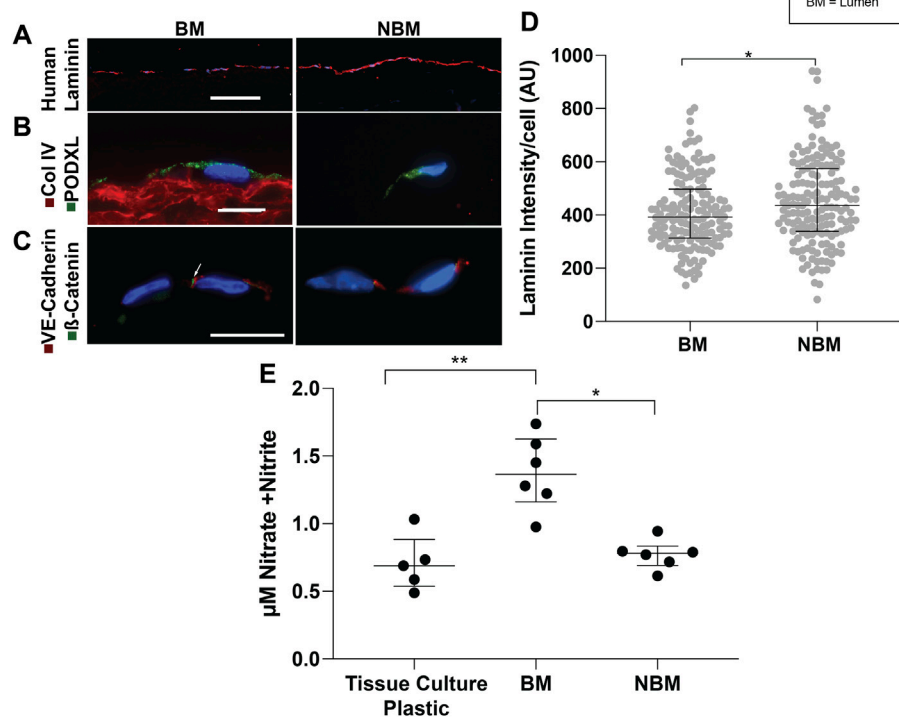
FIGURE 3 | Effects of the presence (BM) versus the absence (NBM) of basement membrane proteins on hAEC phenotypes and functions. Representative images of immunofluorescent staining of human laminin production demonstrates the increased production of human laminin in the hAECs seeded on the non-basement membrane protein (NBM) surface when compared to cells seeded on the BM surface **(A)**. A quantitative analysis of the human laminin production per cell shows a significant higher production of human laminin by the hAECs seeded on the NBM surface versus on the BM surface **(D)**. Representative images of immunofluorescent staining for endothelial cell polarization demonstrates that the BM presence mediates the polarization of podocalyxin (green) to the apical cell surface of seeded hAECs, indicating their quiescent phenotype **(B)**. Conversely, apical polarization of podocalyxin is not present on hAECs seeded on the NBM protein side **(B)**. Similarly, representative images of the adherence junction immunofluorescent staining for VE-cadherin (red) and β-catenin (green) resulted in appropriate expression and co-localization of these adherence junction proteins (indicated by the arrow) in hAECs seeded on the BM surface, while expression and co-localization is not seen in cells seeded on the NBM protein surface **(C)**. A quantitative analysis of nitrate and nitrite secretions (nitric oxide biproducts) of HUVEC-seeded AR-scaffolds, show a significant increase in nitrate and nitrite secretions by cells seeded on the BM protein surface, compared to the cells seeded on the NBM protein surface or tissue culture plastic **(E)**. Scale bar A, 100 μm. Scale bars B and C, 10 μm * = $p < 0.05$, ** = $p < 0.01$.

3.2 Presence of Basement Membrane Proteins Enhances the Rate of Monolayer Formation as Assessed by Endothelial Cell Migration and Proliferation

To determine the effect of basement membrane proteins on the rate of hAEC monolayer formation, proliferation, and migration were assessed for cells seeded in the presence (i.e., basement membrane surface—BM) or absence (i.e., non-basement membrane surface—NMB) of basement membrane proteins. To determine the effect on cell spread due to the combined effect of migration/proliferation, cells were seeded on either the BM or NBM surface of the AR-scaffolds in the same initial seeding diameter (i.e., 3.5 mm disc in the center of a 1 × 1 cm scaffold). While no differences were seen between the two sides at day 1, hAECs seeded on the BM surface covered a larger surface area than those seeded on the NBM surface by 20 days post-seeding (**Figure 2A**). A quantitative analysis of cell migration/proliferation demonstrated that the cells seeded on the BM

surface spread farther each day [0.28 mm/day (0.13–0.37)] when compared to the cells seeded on the NBM surface [0.006 mm/day (0.008–0.01)] at all post-seeding time points [**Figure 2B**; day 4 ($p < 0.001$), day 8 ($p < 0.001$), day 12 ($p < 0.05$), day 16 ($p < 0.01$) and day 20 ($p < 0.01$)]. The effect of basement membrane presence vs the absence on hAEC migration alone was assessed by inhibiting the proliferation with mitomycin. Migration-only experiments demonstrated a significant difference in the maximal radial distance migrated by treated hAECs seeded on the BM surface (BM Mitomyocin, 0.043 mm/day [0.069–0.015]) when compared to treated hAECs seeded on the NBM surface (NBM Mitomyocin, 0.0032 mm/day [0.022–0.018]) at day 4 ($p < 0.05$) and day 8 ($p < 0.05$) post-seeding (**Figure 2C**). Inhibition of proliferation did not significantly reduce early (day 4) migration in the presence of basement membrane components. However, at later timepoints, proliferation inhibition decreased the maximal migratory distance (day 8) compared to combined migration/proliferation in the presence of basement membrane proteins. The effect of the

basement membrane proteins' presence vs absence on EC proliferation was assessed using FUCCI staining. Basement membrane presence (i.e., BM surface) resulted in a significantly higher number of proliferating hAECs [73 (62–78) per scaffold, $p < 0.01$] compared to the number of hAECs proliferating following seeding on the NBM surface [42 (Rieder et al., 2004; Gratzer et al., 2006; Jaffe et al., 2008; Martin-Belmonte and Mostov, 2008; Reing et al., 2009; Lampugnani et al., 2010; Bloch et al., 2012; Tousoulis et al., 2012; Lizama and Zovein, 2013; Yeong, 2013; Heo et al., 2015; Iorio et al., 2015; van Dijk et al., 2020) per scaffold, **Figure 2D**].

3.3 Presence of Basement Membrane Proteins Enhance the Endothelial Cell Quiescent Phenotype and Function in a Confluent Monolayer

The ability of basement membrane proteins in AR-SV scaffolds to drive the quiescent behavior of confluent endothelial cells (i.e., seeded as a monolayer) was determined using immunofluorescence and nitric oxide production. Qualitative assessment of human laminin production using immunofluorescence demonstrated that hAECs seeded on the BM side produced less human laminin that those seeded on the NBM surface (**Figure 3A**). Quantification of human laminin production per cell confirmed significantly lower human laminin production for cells seeded on BM surfaces [392 AU/cell (313.8–497), $p < 0.05$] compared to those on the NBM surface [435.9 AU/cell (338.8–574.2), **Figure 3D**]. Representative images of the immunofluorescence staining demonstrated apical polarization of podocalyxin (PODXL) in hAECs seeded on the BM surface, while polarization was absent in cells seeded on the NBM surface (**Figure 3B**). Similarly, the formation of adherence junctions was evident in hAECs seeded on the BM surface of AR-scaffolds, with appropriate co-localization of VE-cadherin and β-catenin. Conversely, adherence junction formation was lacking in the cells seeded on the NBM surface (**Figure 3C**). Finally., nitric oxide production of HUVECs was higher following BM surface seeding [1.36 μM Nitrate + Nitrite (1.16–1.63)] compared to the cells seeded on tissue culture plastic [0.64 μM Nitrate + Nitrite (0.31–0.81) $p < 0.01$] or the NBM surface [0.78 μM Nitrate + Nitrite (0.69–0.83), $p < 0.05$]. Nitric oxide production was not significantly different between cells seeded on tissue culture plastic and those seeded on the NBM surface ($p > 0.05$, **Figure 3E**).

3.4 Endothelial Cells Seeded as a Monolayer on the Basement Membrane Side of Antigen Removal-ECM Scaffolds Adopt a Transcriptional Phenotype Similar to Simvastatin Treated Human Aortic Endothelial Cells, but Distinct From TNFα Treated Human Aortic Endothelial Cells

To determine the effect of BM presence on hAEC quiescence, cells seeded on AR-scaffolds were compared to quiescent (simvastatin) and activated (TNFα) hAECs *via* RNA sequencing. A total of 415 individual genes were determined to be significantly different in each of the three groups (scaffolds, simvastatin, and TNFα), compared to control. The TNFα group accounted for 306 of these differentially expressed genes, while the scaffold and simvastatin groups contained 59 and 85 differentially expressed genes, respectively. Only five genes (ACP5, CXCL8, FST, NOV, and ST6GALNAC1) were found to be differentially expressed across all three groups. Hierarchial clustering of the heatmap of all significantly differentially expressed genes across all three treatment groups demonstrated each respective group possessed its own distinct transcriptomic signature as evidenced by all six replicates within each treatment group clustering together (**Figure 4A**). Additionally, the scaffold group is seen clustered between the simvastatin and control groups, relatively removed from the TNFα group in the heatmap.

Gene Set Enrichment Analyses (GSEA) were employed to examine the pathways which were significantly enriched in each treatment group, compared to control. A total of 355 pathways (17 positive, 338 negative) were found to be significantly enriched in the scaffold- seeded hAECs from the REACTOME, HALLMARK, and KEGG gene set databases. Comparatively, the simvastatin group had a total of 279 (5 positive, 274 negative) and the TNFα group possessed a total of 133 (124 positive, nine negative) significantly enriched pathways. Bar plots showing the magnitude and directionality of significantly enriched HALLMARK and KEGG pathways for each of the three treatment groups indicated that the scaffold group (**Figure 4C**) was more similar to the simvastatin group (**Figure 4B**), than the TNFα group (**Figure 4D**) with respect to both the directionality and identity of the significantly enriched pathways. Representative GSEA plots for three biologically relevant pathways, including mitosis (**Figure 4E**), programmed cell death (**Figure 4F**), and glucose metabolism (**Figure 4G**) confirm this observation. For all three pathways shown, both the simvastatin and scaffold groups are negatively enriched, while the TNFα group demonstrates a positive enrichment.

3.5 tSNE Clustering Analysis Confirms the Similarity Between Scaffold-Seeded and Simvastatin-Treated Human Aortic Endothelial Cells, and Highlights the Disparity Between the TNFα Group

To further confirm hAECs seeded on the AR-scaffolds had a similar transcriptional profile to the simvastatin-treated cells, compared to the TNFα-treated cells; tSNE clustering analysis was performed based on the top 1,000 variable genes across all samples (**Figure 5A**). The Principal Component 1 (PC1), which accounts for 79.88% of the variance, shows a distinct separation between the TNFα-treated group and the other three groups (simvastatin, control, and scaffold). Interestingly, the Principal Component 2 (PC2), which explains the remaining 20.12% of the variance, highlights a separation between scaffold-seeded cells and the other three treatment groups, which were seeded on tissue culture plastic.
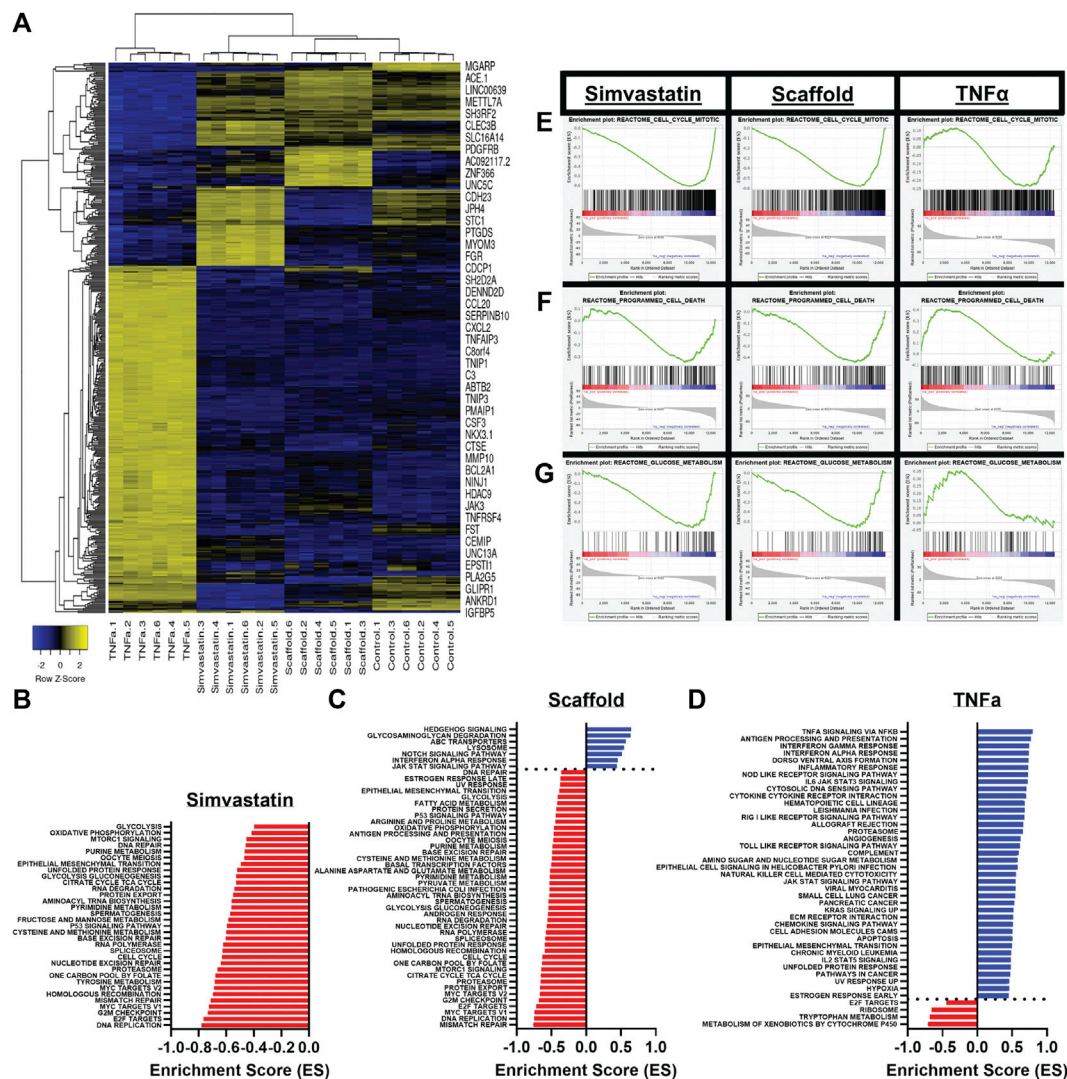
FIGURE 4 | Differential gene expression and the gene set enrichment analysis of scaffold seeded, simvastatin-, and TNFα-treated hAECs. **(A)** Heatmap of all 415 identified significantly differentially expressed genes across all three treatment groups. **(B–D)** Significantly enriched pathways in the KEGG and HALLMARK gene sets following GSEA for simvastatin **(B)**, scaffold **(C)**, and TNFα **(D)** groups. **(E–G)** Representative GSEA plots across all three groups for three biologically relevant pathways, including mitosis **(E)**, programmed cell death **(F)**, and glucose metabolism **(G)**.

In order to better understand the differences between PC1 and PC2, the top 100 genes responsible for driving the differences observed in each Principal Component were extracted. Using the read count data, Z-scores for each of these genes were calculated and heatmaps were generated for both PC1 (**Figure 5B**) and PC2 (**Figure 5C**). PC1 is almost exclusively driven by up-regulated genes in the TNFα group (**Figure 5B**). When we performed an Over-Representation Analysis (ORA) on these genes using WebGestalt, the top ten enriched pathways generally reflected a pro-inflammatory response, of which, TNFα is a potent inducer (**Figure 5D**). Similar to what was observed in the tSNE clustering analysis, the heatmap for the top 100 genes in PC2 (**Figure 5C**) illustrates that there is a distinct difference between the cells seeded on the AR-ECM scaffold and cells seeded on tissue culture

plastic (control, TNFα or simvastatin). Although there is not as distinct of a pattern in the ORA of the PC2 genes, as compared to the PC1 genes, of the top 10 enriched pathways, five (50%) pathways are related to cell chemotaxis and responding to chemokines (**Figure 5E**).

4 DISCUSSION

The success of of-the-shelf small diameter vascular grafts is dependent on the ability of endothelial cells to rapidly form a monolayer on the luminal surface of the graft and to promote quiescent behavior once the monolayer has been established (Lopera Higuita and Griffiths, 2020b). Acellular ECM scaffolds
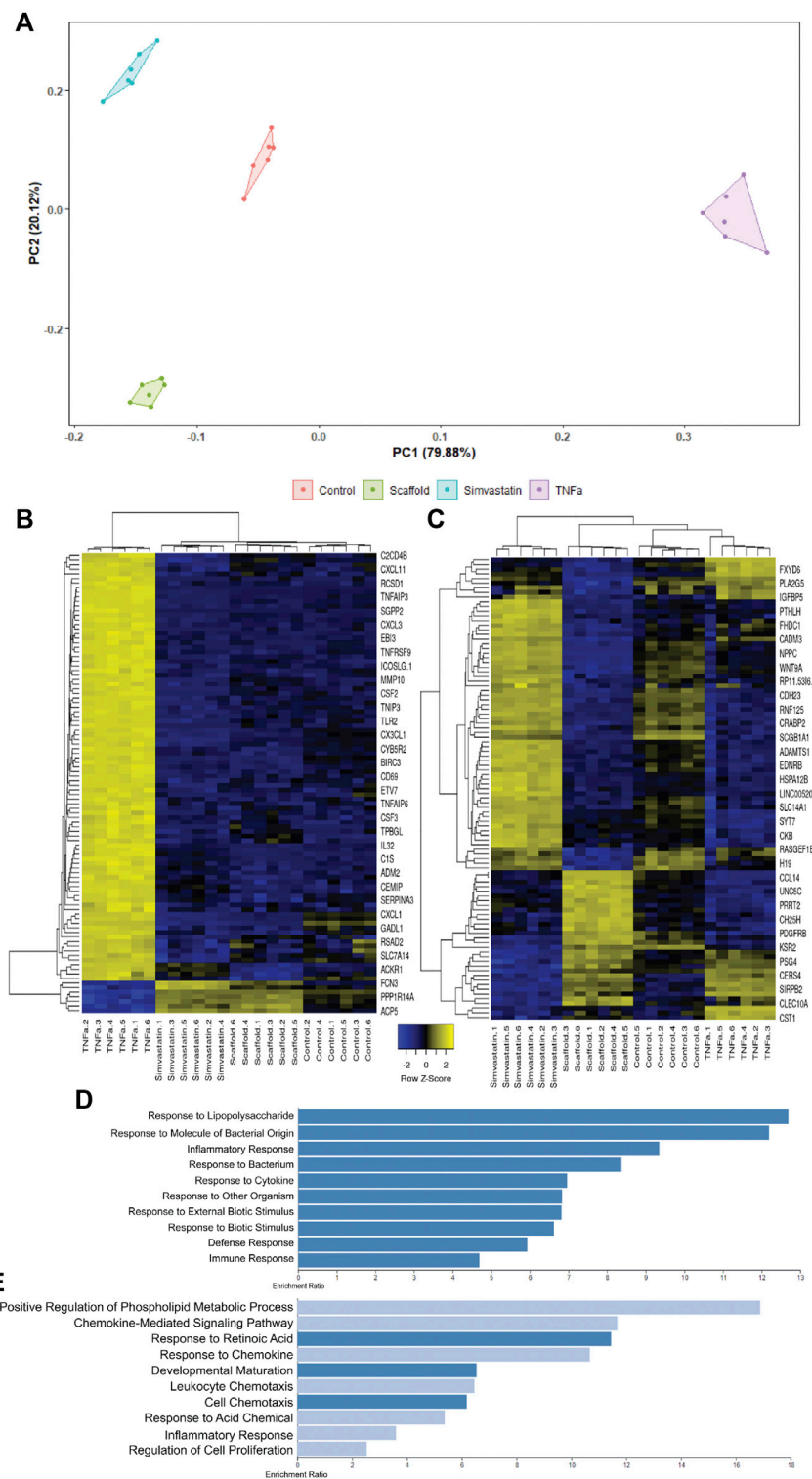
FIGURE 5 | tSNE clustering analysis of scaffold seeded, simvastatin, and TNFα-treated hAECs. The tSNE clustering analysis plot is driven by the top 1,000 variable genes across all samples **(A)**. PC1 accounts for 79.88% of the variance, while PC2 explains the remaining 20.22%. Heatmap of the top 100 genes responsible for driving PC1 **(B)**. PC1 is almost exclusively driven by up-regulated genes in the TNFα group. Enrichment plot of the top 10 enriched gene ontology biological processes for the top 100 genes driving PC1 **(D)**. The top 10 enriched pathways in PC1 are all associated with pro-inflammatory responses. Heatmap of the top 100 genes responsible for driving PC2 **(C)**. PC2 is predominantly driven by up-regulated genes in the scaffold group. Enrichment plot of the top 10 enriched gene ontology biological processes for the top 100 genes driving PC2 **(E)**. 50% of the enriched pathways in PC2 are associated with cellular chemotaxis and respond to chemokines.

derived from their target organs have gained importance in the field of tissue engineering due to their inherent characteristics. ECM proteins secreted by host cells are tailored for the specific needs and functions of each independent organ. In vascular physiology, basement membrane proteins are essential for vessel homeostasis due to their known individual roles in modulating endothelial cell behavior and vascular integrity. Consequently, basement membrane proteins may be expected to play a key role in promoting endothelialization and the resultant function of denuded ECM scaffolds when implanted as vascular grafts. The results in this article demonstrate that the AR process is capable of preserving the major components of native tissue basement membrane complex and the conjoint effect of these complexes modulates endothelial cell migration and proliferation, enhancing the rate of th monolayer formation and drives the quiescent behavior once a cell confluence has been achieved.

The importance of basement membrane proteins in vascular biology highlight the need for tissue-processing methods to retain the structure, composition, and function of this critical vascular component in acellular ECM scaffolds. Unfortunately, the goal of retaining the native vascular basement membrane integrity has proven challenging to achieve (Crapo et al., 2011). Previously reported de-cellularization methods have been shown to result in significant disruption of basement membrane integrity, although the extent to which each individual basement membrane protein is disrupted and/or eliminated varies depending on the de-cellularization process and specific tissue employed (Crapo et al., 2011). In the case of vascular grafts, de-cellularization methods have been universally reported to disrupt the delicate native BM components (Schaner et al., 2004; Crapo et al., 2011; Mancuso et al., 2014). Alternatively, antigen removal (AR) tissue-processing method has been designed to minimize macromolecule denaturation and disruption, while maximizing antigen solubilization and elimination, resulting in the production of ECM scaffolds with retained native ECM, including basement membrane proteins (Liu et al., 2016; Shklover et al., 2019; Xing et al., 2021). Indeed, in the current study, the capability of the AR tissue-processing method to retain both the composition and structural integrity of ECM and basement membrane proteins is clearly shown by the retention of appropriately oriented collagen, elastin, collagen IV (Col IV), and laminin. Consequently, unlike previously reported de-cellularization processes, the results presented here demonstrate the ability of the AR tissue-processing method to retain the integrity of the native small diameter vascular scaffold ECM components, including the delicate basement membrane complex (Bloch et al., 2012; Faulk et al., 2014b).

Basement membrane proteins are a specialized, thin layer of ECM proteins composed by a wide array of different proteins (Col IV, laminin, heparan sulfate proteoglycans, nidogen, fibrillin, collagen III, and osteonectin) that interact with each other to provide important structural and functional support to the overlying endothelial cells. Although being composed by multiple proteins, laminin and Col IV are among the few basement membrane proteins capable of modulating endothelial cell behavior *via* cellular receptors (Xing et al.,

2021). In isolation, Col IV has been shown to facilitate endothelial cell migration and provide migration directionality (Heo et al., 2015). As predicted from single protein studies, the individual effects of Col IV persist in the present study. Endothelial cells seeded on the BM surface, and therefore exposed to Col IV, were able to migrate significantly farther than cells seeded on the NBM side. Although other literature in de-cellularized tissues has reported cell migration into ECM scaffolds, such studies failed to investigate whether a differential effect of the migration on the BM versus NBM environments existed (Rieder et al., 2004; Gratzer et al., 2006; Reing et al., 2009). Since alterations to the ECM proteins play a key role in decreasing cell chemotaxis, the aforementioned effect of de-cellularization on basement membrane integrity would be expected to abolish such differential cell migratory behavior (Rieder et al., 2004; Gratzer et al., 2006; Reing et al., 2009). Indeed, studies in vascular (i.e., saphenous vein) tissues support this contention, showing that destruction of the basement membrane environment by SDS-decellularization eliminates the effect of BM in driving rapid cell migration (Lopera Higuita and Griffiths, 2020a). The ability of the intact basement membrane of AR vascular scaffolds to increase endothelial cell migration in vascular grafts is an extremely desired scaffold attribute due to the absolute need for rapid endothelial cell monolayer formation to avoid scaffold failure *via* a wide array of mechanisms, including thrombosis (Lopera Higuita and Griffiths, 2020b).

Intriguingly, the absence of basement membrane proteins in the NBM surface also modulated differential cell behavior on the cells seeded on this surface. The cells seeded on the NBM surface initiated the over-expression and secretion of human laminin, a behavior that was less prominent in the cells seeded on the BM surface. The increased human laminin secretion can potentially be attributed to the exposure of endothelial cells to structural collagens (e.g. collagen I), to which they are only exposed during vessel injury. After vessel injury, the endothelial cells react by overexpressing basement membrane proteins, including laminin to provide the substrate for endothelial cell migration into the wound to re-establish an intact endothelial cell layer (Iorio et al., 2015). Furthermore, the confounded necessity to produce their own basement membrane proteins is the likely explanation for their decreased proliferative capacity. To undergo mitosis cells, in general, significantly down-regulate their protein trafficking, making it unviable for laminin over-expression and cell proliferation to happen at the same time (Yeong, 2013). Therefore, the need for basement membrane secretion by the endothelial cells seeded on the NBM surface of the scaffolds likely inhibited cell division, resulting in a lower number of proliferating cells.

In addition to promoting the rapid endothelial cell monolayer formation, an ideal vascular scaffold should also modulate quiescence of the re-populated cells once a confluent monolayer is achieved. Surfaces which uncontrollably drive endothelial cell activation result in aberrant endothelial cell signaling, proliferation and/or infiltration, leading to failure by intimal hyperplasia, altered vascular tone, recruitment of inflammatory cells, and/or permanently altered vessel wall

structure (McKavanagh et al., 2017). Laminin, along with other basement membrane and ECM proteins, play an important role in driving endothelial cell maturation from actively growing cells toward a quiescent state (van Dijk et al., 2020). Consequently, laminin integrity is expected to be the key to avoid failure by modulating endothelial cell quiescence. Laminin availability to endothelial cells seeded on the BM surface of the scaffolds likely modulated the observed apicobasal polarization (i.e., podocalyxin covering the apical cell membrane only). Conversely, seeding in the NBM surface resulted in failure of quiescent apicobasal endothelial cell polarization. Apicobasal polarization of endothelial cells is an important characteristic of achieved quiescent state and reflects the capability of endothelial cells to maintain the stability and integrity of the vascular wall (Lizama and Zovein, 2013). Additionally, the appropriate formation of an apicobasal polarization is known to be an absolute requirement for correct lumen organization in any type of vessel (Jaffe et al., 2008; Martin-Belmonte and Mostov, 2008). Furthermore, the expression and formation of adherence junctions between the endothelial cells is an absolute pre-requisite to forming this apicobasal polarization (Lampugnani et al., 2010). Endothelial cell adherence junctions are protein complexes that form in the cell–cell junctions and function as sites of cell attachment, signaling, and regulation of growth and apoptosis, as well as vascular homeostasis. Basement membrane proteins (e.g., Laminin) present in the BM surface of the scaffolds provided the appropriate environment and signaling to modulate endothelial cell expression and formation of adherence junctions as indicated by appropriate VE-Cadherin and β-catenin co-localization. Conversely, the lack of BM proteins in the NMB surface resulted in the lack of formation of adherence junctions and the resultant lack of apicobasal polarization. Failure to maintain apicobasal polarization is known to be associated with decreased Col IV and laminin production resulting in aneurysmal dilation and increased vascular permeability (Lampugnani et al., 2010). Finally, additional evidence of the quiescent endothelial cell phenotype for cells seeded on the BM surface was observed due to their capacity to secrete nitric oxide (NO) in higher concentrations than those cells seeded on the NBM surface or tissue culture plastic. NO is a soluble gas that aids in the control of a wide array of biological processes key for vessel homeostasis and normal endothelial cell function (Tousoulis et al., 2012). Its role in preventing vascular diseases is known to be so essential that significant efforts have been allocated into engineering vascular grafts with the capability of synthetically producing and/or releasing NO (Wang Z et al., 2015; Wang Y et al., 2015). Therefore, the capability of AR-scaffolds to naturally modulate endothelial cells to secrete NO is an important achievement toward the development of a small diameter vascular graft. Collectively, the ability of the intact basement membrane of AR vascular scaffolds to drive apicobasal polarization, adherence junction formation, and NO production demonstrate the capacity of such scaffold environments to promote endothelial cell quiescence.

Finally, in order to conclusively determine that the intact basement membrane of AR vascular scaffolds promotes endothelial cell quiescence in an unbiased manner, RNA-sequencing was performed to compare the transcriptome of scaffold-seeded cells to the transcriptomes of endothelial cells treated with either simvastatin or TNFα. Simvastatin, a member of the statin drug family, commonly prescribed to patients as a means to lower their cholesterol levels. However in vitro, simvastatin has previously been shown to improve endothelial cell function and potentially induce physiologic changes which reduce the risk of thrombosis development (Beckman and Creager, 2006). Conversely, TNFα is a potent pro-inflammatory cytokine, well known to modulate proliferative and inflammatory behaviors in endothelial cells (Rastogi et al., 2012). In this manner, a continuum between cellular quiescence and cellular activation was established. This was utilized to compare the transcriptional profile of endothelial cells seeded on the BM surface of AR-ECM venous scaffolds and determine how the BM surface influenced the cellular phenotype. It is important to point out that RNA sequencing for cells seeded on the NBM side of the scaffolds could not be performed due to the inability to extract non-fractioned RNA from cells when seeded on this surface. Following the bioinformatics analysis, several pieces of evidence were identified which confirmed that endothelial cells seeded on scaffolds adopted a phenotype more closely resembling simvastatin-treated, rather than TNFα-treated cells. Specifically, the unsupervised hierarchial clustering based on all identified significantly differentially expressed genes across all three treatment groups indicated that the scaffold samples had a similar transcriptional signature to the simvastatin samples, and a signature distinct from the TNFα group (**Figure 4A**). Furthermore, when compared head-to-head, gene set enrichment analyses for each of the three treatment groups indicated that scaffold-seeded cells had a similar magnitude and directionality of enrichment for various pathways as the simvastatin group, but opposite to that of the TNFα group. Additionally, many of the commonly enriched pathways between the simvastatin and scaffold groups were related to processes that are commonly down-regulated in quiescent cells. In particular, there was a strong negative enrichment in pathways relating to the cell cycle, programmed cell death, and metabolism in these two groups (Cho et al., 2019; Li et al., 2019). Conversely, however, these processes were positively enriched in the endothelial cells treated with TNFα (**Figures 4E–G**), consistent with the up-regulation of these processes upon cellular activation. Furthermore, tSNE clustering analyses demonstrated distinct differences between the TNFα-treated cells and the other three groups (as evidenced by PC1, which accounted for ~80% of the variance). The main component driving the variance in PC1 is a strong up-regulation of the genes in the TNFα group, which are not up-regulated in the other three groups. An over-representation analysis (ORA) of these PC1 genes confirms this finding, as all 10 of the top 10 most enriched gene ontology-biological processes pathways are pro-inflammatory/regulated by TNFα (**Figure 5C**). Interestingly, PC2 (which explained the remaining ~20% of the variance) showed a separation between the three groups seeded on tissue culture plastic and the cells which were interacting with the BM of AR vascular scaffolds

(**Figure 5A**). Additionally, as suspected based on the tSNE clustering analysis, PC2 appears to be driven primarily between differences between the scaffold group and the other three groups which were seeded on tissue culture plastic (**Figure 5D**). In the same manner, an ORA of these genes indicated that half of the top ten (5/10) most enriched pathways were related to cellular chemotaxis/response to chemokines (**Figure 5E**). It is well established that the extracellular matrix is a reservoir for numerous cell signaling molecules which can modulate cell behaviors (Valiente-Alandi et al., 2016; Poltavets et al., 2018). The fact that cells interacting with AR ECM scaffolds would be enriched for pathways related to chemotaxis further demonstrates that the seeded endothelial cells are interacting in appropriate biologically relevant ways to the active components of ECM. Overall, these results indicate that hAECs seeded on the BM (luminal) side of AR ECM venous scaffolds respond to inherent ECM signals, mediating the observed cellular migration, proliferation, and quiescent phenotype.

5 CONCLUSION

The results in this manuscript indicate that the intact basement membrane proteins present in AR vascular scaffolds positively modulate a wide array of endothelial cellular processes resulting in the rapid re-cellularization and quiescent endothelial cell monolayer formation, which is known to be essential for vascular homeostasis. Therefore, we conclude that the retention of basement membrane proteins by tissue processing methods is essential for the success of small diameter vascular grafts. Due to the capability of AR to retain the macromolecular structure, organization, and composition of the proteins within the ECM scaffold, future work is required to separate the individual effects of each of the basement membrane protein's macromolecular integrity and structure of the resultant surface on resultant endothelial cell responses.

DATA AVAILABILITY STATEMENT

The dataset presented in this study can be found in online at GEO, accession number GSE199281, https://www.ncbi.nlm.nih.gov/geo/query/acc.cgi?acc=GSE199281.

AUTHOR CONTRIBUTIONS

LG contributed to conception and design of the study. ML performed all "wet lab" experiments and their corresponding statistical analysis and wrote the first draft of the manuscript. NS contributed to determining the type of analysis to do on RNA sequence data, created the RNA-seq figures, and wrote section of the manuscript. SD performed the data processing for the RNA sequencing experiments. All authors contributed to the manuscript revision, read, and approved the submitted version.

FUNDING

SUPPLEMENTARY MATERIAL

The Supplementary Material for this article can be found online at: https://www.frontiersin.org/articles/10.3389/fbioe.2022.903907/full#supplementary-material

REFERENCES

Alexander, J. H., and Smith, P. K. (2016). Coronary-Artery Bypass Grafting. *N. Engl. J. Med.* 374 (20), 1954–1964. doi:10.1056/nejmra1406944

Anders, S., Pyl, P. T., and Huber, W. (2015). HTSeq-A Python Framework to Work with High-Throughput Sequencing Data. *Bioinformatics* 31 (2), 166–169. doi:10.1093/bioinformatics/btu638

Babicki, S., Arndt, D., Marcu, A., Liang, Y., Grant, J. R., Maciejewski, A., et al. (2016). Heatmapper: Web-Enabled Heat Mapping for All. *Nucleic Acids Res.* 44 (W1), W147–W153. doi:10.1093/nar/gkw419

Beckman, J. A., and Creager, M. A. (2006). The Nonlipid Effects of Statins on Endothelial Function. *Trends Cardiovasc. Med.* 16 (5), 156–162. doi:10.1016/j.tcm.2006.03.003

Benjamin, E. J., Muntner, P., Alonso, A., Bittencourt, M. S., Callaway, C. W., Carson, A. P., et al. (2019). Heart Disease and Stroke Statistics-2019 Update: A Report from the American Heart Association. *Circulation* 139 (10), e56–e528. doi:10.1161/CIR.0000000000000659

Bloch, O., Erdbrügger, W., Völker, W., Schenk, A., Posner, S., Konertz, W., et al. (2012). Extracellular Matrix in Deoxycholic Acid Decellularized Aortic Heart Valves. *Med. Sci. Monit.* 18 (12), BR487–BR492. doi:10.12659/msm.883618

Cho, I. J., Lui, P. P., Obajdin, J., Riccio, F., Stroukov, W., Willis, T. L., et al. (2019). Mechanisms, Hallmarks, and Implications of Stem Cell Quiescence. *Stem Cell Rep.* 12 (6), 1190–1200. doi:10.1016/j.stemcr.2019.05.012

Crapo, P. M., Gilbert, T. W., and Badylak, S. F. (2011). An Overview of Tissue and Whole Organ Decellularization Processes. *Biomaterials* 32 (12), 3233–3243. doi:10.1016/j.biomaterials.2011.01.057

Dalgliesh, A. J., Parvizi, M., Lopera-Higuita, M., Shklover, J., and Griffiths, L. G. (2018). Graft-specific Immune Tolerance Is Determined by Residual Antigenicity of Xenogeneic Extracellular Matrix Scaffolds. *Acta Biomater.* 79, 253–264. doi:10.1016/j.actbio.2018.08.016

de Vries, M. R., Simons, K. H., Jukema, J. W., Braun, J., and Quax, P. H. A. (2016). Vein Graft Failure: From Pathophysiology to Clinical Outcomes. *Nat. Rev. Cardiol.* 13 (8), 451–470. doi:10.1038/nrcardio.2016.76

Dobin, A., Davis, C. A., Schlesinger, F., Drenkow, J., Zaleski, C., Jha, S., et al. (2013). STAR: Ultrafast Universal RNA-Seq Aligner. *Bioinformatics* 29 (1), 15–21. doi:10.1093/bioinformatics/bts635

Faulk, D. M., Johnson, S. A., Zhang, L., and Badylak, S. F. (2014). Role of the Extracellular Matrix in Whole Organ Engineering. *J. Cell. Physiol.* 229 (8), 984–989. doi:10.1002/jcp.24532

Faulk, D. M., Carruthers, C. A., Warner, H. J., Kramer, C. R., Reing, J. E., Zhang, L., et al. (2014). The Effect of Detergents on the Basement Membrane Complex of a Biologic Scaffold Material. *Acta Biomater.* 10 (1), 183–193. doi:10.1016/j.actbio.2013.09.006

Fryar, C. D., Chen, T., and Li, X. (2012). *Prevalence of Uncontrolled Risk Factors for Cardiovascular Disease: United States, 1999-2010.* No. 103. US Department of Health and Human Services, Centers for Disease Control and Prevention, National Center for Health Statistics.

Gratzer, P. F., Harrison, R. D., and Woods, T. (2006). Matrix Alteration and Not Residual Sodium Dodecyl Sulfate Cytotoxicity Affects the Cellular Repopulation of a Decellularized Matrix. *Tissue Eng.* 12 (10), 2975–2983. doi:10.1089/ten.2006.12.2975

Heo, Y., Shin, Y. M., Lee, Y. B., Lim, Y. M., and Shin, H. (2015). Effect of Immobilized Collagen Type IV on Biological Properties of Endothelial Cells for the Enhanced Endothelialization of Synthetic Vascular Graft Materials. *Colloids Surfaces B Biointerfaces* 134, 196–203. doi:10.1016/j.colsurfb.2015.07.003

Hillis, L. D., Smith, P. K., Anderson, J. L., Bittl, J. A., Bridges, C. R., Byrne, J. G., et al. (2011). 2011 ACCF/AHA Guideline for Coronary Artery Bypass Graft Surgery. A Report of the American College of Cardiology Foundation/American Heart Association Task Force on Practice Guidelines. Developed in Collaboration with the American Association for Thoracic Surgery, Society of Cardiovascular Anesthesiologists, and Society of Thoracic Surgeons. *J. Am. Coll. Cardiol.* 58 (24), e123–210. doi:10.1016/j.jacc.2011.08.009

Hillis, L. D., Smith, P. K., Anderson, J. L., Bittl, J. A., Bridges, C. R., Byrne, J. G., et al. (2012). 2011 ACCF/AHA Guideline for Coronary Artery Bypass Graft Surgery: Executive Summary: A Report of the American College of Cardiology Foundation/American Heart Association Task Force on Practice Guidelines. *J. Thorac. Cardiovasc Surg.* 143 (1), 4–34. doi:10.1016/j.jtcvs.2011.10.015

Huang, G., and Greenspan, D. S. (2012). ECM Roles in the Function of Metabolic Tissues. *Trends Endocrinol. Metabol.* 23 (1), 16–22. doi:10.1016/j.tem.2011.09.006

Iorio, V., Troughton, L. D., and Hamill, K. J. (2015). Laminins: Roles and Utility in Wound Repair. *Adv. Wound Care* 4 (4), 250–263. doi:10.1089/wound.2014.0533

Jaffe, A. B., Kaji, N., Durgan, J., and Hall, A. (2008). Cdc42 Controls Spindle Orientation to Position the Apical Surface during Epithelial Morphogenesis. *J. Cell Biol.* 183 (4), 625–633. doi:10.1083/jcb.200807121

Kalari, K. R., Nair, A. A., Bhavsar, J. D., O'Brien, D. R., Davila, J. I., Bockol, M. A., et al. (2014). MAP-RSeq: Mayo Analysis Pipeline for RNA Sequencing. *BMC Bioinform.* 15, 224. doi:10.1186/1471-2105-15-224

Lampugnani, M. G., Orsenigo, F., Rudini, N., Maddaluno, L., Boulday, G., Chapon, F., et al. (2010). CCM1 Regulates Vascular-Lumen Organization by Inducing Endothelial Polarity. *J. Cell Sci.* 123 (Pt 7), 1073–1080. doi:10.1242/jcs.059329

Lee, C.-H., Yu, C.-Y., Chang, S.-H., Hung, K.-C., Liu, S.-J., Wang, C.-J., et al. (2014). Promoting Endothelial Recovery and Reducing Neointimal Hyperplasia Using Sequential-like Release of Acetylsalicylic Acid and Paclitaxel-Loaded Biodegradable Stents. *Int. J. Nanomedicine* 9, 4117–4133. doi:10.2147/ijn.s67721

Li, X., Sun, X., and Carmeliet, P. (2019). Hallmarks of Endothelial Cell Metabolism in Health and Disease. *Cell Metab.* 30 (3), 414–433. doi:10.1016/j.cmet.2019.08.011

Liao, Y., Jaehnig, E. J., Shi, Z., and Zhang, B. (2019). WebGestalt 2019: Gene Set Analysis Toolkit with Revamped UIs and APIs. *Nucleic Acids Res.* 47 (W1), W199–W205. doi:10.1093/nar/gkz401

Liu, Z. Z., Wong, M. L., and Griffiths, L. G. (2016). Effect of Bovine Pericardial Extracellular Matrix Scaffold Niche on Seeded Human Mesenchymal Stem Cell Function. *Sci. Rep.* 6, 37089. doi:10.1038/srep37089

Lizama, C. O., and Zovein, A. C. (2013). Polarizing Pathways: Balancing Endothelial Polarity, Permeability, and Lumen Formation. *Exp. Cell Res.* 319 (9), 1247–1254. doi:10.1016/j.yexcr.2013.03.028

Lopera Higuita, M., and Griffiths, L. G. (2020). Antigen Removal Process Preserves Function of Small Diameter Venous Valved Conduits, whereas SDS-Decellularization Results in Significant Valvular Insufficiency. *Acta Biomater..* doi:10.1016/j.actbio.2020.03.003

Lopera Higuita, M., and Griffiths, L. G. (2020). Small Diameter Xenogeneic Extracellular Matrix Scaffolds for Vascular Applications. *Tissue Eng. Part B Rev.* 26 (1), 26–45. doi:10.1089/ten.teb.2019.0229

Lopera Higuita, M., Lopera Giraldo, J. F., Sarrafian, T. L., and Griffiths, L. G. (2021). Tissue Engineered Bovine Saphenous Vein Extracellular Matrix Scaffolds Produced via Antigen Removal Achieve High *In Vivo* Patency Rates. *Acta Biomater.* 134, 144–159. doi:10.1016/j.actbio.2021.06.034

Mancuso, L., Gualerzi, A., Boschetti, F., Loy, F., and Cao, G. (2014). Decellularized Ovine Arteries as Small-Diameter Vascular Grafts. *Biomed. Mat.* 9 (4), 045011. doi:10.1088/1748-6041/9/4/045011

Martin-Belmonte, F., and Mostov, K. (2008). Regulation of Cell Polarity during Epithelial Morphogenesis. *Curr. Opin. Cell Biol.* 20 (2), 227–234. doi:10.1016/j.ceb.2008.01.001

McKavanagh, P., Yanagawa, B., Zawadowski, G., and Cheema, A. (2017). Management and Prevention of Saphenous Vein Graft Failure: A Review. *Cardiol. Ther.* 6 (2), 203–223. doi:10.1007/s40119-017-0094-6

Morrissey, M. A., and Sherwood, D. R. (2015). An Active Role for Basement Membrane Assembly and Modification in Tissue Sculpting. *J. Cell Sci.* 128 (9), 1661–1668. doi:10.1242/jcs.168021

Poltavets, V., Kochetkova, M., Pitson, S. M., and Samuel, M. S. (2018). The Role of the Extracellular Matrix and its Molecular and Cellular Regulators in Cancer Cell Plasticity. *Front. Oncol.* 8, 431. doi:10.3389/fonc.2018.00431

Popovic, B., Voillot, D., Maureira, P., Vanhuyse, F., Agrinier, N., Aliot, E., et al. (2013). Bilateral Internal Mammary Artery Bypass Grafting: Long-Term Clinical Benefits in a Series of 1000 Patients. *Heart* 99 (12), 854–859. doi:10.1136/heartjnl-2012-303466

Rastogi, S., Rizwani, W., Joshi, B., Kunigal, S., and Chellappan, S. P. (2012). TNF-α Response of Vascular Endothelial and Vascular Smooth Muscle Cells Involve Differential Utilization of ASK1 Kinase and P73. *Cell Death Differ.* 19 (2), 274–283. doi:10.1038/cdd.2011.93

Reing, J. E., Zhang, L., Myers-Irvin, J., Cordero, K. E., Freytes, D. O., Heber-Katz, E., et al. (2009). Degradation Products of Extracellular Matrix Affect Cell Migration and Proliferation. *Tissue Eng. Part A* 15 (3), 605–614. doi:10.1089/ten.tea.2007.0425

Rieder, E., Kasimir, M.-T., Silberhumer, G., Seebacher, G., Wolner, E., Simon, P., et al. (2004). Decellularization Protocols of Porcine Heart Valves Differ Importantly in Efficiency of Cell Removal and Susceptibility of the Matrix to Recellularization with Human Vascular Cells. *J. Thorac. Cardiovasc. Surg.* 127 (2), 399–405. doi:10.1016/j.jtcvs.2003.06.017

Robinson, M. D., McCarthy, D. J., and Smyth, G. K. (2010). edgeR: A Bioconductor Package for Differential Expression Analysis of Digital Gene Expression Data. *Bioinformatics* 26 (1), 139–140. doi:10.1093/bioinformatics/btp616

Schaner, P. J., Martin, N. D., Tulenko, T. N., Shapiro, I. M., Tarola, N. A., Leichter, R. F., et al. (2004). Decellularized Vein as a Potential Scaffold for Vascular Tissue Engineering. *J. Vasc. Surg.* 40 (1), 146–153. doi:10.1016/j.jvs.2004.03.033

Shklover, J., McMasters, J., Alfonso-Garcia, A., Higuita, M. L., Panitch, A., Marcu, L., et al. (2019). Bovine Pericardial Extracellular Matrix Niche Modulates Human Aortic Endothelial Cell Phenotype and Function. *Sci. Rep.* 9 (1), 16688. doi:10.1038/s41598-019-53230-1

Slovut, D. P., and Lipsitz, E. C. (2012). Surgical Technique and Peripheral Artery Disease. *Circulation* 126 (9), 1127–1138. doi:10.1161/circulationaha.111.059048

Taggart, D. P. (2013). Current Status of Arterial Grafts for Coronary Artery Bypass Grafting. *Ann. Cardiothorac. Surg.* 2 (4), 427–430. doi:10.3978/j.issn.2225-319X.2013.07.21

Tousoulis, D., Kampoli, A.-M., Tentolouris, C., Papageorgiou, N., and Stefanadis, C. (2012). The Role of Nitric Oxide on Endothelial Function. *Curr. Vasc. Pharmacol.* 10 (1), 4–18. doi:10.2174/157016112798829760

Tranbaugh, R. F., Schwann, T. A., Swistel, D. G., Dimitrova, K. R., Al-Shaar, L., Hoffman, D. M., et al. (2017). Coronary Artery Bypass Graft Surgery Using the Radial Artery, Right Internal Thoracic Artery, or Saphenous Vein as the Second Conduit. *Ann. Thorac. Surg.* 104 (2), 553–559. doi:10.1016/j.athoracsur.2016.11.017

Valiente-Alandi, I., Schafer, A. E., and Blaxall, B. C. (2016). Extracellular Matrix-Mediated Cellular Communication in the Heart. *J. Mol. Cell. Cardiol.* 91, 228–237. doi:10.1016/j.yjmcc.2016.01.011

van Dijk, C. G. M., Louzao-Martinez, L., van Mulligen, E., Boermans, B., Demmers, J. A. A., van den Bosch, T. P. P., et al. (2020). Extracellular Matrix Analysis of Human Renal Arteries in Both Quiescent and Active Vascular State. *Int. J. Mol. Sci.* 21 (11), 3905. doi:10.3390/ijms21113905

Wang Y., Y., Chen, S., Pan, Y., Gao, J., Tang, D., Kong, D., et al. (2015). Rapid *In Situ* Endothelialization of a Small Diameter Vascular Graft with Catalytic Nitric Oxide Generation and Promoted Endothelial Cell Adhesion. *J. Mat. Chem. B* 3 (47), 9212–9222. doi:10.1039/c5tb02080h

Wang Z., Z., Lu, Y., Qin, K., Wu, Y., Tian, Y., Wang, J., et al. (2015). Enzyme-functionalized Vascular Grafts Catalyze Iin-Ssitu Release of Nitric Oxide from

Exogenous NO Prodrug. *J. Control. Release* 210, 179–188. doi:10.1016/j.jconrel. 2015.05.283

Xing, Q., Parvizi, M., Lopera Higuita, M., and Griffiths, L. G. (2021). Basement Membrane Proteins Modulate Cell Migration on Bovine Pericardium Extracellular Matrix Scaffold. *Sci. Rep.* 11 (1), 4607. doi:10.1038/s41598-021-84161-5

Yeong, F. M. (2013). Multi-step Down-regulation of the Secretory Pathway in Mitosis: A Fresh Perspective on Protein Trafficking. *Bioessays* 35 (5), 462–471. doi:10.1002/bies.201200144

Conflict of Interest: The authors declare that the research was conducted in the absence of any commercial or financial relationships that could be construed as a potential conflict of interest.

Strategies to improve the therapeutic effect of pluripotent stem cell-derived cardiomyocytes on myocardial infarction

Yang Xiao[1†], Yihuan Chen[1†], Chunlai Shao[2†], Yaning Wang[1], Shijun Hu[1]* and Wei Lei[1]*

[1]Department of Cardiovascular Surgery of the First Affiliated Hospital and Institute for Cardiovascular Science, Collaborative Innovation Center of Hematology, State Key Laboratory of Radiation Medicine and Protection, Suzhou Medical College, Soochow University, Suzhou, China, [2]Department of Cardiology, The Second Affiliated Hospital of Soochow University, Suzhou, China

Myocardial infarction (MI) is a common cardiovascular disease caused by permanent loss of cardiomyocytes and the formation of scar tissue due to myocardial ischemia. Mammalian cardiomyocytes lose their ability to proliferate almost completely in adulthood and are unable to repair the damage caused by MI. Therefore, transplantation of exogenous cells into the injured area for treatment becomes a promising strategy. Pluripotent stem cells (PSCs) have the ability to proliferate and differentiate into various cellular populations indefinitely, and pluripotent stem cell-derived cardiomyocytes (PSC-CMs) transplanted into areas of injury can compensate for part of the injuries and are considered to be one of the most promising sources for cell replacement therapy. However, the low transplantation rate and survival rate of currently transplanted PSC-CMs limit their ability to treat MI. This article focuses on the strategies of current research for improving the therapeutic efficacy of PSC-CMs, aiming to provide some inspiration and ideas for subsequent researchers to further enhance the transplantation rate and survival rate of PSC-CMs and ultimately improve cardiac function.

Introduction

Myocardial infarction (MI), also called heart attack, is the most common form of cardiovascular disease and a leading cause of mortality worldwide (Roth et al., 2020). MI involves the ischemic death of myocardial tissue, usually due to sudden occlusion of the coronary artery caused by plaque rupture and acute thrombosis, resulting in the obstruction of blood flow to a section of the heart. Myocardial cell death triggers an intense inflammatory response and subsequent cardiac fibrosis in the infarction area, ultimately leading to adverse ventricular remodeling (Pfeffer and Braunwald, 1990;
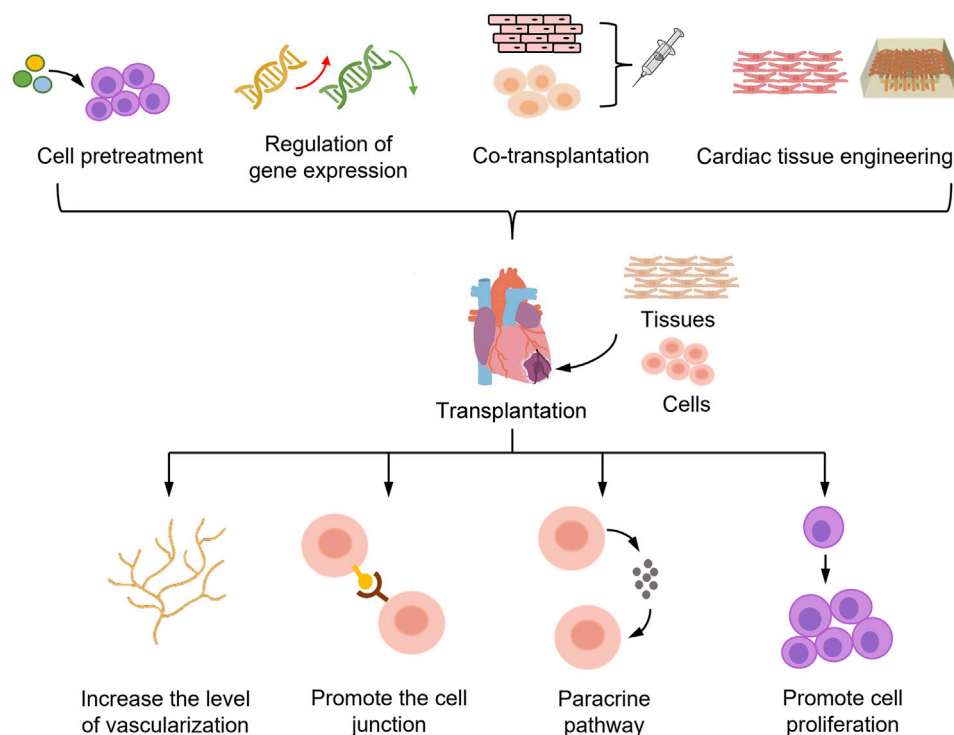
FIGURE 1
Strategies to enhance the efficacy of PSC-CMs in the treatment of myocardial infarction. PSC-CMs transplanted into the myocardial infarct region die in large numbers during the initial stage of transplantation, limiting the potential of PSC-CMs for cell therapy. To improve the survival rate of PSC-CMs, the main strategies adopted are pretreatment of PSC-CMs, gene expression modulation, co-transplantation with other cells, and cardiac tissue engineering. These strategies mainly aim to increase the number of cells and survival of PSC-CMs after transplantation by improving the vascularization level of grafts, enhancing the connection between donor and host cells, and promoting cell proliferation and paracrine pathways. Ultimately, these strategies can be used to achieve the goal of improving the efficacy of PSC-CMs in the treatment of myocardial infarction.

Chiong et al., 2011). Notably, patients who have suffered an MI are at increased risk of recurrence or other cardiovascular diseases. Moreover, patients with MI commonly have other diseases (e.g., diabetes) that may further aggravate the symptoms of MI (Schmitt et al., 2021). Despite advances in MI treatment, current therapeutic strategies remain limited to thrombus removal, blood perfusion, and heart transplantation (Lu et al., 2015). However, these methods are either unable to restore necrotic myocardial cells due to the limited regenerative capacity of the adult heart or difficult to apply at a large scale due to the relative lack of heart donors and the high risk of this procedure.

Cell therapy represents a valuable treatment method for MI. It has been shown to promote a certain degree of functional recovery of infarcted hearts in preclinical studies by orchestrating inflammatory reactions, promoting angiogenesis and cell survival, or replacing lost cells with *de novo* cardiomyocytes. Among the cell types currently used for therapeutic purposes are pluripotent stem cells (PSCs), including embryonic stem cells (ESCs) and induced pluripotent stem cells (iPSCs); adult stem

cells (e.g., mesenchymal stem cells and epithelial stem cells); and somatic cells (e.g., skeletal myoblasts) (Zhang et al., 2021). While adult stem cells have less ability to differentiate into a limited number of cell types, PSCs have the potential to differentiate into any cell type in the body and thus represent a promising source of functional cells for different therapeutic purposes. Compared with adult stem cells, PSCs showed greater ability to restore cardiac function in a porcine MI model (Ishida et al., 2019).

While ESCs are derived from the inner cell mass of the embryonic blastocyst, iPSCs are similar to ESCs and are generated from somatic cells by the transduction of different reprogramming factors, e.g., c-MYC, Klf4, Oct4, and Sox2. There are potential challenges with the use of iPSCs and ESCs in cell therapy that must be addressed to minimize the drawbacks and enhance the benefits. Transplanted exogenous ESCs often elicit immune rejection, which markedly diminishes the therapeutic effect or causes further damage; immune rejection can be suppressed by HLA matching and knocking down the antigen-encoding gene. In contrast, iPSCs derived from autologous cells do not evoke severe immune rejection by the

organism (Zhang et al., 2009). The PSC-derived cardiomyocytes (PSC-CMs) were recently shown to have a significant ameliorative effect on MI, replacing some of the damaged cardiomyocytes and restoring the mechanical contractility of cardiomyocytes after transplantation into the infarcted area (Qiao et al., 2011; Yu et al., 2019; Guan et al., 2020). These data indicate the value of PSC-CMs for the treatment of MI. However, many factors still limit the use of PSC-CMs for MI treatment, including the low transplantation efficiency, short survival time and low survival rate of cardiomyocytes after transplantation, and the possibility of arrhythmia caused by PSC-CM transplantation (Liao et al., 2010). Given the great potential and limitations of PSC-CMs, scientists are developing various strategies to improve the effect of PSC-CMs in the treatment of MI (Figure 1). In this article, we focus on strategies that are currently widely used.

Cell pretreatment

Faced with the limitations of PSC-CM therapies for MI, one possible strategy is to pretreat PSC-CMs before transplantation. Many drugs have been shown to be efficacious in MI, which has led investigators to wonder whether the pretreatment of PSC-CMs with these drugs could improve their efficacy in the treatment of MI. Additionally, pretreatment with non-drug factors, such as hypoxia and starvation, has also been shown to somewhat alleviate the limitations of PSC-CM therapy.

If medications are used for treatment, the first goal is to select the right drug. For example, drugs that increase cell proliferation and promote cell survival in the heart (such as the FGF family and CHIR99021) may be promising. The fibroblast growth factor (FGF) family, also known as the heparin affinity growth factor family, is a class of peptide-like molecules that bind to specific cell membrane receptors. Fibroblast growth factor 1 (FGF1) is involved in several physiological processes, such as development, morphogenesis and proliferation, and FGF1 treatment for acute myocardial injury was found to increase cardiomyocyte mitosis, reduce scar area, and improve cardiac function (Beenken and Mohammadi, 2009). FGF21 also affects a variety of physiological processes, including regulating glucose and lipids and reducing large vessel atherosclerotic plaque formation, and has significant protective effects against MI, myocardial ischemia–reperfusion injury and diabetic cardiomyopathy (Tanajak et al., 2015). There is evidence that FGF21 improves inflammation and myocardial fibrosis in MI via the early growth response protein 1 (EGR1) (Li et al., 2021a). CHIR99021, a potent and highly selective inhibitor of glycogen synthase kinase 3 (GSK3), enhances cell cycle activity by inhibiting GSK3. CHIR99021 can promote PSC-CM proliferation and maintain their immature state; upon removal of CHIR99021, the cells can return to a normal myocardial state. One *in vivo* study in a mouse model found that transplantation of

human iPSC-CMs into myocardial infarct areas after combination pretreatment with CHIR99021 and FGF1 increased cell cycle activity by approximately 4–6-fold and the transplantation rate by approximately 4-fold. The effect of CHIR99021 or FGF1 pretreatment alone was weaker than that of cotreatment but significantly stronger than that of the control (Fan et al., 2020).

There are also drugs that promote vascularization and graft–host cell integration, such as thymosin β4 and Y-27632. Thymosin β4 (Tb4) was found to promote cardiomyocyte survival and proliferation and to enhance angiogenesis. Tan et al. demonstrated *in vitro* that Tb4 could increase AKT activity and BcL-XL expression to protect cultured hiPSC-CMs from hypoxic injury. In a porcine MI model, the combined effect of human iPSC-CMs and Tb4 improved the engraftment rate, vascularization and cardiac function, and no tumor tissue was found in this immunodeficient porcine model (Tan et al., 2021). The enhancement of cellular junctions between transplanted cells and host cells contributes to the survival of transplanted cells. Zhao et al. found that pretreatment of iPSC-CMs with a Rho kinase (ROCK) inhibitor, Y-27632, significantly improved the transplantation rate and the therapeutic effect on MI. ROCK regulates cytoskeletal changes associated with cell adhesion, suggesting that cell–cell junctions play an important role in the therapeutic effect of transplanted PSC-CMs in the MI region (Zhao et al., 2019). Y-27632 is commonly used to promote cell survival and wall attachment during cell passaging.

Faced with the problems of arrhythmia and tachycardia caused by the transplantation of PSC-CMs, one feasible option is to apply drugs to regulate the electrical phenotype of PSC-CMs. Liu et al. found that canonical transient receptor potential isoform 7 (TRPC7) channels play an important role in regulating the automaticity of ESC-CMs. TRPC7 is a receptor-operated Ca^{2+} channel that can be activated by binding to DAG and mediates Ca^{2+} influx, indicating that TRPC7 is an important potential drug target (Liu et al., 2021). Similarly, it has been suggested that TRPC3 has a similar role to TRPC7 in regulating the automaticity of ESC-CMs (Qi et al., 2016), and the identification of drugs targeting these targets could address the problem of rapid arrhythmias after transplantation and improve the therapeutic efficacy of ESC-CMs.

The basic principle of nondrug pretreatment is that unfavorable environments, such as hypoxia and starvation, activate cellular resilience and force PSC-CMs to enhance the utilization of oxygen and nutrients. Yang et al. treated PSC-CMs with Earle's balanced salt solution (EBSS) to simulate starvation *in vivo* and found that EBSS-induced starvation significantly promoted the structural, metabolic and electrophysiological maturation of PSC-CMs. Moreover, this treatment increased the mitochondrial content of ESC-CMs and enhanced their oxidative phosphorylation capacity (Yang et al., 2021). ESCs are derived from the inner cell mass of the embryonic blastocyst stage, and the oxygen content in the embryo is typically 3–5%,

which is lower than that in the external environment. Hypoxic conditions play a very important role in the maintenance of stem cells, and hypoxia-inducible factors (HIFs) regulate the pluripotency of PSCs. Among HIFs, HIF-2α is an upstream regulator of Oct4, and knockdown of HIF-2α leads to the downregulation of Oct4, Nanog and Sox2 (Szablowska-Gadomska et al., 2011). Hu et al. injected mouse mesenchymal stem cells (MSCs) into myocardial infarct areas after pretreatment under hypoxic conditions (0.5% oxygen) for 24 h. The results showed that hypoxic pretreatment increased the expression of proangiogenic and prosurvival factors, such as angiopoietin-1 (Ang-1), vascular endothelial growth factor (VEGF) and erythropoietin. Thus, hypoxic pretreatment enhanced the ability of MSCs to repair the infarcted myocardium, reduced the apoptosis of transplanted cells, and increased angiogenesis (Hu et al., 2008). Therefore, unfavorable environmental factors, such as hypoxia and starvation, can somewhat improve cell viability, and such nondrug pretreatments are feasible options for improving the survival rate of PSC-CMs after transplantation.

Regulation of gene expression

Adult mammalian cardiomyocytes have almost no proliferative capacity; thus, it is difficult to replenish new cardiomyocytes after injury, an important reason for the dramatic impairment of cardiac function after MI. In contrast, during mammalian fetal development, cardiomyocytes have the ability to proliferate, but soon after birth, their proliferative capacity begins to decline until it is lost. This loss of proliferative ability mainly stems from the downregulation of cell cycle maintenance factors as the heart matures, which causes cardiomyocytes to enter G0 of the cell cycle and thus fail to provide new cells at the site of injury after MI. Therefore, researchers have explored ways to increase the proliferative capacity of PSC-CMs from the perspective of gene expression regulation. Overexpressing cell cycle maintenance factors in PSC-CMs may prolong cell cycle progression, allowing more cardiomyocytes to remain in the proliferative phase and increasing the retention of transplanted cells in the infarct zone. Cell cycle protein D (cyclin D) regulates the cell cycle at the G1/S transition, wherein it binds to Cyclin Dependent Kinase 1 (CDK1) and activates CDK1 activity through a series of phosphorylation and dephosphorylation events to move cells from G1 to the replicative S phase. Zhu et al. showed that the overexpression of cyclin D2 in human iPSC-CMs increased graft size and improved myocardial recovery in a mouse model of MI by increasing the proliferation of transplanted cells, which played a significant role in myocardial remyelination and ventricular function recovery (Zhu et al., 2018). Zhao et al. also reported the same ability of cyclin D2 to improve cardiac function in a porcine model of MI (Zhao et al., 2021).

An increased number of PSC-CMs lingering in the infarct zone and increased cell cycle activity can also be achieved by reducing cell death. Many genes are closely related to cell aging and apoptosis, and regulating the expression of these genes can slow cell aging and inhibit apoptosis. Engel et al. showed that p38 activity is one important component of cell cycle regulation in the mammalian myocardium. p38 activity is negatively correlated with cardiac growth, and p38 overexpression inhibits myocardial proliferation (Engel et al., 2005). p38 belongs to the superfamily of mitogen-activated protein kinases (MAPKs), which mediate multiple signaling pathways that regulate cardiomyocyte death (Engel et al., 2006). Fiedler et al. inhibited MAP4K4 activity in hiPSC-CMs by treatment with specific pharmacological agents and confirmed that MAP4K4 inhibition could effectively protect cardiomyocytes from lethal damage (Fiedler et al., 2019).

In addition to increasing the number of PSC-CMs in the MI region by promoting cell proliferation and reducing apoptosis, enhancing the integration between transplanted PSC-CMs and host cells can also improve the therapeutic effect on MI. By expressing certain exogenous genes in PSC-CMs, graft vascularization and cellular junctions between donor and host cells can be improved to achieve functional integration. Tao et al. transfected Ang-1 into human iPSC-CMs and then implanted these genetically altered cells into the anterior wall of the left ventricle after MI in rats. The results showed that Ang-1 improved the survival rate of iPSC-CMs after transplantation, induced mitosis and small artery formation in both host and donor cells, and improved the cell engraftment rate (Tao et al., 2021). Lou et al. found that N-cadherin (CDH2) mediates the adhesion between cardiomyocytes. Therefore, they overexpressed the CDH2 gene in iPSC-CMs and found that CDH2 overexpression improved the therapeutic effect of iPSC-CMs in a mouse model of MI (Lou et al., 2021).

In addition, scientists need to find ways to improve the therapeutic efficacy of PSC-CMs by mitigating problems such as heart rate irregularities that may result from the immature electrical phenotype. The ion channel Kir2.1 is encoded by the KCNJ2 gene and forms inward rectifier potassium current (I_{K1}) channels in a variety of cell types, including cardiomyocytes; therefore, Liao et al. overexpressed the ion channel Kir2.1 in ESC-CMs. I_{K1} can hyperpolarize the resting membrane potential, and I_{K1} expression seems to be a marker of ESC-CM maturation. Although ESC-CMs improved cardiac function after MI with or without the overexpression of Kir2.1, the risk of ventricular tachyarrhythmias and sudden death was significantly reduced by Kir2.1 overexpression (Liao et al., 2013).

Cotransplantation

The heart is not entirely composed of cardiomyocytes but also includes a variety of tissues and cells, such as blood vessels,

connective tissue, smooth muscle cells (SMCs), fibroblasts, and endothelial cells (ECs). Therefore, one idea for improving the therapeutic effect after MI is to transplant PSC-CMs into the infarcted area together with other cells or tissues that could ensure a high survival rate of the transplanted PSC-CMs through paracrine signaling and provide a suitable microenvironment for PSC-CMs. This approach has been shown to significantly improve the therapeutic efficacy of PSC-CMs in MI. Sekine et al. cocultured ECs with cardiomyocytes from newborn mice, and these ECs formed a network structure in cardiomyocyte sheets that significantly increased vascular structure and cytokine secretion; in addition, engineered myocardial tissue consisting of three layers of cardiomyocyte sheets was transplanted into a MI model and significantly improved cardiac function (Sekine et al., 2008). This finding indicates that coculture with ECs increases vascularization in grafts, suggesting that coculturing ECs with PSC-CMs may have similar effects.

Cotransplantation of PSC-CMs with other cells or tissues improves cardiac function through two main ways: promoting vascularization and increasing the secretion of paracrine factors. Vascular regeneration of the graft in the infarct area can provide oxygen and nutrients to the transplanted cells and improve the survival rate of transplanted PSC-CMs. Moreover, the graft provides a favorable microenvironment that promotes cardiomyocyte proliferation, survival, and vascularization by prolonging the secretion of paracrine factors. Park et al. used a patch of human MSCs in conjunction with iPSC-CMs to promote myocardial repair (Park et al., 2019). MSCs secrete a variety of paracrine factors, such as VEGF, fibroblast growth factor 2 (FGF2) and hepatocyte growth factor (HGF), which promote angiogenesis, neovascularization and cell survival. The human MSCs also secrete potent antifibrotic factors (e.g., matrix metalloproteinases) that can inhibit the proliferation of cardiac fibroblasts and thus attenuate fibrosis (Uemura et al., 2006).

Paracrine effects are important for the survival of PSC-CMs after transplantation; these cells exert paracrine effects mainly through exosomes, which contain a variety of bioactive proteins, RNAs and microRNAs that act as cytokines to regulate numerous intra- and intercellular processes. It was reported that exosomes secreted by iPSC-CMs can restore the cell loss caused by MI in pigs, and *in vitro* experiments showed that exosomes protect iPSC-CMs and promote vascularization by inhibiting apoptosis, maintaining intracellular calcium homeostasis, and increasing adenosine 5′-triphosphate synthesis (Gao et al., 2020). Therefore, the transplantation of exosomes together with PSC-CMs into the heart is another feasible approach to mitigate myocardial injury after heart attack.

Transplanted cardiomyocytes die in large numbers in the early posttransplant period due to ischemia, suggesting that enhanced local vascularization and blood perfusion may promote graft cell survival. The importance of vascularization for cardiomyocyte survival *in vivo* has been demonstrated in

several publications (Stevens et al., 2009). Sun et al. injected microvessels isolated from adipose tissue with human iPSC-CMs into a rat model and found that these microvascular grafts increased vascularization and vascular density in the heart and could be maintained in the heart for a long time. Grafting microvessels with iPSC-CMs improved the survival rate of iPSC-CMs by approximately 6-fold, increased the graft area by approximately 5.3-fold, promoted the maturation of iPSC-CMs *in vivo* and restored a portion of the lost ventricular function after MI (Sun et al., 2020).

When transplanting different cell types into the infarcted area, it is important to consider that different cell proportions may exert different therapeutic effects. In the normal heart, the proportion of cardiomyocytes is the largest and can even reach 80% of the total volume of the heart. Thus, when co-transplanting, the cells should be mixed in the appropriate ratio. Giacomelli et al. constructed a scaffold-free structure of microtissues (MTs) using PSC-derived cardiovascular cells in a ratio of 15% endothelial cells, 70% cardiomyocytes, and 15% fibroblasts, showing that PSC-CMs in MTs have improved sarcomere structures with T-tubules, increased contractility, and more mature electrophysiological phenotypes than PSC-CMs alone (Giacomelli et al., 2020). The main cell types in the heart have significant heterogeneity, with different proportions of cells in different regions (Litvinukova et al., 2020). There are also studies that point to differences in healthy hearts between men and women. The proportion of cardiomyocytes in the heart is higher in women than in men, and factors such as the region of infarction and the gender of the patient should be taken into account in the future clinical translation of cell therapy.

Cardiac tissue engineering

Myocardial regeneration strategies have been hampered by the lack of cardiac cell sources and the marked loss of donor cells after transplantation. PSC-CMs are a potential adequate cell source for cell replacement therapy but do not solve the problem of rapid donor cell loss. Cardiac tissue engineering is an interdisciplinary strategy in which bionic scaffolds and seed cells are used to generate tissue replacements aimed at restoring the structure, morphology, and function of damaged cardiac tissue (Cho et al., 2021). Commonly used bionic scaffolds include cardiac patches, hydrogels, and nano/microparticles that can serve as carriers of drugs, proteins, and biologically active substances to provide a suitable extracellular environment for stem cells and improve cell survival after transplantation (Nelson et al., 2011; Li et al., 2012). Cardiomyocyte patch technology allows for the delivery of large numbers of cells to the damaged myocardium without the loss of transplanted cells or damage to the host myocardium. Traditional methods of cardiomyocyte patch fabrication include suspending cells within a scaffold composed of biocompatible materials or growing two-

dimensional sheets that are stacked to form multilayer structures. Recently, advanced techniques such as micropatterning and three-dimensional (3D) bioprinting have allowed for more precise and standardized preparation of cardiomyocyte patches (Wang et al., 2021). The use of autologous myogenic cell patches was previously shown to improve cardiac function (Memon et al., 2005). Kawamura et al. prepared human iPSC-CMs patches and validated their therapeutic activity using a porcine ischemic cardiomyopathy model; these patches restored normal cardiac function by enhancing cardiomyocyte and electromechanical integration (Kawamura et al., 2012). Gao et al. induced the differentiation of iPSCs into smooth muscle cells, cardiomyocytes and endothelial cells and used these three cell types to form cardiomyocyte patches. Such patches had a better therapeutic effect than iPSC-CMs transplanted alone (Gao et al., 2018).

The developmental maturation of cardiomyocytes requires interactions among various regulatory mechanisms within the cell, but the extracellular matrix also plays an important role (Miao et al., 2020). Samura et al. found that components of the extracellular matrix, especially laminin-221, may play important roles in the survival of human iPSC-CMs after transplantation. Laminin-221 enhanced the mechanical and metabolic functions of iPSC-CMs and improved the therapeutic effects of 3D engineered cardiac tissue (ECT) in a rat ischemic cardiomyopathy model (Samura et al., 2020). Yokoyama et al. encapsulated human iPSC-CM-derived 3D cardiac tissue with the extracellular matrix protein fibronectin and implanted this tissue at the site of MI in rats. The results showed that these iPSC-CMs had better tolerance to hypoxia, improved cardiac injury associated with MI, and had the potential to improve the survival and treatment outcomes of patients with ischemic heart disease (Yokoyama et al., 2021).

The development of cardiomyocytes requires an extracellular matrix with appropriate topological properties, and several studies have shown that a stiffer matrix can better recapitulate the *in vivo* myocardial environment and promote the maturation of PSC-CMs, with better myocardial myofibrillar alignment and more ordered electrical properties (Bhana et al., 2010). After transplanting ECT with iPSC-CMs encapsulated in different matrices to MI sites, many investigators found that these matrices promoted the coupling of iPSC-CMs to host cells. Li et al. developed an injectable hydrogel matrix with hyaluronic acid (HA) as the skeleton that was tailored by introducing gold nanoparticles (AuNPs) and RGD adhesion peptides; these modifications enhanced the biophysical properties of the HA matrix gel and provided adhesion sites for cells. The iPSC-CMs were eventually encapsulated into the prepared hydrogel matrix and injected into the mouse heart post infarction. The transplanted iPSC-CMs formed more mature gap junctions in the ischemic myocardial tissue and improved left ventricular electrical conduction in this murine infarction model (Li et al., 2021b).

In addition, a large number of investigators have constructed ECT using ESC-CMs, which also promote remyelination and revascularization of the infarcted myocardial region and achieve improved cardiac function. Caspi et al. demonstrated that ECT constructed from ESC-derived cardiomyocytes, endothelial cells and embryonic fibroblasts has cardiac-specific ultrastructural, molecular and functional properties and is highly vascularized (Caspi et al., 2007). Lesman et al. inoculated ESC-CMs together with ECs (human biliary vein endothelial cells) and embryonic fibroblasts onto biodegradable porous scaffolds. The resulting ECTs were transplanted into rat hearts and formed cardiac tissue grafts, and studies showed that the transplanted tissues successfully and functionally integrated with the host coronary arteries with a higher level of vascularization than ESC-CMs transplanted alone (Lesman et al., 2010).

The alignment of the cells used for cardiac tissue engineering affects the effect of repair on the heart. Jamaiyar et al. inoculated co-cultured ECs and SMCs in an alignment similar to that of blood vessels on a micro-scaffold made from poly (lactic-co-glycolic acid), and then transplanted induced vascular progenitor cells (iVPC) together with 3D cell/polymer micro-beams formed by micro-scaffolds into a mouse model of myocardial infarction, and the results showed that iVPC on microbeam scaffolds had higher survival rates and the ability to treat infarction (Jamaiyar et al., 2017). Similarly, PSC-CMs can be inoculated onto the scaffold according to the arrangement in the heart. The similar cellular alignment makes it easier for PSC-CMs to bind to the host myocardium and also have more similar beating frequency and amplitude of the host myocardium, thereby reducing the risk of post-transplant arrhythmias. On the other hand, this specific structure also provides some mechanical support for the transplanted cells, allowing better binding of the transplanted PSC-CMs to the host and improving the success rate of transplantation.

Conclusion and perspectives

PSC-CMs can provide a suitable cell source for cell replacement therapy. Transplanting PSC-CMs into the heart can restore a portion of the cell loss and scar tissue caused by MI, thus restoring normal physiological function of the heart (Sayed et al., 2016). A major obstacle to cell-based cardiac therapy is the extremely low retention and colonization rate on the host myocardium, which is particularly important because the extent of cell-based cardiac repair is largely dependent on the number of cells that survive and colonize the heart (Ban et al., 2014). It is widely recognized that the retention rate of cardiomyocytes delivered to the heart is incredibly low (Zhang et al., 2001). The survival rate after injection is only 50%, dropping to 10% in as little as 1 week (van Laake et al., 2008). The maximum survival time of human PSC-CMs after direct injection into

the mouse myocardium has been reported to be no more than 12 weeks. Along with the number of cells transplanted, the maturity of the cells is an important aspect that affects the effectiveness of the treatment. Many studies have also used various methods to improve the maturity of transplanted cardiomyocytes, and it has been shown that immature cardiomyocytes have a risk of inducing arrhythmias.

Therefore, to address these problems, scientists have used strategies such as PSC-CM pretreatment, gene expression modulation, cotransplantation with other cells and cardiac tissue engineering to mitigate the limitations of PSC-CM therapies and increase their efficacy in the treatment of MI. Other investigators have developed combination strategies that can achieve better results. Kawamura et al. found that combining cell sheets with the Omental Flap Technique enhanced the therapeutic effect of human iPSC-CMs in a porcine ischemic cardiomyopathy model (Kawamura et al., 2017). Alternatively, a combination of the above strategies may better exploit the potential of PSC-CMs compared to their use alone; such combinations as treating PSC-CMs with bioactive factors or regulating gene expression before cotransplantation with other cells or constructing engineered heart tissue await validation in future studies.

With regard to the clinical translation of autologous stem cell therapy in acute myocardial infarction, two cell types have now completed phase III clinical trials: skeletal myogenic cells and bone marrow mononuclear cells. Large-scale randomized clinical studies have also demonstrated the clinical feasibility and safety of transcoronary infusion of autologous bone marrow-derived mononuclear cells and circulating progenitor cells in patients with acute MI, showing a 9.3% increase in left ventricular ejection fraction and a reduction in myocardial infarct size at 12 months follow-up (Leistner et al., 2011). Ideally, the best cells for regenerating the heart should be precursors of all cardiac lineages, as iPSCs combine the pluripotency of ESCs with the advantages of autologous use, making them a promising source of cells. ESCs are likewise an alternative stem cell, but issues with ESC sources limit their ability to be used clinically. In clinical applications, fibroblasts from patient blood or urine are collected and differentiated to form autologous iPSCs, which are then induced to differentiate into cardiomyocytes. After differentiation to obtain cardiomyocytes, various strategies of treatment, such as treatment with various drugs, co-culture with other cells and preparation of engineered heart tissues, are adopted to improve the maturation and therapeutic potential of iPSC-CMs, and then the treated cardiomyocytes or engineered heart tissues are transplanted to the infarcted area to restore the number of cardiomyocytes in the injured area.

Current research on PSC-CM replacement therapy is limited to animal and *in vitro* experiments; most studies have used mouse, rat, and porcine models of MI, with few performed in primates. The clinical relevance of animal models is limited by significant physiological differences in size, electrical conduction,

and coronary artery formation and distribution between the animal and human heart. Therefore, rigorous clinical trials and the establishment of standard operating procedures are needed to address the safety issues associated with PSC-CM transplantation, such as whether this procedure will cause new heart diseases or lead to tumorigenesis. In addition, the ethical issues associated with the transplantation of PSC-CMs are a major impediment to clinical use. Meanwhile, a standardized and scaled-up culture protocol for PSC-CM treatment in clinical settings is still lacking, and further collaborative research by researchers and medical professionals is needed. Future issues to be addressed in clinical trials may also include determining the appropriate timing of transplantation and the number of cells transplanted. The appropriate number of cells to be transplanted must be determined to ensure efficacy without causing cardiac arrhythmias due to excessive cell numbers. In the future, these strategies can be combined with conventional pharmacological and surgical treatments (e.g., antithrombotic drugs, revascularization, and installation of left ventricular assist devices), which may further improve the therapeutic efficacy of PSC-CMs.

When performing cell transplantation, some undifferentiated and partially differentiated PSCs might be also transplanted together with PSC-CMs into the infarcted region. Since undifferentiated PSCs exhibit intrinsic tumorigenic properties that allow them to form teratomas, cell therapy products containing residual undifferentiated PSCs may lead to tumor formation after transplantation. It has been shown that transplantation of different iPSC lines shows significant differences in tumor incidence, latency of formation, and volume. Cho et al. developed a PSC-specific fluorescent probe, CDy1, which generates reactive oxygen species (ROS) upon visible light irradiation that induces selective PSCs death. Importantly, CDy1 and light irradiation did not have a negative effect on differentiated endothelial cells. Photodynamic treatment of PSCs with CDy1 and visible light irradiation confirmed the inhibition of teratoma formation in mice (Cho et al., 2016). Studies on the inhibition of teratoma formation by PSCs are being further explored, but this risk still cannot be completely avoided. When using PSCs for treatment in the future, it may be advisable to try to ensure complete differentiation of PSCs into cardiomyocytes before using them for treatment.

Although PSC-CMs still predominantly act in a paracrine manner due to low transplantation efficiency and many issues remain to be resolved to achieve clinical translation, the great potential for the treatment of MI encourages researchers to continue exploring and developing better protocols. We believe that with the optimization of PSC-CM pretreatment and transplantation techniques, the goal of PSC-CM transplantation to repair the necrotic myocardium will eventually be achieved.

Author contributions

YX, YC, CS, YW, SH, and WL wrote and revised the manuscript. All authors read, edited and approved the manuscript.

Funding

Conflict of interest

The authors declare that the research was conducted in the absence of any commercial or financial relationships that could be construed as a potential conflict of interest.

Publisher's note

All claims expressed in this article are solely those of the authors and do not necessarily represent those of their affiliated organizations, or those of the publisher, the editors and the reviewers. Any product that may be evaluated in this article, or claim that may be made by its manufacturer, is not guaranteed or endorsed by the publisher.

References

Ban, K., Park, H. J., Kim, S., Andukuri, A., Cho, K. W., Hwang, J. W., et al. (2014). Cell therapy with embryonic stem cell-derived cardiomyocytes encapsulated in injectable nanomatrix gel enhances cell engraftment and promotes cardiac repair. *ACS Nano* 8 (10), 10815–10825. doi:10.1021/nn504617g

Beenken, A., and Mohammadi, M. (2009). The FGF family: Biology, pathophysiology and therapy. *Nat. Rev. Drug Discov.* 8 (3), 235–253. doi:10.1038/nrd2792

Bhana, B., Iyer, R. K., Chen, W. L., Zhao, R., Sider, K. L., Likhitpanichkul, M., et al. (2010). Influence of substrate stiffness on the phenotype of heart cells. *Biotechnol. Bioeng.* 105 (6), 1148–1160. doi:10.1002/bit.22647

Caspi, O., Lesman, A., Basevitch, Y., Gepstein, A., Arbel, G., Habib, I. H. M., et al. (2007). Tissue engineering of vascularized cardiac muscle from human embryonic stem cells. *Circ. Res.* 100 (2), 263–272. doi:10.1161/01.res.0000257776.05673.ff

Chiong, M., Wang, Z. V., Pedrozo, Z., Cao, D. J., Troncoso, R., Ibacache, M., et al. (2011). Cardiomyocyte death: Mechanisms and translational implications. *Cell. Death Dis.* 2, e244. doi:10.1038/cddis.2011.130

Cho, S. J., Kim, S. Y., Park, S. J., Song, N., Kwon, H. Y., Kang, N. Y., et al. (2016). Photodynamic approach for teratoma-free pluripotent stem cell therapy using CDy1 and visible light. *ACS Cent. Sci.* 2 (9), 604–607. doi:10.1021/acscentsci.6b00099

Cho, S., Lee, C., Skylar-Scott, M. A., Heilshorn, S. C., and Wu, J. C. (2021). Reconstructing the heart using iPSCs: Engineering strategies and applications. *J. Mol. Cell. Cardiol.* 157, 56–65. doi:10.1016/j.yjmcc.2021.04.006

Engel, B. F., Hsieh, P. C. H., Lee, R. T., and Keating, M. T. (2006). FGF1/p38 MAP kinase inhibitor therapy induces cardiomyocyte mitosis, reduces scarring, and rescues function after myocardial infarction. *Proc. Natl. Acad. Sci.* 103 (42), 15546–15551. doi:10.1073/pnas.0607382103

Engel, F. B., Schebesta, M., Duong, M. T., Lu, G., Ren, S., Madwed, J. B., et al. (2005). p38 MAP kinase inhibition enables proliferation of adult mammalian cardiomyocytes. *Genes. Dev.* 19 (10), 1175–1187. doi:10.1101/gad.1306705

Fan, C., Tang, Y., Zhao, M., Lou, X., Pretorius, D., Menasche, P., et al. (2020). CHIR99021 and fibroblast growth factor 1 enhance the regenerative potency of human cardiac muscle patch after myocardial infarction in mice. *J. Mol. Cell. Cardiol.* 141, 1–10. doi:10.1016/j.yjmcc.2020.03.003

Fiedler, L. R., Chapman, K., Xie, M., Maifoshie, E., Jenkins, M., Golforoush, P. A., et al. (2019). MAP4K4 inhibition promotes survival of human stem cell-derived cardiomyocytes and reduces infarct size *in vivo*. *Cell. Stem Cell.* 24 (4), 579–591. e512. doi:10.1016/j.stem.2019.01.013

Gao, L., Gregorich, Z. R., Zhu, W., Mattapally, S., Oduk, Y., Lou, X., et al. (2018). Large cardiac muscle patches engineered from human induced-pluripotent stem cell–derived cardiac cells improve recovery from myocardial infarction in swine. *Circulation* 137 (16), 1712–1730. doi:10.1161/circulationaha.117.030785

Gao, L., Wang, L., Wei, Y., Krishnamurthy, P., Walcott, G. P., Menasche, P., et al. (2020). Exosomes secreted by hiPSC-derived cardiac cells improve recovery from myocardial infarction in swine. *Sci. Transl. Med.* 12 (561), eaay1318. doi:10.1126/scitranslmed.aay1318

Giacomelli, E., Meraviglia, V., Campostrini, G., Cochrane, A., Cao, X., van Helden, R. W., et al. (2020). Human-iPSC-Derived cardiac stromal cells enhance maturation in 3D cardiac microtissues and reveal non-cardiomyocyte contributions to heart disease. *Cell. Stem Cell.* 26 (6), 862–879.e11. doi:10.1016/j.stem.2020.05.004

Guan, X., Xu, W., Zhang, H., Wang, Q., Yu, J., Zhang, R., et al. (2020). Transplantation of human induced pluripotent stem cell-derived cardiomyocytes improves myocardial function and reverses ventricular remodeling in infarcted rat hearts. *Stem Cell. Res. Ther.* 11 (1), 73. doi:10.1186/s13287-020-01602-0

Hu, X., Yu, S. P., Fraser, J. L., Lu, Z., Ogle, M. E., Wang, J. A., et al. (2008). Transplantation of hypoxia-preconditioned mesenchymal stem cells improves infarcted heart function via enhanced survival of implanted cells and angiogenesis. *J. Thorac. Cardiovasc. Surg.* 135 (4), 799–808. doi:10.1016/j.jtcvs.2007.07.071

Ishida, M., Miyagawa, S., Saito, A., Fukushima, S., Harada, A., Ito, E., et al. (2019). Transplantation of human-induced pluripotent stem cell-derived cardiomyocytes is superior to somatic stem cell therapy for restoring cardiac function and oxygen consumption in a porcine model of myocardial infarction. *Transplantation* 103 (2), 291–298. doi:10.1097/tp.0000000000002384

Jamaiyar, A., Wan, W., Ohanyan, V., Enrick, M., Janota, D., Cumpston, D., et al. (2017). Alignment of inducible vascular progenitor cells on a micro-bundle scaffold improves cardiac repair following myocardial infarction. *Basic Res. Cardiol.* 112 (4), 41. doi:10.1007/s00395-017-0631-4

Kawamura, M., Miyagawa, S., Fukushima, S., Saito, A., Miki, K., Funakoshi, S., et al. (2017). Enhanced therapeutic effects of human iPS cell derived-cardiomyocyte by combined cell-sheets with omental Flap technique in porcine ischemic cardiomyopathy model. *Sci. Rep.* 7 (1), 8824. doi:10.1038/s41598-017-08869-z

Kawamura, M., Miyagawa, S., Miki, K., Saito, A., Fukushima, S., Higuchi, T., et al. (2012). Feasibility, safety, and therapeutic efficacy of human induced pluripotent stem cell-derived cardiomyocyte sheets in a porcine ischemic cardiomyopathy model. *Circulation* 126 (11), S29–S37. doi:10.1161/circulationaha.111.084343

Leistner, D. M., Fischer-Rasokat, U., Honold, J., Seeger, F. H., Schachinger, V., Lehmann, R., et al. (2011). Transplantation of progenitor cells and regeneration enhancement in acute myocardial infarction (TOPCARE-AMI): Final 5-year results suggest long-term safety and efficacy. *Clin. Res. Cardiol.* 100 (10), 925–934. doi:10.1007/s00392-011-0327-y

Lesman, A., Habib, M., Caspi, O., Gepstein, A., Arbel, G., Levenberg, S., et al. (2010). Transplantation of a tissue-engineered human vascularized cardiac muscle. *Tissue Eng. Part A* 16 (1), 115–125. doi:10.1089/ten.tea.2009.0130

Li, H., Yu, B., Yang, P., Zhan, J., Fan, X., Chen, P., et al. (2021). Injectable AuNP-HA matrix with localized stiffness enhances the formation of gap junction in engrafted human induced pluripotent stem cell-derived cardiomyocytes and promotes cardiac repair. *Biomaterials* 279, 121231. doi:10.1016/j.biomaterials.2021.121231

Li, J., Gong, L., Zhang, R., Li, S., Yu, H., Liu, Y., et al. (2021). Fibroblast growth factor 21 inhibited inflammation and fibrosis after myocardial infarction via EGR1. *Eur. J. Pharmacol.* 910, 174470. doi:10.1016/j.ejphar.2021.174470

Li, Y., Rodrigues, J., and Tomas, H. (2012). Injectable and biodegradable hydrogels: Gelation, biodegradation and biomedical applications. *Chem. Soc. Rev.* 41 (6), 2193–2221. doi:10.1039/c1cs15203c

Liao, S. Y., Liu, Y., Siu, C. W., Zhang, Y., Lai, W. H., Au, K. W., et al. (2010). Proarrhythmic risk of embryonic stem cell-derived cardiomyocyte transplantation in infarcted myocardium. *Heart rhythm.* 7 (12), 1852–1859. doi:10.1016/j.hrthm.2010.09.006

Liao, S. Y., Tse, H. F., Chan, Y. C., Mei-Chu Yip, P., Zhang, Y., Liu, Y., et al. (2013). Overexpression of Kir2.1 channel in embryonic stem cell-derived cardiomyocytes attenuates posttransplantation proarrhythmic risk in myocardial infarction. *Heart rhythm.* 10 (2), 273–282. doi:10.1016/j.hrthm.2012.10.008

Litvinukova, M., Talavera-Lopez, C., Maatz, H., Reichart, D., Worth, C. L., Lindberg, E. L., et al. (2020). Cells of the adult human heart. *Nature* 588 (7838), 466–472. doi:10.1038/s41586-020-2797-4

Liu, X., Zhao, R., Ding, Q., Yao, X., and Tsang, S. Y. (2021). TRPC7 regulates the electrophysiological functions of embryonic stem cell-derived cardiomyocytes. *Stem Cell. Res. Ther.* 12 (1), 262. doi:10.1186/s13287-021-02308-7

Lou, X., Zhao, M., Fan, C., Fast, V. G., Valarmathi, M. T., Zhu, W., et al. (2021). N-cadherin overexpression enhances the reparative potency of human-induced pluripotent stem cell-derived cardiac myocytes in infarcted mouse hearts. *Cardiovasc. Res.* 116 (3), 671–685. doi:10.1093/cvr/cvz179

Lu, L., Liu, M., Sun, R., Zheng, Y., and Zhang, P. (2015). Myocardial infarction: Symptoms and treatments. *Cell. biochem. Biophys.* 72 (3), 865–867. doi:10.1007/s12013-015-0553-4

Memon, I. A., Sawa, Y., Fukushima, N., Matsumiya, G., Miyagawa, S., Taketani, S., et al. (2005). Repair of impaired myocardium by means of implantation of engineered autologous myoblast sheets. *J. Thorac. Cardiovasc. Surg.* 130 (5), 1333–1341. doi:10.1016/j.jtcvs.2005.07.023

Miao, S., Zhao, D., Wang, X., Ni, X., Fang, X., Yu, M., et al. (2020). Retinoic acid promotes metabolic maturation of human Embryonic Stem Cell-derived Cardiomyocytes. *Theranostics* 10 (21), 9686–9701. doi:10.7150/thno.44146

Nelson, D. M., Ma, Z., Fujimoto, K. L., Hashizume, R., and Wagner, W. R. (2011). Intra-myocardial biomaterial injection therapy in the treatment of heart failure: Materials, outcomes and challenges. *Acta Biomater.* 7 (1), 1–15. doi:10.1016/j.actbio.2010.06.039

Park, S. J., Kim, R. Y., Park, B. W., Lee, S., Choi, S. W., Park, J. H., et al. (2019). Dual stem cell therapy synergistically improves cardiac function and vascular regeneration following myocardial infarction. *Nat. Commun.* 10 (1), 3123. doi:10.1038/s41467-019-11091-2

Pfeffer, M. A, E. B., and Braunwald, E. (1990). Ventricular remodeling after myocardial infarction. Experimental observations and clinical implications. *Circulation* 81 (4), 1161–1172. doi:10.1161/01.cir.81.4.1161

Qi, Z., Wong, C. K., Suen, C. H., Wang, J., Long, C., Sauer, H., et al. (2016). TRPC3 regulates the automaticity of embryonic stem cell-derived cardiomyocytes. *Int. J. Cardiol.* 203, 169–181. doi:10.1016/j.ijcard.2015.10.018

Qiao, H., Zhang, H., Yamanaka, S., Patel, V. V., Petrenko, N. B., Huang, B., et al. (2011). Long-term improvement in postinfarct left ventricular global and regional contractile function is mediated by embryonic stem cell-derived cardiomyocytes. *Circ. Cardiovasc. Imaging* 4 (1), 33–41. doi:10.1161/circimaging.110.957431

Roth, G. A., Mensah, G. A., Johnson, C. O., Addolorato, G., Ammirati, E., Baddour, L. M., et al. (2020). Global burden of cardiovascular diseases and risk factors, 1990-2019: Update from the GBD 2019 study. *J. Am. Coll. Cardiol.* 76 (25), 2982–3021. doi:10.1016/j.jacc.2020.11.010

Samura, T., Miyagawa, S., Kawamura, T., Fukushima, S., Yokoyama, J., Takeda, M., et al. (2020). Laminin-221 enhances therapeutic effects of human-induced pluripotent stem cell-derived 3-dimensional engineered cardiac tissue transplantation in a rat ischemic cardiomyopathy model. *J. Am. Heart Assoc.* 9 (16), e015841. doi:10.1161/jaha.119.015841

Sayed, N., Liu, C., and Wu, J. C. (2016). Translation of human-induced pluripotent stem cells: From clinical trial in a dish to precision medicine. *J. Am. Coll. Cardiol.* 67 (18), 2161–2176. doi:10.1016/j.jacc.2016.01.083

Schmitt, V. H., Hobohm, L., Munzel, T., Wenzel, P., Gori, T., and Keller, K. (2021). Impact of diabetes mellitus on mortality rates and outcomes in myocardial infarction. *Diabetes Metab.* 47 (4), 101211. doi:10.1016/j.diabet.2020.11.003

Sekine, H., Shimizu, T., Hobo, K., Sekiya, S., Yang, J., Yamato, M., et al. (2008). Endothelial cell coculture within tissue-engineered cardiomyocyte sheets enhances neovascularization and improves cardiac function of ischemic hearts. *Circulation* 118 (14), S145–S152. doi:10.1161/circulationaha.107.757286

Stevens, K. R., Kreutziger, K. L., Dupras, S. K., Korte, F. S., Regnier, M., Muskheli, V., et al. (2009). Physiological function and transplantation of scaffold-free and vascularized human cardiac muscle tissue. *Proc. Natl. Acad. Sci. U. S. A.* 106 (39), 16568–16573. doi:10.1073/pnas.0908381106

Sun, X., Wu, J., Qiang, B., Romagnuolo, R., Gagliardi, M., Keller, G., et al. (2020). Transplanted microvessels improve pluripotent stem cell–derived cardiomyocyte engraftment and cardiac function after infarction in rats. *Sci. Transl. Med.* 12 (562), eaax2992. doi:10.1126/scitranslmed.aax2992

Szablowska-Gadomska, I., Zayat, V., and Buzanska, L. (2011). Influence of low oxygen tensions on expression of pluripotency genes in stem cells. *Acta Neurobiol. Exp.* 71 (1), 86–93.

Tanajak, P., Chattipakorn, S. C., and Chattipakorn, N. (2015). Effects of fibroblast growth factor 21 on the heart. *J. Endocrinol.* 227 (2), R13–R30. doi:10.1530/joe-15-0289

Tan, S. H., Loo, S. J., Gao, Y., Tao, Z. H., Su, L. P., Wang, C. X., et al. (2021). Thymosin β4 increases cardiac cell proliferation, cell engraftment, and the reparative potency of human induced-pluripotent stem cell-derived cardiomyocytes in a porcine model of acute myocardial infarction. *Theranostics* 11 (16), 7879–7895. doi:10.7150/thno.56757

Tao, Z., Loo, S., Su, L., Tan, S., Tee, G., Gan, S. U., et al. (2021). Angiopoietin-1 enhanced myocyte mitosis, engraftment, and the reparability of hiPSC-CMs for treatment of myocardial infarction. *Cardiovasc. Res.* 117 (6), 1578–1591. doi:10.1093/cvr/cvaa215

Uemura, R., Xu, M., Ahmad, N., and Ashraf, M. (2006). Bone marrow stem cells prevent left ventricular remodeling of ischemic heart through paracrine signaling. *Circulation Res.* 98 (11), 1414–1421. doi:10.1161/01.res.0000225952.61196.39

van Laake, L. W., Passier, R., Doevendans, P. A., and Mummery, C. L. (2008). Human embryonic stem cell-derived cardiomyocytes and cardiac repair in rodents. *Circ. Res.* 102 (9), 1008–1010. doi:10.1161/circresaha.108.175505

Wang, L., Serpooshan, V., and Zhang, J. (2021). Engineering human cardiac muscle patch constructs for prevention of post-infarction LV remodeling. *Front. Cardiovasc. Med.* 8, 621781. doi:10.3389/fcvm.2021.621781

Yang, J., Ding, N., Zhao, D., Yu, Y., Shao, C., Ni, X., et al. (2021). Intermittent starvation promotes maturation of human embryonic stem cell-derived cardiomyocytes. *Front. Cell. Dev. Biol.* 9, 687769. doi:10.3389/fcell.2021.687769

Yokoyama, J., Miyagawa, S., Akagi, T., Akashi, M., and Sawa, Y. (2021). Human induced pluripotent stem cell-derived three-dimensional cardiomyocyte tissues ameliorate the rat ischemic myocardium by remodeling the extracellular matrix and cardiac protein phenotype. *PLoS One* 16 (3), e0245571. doi:10.1371/journal.pone.0245571

Yu, Y., Qin, N., Lu, X. A., Li, J., Han, X., Ni, X., et al. (2019). Human embryonic stem cell-derived cardiomyocyte therapy in mouse permanent ischemia and ischemia-reperfusion models. *Stem Cell. Res. Ther.* 10 (1), 167. doi:10.1186/s13287-019-1271-4

Zhang, J., Bolli, R., Garry, D. J., Marban, E., Menasche, P., Zimmermann, W. H., et al. (2021). Basic and translational research in cardiac repair and regeneration: JACC state-of-the-art review. *J. Am. Coll. Cardiol.* 78 (21), 2092–2105. doi:10.1016/j.jacc.2021.09.019

Zhang, J., Wilson, G. F., Soerens, A. G., Koonce, C. H., Yu, J., Palecek, S. P., et al. (2009). Functional cardiomyocytes derived from human induced pluripotent stem cells. *Circ. Res.* 104 (4), e30–41. doi:10.1161/circresaha.108.192237

Zhang, M., Methot, D., Poppa, V., Fujio, Y., Walsh, K., and Murry, C. E. (2001). Cardiomyocyte grafting for cardiac repair: Graft cell death and anti-death strategies. *J. Mol. Cell. Cardiol.* 33 (5), 907–921. doi:10.1006/jmcc.2001.1367

Zhao, M., Fan, C., Ernst, P. J., Tang, Y., Zhu, H., Mattapally, S., et al. (2019). Y-27632 preconditioning enhances transplantation of human-induced pluripotent stem cell-derived cardiomyocytes in myocardial infarction mice. *Cardiovasc. Res.* 115 (2), 343–356. doi:10.1093/cvr/cvy207

Zhao, M., Nakada, Y., Wei, Y., Bian, W., Chu, Y., Borovjagin, A. V., et al. (2021). Cyclin D2 overexpression enhances the efficacy of human induced pluripotent stem cell-derived cardiomyocytes for myocardial repair in a swine model of myocardial infarction. *Circulation* 144 (3), 210–228. doi:10.1161/circulationaha.120.049497

Zhu, W., Zhao, M., Mattapally, S., Chen, S., and Zhang, J. (2018). CCND2 overexpression enhances the regenerative potency of human induced pluripotent stem cell-derived cardiomyocytes: Remuscularization of injured ventricle. *Circ. Res.* 122 (1), 88–96. doi:10.1161/circresaha.117.311504

Intersection of stem cell biology and engineering towards next generation *in vitro* models of human fibrosis

Erika Yan Wang[1,2], Yimu Zhao[2,3], Sargol Okhovatian[2,3], Jacob B. Smith[3,4] and Milica Radisic[2,3,4]*

[1]David H. Koch Institute for Integrative Cancer Research, Massachusetts Institute of Technology, Cambridge, MA, United States, [2]Institute of Biomedical Engineering, University of Toronto, Toronto, ON, Canada, [3]Toronto General Hospital Research Institute, University Health Network, Toronto, ON, Canada, [4]Department of Chemical Engineering and Applied Chemistry, University of Toronto, Toronto, ON, Canada

Human fibrotic diseases constitute a major health problem worldwide. Fibrosis involves significant etiological heterogeneity and encompasses a wide spectrum of diseases affecting various organs. To date, many fibrosis targeted therapeutic agents failed due to inadequate efficacy and poor prognosis. In order to dissect disease mechanisms and develop therapeutic solutions for fibrosis patients, *in vitro* disease models have gone a long way in terms of platform development. The introduction of engineered organ-on-a-chip platforms has brought a revolutionary dimension to the current fibrosis studies and discovery of anti-fibrotic therapeutics. Advances in human induced pluripotent stem cells and tissue engineering technologies are enabling significant progress in this field. Some of the most recent breakthroughs and emerging challenges are discussed, with an emphasis on engineering strategies for platform design, development, and application of machine learning on these models for anti-fibrotic drug discovery. In this review, we discuss engineered designs to model fibrosis and how biosensor and machine learning technologies combine to facilitate mechanistic studies of fibrosis and pre-clinical drug testing.

KEYWORDS

tissue engineeering, stem cell, fibrosis, disease modeling, organ on a chip (OCC), biosensor, machine learning (ML)

Background: Current challenges in modeling human fibrotic diseases for drug development

Human fibrotic diseases constitute a major health problem worldwide owing to their high incidence rate in most chronic inflammatory diseases (Wynn and Ramalingam, 2012). The data from the government of the United States suggests that fibrosis disorders are collectively responsible for 45% of deaths in the developed world (Wynn, 2004). Human fibrosis involves significant etiological heterogeneity and encompasses a wide

spectrum of diseases affecting various organs. Typical fibrotic disorders include cardiac fibrosis (CF), idiopathic pulmonary fibrosis (IPF), primary myelofibrosis, scleroderma, as well as systemic fibrotic diseases including systemic sclerosis (SSc) and nephrogenic systemic fibrosis (Wells, 2013).

Fibrosis is generally initiated by a tissue repair process, followed by a scarring phase over the regeneration limit (Krenning et al., 2010). The replacement of normal parenchymal components by fibroblasts is often accompanied by a persistent release of fibrogenic cytokines, which in turn stimulates myofibroblast activation and deposition of extracellular matrix (ECM). Compromisation of organ function is a common paradigm in most fibrotic diseases following altered tissue micro-architecture. For example, many clinical cases of heart failure reflect histologic evidence of interstitial cardiac fibrosis (Fan et al., 2012). Cardiac fibrosis is associated with a progressive decline in cardiac performance, including diastolic dysfunction, reduced afterload, and arrhythmia (Leask, 2015). Similarly, idiopathic pulmonary fibrosis (IPF) remains a lethal condition, as it can lead to irreversible stiffening of lung tissue, distortion of the organ architecture, as well as decreased lung volumes and compliance (Lee et al., 2015).

Organ transplantation is the only therapeutic option for many end-stage diseases given the inefficiency and poor prognosis capabilities of fibrosis-modifying therapeutics (Rosenbloom et al., 2013). Drug discovery and development is a lengthy, costly, and risky process, reflected by substantial number of failed clinical trials and market withdrawals. The development of new pharmaceutical solutions for fibrosis has been extremely challenging as a comprehensive understanding of fibrosis etiology and evaluation of effective therapies have been hampered by lack of *in vitro* models that can faithfully recapitulate human pathophysiology.

Conventional disease models mainly rely on animal experiments and *in vitro* monolayer-based assays. Animal models, despite being the gold standards in current drug testing, present considerable discrepancies in both physiology and pathology compared to humans. Moreover, monolayer cell cultures are cost-effective alternatives for pre-clinical studies and have been widely used as established systems for pre-clinical drug testing. However, many of these models poorly replicate pathological factors responsible for disease onset and progression, because they lack of the structural and compositional complexity of native human tissues.

An ideal model for fibrosis studies and drug development should (Wynn and Ramalingam, 2012) produce a precise manifestation of disease phenotypes; and (Wynn, 2004) provide facile and reliable readouts that are important for fibrotic modeling. The major hurdle in new drug development is that the effects of some drugs on preventing or ameliorating the progression of fibrosis in practice cannot be reliably replicated in animals or 2D lab models. Therefore, it is hard to predict which

compounds would have the optimal anti-fibrotic outcomes. A reliable testing system is one that approximates key features of the *in vivo* environment such as functional and structural properties, and molecular and metabolic signatures over the course of drug treatment. Ideally, it should also allow real-time and non-invasive tracking of multiplexed functional outputs (e.g., contractility and electrophysiological properties) in response to drug candidates under investigation.

Bioengineers are leveraging techniques in tissue engineering and microfabrication into the pipeline of human disease modeling. This will give rise to the next generation of *in vitro* models that are not only capable of modelling of fibrotic disease, but also test feasible therapeutic strategies. Organ-on-a-chip (OOC) technology, as a multi-disciplinary field that combines bioengineering, regenerative medicine, and platform manufacturing, has led to the establishment of authentic bio-systems to emulate human biology and diseases. This field has grown appreciably over the past decades with versatile approaches to generate disease- and patient-specific models for preclinical drug testing. Some of the most recent advances in modeling of fibrotic disease will be discussed, with an emphasis on the development of engineering techniques in the aspects of platform design, tissue construction, biosensor integration, and machine learning aided testing (Figure 1).

Engineering of fibrotic models targeting distinct pathological factors

In different organ disorders, fibrosis arises from a variety of origins and involves multifaceted etiology. Replacement of fibroblasts, activation of immune cells, stimulation of growth factors, mechanical stress, and genetic background are some of the key factors that have been implicated in underlying fibrosis. Fibrosis occurs ubiquitously in the human body as a repair

FIGURE 1
Current advances in modelling fibrotic diseases and therapeutic development. Engineered models of human fibrotic disease, incorporation of biosensors and machine learning would facilitate gaining insight into disease mechanisms and development of novel therapeutic agents in higher throughput.
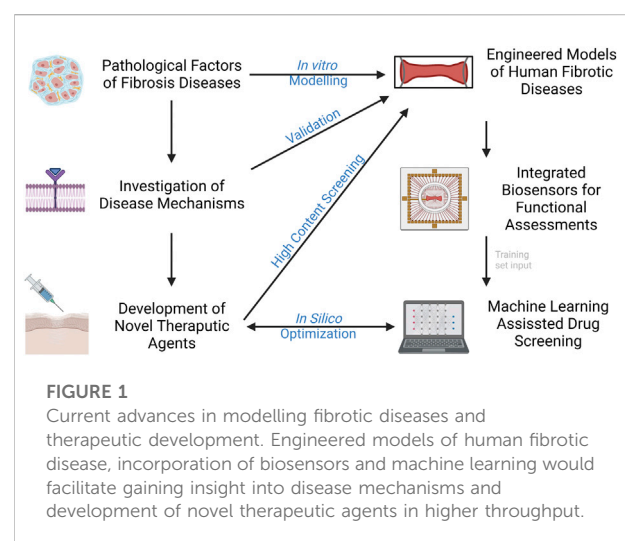
response to tissue injury. In healthy organs, the injury is followed by inflammation responses to cause immune cell infiltration and activation at the injury sites, including T cells, macrophages and neutrophils. These immune cells release profibrotic mediators to activate profibrotic signaling pathways such as TGF-β, WNT, hedgehog and PDGF, and initiate the transformation of vascular cells, resident fibroblasts, circulating fibrocytes and mesenchymal cells into myofibroblast-like phenotypes. Myofibroblast activation contributes to wound contraction and ECM protein deposition. The myoFBs often go through apoptosis after tissue repair in the context of physiological wound healing process. When persisted injury is in place, such process persists with elevated release of inflammatory cytokines and growth factors, abnormal myofibroblast activation, and excessive ECM deposition. The altered microenvironment including profibrotic mediators, ECM composition with increased stiffness and reduced compliance, in turn creates a positive feedback loop to aggravate the activation of myofibroblasts and prolong fibrosis (Distler et al., 2019). Genetic predisposition may also significantly contribute to the pathological activation of myofibroblasts and development of fibrosis.

To address the inherent complexities of fibrosis, novel engineering strategies have to recapitulate the intrinsic niche for fibrosis onset and progression. A rational experimental design to specifically probe individual or inter-related pathological facets and modulate their activities *in vitro* is essential for providing a better understanding of fibrosis pathogenesis and offering a more reliable testing microenvironment. Here we discuss the integration of the aforementioned factors into the model design to assist the precise manifestation of disease phenotypes.

Cellular cues

Fibroblasts, as the cell population that constitutes majority of the stroma of tissues, constantly secrete extracellular matrix molecules and secrete factors to remodel the adjacent ECMs (Cox and Erler, 2011). More importantly, fibroblasts mediate the response to the inflammatory factors and matrix degradation products secreted by macrophages and endothelial cells (Wells, 2013). Fibroblast to myofibroblast activation is the key step in all forms of fibrosis, thus fibroblasts were widely maneuvered as the main switch to turn on fibrosis as well as the primary target for antifibrotic therapy. Scar-in-a-jar is a simplified tool for antifibrotic agent screening targeting fibroblast activation and ECM synthesis (Chen et al., 2009). However, this model is composed only of fibroblasts and does not reflect the physiological cellular diversity of human body. Co-culture of parenchymal cells and fibroblasts in engineered 3D platforms provides highly functional tissue constructs for use in investigational and therapeutic applications. For example, the

model design strategy of the Biowire fibrotic tissues (Wang et al., 2019; Mastikhina et al., 2020; Wang et al., 2022) aims to reproduce the microenvironment involved in common forms of cardiac fibrosis, where the elevated presence of cardiac fibroblasts takes place after the loss of cardiomyocytes. Overpopulation of resident fibroblasts cause enhanced collagen content and tissue stiffening, which in turn activates progressive myofibroblast activation and aggravates more collagen deposition. In this fashion, fibrosis is mediated by a self-reinforcing positive feedback loop (Wang et al., 2019).

Endothelial cells play an integral role in tissue repair and contribute significantly to the development of fibrosis through cytokine secretion and fibroblast activation. Injured vasculature triggers endothelial cells to secrete profibrotic mediators such as TGF-β, connective tissue growth factor/CCN family member 2 (CTGF/CCN2), and plasminogen activator inhibitor-1 (PAI-1), which directly recruit and activate fibroblasts to produce ECM proteins (Leach et al., 2013). In addition, endothelial-to-mesenchymal transition (EndoMT) may occur during chronic wound healing, which further enriches the myofibroblast population and contributes to tissue fibrosis (Hashimoto et al., 2010).

As a key process of wound healing, various immune cells engage in the manifestation of fibrosis after tissue injury. Macrophages are an important source of matrix metalloproteinases (MMPs) and inflammatory mediators that drive the initial tissue response after injury. Specifically, pro-inflammatory macrophages are predominant during the initial phase of wound healing, secretes pro-inflammatory cytokines, and produces MMPs for ECM degradation, which have potential antifibrotic effects. In later phases of wound healing, reparative macrophages secrete anti-inflammatory and profibrotic cytokines, such as Transforming Growth Factor β (TGF-β), Platelet Derived Growth Factor (PDGF), Insulin-Like Growth Factor 1 (IGF-1), and Vascular Endothelial Growth Factor α (VEGF-α), in response to inflammatory factors, such as interleukin 10 (IL-10) (Huang et al., 2020). With the production of these cytokines, reparative macrophages induce proliferation and recruitment of resident and circulating mesenchymal cells and activate these cells into myofibroblast phenotypes to produce ECM for wound contraction and tissue regeneration (Wynn and Vannella, 2016). The involvement of T cells has been shown in orchestrating fibrotic responses. T cell activation and the crosstalk between T cells and fibroblasts become increasingly important for recreating the niche and local environment for various fibrosis embodiments such as dermal fibrosis in burn patients (Zhang and Zhang, 2020). Incorporating endothelial cells and immune cells such as macrophages in engineered disease models can facilitate the precise manifestation of fibrotic phenotypes to study of the interplay of different pathological factors, and evaluation of systemic drug response. Figure 2A summarises cells involved in tissue fibrosis.
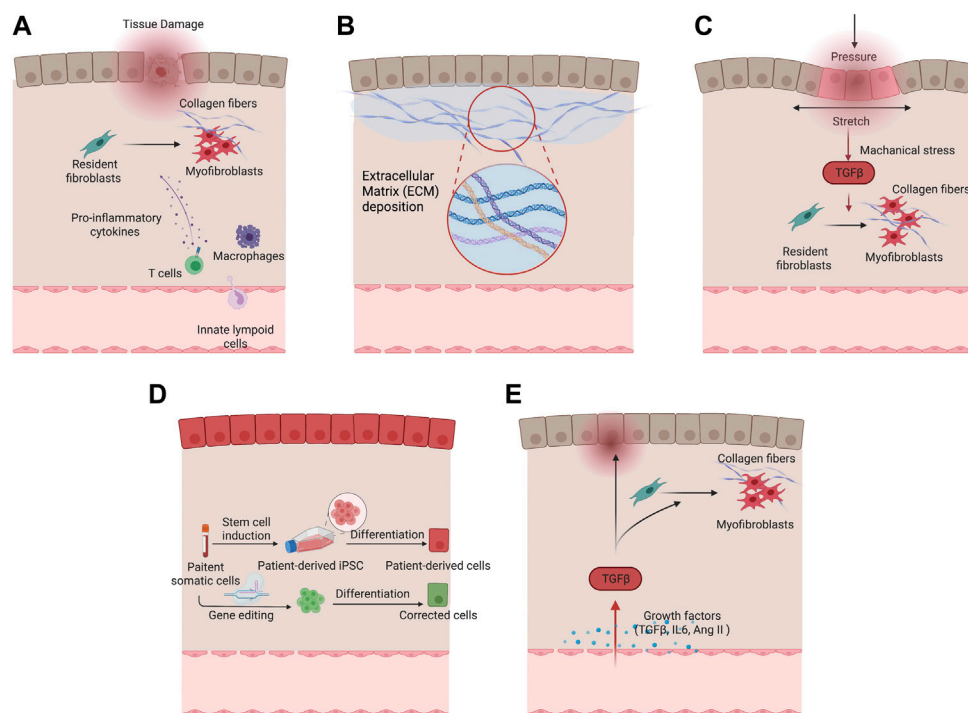
FIGURE 2
Different pathological factors of fibrotic remodeling. **(A)** Cellular factors underlying fibrotic remodeling. **(B)** Increased extracellular matrix deposition in fibrotic condition. **(C)** Mechanical stimulation drives myofibroblast activation and fibrotic remodeling. **(D)** Genetic predisposition in tissue and vascular cells with patient-derived cells serving for fibrotic disease modeling. **(E)** Growth factors including TGF-β and Ang II in fibrosis activation.

Extracellular matrix cues

ECM cues refer to undergoing dynamic, structural and biomechanical changes in the extracellular matrix during fibrotic diseases. Because of the continuous activation of myofibroblasts, extracellular matrix proteins are excessively deposited in the injury sites. A hallmark of all fibrotic tissues is an increase in ECM stiffness. Major drivers of ECM stiffening include phenotypically converted myofibroblasts, activation of TGFβ pathway, and matrix cross-linking. For example, fibrotic myocardium is reported to have up to a 10-fold increase in Young's modulus compared to normal myocardium (Jacot et al., 2010).

The increased stiffness is sensed by the resident cells through mechanotransduction by the surface integrin receptor and triggers downstream pathways such as Hippo followed by YAP/TAZ, which contributes to the upregulation of the profibrotic gene expressions (Kim et al., 2019). The profibrotic signaling pathways, such as PDGF, CTGF, and PAI-1, continue to promote the proliferation of myofibroblasts. Thus, targeting ECM mechanics, by preventing or reversing tissue stiffening or interrupting the cellular response, is an engineering approach to generate fibrotic disease models that offers potential targets for

therapeutic intervention. Many studies aimed to incorporate and study this microenvironmental niche using organ-on-a-chip devices. Caliari et al. (2016) utilized a gradually softening hydrogel to investigate the hepatic stellate cell behavior during fibrosis regression and reinjure. Stellate cells were initially primed on tissue culture plastics to attain myofibroblast phenotypes and persisted when seeded onto the stiff hydrogel with Young's modulus of 20 kPa. During the 2-week period of softening the hydrogel, reversal of myofibroblast phenotype was evident by reduced protein expression of alpha smooth muscle actin (α-SMA) and gene expression of YAP/TAZ signaling pathway. The re-stiffening of the hydrogel triggered reappearance of myofibroblast phenotype which supports the dynamic nature of this process and confirms the ECM as one of the critical microenvironment niches for *in vitro* fibrosis model.

Decellularized ECM may represent an ideal substrate for fibrosis modelling as it preserves the intrinsic biochemical and topographical micro-environments. ECM derived from hypertrophic myocardium in swine model was decellularized and reseeded with human cardiomyocytes (Sewanan et al., 2019). The resulting tissues demonstrated impaired twitch in comparison with the same cardiomyocytes seeded on ECM from healthy animals (Sewanan et al., 2019). Tissues grown

on the diseased matrix exhibited prolonged contractions and poor relaxation. It has been suggested that both the mechanical properties and molecular compositions of ECM contribute to the impaired cardiac function. More recently, Shin et al. (2021) developed hybrid hydrogel bioinks containing partially digested porcine cardiac decellularized ECM and demonstrated the application in printing both healthy and fibrotic cardiac tissues with high shape fidelity and cell viability (Figure 2B).

Mechanical cues

Organs that experience continuous mechanical stimuli, such as the heart and lung, can develop fibrotic phenotypes due to altered mechanical activity (Zhang et al., 2015; Yuan et al., 2018). Myofibroblast activation responsive to extensive strains was evident both *in vitro* and *in vivo* (Yuan et al., 2018; Kong et al., 2019). The activation of YAP/TAZ pathway and MAPK signaling pathways are responsible for the elevated α-SMA expression and myofibroblast transformation (Kim et al., 2019). Interestingly, among the three MAPK kinases (ERK, JNK, P38), only P38 can be activated through tensile stretching, which encourages myofibroblast activation (Zhang et al., 2003). When activated, myofibroblasts express α-SMA, which is incorporated into stress fibers through myosin light-chain phosphorylation *via* RhoA/ROCK pathway (Rouillard and Holmes, 2012). Moreover, mechanical stretching causes release latent TGFβ by opening the ECM bonded TGFβ1 straitjacket activate myofibroblasts to contract and change their mechanical microenvironment, resulting in a positive feedback loop (Rouillard and Holmes, 2012; Rosenbloom et al., 2013; Santos and Lagares, 2018; Roth Gregory et al., 2020).

Many engineered models incorporated external mechanical stimuli to facilitate pathological remodeling. In a three-dimensional microtissues model composed of fibroblasts in macroscopically engineered clefts, Kollmannsberger et al. (2018) discovered that tensile forces drive a reversible fibroblast-to-myofibroblast transition at the highly tensed growth front as the microtissue progressively closed the cleft, in analogy to closing a wound site. In another model, cyclic compressions with gradient magnitudes and tunable frequency were subjected onto gelatin methacryloyl (GelMA) hydrogels laden with CFs in a microdevice. Mechanical compression was observed to induce CFs proliferation and fibrotic phenotype transition, depending on the strain of mechanical load and myofibroblast maturity of CFs encapsulated in GelMA hydrogels (Yuan et al., 2018) (Figure 2C).

Patient-specific genetic background

Patients with genetic diseases ranging from cystic fibrosis to systemic sclerosis, have genetic predispositions that put them at

higher risk of tissue fibrosis. Although the state of art genetic sequencing technology allows high throughput screening and identification of genetic variants that contribute to fibrosis, these genetic variants have extremely high diversity among individuals (Lek et al., 2016). Therefore, a patient-specific *in vitro* model would provide a direct method to validate the correlation between genetic variances and functional deteriorations of fibrosis in patients, as well as to identify the specific disease mechanisms and personalized therapeutic targets (Figure 2D).

Patient-specific disease modeling is often performed by comparative assessments of patient-derived lines with their family-matched controls or gene-edited isogenic cell lines. The development of genome editing technologies has extended our ability to directly modifying genomic sequences. Recent advances in CRISPR-Cas9 system have enabled rapid genome editing in almost all eukaryotic cells with high efficiency and specificity. Up to now, CRISPR-Cas9 has been used to correct a wide spectrum of disorders, ranging from a defect associated with cystic fibrosis in human adult stem cells (Schwank et al., 2013) to a mutation in the calmodulin 2 (CALM2) gene with long QT associated syndrome in iPSC-cardiomyocytes (Limpitikul et al., 2017), leading to a remarkable functional rescue of disease triggered phenotypes.

In a lung-on-a-chip model, healthy and idiopathic fibrosis patient-derived lung fibroblasts were co-cultured with HUVECs in a microfluidic-based platform (Mejías et al., 2020). Strikingly, the idiopathic fibrosis tissues have a high baseline of α-SMA and do not react to TGF-β or clinically used antifibrotic drug (Pirfenidone), whereas the healthy tissues showed superior responses. In a pancreas-on-a-chip model, patient-derived ductal epithelial cells and islets were co-cultured in two-cell culture chambers separated by a thin layer of porous membrane. When compared to the healthy control, cystic fibrosis related insulin disorder was captured in the disease model (Shik Mun et al., 2019). Despite the lack of in-depth investigation of disease mechanisms, these proof-of-concept studies demonstrated the potential of these genetically edited models in the application of precision medicine and drug discovery.

Growth factors

Many studies, both *in vivo* and *in vitro*, concluded that TGF-β is the predominant pathogenic factor that drives fibrosis. Upon tissue injury, TGF-β is released from latent TGF-β binding protein (LTBP) complex in ECMs. Macrophages can also produce TGF-β during the inflammation process. After binding with receptors on the cell surfaces, Smad 2, 3, and 4 will form complex and translocate to the nucleus to upregulate transcription of profibrotic molecules, such as α-SMA, collagen I, and tissue inhibitor of matrix metalloproteinases (TIMP) hence induce myofibroblast

transformation of the cells (Meng et al., 2016). Thus, as a direct modulator, TGF-β has been used in various *in vitro* models to initiate myofibroblast transformation. The common methodology is to subject the culture to TGF-β treatment to stimulate the transformation of resident fibroblasts into myofibroblasts and evaluate the functional and structural changes *in vitro* (Oakley et al., 2019).

Lee et al. (2019a) established self-aggregated cardiac microtissues by co-culturing hESC-MSC and hESC-CM in order to transform of MSCs toward cardiac fibroblast phenotype. After 2 weeks of TGF-β treatment, cardiac microtissues showed impaired contractile behavior, mitochondria deformation, and smaller tissue sizes with a significant portion of CMs going through apoptosis. They also observed increased myofibroblast activation and collagen deposition in the TGF-β treated group, which are consistent with global transcription analysis. Comparable results were presented in the study by Sadeghi et al. (2017), where fibrosis remodeling was activated by the exogenous addition of TGF-β1 in a simplified three-dimensional (3D) hydrogel platform. In a more sophisticated *in vitro* platform developed by Mastikhina et al. (2020) papillary-like cardiac tissue was formed under uniaxial tension, where the force of contraction and tissue stiffness changes were presented to further validate fibrotic nature of the tissues. TGF- β in this system was also shown to significantly reduce the force of contraction and increase local and global tissue stiffness in addition to the genetic and protein level alteration. In contrast to results in 2D culture system, Pirfenidone was shown to reduce the profibrotic gene expressions and tissue stiffness. In a lung-on-a-chip model, Pirfenidone was also shown to minimize the TGF- β induced fibrosis, in terms of α-SMA expression, and passive tensions (Asmani et al., 2018). These results demonstrated the superiority of a more complicated *in vitro* system with precise recapitulation of clinical outcomes.

Angiotensin II (Ang II), the main peptide of Renin-Angiotensin System (RAS), is believed to induce progressive deterioration of organ function. Its upregulation is implicated in various pathological conditions such as cardiac hypertrophy and fibrosis, offering another important mediator for the disease model development. Ang II can induce fibrosis indirectly by activating proinflammatory mediators such as cytokines, chemokines, adhesion molecules, and directly by regulating extracellular matrix synthesis and degradation, increasing tissue stiffness and leading to the impaired function. Horton et al. (2016) utilized a cardiac platform composed of neonatal rat cardiomyocytes on muscular thin films (MTF) to study tissue dysfunction in response to Ang II exposure. This model mimics many features of disease observed *in vivo*, with pathological gene expression profiles including over-expression of B-type natriuretic peptide (BNP), Rho GTPase 1, and T-type calcium
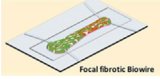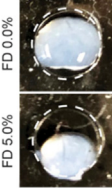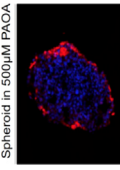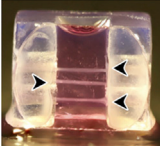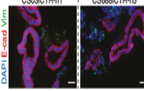
channels, as well as increased proarrhythmic early after depolarization events, along with significantly reduced peak systolic stresses. In a recent study from our group, a Biowire II disease model was constructed to recapitulate myocardial response to Ang II in a temporal manner and evaluate compounds that target Ang II-induced cardiac remodeling (Wang et al., 2021a).

Many other pro-fibrotic mediators recently came into focus, such as IL-10 cytokine family members. These pro-inflammatory cytokines exert host defense mechanisms and facilitate tissue healing (Jennings et al., 2015). Recent studies reveal a close association between IL-10 family cytokines and fibrotic diseases including Interstitial lung disease (Sziksz et al., 2015), renal fibrosis (Jennings et al., 2015), and cardiac fibrosis (Zimmermann et al., 2012). Pro-fibrotic hypoxia signaling pathway was also shown to correlate extensively with fibrosis (Senavirathna et al., 2018; Aquino-Gálvez et al., 2019; Kuo et al., 2019). It has been shown to significantly upregulate the α-SMA expression in idiopathic lung fibrosis patient-derived cells and healthy controls through HIF-1α & HIF-2α (Figure 2E).

Engineered models for studying human fibrotic diseases

Engineered platforms for *in vitro* fibrosis disease modeling have been created to recapitulate chemical, mechanical, and biological conditions in fibrosis of various organs (Tissue-engineered disease models, 2018). Human-induced pluripotent stem cell (hiPSC) technology presents an unprecedented opportunity for disease modeling in association with these platforms (Brandão et al., 2017; Zhang et al., 2018a; Zhao et al., 2019a). Human-based fibrosis-on-a-chip models have been designed to mimic the pathological niche *in vivo* (Besser et al., 2018; Tissue-engineered disease models, 2018; Ulmer and Eschenhagen, 2020). These models have shown promise for deciphering fibrosis mechanisms and discovering effective drugs. Moreover, the advances in differentiation of human pluripotent stem cell hiPSCs into three the germ layer lineages facilitate the development of three-dimensional hiPSC-derived organoid models that recapitulate the native organ with remarkable fidelity (Devarasetty et al., 2018). Organoids, which are self-organizing tissues, provide a new powerful tool for disease modeling and have been increasingly adopted since 2009 (Wörsdörfer et al., 2020). When cultured within an extracellular matrix and provided with suitable culture media and growth factors, they can self-organize into 3D structures that resemble miniature organs composed of various cell types. Organoid models offer a unique approach for studying pathological conditions including fibrosis. Most recent *in vitro* OOC and organoid disease models in the context of various fibrotic disorders in the past 5 years are discussed below.

TABLE 1 Recent models of studying fibrosis *in vitro*. Current models have been able to recapitulate various aspects of fibrosis in cardiac, liver, skeletal muscle, lung and intestine engineered tissues. All figures are reproduced under the terms of CC-BY license.

Organ	00AC model	Key advances	Main readouts	Drug screening	Stage of translation	Opportunity for future works	References
Heart	Biowire II	Heteropolar integrated model of healthy and fibrotic tissue Non-invasive readouts of tissue Constraction	Active and passive force. Excitation threshold (ET). Maximum capture rate (MCR). electrical propagation, tissue compaction force frequency relationship (FFR). Collagen deposition	Furin inhibitors (PCI, Fil, and Fill)	Proof-of-concept	Should Include all myofibroblast origins for phenotypical heterogeneouty Incorporating automated cell seeding or 3D printing technologies to prevent patterning Inconsistencies	Wang et al. (2019) ACS central science
Lung	3D model with multi-component hydrogel	3D fibrous structure of interstitial tissue in idopathic pulmonary fibrosis (IPF)	Collagen deposition, tissue compaction, cellular remodeling	YAP inhibitor (dimethyl fumarate), IPF therapeutics (nintedanib. pirfenidone and their combination)	Proof-of-concept	Matrix remodelling over time Crosstalk among relevant cell types i.e., epithelial cells macrophages and endothelial cells	Matera et al. (2020) Science Advances
Liver	Spheroid	Enables studying molecular mechanisms underlying lipid accumulation during liver fibrosis	Matrix topography myofibroblast activation	Potential therapeutics of NASH (Iiraglutide. elafibranor, vitamin E and obeticholic acid)	Proof-of-concept leading to clinical evaluations	Matrix stiffness at different stages of fibrosis Crosstalk among relevant cell types i.e., epithelial cells, macrophages and endothelial cells	Pingitore et al. (2019) International Journal of Molecular Sciences
Skeletal Muscle	Vacularized sheet of human muscle-derived fibroblasts and muscle cells	Incorporation of endothelial cells within model Enables studying the mechanism of muscle-specific fibroblast recruitement Physiologically relevant architecture	Collagen fiber deposition	N/A	Proof-of-concept	Functional assessments. i.e., changes of muscle contractility. Additional elements to study i.e., matrix compositions, and inflammatory cytokines	Bersini et al. (2018) Cell reports
Intestine	Organoids	Personalized approach for intestinal fibrotic response using hiPSCs	Flow eytometric assessment of cell populations Assessment of N-cadherin, COL5A1. COL1A1 and TIMP1 secretion after TGF-β treatment	N/A	Proof-of-concept	Benchmarking to the clinical data- Further evaluation of fibrosis hallmarks. i.e., functional and ECM changes	Estrada et al. (2021) Inflammatory Bowel Diseases

Cardiac fibrosis

Our group developed a heart-on-chip model of human myocardial fibrosis and used it to establish a compound screening framework. In this platform termed Biowire II, cardiac tissues were cultured around a pair of poly [octamethylene maleate (anhydride) citrate] (POMaC) wires to recapitulate contractile, biomechanical, and electrophysiological complexities of fibrotic myocardium (Table 1). The structural and mechanical properties of the fibrotic tissues were tailored by tuning the cellular composition. Hallmarks of fibrotic myocardium characterized such as myofibroblast activation, excessive collagen deposition, tissue stiffening, impaired contractile and electrical properties, and concomitant arrhythmogenesis were obtained. Additionally, we constructed a heteropolar integrated model where fibrotic and

healthy cardiac tissues were coupled together to capture the regional heterogeneity of scar lesion, border zone, and adjacent healthy myocardium (Wang et al., 2019). Other groups have designed similar heart-on-chip models with tissues attached to polydimethylsiloxane (PDMS)-based wires and observed similar fibrotic responses such as increased tissue stiffness, BNP secretion and collagen deposition (Mastikhina et al., 2020).

Another engineered *in vitro* model of human cardiac fibrosis was developed using human fetal cardiac fibroblasts (hfCF) encapsulated in a gelatin methacryloyl (GelMA) hydrogel. Subsequent TFG-β1 stimulation in hfCF-laden GelMA resulted in a fibrotic phenotype characterized by myofibroblast activation and ECM accumulation. This fibrotic model was utilized to investigate the effect of cardiac progenitor cells (CPC) on the disease process, supporting previous *in vivo* findings of the anti-fibrotic potential of CPC in conjunction with hfCF (Bracco Gartner et al., 2019).

Liver fibrosis

Davidson et al. (2017) developed a micropatterned tri-culture (MPTC) platform that displayed early fibrosis-like hepatic dysfunctions associated with non-alcoholic steatohepatitis (NASH). Clinically relevant hepatic dysfunctions caused by activation of human stellate cells (HSCs) were captured in their multi-well microfabricated platform. The disease model was used for investigating mechanisms in NASH/fibrosis and screening of therapeutics targeted towards the early stages of fibrosis.

In another study, an *in vitro* model of human liver fibrosis was developed in a hepatic organoid system. Multilineage 3D spheroids composed of hepatocytes (HepG2) and hepatic stellate cells (LX-2) were constructed and exposed to free fatty acids to induce steatosis and fibrosis. This fibrotic organoid model was used to study molecular mechanisms underlying lipid accumulation induced fibrogenesis and screen compounds that are in clinical trials for the treatment of NASH (Pingitore et al., 2019) (Table 1).

Pulmonary fibrosis

In the area of pulmonary fibrosis, Matera et al. (2020) developed a 3D model composed of multi-component hydrogel that recapitulates the 3D fibrous structure of interstitial tissue regions in idiopathic pulmonary fibrosis (IPF). Key design criteria were determined by referring to mechanical properties of fibrotic interstitial tissue in a bleomycin-induced lung injury model in mouse. The microengineered pulmonary interstitial matrix resembles mechanical and structural features of fibrotic tissue, as well as key biological events underlying IPF progression. This model was

then applied to study the correlation of altered matrix topography and myofibroblast activation, and to probe fibroblast-ECM interactions. Furthermore, multiple antifibrotic agents were tested in the engineered fibrotic pulmonary interstitial matrices and exhibited aligned antifibrotic efficacy with the previous clinical studies (Table 1).

Another model of idiopathic pulmonary fibrosis was constructed using 3D organoids. Gene-edited embryonic stem cell (ESC)-derived lung organoids were generated and showed to recapitulate important phenotypes of Hermansky-Pudlak syndrome-associated interstitial pneumonia (HPSIP). They further validated the hiPSC-derived lung organoids as a useful tool to identify potential drug targets. Genome-wide expression analysis from the HPSIP mutant fibrotic organoids deciphered the crucial role of interleukin 11 (IL-11) in the fibrotic process (Strikoudis et al., 2019).

Fibrosis in other organs

Fibrosis has been successfully captured in a wide range of engineered *in vitro* models of other organs and tissues. Bersini et al. (2018) reported the generation of a mesoscale human muscle model. This model is composed of differentiated human muscle fibers enveloped by a sheath of human muscle-derived fibroblasts and supported by a vascular network with mural-like cells. This vascularized skeletal muscle model was used to capture key physiological features of fibrosis. Abnormal fibrotic deposition of ECM proteins and myofibroblast activation were observed when Duchenne muscular dystrophy (DMD) fibroblasts were embedded in the 3D vascularized muscle environment (Bersini et al., 2018) (Table 1). Estrada et al. (2021) reported the generation of human intestinal organoids derived from patient derived-induced pluripotent stem cells. These 3D organoids provided a personalized approach for modeling intestinal fibrotic responses *in vitro* (Table 1). Tissue-engineered skin is an emerging tool for identification of novel therapeutic interventions for treating skin injuries and hypertrophic scars, especially for burn patients (Vig et al., 2017). In a work by Varkey et al. (2013) layered fibroblasts and keratinocytes were co-cultured on collagen-glycosaminoglycan scaffolds to build an engineered skin model. This model was used to investigate the role of keratinocytes in fibrotic remodeling.

The incorporation of built-in biosensors for functional assessment

There has been a growing interest in application of novel biosensors in engineered *in vitro* systems. In order to use the microphysiological models to expedite high content and high-
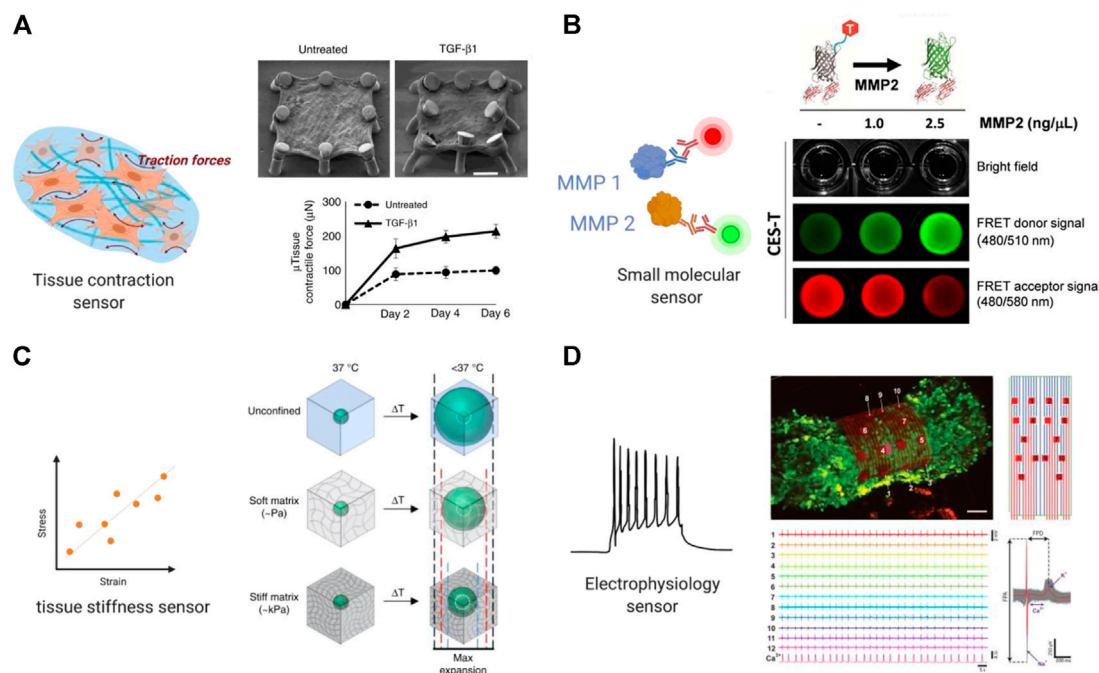
FIGURE 3
Built-in biosensors for anti-fibrotic drug screening. **(A)** Micropillar sensors integrated in a membranous human lung microtissue array to measure spontaneous contraction force generated by fibrotic tissues (Asmani et al., 2018). Reproduced under terms of the CC-BY license. **(B)** A microgel-based biosensor for the direct measurement of mechanical stiffness in local tissues (Mok et al., 2020). Reproduced under terms of the CC-BY license. **(C)** An extracellular FRET biosensor for the visualization of MMP2 activity in a 3D culture system (Lee et al., 2020). Reproduced under terms of the CC-BY license. **(D)** A self-rolled biosensor array to investigate electrogenic cell behavior in 3D human cardiac spheroids (Kalmykov et al., 2019).

throughput compound screening and assess toxicity or evaluate the effectiveness of new anti-fibrotic drugs, their readouts shall be facile and reliable. Biosensors are physical transducing systems that are integrated with the biological components of the engineered models. Implementation of such transducing system enables quantitative study of the interaction between biocomponent and tested therapeutic compounds. An ideal biosensing system should provide a means to collect the drug testing data in real-time non-invasively. To this end, different strategies are applied to incorporate biosensors into engineered OOC systems and performing *in situ*, real-time and automated analyses.

Great efforts have been undertaken to integrate various types of biosensors into OOC platforms. Based on their distinct analytical approaches, OOC biosensors can be classified into several types including electrochemical, optical, and piezoelectric biosensors, etc. (Fahliyani et al., 2020). In the context of fibrotic remodeling, progressive stiffening, contraction of tissue, and the decline in tissue compliance are the key readouts of different fibrosis models. We will mainly focus on primary readouts for anti-fibrotic drug study and summarize existing biosensing systems for functional assessment of tissue contraction, stiffness, and electrical properties in this section.

Biosensor for measuring fibrotic tissue contraction

Tissue contraction is an important determinant of fibrotic phenotype. In fibrotic tissues, myofibroblasts, containing cytoplasmic bundles of microfilaments or stress fibers, are interconnected by gap junctions, and are also connected to the extracellular matrix by a specialized structure called fibronexus, thereby play a pivotal role in tissue contraction. During the fibrosis process, myofibroblasts are responsible for tissue remodeling both by tractional forces and contraction.

By utilizing elastic materials like silicone posts or elastic wires in fabrication of optical biosensors, contractility can be calculated based on deformation of the substrates. For example, the Biowire platform uses wire deflection to continuously measure force values and dynamics, capturing declined force amplitude and increased tractional force in a fibrotic disease model. Non-invasive functional readouts are realized on the basis of the deflection of the intrinsically fluorescent polymer (Wang et al., 2022). By assessing the dynamic change in passive tension, the authors evaluated antifibrotic efficacy of the small-molecule inhibitor of proprotein convertase furin and proofed potential application of the sensing system in preliminary compound screening (Wang et al., 2019; Wang et al., 2022).

In another study, Asmani and coworkers developed a membranous human lung microtissue array, where the spontaneous contraction force generated by individual microtissues was determined from the deflection of micropillars based on cantilever bending theory. They successfully captured progressive stiffening and contraction of alveolar tissue during lung fibrogenesis, and provide proof of principle for using this system for phenotypic analysis of the therapeutic efficacy of two PDA-approved anti-fibrosis drugs (Asmani et al., 2018) (Figure 3A).

Biosensor for measuring tissue stiffness and mechanical properties

Tissue stiffness is a critical physical characteristic and plays a significant role in many biological responses including fibrosis (Wells, 2013). Due to excessive ECM deposition, tissue stiffening is one of the most direct readouts in all kinds of organ fibrosis. Therefore, extracting the drug effect on tissue stiffness is of particular interest for evaluating potential anti-fibrotic compounds.

Various *in situ* biosensors for monitoring cell- or tissue-level stiffness have been developed. Lam et al. (2012) developed a whole-cell cell stiffness sensing system with a subcellular spatial resolution, by using a cell stretching device that allowed quantitative control and real-time measurements of mechanical stimuli and cellular biomechanical responses. This platform is composed of a microfabricated array of silicone elastomeric micro-posts integrated onto a stretchable elastomeric membrane. Changes in micro-post top positions during mechanical stretches were recorded and converted to cell stiffness based on the data of local cell stretching forces and cell area increments.

Mok et al. (2020) developed a thermoresponsive microgel-based biosensor that can be dispersed or injected into tissues and optically tracked to measure mechanical stiffness in tissues. Based on the size-changing of the microgel, internal mechanical profiles of live multicellular spheroids were mapped at high resolutions to reveal spatial rigidity across the tissues. This biosensor also showed promising results in mapping tissue stiffness in an *in vivo* mouse model of breast cancer progression (Figure 3B).

In a more recent work led by Emon et al. (2021) a high-resolution sensor that allows self-assembly and culture of 3D tissue models was described. This sensor was applied to detect single and multiple cell forces in 3D matrices over long-term culture with a high resolution of 1 nN. The design also allowed quantification of the changes in stiffness of the tissue remodeled by the cells. This system originally aimed at testing tissue stiffness in tumor microenvironment but has great potential in fibrotic study and the development of anti-fibrotic compounds.

Biosensor for molecules detection

It is important to enable real-time detection of functional protein molecules in the fibrotic process released from different cell populations and phenotypes to understand the fundamentals of cell responses for disease modeling and drug screening applications. Some of the key molecules that are commonly assessed are MMPs, and inflammatory cytokines (Hasan et al., 2014). MMPs are a group of enzymes in the proteinase family, in concert are closely related to the dynamic degradation of most extracellular matrix proteins during organogenesis, as well pathological remodeling process including fibrosis. Thus, MMPs can serve as real-time biomarkers under fibrotic state and in response to different treatments, which can be measured and quantified using a biosensing system.

Due to low concentration of many biomarkers in the microphysiological system at nanogram and picogram levels, it is important to develop highly sensitive biosensing systems and signal amplification approaches. To this end, Förster or fluorescence resonance energy transfer (FRET) based biosensors were developed to measure molecular events that occur relatively fast in single cells or engineered tissues with high signal to noise ratio and spatio-temporal resolution (Liu et al., 2020).

Utilizing FRET imaging, Ouyang et al. (2008) developed a biosensor that has its sensing element anchoring at the extracellular surface of cell membrane to visualize dynamic MT1-MMP activity in live cells with subcellular resolution. Constructed with a substrate sensitive to MT1-MMP, this biosensor was able to capture drastic FRET changes induced by epidermal growth factor (EGF) in migrating cancer cells, *via* a process dependent upon an intact cytoskeletal network. In a follow-up study, the authors further developed two membrane-anchored FRET biosensors of different spectra and used the system to concurrently visualize the activities of Src and MT1-MMP in a single live cell. The result delineated the temporal and spatial differences between MT1-MMP and Src activation upon EGF stimulation (Ouyang et al., 2010).

In a more recent work, a similar approach using cleavage-based FRET reporters was reported to detect metalloproteinase-2 (MMP2) activity in living cell culture. In this report, Lee et al. (2020) developed an extracellular FRET reporter which consists of an ECM collagen-binding protein and a FRET coupler of an enhanced green fluorescent protein (eGEF) and a small dye molecule. The extracellular FRET reporter can bind to the collagen matrices and enables the visualization of MMP2 activity through fluorescence changes. This system showed feasibility in detecting protease activity in a 3D culture system. (Figure 3C) Many challenges still exist in determination of disease markers using biosensors, such as nonspecific binding and the small size of the target which can be overcome in future studies.

Biosensor for detecting electrical signals

Electrophysiology is an important feature of electroactive tissues including cardiac and neuronal tissues. The fibrotic process is particularly detrimental as the heart is characterized by limited regenerative and repair capacity. In the case of cardiac fibrosis, overpopulated cardiac fibroblasts result in ECM deposition and hence altered cardiomyocyte electrophysiology and disrupted electrical impulse conduction of the myocardium (Ramanathan et al., 2006). The activated myofibroblasts can be coupled to cardiomyocytes through gap junctions and result in partial depolarization of cardiomyocytes (Thompson et al., 2011). Therefore, integration of electrical biosensors can provide targets for potential drug therapies of cardiac fibrosis. An ideal cardiac OOC platform should provide multiplexed measurements of electrophysiological aspects. Concerted efforts in sensor integration in OOC platforms will open a new avenue for spatiotemporal exploration of cardiac disease.

Microelectrode array (MEA) is a widely used approach for recording electrical signal as it can be easily integrated in microphysiological systems. Traditional MEAs are confined to 2D substrates that render spatiotemporal electrical recordings of a single plane. More recently, 3D bioelectrical interfaces were reported, enabling a more complex electrophysiological readout. Kalmykov et al. (2019) developed a self-rolled biosensor array using either built-in active field-effective transistors or passive microelectrodes to interface with encapsulated 3D human cardiac spheroids to investigate electrogenic cell behavior. These arrays provided continuous and stable multiplexed recordings of field potentials, supported with simultaneous calcium imaging (Figure 3D).

Cardiac conduction is another important functional readout of the heart and is often impaired by fibrotic remodeling (Thompson et al., 2011). Optical mapping is the conventional method to measure electrical propagation and arrhythmias. However, the fluorescent dyes induce phototoxicity in longer term application, therefore optical mapping is typically performed as end-point analysis. MEA is also accompanied by low spatial resolution and low signal-to-noise ratio. The development of cytotoxicity-free methods for real-time *in situ* recording of conduction velocity is of increasing research interest. Dou et al. (2020) developed a label-free method based on defocused brightfield imaging to quantify cardiac volume (CV) by analyzing centroid displacements and contraction trajectories of each cardiomyocyte in a 2D iPSC-cardiomyocytes culture without effecting cell viability.

Beyond the cardiac system, integrated electrodes are also applied in other organ models. These applications include the assessment of barrier integrity of cultured cells using trans-endothelial electrical resistance (TEER) measurements. Farooqi et al. (2021) explored TEER measurement's utility for monitoring liver fibrosis development in a dynamic cell culture microphysiological liver system. A glass chip-based embedded TEER and reactive oxygen species (ROS) sensors were employed to gauge the effect of TGF-β1 within the microphysiological system, which promotes a positive feedback response in fibrosis development.

Overall, chip embedded electrochemical sensors could be used as a promising substitute for conventional end-point assays for studying fibrosis in microphysiological systems. In future, this fast-developing field has great value in illuminating mechanisms of diverse fibrotic diseases and accelerating discovery of novel anti-fibrotic drugs.

Potential Therapeutic Targets for Fibrosis

Fibrosis represents a major health problem worldwide, yet there are still limitations in current knowledge of the disease mechanisms. Development of antifibrotic therapies relies on comprehensive understanding of profibrogenic mechanisms in organ-specific systems. Due to heterogeneity in disease etiology and phenotypes, and lack of clinically validated biomarkers, there is a no effective disease-modifying therapeutic agents specific to fibrosis. Conventional treatments rely on pharmaceutical compounds targeting inhibition of fibrosis-related molecular pathways. Various potential novel strategies have been investigated to combat fibrotic tissue damage in different organs (Figure 4).

Transforming growth factor-related pathway inhibition

In the past few decades, research has highlighted potentially targetable pathways and related individual factors involved in the fibrogenesis process. These include transforming growth factor-beta (TGF-β), which has long been recognized as a master activator in fibrosis (Meng et al., 2016). TGF-β acts on multiple cell types to drive pathogenesis of fibrogenic responses in several different organs. TGF-β-induced fibrosis is activated through canonical Smad-dependent or non-canonical Smad-independent pathways and is modulated by various coreceptors and complex interacting networks (Meng et al., 2016).

There is a limited therapeutic feasibility and unpredictable off-target effects in direct targeting of TGF-β, due to the functional pleiotropy of this growth factor in a wide variety of complex biological processes. Recent discoveries in fibrotic pathways and factors regulated by TGF-β have facilitated the identification of alternative therapeutic targets and showed promise in achieving an attainable inhibition of fibrotic response (Akhmetshina et al., 2012).
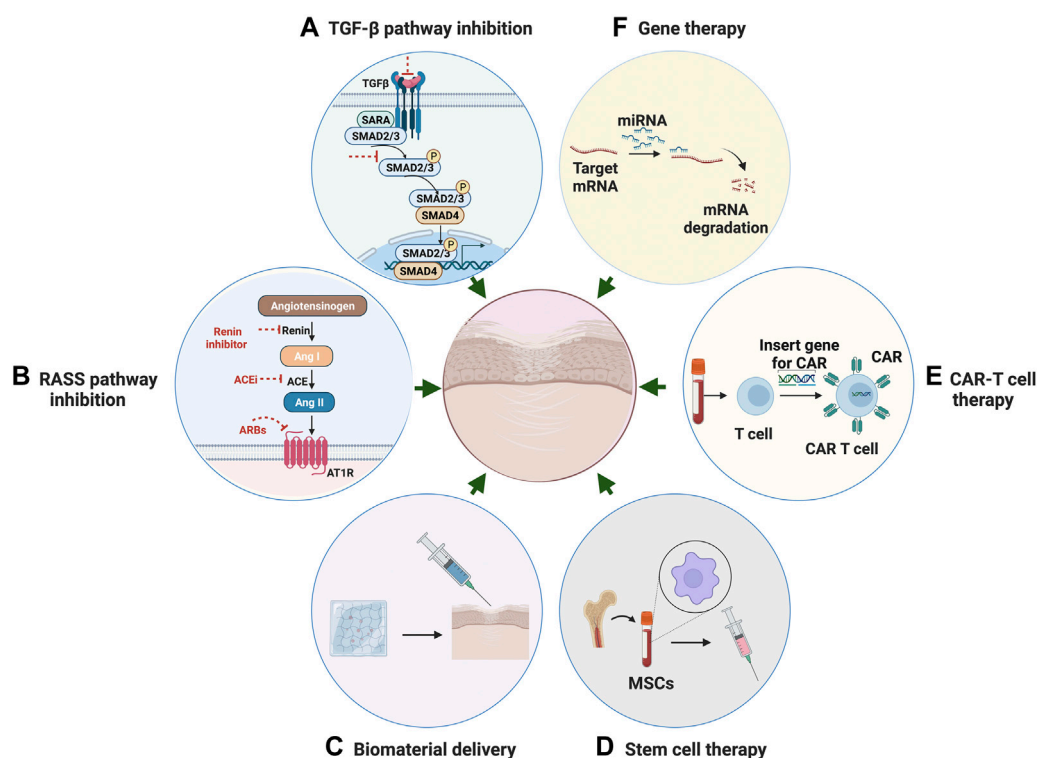
FIGURE 4
Potential Therapeutic strategies for fibrosis. **(A)** Anti-fibrotic therapeutic strategies through inhibition of TGF-β pathway. **(B)** Therapeutic strategies through inhibition of RAS system. **(C)** Targeted anti-fibrotic therapeutic approach through biomaterial-based delivery. **(D)** Stem cell therapy with mesenchymal stromal cells for the treatment of fibrotic disease. **(E)** CAR T-cell therapy using engineered T cells for the treatment of fibrotic disease. **(F)** Gene therapy through mediating miRNA as a novel approach for anti-fibrosis treatment.

Fibroblast growth factor 2 (FGF2), one of the members of the mammalian fibroblast growth factor family, is a cytokine with well-documented cardioprotective effects to attenuate fibroblast activation through antagonizing TGF-β signaling. Svystonyuk et al. (2015) evaluated the effects of low molecular weight fibroblast growth factor (LMW-FGF-2) on myofibroblast-seeded collagen gels, and observed a significant attenuation in TGFβ1 induced myofibroblast activation and ECM remodeling (Fan and Guan, 2016).

Bone morphogenetic protein-7 (BMP7) belongs to the TGF-β super family and is found to have an anti-fibrotic role that is correlated with the inhibition of TGF-β-mediated profibrotic signaling (Hanna and Frangogiannis, 2019). Various studies showed that supplementation with exogenous recombinant BMP-7 can facilitate the reversal of established fibrotic lesions (Tampe and Zeisberg, 2014). Efforts continue to define the therapeutic effectiveness of BMP7 through ongoing *in vitro* and *in vivo* investigations, and to develop small-molecule agonists for systemic administration.

Peroxisome Proliferation Activator Receptors (PPARs) are nuclear transcription factors that form obligate heterodimers with retinoid-X receptors to modulate the transcription of target genes. Preclinical studies have implicated all three PPARs as potential targets for antifibrotic therapy (McVicker and Bennett, 2017).

β-catenin, the central signaling component of the canonical Wnt pathway, is believed to serve a modified target for fibrosis through activation of TGFβ pathway. Hirakawa et al. (2019) evaluated two Wnt/β-catenin signaling inhibitors, ICG-001 and C-82, on the progression of endometriosis. The results suggested that inhibiting the CREB-binding protein (CBP)/β-catenin signal can be a therapeutic target for endometriosis. In another study, Itaba et al. (2019) reported the potent anti-fibrotic therapeutic effect of IC-2, a derivative of ICG-001, on established liver fibrosis.

Recently, several novel components of the TGF β have been discovered, including proprotein convertases (PCSKs), which is in a family of serine proteases that cleave secreted peptides. PCSKs have been reported to be involved in the activation of the TGF-β/Smad signaling pathway. Furin is one of the most ubiquitously expressed PCSK and has been

implicated as a potential therapeutic target in fibrosis (Ichiki et al., 2013).

Rennin–angiotensin–aldosterone system pathway inhibition

The Rennin–angiotensin–aldosterone system (RAAS) plays a critical role in mediating systemic blood pressure, fluid volume, and sodium balance. Overactivity of RAAS is believed to have a pivotal role in the onset of pathological fibrosis. Angiotensin II, the main peptide of the RAS system, has been demonstrated to induce fibrosis in various organs. Many studies reported the critical role of Ang II in the cardiovascular, renal, and pulmonary systems (Murphy et al., 2015) under pathological conditions, such as cardiac hypertrophy and the resultant fibrosis (Murphy et al., 2015). It is now known that angiotensin II acts both independently and in synergy with TGF-β to induce fibrosis via the angiotensin type 1 receptor (AT1) in a multitude of tissues. Ang II can induce fibrosis indirectly by activating proinflammatory mediators such as cytokines, chemokines, adhesion molecules, as well as directly by regulating ECM synthesis and degradation. These studies indicate that therapeutic strategies targeting Ang II are probably an effective way of alleviating fibrosis progression.

The use of RAAS inhibitors, such as renin inhibitors, Angiotensin-converting enzyme (ACE) inhibitors, Angiotensin Receptor Blockers (ARBs), and mineralocorticoid receptor antagonists has been documented to prevent fibrosis and slow the decline of organ function effectively in the process of kidney disease and cardiac hypertrophy (Zhang et al., 2019a). ACE Inhibitors (ACEIs) inhibit the conversion of Ang II from Ang I. A number of ACEIs are currently on the market and used primarily for the treatment of high blood pressure and heart failure. Different ACEIs such as captopril, ramipril, and enalapril, have been extensively tested in both *in vitro* and *in vivo* models and shown effects on reducing fibroblast proliferation, and suppressing collagen deposition and TGF-β1 expression. Similar with ACEIs, ARBs are also frequently prescribed to treat hypertension and have comparable clinical profiles regarding anti-inflammatory and anti-fibrotic outcomes. ARBs compete with the binding of angiotensin II to AT1 receptors, thereby cause angiotensin II receptor blockade. Clinical trials looking at the potential utility of an angiotensin II type 1 receptor blocker (ARB) have demonstrated significant benefit in the prevention of myocardial fibrosis (Zhang et al., 2019a).

Direct Renin Inhibitors (DRIs), Mineralocorticoid Receptor Antagonists (MRAs) as other means of RAAS blockade also have been studied (Zhang et al., 2019a). However, inhibition of RAAS only modestly regresses fibrosis. The combination of different RAAS drugs is an alternative strategy. The use of combination therapy is already established in practice and positive effect has been confirmed.

Developing novel and effective anti-fibrotic therapies through targeting Ang II pathway appears an attractive strategy. Over the past decades, many novel compounds such as kinases inhibitors and hormone peptides showed promising results in alleviating Ang II signaling and compensatory fibrotic remodeling. For example, relaxin, an endogenous peptide hormone in the insulin family, has received much research attention due to the increasing evidence on this peptide hormone's beneficial effects in fibrotic conditions. Relaxin binds with its endogenous receptor, relaxin family peptide receptor 1 (RXFP1), inhibiting the actions of major pro-fibrotic factors including Ang II (Chow et al., 2014; Samuel et al., 2017).

Novel interventions

Biomaterial-based delivery

Current fibrosis therapeutic development technologies are aiming at reducing off-target effects and promoting localized action to affected or fibrotic regions. The development of biomaterial-based delivery methods offers opportunities to improve target specificity and reduce adverse effects. Nano- and micro-particles as carriers for the delivery of can improve transport efficiency and allow more circulation time for the cargo molecules to reach the disease site (Hrkach and Langer, 2020).

Different polymeric microspheres and microparticles have been extensively studied as drug-laden depots to achieve localized delivery of cargos including anti-fibrotic molecules. For example, poly (lactic-co-glycolic acid) (PLGA) microspheres were used to encapsulated resveratrol (RSV) and embedded in a gelatin methacryloyl (GelMA) hydrogel matrix for the treatment of epidural fibrosis (Wang et al., 2021b). Sustained release over weeks was achieved, along with reduced fibroblast proliferation and extracellular matrix deposition. Similarly, low molecular weight heparin (LMWH) loaded PLGA microspheres were administrated in a mouse model of bleomycin-induced lung fibrosis and exerted anti-fibrotic and anti-inflammatory therapeutic effects (Saito et al., 2020). Horejs et al. (2017) developed electrospun polymer matrices incorporated with a fragment of the laminin β1-chain to efficiently modulate MMP expression and activity. They demonstrated that interfacing of the β1-fragment with the mesothelium of the peritoneal membrane *via* a biomaterial abrogates the release of active MMP2 in response to transforming growth factor β1 in a mouse model of peritoneal fibrosis.

In the nanoscale range, there are successful applications of the nanoparticle-based delivery for the treatment of chronic human diseases including cancer, diabetes, and fibrosis. The

advances in target-oriented delivery facilitate the therapeutic agents to anchor to their target location for maximized therapeutic function and reduced off-target effects. Controlled systems for delivering therapeutic agents to myofibroblasts have been explored for the treatment of fibrosis (Yazdani et al., 2017). Cell surface ligands such as peptides, antibodies, aptamers, or other moieties are designed against myofibroblast-specific receptors. Activation of hepatic stellate cells (HSCs) is the hallmark of liver fibrogenesis. Targeted delivery of therapeutic agents to activated HSCs has been extensively studied for the treatment of liver fibrosis. Azzam et al. reported a chitosan-nanoparticles (CS-NPs) based delivery system for anti-TGF-β siRNA delivery, promoting delivery into HSCs via modification with PDGF receptor-beta binding peptides. The peptide-modified CS-NPs allow for efficient targeting of fibrotic livers and increased NP uptake by target cells, offering a powerful strategy for improving therapeutic outcomes (Yazdani et al., 2017). In future, targeted delivery to subpopulations of myofibroblasts will remain a highly appealing approach to suppress interstitial fibrosis. However, this field is still in its infancy, as the surface markers delineating these populations are yet to be identified and fully understood.

Cell therapy

Cell therapy aims to introduce new, healthy cells into a diseased or injured locus, to replace the pathological or missing native cells and to restore organ function. Mesenchymal stromal cells (MSCs) have shown great potential in the treatment of inflammatory diseases and mediating profibrotic factors through their immunoregulatory properties (Usunier et al., 2014). Averyanov et al. (2020) reported the first-in-human stem cell therapy in idiopathic pulmonary fibrosis using a high cumulative dose of bone marrow MSCs. The treatment was demonstrated to contribute to an increase in lung function. However, various challenges still exist. Underlying immunocompatibility, stability, heterogeneity, and migratory capacity should be optimized before moving to large-scale clinical trials (Yang et al., 2020).

Chimeric antigen Receptor (CAR) T-cell therapy is a form of immunotherapy that uses engineered T cells to target specific antigens on cancer cells. Patient-derived T cells are collected and modified to produce a modified T cell receptor or CARs on their surface (Aghajanian et al., 2019). Recent advances in CAR-T cell therapy have led to increased interest in their use as a new therapeutic method to address not only cancer but also chronic inflammation associated with fibrosis. Aghajanian et al. (2019) reported the success in using redirected T cell immunotherapy to target pathological cardiac fibrosis in mice. Cardiac fibroblasts that express a xenogeneic antigen were targeted and significantly ablated by the adoptive transfer of antigen-specific CD8^{+} T cells.

However, establishing the Car-T cell therapy in humans could take years of development. The therapy is also very expensive and accompanied by severe off-target and side effects. Continued efforts in the identification of antigens that are expressed by activated cardiac fibroblasts may contribute to the development of T cell therapy of fibrosis.

Gene therapy

Gene therapy has shown promising results in the treatment of a wide spectrum of human diseases. Gene therapy is normally generated by transferring specific genetic information into target cells to correct mutated genes that cause diseases. Many recent technologies, including genetic editing, recombinant DNA technique, mRNA, and miRNA technology, have been utilized in improving the performance of gene therapy in disease context.

MicroRNAs (miRNAs) are a class of small non-coding RNAs that play a role in regulating the expression of messenger RNAs (mRNAs). miRNAs are thought to be involved in diverse biological processes, including fibrosis (Marquez and McCaffrey, 2008). Mediating miRNA by gene therapy provides an attractive approach for therapeutic development of anti-fibrosis drugs. Recent studies have indicated the critical role of a number of microRNAs in the pathogenesis of different forms of human fibrotic disease. For example, Ji et al. (2015) performed genome-wide profiling of miRNA expression in a silica-induced mouse model of pulmonary fibrosis using microarrays. Their results suggested that miR-486-5p is downregulated in the disease model and may act as an anti-fibrotic effector in the development of pulmonary fibrosis.

Machine learning assisted drug screening

Machine learning in fibrotic drug discovery and screening

Machine learning (ML) is a rapidly growing field of artificial intelligence research influencing drug screening approaches and enabling new methods of drug discovery (Vamathevan et al., 2019). Generally, ML algorithms are divided into three main categories, supervised, unsupervised, and reinforcement learning. Supervised ML uses labeled datasets to train an algorithm that can later classify data or better predict outcomes of potential inputs to the system (Benjamins et al., 2019). Supervised algorithms include regression analysis, k-nearest neighbour (kNN), Bayesian probabilistic learning, support vector machines (SVMs), random forests and neural networks (Shrestha and Mahmood, 2019). A neural network is one of the most common subsets of machine learning meant to mimic human brain by containing a series of connected nodes,

organized in several layers (Yegnanarayana, 2009).Deep learning utilizes neural network approach but contains a much greater quality of hidden layers between data input and output, in comparison to the relatively small number of hidden layers in traditional neural networks (LeCun et al., 2015). Unsupervised ML algorithms analyze and cluster the unlabelled datasets from their potential hidden patterns (Jordan and Mitchell, 2015). Some of the most commonly utilized methods of unsupervised ML are principal component analysis, independent components analysis (ICA), hierarchal learning, data clustering, outlier detection, and singular value decomposition (SVD) (Usama et al., 2019). In reinforcement learning, the algorithm is given a challenge, and is instructed to accomplish a specific goal by optimize a custom function. As the algorithm explores the challenge, it is given a "reward" a representation of our result's approximate to the desired goal. In this way, the algorithm progressively makes decisions to find the optimal method of reaching the set goal, as it is maximizing the reward (Sugiyama, 2015).

A variety of ML methods were applied to uncover drug candidates or putative targets for drug discovery, for instance the use of support vector machines, optical flow, and tree bagger algorithms, among others. The targets of ML in the drug screening field have focused on analyzing the effects of drugs on tissue contraction, cardiotoxicity, and electrophysiology. Although current drug-centric ML approaches have not specifically focused on anti-fibrosis drugs, we will briefly review several machine learning-based methods for drug discovery and screening applications. We believe these current implementations will help establish the groundwork for future ML studies related to fibrosis as they involve similar assays and datasets.

Machine learning-based method for drug discovery

In the early stages of drug discovery there are frequently thousands, or tens of thousands of potential candidate molecules. Manual analysis of such tremendous volumes of candidates is extremely labour intensive, thus, recently this process is being enhanced using novel ML methods.

Drug repositioning is a common technique in industry where after research and testing, a molecule is found to be effective on treating a different condition. Due to tremendous volume of approved compounds, ML approaches lend themselves well to determining potential repurposing targets. A novel ML approach for this problem was developed by Wu et al. (2020) with the development of DR AFC (Drug Repositioning based on Anti-Fibrosis Characteristics), which predicts anti-fibrosis drug repositioning candidates through molecular structure and biological profile analysis. Using logistical regression,

decision tree, random forest and gradient boosting algorithms, DR AFC was trained on a labelled database of anti-fibrotic and non-anti-fibrotic compounds using molecule structure and biological profile. DR AFC was then applied to experimental drugs in the DrugBank database to locate potential anti-fibrotic drugs for repositioning. DR AFC determined that the molecule Quercetin and the natural compounds of turmeric and curcumin could have potential anti-fibrotic properties based on the activated gene pathways and structure (Wu et al., 2020).

To reduce the large volume of drug candidates, a compound's molecular structure can be investigated to predict how it may interact with desired biological bind sites. This can be accomplished through computing the standard binding free energy between particular compound and a binding site. Ding and Zhang (2021) developed a platform to determine the standard binding free energy using a deep generative model based on Bennet acceptance ratio, called DeepBAR. Their technology does not require calculation of the intermediate binding steps of the compound, and only requires data regarding the end states of binding sites. The authors tested effectiveness of their system by testing its prediction capabilities of compound binding to the commonly used achiral ring molecule cucurbituril (Sgalla et al., 2018). They found that DeepBAR requires significantly less computational power compared to traditional methods, yet still maintains the high degree of accuracy required for complex testing (Ding and Zhang, 2021).

Machine learning-based method for assessing tissue contraction

Using the technique of optical flow to measure cardiomyocyte monolayer contractions, Lee et al. (2015) developed a ML-based drug screening platform to identify cardioactive drugs. The ML system was designed to distinguish between the effects of the drugs E-4031, verapamil, and blebbistatin on cardiomyocyte contraction. The motion vector maps of monolayer contraction captured by optical flow were reduced to a single contraction profile using principal component analysis. Twelve parameters were extracted from the contraction profile and used to train a supervised ML algorithm based on the Support Vector Machine (SVM) framework. The trained algorithm categorized the contraction profiles of samples as having either normal or abnormal cardiomyocyte behaviour when exposed to drug treatment. A follow up study by Lee et al. (2017) applied a two-step ML algorithm using SVM to anticipate a cardioactive drug's mechanism of action on contractility in cardiac tissue strips. In the first step, supervised ML was used to binarily classify each of the 12 compounds as cardioactive or not by observing changes in contractility. The second stage

consisted of training a multiclass SVM algorithm with half the compounds to create distinct classification of compounds based on their effects on the cardiac tissue strips. The remaining, unclassified compounds were tested on this algorithm to determine its prediction ability of drug class as an indicator of mechanism of action.

Machine learning-based method for assessing cardiotoxicity

The effects caused by a compound on the human ether-à-go-go-related gene (hERG) pathway is an important factor when testing for cardiotoxicity as inhibition can cause fatal cardiac arrhythmias (Sanguinetti and Tristani-Firouzi, 2006). To predict if compounds may affect the hERG channel, Cai et al. (2019) developed a multitask deep neural network (DNN) called deephERG. DeephERG operates by using the Molecular Operating Environment (MOE) to generate the properties and vector representation of each drug being analyzed. A subset of this dataset is then input into the multitask DNN for training and validation to determine the cardiotoxicity prediction accuracy. The authors subsequently applied deephERG to analyze 1824 FDA approved drugs for their potential effects on hERG and predicted that 539 candidates could be problematic. DeephERG leverages Mol2Vec descriptors, which is an unsupervised machine learning approach that converts molecular substructures into a vector representation (Cai et al., 2019). Molecules that have comparable substructures end up as similar vectors. Mol2Vec is developed based on application of machine learning on Word2Vec algorithm which a Natural Processing technique for identification and process of closely related molecular substructures and translating them into a vector representation (Jaeger et al., 2018).

A similar study on identifying hERG pathway cardiotoxicity using ML was done by Lee et al. (2019b) through the analysis of molecular physicochemical descriptors associated with cardiotoxicity. After training six different ML algorithms, each was tested on its ability to distinguish cardiotoxicity on a dataset of 2130 compounds. Evaluation of the model showed it had an accuracy of 90.1% at determining potential cardiotoxicity compounds (Lee et al., 2019b).

Machine learning-based method for electrophysiological assessments

Heylman et al. (2015) created a supervised ML algorithm that compares differences in cardiomyocyte electrical membrane depolarization when treated with propranolol and isoproterenol. A two-photon laser scanning microscope was used to scan individual cardiomyocytes exposed to a fluorescent voltage sensitive dye to extract a membrane depolarization waveform. The TreeBagger random forest algorithm was used as the basis for the supervised ML platform, and functions by comparing the waveform's upslope, downslope, peak width, maximum height, and

plateau height. After training the algorithm to distinguish between treatment groups, the accuracy of group determination for unknown waveforms was found to be 70% for a single depolarization, and 100% for 1-min recordings (Heylman et al., 2015).

A method developed by Juhola et al. (2018) utilized several different supervised ML algorithms such as least-squares-SVM, k-nearest neighbor and random forest to classify calcium transients from patient cardiomyocytes with genetic diseases. The calcium transients were analyzed based on ten different variables extracted from peak information of each sample. These variables include transient peak amplitude, duration, and area under the peak. After training the algorithm, each ML algorithm was applied to a pool of unclassified transients to separate them into the three different diseased groups or as healthy controls. The random forest algorithm was determined to be the most accurate, with 78.6% accuracy at correctly predicting the groups. Despite the fact that the focus of this research was on identification of genetic cardiac diseases, this research may be translatable to investigating changes in calcium transients during drug screening (Juhola et al., 2018).

Current challenges and future directions in the application of engineered approaches in fibrotic remodeling

The use of OOC disease models, as a viable alternative to traditional pre-clinical testing methods, is improving in verifications with regulatory environment and facing increasing industrial acceptance in the past decade. The upward trend in optimization, regulation, ratification, and adoption of these engineered models promises to lay the foundation of next-generation precise medicine. However, stumbling blocks remain for the widespread adoption of OOC disease models.

Lineage variability

One of the biggest challenges of hiPSC-based disease modeling is the experimental heterogeneity due to lineage variability and instability. Heterogeneity can result from a multitude of factors such as donor-specific genetic and epigenetic status, as well as clonal variations including incomplete reprogramming and changes during culture. This can hinder reproducibility and confound biological phenotypical differences. In the context of fibrotic disorders, the synergistic interaction of multiple cell types is often involved to manifest specific disease phenotypes. As a result, it is of great importance to construct the model using subpopulations of the same genetic background. The use of standardized differentiation and maturation protocols and cell sorting-based phenotypic selection can potentially minimize variability and thereby increase the reliability of phenotype comparisons in disease modeling. In addition, recent studies

describe elegant protocols for the derivation of cardiac fibroblasts from genetically defined hiPSCs (Zhang et al., 2019b). Alternative sources of genetically matched cardiac fibroblasts could be obtained through selective adhesion or cell sorting from the mixed differentiation culture. Other genetically matched cells, such as ECs (Gu, 2018) and macrophages (Sturgeon et al., 2014), can be differentiated from iPSC with established differentiation methods. Isogenic controls, conventionally used in animal models, have been an effective tool for hiPSC-based disease modeling via CRISPR correction of mutated loci. The isogenic cell lines are typically established and cultured in parallel with the fibrosis diseased lines to study epigenetic changes resulting from a specific allele. The disease phenotypes would be corrected in isogenic control and the disease mechanisms can be therefore investigated for potential therapeutic interventions (Merkert et al., 2017). As obtaining hiPSC with disease-causing genetic mutations can be unpredictable and time-consuming, a faster and easier approach is to obtain the healthy iPSC cell lines and CRISPR editing the known mutation into the genome to investigate the epigenetic changes regarding to the specific mutation (Wang et al., 2014; Valley et al., 2019). In comparison to iPSC control from an unaffected family member, the isogenic control would significantly reduce the variability resulting from the different genetic backgrounds and identify the disease relevant molecular changes (Wang et al., 2014; Valley et al., 2019). In future studies, these cells could be used to provide genetically matched cell sources and isogenic controls for robust 3D disease models.

Tissue maturation

The structural and functional immaturity of hiPSC-derived cells poses another challenge for the direct application of OOC disease models. To this end, enhanced tissue maturation can be achieved using external signals, including electrical, mechanical, and hormonal stimuli. Zhao et al. (2019b) applied electrical stimulation at a gradually increasing intensity to generate electrophysiologically distinct atrial and ventricular tissues with chamber-specific drug responses and gene expression. Ulmer and Eschenhagen (2020) achieved cardiac metabolic maturation through the cultivation of 3D cardiac tissues against a mechanical load, allowing *in vitro* study of metabolic cardiomyopathies. Whilst maturity level in these engineered models is still not on par with the human level, these methods provide a significantly more adult-like hiPSC-derived cardiomyocytes. Continuous effort in improving tissue maturation is essential for developing more physiological relevant disease models.

Integration of vasculature and local and circulating immune cells

A functional vascular system is a key element in promoting tissue function and evaluating pharmacokinetics and drug effects. However, integrating a vascular interface to multi-OOC systems remains a major challenge without a universal solution. Over the decades, there has been considerable interest in the development of microfluidic OOC platforms with a perfusable vascular network. Co-culture of hiPSC-CMs with endothelial cells can result in primitive vessel-like structures with the potential for *in vivo* anastomosis (Zhang et al., 2018b). The next essential step will be the development of 3D engineered tissue constructs with perfusable vasculature, and include the immune response. Human physiomimetic models that support the cultivation of organ models and circulating immune cells will fundamentally facilitate the study of complex human diseases such as fibrosis, pre-clinical drug development, and precision medicine.

Scale-up and manufacturing

In terms of platform development, although the culture-based *in vitro* disease models are useful tools to study the disease mechanism and the development of anti-fibrotic drugs, reproducibility, and manufacture of the platform devices are significant challenges. The success of commercial use of organ-on-a-chip model depends heavily on their manufacturability, reproducibility, and availability for large-scale studies. Most lab-used OOC platforms are of relatively low yield due to manual handling in microfabrication and assembly procedures. Standard operation protocol and good manufacture procedures are necessary to develop more standardized and reproducible platform fabrication and end use. Nevertheless, such models are more appropriate to use at a later stage and not suitable for early developmental stage where high-throughput screening for thousands of hits within a limited time window.

The construction of OOC platform involve two key components, the platform fabrication and tissue construction. Platform fabrication relies on microfabrication or microfluidics techniques to build the device for tissue cultivation; tissue construction refers to cultivation of live tissues in a 3D format. The development of more automated and cost-effective manufacturing technologies, such as one-step multi-material 3D printing (134, 135) or hot-embossing (136), can significantly scale up the production of OOC platforms. On the tissue construction side, self-assembly is a widely used process by which cellular components adopt a defined structure without external guidance to achieve complex tissue and organ-level organization and function (75, 137). Additionally, recent advances in 3D bioprinting facilitated multi-scale cell micropatterning and construction of tissues with complex topography (24, 138). These techniques collectively allow rapid and reproducible automated construction of biomimetic organ-like structures. Once the manufacturing process becomes more streamlined and reproducible, widespread adoption of OOC disease models will be accelerated.

Concluding remarks

While the field is still in the early stage of development, OOC has indeed delivered a breakthrough in disease modeling, allowing for the creation of sophisticated *in vitro* models to understand the processes regulating complex human physiology and pathology. Although the application of these platforms is still confined within the research laboratories, awareness of this technology is spreading fast. The potential for wide adoption across the broader scientific community, industry, and regulatory agencies is encouraging.

Faithfully modelling disease phenotypes and providing clinically meaningful readouts are the important features of an ideal experimental system for drug development. Engineered microtissues, organoids, spheroids, and microfluidic cultures are enjoying rapid growth in the past decade. In terms of fibrosis remodeling, various engineered tools with the capacity to identify pathological factors and potential therapeutics have been devised. Such clinically relevant findings cannot be easily achieved from other commonly used *in vivo* or *in vitro* approaches which are limited by the absence of physiologically relevant hallmarks of human fibrosis.

OOC models are broadly applicable as novel tools for better understating the underlying mechanisms of pathological development of fibrotic diseases, and the inhibition or prevention of fibrotic phenotypes through therapeutic interventions. Each model system exhibits its unique limitations. It may be challenging to find an appropriate model to meet all kinds of experimental requirements and the efficacy of each model is mostly based on the desired assay or translational applications. Current OOC are used to identify the problem and design the system based on the elements needed by this problem, therefore, we do not need everything in the system, but only elements that are critical to reproduce the desired function. The value that OOCs bring is the ability to recapitulate these essential factors *in vitro*. A further boost to these platforms could be achieved using multiple techniques in conjunction, such as hiPSC-derived 3D microtissues on a chip where the real-time properties can be monitored using a buit-in sensor. In addition, automation capacity is strongly desired for chronological tissue assessment and for retrieving useful data from the system. Machine learning applications through analysis of tissue contractions, electrophysiology, calcium flux, and overall toxicity are applicable to fibrosis-related drug screening. In the future, these algorithms could be integrated into anti-fibrosis drug screening pipelines to enhance screening throughput and detection of novel compounds. With highly controlled and formulated micro-environments, these avatars of the human organs can faithfully replicate disease phenotypes. These biosystems present a promising tool with unique features that can propel them to transform the present disease study and drug discovery with superior biofidelity, outperforming the conventional animal and monolayer disease models. Although tumbling blocks still exist in the widespread application of OOC models, we are optimistic that the coherent efforts from the engineers, biologists, and clinicians will entail this complex issue.

Author contributions

EW and MR contributed to conceptualization and design of the paper. EW, YZ, and JS wrote the initial manuscript, which was edited by MR and SO. MR approved the final manuscript.

Funding

Acknowledgments

Conflict of interest

The authors declare that the research was conducted in the absence of any commercial or financial relationships that could be construed as a potential conflict of interest.

Publisher's note

All claims expressed in this article are solely those of the authors and do not necessarily represent those of their affiliated organizations, or those of the publisher, the editors and the reviewers. Any product that may be evaluated in this article, or claim that may be made by its manufacturer, is not guaranteed or endorsed by the publisher.

References

Aghajanian, H., Kimura, T., Rurik, J. G., Hancock, A. S., Leibowitz, M. S., Li, L., et al. (2019). Targeting cardiac fibrosis with engineered T cells. *Nature* 573 (7774), 430–433. doi:10.1038/s41586-019-1546-z

Akhmetshina, A., Palumbo, K., Dees, C., Bergmann, C., Venalis, P., Zerr, P., et al. (2012). Activation of canonical Wnt signalling is required for TGF-β-mediated fibrosis. *Nat. Commun.* 3 (1), 735. doi:10.1038/ncomms1734

Aquino-Gálvez, A., González-Ávila, G., Jiménez-Sánchez, L. L., Maldonado-Martínez, H. A., Cisneros, J., Toscano-Marquez, F., et al. (2019). Dysregulated expression of hypoxia-inducible factors augments myofibroblasts differentiation in idiopathic pulmonary fibrosis. *Respir. Res.* 20 (1), 130. doi:10.1186/s12931-019-1100-4

Asmani, M., Velumani, S., Li, Y., Wawrzyniak, N., Hsia, I., Chen, Z., et al. (2018). Fibrotic microtissue array to predict anti-fibrosis drug efficacy. *Nat. Commun.* 9 (1), 2066. doi:10.1038/s41467-018-04336-z

Averyanov, A., Koroleva, I., Konoplyannikov, M., Revkova, V., Lesnyak, V., Kalsin, V., et al. (2020). First-in-human high-cumulative-dose stem cell therapy in idiopathic pulmonary fibrosis with rapid lung function decline. *STEM CELLS Transl. Med.* 9 (1), 6–16. doi:10.1002/sctm.19-0037

Benjamins, J. W., Hendriks, T., Knuuti, J., Juarez-Orozco, L. E., and van der Harst, P. (2019). A primer in artificial intelligence in cardiovascular medicine. *Neth. Heart J.* 27 (9), 392–402. doi:10.1007/s12471-019-1286-6

Bersini, S., Gilardi, M., Ugolini, G. S., Sansoni, V., Talò, G., Perego, S., et al. (2018). Engineering an environment for the study of fibrosis: A 3D human muscle model with endothelium specificity and endomysium. *Cell. Rep.* 25 (13), 3858–3868.e4. e4. doi:10.1016/j.celrep.2018.11.092

Besser, R. R., Ishahak, M., Mayo, V., Carbonero, D., Claure, I., and Agarwal, A. (2018). Engineered microenvironments for maturation of stem cell derived cardiac myocytes. *Theranostics* 8 (1), 124–140. doi:10.7150/thno.19441

Bracco Gartner, T. C. L., Deddens, J. C., Mol, E. A., Magin Ferrer, M., van Laake, L. W., Bouten, C. V. C., et al. (2019). Anti-fibrotic effects of cardiac progenitor cells in a 3D-model of human cardiac fibrosis. *Front. Cardiovasc. Med.* 6, 52. doi:10.3389/fcvm.2019.00052

Brandão, K. O., Tabel, V. A., Atsma, D. E., Mummery, C. L., and Davis, R. P. (2017). Human pluripotent stem cell models of cardiac disease: From mechanisms to therapies. *Dis. Model. Mech.* 10 (9), 1039–1059. doi:10.1242/dmm.030320

Cai, C., Guo, P., Zhou, Y., Zhou, J., Wang, Q., Zhang, F., et al. (2019). Deep learning-based prediction of drug-induced cardiotoxicity. *J. Chem. Inf. Model.* 59 (3), 1073–1084. doi:10.1021/acs.jcim.8b00769

Caliari, S. R., Perepelyuk, M., Soulas, E. M., Lee, G. Y., Wells, R. G., and Burdick, J. A. (2016). Gradually softening hydrogels for modeling hepatic stellate cell behavior during fibrosis regression. *Integr. Biol.* 8 (6), 720–728. doi:10.1039/c6ib00027d

Chen, C., Peng, Y., Wang, Z., Fish, P., Kaar, J., Koepsel, R., et al. (2009). The scar-in-a-jar: Studying potential antifibrotic compounds from the epigenetic to extracellular level in a single well. *Br. J. Pharmacol.* 158 (5), 1196–1209. doi:10.1111/j.1476-5381.2009.00387.x

Chow, B. S. M., Kocan, M., Bosnyak, S., Sarwar, M., Wigg, B., Jones, E. S., et al. (2014). Relaxin requires the angiotensin II type 2 receptor to abrogate renal interstitial fibrosis. *Kidney Int.* 86 (1), 75–85. doi:10.1038/ki.2013.518

Cox, T. R., and Erler, J. T. (2011). Remodeling and homeostasis of the extracellular matrix: Implications for fibrotic diseases and cancer. *Dis. Model. Mech.* 4 (2), 165–178. doi:10.1242/dmm.004077

Davidson, M. D., Kukla, D. A., and Khetani, S. R. (2017). Microengineered cultures containing human hepatic stellate cells and hepatocytes for drug development. *Integr. Biol.* 9 (8), 662–677. doi:10.1039/c7ib00027h

Devarasetty, M., Mazzocchi, A. R., and Skardal, A. (2018). Applications of bioengineered 3D tissue and tumor organoids in drug development and precision medicine: Current and future. *BioDrugs* 32 (1), 53–68. doi:10.1007/s40259-017-0258-x

Ding, X., and Zhang, B. (2021). DeepBAR: A fast and exact method for binding free energy computation. *J. Phys. Chem. Lett.* 12 (10), 2509–2515. doi:10.1021/acs.jpclett.1c00189

Distler, J. H. W., Györfi, A-H., Ramanujam, M., Whitfield, M. L., Königshoff, M., and Lafyatis, R. (2019). Shared and distinct mechanisms of fibrosis. *Nat. Rev. Rheumatol.* 15 (12), 705–730. doi:10.1038/s41584-019-0322-7

Dou, W., Zhao, Q., Malhi, M., Liu, X., Zhang, Z., Wang, L., et al. (2020). Label-free conduction velocity mapping and gap junction assessment of functional iPSC-Cardiomyocyte monolayers. *Biosens. Bioelectron.* 167, 112468. doi:10.1016/j.bios.2020.112468

Emon, B., Li, Z., Joy, M. S. H., Doha, U., Kosari, F., and Saif, M. T. A. (2021). A novel method for sensor-based quantification of single/multicellular force dynamics and stiffening in 3D matrices. *Sci. Adv.* 7 (15), eabf2629. doi:10.1126/sciadv.abf2629

Estrada, H., Patel, S., Rabizadeh, S., Targan, S., and Barrett, R. (2021).Development of a personalized model of intestinal fibrosis using human intestinal organoids derived from induced pluripotent stem cells, *Inflamm. Bowel Dis.*, 27, S35. doi:10.1093/ibd/izaa347.085

Fahliyani, S. A., Rastegari, A. A., Yadav, A. N., and Yadav, N. (2020). "Chapter 4 - microbially derived biosensors for diagnosis, monitoring, and epidemiology for future biomedicine systems," in *New and future developments in microbial Biotechnology and bioengineering*. Editors A. A. Rastegari, A. N. Yadav, and N. Yadav (Amsterdam, Netherlands: Elsevier), 43–65.

Fan, D., Takawale, A., Lee, J., and Kassiri, Z. (2012). Cardiac fibroblasts, fibrosis and extracellular matrix remodeling in heart disease. *Fibrogenes. Tissue Repair* 5 (1), 15. doi:10.1186/1755-1536-5-15

Fan, Z., and Guan, J. (2016). Antifibrotic therapies to control cardiac fibrosis. *Biomater. Res.* 20, 13. doi:10.1186/s40824-016-0060-8

Farooqi, H. M. U., Kang, B., Khalid, M. A. U., Salih, A. R. C., Hyun, K., Park, S. H., et al. (2021). Real-time monitoring of liver fibrosis through embedded sensors in a microphysiological system. *Nano Converg.* 8 (1), 3. doi:10.1186/s40580-021-00253-y

Gu, M. (2018). Efficient differentiation of human pluripotent stem cells to endothelial cells. *Curr. Protoc. Hum. Genet.* 98, e64. doi:10.1002/cphg.64

Hanna, A., and Frangogiannis, N. G. (2019). The role of the TGF-β superfamily in myocardial infarction. *Front. Cardiovasc. Med.* 6, 140. doi:10.3389/fcvm.2019.00140

Hasan, A., Nurunnabi, M., Morshed, M., Paul, A., Polini, A., Kuila, T., et al. (2014). Recent advances in application of biosensors in tissue engineering. *BioMed Res. Int.* 2014, 1–18. doi:10.1155/2014/307519

Hashimoto, N., Phan, S. H., Imaizumi, K., Matsuo, M., Nakashima, H., Kawabe, T., et al. (2010). Endothelial-mesenchymal transition in bleomycin-induced pulmonary fibrosis. *Am. J. Respir. Cell. Mol. Biol.* 43 (2), 161–172. doi:10.1165/rcmb.2009-0031oc

Heylman, C., Datta, R., Sobrino, A., George, S., and Gratton, E. (2015). Supervised machine learning for classification of the electrophysiological effects of chronotropic drugs on human induced pluripotent stem cell-derived cardiomyocytes. *PloS one* 10 (12), e0144572. doi:10.1371/journal.pone.0144572

Hirakawa, T., Nasu, K., Miyabe, S., Kouji, H., Katoh, A., Uemura, N., et al. (2019). β-catenin signaling inhibitors ICG-001 and C-82 improve fibrosis in preclinical models of endometriosis. *Sci. Rep.* 9 (1), 20056. doi:10.1038/s41598-019-56302-4

Horejs, C-M., St-Pierre, J-P., Ojala, J. R. M., Steele, J. A. M., da Silva, P. B., Rynne-Vidal, A., et al. (2017). Preventing tissue fibrosis by local biomaterials interfacing of specific cryptic extracellular matrix information. *Nat. Commun.* 8 (1), 15509. doi:10.1038/ncomms15509

Horton, R. E., Yadid, M., McCain, M. L., Sheehy, S. P., Pasqualini, F. S., Park, S-J., et al. (2016). Angiotensin II induced cardiac dysfunction on a chip. *PLOS ONE* 11 (1), e0146415. doi:10.1371/journal.pone.0146415

Hrkach, J., and Langer, R. (2020). From micro to nano: Evolution and impact of drug delivery in treating disease. *Drug Deliv. Transl. Res.* 10 (3), 567–570. doi:10.1007/s13346-020-00769-6

Huang, E., Peng, N., Xiao, F., Hu, D., Wang, X., and Lu, L. (2020). The roles of immune cells in the pathogenesis of fibrosis. *Int. J. Mol. Sci.* 21 (15), 5203. doi:10.3390/ijms21155203

Ichiki, T., Boerrigter, G., Huntley, B. K., Sangaralingham, S. J., McKie, P. M., Harty, G. J., et al. (2013). Differential expression of the pro-natriuretic peptide convertases corin and furin in experimental heart failure and atrial fibrosis. *Am. J. Physiology-Regulatory, Integr. Comp. Physiology* 304 (2), R102–R109. doi:10.1152/ajpregu.00233.2012

Itaba, N., Kono, Y., Watanabe, K., Yokobata, T., Oka, H., Osaki, M., et al. (2019). Reversal of established liver fibrosis by IC-2-engineered mesenchymal stem cell sheets. *Sci. Rep.* 9 (1), 6841. doi:10.1038/s41598-019-43298-0

Jacot, J. G., Martin, J. C., and Hunt, D. L. (2010). Mechanobiology of cardiomyocyte development. *J. Biomech.* 43 (1), 93–98. doi:10.1016/j.jbiomech.2009.09.014

Jaeger, S., Fulle, S., and Turk, S. (2018). Mol2vec: Unsupervised machine learning approach with chemical intuition. *J. Chem. Inf. Model.* 58 (1), 27–35. doi:10.1021/acs.jcim.7b00616

Jennings, P., Crean, D., Aschauer, L., Limonciel, A., Moenks, K., Kern, G., et al. (2015). Interleukin-19 as a translational indicator of renal injury. *Arch. Toxicol.* 89 (1), 101–106. doi:10.1007/s00204-014-1237-3

Ji, X., Wu, B., Fan, J., Han, R., Luo, C., Wang, T., et al. (2015). The anti-fibrotic effects and mechanisms of MicroRNA-486-5p in pulmonary fibrosis. *Sci. Rep.* 5 (1), 14131. doi:10.1038/srep14131

Jordan, M. I., and Mitchell, T. M. (2015). Machine learning: Trends, perspectives, and prospects. *Science* 349 (6245), 255–260. doi:10.1126/science.aaa8415

Juhola, M., Joutsijoki, H., Penttinen, K., and Aalto-Setälä, K. (2018). Detection of genetic cardiac diseases by Ca2+ transient profiles using machine learning methods. *Sci. Rep.* 8 (1), 9355–9410. doi:10.1038/s41598-018-27695-5

Kalmykov, A., Huang, C., Bliley, J., Shiwarski, D., Tashman, J., Abdullah, A., et al. (2019). Organ-on-e-chip: Three-dimensional self-rolled biosensor array for electrical interrogations of human electrogenic spheroids. *Sci. Adv.* 5 (8), eaax0729. doi:10.1126/sciadv.aax0729

Kim, C.-L., Choi, S.-H., and Mo, J.-S. (2019). Role of the Hippo pathway in fibrosis and cancer. *Cells* 8 (5), 468. doi:10.3390/cells8050468

Kollmannsberger, P., Bidan, C. M., Dunlop, J. W. C., Fratzl, P., and Vogel, V. (2018). Tensile forces drive a reversible fibroblast-to-myofibroblast transition during tissue growth in engineered clefts. *Sci. Adv.* 4 (1), eaao4881. doi:10.1126/sciadv.aao4881

Kong, M., Lee, J., Yazdi, I. K., Miri, A. K., Lin, Y.-D., Seo, J., et al. (2019). Cardiac fibrotic remodeling on a chip with dynamic mechanical stimulation. *Adv. Healthc. Mat.* 8 (3), 1801146. doi:10.1002/adhm.201801146

Krenning, G., Zeisberg, E. M., and Kalluri, R. (2010). The origin of fibroblasts and mechanism of cardiac fibrosis. *J. Cell. Physiol.* 225 (3), 631–637. doi:10.1002/jcp.22322

Kuo, Y.-L., Jou, I. M., Jeng, S.-F., Chu, C.-H., Huang, J.-S., Hsu, T.-I., et al. (2019). Hypoxia-induced epithelial-mesenchymal transition and fibrosis for the development of breast capsular contracture. *Sci. Rep.* 9 (1), 10269. doi:10.1038/s41598-019-46439-7

Lam, R. H. W., Weng, S., Lu, W., and Fu, J. (2012). Live-cell subcellular measurement of cell stiffness using a microengineered stretchable micropost array membrane. *Integr. Biol.* 4 (10), 1289–1298. doi:10.1039/c2ib20134h

Leach, H. G., Chrobak, I., Han, R., and Trojanowska, M. (2013). Endothelial cells recruit macrophages and contribute to a fibrotic milieu in bleomycin lung injury. *Am. J. Respir. Cell. Mol. Biol.* 49 (6), 1093–1101. doi:10.1165/rcmb.2013-0152oc

Leask, A. (2015). Getting to the heart of the matter: New insights into cardiac fibrosis. *Circulation Res.* 116, 1269–1276. doi:10.1161/CIRCRESAHA.116.305381

LeCun, Y., Bengio, Y., and Hinton, G. (2015). Deep learning. *Nature* 521 (7553), 436–444. doi:10.1038/nature14539

Lee, E. K., Kurokawa, Y. K., Tu, R., George, S. C., and Khine, M. (2015). Machine learning plus optical flow: A simple and sensitive method to detect cardioactive drugs. *Sci. Rep.* 5 (1), 11817–11912. doi:10.1038/srep11817

Lee, E. K., Tran, D. D., Keung, W., Chan, P., Wong, G., Chan, C. W., et al. (2017). Machine learning of human pluripotent stem cell-derived engineered cardiac tissue contractility for automated drug classification. *Stem Cell. Rep.* 9 (5), 1560–1572. doi:10.1016/j.stemcr.2017.09.008

Lee, H., Kim, S-j., Shin, H., and Kim, Y-P. (2020). Collagen-immobilized extracellular FRET reporter for visualizing protease activity secreted by living cells. *ACS Sens.* 5 (3), 655–664. doi:10.1021/acssensors.9b01456

Lee, H-M., Yu, M-S., Kazmi, S. R., Oh, S. Y., Rhee, K-H., Bae, M., et al. (2019). Computational determination of hERG-related cardiotoxicity of drug candidates. *BMC Bioinforma.* 20 (10), 250–273. doi:10.1186/s12859-019-2814-5

Lee, M-O., Jung, K. B., Jo, S-J., Hyun, S-A., Moon, K-S., Seo, J-W., et al. (2019). Modelling cardiac fibrosis using three-dimensional cardiac microtissues derived from human embryonic stem cells. *J. Biol. Eng.* 13 (1), 15. doi:10.1186/s13036-019-0139-6

Lek, M., Karczewski, K. J., Minikel, E. V., Samocha, K. E., Banks, E., Fennell, T., et al. (2016). Analysis of protein-coding genetic variation in 60, 706 humans. *Nature* 536 (7616), 285–291. doi:10.1038/nature19057

Limpitikul, W. B., Dick, I. E., Tester, D. J., Boczek, N. J., Limphong, P., Yang, W., et al. (2017). A precision medicine approach to the rescue of function on malignant calmodulinopathic long-QT syndrome. *Circ. Res.* 120 (1), 39–48. doi:10.1161/circresaha.116.309283

Liu, L., He, F., Yu, Y., and Wang, Y. (2020). Application of FRET biosensors in mechanobiology and mechanopharmacological screening. *Front. Bioeng. Biotechnol.* 8, 595497. doi:10.3389/fbioe.2020.595497

Marquez, R. T., and McCaffrey, A. P. (2008). Advances in microRNAs: Implications for gene therapists. *Hum. Gene Ther.* 19 (1), 27–38. doi:10.1089/hum.2007.147

Mastikhina, O., Moon, B-U., Williams, K., Hatkar, R., Gustafson, D., Mourad, O., et al. (2020). Human cardiac fibrosis-on-a-chip model recapitulates disease

hallmarks and can serve as a platform for drug testing. *Biomaterials* 233, 119741. doi:10.1016/j.biomaterials.2019.119741

Matera, D. L., DiLillo, K. M., Smith, M. R., Davidson, C. D., Parikh, R., Said, M., et al. (2020). Microengineered 3D pulmonary interstitial mimetics highlight a critical role for matrix degradation in myofibroblast differentiation. *Sci. Adv.* 6 (37), eabb5069. doi:10.1126/sciadv.abb5069

McVicker, B. L., and Bennett, R. G. (2017). Novel anti-fibrotic therapies. *Front. Pharmacol.* 8, 318. doi:10.3389/fphar.2017.00318

Mejías, J. C., Nelson, M. R., Liseth, O., and Roy, K. (2020). A 96-well format microvascularized human lung-on-a-chip platform for microphysiological modeling of fibrotic diseases. *Lab. Chip* 20 (19), 3601–3611. doi:10.1039/d0lc00644k

Meng, X-m., Nikolic-Paterson, D. J., and Lan, H. Y. (2016). TGF-B: The master regulator of fibrosis. *Nat. Rev. Nephrol.* 12 (6), 325–338. doi:10.1038/nrneph.2016.48

Merkert, S., Bednarski, C., Gohring, G., Cathomen, T., and Martin, U. (2017). Generation of a gene-corrected isogenic control iPSC line from cystic fibrosis patient-specific iPSCs homozygous for p.Phe508del mutation mediated by TALENs and ssODN. *Stem Cell. Res.* 23, 95–97. doi:10.1016/j.scr.2017.07.010

Mok, S., Al Habyan, S., Ledoux, C., Lee, W., MacDonald, K. N., McCaffrey, L., et al. (2020). Mapping cellular-scale internal mechanics in 3D tissues with thermally responsive hydrogel probes. *Nat. Commun.* 11 (1), 4757. doi:10.1038/s41467-020-18469-7

Murphy, A. M., Wong, A. L., and Bezuhly, M. (2015). Modulation of angiotensin II signaling in the prevention of fibrosis. *Fibrogenes. Tissue Repair* 8 (1), 7. doi:10.1186/s13069-015-0023-z

Oakley, F., Gee, L. M., Sheerin, N. S., and Borthwick, L. A. (2019). Implementation of pre-clinical methodologies to study fibrosis and test anti-fibrotic therapy. *Curr. Opin. Pharmacol.* 49, 95–101. doi:10.1016/j.coph.2019.10.004

Ouyang, M., Huang, H., Shaner, N. C., Remacle, A. G., Shiryaev, S. A., Strongin, A. Y., et al. (2010). Simultaneous visualization of protumorigenic Src and MT1-MMP activities with fluorescence resonance energy transfer. *Cancer Res.* 70 (6), 2204–2212. doi:10.1158/0008-5472.can-09-3698

Ouyang, M., Lu, S., Li, X-Y., Xu, J., Seong, J., Giepmans, B. N. G., et al. (2008). Visualization of polarized membrane type 1 matrix metalloproteinase activity in live cells by fluorescence resonance energy transfer imaging. *J. Biol. Chem.* 283 (25), 17740–17748. doi:10.1074/jbc.m709872200

Pingitore, P., Sasidharan, K., Ekstrand, M., Prill, S., Lindén, D., and Romeo, S. (2019). Human multilineage 3D spheroids as a model of liver steatosis and fibrosis. *Int. J. Mol. Sci.* 20 (7), 1629. doi:10.3390/ijms20071629

Ramanathan, C., Jia, P., Ghanem, R., Ryu, K., and Rudy, Y. (2006). Activation and repolarization of the normal human heart under complete physiological conditions. *Proc. Natl. Acad. Sci. U. S. A.* 103 (16), 6309–6314. doi:10.1073/pnas.0601533103

Rosenbloom, J., Mendoza, F. A., and Jimenez, S. A. (2013). Strategies for anti-fibrotic therapies. *Biochimica Biophysica Acta (BBA) - Mol. Basis Dis.* 1832 (7), 1088–1103. doi:10.1016/j.bbadis.2012.12.007

Roth Gregory, A., Mensah George, A., Johnson Catherine, O., Addolorato, G., Ammirati, E., Baddour Larry, M., et al. (2020). Global burden of cardiovascular diseases and risk factors, 1990-2019: Update from the GBD 2019 study. *J. Am. Coll. Cardiol.* 76 (25), 2982–3021. doi:10.1016/j.jacc.2020.11.010

Rouillard, A. D., and Holmes, J. W. (2012). Mechanical regulation of fibroblast migration and collagen remodelling in healing myocardial infarcts. *J. Physiology* 590 (18), 4585–4602. doi:10.1113/jphysiol.2012.229484

Sadeghi, A. H., Shin, S. R., Deddens, J. C., Fratta, G., Mandla, S., Yazdi, I. K., et al. (2017). Engineered 3D cardiac fibrotic tissue to study fibrotic remodeling. *Adv. Healthc. Mat.* 6 (11), 1601434. doi:10.1002/adhm.201601434

Saito, T., Kotani, T., and Suzuki, K. (2020). Antifibrotic therapy by sustained release of low molecular weight heparin from poly(lactic-co-glycolic acid) microparticles on bleomycin-induced pulmonary fibrosis in mice. *Sci. Rep.* 10 (1), 19019. doi:10.1038/s41598-020-76034-0

Samuel, C. S., Royce, S. G., Hewitson, T. D., Denton, K. M., Cooney, T. E., and Bennett, R. G. (2017). Anti-fibrotic actions of relaxin. *Br. J. Pharmacol.* 174 (10), 962–976. doi:10.1111/bph.13529

Sanguinetti, M. C., and Tristani-Firouzi, M. (2006). hERG potassium channels and cardiac arrhythmia. *Nature* 440 (7083), 463–469. doi:10.1038/nature04710

Santos, A., and Lagares, D. (2018). Matrix stiffness: The conductor of organ fibrosis. *Curr. Rheumatol. Rep.* 20 (1), 2. doi:10.1007/s11926-018-0710-z

Schwank, G., Koo, B-K., Sasselli, V., Dekkers Johanna, F., Heo, I., Demircan, T., et al. (2013). Functional repair of CFTR by CRISPR/Cas9 in intestinal stem cell organoids of cystic fibrosis patients. *Cell. Stem Cell.* 13 (6), 653–658. doi:10.1016/j.stem.2013.11.002

Senavirathna, L. K., Huang, C., Yang, X., Munteanu, M. C., Sathiaseelan, R., Xu, D., et al. (2018). Hypoxia induces pulmonary fibroblast proliferation through NFAT signaling. *Sci. Rep.* 8 (1), 2709. doi:10.1038/s41598-018-21073-x

Sewanan, L. R., Schwan, J., Kluger, J., Park, J., Jacoby, D. L., Qyang, Y., et al. (2019). Extracellular matrix from hypertrophic myocardium provokes impaired twitch dynamics in healthy cardiomyocytes. *JACC Basic Transl. Sci.* 4 (4), 495–505. doi:10.1016/j.jacbts.2019.03.004

Sgalla, G., Iovene, B., Calvello, M., Ori, M., Varone, F., and Richeldi, L. (2018). Idiopathic pulmonary fibrosis: Pathogenesis and management. *Respir. Res.* 19 (1), 32–18. doi:10.1186/s12931-018-0730-2

Shik Mun, K., Arora, K., Huang, Y., Yang, F., Yarlagadda, S., Ramananda, Y., et al. (2019). Patient-derived pancreas-on-a-chip to model cystic fibrosis-related disorders. *Nat. Commun.* 10 (1), 3124. doi:10.1038/s41467-019-11178-w

Shin, Y. J., Shafranek, R. T., Tsui, J. H., Walcott, J., Nelson, A., and Kim, D-H. (2021). 3D bioprinting of mechanically tuned bioinks derived from cardiac decellularized extracellular matrix. *Acta Biomater.* 119, 75–88. doi:10.1016/j.actbio.2020.11.006

Shrestha, A., and Mahmood, A. (2019). Review of deep learning algorithms and architectures. *IEEE Access* 7, 53040–53065. doi:10.1109/access.2019.2912200

Strikoudis, A., Cieślak, A., Loffredo, L., Chen, Y-W., Patel, N., Saqi, A., et al. (2019). Modeling of fibrotic lung disease using 3D organoids derived from human pluripotent stem cells. *Cell. Rep.* 27 (12), 3709–3723.e5. e5. doi:10.1016/j.celrep.2019.05.077

Sturgeon, C. M., Ditadi, A., Awong, G., Kennedy, M., and Keller, G. (2014). Wnt signaling controls the specification of definitive and primitive hematopoiesis from human pluripotent stem cells. *Nat. Biotechnol.* 32 (6), 554–561. doi:10.1038/nbt.2915

Sugiyama, M. (2015). *Statistical reinforcement learning: Modern machine learning approaches*. Florida, United States: CRC Press.

Svystonyuk, D. A., Ngu, J. M., Mewhort, H. E., et al. (2015). Fibroblast growth factor-2 regulates human cardiac myofibroblast-mediated extracellular matrix remodeling. *J. Transl. Med.* 13 (147), 1–11. doi:10.1186/s12967-015-0510-4

Sziksz, E., Pap, D., Lippai, R., Béres, N. J., Fekete, A., Szabó, A. J., et al. (2015). Fibrosis related inflammatory mediators: Role of the IL-10 cytokine family. *Mediat. Inflamm.* 2015, 764641–764715. doi:10.1155/2015/764641

Tampe, D., and Zeisberg, M. (2014). Potential approaches to reverse or repair renal fibrosis. *Nat. Rev. Nephrol.* 10 (4), 226–237. doi:10.1038/nrneph.2014.14

Thompson, S. A., Copeland, C. R., Reich, D. H., and Tung, L. (2011). Mechanical coupling between myofibroblasts and cardiomyocytes slows electric conduction in fibrotic cell monolayers. *Circulation* 123 (19), 2083–2093. doi:10.1161/circulationaha.110.015057

Tissue-engineered disease models. *Nat. Biomed. Eng.* 2018 2 (12):879–880. doi:10.1038/s41551-018-0339-2

Ulmer, B. M., and Eschenhagen, T. (2020). Human pluripotent stem cell-derived cardiomyocytes for studying energy metabolism. *Biochimica Biophysica Acta (BBA) - Mol. Cell. Res.* 1867 (3), 118471. doi:10.1016/j.bbamcr.2019.04.001

Usama, M., Qadir, J., Raza, A., Arif, H., Yau, K-L. A., Elkhatib, Y., et al. (2019). Unsupervised machine learning for networking: Techniques, applications and research challenges. *IEEE access* 7, 65579–65615. doi:10.1109/access.2019.2916648

Usunier, B., Benderitter, M., Tamarat, R., and Chapel, A. (2014). Management of fibrosis: The mesenchymal stromal cells breakthrough. *Stem Cells Int.* 2014, 1–26. doi:10.1155/2014/340257

Valley, H. C., Bukis, K. M., Bell, A., Cheng, Y., Wong, E., Jordan, N. J., et al. (2019). Isogenic cell models of cystic fibrosis-causing variants in natively expressing pulmonary epithelial cells. *J. Cyst. Fibros.* 18 (4), 476–483. doi:10.1016/j.jcf.2018.12.001

Vamathevan, J., Clark, D., Czodrowski, P., Dunham, I., Ferran, E., Lee, G., et al. (2019). Applications of machine learning in drug discovery and development. *Nat. Rev. Drug Discov.* 18 (6), 463–477. doi:10.1038/s41573-019-0024-5

Varkey, M., Ding, J., and Tredget, E. E. (2013). Fibrotic remodeling of tissue-engineered skin with deep dermal fibroblasts is reduced by keratinocytes. *Tissue Eng. Part A* 20 (3-4), 716–727. doi:10.1089/ten.tea.2013.0434

Vig, K., Chaudhari, A., Tripathi, S., Dixit, S., Sahu, R., Pillai, S., et al. (2017). Advances in skin regeneration using tissue engineering. *Int. J. Mol. Sci.* 18 (4), 789. doi:10.3390/ijms18040789

Wang, E. Y., Kuzmanov, U., Smith, J. B., Dou, W., Rafatian, N., Lai, B. F. L., et al. (2021). An organ-on-a-chip model for pre-clinical drug evaluation in progressive non-genetic cardiomyopathy. *J. Mol. Cell. Cardiol.* 160, 97–110. doi:10.1016/j.yjmcc.2021.06.012

Wang, E. Y., Rafatian, N., Zhao, Y., Lee, A., Lai, B. F. L., Lu, R. X., et al. (2019). Biowire model of interstitial and focal cardiac fibrosis. *ACS Cent. Sci.* 5 (7), 1146–1158. doi:10.1021/acscentsci.9b00052

Wang, E. Y., Smith, J., and Radisic, M. (2022). "Design and fabrication of biological WiresBiological wires for cardiac FibrosisFibrosis disease modeling," in *Cardiac tissue engineering: Methods and protocols*. Editors K. L. K. Coulombe and L. D. BlackIii (New York, NY: Springer US), 175–190.

Wang, S., Shi, K., Lu, J., Sun, W., Han, Q., Che, L., et al. (2021). Microsphere-embedded hydrogel sustained-release system to inhibit postoperative epidural fibrosis. *ACS Appl. Bio Mat.* 4 (6), 5122–5131. doi:10.1021/acsabm.1c00347

Wang, Y., Liang, P., Lan, F., Wu, H., Lisowski, L., Gu, M., et al. (2014). Genome editing of isogenic human induced pluripotent stem cells recapitulates long QT phenotype for drug testing. *J. Am. Coll. Cardiol.* 64 (5), 451–459. doi:10.1016/j.jacc.2014.04.057

Wells, R. G. (2013). Tissue mechanics and fibrosis. *Biochimica Biophysica Acta (BBA) - Mol. Basis Dis.* 1832 (7), 884–890. doi:10.1016/j.bbadis.2013.02.007

Wörsdörfer, P., Takashi, I., Asahina, I., Sumita, Y., and Ergün, S. (2020). Do not keep it simple: Recent advances in the generation of complex organoids. *J. Neural Transm.* 127 (11), 1569–1577. doi:10.1007/s00702-020-02198-8

Wu, D., Gao, W., Li, X., Tian, C., Jiao, N., Fang, S., et al. (2020). Dr AFC: Drug repositioning through anti-fibrosis characteristic. *Brief. Bioinform.* 22 (3), bbaa115. doi:10.1093/bib/bbaa115

Wynn, T. A. (2004). Fibrotic disease and the TH1/TH2 paradigm. *Nat. Rev. Immunol.* 4 (8), 583–594. doi:10.1038/nri1412

Wynn, T. A., and Ramalingam, T. R. (2012). Mechanisms of fibrosis: Therapeutic translation for fibrotic disease. *Nat. Med.* 18 (7), 1028–1040. doi:10.1038/nm.2807

Wynn, T. A., and Vannella, K. M. (2016). Macrophages in tissue repair, regeneration, and fibrosis. *Immunity* 44 (3), 450–462. doi:10.1016/j.immuni.2016.02.015

Yang, X., Meng, Y., Han, Z., Ye, F., Wei, L., and Zong, C. (2020). Mesenchymal stem cell therapy for liver disease: Full of chances and challenges. *Cell. Biosci.* 10 (1), 123. doi:10.1186/s13578-020-00480-6

Yazdani, S., Bansal, R., and Prakash, J. (2017). Drug targeting to myofibroblasts: Implications for fibrosis and cancer. *Adv. Drug Deliv. Rev.* 121, 101–116. doi:10.1016/j.addr.2017.07.010

Yegnanarayana, B. (2009). *Artificial neural networks*. Patparganj Industrial Area, New Delhi,: PHI Learning Pvt. Ltd.

Yuan, Y., Li, M., To, C. H., Lam, T. C., Wang, P., Yu, Y., et al. (2018). The role of the RhoA/ROCK signaling pathway in mechanical strain-induced scleral myofibroblast differentiation. *Invest. Ophthalmol. Vis. Sci.* 59 (8), 3619–3629. doi:10.1167/iovs.17-23580

Zhang, B., Korolj, A., Lai, B. F. L., and Radisic, M. (2018). Advances in organ-on-a-chip engineering. *Nat. Rev. Mat.* 3 (8), 257–278. doi:10.1038/s41578-018-0034-7

Zhang, B., Lai, B. F. L., Xie, R., Davenport Huyer, L., Montgomery, M., and Radisic, M. (2018). Microfabrication of AngioChip, a biodegradable polymer scaffold with microfluidic vasculature. *Nat. Protoc.* 13 (8), 1793–1813. doi:10.1038/s41596-018-0015-8

Zhang, H., Tian, L., Shen, M., Tu, C., Wu, H., Gu, M., et al. (2019). Generation of quiescent cardiac fibroblasts from human induced pluripotent stem cells for *in vitro* modeling of cardiac fibrosis. *Circ. Res.* 125 (5), 552–566. doi:10.1161/circresaha.119.315491

Zhang, M., and Zhang, S. T. (2020). T cells in fibrosis and fibrotic diseases. *Front. Immunol.* 11, 1142. doi:10.3389/fimmu.2020.01142

Zhang, R., Pan, Y., Fanelli, V., Wu, S., Luo, A. A., Islam, D., et al. (2015). Mechanical stress and the induction of lung fibrosis via the midkine signaling pathway. *Am. J. Respir. Crit. Care Med.* 192 (3), 315–323. doi:10.1164/rccm.201412-2326oc

Zhang, W., Elimban, V., Nijjar, M. S., Gupta, S. K., and Dhalla, N. S. (2003). Role of mitogen-activated protein kinase in cardiac hypertrophy and heart failure. *Exp. Clin. Cardiol.* 8 (4), 173–183.

Zhang, Y-Y., Yu, Y., and Yu, C. (2019). Antifibrotic roles of RAAS blockers: Update. *Adv. Exp. Med. Biol.* 1165, 671–691. doi:10.1007/978-981-13-8871-2_33

Zhao, Y., Kankala, R. K., Wang, S-B., and Chen, A-Z. (2019). Multi-Organs-on-Chips: Towards long-term biomedical investigations. *Molecules* 24 (4), 675. doi:10.3390/molecules24040675

Zhao, Y., Rafatian, N., Feric, N. T., Cox, B. J., Aschar-Sobbi, R., Wang, E. Y., et al. (2019). A platform for generation of chamber-specific cardiac tissues and disease modeling. *Cell.* 176 (4), 913–927.e18. e18. doi:10.1016/j.cell.2018.11.042

Zimmermann, O., Homann, J. M., Bangert, A., Müller, A-M., Hristov, G., Goeser, S., et al. (2012). Successful use of mRNA-nucleofection for overexpression of interleukin-10 in murine monocytes/macrophages for anti-inflammatory therapy in a murine model of autoimmune myocarditis. *J. Am. Heart Assoc.* 1 (6), e003293–e. doi:10.1161/jaha.112.003293

Cooperation between myofibril growth and costamere maturation in human cardiomyocytes

Huaiyu Shi[1,2], Chenyan Wang[1,2], Bruce Z. Gao[3], James H. Henderson[1,2] and Zhen Ma[1,2]*

[1]Department of Biomedical & Chemical Engineering, Syracuse University, Syracuse, NY, United States, [2]BioInspired Institute for Materials and Living Systems, Syracuse University, Syracuse, NY, United States, [3]Department of Bioengineering, Clemson University, Clemson, SC, United States

Costameres, as striated muscle-specific cell adhesions, anchor both M-lines and Z-lines of the sarcomeres to the extracellular matrix. Previous studies have demonstrated that costameres intimately participate in the initial assembly of myofibrils. However, how costamere maturation cooperates with myofibril growth is still underexplored. In this work, we analyzed zyxin (costameres), α-actinin (Z-lines) and myomesin (M-lines) to track the behaviors of costameres and myofibrils within the cardiomyocytes derived from human induced pluripotent stem cells (hiPSC-CMs). We quantified the assembly and maturation of costameres associated with the process of myofibril growth within the hiPSC-CMs in a time-dependent manner. We found that asynchrony existed not only between the maturation of myofibrils and costameres, but also between the formation of Z-costameres and M-costameres that associated with different structural components of the sarcomeres. This study helps us gain more understanding of how costameres assemble and incorporate into the cardiomyocyte sarcomeres, which sheds a light on cardiomyocyte mechanobiology.

1 Introduction

Functioning as the mediators of cell-extracellular matrix (ECM) interactions, focal adhesions are responsible for sensing and transducing extracellular signals to regulate cell behaviors and functions (González-García et al., 2010; Seo et al., 2013; Yip et al., 2018; Natale et al., 2019; Fedele et al., 2020). Cardiomyocytes exhibit two distinct focal adhesion structures: periphery focal adhesions (pFAs) close to the cell perimeter, which are laterally parallel along the myofibrils; and costameres registered with sarcomeres, which are transverse across the myofibrils. Costameres, as striated muscle-specific cell adhesion structures, were first described as vinculin-containing structures located between the sarcolemma and myofibrils (Pardo et al., 1983). Except for vinculin, costameres have been
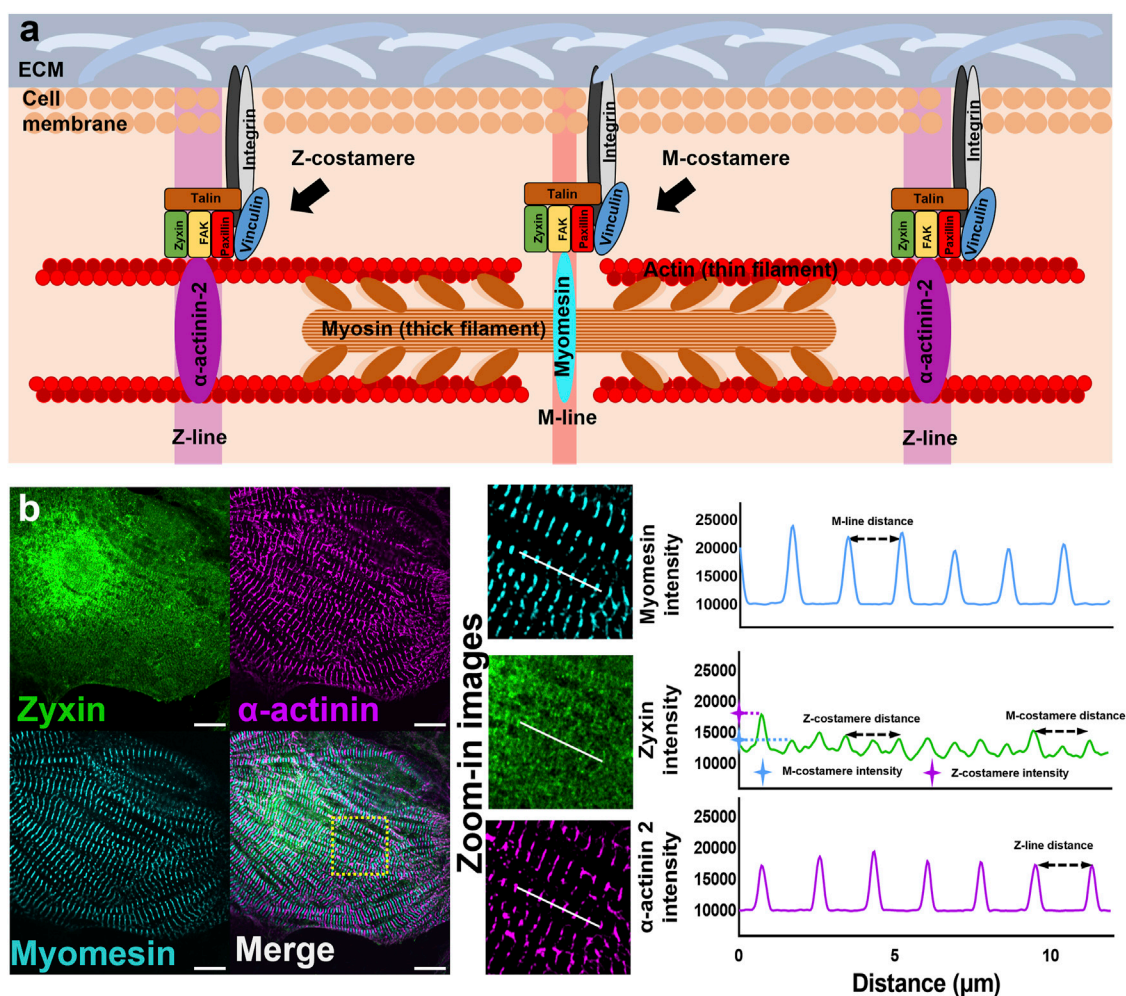
FIGURE 1
Myofibrils and costameres in cardiomyocytes **(A)** Schematics showing the components of sarcomeres and costameres in cardiomyocytes. **(B)** Fluorescent images of Z-lines (α-actinin), M-lines (myomesin), and costameres (zyxin). Intensity profiles to demonstrate the measurement of Z/M-line distance, Z/M-costamere distance, and Z/M-costamere intensity. Scale bar: 10 μm.

proved to share similar components with pFAs (e.g., integrins (McDonald et al., 1995), FAK (Kovačič-Milivojević et al., 2001), and talin (Belkin et al., 1986)). This multiprotein architecture serves as the linkages between sarcomeres and ECMs, thus regulates the contractile functions of muscular tissues (Lyon et al., 2015). Previous studies have shown that muscle atrophy resulting from the reduction in mechano-loading might be accompanied by decreased expression of costamere components (Li et al., 2013; Ruoss et al., 2018; Gorza et al., 2021). In addition, costamere formation is also affected by the mechanical properties of ECM (Galie et al., 2013). These studies indicated that costameres are highly regulated by the extracellular mechanical microenvironment, and responsible for transducing contractile force from myofibrils to ECMs. Despite extensive studies focusing on focal adhesions in general, behaviors of

costameres are less investigated, leaving unanswered questions of how costameres interact with myofibrils to mediate cardiomyocyte contraction.

Myofibrils make up the contractile machinery of individual cardiomyocytes consisting of serially arranged sarcomeres comprising thick filaments (myosin and associated proteins), thin filaments (actin and associated proteins), and Z-discs (α-actinin). Myofibrillogenesis was proposed to occur *via* a three-step process: pre-myofibrils to nascent myofibrils to mature myofibrils (Sanger et al., 2006; Sanger et al., 2010; Sanger et al., 2017). Pre-myofibrils are composed of mini-sarcomeres that are bordered by Z-bodies containing muscle α-actinin. The bipolar arrangement of the actin filaments in the mini-sarcomeres are held together by bipolar non-muscle myosin II filaments. Nascent myofibrils are formed by adding titin

molecules and overlapping thick muscle myosin filaments to the former pre-myofibrils. The mature myofibrils result from the elimination of non-muscle myosin II, the alignment and fusion of several Z-bodies to form Z-bands, and the alignment of muscle myosin II filaments to form A-bands. Furthermore, late assembling proteins are added to form the mature myofibrils: telethonin, a titin binding protein in the Z-bands; muscle myosin II binding C protein in the cross-bridge regions of the A-bands; the incorporation of myomesin into the middle of the A-bands to form M-bands.

During this process, the costameres provide anchors for the initial recruitment and stability of the sarcomeres (Myhre and Pilgrim, 2012). Particularly, costameres are registered with the Z-discs (Z-costameres) and the central M-line of the A-band (M-costameres), showing a striated rib-like pattern upon becoming mature costameres (also called costamere maturation) (Figure 1A) (di Mauro et al., 2009). However, the process of costamerogenesis and particularly how costameres assemble and mature into the striated pattern is poorly studied. Early work found complete devastation of mature costamere structures associated with a decreased proportion of mature myofibrils in FAK-inhibited cardiomyocytes, which led to a hypothesized model discussing the interdependence between costamerogenesis and myofibrillogenesis (Quach and Rando, 2006). This theory was reinforced by a recent investigation in which the cardiomyocyte contractile force was impaired in a vinculin knockout cell line and myofibril-flawed cell lines. Neither mature costameres nor organized myofibrils were found in these contraction-deficient cells (Chopra et al., 2018). These studies elucidated that the formation of costameres was driven by the contractile force, which in return played a critical role in maintaining the contractions of cardiomyocytes. Most of these early studies on costamere biology focused on the Z-costameres, while biological role and behaviors of M-costameres are much less investigated (Porter et al., 1992; Hresko et al., 1994; Anastasi et al., 2003). More importantly, how M-costameres and Z-costameres assemble and incorporate in the sarcomeres during costamerogenesis remains unclear.

In this study, we utilized human-induced pluripotent stem cell-derived cardiomyocytes (hiPSC-CMs) to study the assembly and maturation of costameres during cell attachment and spreading. Compared to adult cardiomyocytes containing mature myofibrils and costameres in both peripheral area and center area of the cells, hiPSC-CMs provide a developmental framework to investigate the process from de-novo assembly to maturation of costameres and myofibrils in vitro. Herein, we focus on the maturation of myofibril-costamere cytoarchitecture into striated patterns, instead of the maturation of stem cell-derived embryonic-like cardiomyocytes into adult-like phenotypes. To understand how costameres were assembled and incorporated with the sarcomeres, we characterized the behavior of costameres and myofibrils during the initial stage of cell attachment from Hour four to Hour eight post-hiPSC-

CMs seeding. To examine the maturation process of costameres and myofibrils, we characterized the behavior of costamere and myofibril during the later stage of cell spreading at Hour 8, Hour 12, Hour 24, and Hour 48 post-hiPSC-CMs seeding.

Zyxin was used to track the distribution of costameres within hiPSC-CMs. Z-costameres and M-costameres were distinguished by the colocalization with sarcomere α-actinin (Z-line protein) and myomesin (M-line protein) respectively. By temporal sampling the hiPSC-CMs after cell seeding, we quantified the activities of Z-costameres and M-costameres from de-novo assembly to the maturation during costamerogenesis. We also tracked the behavior of M-lines and Z-lines to profile the coordination between myofibrillogenesis and costamerogenesis. We found that the de-novo assembly of M-costamere and Z-costamere proceeded simultaneously while the maturation of Z-costameres and M-costameres were asynchronous. Moreover, we grew hiPSC-CMs on stiffness-tunable polyacrylamide hydrogel to investigate how costamere formation could be affected by the substrate mechanical properties. This study provides detailed evidence to fill in the knowledge gap of how costameres interact with myofibrils to maintain the contractile functions of cardiomyocytes, which should enable future progress in understanding the process of cardiomyocyte mechanobiology in vitro.

2 Method and materials

2.1 hiPSC-CMs differentiation and purification

hiPSC-CMs were differentiated from mEGFP-tagged ACTN2 WTC hiPSC line edited with CRISPR/Cas9 technology (Coriell Institute, Ca# AICS-0075-085), which have fluorescent reporter on sarcomere α-actinin under 488 nm excitation in the differentiated hiPSC-CMs. The hiPSCs were cultured in Essential 8 (E8) media (Thermo Fisher Scientific, Ca# A1517001) with media refreshment every 24 h on 6-well plates pre-coated with Geltrex (Thermo Fisher Scientific, Ca# A1413302). The cell passaging was performed every 3 days at the seeding density of 2.5×10^4 cells/cm^2 in the E8 media supplemented with ROCK inhibitor (10 μM, Y-27632; BioVision, Ca# 1994) for the first 24 h. The differentiation procedures have been detailed in our previous publications (Hoang et al., 2018). Briefly, differentiation was initialized by modulating the WNT pathway using two small molecules, GSK3 inhibitor (6 μM, CHIR99021; Stemgent, Ca# 04-0004) and WNT inhibitor (5 μM, IWP4; Stemgent, Ca# 04-0036) in RPMI 1640 media (Thermo Fisher Scientific, Ca# A1517001) with B27 supplement minus insulin (Thermo Fisher Scientific, Ca# A1895601) (RPMI-B27-I). Then, cells were cultured in RPMI 1640 media with B27 complete supplement

(Thermo Fisher Scientific, Ca# 17504044) (RPMI-B27 + C) until Day 16 for purification procedures. The differentiated hiPSC-CMs were disassociated and replated on Geltrex pre-coated 6-well plates with RPMI-B27 + C media supplemented with ROCK inhibitor. After 2-day recovery in RPMI-B27 + C media, cells were purified in a media of DMEM without glucose (Thermo Fisher Scientific, Ca# 11966-025) supplemented with NEAA (Thermo Fisher Scientific, Ca# 11140050), GlutaMAX (Thermo Fisher Scientific, Ca# 35050061) and 4 mM lactate (Sigma Aldrich, Ca# L7022) for 6 days with media refreshment every 2 days. The purified hiPSC-CMs were maintained in RPMI-B27 + C media refreshed every 2 days.

2.2 Cell seeding and sampling

Differentiated hiPSC-CMs were dissociated from the 6-well plates and seeded on the substrates pre-coated with Geltrex. To investigate the *de-novo* formation of costameres and myofibrils at the initial stage of hiPSC-CMs attachment, we sampled the hiPSC-CMs hourly during Hours 4-8 post cell seeding. To investigate the activities of costameres and myofibrils at the later stage of hiPSC-CMs spreading, we sampled the hiPSC-CMs at Hours 8, 12, 24, and 48 post cell seeding. We then performed immunofluorescence staining on the selected samples for further measurements. To study how costameres and myofibrils would be affected by extracellular mechanical properties, we seeded hiPSC-CMs on the substrates pre-coated by PA hydrogels of varying stiffness (see *Traction force microscopy analysis*). At 48 h, the hiPSC-CMs were transferred to an on-stage incubator and motion videos for traction force microscopy were recorded using a Nikon Eclipse Ti microscope with Zyla 4.2 PLUS sCMOS camera. After the video recording, the hiPSC-CMs were fixed and stained for further measurements on costameres and sarcomeres.

2.3 Immunocytochemistry

Cell samples were fixed in 4% PFA solution for 20 min, permeabilized with 0.2% triton solution for 5 min, and blocked with 2% bovine serum albumin (BSA; Sigma Aldrich, Ca# A8022) for 30 min. The fixed samples were then incubated in primary antibody solution (Supplementary Table S1) for 2 h, washed with PBS three times, and incubated with secondary antibodies for 2 h. After three times of PBS washing, the cell samples were ready to image. The bright-field and epifluorescence microscopy was performed on a Nikon Eclipse Ti microscope with Zyla 4.2 PLUS sCMOS camera. The confocal microscopy was performed on a Zeiss LSM 980 with Airyscan two confocal microscope.

2.4 Quantification of costamere and myofibril properties

To analyze the myofibril structure, the M-line component myomesin and Z-line component α-actinin were stained and imaged using the confocal microscope. For the myofibril characterizations, the distance between two adjacent Z-lines (Z-line distance) and Z-line density were quantified to examine the Z-disc assembly. The distance between two adjacent M-lines and M-line density were quantified to examine the M-band assembly. The Z-line length and M-line length were measured to examine the maturation of myofibrils. M-line distance, Z-line distance, Z-line length, M-line length, Z-line number and M-line number were characterized using a Matlab-based software (Morris et al., 2020). Cell area was measured using Fiji ImageJ. Z-line density and M-line density were calculated as follows:

$$Z - line\ density = \frac{M - line\ number\ (count)}{Cell\ area\ (\mu m^2)}$$

$$M - line\ density = \frac{M - line\ number\ (count)}{Cell\ area\ (\mu m^2)}$$

The analysis of costameres was performed using the fluorescent images of costamere component zyxin. Fiji ImageJ was used to plot the intensity profile of costameres and myofibrils. Based on the intensity profiles, Z-costameres were identified by the colocalization of costamere peaks with actinin peaks, while the M-costameres were identified by the co-localization of costamere peaks with myomesin peaks (Figure 1B). To characterize the assembly of costameres, the distances between two adjacent Z/M-costameres were characterized by the distance between two fluorescent peaks from the intensity profiles of Z/M costameres. To characterize the maturation of costameres, the intensity of costameres was characterized by the amplitude of the fluorescent peak and then normalized by the intensity value of fluorescent background from the regions without cells or debris.

2.5 Traction force microscopy analysis

To analyze how costameres respond to different substrates stiffnesses, the hiPSC-CMs were cultured on polyacrylamide (PA) hydrogels with stiffness of 10 kPa and 40 kPa (Tse and Engler, 2010; Simmons et al., 2013). The fabrication of PA hydrogel followed a standard protocol (Ribeiro et al., 2016), starting at the preparation of prepolymer solution, made of acrylamide (BIO-RAD Ca# 1610140), bis-acrylamide (BIO-RAD Ca# 1610142), 35 mM HEPES buffer (SIGMA Ca# 7365-45-9), 0.1% w/v ammonium persulfate (BIO-RAD Ca# 1610700), 0.1% v/v N′-Tetramethylethylenediamine (TEMED, BIO-RAD Ca# 161-0801) and Milli-Q water. The stiffness of the

hydrogels is mediated by altering the concentration of acrylamide (40 kPa, 8%; 10 kPa, 10%) and bisacrylamide (40 kPa, 0.48%; 10 kPa, 0.1%) used in the prepolymer solution (Ribeiro et al., 2015). To enable the measurement of hiPSC-CM force generation, fluorescent microbeads (Thermo Fisher Scientific, Ca# F8805) were incorporated to the prepolymer solution with a final concentration of 6×10^9 microbeads/mL. To create a PA hydrogel with flat surface, 15 ml of prepolymer solution was dripped on a glass slide precoated with fibronectin. A glass coverslip, silane-treated with 0.4% 3-(trimethoxysilyl) propyl methacrylate (SIGMA Ca# 2530-85-0) for 1 h, was gently placed on the top of the prepolymer solution drop. After 15 min polymerization, the hydrogel together with the glass slide was immersed in phosphate-buffered saline (PBS) solution for 1 h to allow the hydration of hydrogel. After the hydration, the PA hydrogel-coated cover glass was gently removed from the glass slide using a razor blade. Before cell seeding, the PA hydrogel was immersed in PBS solution overnight to further rinse out unreacted monomer.

For traction force microscopy, videos containing dispersed fluorescent beads were captured under 330 nm excitation with a frame rate of 18 fps (Supplementary Movie S1). The videos were analyzed using a Matlab-based software to generate the plots of hiPSC-CMs contractile force (Supplementary Movie S2) and contractile energy (SupplementaryMovie S3) (Sergé et al., 2008; Mandal et al., 2014; Kumari et al., 2019; Kumari et al., 2020). These plots were applied to an in-house MATLAB script to calculate the maximum contractile energy, maximum upstroke power, maximum upstroke force (Ma et al., 2018).

2.6 Sarcomere shortening analysis

To investigate how different substrate stiffness could affect the contraction of hiPSC-CMs, the sarcomere shortening was measured by tracking the position of individual Z-lines in a beating video. The videos containing the Z-line movements in live hiPSC-CMs were captured under the excitation of 488 nm excitation with a frame rate of 20 fps (Supplementary Movie S4) and analyzed using a Python 3.6-based algorithm to identify the sarcomere shortening percentile, sarcomere contraction duration, and sarcomere relaxation duration.

2.7 Statistical analysis

One-way ANOVA with Tukey multiple t-test was used to compare the difference among groups. The statistical significance was determined as p-value <0.05 (*), <0.01(**), <0.001 (***) and <0.0001 (****), respectively. For each condition, more than 20 hiPSC-CMs were selected for quantification. In myofibril measurement, all clean Z-line and M-line within individual hiPSC-CMs were measured for each condition. In costamere

analysis, four different locations containing myofibrils were randomly selected in each hiPSC-CM for measurement. Data visualization, including box plots showing the minimum, maximum, median, and 25th and 75th percentiles, was performed by software GraphPad Prism 6.

3 Results

3.1 Assembly of costameres in hiPSC-CMs during cell attachment

We investigated the formation of myofibrils and costameres at the initial stage of cell attachment by sampling hiPSC-CMs hourly from Hour four to Hour eight post cell seeding (Figure 2A). From the confocal fluorescent images of zyxin-actinin-myomesin co-staining, we found that the zyxin pre-costameres colocalized with both pre-myofibrils containing Z-bodies in the peripheral region of hiPSC-CMs and the nascent myofibrils containing striated-like Z-lines but no M-lines. The striated mature costameres only existed in the mature myofibrils containing striated Z-lines and M-lines (Figure 2B). During hiPSC-CMs attachment, Z-bodies aggregated in the peripheral region and close to the mature myofibrils with striated Z- and M-lines at Hour four and Hour 5, when the pre-costameres showed no obvious striated repeating pattern (Supplementary Figure S1). From Hour six to Hour 8, the striated sarcomeric Z-lines and M-lines were colocalized in both the peripheral and center areas of the cells, indicating the maturation of myofibrils. Moreover, during Hours 6–8, the Z-costameres and the M-costameres were assembled to a detectable level, which showed the striated pattern colocalizing with the mature myofibrils (Supplementary Figure S1).

To study the myofibril assembly and growth, we characterized the properties of Z-lines and M-lines of the hiPSC-CMs, including distance, length, and density from fluorescent images of α-actinin and myomesin. Both Z-line density and M-line density had a trend of an increase from Hour 4 to Hour 5, followed by a clear decrease from Hour 5 to Hour 8, with a peak value at Hour 5 (Figures 2C,D). These results indicated a fast *de-novo* assembly of Z-lines and M-lines at Hour 5, which was slowed down during Hours 6–8 due to a rapid increase of cell area (Supplementary Figure S2). We also found that both Z-line distance and M-line distance during Hours 5–8 were significantly longer than at Hour 4, indicating a progressive transition from pre-myofibrils to nascent myofibrils during the initial stage of cell attachment would increase the sarcomere distance (Figures 2E,F). Using Z-line length and M-line length as sarcomere maturity measurement, we found that Z-line length increased significantly during Hours 7-8, while the M-line length increased significantly during Hours 6–8 (Figures 2G,H). These results suggested the growth of Z-lines and M-lines starts immediately after *de-novo* assembly of the sarcomeres.
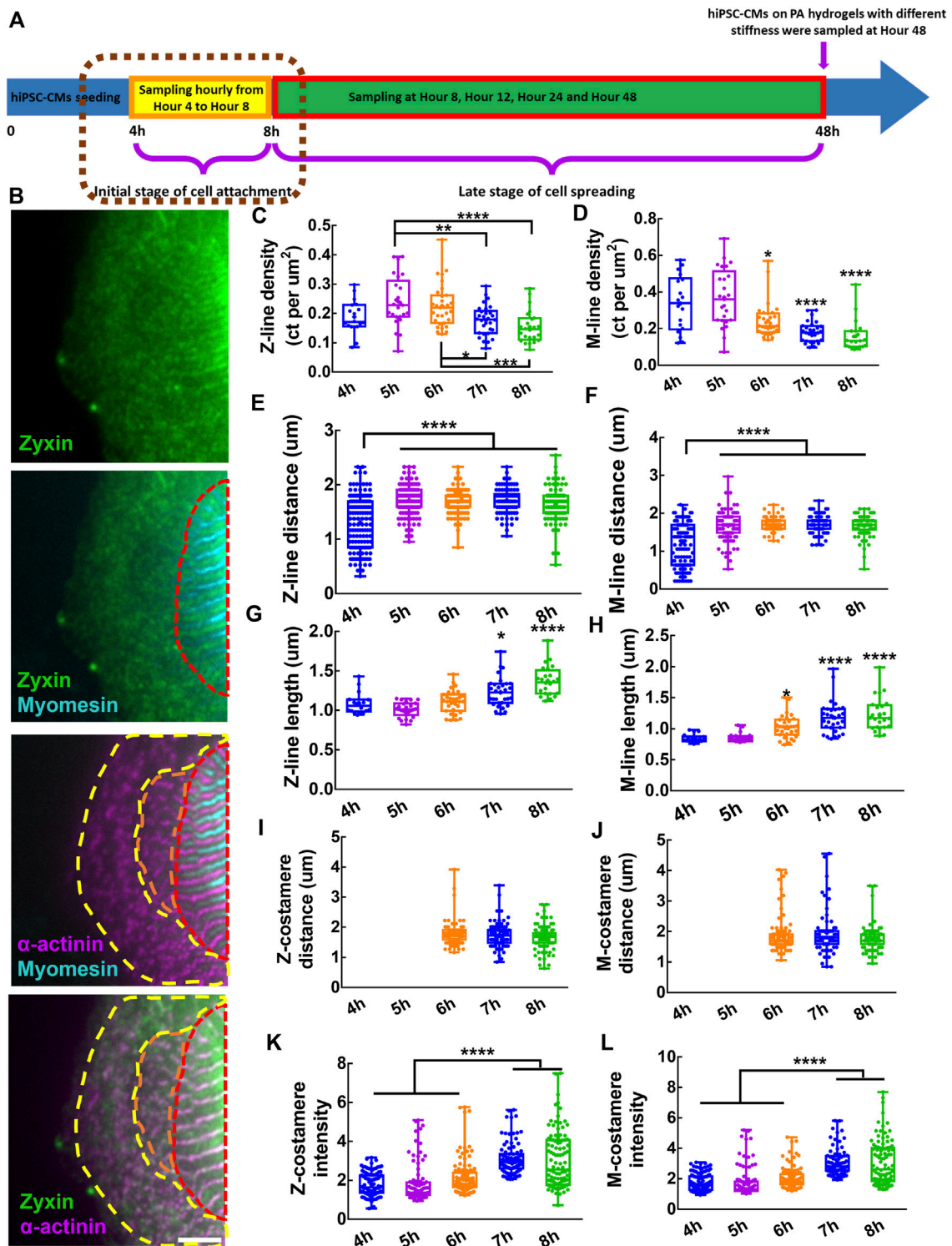
FIGURE 2
Assembly of costameres in hiPSC-CMs during cell attachment. **(A)** Schematics showing the sampling of hiPSC-CMs in the initial stage of cell attachment. **(B)** Fluorescent images of Z-lines, M-lines and costameres. The region containing mature costameres and mature myofibrils is indicated by a red dashed line. Nascent myofibrils with striated-like Z-lines colocalized with pre-costameres are indicated by an orange dashed line. Pre-myofibrils with Z-bodies colocalized with pre-costameres in the cell peripheral region are indicated by a yellow dashed line. Scale bar: 5 µm. To characterize the assembly and growth of myofibrils within hiPSC-CMs during cell attachment, we measured the **(C)** Z-line density, **(D)** M-line density, **(E)** Z-line distance, **(F)** M-line distance, **(G)** Z-line length and **(H)** M-line length. To track the assembly of costameres, we quantified the **(I)** Z-costamere distance **(J)** M-costamere distance **(K)** Z-costamere intensity and **(L)** M-costamere intensity. *$p < 0.05$, **$p < 0.01$, ***$p < 0.001$ and ****$p < 0.0001$.
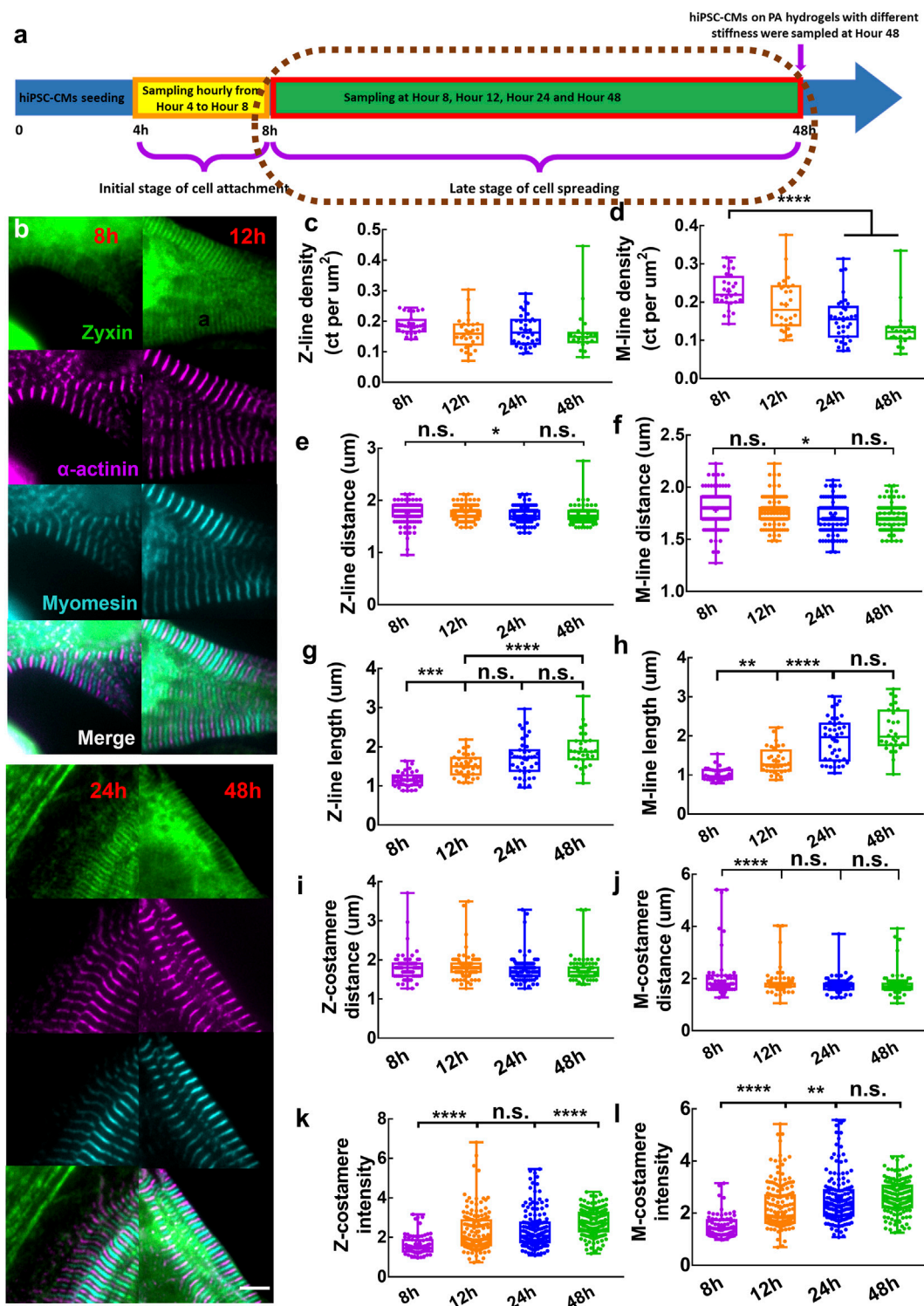
FIGURE 3
(A) Schematics showing sampling of hiPSC-CMs in the late stage of cell spreading. **(B)** Zoom-in images showing mature Z/M-costameres together with mature myofibrils within the hiPSC-CMs. Scale bar: 5 μm. To track the myofibril growth within hiPSC-CMs during cell spreading, we measured the **(C)** Z-line density, **(D)** M-line density, **(E)** Z-line distance, **(F)** M-line distance, **(G)** Z-line length and **(H)** M-line length. To track the costamere growth during cell spreading, we quantified **(I)** Z-costamere distance **(J)** M-costamere distance **(K)** Z-costamere intensity and **(L)** M-costamere intensity. *p <0.05, **p <0.01, ***p <0.001 and ****p <0.0001.

To examine the assembly of Z-costameres and M-costameres, we measured the Z-costamere distance, M-costamere distance, Z-costamere intensity, and M-costamere intensity based on zyxin staining colocalized with α-actinin and myomesin. From the fluorescent images, we only found clear Z-costameres and M-costameres appearing at Hour 6, which was later than the formation of striated myofibrils starting at Hour 4 (Supplementary Figure S1). No significant difference was found in Z-costamere distance and M-costamere distance among different time points (Figures 2I,J). Though the observable costameres occurred at Hour 6, we found that zyxin accumulated to form pre-costameres at the positions of Z-lines and M-lines and that the pre-costameres' fluorescent intensity could be quantified as early as the Hour 4-5 time points. The results showed that the fluorescent intensity of both Z-costameres and M-costameres at Hour 7-8 was significantly higher than the ones at Hour 4–6, indicating that fully assembled costameres had more zyxin components than the *de-novo* clusters of early costameres (Figure 2k,L). From Hour 4 to Hour 8, no significant difference on the zyxin fluorescent intensity was found between Z-costameres and M-costameres (Supplementary Figure S2), suggesting that the zyxin was equally recruited to the Z-costameres and M-costameres during hiPSC-CMs attachment. We also found that there was no significant difference in distance between Z-costameres and Z-lines (Supplementary Figure S2), while the M-line distance was significantly shorter than the M-costamere distance during Hours 6–8 (Supplementary Figure S2). These results suggested that the Z-lines intimately associate with Z-costameres during myofibril growth and maturation, while some M-lines might not be registered to M-costameres in the middle of the myofibrils (Supplementary Figure S2).

3.2 Maturation of costameres during cell spreading

To elucidate how costamerogenesis cooperates with myofibrillogenesis in a later stage of cell spreading, we characterized the temporal behavior of myofibrils and costameres at Hour 8, Hour 12, Hour 24, and Hour 48 post cell seeding (Figure 3A). The myomesin-containing M-lines were in the center of two adjacent actinin-containing Z-lines, showing an alternative striated pattern of the mature myofibrils observed from all the timepoints (Supplementary Figure S3). Z-costameres and M-costameres showed a striated pattern of mature costameres (Figure 3B). We found a progressive increase of cell area, reaching a significant larger area at Hour 48 comparing to Hour 8 (Supplementary Figure S4). By tracking the myofibril growth during cell spreading, we found Z-line density maintained a stable level, indicating a relative fast assembly of Z-lines for myofibril growth to meet the increase of cell area (Figure 3C). In contrast, we found a significant decrease of M-line density from Hour eight to

Hour 48 (Figure 3D), suggesting the M-line assembly was slower than the Z-lines, indicating the myofibril maturation was delayed during the cell spreading. The Z-line distance and M-line distance showed a consistent decreasing trend from Hour eight to Hour 24, which also indicated a progressive formation of new Z-lines and M-lines within the myofibrils (Figures 3E,F). Meanwhile, we found that the Z-line length showed a rapid increase from Hour eight to Hour 12, followed by a slow growth from Hour 12 to Hour 48 (Figure 3G). The M-line length showed a similar increasing trend from Hour eight to Hour 48, but the rapid growth occurred from Hour 12 to Hour 24 (Figure 3H). These results indicated that the maturation of the M-lines was later than the Z-lines during myofibrillogenesis.

We quantified the features of Z-costameres and M-costameres from Hour eight to Hour 48 post cell seeding to investigate their distinct roles during costamerogenesis. The Z-costamere distance showed no significant difference from Hour eight to Hour 48, suggesting the assembly of Z-costameres had been completed before Hour 8 (Figure 3I). In contrast, the M-costamere distance at Hour eight was significantly longer than Hour 12–48 (Figure 3J), indicating a delayed assembly of the M-costameres than the Z-costameres. We found that the intensity of both Z-costameres and M-costameres showed an increasing trend Hour eight to Hour 48. Interestingly, the accumulation of zyxin in Z-costameres and M-costameres demonstrated an alternating pattern of increasing fluorescent intensity. A significant increase of M-costamere intensity occurred between Hour 12 and Hour 24, while the Z-costamere intensity was unchanged. While the intensity of M-costameres reached a stable level at Hour 24, a significant increase of Z-costamere intensity was observed during Hours 24–48 (Figures 3K,L). These results revealed distinct costamerogenesis processes between Z-costameres (early formation but late maturation) and M-costameres (late formation but early maturation). We also found a significantly higher intensity of Z-costameres than of M-costameres at Hour 48, indicating the abundance of Z-costameres in long-term culture of hiPSC-CMs (Supplementary Figure S4). For the distance comparison between myofibrils (Z-lines and M-lines) and costameres (Z-costameres and M-costameres), we found similar results as at earlier timepoints (Hour 4–8). Z-line distance and Z-costamere distance showed no significant difference (Supplementary Figure S4). We found a larger M-costamere distance than M-line distance at Hour 8 (Supplementary Figure S4), which was consistent with early timepoints (Supplementary Figure S2), but such difference was no longer obvious in the later timepoints, indicating that M-lines were fully registered to the M-costameres during myofibril maturation.

3.3 Costamere maturation on the substrates of different stiffness

To investigate the role of costameres in sustaining the contractile function of hiPSC-CMs, we seeded hiPSC-CMs on PA hydrogel with moduli of 10 kPa and 40 kPa, respectively, for

FIGURE 4
Costameres of hiPSC-CMs on different substrates. **(A)** Schematics showing the experiment of hiPSC-CMs seeding on PA hydrogels with different stiffness. **(B)** hiPSC-CMs cultured on the PA hydrogels with 10 kPa and 40 kPa modulus were analyzed for their mechanical output based on traction force microscopy. Scale bar: 10 μm. To characterize the responsiveness of myofibrils to different substrate stiffness, we measured the **(C)** Z-line density, **(D)** M-line density, **(E)** Z-line distance, **(F)** M-line distance, **(G)** Z-line length, **(H)** M-line length. To investigate the behaviors of Z-costameres and M-costameres of hiPSC-CMs on different substrates, we quantified the **(I)** Z-costamere distance **(J)** M-costamere distance **(K)** Z-costamere intensity and **(L)** M-costamere intensity. *$p < 0.05$, **$p < 0.01$, ***$p < 0.001$ and ****$p < 0.0001$.

48 h (Figure 4A). No significant difference was found on cell area of the hiPSC-CMs on the different substrates (Supplementary Figure S5). We performed traction force microscopy (TFM) for the hiPSC-CMs (Figure 4B) and found that the hiPSC-CMs on 40 kPa PA hydrogels showed impaired contractions, manifesting as significant deterioration of maximum contractile energy, maximum upstroke power, and maximum upstroke force (Supplementary Figure S5). When we characterized the responsiveness of myofibrils of hiPSC-CMs to different substrate stiffnesses, we found that the Z-line distance and M-line distance were increased significantly on the 40 kPaPA hydrogel compared to the 10 kPa PA hydrogel (Figures 4C,D). No significant difference was found in Z-line length Z-line density within the hiPSC-CMs between the 10 kPa and 40 kPa groups (Figures 4E,G), suggesting the maturity of the Z-lines was

unchanged in response to the substrates with different stiffness. However, M-line length of the hiPSC-CMs on the 40 kPa substrate was significantly shorter than those of cells on the 10 kPa substrate, suggesting the M-lines were more sensitive to extracellular mechanical microenvironment (Figure 4H). In sarcomere shortening analysis, we found the sarcomere shortening was significantly decreased on the 40 kPa PA hydrogel compared to the 10 kPa PA hydrogel. No significant difference was found in sarcomere contraction duration and sarcomere relaxation duration (Supplementary Figure S5). When we investigated the behaviors of Z-costameres and M-costameres of hiPSC-CMs on different substrates, we found that Z-costamere distance showed no significant difference between the 10 kPa group and 40 kPa group (Figure 4I). However, a significantly longer M-costamere distance was

observed in the 40 kPa group, which was consistent with the increase in M-line distance (Figure 4J). We found that both Z-costamere intensity and M-costamere intensity were significantly lower in hiPSC-CMs on the 40 kPa hydrogel compared to the ones on the 10 kPa PA hydrogel, indicating that high substrate stiffness jeopardized costamere expression of the hiPSC-CMs (Figures 4K,L).

4 Discussion

The multiple steps of myofibril growth are widely described as the models of myofibrillogenesis (Sanger et al., 2000). Newer results indicated that recruitment of Z-bodies during *de-novo* assembly of myofibrils was initialized at the integrin, vinculin, and talin-containing adhesion sites, which were termed as pre-costameres (Sparrow and Schöck, 2009). In mature myofibrils, the costameres, showing periodic rib-like patterns, were considered as the myofibril-sarcolemma connections registering with Z-lines and M-lines of the sarcomeres (ErvastiCostameres, 2003). From the observation of the pleat-like wrinkles forming on the flexible substrate during cardiomyocyte contraction, the costameres were proposed as the transmitters that mediated the force transmission from myofibrils to environmental ECM (Danowski et al., 1992). Despite the progress in elucidating details of the models of myofibrillogenesis and costamerogenesis, current understanding of how pre-costameres mature into costameres within the cardiomyocytes is still unclear. To address this gap in understanding, in previous work we documented costamere dynamics of the hiPSC-CMs during topography-induced cardiomyocyte reorganization (Shi et al., 2022). To better understand the process of costameres associated with different myofibril components (Z-lines and M-lines), in the present work we utilized hiPSC-CMs to profile the time-dependent costamerogenesis during cell attachment and spreading. By seeding hiPSC-CMs on PA hydrogel of different stiffnesses, we also studied how extracellular mechanical microenvironment affect myofibril and costamere structures.

4.1 Costamerogenesis and myofibrillogenesis occurred alternatively

Previous works indicated the irreplaceable role of costameres in the initial assembly of myofibrils (Chopra et al., 2018). In our study, though no distinguishable striated costameres were found at Hour 4-5, zyxin showed an early aggregation at the positions of Z-bodies in the pre-myofibrils and the interface between pre-myofibrils and nascent myofibrils. We believe that the *de-novo* assembly of pre-costameres participated in the recruitment of actinin to form the Z-bodies within pre-myofibrils and nascent myofibril at the early stage of myofibrillogenesis (Supplementary

Figure S1, Figure 2B). It has been reported that in the later stage of costamerogenesis, the maturation of costameres relied on the integrity of mature myofibrils (Quach and Rando, 2006). The non-muscle myosin II diffusely existed in pre-myofibrils and nascent myofibrils but only aggregated near the bottom side of the cell membrane in cardiomyocytes with mature myofibrils, suggesting the non-muscle myosin may serve as the navigator in the cell-ECM interface to guide the maturation of costameres (Wang et al., 2018). In our research, both Z-costameres and M-costameres were assembled into an observable striated pattern at Hour 6, at which point the hiPSC-CMs show clear striated Z-lines and M-lines, indicating the maturation of myofibrils was prior to the maturation of costameres (Supplementary Figure S1, Figure 2B). We found that the Z-line distance and M-line distance showed no significant difference from Hour five to Hour 12, but the intensity of Z-costameres and M-costameres increased significantly during the same period (Figure 2 and Figure 3). This temporal alternation of costamere maturation and myofibril maturation suggests that the development of mature Z-lines and M-lines within the myofibrils is a prerequisite for costamere maturation.

4.2 Maturation of Z-costameres and M-costameres was asynchronous

The costameres registered with Z-lines were widely documented in previous cardiac studies, while the M-costameres have been rarely observed. In our previous study, we found that the ratio between costamere density and Z-line density within the hiPSC-CMs was higher than one but not equal to two, suggesting that the M-costameres and M-bands were not strictly paired. Moreover, we found that M-costameres were less detectable than the Z-costameres, suggesting that M-costameres were less expressed than the Z-costameres in hiPSC-CMs (Shi et al., 2022). In this study, we temporally quantified the intensity of Z-costameres and M-costameres after cell seeding to characterize the process of costamere maturation. We found that the intensity of Z-costameres and M-costameres increased in an alternating fashion, indicating the maturation of Z-costameres and M-costamere were asynchronous from Hour 12 to Hour 48 (Figures 3K,L). At Hour 48, the intensity of Z-costameres was significantly higher than M-costameres, suggesting that the Z-costameres were more predominant than the M-costameres in the hiPSC-CMs (Supplementary Figure S4).

4.3 Costameres of cardiomyocytes on substrates with different stiffness

It has been found that cardiomyocytes are able to adapt their contraction forces to environmental stiffening (Hersch et al.,

2013). In our research, hiPSC-CMs on the 10 kPa substrates had higher force output than the ones on the 40 kPa substrates (Supplementary Figure S5), which was consistent with another study showing that hiPSC-CMs on stiffer substrates produced lower contractile force (Ribeiro et al., 2015). In addition, previous study reported that cardiomyocytes on a stiff substrate showed a decreased cell shortening (van Deel et al., 2017), which is consistent with our results showing a decrease in sarcomere shortening of hiPSC-CMs on 40 kPa PA hydrogel. We believe that the impaired sarcomere shortening may contribute to the impaired contractile function of hiPSC-CMs on 40 kPa PA hydrogel. It was also reported that cardiomyocytes on stiffer substrates developed disrupted myofibrils (Corbin et al., 2019). In this work, we found that the hiPSC-CMs on 40 kPa PA hydrogels showed shortened M-line length (Figure 4I), suggesting impairment of M-lines formation might lead to lower contractile force generation. In addition, we also found that both Z-line distance and M-line distance were increased in the hiPSC-CMs on the 40 kPa substrate (Figures 4C,D), which was consistent with previous work showing an increase of sarcomere length in a stiffer environment (Rodriguez et al., 2011). Showing a similar trend as the M-lines, M-costamere distance increased in the 40 kPa group (Figures 4D,J). This suggested that maturation of M-costameres required M-lines as the template. It has been reported that costameres function as the force transmitters during cardiomyocyte contractions (Danowski et al., 1992). It has been reported that costameres function as the force transmitters during cardiomyocyte contractions, while formation of mature striated costameres is intimately regulated by the contraction of cardiomyocytes (Danowski et al., 1992; Shakp et al., 1997). In our work, both Z-costameres and M-costameres showed lower intensity in contractile force-deficient hiPSC-CMs in the 40 kPa group (Figures 4K,L). We believe that the zyxin expression and costamere maturation does not directly respond to the substrate stiffness but might be mechanosensitive to the contractile force transmitted from sarcomeres to the extracellular matrices.

5 Conclusions and future work

In this study, we utilized hiPSC-CMs to study the assembly and maturation of costameres associated with the myofibrillogenesis processes. By temporally tracking the behaviors of costameres and myofibrils of the hiPSC-CMs, we found that costamerogenesis and myofibrillogenesis occurred in an alternating fashion. Early assembled pre-costameres participated in the recruitment of α-actinin to form pre-myofibrils and nascent myofibrils, leading to myofibril maturation. Next, using Z-lines and M-lines as templates in the myofibrils, pre-costameres grew into mature costameres with a striated pattern. During this

process, the maturation of M-costameres and Z-costameres was asynchronous: Z-costameres showed a pattern of early formation but late maturation, while M-costameres showed a pattern of late formation but early maturation. By seeding hiPSC-CMs on PA hydrogels with different stiffness, we found that costamere maturation was regulated by the contractile function of cardiomyocytes. In future, the confocal microscopy with 3D Z-scanning of individual hiPSC-CMs with other components of costameres (e.g., integrin, vinculin, dystrophin) in a time-dependent manner will further enhance our understanding of how costameres incorporating with myofibrils would affect cardiomyocyte mechanobiology.

Data availability statement

The raw data supporting the conclusions of this article will be made available by the authors, without undue reservation.

Author contributions

Funding

Conflict of interest

The authors declare that the research was conducted in the absence of any commercial or financial relationships that could be construed as a potential conflict of interest.

Publisher's note

All claims expressed in this article are solely those of the authors and do not necessarily represent those of their affiliated organizations, or those of the publisher, the editors and the reviewers. Any product that may be evaluated in this article, or claim that may be made by its manufacturer, is not guaranteed or endorsed by the publisher.

Supplementary material

The Supplementary Material for this article can be found online at: https://www.frontiersin.org/articles/10.3389/fbioe.2022.1049523/full#supplementary-material

References

Anastasi, G., Amato, A., Tarone, G., Vita, G., Monici, M., Magaudda, L., et al. (2003). Distribution and localization of vinculin-talin-integrin system and dystrophin-glycoprotein complex in human skeletal muscle. *Cells Tissues Organs* 175, 151–164. doi:10.1159/000074631

Belkin, A. M., Zhidkova, N. I., and Koteliansky, V. E. (1986). Localization of talin in skeletal and cardiac muscles. *FEBS Lett.* 200, 32–36. doi:10.1016/0014-5793(86) 80505-1

Chopra, A., Kutys, M. L., Zhang, K., Polacheck, W. J., Sheng, C. C., Luu, R. J., et al. (2018). Force generation via β-cardiac myosin, titin, and α-actinin drives cardiac sarcomere assembly from cell-matrix adhesions. *Dev. Cell* 44, 87–96. doi:10.1016/j.devcel.2017.12.012

Corbin, E. A., Vite, A., Peyster, E. G., Bhoopalam, M., Brandimarto, J., Wang, X., et al. (2019). Tunable and reversible substrate stiffness reveals a dynamic mechanosensitivity of cardiomyocytes. *ACS Appl. Mat. Interfaces* 11, 20603–20614. doi:10.1021/acsami.9b02446

Danowski, B. A., Imanaka-Yoshida, K., Sanger, J. M., and Sanger, J. W. (1992). Costameres are sites of force transmission to the substratum in adult rat cardiomyocytes. *J. Cell Biol.* 118, 1411–1420. doi:10.1083/jcb.118.6.1411

di Mauro, D., Gaeta, R., Arco, A., Milardi, D., Lentini, S., Runci, A., et al. (2009). Distribution of costameric proteins in normal human ventricular and atrial cardiac muscle. *Folia histochem. Cytobiol.* 47, 605–608. doi:10.2478/v10042-009-0114-z

ErvastiCostameres, J. M. (2003). Costameres: The achilles' heel of herculean muscle. *J. Biol. Chem.* 278, 13591–13594. doi:10.1074/jbc.r200021200

Fedele, C., Mantyla, E., Belardi, B., Hamkins-Indik, T., Cavalli, S., Netti, P. A., et al. (2020). Azobenzene-based sinusoidal surface topography drives focal adhesion confinement and guides collective migration of epithelial cells. *Sci. Rep.* 10, 15329–15415. doi:10.1038/s41598-020-71567-w

Galie, P. A., Khalid, N., Carnahan, K. E., Westfall, M. v., and Stegemann, J. P. (2013). Substrate stiffness affects sarcomere and costamere structure and electrophysiological function of isolated adult cardiomyocytes. *Cardiovasc. Pathol.* 22, 219–227. doi:10.1016/j.carpath.2012.10.003

González-García, C., Sousa, S. R., Moratal, D., Rico, P., and Salmerón-Sánchez, M. (2010). Effect of nanoscale topography on fibronectin adsorption, focal adhesion size and matrix organisation. *Colloids Surfaces B Biointerfaces* 77, 181–190. doi:10.1016/j.colsurfb.2010.01.021

Gorza, L., Sorge, M., Seclì, L., and Brancaccio, M. (2021). Master regulators of muscle atrophy: Role of costamere components. *Cells* 10, 61–37. doi:10.3390/cells10010061

Hersch, N., Wolters, B., Dreissen, G., Springer, R., KirchgeBner, N., Merkel, R., et al. (2013). The constant beat: cardiomyocytes adapt their forces by equal contraction upon environmental stiffening. *Biol. Open* 2, 351–361. doi:10.1242/bio.20133830

Hoang, P., Wang, J., Conklin, B. R., Healy, K. E., and Ma, Z. (2018). Generation of spatial-patterned early-developing cardiac organoids using human pluripotent stem cells. *Nat. Protoc.* 13, 723–737. doi:10.1038/nprot.2018.006

Hresko, M. C., Williams, B. D., and Waterston, R. H. (1994). Assembly of body wall muscle and muscle cell attachment structures in *Caenorhabditis elegans*. *J. Cell Biol.* 124, 491–506. doi:10.1083/jcb.124.4.491

Kovačič-Milivojević, B., Roediger, F., Almeida, E. A., Damsky, C. H., Gardner, D. G., and Ilic, D. (2001). Focal adhesion kinase and p130Cas mediate both sarcomeric organization and activation of genes associated with cardiac myocyte hypertrophy. *Mol. Biol. Cell* 12, 2290–2307. doi:10.1091/mbc.12.8.2290

Kumari, A., Pineau, J., Lennon-Duménil, A. M., Balland, M., and Pierobon, P. (2020). Traction force microscopy to study B lymphocyte activation. *J. Vis. Exp.* 2020, e60947. doi:10.3791/60947

Kumari, A., Pineau, J., Saez, P. J., Maurin, M., Lankar, D., San Roman, M., et al. (2019). Actomyosin-driven force patterning controls endocytosis at the immune synapse. *Nat. Commun.* 10, 2870–2914. doi:10.1038/s41467-019-10751-7

Li, R., Narici, M. V., Erskine, R. M., Seynnes, O. R., Rittweger, J., Pisot, R., et al. (2013). Costamere remodeling with muscle loading and unloading in healthy young men. *J. Anat.* 223, 525–536. doi:10.1111/joa.12101

Lyon, R. C., Zanella, F., Omens, J. H., and Sheikh, F. (2015). Mechanotransduction in cardiac hypertrophy and failure. *Circ. Res.* 116, 1462–1476. doi:10.1161/circresaha.116.304937

Ma, Z., Huebsch, N., Koo, S., Mandegar, M. A., Siemons, B., Boggess, S., et al. (2018). Contractile deficits in engineered cardiac microtissues as a result of MYBPC3 deficiency and mechanical overload. *Nat. Biomed. Eng.* 2, 955–967. doi:10.1038/s41551-018-0280-4

Mandal, K., Wang, I., Vitiello, E., Orellana, L. A. C., and Balland, M. (2014). Cell dipole behaviour revealed by ECM sub-cellular geometry. *Nat. Commun.* 5 (1), 5749–5810. doi:10.1038/ncomms6749

McDonald, K. A., Lakonishok, M., and Horwitz, A. F. (1995). Alpha v and alpha 3 integrin subunits are associated with myofibrils during myofibrillogenesis. *J. Cell Sci.* 108, 975–983. doi:10.1242/jcs.108.3.975

Morris, T. A., Naik, J., Fibben, K. S., Kong, X., Kiyono, T., Yokomori, K., et al. (2020). Striated myocyte structural integrity: Automated analysis of sarcomeric z-discs. *PLoS Comput. Biol.* 16, e1007676. doi:10.1371/journal.pcbi.1007676

Myhre, J. L., and Pilgrim, D. B. (2012). At the start of the sarcomere: A previously unrecognized role for myosin chaperones and associated proteins during early myofibrillogenesis. *Biochem. Res. Int.* 2012, 1–16. doi:10.1155/2012/712315

Natale, C. F., Lafaurie-Janvore, J., Ventre, M., Babataheri, A., and Barakat, A. I. (2019). Focal adhesion clustering drives endothelial cell morphology on patterned surfaces. *J. R. Soc. Interface* 16, 20190263. doi:10.1098/rsif.2019.0263

Pardo, J. v., D'Angelo Siliciano, J., and Craig, S. W. (1983). A vinculin-containing cortical lattice in skeletal muscle: Transverse lattice elements ('costameres') mark sites of attachment between myofibrils and sarcolemma. *Proc. Natl. Acad. Sci. U. S. A.* 80, 1008–1012. doi:10.1073/pnas.80.4.1008

Porter, G. A., Dmytrenko, G. M., Winkelmann, J. C., and Bloch, R. J. (1992). Dystrophin colocalizes with beta-spectrin in distinct subsarcolemmal domains in mammalian skeletal muscle. *J. Cell Biol.* 117, 997–1005. doi:10.1083/jcb.117.5.997

Quach, N. L., and Rando, T. A. (2006). Focal adhesion kinase is essential for costamerogenesis in cultured skeletal muscle cells. *Dev. Biol. (N. Y. 1985.* 293, 38–52. doi:10.1016/j.ydbio.2005.12.040

Ribeiro, A. J. S., Ang, Y. S., Fu, J. D., Rivas, R. N., Mohamed, T. M. A., Higgs, G. C., et al. (2015). Contractility of Single cardiomyocytes differentiated from pluripotent stem cells depends on physiological shape and substrate stiffness. *Proc. Natl. Acad. Sci. U. S. A.* 112, 12705–12710. doi:10.1073/pnas.1508073112

Ribeiro, A. J. S., Denisin, A. K., Wilson, R. E., and Pruitt, B. L. (2016). For whom the cells pull: Hydrogel and micropost devices for measuring traction forces. *Methods* 94, 51–64. doi:10.1016/j.ymeth.2015.08.005

Rodriguez, A. G., Han, S. J., Regnier, M., and Sniadecki, N. J. (2011). Substrate stiffness increases twitch power of neonatal cardiomyocytes in correlation with

changes in myofibril structure and intracellular calcium. *Biophys. J.* 101, 2455–2464. doi:10.1016/j.bpj.2011.09.057

Ruoss, S., Kindt, P., Oberholzer, L., Rohner, M., Jungck, L., Abdel-Aziz, S., et al. (2018). Inhibition of calpain delays early muscle atrophy after rotator cuff tendon release in sheep. *Physiol. Rep.* 6, e13833. doi:10.14814/phy2.13833

Sanger, J. W., Ayoob, J. C., Chowrashi, P., and Zurawski, D. (2000). Assembly of myofibrils in cardiac muscle cells. *Adv. Exp. Med. Biol.* 481, 89–102. doi:10.1007/978-1-4615-4267-4_6

Sanger, J. W., Kang, S., Siebrands, C. C., Freeman, N., Du, A., Wang, J., et al. (2006). How to build a myofibril. *J. Muscle Res. Cell Motil.* 26, 343–354. doi:10.1007/s10974-005-9016-7

Sanger, J. W., Wang, J., Fan, Y., White, J., Mi-Mi, L., Dube, D. K., et al. (2017). Assembly and maintenance of myofibrils in striated muscle. *Handb. Exp. Pharmacol.* 235, 39–75. doi:10.1007/164_2016_53

Sanger, J. W., Wang, J., Fan, Y., White, J., and Sanger, J. M. (2010). Assembly and dynamics of myofibrils. *J. Biomed. Biotechnol.* 2010, 1–8. doi:10.1155/2010/858606

Seo, C. H., Jeong, H., Furukawa, K. S., Suzuki, Y., and Ushida, T. (2013). The switching of focal adhesion maturation sites and actin filament activation for MSCs by topography of well-defined micropatterned surfaces. *Biomaterials* 34, 1764–1771. doi:10.1016/j.biomaterials.2012.11.031

Sergé, A., Bertaux, N., Rigneault, H., and Marguet, D. (2008). Dynamic multiple-target tracing to probe spatiotemporal cartography of cell membranes. *Nat. Methods* 5, 687–694. doi:10.1038/nmeth.1233

Shakp, W. W., Simpson, D. G., Borg, T. K., Samarel, A. M., and Terracio, L. (1997). Mechanical forces regulate focal adhesion and costamere assembly in cardiac myocytes. *Am. J. Physiol.* 273, H546. doi:10.1152/ajpheart.1997.273.2.H546

Shi, H., Wu, X., Sun, S., Wang, C., Vangelatos, Z., Ash-Shakoor, A., et al. (2022). Profiling the responsiveness of focal adhesions of human cardiomyocytes to extracellular dynamic nano-topography. *Bioact. Mat.* 10, 367–377. doi:10.1016/j.bioactmat.2021.08.028

Simmons, C. S., Ribeiro, A. J. S., and Pruitt, B. L. (2013). Formation of composite polyacrylamide and silicone substrates for independent control of stiffness and strain. *Lab. Chip* 13, 646–649. doi:10.1039/c2lc41110e

Sparrow, J. C., and Schöck, F. (2009). The initial steps of myofibril assembly: integrins pave the way. *Nat. Rev. Mol. Cell Biol.* 10, 293–298. doi:10.1038/nrm2634

Tse, J. R., and Engler, A. J. (2010). Preparation of hydrogel substrates with tunable mechanical properties. *Curr. Protoc. Cell Biol.* 10, Unit 10.16. doi:10.1002/0471143030.cb1016s47

van Deel, E. D., Najafi, A., Fontoura, D., Valent, E., Goebel, M., Kardux, K., et al. (2017). *In vitro* model to study the effects of matrix stiffening on Ca²⁺ handling and myofilament function in isolated adult rat cardiomyocytes. *J. Physiol.* 595, 4597–4610. doi:10.1113/jp274460

Wang, J., Fan, Y., Sanger, J. M., and Sanger, J. W. (2018). Nonmuscle myosin II in cardiac and skeletal muscle cells. *Cytoskelet. Hob.* 75, 339–351. doi:10.1002/cm.21454

Yip, A. K., Nguyen, A. T., Rizwan, M., Wong, S. T., Chiam, K. H., and Yim, E. K. (2018). Anisotropic traction stresses and focal adhesion polarization mediates topography-induced cell elongation. *Biomaterials* 181, 103–112. doi:10.1016/j.biomaterials.2018.07.057

Recent advancements and future requirements in vascularization of cortical organoids

Erin LaMontagne[1], Alysson R. Muotri[2,3,4]* and Adam J. Engler[1,4]*

[1]Department of Bioengineering, University of California, San Diego, La Jolla, CA, United States, [2]Department of Pediatrics, University of California, San Diego, La Jolla, CA, United States, [3]Department of Cellular and Molecular Medicine, University of California, San Diego, La Jolla, CA, United States, [4]Sanford Consortium for Regenerative Medicine, La Jolla, CA, United States

The fields of tissue engineering and disease modeling have become increasingly cognizant of the need to create complex and mature structures *in vitro* to adequately mimic the *in vivo* niche. Specifically for neural applications, human brain cortical organoids (COs) require highly stratified neurons and glial cells to generate synaptic functions, and to date, most efforts achieve only fetal functionality at best. Moreover, COs are usually avascular, inducing the development of necrotic cores, which can limit growth, development, and maturation. Recent efforts have attempted to vascularize cortical and other organoid types. In this review, we will outline the components of a fully vascularized CO as they relate to neocortical development *in vivo*. These components address challenges in recapitulating neurovascular tissue patterning, biomechanical properties, and functionality with the goal of mirroring the quality of organoid vascularization only achieved with an *in vivo* host. We will provide a comprehensive summary of the current progress made in each one of these categories, highlighting advances in vascularization technologies and areas still under investigation.

KEYWORDS

brain organoid, vasculature, tissue engineering, organ-on-a-chip, microenvironment

1 Introduction

Organoids are self-organizing, three-dimensional cell clusters that are often derived from pluripotent stem cells (PSCs) (Rossi et al., 2018). They form with minimal direction from exogenous biochemical factors and create a tissue-specific niche where cells replicate some aspects of organ function or complexity (Qian et al., 2019). Embryonic and induced pluripotent stem cell (iPSC)-derived organoids provide a rare window into early cellular events that give rise to tissues and diseases (Lancaster and Knoblich, 2014; Pasca et al., 2015). Because organoids are generated from PSCs, strategies to prevent uncontrolled tumorigenicity, such as confirming the absence of pluripotent markers in differentiated cells or incorporating a suicidal gene to eliminate residual pluripotent cells, must be employed. Additionally, brain organoid protocols are still quite variable and thus, strong quality controls are necessary to reduce the experimental heterogeneity. Nevertheless, brain organoids have proven particularly useful for studying the human brain, which we
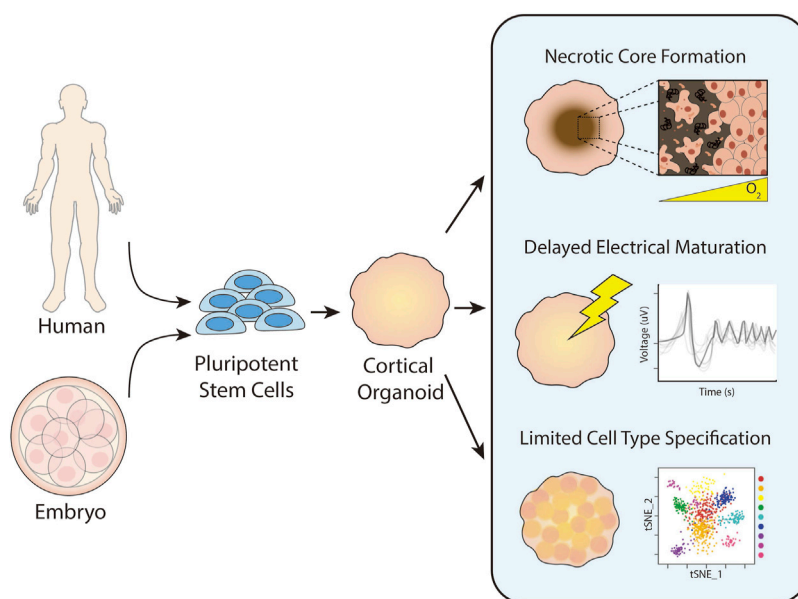
FIGURE 1
Historic challenges in cortical organoid culture. Cortical organoids are generated from pluripotent stem cells harvested from an embryo or reprogrammed from somatic cells. Upon prolonged culture, cortical organoids commonly form necrotic cores due to insufficient distribution of oxygen and nutrients. They also exhibit delayed electrical maturation with spontaneous action potentials occurring only after months of culture with minimal improvement over time. Finally, cortical organoids have limited cell type specification and differentiation after prolonged culture.

have limited opportunities to observe and differs from those of animal models (Marshall and Mason, 2019). The cerebral cortex is perhaps the most interesting region of the human brain, as it is significantly larger and more complex than that of our evolutionary predecessors and regulates higher order functions like consciousness and thought. Cortical organoids (COs) have been used to study human-relevant neurodevelopment (Trujillo and Muotri, 2018), disease pathophysiology (Di Lullo and Kriegstein, 2017), and brain evolution (Giandomenico and Lancaster, 2017). Despite these advances, the absence of vasculature in organoid models leads to numerous problems beyond a lack of tissue complexity. A primary issue faced with organoids is the formation of a necrotic core due to insufficient mass transfer of oxygen and nutrients. Most cells can only survive ~200 μm away from a vessel (Jain et al., 2005), but organoids can grow up to a few millimeters in diameter, resulting in heightened expression of hypoxia- and apoptosis-related genes and activation of metabolic stress pathways that negatively impact neural development and migration (Qian et al., 2019; Bhaduri et al., 2020). COs are also limited to immature fetal states, defined in part by less distinct cell types, rudimentary cortical layer formation, and variable electrophysiological activity (Luo et al., 2016; Qian et al., 2019; Puppo and Muotri, 2022) (Figure 1). Vascularizing brain organoids has alleviated these issues to varying degrees, but there remains a need for a reliable and effective method of CO vascularization.

To successfully vascularize COs, it is important to consider both form and function. Vasculature primarily transports oxygen and nutrients essential for cellular survival and function, but also it plays roles in cell signaling, inter-organ crosstalk, and tissue-specific maturation (Carmeliet, 2005). The brain is one of the most densely vascularized tissues in the body, receiving 15–20% of the cardiac output to meet its high metabolic demands (Xing et al., 2017). Neurons, glial cells, and vascular cells work together to form a neurovascular unit, which regulates selective permeability of the blood brain barrier (BBB) and controls cerebral blood flow and stabilizes neuronal circuits via neurovascular coupling (Cipolla, 2009). The cerebral cortex exhibits unique vascular patterning in which large superficial vessels located in the pia mater branch off into venules and arterioles at 90-degree angles that penetrate the cortex columns. Small microvessels sprout between these penetrating vessels, forming dense microvascular beds located about ~200 μm apart (Cipolla, 2009; Marín-Padilla and Knopman, 2011). This complex patterning is orchestrated by biochemical signals, cell-extracellular matrix (ECM) interactions, and biophysical cues provided by blood and cerebrospinal fluids (Figure 2). In this review, we examine the different approaches taken to vascularize COs, evaluate their successes and limitations, and identify key features that facilitate neurovascular development and can be leveraged to improve tissue models.

FIGURE 2
Cortical organoid vascularization components and considerations. Cellular signalling between neural and vascular cells is essential for complex network architecture. Hemodynamic forces that exude pressure and shear stresses on vessel walls can be mimicked using microfluidics. The extracellular matrix provides support and aids in mechanotransduction. Cortical organoids may be implanted into animal hosts to connect with or be invaded by host vasculature.

2 Biological self-organization of cortical vessels

The cellular and molecular signaling that direct cortical vasculogenesis *in vivo* are complex but offer a blueprint for the self-organization of vascular networks in COs (Figure 3). The goals of this process for COs are two-fold: First, most cell types of the BBB are neuroepithelium-derived, including astrocytes, pericytes, and neurons, and can arise spontaneously in COs. However, traditional COs lack the capacity to generate vascular endothelial cells (ECs) due to their mesodermal origins, so they must be added by other means. Second, signals must be provided to induce vascular network formation.

2.1 Vascular endothelial cell signaling in neocortical development

Proper brain development depends on the co-expansion of intercalated neural and vascular tissues. In neurodevelopment, ECs respond to pro- and anti-angiogenic factors to produce vascular networks and recruit other cells to the BBB. Vascular progenitor cells do not originate in the brain, rather, they are born in the vascular plexus that surrounds the central nervous system and ingress into the neural tube in response to hypoxic signals released by neural progenitor cells (NPCs). Subsequent signaling between vascular and NPCs activates neurogenesis and pro-angiogenic pathways that enable fetal brain growth and function (Carmeliet and Tessier-Lavigne, 2005; Ma et al., 2013).

In early corticogenesis, radial glial cells interact with ECs through both paracrine signaling and direct contact. Canonical Wnt signaling from radial glia regulates EC activation and vessel stabilization. In particular, Wnt7a and Wnt7b are expressed in a highly regulated and stage-specific manner that guides vascular network formation in the neural tube and forebrain (Ma et al., 2013). Radial glia also secrete transforming growth factor beta 1 (TGF-β1), an essential angiogenic factor that activates ECs, promotes EC migration, and supports tight junction formation (Siqueira et al., 2018). Simultaneously, Wnt family proteins, vascular endothelial growth factor (VEGF), and angiopoietins secreted from ECs regulate the self-renewal and differentiation of neural stem cells and induce the lateral expansion of the cortical epithelium (Carmeliet and Tessier-Lavigne, 2005). As a result of the signaling between radial glia and ECs, the regional density of radial glia correlates to vessel density and branching frequency (Ma et al., 2013). On the other hand, in late corticogenesis, neurons primarily coordinate vasculogenesis.
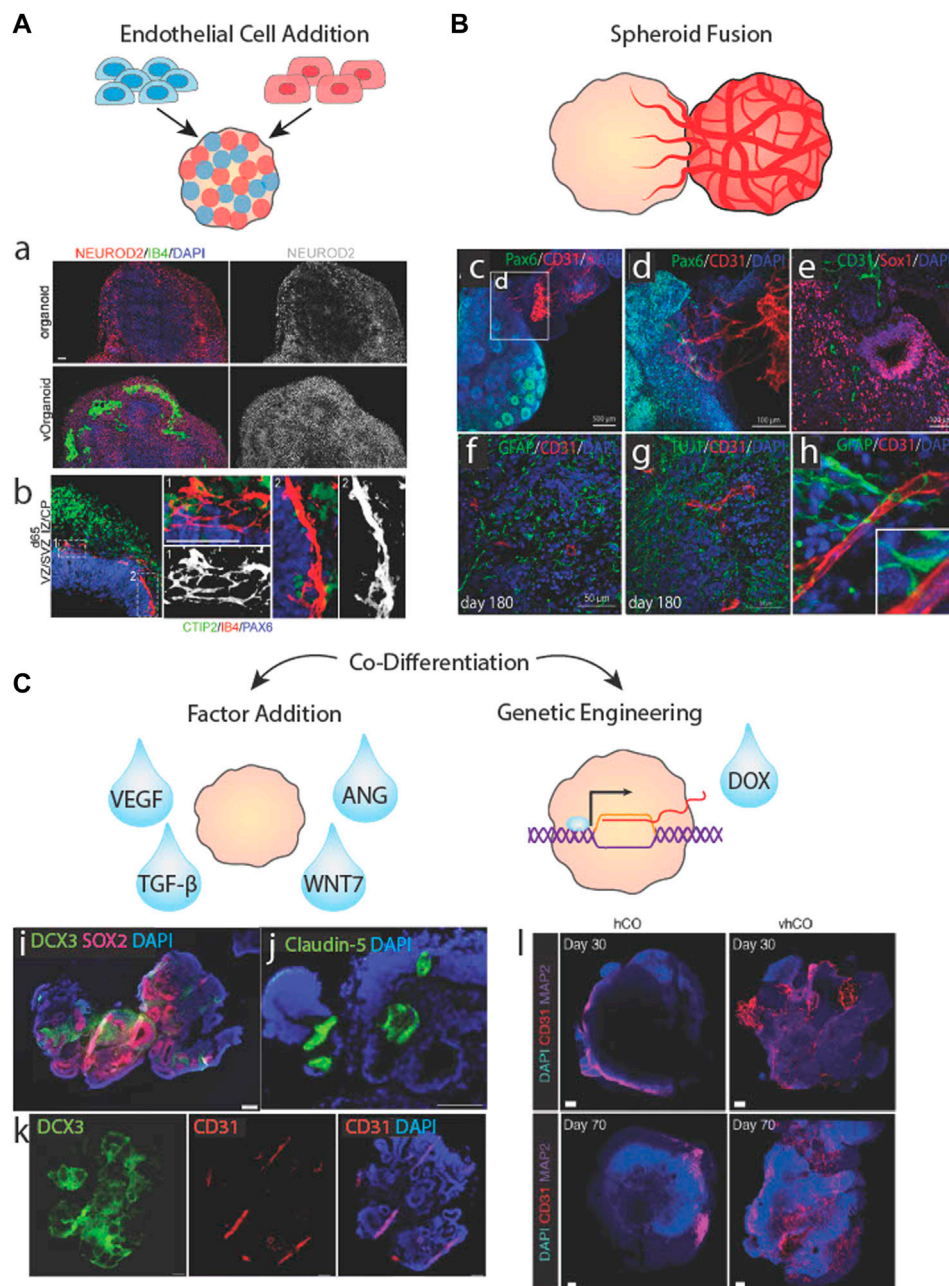
FIGURE 3
Biological approaches to brain organoid vascularization. **(A)** Schematic of organoid vascularization by mixing pluripotent stem cells with endothelail cells. a.b. Vascularized brain organoids generated by mixing HUVECs with stem cells showing localized clusters of vessel-like structures and vascular cells interacting with neurites. Adapted from (Shi et al., 2020). **(B)** Schematic of a brain organoid fused to a vascular spheroid. c.d.e. Vessels from a vascular spheroid invading the neuroepithelium of a brain organoid. f.g.h. Vessels from a vascular spheroid interacting with neurons and astrocytes/radial glia. Adapted from (Wörsdörfer et al., 2019). **(C)** Schematic of brain organoid vascularization by the addition of soluble factors or genetic engineering of inducible transcription factor systems. i.j.k Co-differentiated vascularized brain organoid stained for neural cell, vasucular cell, and tight junction markers. Adapted from Ham et al. (2020). Vascular markers in control (hCO) versus vascularized cortical organoids (vhCO), which carry an inducible Ets variant transcription factor 2 (*ETV2*) genetic system. Adapted from (Cakir et al., 2019).

VEGF, known as the master regulator of vascular growth, is released by both hypoxic tissues and neuronal axons (Carmeliet and Tessier-Lavigne, 2005). VEGF gradients activate ECs and induce the generation of tip cells, which delaminate the basement membrane and migrate *via* filipodia to make new vessel branches (Abe et al., 2019). VEGF-induced migration is inhibited by

interactions between roundabout 4 (ROBO4) on EC membranes and SLIT2 on axons that subsequently upregulate cell adhesion and permeability pathways in ECs such as E-cadherin, β-catenin, and cadherin 5 (CDH5) and claudin 5 (CLDN5) (Bekes et al., 2017). But VEGF is not only important for ECs; it also plays key roles in neurogenesis and neuroprotection (Rosenstein et al., 2010). These are just a few of the numerous factors in the brain that guide both axon and vessel growth (Carmeliet and Tessier-Lavigne, 2005), though they illustrate the interdependence of axon and vessel signaling and how vessel and neuron density scale with each other (Tsai et al., 2009).

2.2 Addition of exogenous endothelial cells to cortical organoids

Terminally differentiated ECs in 3D environments spontaneously form tubular mesh networks in response to signals from neighboring ECs or other cells (Jeon et al., 2014), but it is important to consider what type of ECs are most appropriate to form networks that recapitulate BBB functions in COs. Human umbilical vein endothelial cells (HUVECs) are commonly used due to their commercial availability, ability to form tight junctions and tubes, and terminally differentiated state, negating the need for differentiation factors. However, HUVECs lack BBB-specific characteristics, including the expression of important surface and junction proteins and brain-specific transporters (Lee et al., 2020; Salmon et al., 2022). Some studies have noted that HUVECs in COs demonstrate transcriptional plasticity by adopting brain-specific vascular signatures, inducing the efflux transporter P-glycoprotein (Shi et al., 2020) and von Willebrand factor (vWF) (Kook et al., 2022). Skylar-Scott et al. (2022) also reported that HUVECs have difficulty adhering to iPSCs, possibly due to disparities in cell adhesion proteins, although high iPSC: HUVEC ratios in Shi et al. (2020) may have enabled the formation of hybrid spheroids (Figures 3Aa,b). The consequences of adding non-tissue-specific vascular cells to COs has not yet been explored, but with the previously described knowledge of cell signaling during neural differentiation, it is possible that adding such cells may disrupt neural patterning and differentiation. Primary human brain microvessel endothelial cells (BMECs) are another option but they have been minimally explored because they are difficult to acquire, quickly lose their brain-specific characteristics when cultured (Rubin et al., 1991), and form large, discontinuous vessels in vitro (Campisi et al., 2018; Lee et al., 2020). Similarly, BBB organoids formed from primary BMECs, astrocytes, and pericytes lack complex vascular morphology (Bergmann et al., 2018), likely due to the absence of tissue-specific biochemical and biomechanical signals provided by the brain microenvironment.

iPSC-derived ECs, on the other hand, are relatively readily available, can have the same genotype as their CO counterparts, and can undergo tissue-specific maturation, adopting brain-specific vascular signatures in the presence of neurons (Campisi et al., 2018; Salmon et al., 2022). iPSC-ECs transcriptomic identities and vascular functionalities depend on the ability of a protocol to reproduce the in vivo microenvironment while supplying sufficient differentiation cues (Pasut et al., 2021). Non-tissue-specific iPSC-ECs exhibit fundamental EC qualities, including EC-specific adhesion protein expression, solute impermeability, and tube formation both in vitro and in vivo (James et al., 2010; Patsch et al., 2015; Lee et al., 2020). However, they lack important qualities that contribute to the BBB and neurovascular development. Lippmann et al. (2012) developed a BMEC differentiation protocol that mimics the co-development of neural and vascular cells in vivo by combining soluble factors with physical cues from ECM substrates to co-differentiate neurons and ECs. The resulting iPSC-BMECs harbor highly organized tight junctions and elevated transendothelial electrical resistance. However, these cells neither express brain-specific transporters nor canonical EC genes and are unable to form continuous lumens in vivo. Notably, iPSC-BMECs have strong epithelial transcriptomic signatures, likely a result of naïve EC plasticity during co-differentiation with neuroepithelial cells, impairing proper EC-type specification (Lippmann et al., 2012; Lu et al., 2021). iPSC-BMECs can obtain canonical vascular EC characteristics via introduction of EC-specific ETS family factors, but this in turn erases their brain-specific qualities (Lu et al., 2021). Consequently, adding non-tissue-specific iPSC-ECs to COs and allowing them to acquire brain-specific characteristics via microenviromental signaling within the CO may be a very promising choice for CO vascularization.

Vascular network localization and density is impacted by the stage of CO differentiation when ECs are added and by their delivery method. ECs added during embryoid body formation are mixed as single cells with PSCs resulting in mixed spheroids (Figure 3A). Upon CO differentiation, the ECs assemble into vessels uniformly and densely across the organoid (Figures 3Aa,b,Cl), although these vessels may not be as interconnected or impermeable as some vascular networks generated using other methods (Cakir et al., 2019; Shi et al., 2020; Skylar-Scott et al., 2022). One concern of adding ECs during embryoid body formation is potential interference with neural induction, although Shi et al. (2020) conversely showed that such approaches may enhance neural differentiation. Still, some protocols opt to add vascular cells to COs after the neural induction phase by Matrigel encapsulation. This method relies on angiogenic and hypoxia chemokine gradients radiating from the CO core to guide vessel sprouting. However, minimal penetration into the CO has been reported, with the highest vessel density localized to the neuron-dense outermost layers (Pham et al., 2018). Minimal vessel penetration may be due to a

number of causes: insufficient tip cell response, hypoxia signals, or NPC-EC signaling due to the distance between the ECs at the organoid surface and NPCs buried in the organoid body. A potential solution may be to incorporate biomaterials capable of releasing pro-angiogenic factors into the COs to encourage vessel sprouting, although this has not been attempted (Mastrullo et al., 2020; Seah et al., 2020).

2.3 Fusing vascular spheroids with cortical organoids

An alternative to mixed organoids is to propagate cell types separately as spheroids and subsequently fuse them together (Figure 3B). In this approach, vascular spheroids containing iPSC-ECs with fully formed networks have been fused to neural spheroids and cultured for long periods of time. Although the majority of neural and vascular cells remain regionally localized, a number of vessels sprout into radial glia-containing regions of the core after months of culturing (Figures 3Bc,e) (Wörsdörfer et al., 2019; Kook et al., 2022). Sprout penetration may be enhanced by EC-radial glia communication as a result of direct contact between the vascular cells and radial glial cells shortly upon fusion (Figures 3Bf–h). Despite relatively successful penetration and maturity of CO vessels formed *via* fusion, network formation and expansion was unresponsive to exogenous pro- and anti-angiogenic factors, (Wörsdörfer et al., 2019). As an alternative approach, Ahn et al. (2021) prevented the regional localization of vessels by dissociating HUVEC vascular spheroids prior to adding them to COs. Long vessels coated with pericytes were found throughout the organoid, but GFAP + astrocytes, although present, did not associate closely with these vessels. This may be due to the non-BBB characteristics of HUVECs or the lack of vessel branches and low vessel densities.

2.4 Co-differentiating endothelial cells and neurons

A third cell-based option found in the literature is to co-differentiate ECs and neurons within the same organoid (Figure 3C). This has been accomplished using exogenous differentiation factors, e.g., VEGF treatment, as early as 6 days after embryonic body formation to induce vascular differentiation without inhibiting neural differentiation and forebrain specification. However, this method does not produce a branched network, and only generates a few large, disconnected vessels that span the entirety of the CO (Figures 3Ci–k) (Ham et al., 2020). This result aligns with other studies that indicate VEGF is sufficient in generating vascular networks *in vitro* but composed of large and simple vessels. The addition of TGF-β1 or ANG1 significantly increased branching frequency

and reduced vessel diameter (Jeon et al., 2014), although this has not been tested in vascularized CO culture.

An alternative to exogenous factors is to use genetically engineered PSCs harboring inducible transcription factor systems (Figure 3C). These cells undergo differentiation *via* lineage-specific gene expression when triggered by a chemical regulator like doxycycline. Ets variant transcription factor 2 (*ETV2*), a gene encoding a chromatin remodeling protein that activates tubulogenic pathways, has become a target for inducible-differentiation of vascular ECs (Palikuqi et al., 2020). Cakir et al. (2019) generated embryoid bodies containing unaltered iPSCs and iPSCs harboring *ETV2*-inducible expression systems then induced vascular expression *via* doxycycline at day 18 of CO differentiation. The result was a highly integrated, branched network spanning most of the organoid (Figure 3Cl). They also reported increased BBB marker expression and significantly improved electrophysiological activity. A reverse approach was taken by Dailamy et al. (2021) where iPSCs and inducible neurons were incorporated into vascular organoids and neuronal expression was induced on day 15 of vascular differentiation. This approach resulted in clusters of neural and vascular networks with some co-localization at their borders but without spanning the organoid uniformly. These biologically-based methods produced some vascularization, but as noted at the outset of this paper, a fully matured vascular network would contain small, highly branched vessels that span the entirety of the organoid. Since none of the methods resulted in such a network, other cues are likely important.

3 Extracellular matrix composition and mechanical properties

ECM-cell interactions also direct cortical vasculogenesis *in vivo*. The goal of ECM-based vascularization approaches is to recreate the brain's extracellular microenvironment, which provides cells with structure to facilitate tissue growth and spatial-temporal regulation of biochemical and mechanical signals for patterning and maturation.

3.1 Extracellular matrix influence on angiogenesis during neocortical development

ECM is an essential component of any tissue microenvironment that supports differentiating cells. While it is perhaps an underappreciated element of the niche, brain ECM constitutes 20% of human brain mass (Rauch, 2007). The brain sees significant change in its ECM composition throughout development that affects mechanical characteristics such as diffusivity through extracellular spaces and tissue

viscoelasticity, which regulates synapse development and functionality. ECM proteins help sequester cells and bind signaling molecules, in order to generate complex gradients and form the laminated structures of the cortex. In COs and the embryonic brain, the ECM maintains NPCs in regional layers and guides radial migration of neurons from the laminin-rich basement membrane of the cortical plate-like structure (Sood et al., 2016).

ECs secrete, degrade, deform, and are deformed by surrounding matrix to generate vascular networks in response to tissue needs (Du et al., 2016). ECs primarily produce and interact with fibrillar matrix proteins like fibronectin and collagen, which they reorganize to serve as scaffolding for migrating and elongating vessel sprouts (Zhou et al., 2008; McCoy et al., 2018). Despite its significant ECM mass, the brain has a relatively low concentration of fibrillar proteins compared to other tissues and the proportion of collagen to other ECM proteins decreases during development (Sood et al., 2016; Cho et al., 2021). In fact, fibrillar collagens in the adult brain almost exclusively surround the basal lamina of cerebral vessels. The bulk of brain ECM is composed of glycoproteins, which provide frameworks for synaptic junctions and play roles in regulating BBB permeability, and proteoglycans, namely chondroitin sulfates and heparan sulfate proteoglycans, which bind to hyaluronic acid molecules to generate soft aggregates that act as a supportive framework around cells (Maeda, 2015).

Beyond composition, the brain's ECM exhibits unique structural and mechanical properties. The adult brain is an extremely soft, viscoelastic tissue, with an elastic modulus in the 100s of Pascal (Pa or N/m^2; a unit of stiffness) (Fallenstein et al., 1969; Canovic et al., 2016). During development, the brain's non-homogenous stiffness profile causes folding of the cerebral cortex (Budday and Steinmann, 2018), a characteristic important for cortical thickness and cellular density (Jalil Razavi et al., 2015). Similarly, organoids embedded in soft ECM hydrogels experience wrinkling and folding caused by differential swelling *via* solvent absorption. These features affect tissue growth, including organoid size, neuronal migration (Karzbrun et al., 2018) and number of rosettes (Cassel De Camps et al., 2022). Conversely, greater stiffness impairs overall growth and skews differentiation towards mature neuronal types (Cassel De Camps et al., 2022). While the effects of stiffness on EC growth in 3D tissues is understudied, it is well known that substrate stiffness greatly impacts ECs in 2D, with stiffer substrates inducing EC spreading and elongation, higher contractile forces, and increased proliferation (Yeung et al., 2005; Yeh et al., 2012). ECs are also sensitive to curvature, and will align and elongate along regions of high curvature (Cheng et al., 2019; Mandrycky et al., 2020). Ye et al. (2014) showed that HBMECs exhibit these effects more strongly than HUVECS.

3.2 Matrigel and extracellular matrix proteins

COs are commonly embedded in ECM proteins to provide structural support, promote neuroepithelial formation, and enhance growth and differentiation (Lancaster et al., 2013; Qian et al., 2016). While other matrix proteins have been used, Matrigel is the most common and, to our knowledge, the only matrix mixture currently used to vascularize brain organoids. Matrigel is a complex mixture of thousands of peptides but is mainly composed of laminin, collagen IV, and entactin. Matrigel also has significantly higher proportions of glycoproteins compared to native brain ECM but lacks important brain-specific secreted factors and ECM regulators (Cho et al., 2021; Simsa et al., 2021). However, its stiffness is tunable depending on its concentration, with Young's moduli from 5 to 300 Pa (Chaudhuri et al., 2014), which encompasses the range of relevant brain ECM stiffness (Borries et al., 2020; Cho et al., 2021; Simsa et al., 2021).

Since angiogenesis depends on integrin-mediated interactions between vascular ECs and fibrillar ECM proteins, Matrigel is highly supportive for vascular network formation. A thorough ECM proteomic and biomechanical analysis of COs cultured in the absence of Matrigel has yet to be performed, so it is uncertain if cells within COs produce enough fibrillar proteins to sustain vascular networks. On the other hand, embedding COs in Matrigel impairs endogenous expression of ECM proteins, which may negatively impact neural patterning and maturation (Luo et al., 2016). Curiously, when COs are encapsulated with EC-containing Matrigel, complex and dense vascular networks form within the Matrigel shell but struggle to penetrate the CO (Pham et al., 2018), suggesting the CO microenvironment may not be favorable for angiogenesis.

Other ECM protein cocktails have not been used to vascularize COs, perhaps because they are less successful at facilitating CO differentiation. Strobel et al. (2021) showed that the addition of collagen to vascularized mesenchymal organoids did not enhance angiogenesis, and like Matrigel-coated organoids, organoids embedded in collagen secreted less ECM proteins. Similarly, Lancaster et al. (2017) showed that the addition of laminin, collagen, and entactin to Matrigel enhanced laminin-rich basement membrane maintenance and denser cortical plate organization similar to Matrigel alone, but using these matrix proteins in the absence of Matrigel did not recapitulate these effects. Even dissolving Matrigel into the organoid media has been shown to condense neurons and enhance radial organization (Lancaster et al., 2013), prolong NPC maintenance (Kadoshima et al., 2013), and reduce apoptosis (Qian et al., 2016). The exact reasons as to why Matrigel is particularly beneficial for CO culture are not well understood and Matrigel formulas are not fully defined, contributing to heterogeneity in brain organoids and making identification of prolific factors a challenge (Sood et al., 2016).

Despite the unclear relationship between COs and Matrigel, ECs are capable of forming tubular networks on a variety of different purified ECMs, including collagen, laminin, and fibronectin (Andrée et al., 2019).

3.3 Decellularized extracellular matrices

Vascular network formation and stabilization has been improved in other organoid types by the addition of peptides from native tissue ECM, but this has not been tested in COs (Jin et al., 2022). Native tissue ECM hydrogels are thought to contain biochemical and biomechanical signals that recreate biological niches better than non-tissue-specific matrices (Cho et al., 2021). Cells cultured with tissue-matched ECM proteins maintain greater proliferation, phenotypic maintenance, and differentiation capacities than those grown on non-specific ECMs, highlighting the importance of ECM on cell specification and function (Zhang et al., 2009). Neurons cultured on brain ECM-containing substrates exhibit improved neural network formation and enhanced spontaneous firing. These effects are particularly exaggerated on substrates containing fetal brain ECM (Simsa et al., 2021), which has higher collagen content contributing to a stiffer mechanical profile than adult brain ECM (Sood et al., 2016). Like Matrigel, extracted brain ECM is significantly higher in collagen and other glycoproteins than native brain tissues, resulting in similar viscoelastic properties including low stiffness and high storage modulus (Borries et al., 2020; Cho et al., 2021; Simsa et al., 2021). Brain ECM-embedded COs have increased NPC populations, greater survival, stronger forebrain identity, and enhanced electrophysical maturity relative to Matrigel-embedded COs (Cho et al., 2021). In contrast, another study found that brain ECM-embedding causes differences in neuroepithelium budding but is equally as supportive of neuronal maturation as Matrigel (Simsa et al., 2021). Due to the sensitivity of ECs to ECM cues (Katt et al., 2018; Gifre-Renom et al., 2022), growing ECs on brain ECM may drive them towards BMEC specification or make them more compatible for vascularizing COs. However, significant further study is clearly needed to understand to what extent and how exogenous matrix modulates cell behavior within COs.

4 Fluid forces in perfusable vessels

Fluid forces give rise to, mature, and maintain vasculature in the cerebral cortex. Neural tissues receive nutrients and oxygen from the vasculature and expel wastes through cerebrospinal fluid in perivascular spaces. In static culture, solutes travel through organoids *via* diffusion, resulting in a lower concentration of nutrients like glucose, which is crucial for neural function, and oxygen, which has a diffusion limit of

~200 μm (Magliaro et al., 2019), at their cores (Cho et al., 2021). Connecting COs to a flowing media source as a method of delivering nutrients and removing wastes would maintain a more stable metabolic profile, perhaps alleviating culture-related stress and enhancing maturation. Here, we will discuss the benefits of incorporating fluid flow into CO culture as well as current efforts to direct vasculogenesis in COs *via* perfusion.

4.1 Hemodynamic forces during neocortical angiogenesis

ECs lining blood vessel lumens are constantly exposed to fluid shear stresses and plasma interstitial forces resulting from blood flow. Astrocytes mediate the transport of interstitial fluids across the BBB into the ECM, exposing non-vascular cells to bulk convection flow carrying soluble nutrients. This highly regulated process depends on ECs modulating their functions in response to mechanical signals from hemodynamic forces. Shear stresses can alter EC cytoskeletal organization, gene expression, alignment, and migration. High shear stresses reduce EC proliferation and migration needed for early vessel formation, induce cell elongation, and initiate junction formation associated with vessel maturation (Dewey et al., 1981; Cucullo et al., 2013). These effects can be replicated *in vitro* by exposing ECs to shear stresses greater than ~5 dyn/cm^2 (Dewey et al., 1981). In the brain, shear stresses also regulate BBB-specific characteristics such as production of junction proteins that control permeability and transendothelial electrical resistance (Cucullo et al., 2013). The direction and magnitude of shear stresses direct microvascular network formation and autoregulation of cerebral blood flow. Interstitial flow can also contribute to angiogenesis as ECs guide newly forming sprouts towards regions of draining interstitial fluid flow in order to connect capillary beds (Galie et al., 2014). Interstitial flow *in vitro* increases vascular sprouting, network extension, and branching (Abe et al., 2019). Hence, the contribution that these forces have on vessel function cannot be ignored in attempting to form vessels in COs.

4.2 Convective flow in cortical organoid culture

Bioreactors incorporate patterns of fluid movement to improve the efficiency of nutrient transfer by convection rather than diffusion alone. Orbital shakers and spinning bioreactors are commonplace in labs now for organoid culture. In addition to reducing cellular stress, minimizing organoid variability, and supporting the growth of larger and more complex COs, they can support hundreds to thousands of organoids at a time (Qian et al., 2016; Monzel et al., 2017; Trujillo
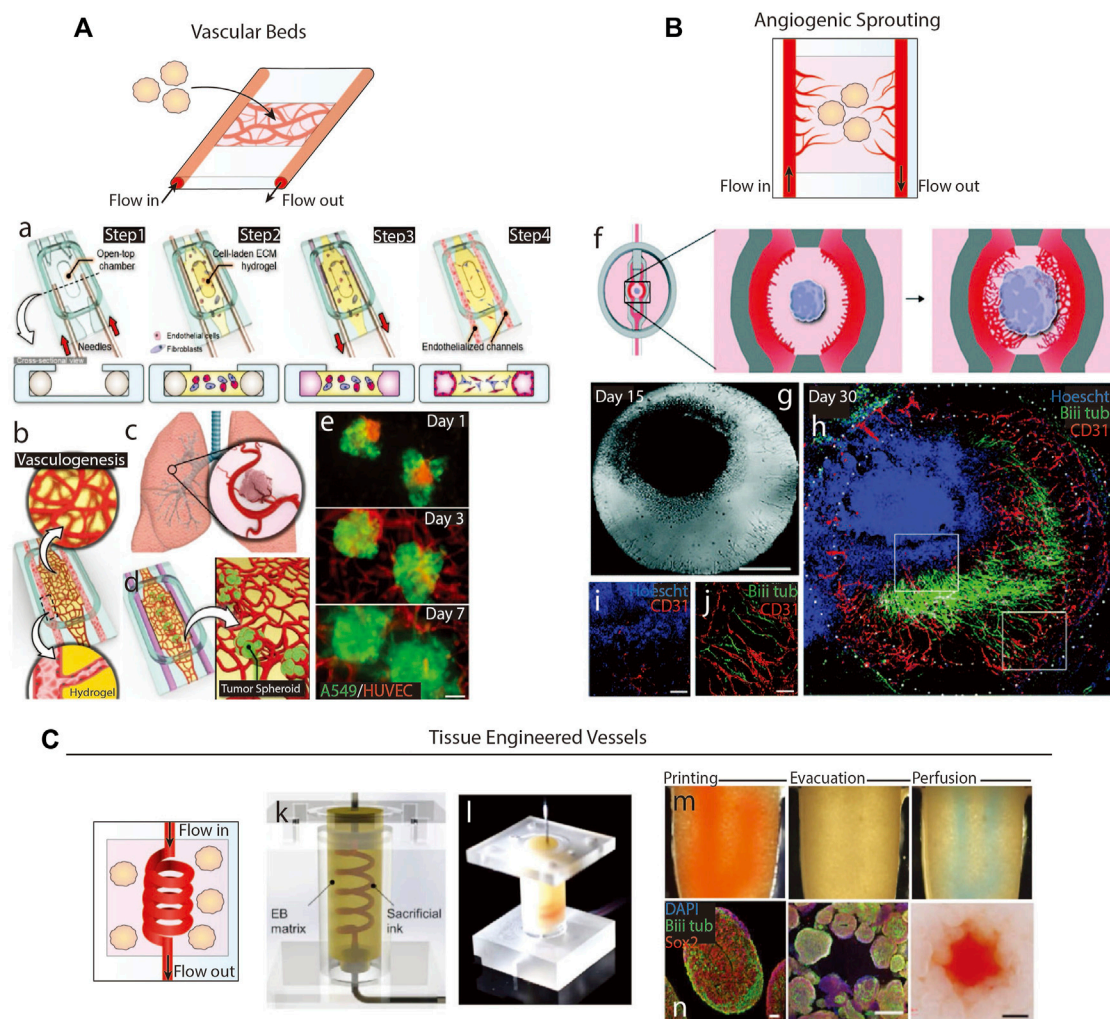
FIGURE 4
Microfluidics-based methods of vascularization. **(A)** Schematic of organoid vascularization using a microfluidic-generated vascular bed. a.b. Schematic showing the fabrication of a vascular bed. c.d.e. Introduction of lung tumor spheroids to the vascular bed. Adapted from (Paek et al., 2019). **(B)** Schematic of organoid vascularization by angiogenic sprouting towards a central brain organoid. g. Image of the organoid and angiogenic sprouts. h.i.j. Organoid and angiogenic sprouts fluorescently stained to show interaction between vessels and neurites. Adapted from (Salmon et al., 2022). **(C)** Schematic of tissue engineered vessel through a matrix containing organoids. k.l. A microfluidic device formed from a sacrificial ink in an embryoid body matrix. When a sacrificial ink is evacuated, the system is then perfusable. n. Images of brain organoids in the device after perfusion. Adapted from (Skylar-Scott et al., 2019).

et al., 2019). However, these bioreactors lack the ability to balance velocities and shear stresses resulting in turbulent flow profiles, which are known to impact brain organoid development and morphology (Goto-Silva et al., 2019; Suong et al., 2021) and angiogenesis. Thus, microfluidic chips have been designed to produce specific and highly accurate flow profiles. When connected to peristaltic pumps, they can produce pulsatile, laminar flow with stable fluid shear stresses like those seen in blood vessels. Studies that have applied laminar flow to COs saw increased metabolic and dopaminergic maturation (Berger et al., 2018), organoid size, and electrophysiological activity (Cho et al., 2021) compared to COs grown in conventional bioreactors. In a

study by Lee et al. (2020) laminar flow even induced the spontaneous formation of superficial but patent vascular networks on organoid surfaces. The next section will discuss how microfluidics have been used to generate perfusing vessels in COs.

4.3 Cortical organoids with vascular beds and tissue engineered vessels

One avenue of vascularizing organoids uses microfluidic devices to generate vascular beds through an organoid-

containing matrix (Figure 4A). Shear stress is applied to two parallel EC-coated channels to induce EC migration into the central organoid-containing matrix until ECs from opposite channels meet to form a vessel. These systems have been applied to a variety of 3D tissues, including cancer spheroids (Figures 4Aa–e) (Paek et al., 2019), lung cell spheroids (Nashimoto et al., 2017), and COs (Salmon et al., 2022), and generate vascular networks with small inner-diameters and continuous lumens capable of transporting solutes (Paek et al., 2019; Lee et al., 2020). Similarly, organoids may be placed in an avascular hydrogel matrix between perfusing microfluidic channels from which ECs sprout towards the organoids in response to signaling gradients (Figure 4B). Salmon et al. (2022) showed that applying this method to COs resulted in short, highly branched vessels with heightened expression of functional vascular markers. While vessel invasion along COs' edges was frequent, less than half of the COs saw vessel invasion into their cores, suggesting that additional approaches are necessary to achieve fully integrated vessels (Figures 4Bf–h).

A second microfluidic method is to encapsulate organoids and a sacrificial scaffold in a hydrogel, remove the sacrificial scaffold, and perfuse media through the empty space (Figure 4C). These channels can be seeded with vascular cells, either by coating the sacrificial scaffold with cells or backfilling the empty space with cells, to generate a cell layer representing vascular luminal layers. Simple sacrificial scaffolds include needles, strings, or solid structures that can be manually removed from hydrogels, resulting in linear channels with diameters matching the structure's diameter, usually greater than 100 μm (Neumann et al., 2003; Chrobak et al., 2006). Biomaterials can be used to make sacrificial scaffolds of more complex geometries and sizes by various fabrication methods. Common sacrificial materials include natural polymers, e.g., alginate and gelatin, or synthetic polymers, e.g., pluronics, Gel-Methacrylate, poly (vinyl alcohol), and poly (ethylene glycol), that undergo a phase transition when exposed to a specific environmental condition. For example, Skylar-Scott et al. (2019) 3D printed a gelatin scaffold through a matrix containing brain organoids, degraded the scaffold *via* heat, and backfilled the empty space with HUVECs (Figures 4Ck–n). Over 20 h of perfusion, no angiogenic sprouting into the organoid matrix was noted, but they found organoid viability increased. Similar studies using tumor fragments (Hu et al., 2018) and spheroids (Kwak and Lee, 2020) embedded in fibrin gels also saw increased viability, but only the later study observed sprouting. Even though Kwak & Lee only perfused their systems for 5 days, they used higher shear stresses at 5 dyn/cm^2, which is sufficient to induce sprouting (Dewey et al., 1981). Vascular network formation was enhanced by coating the tumor spheroids with ECs, which sprouted towards the tissue engineered (TE) vessel in return. Alternatively, sprouting from the perfusing TE vessels may be achievable by inserting artificial chemokine gradients (Seah et al., 2020), since organoids may not produce strong enough signals to induce angiogenesis in low shear stress conditions.

4.4 Cortical organoid engraftment into non-human hosts

Organoids implanted into animal hosts offer a less controlled but efficient method to becoming vascularized. A host's vessels invade an engrafted organoid in response to proangiogenic signals, in order to prevent graft death (Figure 5A). Mansour et al. (2018) transplanted brain organoids into mice cortices and identified vascular invasion as early as 5 days post-transplantation that directly correlated with decreased apoptosis and survivability of the graft (Figures 5Aa–e). Engrafted organoids also were invaded by host immune cells and made synaptic connections with host neurons across different regions of the brain, resulting in neuronal synchronization. Extensive host vascularization also increases neuronal differentiation and activity, enhanced survival (Daviaud et al., 2018; Bao et al., 2021), and reduced cellular stress (Bhaduri et al., 2020).

Engraftment of pre-vascularized tissues supports better vessel invasion and graft survivability than avascular grafts (Figures 5Af–h) (Ben-Shaul et al., 2019; Shi et al., 2020; Wassmer et al., 2022). With brain organoids, such experiments have been performed in mouse cortical tissue (Pham et al., 2018; Cakir et al., 2019; Shi et al., 2020), subcutaneous tissue (Cakir et al., 2019), and chicken chorion allantois membranes (Wörsdörfer et al., 2019) to highlight the ability of *in vitro*-derived vessels to sustain hemodynamic mechanical forces and retain solutes as evidence functional luminal junctions. However, it is uncertain if *in vitro*-derived vessels obtain these capabilities because of *in vivo* hemodynamic forces or host-graft cell signaling rather than acquiring these mature functional characteristics as a result of *in vitro* vascularization efforts.

5 Successes and challenges in cortical organoid vascularization

To assess the accomplishments and describe future directions that CO vascularization should take, here we summarize what we believe will be necessary to achieve fully functional CO vascularization in the context of current methods (Table 1). These criteria cover vascular architecture, mature BBB characteristics, and neurovascular function. Of these categories, engrafted organoids *in vivo* are most successful. They vascularized robustly and show strongest evidence of vessel maturity and perfusability, but because they rely on non-human hosts, COs vascularized *in vivo* are rendered imperfect representations of human neurovasculature and unsuitable for modeling human disease or development. For this reason, they are not a reliable approach to CO vascularization, although they may provide insight on biological cues needed to further the
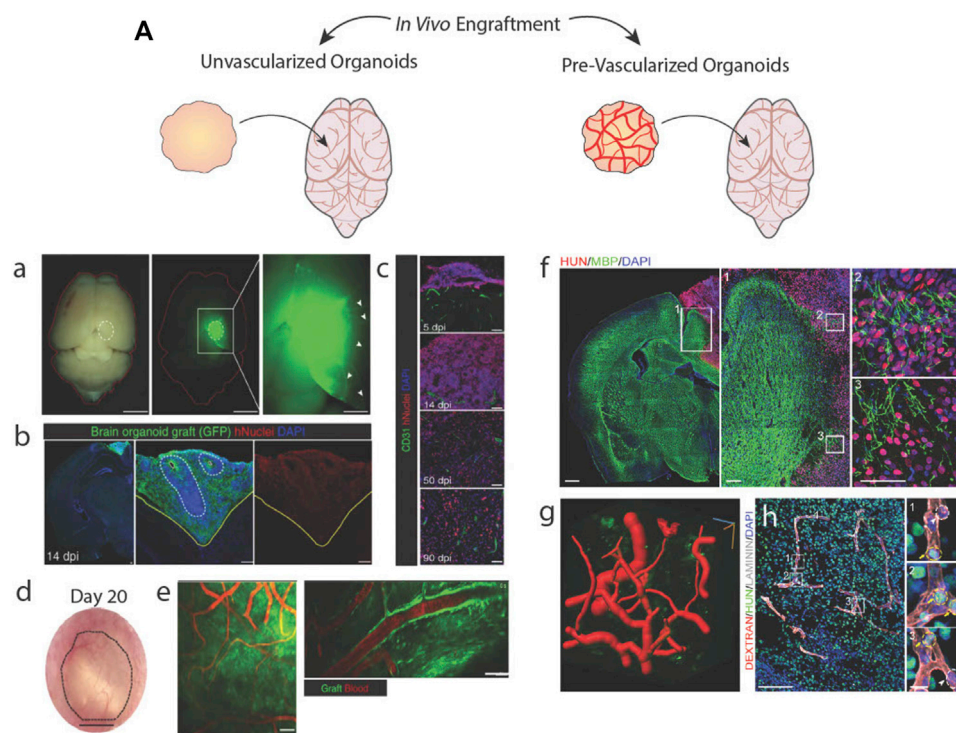
FIGURE 5
Brain organoid vascularization by engraftment into animal hosts. **(A)** Schematic of unvascularized or pre-vascularized organoids being engrafted in living mice brains. a.b. An unvascularized GFP + brain organoid located in a mouse brain stains positive for a human-specific nuclear marker. c.d. Engrafted brain organoid exhibits invasive host vessels. e. Vessels located in the graft perfuse blood. Adapted from (Mansour et al., 2018). A vascularized brain organoid located in a mouse brain stains positive for a human-specific marker and interacts with host tissues. g. Computational rendering of vessels within the organoid graft. h. Vessels within the graft perfuse a labelled dextran injected into the host mouse. Adapted from (Shi et al., 2020).

vascularization field. We will continue with a comparison of *in vitro* methods.

Cortical microvasculature is dense, highly branched with narrow vessels and a continuous interconnected lumen. *In vitro* approaches using self-organizing vessels have reached the greatest success to date in recapitulating these features. The best of these being EC addition during organoid formation, which results in dense and highly branched networks that span the majority of the organoid, with vessels preferentially localized in outermost neuronal layers (Cakir et al., 2019; Shi et al., 2020). Yet, biologically-based self-organization approaches may be incapable of accomplishing the same level of vessel interconnectedness as models that incorporate flow, since the development of this feature relies on fluid forces. Methods that utilize angiogenic sprouting–vascular spheroid fusion, vascular bed devices, and angiogenic sprouting devices–benefit from incorporating 3D pre-assembled vascular networks, which arise from a process we do not yet fully understand and thus have been challenging to recreate in organoids. TE vessels currently fall short in producing realistic vasculature, often generating vessels adjacent to organoids rather than through them. This lack of integration is accompanied by a general lack of complexity, as

TE vessels are usually significantly larger than cortical microvessels and lack branches due to limitations by their fabrication methods (Chen et al., 2021). Realistic vascular architecture may remain unachievable in the tissue engineering field until fabrication methods capable of smaller, more exact features are available.

Maturity of neurovascular tissue is indicated by neuronal electrical activity, cell-type specification, and properties of the BBB, such as EC tight junction formation and recruitment of pericytes and astrocytes. ECs in COs typically accelerate neural differentiation, decrease cell death, and enhance spontaneous electrical activity in COs (Cakir et al., 2019; Shi et al., 2020; Kook et al., 2022), regardless of vascular architecture. Most biological vascularization methods also note mature BBB characteristics, focusing on junction-associated protein expression and changes to astrocyte populations. Vessels formed *via* sprouting from a perfusion source, e.g., those that use microfluidic devices, presumably have fully formed tight junctions necessary for sustaining fluid flow, therefore this is not always reported. However, the effects of vascularization of COs by engineering methods as a whole are understudied. While convective flow is

TABLE 1 Comparison of organoid vascularization methods. Table outlining the success of each organoid vascularization method at achieving realistic vessel architecture, perfusability, and mature blood brain barrier characteristics.

	Biological self-organization			Microfluidic engineering			Living tissues
	Endothelial Cell Addition	Spheroid Fusion	Co-Differentiation	Vascular Beds	Angiogenic Sprouting	Tissue Engineered Blood Vessels	*In Vivo* Engraftment
Human-Only	Yes	Yes	Yes	Yes	Yes	Yes	No
Integrated	Variable	Variable	Variable	Variable	Variable	No	Yes
Complex	Yes	Yes	Variable	Yes	Yes	No	Yes
Continuous	Yes	Yes	Variable	Yes	Yes	Yes	Yes
Perfusable	No	No	No	Yes	Yes	Yes	Yes
Tight Junction Formation	Yes	Yes	Yes	Yes	Yes	Yes	To be determined
Reduced Hypoxia	Variable	To be determined	Variable	Yes	Yes	Yes	To be determined
Reduced Necrosis/ Apoptosis	Variable	Variable	Variable	To be determined	To be determined	Yes	Yes
Accelerated Neural Maturation	Variable	Variable	Variable	To be determined	Yes	To be determined	To be determined
Pericyte Recruitment	Variable	Yes	Variable	To be determined	To be determined	To be determined	To be determined
Enriched Astrocyte Population	Variable	Yes	Variable	To be determined	To be determined	To be determined	Yes
Enhanced Electrical Activity	Variable	To be determined	Variable	To be determined	To be determined	To be determined	Variable

known to be highly beneficial for CO culture (Qian et al., 2016; Monzel et al., 2017; Trujillo et al., 2019; Cho et al., 2021), most microfluidics-based organoid vascularization methods focus on reducing hypoxia and neglect addressing other areas of neurovascular maturity (Skylar-Scott et al., 2019). Thus, without proper evaluation of maturity criteria in engineering-based approaches, we can only conclude that biological self-organized vessels currently have the greatest benefits towards neurovascular maturity.

Since sustaining blood flow is a key function of vasculature, it is important for vascularized COs to be patent and perfusable. COs vascularized by biological approaches are unable to be connected directly to a flow source or fluidics pump. Some studies add fluorophore-conjugated dextrans to culture media and allow these sugars to flow into biologically-vascularized COs *via* diffusion or convective flow in bioreactors, suggesting that the vessels are patent (Cakir et al., 2019; Shi et al., 2020). Vascularization methods dependent on microfluidic systems provide the most reliably patent and perfusable vasculature. Because they are hooked up to pumps with controllable perfusion rates, realistic shear stresses and flow profiles and a

constant supply of nutrients are easily achievable. Thus, microfluidic-based methods are the best models for replicating hemodynamic forces and perfusion.

6 Conclusion

Vasculature provides tissues with means to transport nutrients and oxygen, metabolites, and cellular signals that facilitate growth and maintain homeostasis. Without vasculature, brain organoids are limited in their differentiation capabilities, morphological patterning, and electrophysiological functions. Here, we have identified different methods of CO vascularization from the most recent and notable published studies and evaluated their successes and drawbacks as they relate to cortical vasculature *in vivo*. Each of the discussed methods has their own advantages, but none fully capture the form and function of an *in vivo* neurovascular unit. Nevertheless, these studies have elucidated important relationships between cells and biochemical and biophysical forces and highlighted the capabilities of *in vitro* cultures in recapitulating aspects of the neurovascular microenvironment. Moving forward, the CO vascularization field

may benefit from combining current approaches and looking into the use of new biomaterials and ECM technologies as well as improving existing techniques.

Data availability statement

The original contributions presented in the study are included in the article/Supplementary Material, further inquiries can be directed to the corresponding authors.

Author contributions

EL, AM, and AE conceived of and wrote the manuscript.

Funding

Acknowledgments

Conflict of interest

AM is a co-founder and has an equity interest in TISMOO, a company dedicated to genetic analysis and brain organoid modeling focusing on therapeutic applications customized for autism spectrum disorder and other neurological disorders with genetic origins. The terms of this arrangement have been reviewed and approved by the University of California San Diego in accordance with its conflict-of-interest policies.

The remaining authors declare that the research was conducted in the absence of any commercial or financial relationships that could be construed as a potential conflict of interest.

Publisher's note

All claims expressed in this article are solely those of the authors and do not necessarily represent those of their affiliated organizations, or those of the publisher, the editors and the reviewers. Any product that may be evaluated in this article, or claim that may be made by its manufacturer, is not guaranteed or endorsed by the publisher.

Supplementary material

The Supplementary Material for this article can be found online at: https://www.frontiersin.org/articles/10.3389/fbioe.2022.1048731/full#supplementary-material

References

Abe, Y., Watanabe, M., Chung, S., Kamm, R. D., Tanishita, K., and Sudo, R. (2019). Balance of interstitial flow magnitude and vascular endothelial growth factor concentration modulates three-dimensional microvascular network formation. *Apl. Bioeng.* 3, 036102. doi:10.1063/1.5094735

Ahn, Y., An, J. H., Yang, H. J., Lee, D. G., Kim, J., Koh, H., et al. (2021). Human blood vessel organoids penetrate human cerebral organoids and form a vessel-like system. *Cells* 10, 2036. doi:10.3390/CELLS10082036

Andrée, B., Ichanti, H., Kalies, S., Heisterkamp, A., Strauß, S., Vogt, P. M., et al. (2019). Formation of three-dimensional tubular endothelial cell networks under defined serum-free cell culture conditions in human collagen hydrogels. *Sci. Rep.* 9, 5437. doi:10.1038/s41598-019-41985-6

Bao, Z., Fang, K., Miao, Z., Li, C., Yang, C., Yu, Q., et al. (2021). Human cerebral organoid implantation alleviated the neurological deficits of traumatic brain injury in mice. *Oxid. Med. Cell. Longev.* 2021, 1–16. doi:10.1155/2021/6338722

Bekes, I., Haunerdinger, V., Sauter, R., Holzheu, I., Janni, W., Wöckel, A., et al. (2017). Slit2/Robo4 signaling: Potential role of a VEGF-antagonist pathway to regulate luteal permeability. *Geburtshilfe Frauenheilkd.* 77, 73–80. doi:10.1055/S-0042-113461

Ben-Shaul, S., Landau, S., Merdler, U., and Levenberg, S. (2019). Mature vessel networks in engineered tissue promote graft–host anastomosis and prevent graft thrombosis. *Proc. Natl. Acad. Sci. U. S. A.* 116, 2955–2960. doi:10.1073/pnas.1814238116

Berger, E., Magliaro, C., Paczia, N., Monzel, A. S., Antony, P., Linster, C. L., et al. (2018). Millifluidic culture improves human midbrain organoid vitality and differentiation. *Lab. Chip* 18, 3172–3183. doi:10.1039/C8LC00206A

Bergmann, S., Lawler, S. E., Qu, Y., Fadzen, C. M., Wolfe, J. M., Regan, M. S., et al. (2018). Blood–brain-barrier organoids for investigating the permeability of CNS therapeutics. *Nat. Protoc.* 1312 (13), 2827–2843. doi:10.1038/s41596-018-0066-x

Bhaduri, A., Andrews, M. G., Mancia Leon, W., Jung, D., Shin, D., Allen, D., et al. (2020). Cell stress in cortical organoids impairs molecular subtype specification. *Nature* 578, 142–148. doi:10.1038/s41586-020-1962-0

Borries, M., Barooji, Y. F., Yennek, S., Grapin-Botton, A., Berg-Sørensen, K., and Oddershede, L. B. (2020). Quantification of visco-elastic properties of a Matrigel for organoid development as a function of polymer concentration. *Front. Phys.* 8, 475. doi:10.3389/fphy.2020.579168

Budday, S., and Steinmann, P. (2018). On the influence of inhomogeneous stiffness and growth on mechanical instabilities in the developing brain. *Int. J. Solids Struct.* 132-133, 31–41. doi:10.1016/j.ijsolstr.2017.08.010

Cakir, B., Xiang, Y., Tanaka, Y., Kural, M. H., Parent, M., Kang, Y. J., et al. (2019). Engineering of human brain organoids with a functional vascular-like system. *Nat. Methods* 1611 (16), 1169–1175. doi:10.1038/s41592-019-0586-5

Campisi, M., Shin, Y., Osaki, T., Hajal, C., Chiono, V., and Kamm, R. D. (2018). 3D self-organized microvascular model of the human blood-brain barrier with endothelial cells, pericytes and astrocytes. *Biomaterials* 180, 117–129. doi:10.1016/J.BIOMATERIALS.2018.07.014

Canovic, E. P., Qing, B., Mijailovic, A. S., Jagielska, A., Whitfield, M. J., Kelly, E., et al. (2016). Characterizing multiscale mechanical properties of brain tissue using atomic force microscopy, impact indentation, and rheometry. *J. Vis. Exp.* (115), 54201. doi:10.3791/54201

Carmeliet, P. (2005). Angiogenesis in life, disease and medicine. *Nature* 438, 932–936. doi:10.1038/nature04478

Carmeliet, P., and Tessier-Lavigne, M. (2005). Common mechanisms of nerve and blood vessel wiring. *Nature* 436, 193–200. doi:10.1038/nature03875

Cassel De Camps, C., Aslani, S., Stylianesis, N., Nami, H., Mohamed, N. V., Durcan, T. M., et al. (2022). Hydrogel mechanics influence the growth and development of embedded brain organoids. *ACS Appl. Bio Mat.* 5, 214–224. doi:10.1021/acsabm.1c01047

Chaudhuri, O., Koshy, S. T., Branco Da Cunha, C., Shin, J. W., Verbeke, C. S., Allison, K. H., et al. (2014). Extracellular matrix stiffness and composition jointly regulate the induction of malignant phenotypes in mammary epithelium. *Nat. Mat.* 1310 (13), 970–978. doi:10.1038/nmat4009

Chen, E. P., Toksoy, Z., Davis, B. A., and Geibel, J. P. (2021). 3D bioprinting of vascularized tissues for *in vitro* and *in vivo* applications. *Front. Bioeng. Biotechnol.* 9, 664188. doi:10.3389/fbioe.2021.664188

Cheng, D., Jayne, R. K., Tamborini, A., Eyckmans, J., White, A. E., and Chen, C. S. (2019). Studies of 3D directed cell migration enabled by direct laser writing of curved wave topography. *Biofabrication* 11, 021001. doi:10.1088/1758-5090/AB047F

Cho, A. N., Jin, Y., An, Y., Kim, J., Choi, Y. S., Lee, J. S., et al. (2021). Microfluidic device with brain extracellular matrix promotes structural and functional maturation of human brain organoids. *Nat. Commun.* 121 (12), 4730–4823. doi:10.1038/s41467-021-24775-5

Chrobak, K. M., Potter, D. R., and Tien, J. (2006). Formation of perfused, functional microvascular tubes *in vitro*. *Microvasc. Res.* 71, 185–196. doi:10.1016/J.MVR.2006.02.005

Cipolla, M. J. (2009). Anatomy and ultrastructure. Available at: https://www.ncbi.nlm.nih.gov/books/NBK53086/(Accessed September 14, 2022).

Cucullo, L., Hossain, M., Tierney, W., and Janigro, D. (2013). A new dynamic *in vitro* modular capillaries-venules modular system: Cerebrovascular physiology in a box. *BMC Neurosci.* 14, 18–12. doi:10.1186/1471-2202-14-18

Dailamy, A., Parekh, U., Katrekar, D., Kumar, A., McDonald, D., Moreno, A., et al. (2021). Programmatic introduction of parenchymal cell types into blood vessel organoids. *Stem Cell. Rep.* 16, 2432–2441. doi:10.1016/j.stemcr.2021.08.014

Daviaud, N., Friedel, R. H., and Zou, H. (2018). Vascularization and engraftment of transplanted human cerebral organoids in mouse cortex. *eNeuro* 5, ENEURO.0219–18.2018. doi:10.1523/ENEURO.0219-18.2018

Dewey, C. F., Bussolari, S. R., Gimbrone, M. A., and Davies, P. F. (1981). The dynamic response of vascular endothelial cells to fluid shear stress. *J. Biomech. Eng.* 103, 177–185. doi:10.1115/1.3138276

Di Lullo, E., and Kriegstein, A. R. (2017). The use of brain organoids to investigate neural development and disease. *Nat. Rev. Neurosci.* 18, 573–584. doi:10.1038/nrn.2017.107

Du, Y., Herath, S. C. B., Wang, Q. G., Wang, D. A., Asada, H. H., and Chen, P. C. Y. (2016). Three-dimensional characterization of mechanical interactions between endothelial cells and extracellular matrix during angiogenic sprouting. *Sci. Rep.* 6, 21362. doi:10.1038/srep21362

Fallenstein, G. T., Hulce, V. D., and Melvin, J. W. (1969). Dynamic mechanical properties of human brain tissue. *J. Biomech.* 2, 217–226. doi:10.1016/0021-9290(69)90079-7

Galie, P. A., Nguyen, D. H. T., Choi, C. K., Cohen, D. M., Janmey, P. A., and Chen, C. S. (2014). Fluid shear stress threshold regulates angiogenic sprouting. *Proc. Natl. Acad. Sci. U. S. A.* 111, 7968–7973. doi:10.1073/pnas.1310842111

Giandomenico, S. L., and Lancaster, M. A. (2017). Probing human brain evolution and development in organoids. *Curr. Opin. Cell. Biol.* 44, 36–43. doi:10.1016/J.CEB.2017.01.001

Gifre-Renom, L., Daems, M., Luttun, A., and Jones, E. A. V. (2022). Organ-specific endothelial cell differentiation and impact of microenvironmental cues on endothelial heterogeneity. *Int. J. Mol. Sci.* 23, 1477. doi:10.3390/IJMS23031477

Goto-Silva, L., Ayad, N. M. E., Herzog, I. L., Silva, N. P., Lamien, B., Orlande, H. R. B., et al. (2019). Computational fluid dynamic analysis of physical forces playing a role in brain organoid cultures in two different multiplex platforms. *BMC Dev. Biol.* 19, 3–10. doi:10.1186/s12861-019-0183-y

Ham, O., Jin, Y. B., Kim, J., and Lee, M. O. (2020). Blood vessel formation in cerebral organoids formed from human embryonic stem cells. *Biochem. Biophys. Res. Commun.* 521, 84–90. doi:10.1016/J.BBRC.2019.10.079

Hu, M., Dailamy, A., Lei, X. Y., Parekh, U., McDonald, D., Kumar, A., et al. (2018). Facile engineering of long-term culturable *ex vivo* vascularized tissues using biologically derived matrices. *Adv. Healthc. Mat.* 7, 1800845. doi:10.1002/adhm.201800845

Jain, R. K., Au, P., Tam, J., Duda, D. G., and Fukumura, D. (2005). Engineering vascularized tissue. *Nat. Biotechnol.* 23, 821–823. doi:10.1038/nbt0705-821

Jalil Razavi, M., Zhang, T., Liu, T., and Wang, X. (2015). Cortical folding pattern and its consistency induced by biological growth. *Sci. Rep.* 5, 14477–14514. doi:10.1038/srep14477

James, D., Nam, H. S., Seandel, M., Nolan, D., Janovitz, T., Tomishima, M., et al. (2010). Expansion and maintenance of human embryonic stem cell–derived endothelial cells by TGFβ inhibition is Id1 dependent. *Nat. Biotechnol.* 28, 161–166. doi:10.1038/nbt.1605

Jeon, J. S., Bersini, S., Whisler, J. A., Chen, M. B., Dubini, G., Charest, J. L., et al. (2014). Generation of 3D functional microvascular networks with human mesenchymal stem cells in microfluidic systems. *Integr. Biol.* 6, 555–563. doi:10.1039/C3IB40267C

Jin, Y., Hyun Heo, J., Kang, D., and Ju Seo, S. (2022). Engineering the extracellular matrix for organoid culture. *Int. J. Stem Cells* 15, 60–69. doi:10.15283/ijsc21190

Kadoshima, T., Sakaguchi, H., Nakano, T., Soen, M., Ando, S., Eiraku, M., et al. (2013). Self-organization of axial polarity, inside-out layer pattern, and species-specific progenitor dynamics in human ES cell-derived neocortex. *Proc. Natl. Acad. Sci. U. S. A.* 110, 20284–20289. doi:10.1073/pnas.1315710110

Karzbrun, E., Kshirsagar, A., Cohen, S. R., Hanna, J. H., and Reiner, O. (2018). Human brain organoids on a chip reveal the physics of folding. *Nat. Phys.* 14, 515–522. doi:10.1038/S41567-018-0046-7

Katt, M. E., Linville, R. M., Mayo, L. N., Xu, Z. S., and Searson, P. C. (2018). Functional brain-specific microvessels from iPSC-derived human brain microvascular endothelial cells: The role of matrix composition on monolayer formation. *Fluids Barriers CNS* 15, 7–12. doi:10.1186/s12987-018-0092-7

Kook, M. G., Lee, S. E., Shin, N., Kong, D., Kim, D. H., Kim, M. S., et al. (2022). Generation of cortical brain organoid with vascularization by assembling with vascular spheroid. *Int. J. Stem Cells* 15, 85–94. doi:10.15283/IJSC21157

Kwak, T. J., and Lee, E. (2020). *In vitro* modeling of solid tumor interactions with perfused blood vessels. *Sci. Rep.* 10, 20142–20149. doi:10.1038/s41598-020-77180-1

Lancaster, M. A., Corsini, N. S., Wolfinger, S., Gustafson, E. H., Phillips, A. W., Burkard, T. R., et al. (2017). Guided self-organization and cortical plate formation in human brain organoids. *Nat. Biotechnol.* 35, 659–666. doi:10.1038/nbt.3906

Lancaster, M. A., and Knoblich, J. A. (2014). Generation of cerebral organoids from human pluripotent stem cells. *Nat. Protoc.* 9, 2329–2340. doi:10.1038/nprot.2014.158

Lancaster, M. A., Renner, M., Martin, C. A., Wenzel, D., Bicknell, L. S., Hurles, M. E., et al. (2013). Cerebral organoids model human brain development and microcephaly. *Nature* 501, 373–379. doi:10.1038/nature12517

Lee, S. W. L., Campisi, M., Osaki, T., Possenti, L., Mattu, C., Adriani, G., et al. (2020). Modeling nanocarrier transport across a 3D *in vitro* human blood-brain–barrier microvasculature. *Adv. Healthc. Mat.* 9, 1901486. doi:10.1002/ADHM.201901486

Lippmann, E. S., Azarin, S. M., Kay, J. E., Nessler, R. A., Wilson, H. K., Al-Ahmad, A., et al. (2012). Derivation of blood-brain barrier endothelial cells from human pluripotent stem cells. *Nat. Biotechnol.* 30, 783–791. doi:10.1038/nbt.2247

Lu, T. M., Houghton, S., Magdeldin, T., Barcia Durán, J. G., Minotti, A. P., Snead, A., et al. (2021). Pluripotent stem cell-derived epithelium misidentified as brain microvascular endothelium requires ETS factors to acquire vascular fate. *Proc. Natl. Acad. Sci. U. S. A.* 118, e2016950118. doi:10.1073/pnas.2016950118

Luo, C., Lancaster, M. A., Castanon, R., Nery, J. R., Knoblich, J. A., and Ecker, J. R. (2016). Cerebral organoids recapitulate epigenomic signatures of the human fetal brain. *Cell. Rep.* 17, 3369–3384. doi:10.1016/J.CELREP.2016.12.001

Ma, S., Kwon, H. J., Johng, H., Zang, K., and Huang, Z. (2013). Radial glial neural progenitors regulate nascent brain vascular network stabilization via inhibition of Wnt signaling. *PLoS Biol.* 11, e1001469. doi:10.1371/JOURNAL.PBIO.1001469

Maeda, N. (2015). Proteoglycans and neuronal migration in the cerebral cortex during development and disease. *Front. Neurosci.* 9, 98. doi:10.3389/fnins.2015.00098.NLM

Magliaro, C., Mattei, G., Iacoangeli, F., Corti, A., Piemonte, V., and Ahluwalia, A. (2019). Oxygen consumption characteristics in 3D constructs depend on cell density. *Front. Bioeng. Biotechnol.* 7, 251. doi:10.3389/fbioe.2019.00251

Mandrycky, C., Hadland, B., and Zheng, Y. (2020). 3D curvature-instructed endothelial flow response and tissue vascularization. *Sci. Adv.* 6, 3629–3645. doi:10.1126/sciadv.abb3629

Mansour, A. A., Gonçalves, J. T., Bloyd, C. W., Li, H., Fernandes, S., Quang, D., et al. (2018). An *in vivo* model of functional and vascularized human brain organoids. *Nat. Biotechnol.* 36, 432–441. doi:10.1038/nbt.4127

Marín-Padilla, M., and Knopman, D. S. (2011). Developmental aspects of the intracerebral microvasculature and perivascular spaces: Insights into brain response

to late-life diseases. *J. Neuropathol. Exp. Neurol.* 70, 1060–1069. doi:10.1097/NEN. 0b013e31823ac627

Marshall, J. J., and Mason, J. O. (2019). Mouse vs man: Organoid models of brain development & disease. *Brain Res.* 1724, 146427. doi:10.1016/J.BRAINRES.2019. 146427

Mastrullo, V., Cathery, W., Velliou, E., Madeddu, P., and Campagnolo, P. (2020). Angiogenesis in tissue engineering: As nature intended? *Front. Bioeng. Biotechnol.* 8, 188. doi:10.3389/fbioe.2020.00188

McCoy, M. G., Wei, J. M., Choi, S., Goerger, J. P., Zipfel, W., and Fischbach, C. (2018). Collagen fiber orientation regulates 3D vascular network formation and alignment. *ACS Biomater. Sci. Eng.* 4, 2967–2976. doi:10.1021/acsbiomaterials. 8b00384

Monzel, A. S., Smits, L. M., Hemmer, K., Hachi, S., Moreno, E. L., Van Wuellen, T., et al. (2017). Derivation of human midbrain-specific organoids from neuroepithelial Stem Cells. *Stem Cell. Rep.* 8, 1144–1154. doi:10.1016/j.stemcr. 2017.03.010

Nashimoto, Y., Hayashi, T., Kunita, I., Nakamasu, A., Torisawa, Y. S., Nakayama, M., et al. (2017). Integrating perfusable vascular networks with a three-dimensional tissue in a microfluidic device. *Integr. Biol.* 9, 506–518. doi:10.1039/C7IB00024C

Neumann, T., Nicholson, B. S., and Sanders, J. E. (2003). Tissue engineering of perfused microvessels. *Microvasc. Res.* 66, 59–67. doi:10.1016/S0026-2862(03) 00040-2

Paek, J., Park, S. E., Lu, Q., Park, K. T., Cho, M., Oh, J. M., et al. (2019). Microphysiological engineering of self-assembled and perfusable microvascular beds for the production of vascularized three-dimensional human microtissues. *ACS Nano* 13, 7627–7643. doi:10.1021/acsnano.9b00686

Palikuqi, B., Nguyen, D. H. T., Li, G., Schreiner, R., Pellegata, A. F., Liu, Y., et al. (2020). Adaptable haemodynamic endothelial cells for organogenesis and tumorigenesis. *Nature* 585, 426–432. doi:10.1038/s41586-020-2712-z

Pasca, A. M., Sloan, S. A., Clarke, L. E., Tian, Y., Makinson, C. D., Huber, N., et al. (2015). Functional cortical neurons and astrocytes from human pluripotent stem cells in 3D culture. *Nat. Methods* 12, 671–678. doi:10.1038/nmeth.3415

Pasut, A., Becker, L. M., Cuypers, A., and Carmeliet, P. (2021). Endothelial cell plasticity at the single-cell level. *Angiogenesis* 24, 311–326. doi:10.1007/S10456-021-09797-3

Patsch, C., Challet-Meylan, L., Thoma, E. C., Urich, E., Heckel, T., O'Sullivan, J. F., et al. (2015). Generation of vascular endothelial and smooth muscle cells from human pluripotent stem cells. *Nat. Cell. Biol.* 17, 994–1003. doi:10.1038/NCB3205

Pham, M. T., Pollock, K. M., Rose, M. D., Cary, W. A., Stewart, H. R., Zhou, P., et al. (2018). Generation of human vascularized brain organoids. *Neuroreport* 29, 588–593. doi:10.1097/WNR.0000000000001014

Puppo, F., and Muotri, A. R. (2022). Network and microcircuitry development in human brain organoids. *Biol. Psychiatry* S0006-3223 (22), 01437–01438. doi:10. 1016/j.biopsych.2022.07.006

Qian, X., Nguyen, H. N., Song, M. M., Hadiono, C., Ogden, S. C., Hammack, C., et al. (2016). Brain-region-specific organoids using mini-bioreactors for modeling ZIKV exposure. *Cell.* 165, 1238–1254. doi:10.1016/j.cell.2016.04.032

Qian, X., Song, H., and Ming, G. L. (2019). Brain organoids: Advances, applications and challenges. *Development* 146, dev166074. doi:10.1242/dev. 166074

Rauch, U. (2007). Brain matrix: Structure, turnover and necessity. *Biochem. Soc. Trans.* 35, 656–660. doi:10.1042/BST0350656

Rosenstein, J., Krum, J., and Ruhrberg, C. (2010). VEGF in the nervous system. *Organogenesis* 6, 107–114. doi:10.4161/ORG.6.2.11687

Rossi, G., Manfrin, A., and Lutolf, M. P. (2018). Progress and potential in organoid research. *Nat. Rev. Genet.* 19, 671–687. doi:10.1038/s41576-018-0051-9

Rubin, L. L., Hall, D. E., Porter, S., Barbu, K., Cannon, C., Horner, H. C., et al. (1991). A cell culture model of the blood-brain barrier. *J. Cell. Biol.* 115, 1725–1735. doi:10.1083/JCB.115.6.1725

Salmon, I., Grebenyuk, S., Abdel Fattah, A. R., Rustandi, G., Pilkington, T., Verfaillie, C., et al. (2022). Engineering neurovascular organoids with 3D printed microfluidic chips. *Lab. Chip* 22, 1615–1629. doi:10.1039/D1LC00535A

Seah, I., Zhao, X., Lin, Q., Liu, Z., Su, S. Z. Z., Yuen, Y. S., et al. (2020). Use of biomaterials for sustained delivery of anti-VEGF to treat retinal diseases. *Eye* 348 (34), 1341–1356. doi:10.1038/s41433-020-0770-y

Shi, Y., Sun, L., Wang, M., Liu, J., Zhong, S., Li, R., et al. (2020). Vascularized human cortical organoids (vOrganoids) model cortical development *in vivo*. *PLoS Biol.* 18, e3000705. doi:10.1371/JOURNAL.PBIO.3000705

Simsa, R., Rothenbücher, T., Gürbüz, H., Ghosheh, N., Emneus, J., Jenndahl, L., et al. (2021). Brain organoid formation on decellularized porcine brain ECM hydrogels. *PLoS One* 16, e0245685. doi:10.1371/JOURNAL.PONE.0245685

Siqueira, M., Francis, D., Gisbert, D., Gomes, F. C. A., and Stipursky, J. (2018). Radial glia cells control angiogenesis in the developing cerebral cortex through TGF-β1 signaling. *Mol. Neurobiol.* 55, 3660–3675. doi:10.1007/s12035-017-0557-8

Skylar-Scott, M. A., Huang, J. Y., Lu, A., Ng, A. H. M., Duenki, T., Liu, S., et al. (2022). Orthogonally induced differentiation of stem cells for the programmatic patterning of vascularized organoids and bioprinted tissues. *Nat. Biomed. Eng.* 64 (6), 449–462. doi:10.1038/s41551-022-00856-8

Skylar-Scott, M. A., Uzel, S. G. M., Nam, L. L., Ahrens, J. H., Truby, R. L., Damaraju, S., et al. (2019). Biomanufacturing of organ-specific tissues with high cellular density and embedded vascular channels. *Sci. Adv.* 5, eaaw2459. doi:10. 1126/sciadv.aaw2459

Sood, D., Chwalek, K., Stuntz, E., Pouli, D., Du, C., Tang-Schomer, M., et al. (2016). Fetal brain extracellular matrix boosts neuronal network formation in 3D bioengineered model of cortical brain tissue. *ACS Biomater. Sci. Eng.* 2, 131–140. doi:10.1021/acsbiomaterials.5b00446

Strobel, H. A., Gerton, T., and Hoying, J. B. (2021). Vascularized adipocyte organoid model using isolated human microvessel fragments. *Biofabrication* 13, 035022. doi:10.1088/1758-5090/ABE187

Suong, D. N. A., Imamura, K., Inoue, I., Kabai, R., Sakamoto, S., Okumura, T., et al. (2021). Induction of inverted morphology in brain organoids by vertical-mixing bioreactors. *Commun. Biol.* 4, 1213. doi:10.1038/S42003-021-02719-5

Trujillo, C. A., Gao, R., Negraes, P. D., Gu, J., Buchanan, J., Preissl, S., et al. (2019). Complex oscillatory waves emerging from cortical organoids model early human brain network development. *Cell. Stem Cell.* 25, 558–569.e7. e7. doi:10.1016/J. STEM.2019.08.002

Trujillo, C. A., and Muotri, A. R. (2018). Brain organoids and the study of neurodevelopment. *Trends Mol. Med.* 24, 982–990. doi:10.1016/j.molmed.2018. 09.005

Tsai, P. S., Kaufhold, J. P., Blinder, P., Friedman, B., Drew, P. J., Karten, H. J., et al. (2009). Correlations of neuronal and microvascular densities in murine cortex revealed by direct counting and colocalization of nuclei and vessels. *J. Neurosci.* 29, 14553–14570. doi:10.1523/JNEUROSCI.3287-09.2009

Wassmer, C.-H., Lebreton, F., Bellofatto, K., Perez, L., Cottet-Dumoulin, D., Andres, A., et al. (2022). Bio-engineering of pre-vascularized islet organoids for the treatment of type 1 diabetes. *Transpl. Int.* 0, 10214. doi:10.3389/TI.2021.10214

Wörsdörfer, P., Dalda, N., Kern, A., Krüger, S., Wagner, N., Kwok, C. K., et al. (2019). Generation of complex human organoid models including vascular networks by incorporation of mesodermal progenitor cells. *Sci. Rep.* 9, 15663–15713. doi:10.1038/s41598-019-52204-7

Xing, C. Y., Tarumi, T., Liu, J., Zhang, Y., Turner, M., Riley, J., et al. (2017). Distribution of cardiac output to the brain across the adult lifespan. *J. Cereb. Blood Flow. Metab.* 37, 2848–2856. doi:10.1177/0271678X16676826

Ye, M., Sanchez, H. M., Hultz, M., Yang, Z., Bogorad, M., Wong, A. D., et al. (2014). Brain microvascular endothelial cells resist elongation due to curvature and shear stress. *Sci. Rep.* 41 (4), 4681–4686. doi:10.1038/srep04681

Yeh, Y. T., Hur, S. S., Chang, J., Wang, K. C., Chiu, J. J., Li, Y. S., et al. (2012). Matrix stiffness regulates endothelial cell proliferation through septin 9. *PLoS One* 7, e46889. doi:10.1371/JOURNAL.PONE.0046889

Yeung, T., Georges, P. C., Flanagan, L. A., Marg, B., Ortiz, M., Funaki, M., et al. (2005). Effects of substrate stiffness on cell morphology, cytoskeletal structure, and adhesion. *Cell. Motil. Cytoskelet.* 60, 24–34. doi:10.1002/CM.20041

Zhang, Y., He, Y., Bharadwaj, S., Hammam, N., Carnagey, K., Myers, R., et al. (2009). Tissue-specific extracellular matrix coatings for the promotion of cell proliferation and maintenance of cell phenotype. *Biomaterials* 30, 4021–4028. doi:10.1016/J.BIOMATERIALS.2009.04.005

Zhou, X., Rowe, R. G., Hiraoka, N., George, J. P., Wirtz, D., Mosher, D. F., et al. (2008). Fibronectin fibrillogenesis regulates three-dimensional neovessel formation. *Genes. Dev.* 22, 1231–1243. doi:10.1101/GAD.1643308

Wnt signaling directs human pluripotent stem cells into vascularized cardiac organoids with chamber-like structures

Po-Yu Liang[1†], Yun Chang[1,2†], Gyuhyung Jin[1,2], Xiaojun Lian[3*] and Xiaoping Bao[1,2*]

[1]Davidson School of Chemical Engineering, Purdue University, West Lafayette, IN, United States, [2]Purdue University Center for Cancer Research, West Lafayette, IN, United States, [3]Department of Biomedical Engineering, The Huck Institutes of the Life Sciences, Department of Biology, The Pennsylvania State University, University Park, PA, United States

Heart diseases are leading cause of death around the world. Given their unique capacity to self-renew and differentiate into all types of somatic cells, human pluripotent stem cells (hPSCs) hold great promise for heart disease modeling and cardiotoxic drug screening. hPSC-derived cardiac organoids are emerging biomimetic models for studying heart development and cardiovascular diseases, but it remains challenging to make mature organoids with a native-like structure *in vitro*. In this study, temporal modulation of Wnt signaling pathway co-differentiated hPSCs into beating cardiomyocytes and cardiac endothelial-like cells in 3D organoids, resulting in cardiac endothelial-bounded chamber formation. These chambered cardiac organoids exhibited more mature membrane potential compared to cardiac organoids composed of only cardiomyocytes. Furthermore, a better response to toxic drugs was observed in chamber-contained cardiac organoids. In summary, spatiotemporal signaling pathway modulation may lead to more mature cardiac organoids for studying cardiovascular development and diseases.

KEYWORDS

human pluripotent stem cells, cardiomyocyte, cardiac endothelial cells, heart organoid, disease modeling

Introduction

Cardiovascular disorders, including congenital heart defects and cardiovascular disease, remain as a global health issue due to their high mortality worldwide (Balakumar and Kaur, 2009; Kadooka et al., 2021; Zhao et al., 2021). Developing new therapies is also challenging, since few drug candidates succeed to pass pre- or clinical trials and many of them are removed from the market due to severe cardiac toxicity (Balakumar and Kaur, 2009; Matoba and Egashira, 2011). To quickly screen effective and safe therapies, more authentic models of human heart are needed to be developed for pre-clinical research (Balakumar and Kaur, 2009; Matoba and Egashira, 2011; Jiang et al., 2017). For the past decades, animal model-based cardiac research has provided the basis

for understanding heart development and diseases (Camacho et al., 2016). Due to the natural species difference, novel *in vitro* human cardiac models are urgently needed for a better understanding of tissue changes during development and diseases (Coales et al., 2016; Mathur et al., 2016; Veldhuizen et al., 2019). Human pluripotent stem cells (hPSCs) have been differentiated into cardiomyocytes (CMs) for heart disease modeling and cardiotoxic drug testing (Lian et al., 2013, 2015). However, commonly used two-dimensional (2D) culture models could not fully recapitulate the three-dimensional (3D) complexity of native human heart, in which the presence of various cardiovascular cell types in the defined geometry and cell-cell as well as cell-extracellular matrix (ECM) interactions play an essential role.

hPSCs are capable of differentiating and self-organizing into 3D tissue structures, termed organoids that resemble embryo-like tissues or organs (Drakhlis et al., 2021; Lewis-Israeli et al., 2021; Tan et al., 2021). While native-like organoid models have been widely implemented for various organs, the implementation of heart-like organoids remains challenging. Classic heart muscle engineering approaches that assemble pre-differentiated or primary cardiac cell types into 3D aggregates were commonly used to form cardiac microtissues that mimic adult-like heart tissue (Giacomelli et al., 2017). For example, Voges et al. (2017) and Mills et al. (2019) embedded hPSC-derived CMs in mixed collagen I-Matrigel substrates to form cardiac organoids that reproduced some aspects of native human heart, including structured endothelial networks and epicardium. Vessel-like structures were observed in some areas of cardiac organoids, formed similarly by embedding hPSC aggregates in Matrigel (Drakhlis et al., 2021). Addition of exogenous VEGF in the cardioids has occasionally led to an intact endothelial layer that lines cardiac cavity (Hofbauer et al., 2021). Cardiac organoid studies that focus on native heart-like morphological aspects are still lacking. During embryo development, heart-forming progenitor cells extend across the midline and fuse into the heart tube, which then give rise to the myocardium and endocardium. After undergoing looping, the heart tube forms chambers (Tan and Lewandowski, 2020). To better recapitulate the complex native heart, there is a strong demand to bridge this technological and knowledge gap.

We have previously identified the temporal roles of canonical Wnt signaling during CM and epicardial cell differentiation from hPSCs (Bao et al., 2017b). Here, we first demonstrated reactivation of Wnt signaling at cardiac progenitor stage directed hPSCs into VE-cadherin (VE-cad)+ cardiac endothelial-like cells, which were incorporated into cardiac organoid differentiation and led to endothelial-bounded chamber formation. The resulting chambered cardiac organoids contained structured endothelial cells and CMs, and exhibited more mature membrane potential compared to cardiac organoids composed of only CMs. Furthermore, vascularized cardiac organoids were better in modeling cardiac response to

toxic drugs. In summary, hPSC-derived vascularized cardiac organoids hold great potential for heart disease modeling and therapeutic drug screening.

Materials and methods

Maintenance of human pluripotent stem cells

H9 and H13 cell lines were purchased from WiCell and maintained on Matrigel- or iMatrix 511-coated plates in mTeSR plus medium at 37°C in humidified atmosphere with 5% CO_2 according to our previously published method (Chang et al., 2022b).

Hanging drop preparation for embryoid body formation

For embryoid body (EB) formation, 20 µl droplets were formed by pipetting on the inner side of a 96-well U-bottom culture plate lid. Droplets contained 100,000 hPSCs/ml and were composed of mTeSR Plus supplemented with 5 µM Y-27632 (Cayman Chemical) and iMatrx-511 (1:100). 100 µl PBS was added to each well before returning the lid to culture plate. After 24 h, EBs were transferred with a pipette to a new 96-well U-bottom culture plate and cultured in mTeSR Plus +5 µM Y-27632 for 1 day. The resulting EBs were then ready for further differentiation.

Cardiovascular differentiation of hPSCs in 2D or 3D embryoid body cultures

For cardiac differentiation, hPSCs were seeded onto Matrigel-coated 6-well plate in mTeSR plus medium with 5 µM Y27632 at a cell density between 10,000 and 80,000 cell/cm^2 after dissociating with 1 ml Versene solution. At day 0, hPSCs were treated with 6 µM CHIR99021 (Cayman Chemical) in RPMI for 24 h. At day 1 and day 2, the medium was switched to RPMI + B27 without insulin. At day 3 and day 4, 50% of medium was replaced with RPMI + B27 without insulin containing 4 µM Wnt-C59. At day 5, RPMI + B27 medium was used and changed every 3 days for CM differentiation. For cardiac organoid differentiation, EBs were treated with 9 µM CHIR99021 in RPMI medium for 24 h. At day 1 and day 2, the medium was switched to RPMI + B27-insulin medium. At day 3 and day 4, 50% of medium was replaced with RPMI + B27-insulin medium containing 4 µM Wnt-C59. At day 5, RPMI + B27 medium was used. At day 7, EBs were treated with EBM™ endothelial cell medium (Lonza) containing 50 µg VEGF (Peprotech) and 4.5 µM CHIR99021. At day 8 and day 9,

medium change with EBM medium containing 50 μg VEGF. Between day 10 to day 15, EBs were treated with EBM medium containing 50 μg VEGF and 2.5 μM TGFβ inhibitor A83-001.

Immunostaining and flow cytometry analysis

Immunostaining analysis was performed as described in an earlier publication (Chang et al., 2022a). Briefly, cells were fixed in PBS −/− containing 4% formaldehyde for 15 min in dark and incubated with appropriate antibodies in 5% nonfat dry-milk solution containing 0.4% Triton X-100. After gently washing and nuclei staining, cells were then imaged in a Leica DMi-8 microscope and processed in ImageJ. To collect differentiated cells for flow cytometry analysis, a 70 μm strainer was used to filter cells, followed by centrifugation and fixation in PBS −/− containing 1% formaldehyde for 20 min. The resulting cells were then permeabilized with ice-cold 90% methanol for at least 30 min and washed with PBS −/− solution containing 1% bovine serum albumin (BSA) and 0.1% Triton X-100. The cells were then stained with antibodies and analyzed in an Accuri C6 plus flow cytometry (Beckton Dickinson). Flow Jo software was used to process collected flow data.

FluoVolt™ membrane potential kit analysis

Prepare labeling solution by adding FluoVolt™ dye (Invitrogen) into RPMI + B27 medium (1:50), and remove old medium from human heart organoid cultures. After washing heart organoids with PBS twice, organoids were treated with 100 μl of labeling solution under room temperature for 20 min. After removing dye solution and washing with PBS twice, organoids were kept in a 96-well U-bottom culture plate with 100 μl of PBS. The resulting cells were then live imaged in a Leica DMi-8 microscope.

Hematoxylin and eosin staining of cardiac organoids

Differentiated cardiac organoids were fixed in 4% formaldehyde for 30 min, and embedded in paraffin. Slices with a thickness of 5 μm were incised for H&E staining, and the stained slice was imaged in a digital microscope.

Cardiac organoids for drug treatment

The viability of cardiac organoids was assessed by the MTS assay. Differentiated cardiac organoids were incubated with

50 μg/ml of Temozolomide and subjected for MTS assay analysis at different time points. After Temozolomide treatment, old medium was aspirated and 100 μl of fresh culture medium containing 16.7% MTS stock solution was added into each well for 4 h at 37°C. The plates were then centrifuged at 2,000 rpm for 10 min. 80 μl supernatant in each cell culture well was pipetted into a well of 96-well microplate and measured at 490 nm for the absorbance of formazan through a SpectraMax iD3 microplate reader.

Results and discussion

Wnt signaling regulates cardiac endothelial cell specification

Cardiac endothelial cells arise from ISL1+NKX2.5 + progenitors during embryo development (Roden, 2013; Coales et al., 2016; Vermeulen et al., 2019) and we have previously identified ISL1+NKX2.5 + progenitor cells during cardiac differentiation from hPSCs (Bao et al., 2017c). To identify signaling pathways regulating cardiac endothelial cell specification, we used the H13 VE-cad-GFP reporter cell line that we previously made (Bao et al., 2017a) (Figure 1A) and expressed high levels of pluripotent markers (Supplementary Figures S1A–C). Day 6 cardiac progenitors derived from VE-cad-GFP reporter hPSCs were treated with different small molecules for 48 h (day 7 to day 9) (Figure 1B). CHIR99021 (CHIR), a GSK-3β inhibitor, significantly enhanced the expression of VE-Cad + cells (Figures 1C,D), which was blocked by a Wnt inhibitor Wnt-C59. Treatment with SB431542, a TGFβ signaling inhibitor, further promoted VE-Cad + cell generation (Figure 1D). The resulting cardiac endothelial cells did not express endocardium marker NFATc1 (Figure 1E), indicating their potential identity of cardiac microvascular endothelial cells. Notably, CHIR treatment from day 7–8 did not eliminate CM differentiation and led to co-differentiation of CM and cardiac endothelial cells, highlighting their application in multicellular cardiac organoid differentiation.

Transcriptome analysis of hPSC-derived cardiac endothelial cells

To further confirm the identity of cardiac endothelial cells (CECs) derived from hPSCs, we sorted day 15 VE-cad + cells and performed bulk RNA sequencing (RNA-seq) analysis. Hierarchical clustering analysis of RNA-seq expression data demonstrated that day 15 CECs were closely clustered to primary human cardiac microvascular endothelial cells (hCMEC) (Figure 2A). Notably, examination of specific
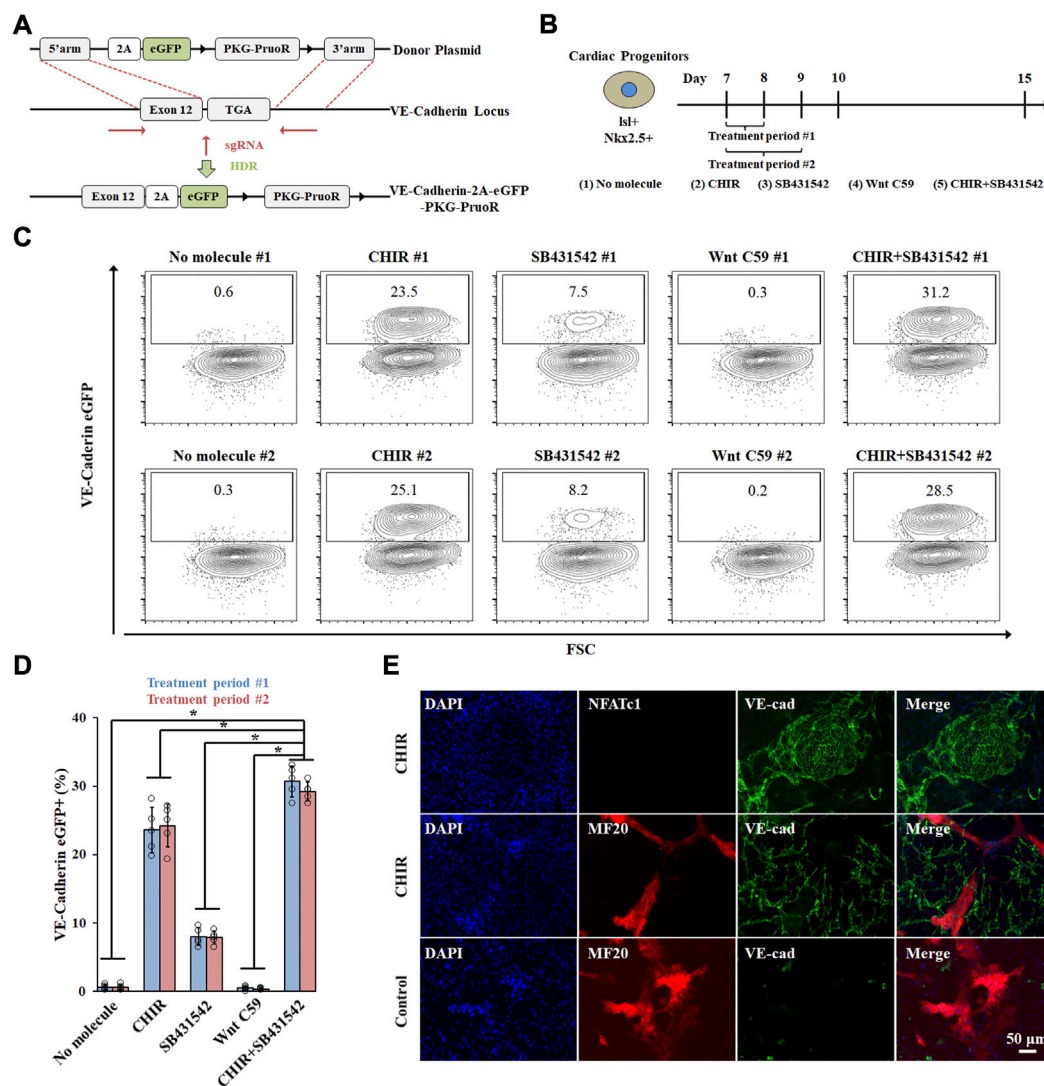
FIGURE 1
Cardiac endothelial cell generation by modulating Wnt signaling pathway. **(A)** Schematic illustration of knock-in strategy at the AAVS1 safe harbor locus. **(B)** Schematic of the protocol used to differentiate hPSCs towards cardiac endothelial cells. Conditions of 1–5 were applied to cardiovascular differentiation either from day 7–8 (period #1) or day 7–9 (period #2). VE-cad-GFP expression was analyzed by flow cytometry **(C)** and quantitated in **(D)**, n = 5, *$p < 0.05$. **(E)** Immunostaining images of cardiomyocytes and cardiac endothelial cells.

endocardial endothelial cell (EEC) genes revealed that hPSC-derived CECs displayed higher expression levels of EEC and barrier makers as compared to hCMEC and HUVEC (Figure 2B). Hierarchical clustering analysis revealed all endothelial cell populations were clustered together as compared to undifferentiated hPSCs, though hPSC-derived CECs were relatively far away from primary hCMEC and HUVEC, indicating the relative immaturity of hPSC-derived CECs. Consistent with this data, relatively lower expression levels of general endothelial and vascular endothelial cell (VEC) markers were also observed in hPSC-derived CECs. In summary, bulk RNA-seq analysis suggested the similarity between our hPSC-derived CECs and primary hCMEC in global transcriptome expression.

Vascularized cardiac organoids derived from hPSCs

To better recapitulate multicellular heart development *in vivo*, we incorporated our 2D co-differentiation protocol into the classic hanging drop platform for embryoid body (EB) formation in 3D. hPSC EBs were cultured and expanded for 2 days prior to cardiac differentiation. Similar to 2D monolayer
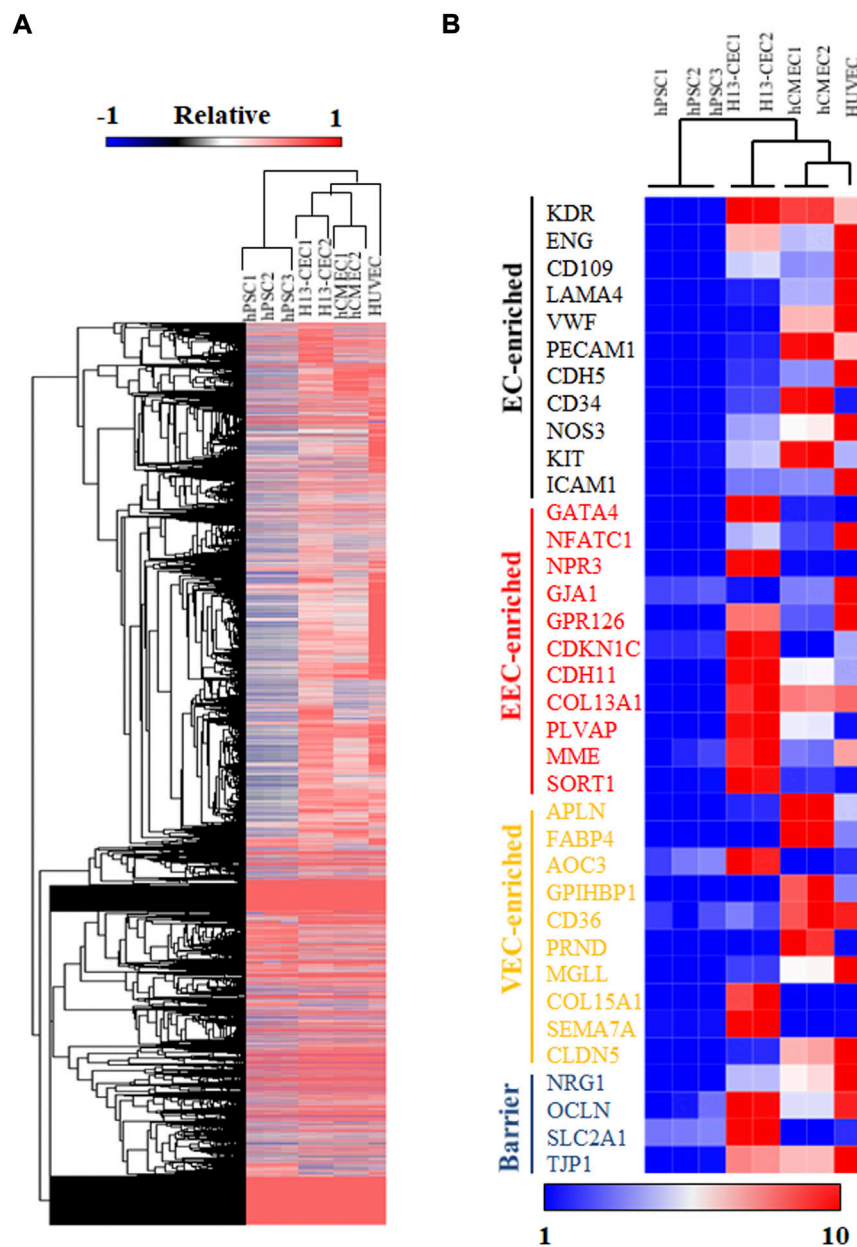
FIGURE 2
RNA sequencing (RNA-seq) analysis was performed on hPSC-differentiated cardiac endothelial cells (CECs). **(A)** Hierarchical clustering of RNA-seq expression data of hPSCs, H13-derived cardiac endothelial cells (CEC), primary human cardiac microvascular endothelial cells (hCMEC), and human umbilical vein endothelial cells (HUVEC). **(B)** Heatmap and hierarchical clustering analysis of selected endothelial cell markers.

culture, GiWi method was used to induce cardiac progenitor generation in 3D EBs (Figure 3A). After day 6, EBs were treated with CHIR and vascular endothelial growth factor (VEGF) to form vascularized cardiac organoids *via* co-differentiation of CMs and CECs in 3D, or left untreated to form regular cardiac organoids composed of CMs only. VEGF is a commonly used growth factor for inducing vascularization in

tissues (Shibuya, 2011; Poldervaart et al., 2014). While both kinds of organoids showed a significant increase in size throughout the differentiation protocol (Figure 3B and Supplementary Figure S2A), vascularized cardiac organoids displayed obvious chamber formation, which was also confirmed by H&E staining of sliced organoids (Figures 3C,D, Supplementary Figure S2B). Immunostaining analysis on sliced cardiac organoids
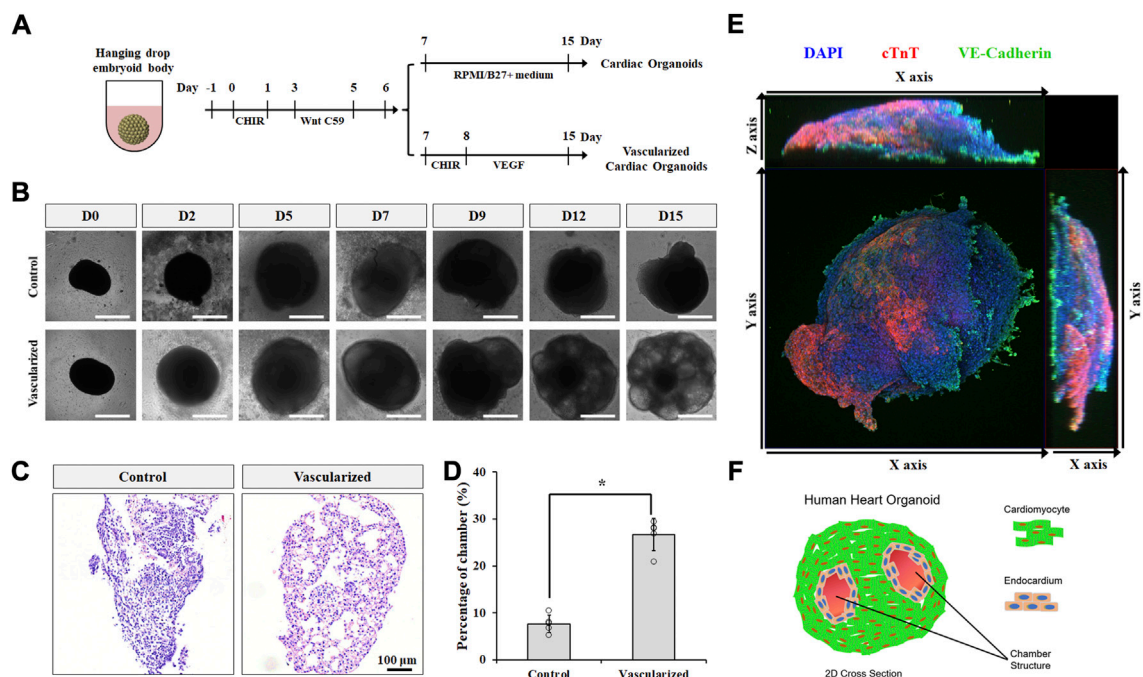
FIGURE 3
Vascularized cardiac organoids were derived from hPSCs. **(A)** Schematic of the protocol used to differentiate hPSCs towards vascularized cardiac organoids. **(B)** Brightfield images of hPSC-derived cardiac organoids at indicated days. **(C)** H&E staining showed sliced cardiac organoids. **(D)** Chamber area quantification in different cardiac organoids. n = 4. Confocal microscope image **(E)** and illustration **(F)** of vascularized cardiac organoids.
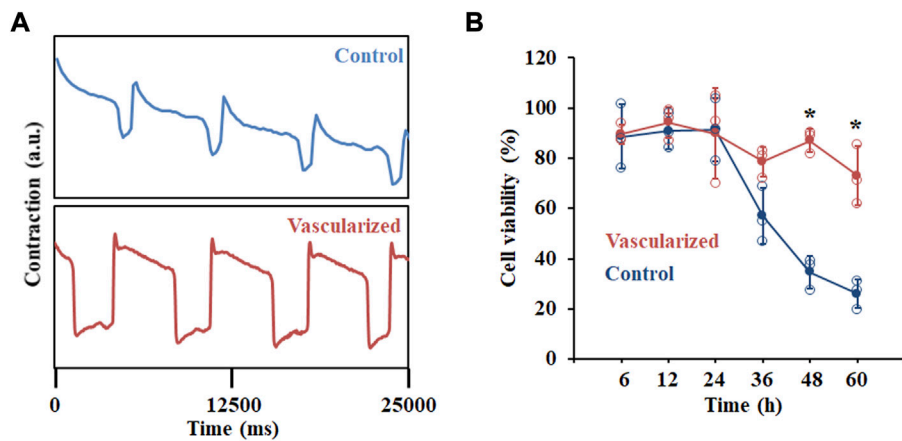
FIGURE 4
Functional analysis of hPSC-derived cardiac organoids. **(A)** Representative contraction amplitude plots of hPSC-derived cardiac organoids using a voltage dye. **(B)** Cell viability analysis of hPSC-derived cardiac organoids after Temozolomide treatment at indicated time points. n = 3.

confirmed the presence of structured endothelial cells and CMs in 3D (Figure 3E). Flow cytometry analysis showed about 2% CECs and 62% CMs, and 19% CECs and 48% CMs presented in control and vascularized organoids (Supplementary Figures S3A,B), respectively. Overall, the resulting vascularized cardiac organoids contained significantly more chambers, mimicking the anatomical structure of the developing embryonic heart (Figure 3F).

hPSC-derived vascularized cardiac organoids better respond to cardiotoxic drugs

A critical feature of *in vitro*-derived organoids is to recapitulate at least one specialized aspect of the native tissues or organs. In terms of cardiac tissue, the contractile activity of hPSC-derived cardiac organoids is an important function. We first analyzed the beating rates of our hPSC-derived cardiac organoids with a highly sensitive voltage dye (Figure 4A). Compared with CM organoids, vascularized cardiac organoids contain more cell types with human heart-like layered structures. In addition, CECs were reported to promote the trabeculation and maturation of CMs (Mikryukov et al., 2021). All these additional features of our vascularized cardiac organoids may lead to a better cardiac model for cardiotoxic drug testing. To test this hypothesis, we studied the possibility of modelling chemotherapy drug-induced cardiotoxicity with cardiac organoids derived from hPSCs by treating them with supernatant medium of chemical drug Temozolomide (Temo)-treated tumor cells. This drug was widely used for glioblastoma treatment, which though induced cardiotoxic and pro-fibrotic effects, causing or exacerbating heart failure. hPSC-derived cardiac organoids were treated with 0.2 and 2 µg/ml Temo, which broke the integral morphology of cardiac organoids (Supplementary Figure S4), possibly due to cell death induced by the drug (Figure 4B).

Conlusion

In this study, we identified that Wnt signaling regulates hPSC differentiation into cardiac endothelial cells (CECs) *in vitro*, consistent with its role in native heart development *in vivo*. (Mukhopadhyay, 2021). Modulation of Wnt signaling also enabled the co-differentiation of CM and CEC differentiation in 2D and 3D cultures. Notably, cardiac organoids treated with the Wnt activator CHIR99021 displayed more chamber formation and more mature beating curve compared with cardiac organoids composed of only CMs. The resulting vascularized cardiac organoids also served as a better model for toxicity analysis of antitumor drugs. In conclusion, hPSC-derived vascularized cardiac organoids hold great potential for heart disease modeling and therapeutic drug screening.

Data availability statement

The datasets presented in this study can be found in online repositories. The names of the repository/repositories and accession number(s) can be found in the article/ Supplementary Material.

Author contributions

P-YL, YC, XL, and XB conceived and designed the experiments. P-YL, YC, and GJ contributed to the study design and assisted in data collection and analysis. P-YL, YC, and XB wrote the manuscript with support from all authors.

Conflict of interest

The authors declare that the research was conducted in the absence of any commercial or financial relationships that could be construed as a potential conflict of interest.

Publisher's note

All claims expressed in this article are solely those of the authors and do not necessarily represent those of their affiliated organizations, or those of the publisher, the editors and the reviewers. Any product that may be evaluated in this article, or claim that may be made by its manufacturer, is not guaranteed or endorsed by the publisher.

Supplementary material

The Supplementary Material for this article can be found online at: https://www.frontiersin.org/articles/10.3389/fbioe.2022.1059243/full#supplementary-material

References

Balakumar, P., and Kaur, J. (2009). Arsenic exposure and cardiovascular disorders: An overview. *Cardiovasc. Toxicol.* 9, 169–176. doi:10.1007/s12012-009-9050-6

Bao, X., Bhute, V. J., Han, T., Qian, T., Lian, X., and Palecek, S. P. (2017a). Human pluripotent stem cell-derived epicardial progenitors can differentiate to endocardial-like endothelial cells. *Bioeng. Transl. Med.* 2, 191–201. doi:10.1002/btm2.10062

Bao, X., Lian, X., Hacker, T. A., Schmuck, E. G., Qian, T., Bhute, V. J., et al. (2017b). Long-term self-renewing human epicardial cells generated from pluripotent stem cells under defined xeno-free conditions. *Nat. Biomed. Eng.* 1, 0003. doi:10.1038/s41551-016-0003

Bao, X., Lian, X., Qian, T., Bhute, V. J., Han, T., and Palecek, S. P. (2017c). Directed differentiation and long-term maintenance of epicardial cells derived from human pluripotent stem cells under fully defined conditions. *Nat. Protoc.* 12, 1890–1900. doi:10.1038/nprot.2017.080

Camacho, P., Fan, H., Liu, Z., and He, J. Q. (2016). Small mammalian animal models of heart disease. *Am. J. Cardiovasc. Dis.* 6, 70–80.

Chang, Y., Syahirah, R., Oprescu, S. N., Wang, X., Jung, J., Cooper, S. H., et al. (2022a). Chemically-defined generation of human hemogenic endothelium and definitive hematopoietic progenitor cells. *Biomaterials* 285, 121569. doi:10.1016/j.biomaterials.2022.121569

Chang, Y., Syahirah, R., Wang, X., Jin, G., Torregrosa-Allen, S., Elzey, B. D., et al. (2022b). Engineering chimeric antigen receptor neutrophils from human pluripotent stem cells for targeted cancer immunotherapy. *Cell Rep.* 40, 111128. doi:10.1016/J.CELREP.2022.111128

Coales, P., Sumigray, K. D., Terwilliger, M., Lechler, T., Bajka, B. H., Rigby, N. M., et al. (2016). *Principles of anatomy & physiology, cardiovascular system: Blood vessels and hemodynamics.* 13th ed. New York, United States: John Wiley & Sons, 816. ISBN 978-0470-56510-0. Nature.

Drakhlis, L., Biswanath, S., Farr, C. M., Lupanow, V., Teske, J., Ritzenhoff, K., et al. (2021). Human heart-forming organoids recapitulate early heart and foregut development. *Nat. Biotechnol.* 39, 737–746. doi:10.1038/s41587-021-00815-9

Giacomelli, E., Bellin, M., Sala, L., van Meer, B. J., Tertoolen, L. G. J., Orlova, V. V., et al. (2017). Three-dimensional cardiac microtissues composed of cardiomyocytes and endothelial cells co-differentiated from human pluripotent stem cells. *Development* 144, 1008–1017. doi:10.1242/dev.143438

Hofbauer, P., Jahnel, S. M., Papai, N., Giesshammer, M., Deyett, A., Schmidt, C., et al. (2021). Cardioids reveal self-organizing principles of human cardiogenesis. *Cell* 184, 3299–3317.e22. doi:10.1016/j.cell.2021.04.034

Jiang, W., Rutherford, D., Vuong, T., and Liu, H. (2017). Nanomaterials for treating cardiovascular diseases: A review. *Bioact. Mat.* 2, 185–198. doi:10.1016/j.bioactmat.2017.11.002

Kadooka, K., Miyachi, H., Kimura, T., Asano, K., Onodera, K., Masunaga, N., et al. (2021). Non-cardiovascular disorders in a contemporary cardiovascular intensive care unit in Japan. *J. Cardiol.* 78, 166–171. doi:10.1016/j.jjcc.2021.03.002

Lewis-Israeli, Y. R., Wasserman, A. H., Gabalski, M. A., Volmert, B. D., Ming, Y., Ball, K. A., et al. (2021). Self-assembling human heart organoids for the modeling of cardiac development and congenital heart disease. *Nat. Commun.* 12, 5142. doi:10.1038/s41467-021-25329-5

Lian, X., Bao, X., Zilberter, M., Westman, M., Fisahn, A., Hsiao, C., et al. (2015). Chemically defined, albumin-free human cardiomyocyte generation. *Nat. Methods* 12, 595–596. doi:10.1038/nmeth.3448

Lian, X., Zhang, J., Azarin, S. M., Zhu, K., Hazeltine, L. B., Bao, X., et al. (2013). Directed cardiomyocyte differentiation from human pluripotent stem cells by modulating Wnt/β-catenin signaling under fully defined conditions. *Nat. Protoc.* 8, 162–175. doi:10.1038/nprot.2012.150

Mathur, A., Ma, Z., Loskill, P., Jeeawoody, S., and Healy, K. E. (2016). *In vitro* cardiac tissue models: Current status and future prospects. *Adv. Drug Deliv. Rev.* 96, 203–213. doi:10.1016/j.addr.2015.09.011

Matoba, T., and Egashira, K. (2011). Anti-inflammatory gene therapy for cardiovascular disease. *Curr. Gene Ther.* 11, 442–446. doi:10.2174/156652311798192888

Mikryukov, A. A., Mazine, A., Wei, B., Yang, D., Miao, Y., Gu, M., et al. (2021). BMP10 signaling promotes the development of endocardial cells from human pluripotent stem cell-derived cardiovascular progenitors. *Cell Stem Cell* 28, 96–111.e7. doi:10.1016/j.stem.2020.10.003

Mills, R. J., Parker, B. L., Quaife-Ryan, G. A., Voges, H. K., Needham, E. J., Bornot, A., et al. (2019). Drug screening in human PSC-cardiac organoids identifies pro-proliferative compounds acting via the mevalonate pathway. *Cell Stem Cell* 24, 895–907.e6. doi:10.1016/j.stem.2019.03.009

Mukhopadhyay, M. (2021). Recapitulating early cardiogenesis *in vitro*. *Nat. Methods* 18, 331. doi:10.1038/s41592-021-01118-2

Poldervaart, M. T., Gremmels, H., Van Deventer, K., Fledderus, J. O., Öner, F. C., Verhaar, M. C., et al. (2014). Prolonged presence of VEGF promotes vascularization in 3D bioprinted scaffolds with defined architecture. *J. Control. Release* 184, 58–66. doi:10.1016/j.jconrel.2014.04.007

Roden, D. M. (2013). Cardiovascular pharmacogenomics: The future of cardiovascular therapeutics? *Can. J. Cardiol.* 29, 58–66. doi:10.1016/j.cjca.2012.07.845

Shibuya, M. (2011). Vascular endothelial growth factor (VEGF) and its receptor (vegfr) signaling in angiogenesis: A crucial target for anti- and pro-angiogenic therapies. *Genes Cancer* 2, 1097–1105. doi:10.1177/1947601911423031

Tan, C. M. J., and Lewandowski, A. J. (2020). The transitional heart: From early embryonic and fetal development to neonatal life. *Fetal diagn. Ther.* 47, 373–386. doi:10.1159/000501906

Tan, J. J., Guyette, J. P., Miki, K., Xiao, L., Kaur, G., Wu, T., et al. (2021). Human iPS-derived pre-epicardial cells direct cardiomyocyte aggregation expansion and organization *in vitro*. *Nat. Commun.* 12, 4997. doi:10.1038/s41467-021-24921-z

Veldhuizen, J., Migrino, R. Q., and Nikkhah, M. (2019). Three-dimensional microengineered models of human cardiac diseases. *J. Biol. Eng.* 13, 29. doi:10.1186/s13036-019-0155-6

Vermeulen, Z., Mateiu, L., Dugaucquier, L., De Keulenaer, G. W., and Segers, V. F. M. (2019). Cardiac endothelial cell transcriptome in neonatal, adult, and remodeling hearts. *Physiol. Genomics* 51, 186–196. doi:10.1152/physiolgenomics.00002.2019

Voges, H. K., Mills, R. J., Elliott, D. A., Parton, R. G., Porrello, E. R., and Hudson, J. E. (2017). Development of a human cardiac organoid injury model reveals innate regenerative potential. *Development* 144, 1118–1127. doi:10.1242/dev.143966

Zhao, S., Kusminski, C. M., and Scherer, P. E. (2021). Adiponectin, leptin and cardiovascular disorders. *Circ. Res.* 128, 136–149. doi:10.1161/CIRCRESAHA.120.314458

Strategies to counteract adverse remodeling of vascular graft: A 3D view of current graft innovations

Wei Tan[1]*, Parnaz Boodagh[2], Prakash Parthiban Selvakumar[3] and Sean Keyser[1]

[1]Department of Mechanical Engineering, University of Colorado Boulder, Boulder, CO, United States,
[2]McGowan Institute for Regenerative Medicine, University of Pittsburgh, Pittsburgh, PA, United States,
[3]Department of Mechanical Engineering, North Dakota State University, Fargo, ND, United States

Vascular grafts are widely used for vascular surgeries, to bypass a diseased artery or function as a vascular access for hemodialysis. Bioengineered or tissue-engineered vascular grafts have long been envisioned to take the place of bioinert synthetic grafts and even vein grafts under certain clinical circumstances. However, host responses to a graft device induce adverse remodeling, to varied degrees depending on the graft property and host's developmental and health conditions. This in turn leads to invention or failure. Herein, we have mapped out the relationship between the design constraints and outcomes for vascular grafts, by analyzing impairment factors involved in the adverse graft remodeling. Strategies to tackle these impairment factors and counteract adverse healing are then summarized by outlining the research landscape of graft innovations in three dimensions—cell technology, scaffold technology and graft translation. Such a comprehensive view of cell and scaffold technological innovations in the translational context may benefit the future advancements in vascular grafts. From this perspective, we conclude the review with recommendations for future design endeavors.

KEYWORDS

vascular grafts, adverse remodeling, impairment factor, scaffold technology, cell technology

1 Introduction

Vascular grafts are widely used for vascular surgeries. Their uses occur in a variety of forms, including vascular access for hemodialysis, as well as surgical bypass for diseased coronary artery, cerebral artery, or peripheral artery in the abdomen (e.g., aorto-iliac bypass) or in the leg (e.g., femoro-popliteal bypass), routing blood flow around an area of blockage or narrowing. A vascular graft can be a native artery or vein, or fabricated from synthetic or natural biomaterials. The current gold standard for a graft is autologous blood vessels such as a saphenous vein, which has better clinical outcomes than biomaterials-based grafts (Caliskan et al., 2020), even those made with tissue engineering approaches (Zilla et al., 2020). A vein fistula for dialysis access, for example, shows better primary patency than a polytetrafluoroethylene (PTFE) graft (Stegmayr et al., 2021). Similarly, for femoro-popliteal bypass, the 5-year patency rate of a vein graft is higher than a PTFE graft (van der Slegt et al., 2014). However, a quality vein suitable for grafting may be unavailable for many patients, particularly elders (Conte, 2012; AbuRahma,

Abbreviations: ECM, extracellular matrix; iPSCs, induced pluripotent stem cells; MSC, mesenchymal stem cell; NO, nitric oxide; PTFE, polytetrafluoroethylene; SMC, smooth muscle cell; TEVG, tissue-engineered vascular grafts.

2018). Also, to become a dialysis access, a vein must undergo a prolonged process to gain sufficient strength until its maturation into artery-like property. The maturation of a vein fistula requires several weeks up to months, during which compromised dialysis access may deteriorate patients' health (Robbin et al., 2016). To make it worse, the incidence of fistula non-maturation varies between 20 and 60% (Kosa et al., 2015; Siddiqui et al., 2017).

Thus, bioengineered or tissue-engineered vascular grafts (TEVGs) have long been envisioned to take the place of synthetic grafts and even vein grafts under certain clinical circumstances. Selective TEVGs have gradually progressed into clinical trials, for both adult patients (Lawson et al., 2016; Kirkton et al., 2019) and pediatric patients with congenital heart diseases (Hibino et al., 2010; Drews et al., 2017; Sugiura et al., 2018; Drews et al., 2020), showing some promises despite yet limited successes. The clinical potentials of TEVGs, acellular or cellular, still require tremendous efforts to unveil (Zilla et al., 2020; Fang et al., 2021a). One possible route is to cater the TEVG development to a specific grafting need or a patient cohort, in which factors that impair healing or regeneration around the vascular graft can be well defined and targeted for graft design and engineering.

To this end, this review starts with analyzing healing- or regeneration-impairment factors, which are tackled by recent graft innovations. To withstand or override the influences of impairment factors, pro-healing and/or pro-regenerative environments could be precisely defined and built into a graft through structural optimizations, signal molecule incorporations, and integration of bioactive materials, cells or cell products. As illustrated in Figure 1, major healing-impairing factors are identified according to their roles in causing the dysfunction of a graft and/or neighboring blood vessels. A number of studies have been designed to reveal cause-effect relationships and unravel underlying molecular mechanisms. To counteract these impairing factors, a variety of strategies that promote design optimization, graft healing or regeneration have emerged. We focused a literature review on those published in recent years and placed them in the landscape of graft innovations in translation, scaffold and cell technologies. Essential to the future graft development is a continual effort to balance the multi-dimensional graft innovations with the fundamental mechanistic understandings underlying adverse graft remodeling.

2 Factors impairing healing or regeneration around vascular grafts

In clinic, graft outcomes in the treatment of vascular diseases are often determined by the size and location of the devices as well as the patients' developmental and health conditions, besides the graft type (i.e., native vessel vs. synthetic graft). Herein, we examined these graft design constraints and associated clinical outcomes, by analyzing relevant impairment factors such as flow-graft interactions, cellular and molecular environments around grafts, and graft bioinertness.

2.1 Graft location, size and compliance: Related to flow-graft interactions

Abnormal blood flow in the graft has long been known as a key impairment factor that alters graft healing and overall patency (Schwarz et al., 2021). Computational flow dynamics tools, with the inputs of graft location, diameter, length and/or compliance together with graft design, have been applied to predict not only flow conditions but also consequent remodeling of a graft (Lu et al., 2014; Ramachandra et al., 2017; Donadoni et al., 2020). Variations in these physical characteristics of a graft delicately influence local fluid stresses in a blood vessel or a graft. Abnormal hemodynamic stresses may further result in impaired graft endothelialization, impaired graft healing and endothelial disruption in neighboring vessels (Chistiakov et al., 2017). Irregularities in the wall shear stress are known to induce endothelial dysfunctions, leading to negative clinical outcomes such as intimal hyperplasia, wherein smooth muscle cells (SMCs) grow to restrict the lumen of a vessel or a graft (Chistiakov et al., 2017; Ng et al., 2017; Totorean et al., 2019). Interestingly, in the case of dialysis access graft, hyperplasia develops predominantly in the vein or anastomotic regions, particularly toe and heel of distal anastomosis, where flow disturbances and altered hemodynamic factors are most prevalent (Sottiurai et al., 1989; Bassiouny et al., 1992). Quantitatively, low shear stress values ($<.5$ Pa) or oscillatory values ($\pm.1–.2$ Pa), as opposed to physiological values ($1–2$ Pa), were shown to induce endothelial dysfunction and subsequent hyperplasia development (Dhawan et al., 2010). The graft location determines flow environments

FIGURE 1
Illusration of impairment factors vs. regenerative signals for vascular grafts.
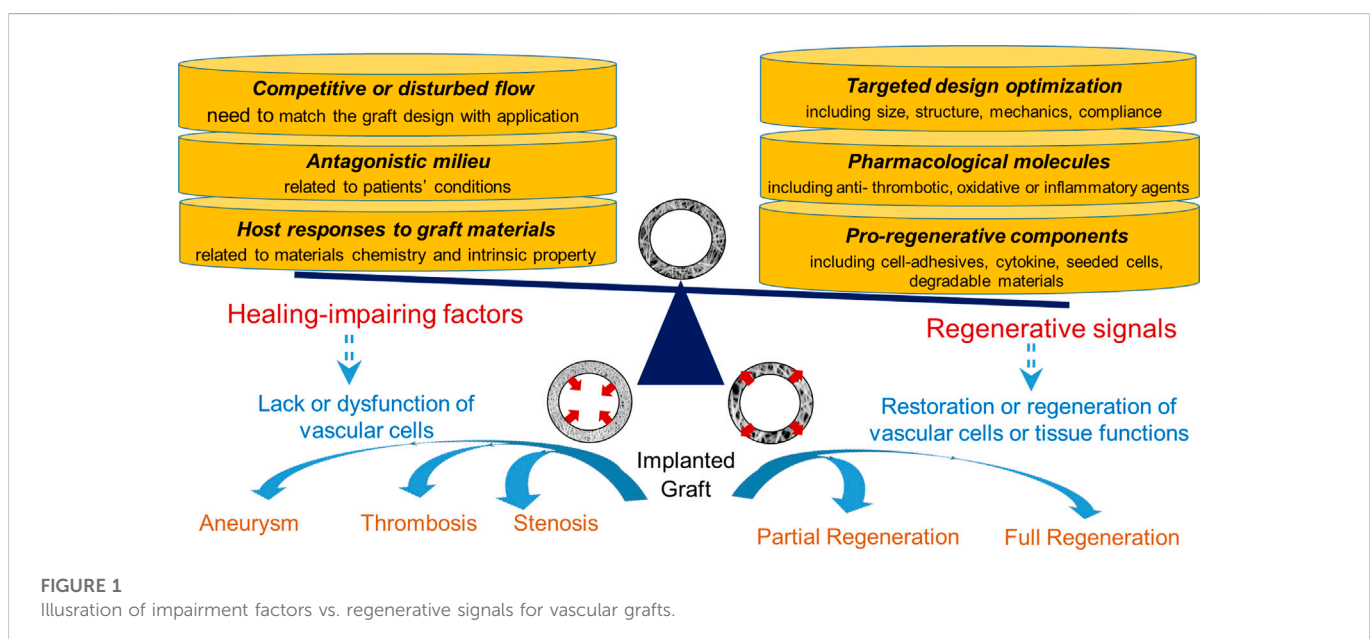
around a graft (Chiu and Chien, 2011); abnormal flow patterns might occur in arteries with branches or curvatures or grafts such as looped vascular access or brachial arterial grafts as compared to aortic grafts.

The graft diameter is key to reach a hemodynamic balance. Bypass grafts with unfavorable diameter ratios to the original vessel can result in competitive flow, ultimately leading to graft failure. Competitive flows occur when a partially stenotic blood vessel is bypassed with a graft, but still retains some of its throughput, thereby competing with the newly grafted path and causing irregular flow through it (Gaudino et al., 2016). A high competitive flow decreases the amount of blood that reaches the graft, creating low shear stresses that increase the levels of hyperplasia at the graft's anastomosis (Jin and Liu, 2019). Clinical findings suggest that more stenotic vessels with lower competitive flow, compared to less stenotic vessels, were better tolerated by coronary bypasses, and arterial grafts were more susceptible to competitive flow-induced impairment than venous grafts (Nordgaard et al., 2010; Gaudino et al., 2016; Sabik Joseph, 2016). The presence of chronic competitive flow is inversely related to internal mammary graft patency (Binns et al., 1989; Sabik et al., 2003). Intriguingly, saphenous vein graft patency did not decrease with increasing competitive flow (Ding et al., 2012; Swillens et al., 2012; Sugiura et al., 2018). Such difference could be attributed to cell and tissue differences between venous and arterial grafts (Harskamp et al., 2016; Sabik Joseph, 2016). Thus, the graft diameter in comparison with the original vessel is an important consideration for reducing flow-induced impairment, in particular for some graft types.

The roles of graft compliance and length in determining the graft patency are also well known (Skovrind et al., 2019). Compliance mismatch was recognized as a major contributor to graft failure (Tiwari et al., 2003). Though the influence of graft length on patency rates was insignificant for a similar grafting application (Tinica et al., 2018; Bosiers et al., 2020), applications that require long grafts, such as femoral artery lesion and hemodialysis access, often yielded low patency rates (Connors et al., 2011; Boutrous et al., 2019). This may be attributed to a wide range of biomechanical forces across a long graft with a large surface area. These forces consist of a complex loading combination from varying amounts of radial deformation, bending, extension/contraction, and torsion/flexion, which significantly impact the cell-graft interactions.

2.2 Patient's conditions: Related to cellular and molecular environments around grafts

The graft failure in the cases of coronary bypass, dialysis access, or stent graft have been variably associated to age, diabetes mellitus, hypertension or other health conditions (Gaudino et al., 2017; AbuRahma, 2018; Misskey et al., 2018). Sex may serve as a possible compounding factor (Blum et al., 2021). Diabetes mellitus in particular causes a high risk of platelet aggregation in the blood and increases the release of von Willebrand factor, which promotes platelet aggregation and results in significant endothelial damage and arterial stiffening (Creager et al., 2003). This vascular intima damage coupled with the pathophysiological mechanism of diabetes leads to the increased formation of thrombosis (Reddy et al., 2013), and thus sooner obstruction of a graft such as arteriovenous fistula (Afsar and Elsurer, 2012). The primary failure of fistulas is associated with an enormous overall cost. Interestingly, arteriovenous fistula showed even higher primary failure rates than synthetic grafts in patients

with diabetes mellites (Qin et al., 2016). To make it worse, failure of a fistula reduces the number of possible sites for an alternate access, exposing the patients to risks from salvaging attempts (Schinstock et al., 2011). Therefore, using hemodialysis access for diabetic patients as an example, it is clear that patients' health conditions complicate cellular and molecular environments around grafts, worsening the ultimate fate of grafts, in particular biological grafts. For above-knee femoropopliteal bypass, diseases including diabetes and ischemia significantly reduced graft patency in both vein and PTFE grafts, but showing similar reduction rates for both types of grafts (Klinkert et al., 2004). Furthermore, during atherosclerosis such as coronary artery diseases, systemic biological factors (e.g., diabetes mellitus, dyslipidemia, sex, age, hypertension, and smoking) and local biological mechanisms (e.g., increased oxidative stress, vascular inflammation, and endothelial dysfunction) all contribute to the initial plaque formation and subsequent progression (Gaudino et al., 2017). These classic cardiovascular risk factors, particularly diabetes mellitus, seem to play a role in determining graft failure. For instance, the impact of diabetes mellitus on arterial and venous bypass grafts has been investigated by several groups, with most but not all, showing a detrimental effect on graft patency (Gaudino et al., 2017).

Besides comorbid diseases, the patency of a biological graft, compared to an inert synthetic graft, might be more influenced by cellular and molecular environments associated with older age. Older patient's arteries tend to be more easily calcified making them more prone to abnormal shear stress, inflammation and other endothelial dysfunction (Tesauro et al., 2017). Due to significant comorbidities in elderly patients, a vein fistula is more likely to fail due to the deteriorating condition of blood vessels (Miller et al., 1999; Ponce, 2001; Lazarides et al., 2007). The use of synthetic PTFE grafts instead of vein fistula in elderly patients and those with compromised vessels might improve primary patency rates (Staramos et al., 2000; Rooijens et al., 2005). Clinical data point to advanced age as a significant factor in adversely affecting outcome of dialysis graft (Sugimoto et al., 2003; Moist et al., 2012). Meanwhile, almost half of all patients initiating dialysis are 65 years of age or older in the United States and the percentage of elderly patients is even higher in Canada and Europe (Ahmed and Catic, 2018), which makes the age as an important consideration for the graft design. It is increasingly recognized that an advanced age is associated with adverse graft remodeling and differentially altered remodeling of vein fistula and synthetic graft, likely through aged-related changes in vascular cells and molecular environments initiated by increases in pro-inflammatory cytokines, pro-calcification signaling, advanced glycation end products, and/or extracellular matrix stiffness. Similarly, when a bioengineered graft or TEVG include a cellular and/or molecular component, its design should consider adverse environments related to clinical conditions such as aging. In the case of vein fistula for dialysis access, its risk of failure is greatest among older patients and/or obese patients (Lok et al., 2006; Peterson et al., 2008; Shingarev et al., 2011).

2.3 Bioinertness of grafts

Graft bioinertness, or lack of biointegration, is another major impairment factor for long-term graft patency. It is mainly related to commercial grafts such as those made of PTFE or Dacron, but could be variably applicable to different TEVGs, particularly prior to the completion of vascular tissue regeneration. Previous review articles
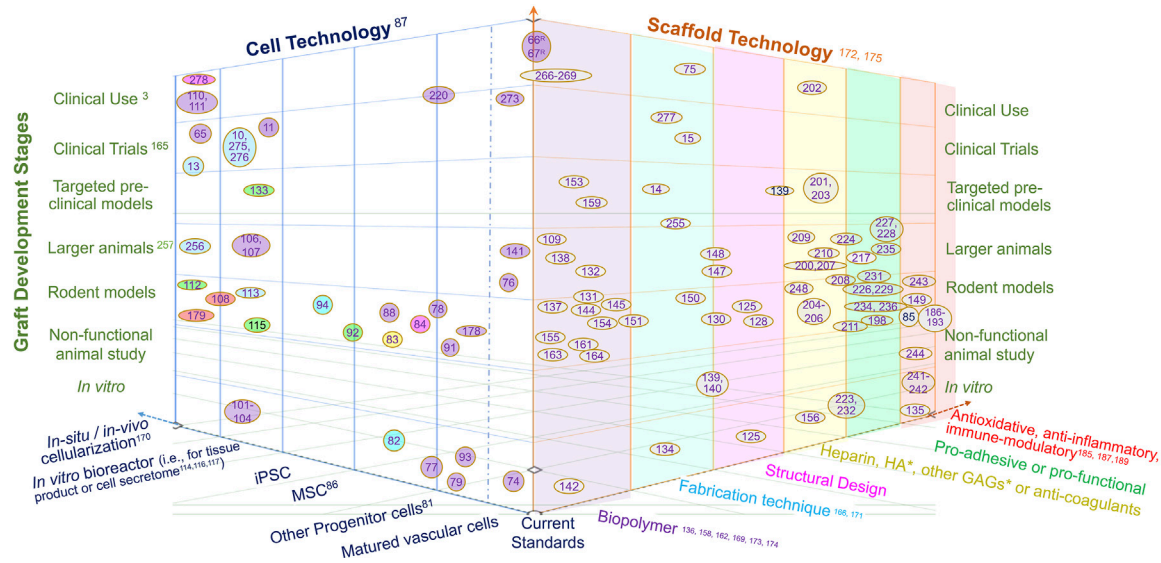
FIGURE 2
The landscape of vascular graft research in three dimensions, namely cell technology, scaffold technology and development stage. The citations of references used here are the numbered references listed in numerical order as they appear in the paper, as shown in Supplementary Material. The reference literatures are mapped in this landscape by locating research studies in the 3-dimensional space with reviews with various scopes labeled on the axes. The colors of oval boxes in the space of cell technology are correlated to the axis scaffold, showing the scaffold technology utilizied in these studies. Herein, "Current standards" refer to autologous graft (vein or artery) or bioinert graft (mostly PTFE-based); "Targeted preclinical models" refer to animal studies targeted at a clinical application such as dialysis access, Fontan graft, bypass for coronary, femoral or other arteries; "Larger animal" refer to animal models larger than rodents, such as rabbit, sheep, pig, dog and balloon; "Non-functional animal study" refer to non-vascular implants (often subcutaneous) or those used in *ex vivo* circulation; "In situ or in vivo cellularization" refer to the cellularization and/or tissue production by implanting acellular polymer; "Matured vascular cells" refer to vascular endothelial, smooth muscle and fibroblast cells; "Other progenitor cells" including endothelial progenitor cell and smooth muscle progenitor cell; "Biopolymer" includes biodegradable polymer , biologically-derived polymer, decellularized ECM or vessel, bioinert polymer, etc. *HA, hyaluronic acid; GAGs, glycosaminnoglycans.

have elaborated the main issues with the graft inertness, which include thrombosis, inflammation and intimal hyperplasia of a graft. Infection can also be a serious issue (Kirkton et al., 2018), in particular for dialysis graft requiring continuous needle access (Halbert et al., 2020; Kostokis and Loukopoulos, 2020; Stegmayr et al., 2021). A generally accepted root cause of these issues is the poor interaction of cells and the non-specific adsorption of proteins onto the graft, which lead to platelet aggregation but fail to form organized endothelium and/or matured smooth muscle. To circumvent these issues, bioengineering strategies including chemical coatings, materials modifications with peptides, proteins or other biomolecules, and seedings of endothelial cells or stem cells on inert or degradable grafts, have been utilized, with the goal of better integrating grafts with the native vasculature (Hielscher et al., 2018; Wang et al., 2020; Ham et al., 2021; Liu et al., 2021; Yu et al., 2021). Results with these strategies demonstrated improved endothelialization and/or inhibited thrombosis, inflammation, intimal hyperplasia, or infection. More recent approaches involve degradable, bioactive materials, as described below.

3 Counteracting adverse remodeling with regenerative signals

To tackle above-mentioned factors involved in adverse graft remodeling, we summarize a three-thronged approach being taken in this field. A focused literature review of recent publications is taken

to map out the research landscape of graft innovations in three dimensions, namely innovations in cell technology, scaffold technology and translation (Figure 2). Each referred study is a data point plotted on three axes in the attempt to show the relationship of the study in the context of the three innovations. Thus, a comprehensive perspective is taken for a combined view of both cell and scaffold technological innovations in the translational context.

3.1 Cell technology

The contribution of cell technology to counteract adverse remodeling is to enhance graft acceptance and integration with native vessels, including attenuating chronic inflammation, reducing thrombogenicity, and promoting fast healing and vascular regeneration. The cell technology includes the technology to isolate, culture and use different types of cells for vascular graft applications, the technology to recruit cells into grafts, and the technology to produce cell products crucial for regeneration. Herein, a brief overview is taken on each cell type used for vascular grafting, highlighting recent innovations in tissue bank, immune-tolerant cells, and bioreactors. Recent cell technology has been expanded to include the use of cell secretomes, while on the other end adding a range of *in situ* or *in vivo* cellularization technique into the realm of cell technology.

Autologous matured vascular cells, such as SMCs, endothelial cells and fibroblasts (McAllister et al., 2009; Syedain et al., 2011; Amensag

and McFetridge, 2012), were employed for the TEVG creation in early preclinical and clinical studies. They are not immunogenic, but their disadvantages include invasive harvest of vascular cells, limited availability, varied quality, and low potential of replication and regeneration.

Progenitor cells, compared to matured cells, are isolated using less invasive procedures, from blood, bone marrow, umbilical cord, adipose or other tissues, and they demonstrate greater proliferative capacities despite their scarcity in tissues. For example, bone marrow-derived smooth muscle progenitor cells, compared to adult vascular SMCs, produced stronger and tougher TEVGs *in vitro*, and consequently progenitor seeded-grafts produced more organized elastin when implanted *in vivo* as jugular replacements in lambs (Swartz et al., 2005; Liu et al., 2007). Similarly, endothelial progenitor cells have been used to seed TEVG (Melchiorri et al., 2016; Muniswami et al., 2020; Tamma et al., 2020), but their high heterogeneity and rare presence could complicate the translation process (Munisso and Yamaoka, 2020). Mesenchymal stem cell (MSC), a type of progenitor cell with the potential of generating various vascular cell types (Gong and Niklason, 2008), lacks major histocompatibility complexes or other immune-stimulatory molecules while secreting anti-thrombotic and anti-inflammatory molecules, such as IL-10 (Fukunishi et al., 2018; Mirhaidari et al., 2020), and TGF-β receptor 1 (Lee et al., 2016). These characteristics make MSC an excellent allogeneic cell candidate for the TEVG production (Wang et al., 2016; Afra and Matin, 2020). In particular, adipose-derived MSCs are advantageous for their easy extraction in high quantities and high regenerative potency in a way unaffected by age (Harris et al., 2011; Zhang et al., 2011; Krawiec et al., 2016; Krawiec et al., 2017; Haskett et al., 2018). Finally, other new types of progenitor cells such as pericardial effusion-derived progenitor cells (Wang et al., 2021) can be potential candidates for cellularizing vascular grafts.

Induced pluripotent stem cells (iPSCs) have the potential of generating patient-specific SMCs, endothelial cells, and fibroblasts for TEVGs (Generali et al., 2019; Luo et al., 2020; Shi et al., 2021). The availability of iPSC-derived cell sources may eliminate the problems with variation in the cell quality and address the timing issue for "off-the-shelf" availability, both of which are concerns relevant to progenitor cells. Nevertheless, a bottleneck of using human iPSC derivatives is their tumorigenicity and immunogenicity (de Almeida et al., 2013). Thus, human leukocyte antigen-matched iPSC tissue banks would be a valuable source for personalized grafts (Jin et al., 2016; Petrus-Reurer et al., 2021). Additionally, genetically engineered master human iPSC lines, which give rise to immune-tolerant (immune-evasive or immune-suppressive) iPSC derivatives (Riolobos et al., 2013), might yield universal "off-the-shelf" cell sources for hypo-immunogenic TEVGs.

Cell seeding *in vitro* often requires an incubation time ranging from days to months in a dish or in a sophisticated bioreactor. Bioreactor designs vary from a rotary bioreactor for stem cell differentiation (Xing et al., 2017; Li et al., 2019a), a closed apparatus for standardizing cell technology (Kurobe et al., 2015), a biaxial stretching system for tissue matrix maturation (Huang et al., 2015; Huang et al., 2016), a semi-automated cell seeding device (Cunnane et al., 2020a), to a perfusion bioreactor for applying flow stresses (Melchiorri et al., 2016) and individualized graft conditioning (Håkansson et al., 2021). Another recent innovation in the *in vitro* cell seeding technology is to exploit 3D bioprinting techniques for printing patterned cell-laden hydrogels, utilizing a mixture of cells and hydrogel as the bioink to create vascular grafts with precisely-defined structures.

Recently, *in situ* or *in vivo* cellularization, utilizing human (or animal) body as a bioreactor, added a novel option into the cell technology for vascular grafts. This approach starts with placing a tube composed of Teflon (Wang et al., 2019a; Qiu et al., 2021), silicone (Fujita et al., 2020) or collagen (Nakayama et al., 2020), as a subcutaneous or peritoneal cavity implant or in an *ex vivo* location, allowing fibrous tissues to grow and form an tubular structure, which is then explanted and subsequently implanted as an autologous graft (Chen et al., 2019; Nakayama et al., 2020) or as an allograft after decellularization (Wang et al., 2019a; Fujita et al., 2020; Qiu et al., 2021). Preclinical or clinical studies showed some encouraging outcomes.

Last but not least is that the future cell technology for vascular grafts will surely see an increased use of stem cell secretomes (Chen et al., 2018; Cunnane et al., 2018; Cunnane et al., 2020b), as their therapeutic and regenerative values are being unveiled (Ahangar et al., 2020; Baruah and Wary, 2020; Nikfarjam et al., 2020; Tang et al., 2021) and recently exploited in other cardiovascular implants (Li et al., 2019b; Baruah and Wary, 2020; Hu et al., 2021).

3.2 Scaffold technology

The scaffold technology encompasses the techniques to improve the graft structure and mechanics and those to improve the biological integration. The former includes design innovations involving novel computational tools, biopolymers, or scaffold fabrication techniques ranging from decellularization to electrospinning and 3D printing. The scaffold technology for improved biological integration often involves the incorporation of a range of bioactive functional biomolecules on the surface or within a biopolymer, in order to modulate immune responses and/or to promote regeneration.

3.2.1 Structural optimization and scaffold fabrication

As described in Section 2.1, the patency of vascular grafts is largely determined by the structural and mechanical interactions between blood flow and vascular graft, which continuously alter neotissue growth and graft remodeling. The neotissue growth and graft remodeling in turn change the flow-graft interactions. Therefore, computational models simulate such interactions as well as advanced statistical analyses of a parametric cause-effect relationship have been exploited to accelerate the rational optimization of vascular grafts (Keshavarzian et al., 2019; Tamimi et al., 2019; Khosravi et al., 2020). Recently, data-informed models have been developed to improve graft designs, even toward patient-specific design (Best et al., 2018), for desired graft performances in terms of lumen diameter, extracellular matrix (ECM) production, and levels of inflammation (Best et al., 2019; Drews et al., 2020). Model parameters comprise not only graft compliance, pore size, fiber diameter and degradation rate (Szafron et al., 2019; Tamimi et al., 2019; Furdella et al., 2021), but possibly also polymer chemistry, cytokine and other biological inputs (Szafron et al., 2018; Khosravi et al., 2020). Importantly, model outputs were compared to experimental outcomes and further predicting outcomes, which thus unravel mechano-biological mechanisms of neovessel formation and graft degradation *in vivo*. For example, models have been used to guide the design of mechanocompatible grafts (Furdella

FIGURE 3
Adverse remodeling versus regeneration of a vascular graft.
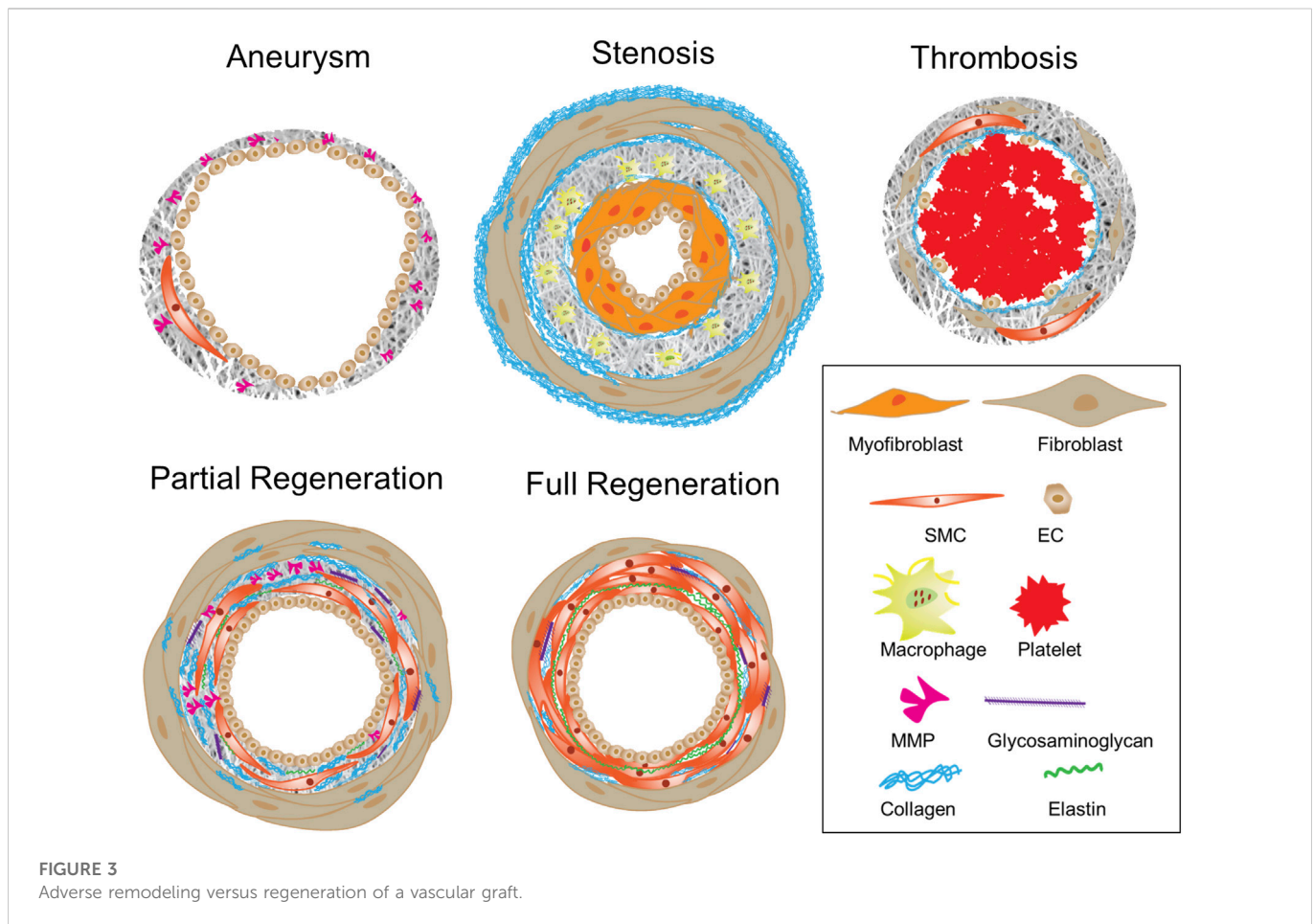
et al., 2021), to examine the role of inflammation activity using immuno-compromised animals (Szafron et al., 2018), or to parametrically explore graft narrowing (Drews et al., 2020; Khosravi et al., 2020). Besides computational models, statistical methods were used to reveal the roles of specialized design variables such as braiding angle, braiding density and coating structure in the graft development (Zbinden et al., 2020). Collectively, these studies have confirmed the well-accepted tissue engineering principle—the successful neovessel formation requires neotissue development to balance the scaffold degradation. However, such balance varies greatly with the animal model (Fukunishi et al., 2020). Lack of a balanced coordination over the time can result in adverse remodeling such as excessive degradation, impaired ECM synthesis, elevated inflammation and neotissue overgrowth in the lumen, leading to aneurysm (Best et al., 2019) or stenosis (Drews et al., 2020), and ultimately graft failure (Stowell et al., 2020). Figure 3 illustrates graft wall remodeling in various scenarios, where physiological routes ended up with partial or complete regeneration.

In parallel with the development of scaffold optimization tools, equally important is a rich availability of scaffold fabrication techniques and biopolymer choices, both of which promote parametric control for optimizations. Some recent developments in the graft fabrication include: 1) Shortening the production time for cell sheet self-assembly method (von Bornstädt et al., 2018); 2) loading drugs, anti-thrombogenic or pro-regenerative molecules for electrospun grafts or 3D printed grafts (Zhang et al., 2019;

Domínguez-Robles et al., 2021); 3) refining decellularization protocols for reduced immunological responses (Schneider et al., 2018; Valencia-Rivero et al., 2019; Kimicata et al., 2020; Lopera Higuita et al., 2021); 4) improving the precision of pore generation in scaffold (Zhen et al., 2021); 5) enhancing recellularization for allogenic or xenogenic decellularized grafts (Dahan et al., 2017; Lin et al., 2019; Fayon et al., 2021); 6) expediting degradation with scaffold composition (Fukunishi et al., 2021) or textile technique (Fukunishi et al., 2019) to enhance matrix remodeling; 7) mimicking the structure and/or composition of vascular ECM using electrochemical fabrication (Nguyen et al., 2018) or an automated technology combining dip-spinning with solution blow spinning (Akentjew et al., 2019); 8) creating patient-specific grafts (Fukunishi et al., 2017); and 9) hybrid approaches, for example, combining electrospinning with decellularized matrices (Gong et al., 2016; Ran et al., 2019; Wu et al., 2019; Yang et al., 2019).

Biopolymers used for the graft construction kept diversifying the graft repertoire. For instance, the recent addition of shape memory polymer as a self-enclosable external support to a graft reduced stenosis (Yi et al., 2021). Currently, graft biopolymers consist of biologically-derived biomaterials such as silk fibroin (Zamani et al., 2017; Gupta et al., 2020; Tanaka et al., 2020), collagen (Li et al., 2017; Copes et al., 2019) and fibrin (Syedain et al., 2017), and synthetic polymers mostly degradable polymers such as polycaprolactone (Mrówczyński et al., 2014), polyglycolic acid (Sugiura et al., 2017), polyurethane (Zhen et al., 2021; Fathi-Karkan et al., 2022),

polycarbonate urethane (Eilenberg et al., 2020), polylactic acid, and poly (l-lactide-co-ε-caprolactone) (Zhu et al., 2018). Hybrid graft materials composed of both biological polymers and synthetic polymers further leveraged the benefits offered by both materials for the mechanics and biological recognition of a graft. For further information, a number of reviews have provided historical views and in-depth analyses of graft fabrication techniques and graft polymers (Hiob et al., 2017; Pagel and Beck-Sickinger, 2017; Song et al., 2018; Chandra and Atala, 2019; Gentile et al., 2020; Niklason and Lawson, 2020; Syedain et al., 2020; Yuan et al., 2020; Gupta and Mandal, 2021; Heng et al., 2021; Zhang et al., 2021).

By and large, a long-term, dynamic, mechanistic view is taken into the design parameters and optimizations for vascular grafts, while continuous advancements in fabrication techniques and materials allow diverse choices and better controls over design parameters. A central finding in the graft optimization is that dynamically evolving mechanical properties can dictate the levels of inflammation and stress shielding of cells, and in turn affect mechanobiologically-mediated ECM production, remodeling and degradation (Szafron et al., 2019; Tamimi et al., 2019; Khosravi et al., 2020; Furdella et al., 2021). Therefore, adjusting the material chemistry and fabrication technique for desired dynamic profiles of graft mechanics in a specific clinical setting would be essential to future improvements.

3.2.2 Starting right at the onset—molecular designs for anti-thrombotic and anti-inflammatory control

Events immediately occurring upon vascular grafting in the body involve endothelial injury platelet activation, and acute inflammation. Properly regulating these early events is crucial to the fate of a graft, either promoting regeneration or preventing failure from thrombosis or intimal hyperplasia (Roh et al., 2010; Tseng et al., 2014; Wissing et al., 2017). Talacua et al. (2015) showed that modulating the initial inflammatory phase in the first days remarkably improved the 3-month implantation outcome. In fact, the immune response is always pivotal to tissue regeneration: on one hand, it is indispensable for proper healing; on the other hand, extensive, prolonged inflammation prevent regeneration (Julier et al., 2017). Ideally, after acute inflammation, a vascular graft would start healing, gradually reach long-term structural stability, restore the normal vascular flow, and regenerate vascular functions. However, when a graft undergoes a healing process with a prolonged presence of inflammatory cells and non-vascular replacement tissues, fibrous formation and fibrous encapsulation may dominate, compromising graft mechanics, vascular flow and flow-dependent vascular cell functions and tissue regeneration (Boccafoschi et al., 2014).

Critical in the initial healing process is the macrophage activity, which determines ultimate graft remodeling or regeneration (Rodriguez-Soto et al., 2021). Macrophage functions are often performed through macrophage polarization (M1/M2) as well as their secreted factors including cytokines acting directly or indirectly on the vascular cells to regulate arteriogenesis (Boccafoschi et al., 2014). Cytokines such as IL-4 and IL-10 have been implicated in the transition of macrophages from a pro-inflammatory phenotype to an anti-inflammatory, pro-healing phenotype in vivo (Browne and Pandit, 2015). The biomaterials form, crosslinking level, degradability, hydrophilicity, topography, and materials choice of an implant can all affect the immune system, triggering varied inflammation (Boccafoschi et al., 2014; Browne and Pandit, 2015). Macrophage infiltration and

polarization provides a strategy for predicting, detecting, and inhibiting stenosis in TEVGs (Szafron et al., 2018).

Because of the pivotal roles of macrophages at the onset of grafting (Zhang and King, 2022), recent strategies towards regulating macrophage functions include the use of immunomodulatory agents, drugs, cytokines, and cells such as progenitor cells. Immunomodulatory agents such as losartan (an angiotensin-II type1 receptor antagonist), zoledronate (a bisphosphonate), and aspirin-triggered resolvin D1, for example, significantly reduce macrophage infiltration or expedite inflammation resolution, thus attenuating graft stenosis and/or promoting regeneration (Ruiz-Rosado et al., 2018; Shi et al., 2019a; Chang et al., 2021). Grafts loaded with immunomodulatory cytokines, such as IL-4 (Tan et al., 2019) or human Wharton's jelly matrix (rich in immunomodulatory cytokines) (Gupta et al., 2021), enhanced M2 macrophage percentage, which suppressed intimal hyperplasia (Tan et al., 2019) or promoted functional regeneration (Gupta et al., 2021). Similarly, immunomodulatory cells, either by in vitro cell seeding or by circulating cell recruitment via ligands immobilized to a graft, successfully regulated macrophage polarization and inflammation process. Fukunishi et al., for instance, seeded mononuclear cells onto electrospun TEVG scaffolds, which reduced platelet activation and attenuated graft stenosis through a higher M2 macrophage percentage and lower macrophage infiltration (Fukunishi et al., 2018). Lorentz et al. loaded microparticles with monocyte recruitment factor (C-C motif chemokine ligand 2) to induce tissue remodeling of vascular grafts (Lorentz et al., 2021). Shafiq et al. (2018) used Substance P and stromal cell–derived factor-1α peptide, both of which encouraged the recruitment of bone marrow cells to initiate healing and anti-inflammatory response. Similarly, Kim et al. (2019) also used Substance P for cell recruitment and accelerated regeneration.

Thrombosis is another early adverse event for a vascular graft and is caused by the lack of a functional endothelium which prevents the aggregation of blood components. Due to the essential roles of endothelial cells in the regulation of thrombogenesis, the in vitro endothelialization of a vascular graft was used prior to implantation. But for acellular grafts, if antithrombotic therapy is not used (Fang et al., 2021b), anti-fouling polymers or anticoagulants such as heparin must be attached to the graft surface for thrombogenic reduction through the prevention of platelet adhesion and/or activation (Radke et al., 2018). Long, flexible hydrophilic polymer chains can offer protein-repellent backgrounds for anti-coagulation (Thalla et al., 2012; Strang et al., 2014); multi-armed hydrophilic polymers further allow other functional molecules to be clickable to the graft surface (Iglesias-Echevarria et al., 2021). Binding of heparin to vascular grafts continues to be the most effective and widely-used method to prevent thrombosis, meanwhile heparin has anti-inflammatory effect and inhibitory effect on intima hyperplasia (Poterucha et al., 2017). Heparin binding can be via chemical conjugations or physical methods, but chemical bonding may compromise mechanical compatibility (Jiang et al., 2016). Regardless of graft materials or fabrication methods, heparinized grafts, including ePTFE grafts (Samson et al., 2016; Freeman et al., 2018), electrospun grafts (Qiu et al., 2017; Xu et al., 2018; Shi et al., 2019b; Matsuzaki et al., 2021; Zhu et al., 2021), and decelluarized grafts (Kong et al., 2019), all outperformed those without heparin in terms of graft patency, showing critical roles of heparin in the thromboresistance and in situ endothelialization. Besides heparin,
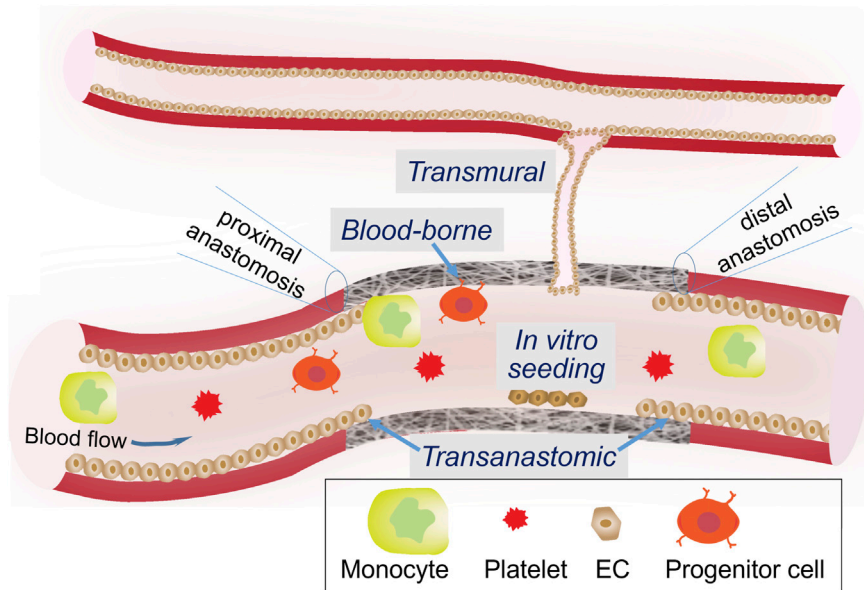
FIGURE 4
Possible mechanisms underlying graft endothelization.

anticoagulation methods include the incorporation of anti-thrombotic drugs (Lee et al., 2022), hyaluronic acid (Dimitrievska et al., 2020) or more sophisticated ECM secreted by thrombospondin-2 knockout cells on decellularized aorta grafts (Kristofik et al., 2017).

In summary, regulating the platelet activity and immune response to a graft is pivotal to initiate graft healing and determine regeneration—galvanize or depress it. The final stage of immune responses involves the coordination of macrophages, endothelial cells and SMCs. The migration and proliferation of the latter two result in the regeneration of new functional arterial tissues. Disruption to the collaborative efforts of these cells as well as any negative exogenous factors such as infection, stresses or environmental factors, can lead to thrombosis and hyperplasia, and eventually graft failure. Therefore, factors influencing graft inflammation at the onset may largely determine its long-term patency. Additional factors affecting the long-term graft patency include physiochemical properties of biomaterials, such as hydrophobicity, stiffness and bioinertness. The current graft material, PTFE, for example, in some cases, induces severe graft calcification, resulting in suboptimal mid-term and long-term outcomes.

3.2.3 Biological functionalization of a graft for vascular regeneration

Due to indispensable, protective roles of endothelial cells throughout the vasculature, it is widely accepted that the endothelialization of a vascular graft is of the utmost importance to graft designers. Reinstitution of a continuous endothelium monolayer on the lumen surface of a graft is the best way to avoid the activation of coagulation cascade and progression of intimal hyperplasia (Heath, 2017). Four endothelialization mechanisms have been identified (Figure 4). The pros and cons of each are summarized in Table 1. Transanastomotic growth refers to the migration of matured endothelial cells from the native vessel onto the luminal surface of the graft across the anastomoses, where a vascular graft is connected to

a native vessel. It served as a major endothelialization mechanism in animal models, but did not extend beyond 1 cm in humans (Zilla et al., 2007; Zilla et al., 2020). Therefore, to endothelialize the middle section of a longer graft, other mechanisms must be considered. Transmural growth occurs through cellular and vascular infiltration from an adjacent blood vessel (Pennel et al., 2013). Blood-borne growth is through cells in the circulation with the capacity of differentiation into endothelial phenotypes, such as endothelial progenitor cells. Such endothelialization modality requires a strong binding between the circulating cell and the graft surface, which may be offered by progenitor-specific antibodies or ligand (Lu et al., 2013; Hao et al., 2020) or adhesive peptides (Choi et al., 2016; Hao et al., 2017; Liu et al., 2021) immobilized on the lumen surface. Since all three in situ mechanisms are still insufficient to create a continuous endothelium throughout a long vascular graft in human patients, ex vivo or in vitro seeding of matured vascular cells (Dahan et al., 2017), progenitor/stem cells (Olausson et al., 2012; Ardila et al., 2019), or genetically modified autologous cells expressing fibulin-5 and VEGF, onto the graft lumen have been employed (Sánchez et al., 2018).

For in situ endothelialization and in situ smooth muscle regeneration, strategies to functionalize graft lumen or an inner layer, have been under continuous development to improve the regeneration speed and quality. To encourage the adhesion, migration, differentiation and proliferation of matured or progenitor-derived vascular cells, bioactive molecules utilized for graft functionalization include: (a) growth factors, (b) genes, (c) peptides, and (d) antioxidants. Figure 5 illustrates functionalization strategies for graft endothelialization.

One of the most adopted growth factors is VEGF (Koobatian et al., 2016; Wang et al., 2019b). Despite an early study showing undesired inflammation and intimal hyperplasia on a decellularized vascular graft with a coating of FGF and VEGF (Heidenhain et al., 2011), a number of recent studies using these or other angiogenic or stem cell-

TABLE 1 Summary of comparisons among four endothelialization mechanisms.

Endothelialization mechanisms	Pros	Cons
Trans-anastomotic growth	Effective in small animals; *in situ*	Irrelevant or ineffective in most clinical applications; complicated by inflammatory responses
Transmural growth	Essential for graft healing; *in situ*	Inconsistent results due to the complexity of angiogenic process; influenced by physical properties of the scaffold
Blood borne growth	Regenerative poten-tial; *in situ* seeding	Scarcity of circulating cells and limited regenerative capability of cells in the circulation
in vitro seeding	Formation of a confluent cell layer	No "off-the-shelf"; possible cell loss *in vivo*; Efficiency and outcome depend on cell source, culture and seeding techniques

FIGURE 5
Surface engineering strategies of grafts Biomolecules conjugated to the surface graft materials are designed to interact with the blood components including blood cells, progenitor cells and platelets.
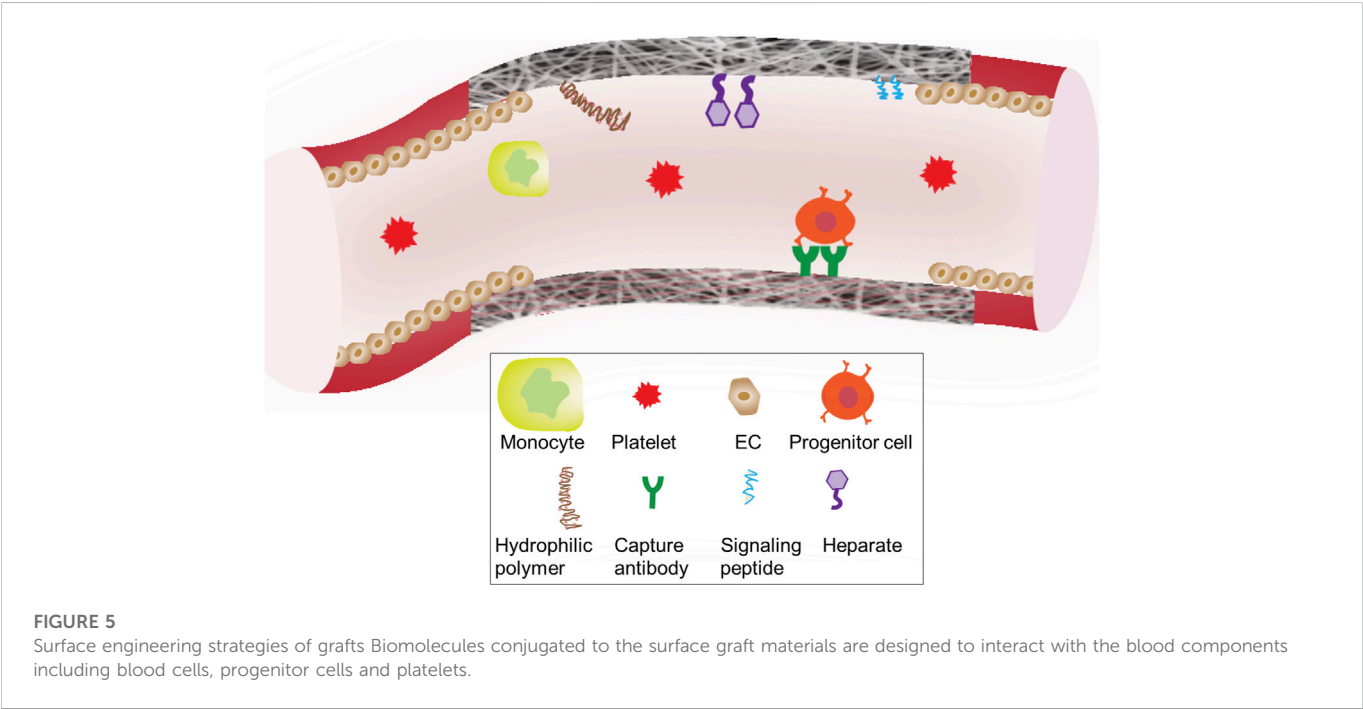
homing molecules demonstrated their positive influences on graft performances. For example, the incorporation of triple factors, VEGF, bFGF, and SDF-1α into a two-layered graft was found to improve endothelialization, SMC layer formation, and thus graft patency compared with VEGF alone (Antonova et al., 2021). Allogeneic decellularized vascular scaffold grafted with VEGF, bFGF, and heparin exhibited similar mechanical properties to the natural vessels, and positive expression of factor VIII and α2-actin (Kong et al., 2019). Smith et al. (2019) and Smith et al. (2020) developed a vascular graft based on small intestinal submucosa with immobilized heparin and VEGF on the graft lumen to capture VEGF receptor-expressing circulating angiogenic cells from the blood, which promoted the formation of artery-mimic structure with endothelial and medial layers. Besides VEGF, other signaling mediators, including brain-derived neurotrophic factors (Zeng et al., 2012), dickkopf-3 glycoprotein (Issa Bhaloo et al., 2018), and SDF-1α (Shafiq et al., 2018; Wang et al., 2019c), were used to improve graft patency through progenitor cell homing and/or paracrine mechanisms for graft endothelialization and smooth muscle formation. Furthermore, these cell-recruiting molecules were used in combination with

anticoagulant and immunomodulatory molecules. For example, the PTFE graft covalently coupled with heparin, SDF-1α and CD47 reduced thrombogenicity, facilitated the recruitment of progenitor cells, and alleviated the immune responses (Gao et al., 2017). Indeed, fast, high-quality *in situ* vascular regeneration could benefit from an exquisite graft design orchestrating the functions of multiple signaling molecules.

The gene incorporation into a graft can also effectively enhance vascular regeneration. Genes such as miRNAs and vectors encoding VEGF receptor-2 ligands (Hytönen et al., 2019) were used instead of functional proteins or peptides. In particular, miRNAs, such as miRNA-126 which accelerates the synthesis of VEGF and FGF and miRNA-145 which modulates the contractile SMC phenotype, were loaded into grafts: miRNA-126 alone was found to accelerate graft endothelialization (Zhou et al., 2016), while dual miRNA loading further improved contractile SMC regeneration and promoted vascular ECM formation (Wen et al., 2020). However, the lack of cell-specific transfection and release kinetics as well as potential toxicity and inflammation are several challenges for the gene approach.

The antioxidant approach could address both regenerative need for a functional endothelium and therapeutic need for inhibiting neointimal growth or calcification, which is related to oxidative stress-caused cellular damage (Gaudino et al., 2017; Washington and Bashur, 2017). A natural antioxidant, oxide (NO) is consistently secreted by endothelial cells, providing essential signaling to prevent thrombosis, SMC proliferation or intimal hyperplasia (Napoli et al., 2006; Strijdom et al., 2009; Devine et al., 2020). Therefore, NO-producing mechanisms, including NO-releasing coating and NO-generating coating such as NO-catalytic bioactive coating that generates NO from endogenous S-nitrosothiols, are integrated into vascular grafts (Wang et al., 2015; Tang et al., 2018; Dou et al., 2020; Li et al., 2020; Enayati et al., 2021) and stents (Yang et al., 2015; Yang et al., 2020), to promote endothelialization and reduce restenosis. Another type of antioxidant used was poly (1,8-octamethylenecitrate-co-cysteine), which was found to inhibit the calcification of decellularized grafts (Jiang et al., 2017).

4 Translation of vascular grafts for clinics: Success measures

Essential to the future development is continual efforts to balance the mechanistic understandings underlying adverse graft remodeling in clinic with the innovations in grafting technologies. Translational innovations are as important as innovations in cell technology and scaffold technology. Assessment tests and preclinical models for vascular grafts are to be properly matched to the targeted clinical application (Zilla et al., 2020), in terms of the anatomic structure such as graft diameter, length and looping, graft functions such as regular needle access for dialysis grafts, and regeneration potential related to clinical use, patient's age and disease condition. Ideally, grafts with regenerated tissues could also simulate vasoreactivity and pharmacological responses of a native vessel, for the long-term success (Strobel et al., 2018).

4.1 Device function tests

Related to tubular vascular implants, FDA guidance documents have specified testing criteria for a number of physical and mechanical properties of grafts, including porosity, burst strength, compliance, elastic modulus, water permeability, compliance, and kink diameter (ANSI, 2010). Vascular grafts for a specific application such as arteriovenous graft access may require additional guidelines for function testing (Vascular Access Society, 2021). For example, when the synthetic grafts are placed a loop configuration, e.g., for vascular access, preventing graft kinking is crucial (Wu et al., 2020). Nevertheless, all the test guidelines refer to traditional, permanent graft materials. When biodegradable materials, synthetic or natural, are used to construct grafts, it may be necessary to test the temporal changes of physical and mechanical properties, in order to avoid devastating events such as aneurysm. Besides physical and mechanical properties, *in vitro* device tests also include biological function assessment. As TEVG improvements focus on the graft development by attending to the main causes of graft failure—thrombus formation and intimal hyperplasia, *in vitro* thrombogenicity tests as well as proliferation and migration tests of vascular cells have been widely employed.

4.2 Preclinical assessment with animals

The goal of TEVG regeneration studies is to translate new findings to human clinical therapy, which relies on animal models to generate enormous data useful to the translation. Ideally, the selection of animal model considers the animal's analog close to human patients in terms of similarities in anatomical, structural, pathological and/or functional aspects. Immunodeficient animal models further allow long-term accommodation of humanized vascular grafts (Itoh et al., 2019). To evaluate the biochemical, structural and functional similarities between a TEVG implant and a native artery in animals, measures taken on the implants include ultrasonic scan, flow Doppler and X-ray/angiography, as well as on explant analyses, such as mechanics (i.e., strength, compliance), histological analyses such as geometry (i.e., lumen size, thickness), layer structure, cells (e.g., inflammatory cells, circulating cells, vascular endothelial cells and SMC, cells related to fibrotic or calcified remodeling), ECM (e.g., elastin, collagen types I/III/IV), and biomolecules through gene and/or protein assays.

A closer analog to clinical conditions allows one to better predict graft healing and regeneration in clinic. A huge discrepancy exists between endothelialization outcomes in animal models and those occurring in clinic (Zilla et al., 2007; Sánchez et al., 2018; Cai et al., 2021). Despite increased graft assessments in different animal models, most studies still use young, healthy small animals. It could be attributed to drastic differences in the vascular anatomy and physiology between human and rodents, which are used for evaluations in the majority of animal studies. The re-endothelization of a vein graft was reported to complete after several weeks of post-surgery in rodents, but re-endothelization duration in human took much longer. More important than the late presence of an endothelium on TEVG in human is a mismatch in the endothelialization mechanism—mainly trans-anastomotic mechanism in short grafts for rodents versus mainly transmural or blood-borne endothelialization in much longer grafts for humans (Zilla et al., 2007). In the clinical context of PTFE grafts, trans-anastomotic endothelialization covers only the immediate peri-anastomotic graft region in patients. Based on the analysis in a senescent non-human primate model, Zilla et al. (2007) and Zilla et al. (2020), concluded that a major issue with the development of prosthetic vascular grafts lied in wrong animal models, which led to wrong questions and no healing. Large animal models such as sheep, pigs, and baboons, though less available and more costly, mimic human physiology, in terms of vascular anatomy, thrombogenicity, inflammatory responses and regenerative potentials (Fukunishi et al., 2016; Rothuizen et al., 2016; Ju et al., 2017; Ma et al., 2017; Syedain et al., 2017; Liu et al., 2018; Schleimer et al., 2018; Fang et al., 2021b).

Overall, the design of future preclinical studies would better address the clinical relevance, for example, dialysis access (Gage and Lawson, 2017; Ong et al., 2017) and meso-Rex bypass (Maxfield et al., 2017), by providing further insight into the mechanisms through experimental designs that are aligned with the purpose and scope of specific clinical applications. In selecting animal models that prematurely terminate adverse remodeling events, the factors that impair vascular regeneration around grafts in clinic may remain largely overlooked. Besides the type of animal models, the significant "impairment factors" as listed in Section 2 include age and disease conditions, e.g., diabetes and ischemia. Additionally, temporal and spatial characterizations of the host responses in animals would be crucial to improve our mechanistic understandings of TEVG remodeling.
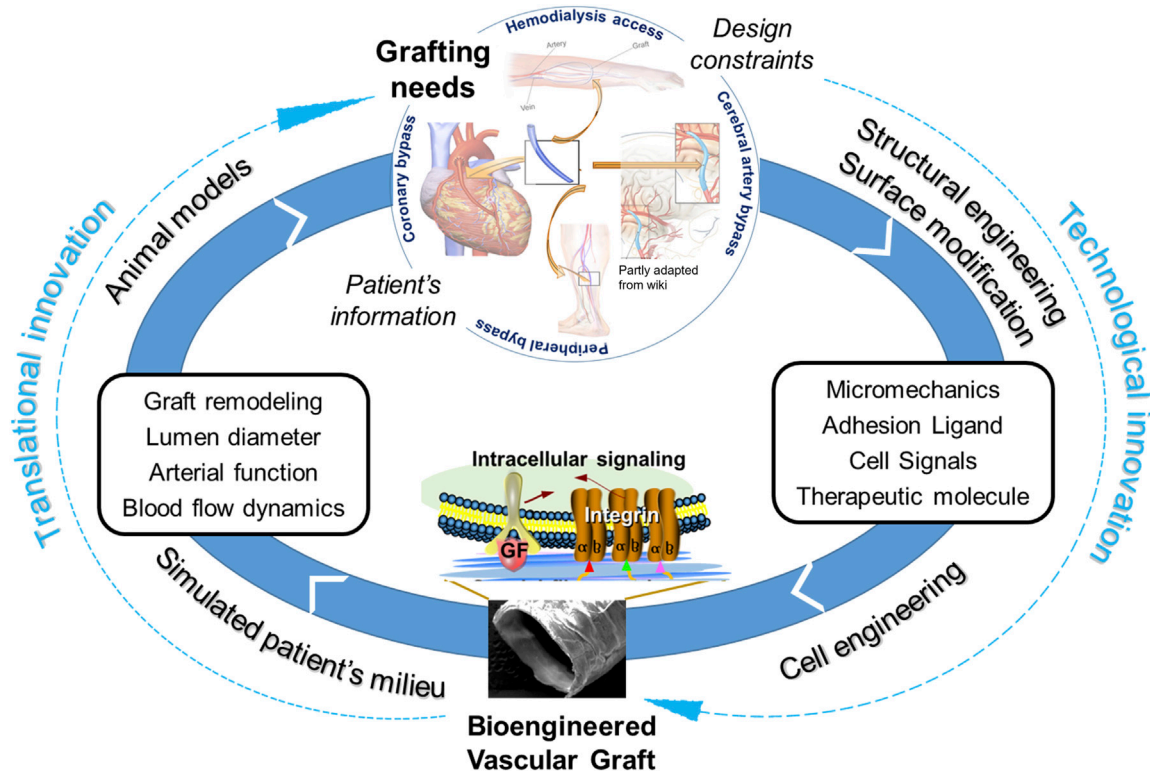
FIGURE 6
Coupling of technological innovations with translational innovations to tackle adverse remodeling of vascular grafts for clinical applications.

4.3 Clinical trials and potential commercialization values

Clinical trials are a true success measure and a determinant to the commercial value of any graft innovation. Prior trials have been performed on three types of grafts: Biological grafts (i.e., xenografts or allografts), bioreactor-manufactured grafts, and readily implantable grafts. Though trial results are encouraging and enlightening for future TEVG strategies, the overall success is still limited.

Biological grafts, referring to acellular blood vessels from human or animal (e.g., bovine) origin, have undergone clinical trials for decades. Bovine carotid artery grafts, such as those commercialized as Artegraft™, were used as arteriovenous fistula in patients undergoing chronic hemodialysis. These grafts outperformed PTFE grafts, though incrementally (Hutchin et al., 1975; Kennealey et al., 2011; Arhuidese et al., 2017). Lindsey et al. (2018) did a 15-year follow-up study on Artegaft used in lower extremity bypass surgery of 120 patients, yielding positive results for patency and salvage limb rates. Recently, the concern regarding the immunologic sensitization of artery xenografts in patients was also addressed (Dyer-Kindy et al., 2020). Similar to an artery graft, a vein xenograft such as bovine vein-derived ProCol™ demonstrated their candidacy as an alternative to synthetic grafts through clinical trials in both hemodialysis patients and patients with critical limb ischemia for 14–20 months (Hatzibaloglou et al., 2004; Schmidli et al., 2004). Vein allografts derived from human cadaveric veins were also a possible alternative. Cryopreserved allografts were used in 90 patients, showing similar patency, more resistant to infection but significantly more susceptible to aneurysms, when compared to PTFE grafts (Madden et al., 2004). More recently, 15 vein allografts seeded with autologous endothelial cells were used in coronary artery bypass surgery with 12 patients, showing patency up to 32 months (Herrmann et al., 2019). Autologous stem cells were also used to recellularize vein allografts and successfully tried on one pediatric patient for vascular vein shunts without the need for immunosuppression (Olausson et al., 2012). Overall, decades of clinical trials have shown that an artery- or vein-based xenografts or allografts can be considered as an alternative to synthetic PTFE or Dacron grafts. However, significant improvements over these graft products, in particular decellularization and recellularization as well as deproteinization and surface engineering to address complications- and/or rejections-derived from immune responses (Merola et al., 2017), are needed before they may gain a bit market share.

Bioreactor-manufactured grafts produce TEVG by culturing human autologous cells and/or allogeneic cells with or without a scaffold in a bioreactor with controlled physical, mechanical and/or biological environments. Clinical trials have illuminated promises and challenges with current methods. Lawson et al. (2016) seeded allogeneic human VSMCs onto polyglycolic acid scaffold, subjected the cell-loaded scaffold to pulsatile cyclic distension for 8 weeks before decellularization for final acellular implant. The patency of these grafts (Humacyte™) on 60 hemodialysis patients was 63% at 6 months and 28% at 18 months, with no evidence of immune response or aneurysm formation. From this trial, 16 tissue samples were acquired from 16 to 200 weeks for the characterization of vascular remodeling, showing recellularization of grafts by non-inflammatory host progenitor and vascular cells (Kirkton et al., 2019). A recent follow-up report provided 5-year (phase II) results on 11 patients who completed the study

(Jakimowicz et al., 2022). Results showed that one patient maintained primary patency, and 10 maintained secondary patency. Like PTFE grafts, such acellular grafts showed better clinical outcomes when used as above-knee, femoral-to-popliteal arterial bypass conduits in 20 patients (Gutowski et al., 2020). As an example for scaffold-free cell-engineered graft, Cytograft™ employed patients' fibroblasts to create an autologous TEVG through a prolonged fabrication procedure, either finishing with autologous endothelial seeding or implanting as it is. Its clinical trial with hemodialysis grafts on ten patients showed 1-month patency of 78% and 6-month patency of 60% (McAllister et al., 2009). Later, L'Heureux's group modified the graft production into an "off-the-shelf" design—allogeneic Lifeline™ graft. Prior to implantation in patients for hemodialysis access, frozen cell-sheet based scaffolds were thawed, rehydrated and seeded with autologous endothelial cells the luminal side. All three implanted grafts worked well till 11 months (Wystrychowski et al., 2014).

More readily implantable grafts are desirable in clinic, as they require minimal or no need of cell culture time, relying on *in vivo* degradation, remodeling, regeneration and maturation. One recent approach is embedding a biotube in subcutaneous spaces of a patient for months, using patient's body to fabricate a graft. This has been used successfully as a pulmonary artery substitute in pediatric patients (Kato et al., 2016; Fujita et al., 2020; Nakatsuji et al., 2021; Higashita et al., 2022). Another approach was employing biodegradable scaffolds in combination with autologous bone marrow mononuclear cells. Their clinical trials investigated these TEVGs in congenital heart surgery (Sugiura et al., 2018). Researchers observed postoperative growth of a TEVG as well as frequent graft narrowing in pediatric patients, but there was no graft-related mortality during the 11-year follow-up period.

5 Challenge and future

In conclusion, we reviewed the studies in the context of three innovations, i.e., cell technology, scaffold technology, and translational stages. Regenerative medicine has demonstrated great promises in the TEVG context. Future endeavors require the technological innovations to be coupled with translational innovations, in order to tackle the adverse remodeling of vascular grafts (Figure 6). This is critical to our fundamental understandings of the regenerative mechanisms and eventual transfer of the understandings into improved products for clinical practices. The complex nature of vascular remodeling and regeneration mechanisms in the spatial and temporal dimensions demands more sophisticated designs of *in vitro* studies and animal models. A combined approach employing both experimental and computational tools could significantly expedite the determination of optimal design parameters in a disease- or host-specific condition. From a perspective of clinical translation and graft commercialization, the considerations about costs and graft processing logistics become more and more important and are also highlighted in other recent reviews and studies. To address scientific questions to the point of clinical relevance, it is critical to highlight and increase the use of appropriate cell models, such as 3D cell models in diseased conditions, appropriate animal models, such as senescent animals, diseased animals, animals with slow vascular regenerative rates. Additionally, to more quantitatively and systematically understand the mechanisms, it would be helpful to standardize protocols such as sampling times across studies to obtain critical mechanobiological modeling inputs such as material degradation, inflammation, growth/remodeling/regeneration parameters.

Also, it is expected that the adaptation and integration of bioengineered or tissue-engineered vascular grafts to human patients are heterogeneous because of cells' varied ability to adapt to new microenvironments. A comparable case of graft heterogeneity in clinic is the use of vein grafts. Some veins are poor remodelers due to lack of adaptation, which had a 13-fold increased risk of failure at 2 years compared with "robust remodelers" (Owens et al., 2015). One factor in this lack of adaptation is biological incompatibility between cells and host endothelium. Cellular heterogeneity arises due to reasons not fully understood yet. For example, iPSC-derived arterial endothelial cells exhibit functional differences from iPSC-derived venous endothelial cells, including nitric oxide production and elongation under shear stress (Rosa et al., 2019). At present, the limitation of cellular heterogeneity is also a direct consequence of difficulty in identifying and precisely isolating progenitor cells which has limited their use in TEVGs. Therefore, improving methods of cell isolation and differentiation as well as reducing heterogeneity between cells in grafts and host vessels could be a solution to better integrate TEVGs into native vasculature.

We acknowledge several limitations of this review study, which include the lack of in-depth analyses and justifications of graft design, fabrication, biomaterials, and molecular mechanisms underlying graft failure and integration.

Author contributions

WT, SK, and PB drafted and wrote the manuscript, and PS edited it.

Funding

Conflict of interest

The authors declare that the research was conducted in the absence of any commercial or financial relationships that could be construed as a potential conflict of interest.

Publisher's note

All claims expressed in this article are solely those of the authors and do not necessarily represent those of their affiliated organizations, or those of the publisher, the editors and the reviewers. Any product that may be evaluated in this article, or claim that may be made by its manufacturer, is not guaranteed or endorsed by the publisher.

Supplementary Material

The Supplementary Material for this article can be found online at: https://www.frontiersin.org/articles/10.3389/fbioe.2022.1097334/full#supplementary-material

References

AbuRahma, A. F. (2018). When are endovascular and open bypass treatments preferred for femoropopliteal occlusive disease? *Ann. Vasc. Dis.* 11 (1), 25–40. doi:10.3400/avd.ra.18-00001

Afra, S., and Matin, M. M. (2020). Potential of mesenchymal stem cells for bioengineered blood vessels in comparison with other eligible cell sources. *Cell Tissue Res.* 380 (1), 1–13. doi:10.1007/s00441-019-03161-0

Afsar, B., and Elsurer, R. (2012). The primary arteriovenous fistula failure—a comparison between diabetic and non-diabetic patients: Glycemic control matters. *Int. Urol. Nephrol.* 44 (2), 575–581. doi:10.1007/s11255-011-9978-x

Ahangar, P., Mills, S. J., and Cowin, A. J. (2020). Mesenchymal stem cell secretome as an emerging cell-free alternative for improving wound repair. *Int. J. Mol. Sci.* 21 (19), 7038. doi:10.3390/ijms21197038

Ahmed, F. A., and Catic, A. G. (2018). Decision-making in geriatric patients with end-stage renal disease: Thinking beyond nephrology. *J. Clin. Med.* 8 (1), 5. doi:10.3390/jcm8010005

Akentjew, T. L., Terraza, C., Suazo, C., Maksimcuka, J., Wilkens, C. A., Vargas, F., et al. (2019). Rapid fabrication of reinforced and cell-laden vascular grafts structurally inspired by human coronary arteries. *Nat. Commun.* 10 (1), 3098. doi:10.1038/s41467-019-11090-3

Amensag, S., and McFetridge, P. S. (2012). Rolling the human amnion to engineer laminated vascular tissues. *Tissue Eng. Part C Methods* 18 (11), 903–912. doi:10.1089/ten.tec.2012.0119

ANSI 2010. ANSI/AAMI/ISO 7198:1998/2001 (R2010) - cardiovascular implants - tubular vascular prostheses. Accessed December 15, 2021. Available at: https://webstore.ansi.org/standards/aami/ansiaamiiso719819982001r2010.

Antonova, L., Kutikhin, A., Sevostianova, V., Velikanova, E., Matveeva, V., Glushkova, T., et al. (2021). bFGF and SDF-1α improve *in vivo* performance of VEGF-incorporating small-diameter vascular grafts. *Pharm. Basel Switz.* 14 (4), 302. doi:10.3390/ph14040302

Ardila, D. C., Liou, J. J., Maestas, D., Slepian, M., Badowski, M., Wagner, W., et al. (2019). Surface modification of electrospun scaffolds for endothelialization of tissue-engineered vascular grafts using human cord blood-derived endothelial cells. *J. Clin. Med.* 8 (2), E185. doi:10.3390/jcm8020185

Arhuidese, I., Reifsnyder, T., Islam, T., Karim, O., Nejim, B., Obeid, T., et al. (2017). Bovine carotid artery biologic graft outperforms expanded polytetrafluoroethylene for hemodialysis access. *J. Vasc. Surg.* 65 (3), 775–782. doi:10.1016/j.jvs.2016.10.080

Baruah, J., and Wary, K. K. (2020). Exosomes in the regulation of vascular endothelial cell regeneration. *Front. Cell Dev. Biol.* 7, 353. doi:10.3389/fcell.2019.00353

Bassiouny, H. S., White, S., Glagov, S., Choi, E., Giddens, D. P., and Zarins, C. K. (1992). Anastomotic intimal hyperplasia: Mechanical injury or flow induced. *J. Vasc. Surg.* 15 (4), 708–717. doi:10.1016/0741-5214(92)90019-5

Best, C., Strouse, R., Hor, K., Pepper, V., Tipton, A., Kelly, J., et al. (2018). Toward a patient-specific tissue engineered vascular graft. *J. Tissue Eng.* 9, 204173141876470. doi:10.1177/2041731418764709

Best, C. A., Szafron, J. M., Rocco, K. A., Zbinden, J., Dean, E. W., Maxfield, M. W., et al. (2019). Differential outcomes of venous and arterial tissue engineered vascular grafts highlight the importance of coupling long-term implantation studies with computational modeling. *Acta Biomater.* 94, 183–194. doi:10.1016/j.actbio.2019.05.063

Binns, R. L., Ku, D. N., Stewart, M. T., Ansley, J. P., and Coyle, K. A. (1989). Optimal graft diameter: Effect of wall shear stress on vascular healing. *J. Vasc. Surg.* 10 (3), 326–337. doi:10.1016/0741-5214(89)90449-7

Blum, K. M., Roby, L. C., Zbinden, J. C., Chang, Y. C., Mirhaidari, G. J. M., Reinhardt, J. W., et al. (2021). Sex and Tamoxifen confound murine experimental studies in cardiovascular tissue engineering. *Sci. Rep.* 11(1), 8037. doi:10.1038/s41598-021-87006-3

Boccafoschi, F., Mosca, C., and Cannas, M. (2014). Cardiovascular biomaterials: When the inflammatory response helps to efficiently restore tissue functionality? *J. Tissue Eng. Regen. Med.* 8 (4), 253–267. doi:10.1002/term.1526

Bosiers, M. J., Panuccio, G., Bisdas, T., Stachmann, A., Donas, K. P., Torsello, G., et al. (2020). Longer bridging stent-grafts in iliac branch endografting does not worsen outcome and expands its applicability, even in concomitant diseased hypogastric arteries. *J. Cardiovasc Surg. (Torino)* 61 (2), 191–195. doi:10.23736/S0021-9509.18.10504-0

Boutrous, M. L., Alvarez, A. C., Okoye, O. T., Laws, J. C., Jacobs, D. L., and Smeds, M. R. (2019). Stent-graft length is associated with decreased patency in treatment of central venous stenosis in hemodialysis patients. *Ann. Vasc. Surg.* 59, 225–230. doi:10.1016/j.avsg.2019.01.024

Browne, S., and Pandit, A. (2015). Biomaterial-mediated modification of the local inflammatory environment. *Front. Bioeng. Biotechnol.* 3, 67. doi:10.3389/fbioe.2015.00067

Cai, Q., Liao, W., Xue, F., Wang, X., Zhou, W., Li, Y., et al. (2021). Selection of different endothelialization modes and different seed cells for tissue-engineered vascular graft. *Bioact. Mater* 6 (8), 2557–2568. doi:10.1016/j.bioactmat.2020.12.021

Caliskan, E., de Souza, D. R., Böning, A., Liakopoulos, O. J., Choi, Y. H., Pepper, J., et al. (2020). Saphenous vein grafts in contemporary coronary artery bypass graft surgery. *Nat. Rev. Cardiol.* 17 (3), 155–169. doi:10.1038/s41569-019-0249-3

Chandra, P., and Atala, A. (2019). Engineering blood vessels and vascularized tissues: Technology trends and potential clinical applications. *Clin. Sci. Lond Engl.* 133 (9), 1115–1135. doi:10.1042/CS20180155

Chang, Y. C., Li, J., Mirhaidari, G., Zbinden, J., Barker, J., Blum, K., et al. (2021). Zoledronate alters natural progression of tissue-engineered vascular grafts. *FASEB J. Off. Publ. Fed. Am. Soc. Exp. Biol.* 35 (10), e21849. doi:10.1096/fj.202001606RR

Chen, C. L., Guo, H. R., Wang, Y. J., Chang, H. T., Pan, C. Y., Tuan-Mu, H. Y., et al. (2019). Combination of inductive effect of lipopolysaccharide and *in situ* mechanical conditioning for forming an autologous vascular graft *in vivo*. *Sci. Rep.* 9 (1), 10616. doi:10.1038/s41598-019-47054-2

Chen, W., Yang, M., Bai, J., Li, X., Kong, X., Gao, Y., et al. (2018). Exosome-modified tissue engineered blood vessel for endothelial progenitor cell capture and targeted siRNA delivery. *Macromol. Biosci.* 18 (2), 1700242. doi:10.1002/mabi.201700242

Chistiakov, D. A., Orekhov, A. N., and Bobryshev, Y. V. (2017). Effects of shear stress on endothelial cells: Go with the flow. *Acta Physiol.* 219 (2), 382–408. doi:10.1111/apha.12725

Chiu, J. J., and Chien, S. (2011). Effects of disturbed flow on vascular endothelium: Pathophysiological basis and clinical perspectives. *Physiol. Rev.* 91 (1), 327–387. doi:10.1152/physrev.00047.2009

Choi, W. S., Joung, Y. K., Lee, Y., Bae, J. W., Park, H. K., Park, Y. H., et al. (2016). Enhanced patency and endothelialization of small-caliber vascular grafts fabricated by coimmobilization of heparin and cell-adhesive peptides. *ACS Appl. Mater Interfaces* 8 (7), 4336–4346. doi:10.1021/acsami.5b12052

Connors, G., Todoran, T. M., Engelson, B. A., Sobieszczyk, P. S., Eisenhauer, A. C., and Kinlay, S. (2011). Percutaneous revascularization of long femoral artery lesions for claudication: Patency over 2.5 years and impact of systematic surveillance. *Catheter Cardiovasc Interv. Off. J. Soc. Card. Angiogr. Interv.* 77 (7), 1055–1062. doi:10.1002/ccd.22802

Conte, M. S. (2012). Diabetic revascularization: Endovascular versus open bypass—do we have the answer? *Semin. Vasc. Surg.* 25 (2), 108–114. doi:10.1053/j.semvascsurg.2012.04.004

Copes, F., Pien, N., Van Vlierberghe, S., Boccafoschi, F., and Mantovani, D. (2019). Collagen-based tissue engineering strategies for vascular medicine. *Front. Bioeng. Biotechnol.* 7, 166. doi:10.3389/fbioe.2019.00166

Creager, M. A., Lüscher, T. F., Beckman, J. A., and Cosentino, T. F. (2003). Diabetes and vascular disease:pathophysiology, clinical consequences, and medical therapy: Part I. *Circulation* 108(12), 1527–1532. doi:10.1161/01.CIR.0000091257.27563.32

Cunnane, E. M., Lorentz, K. L., Ramaswamy, A. K., Gupta, P., Mandal, B. B., O'Brien, F. J., et al. (2020). Extracellular vesicles enhance the remodeling of cell-free silk vascular scaffolds in rat aortae. *ACS Appl. Mater Interfaces* 12 (24), 26955–26965. doi:10.1021/acsami.0c06609

Cunnane, E. M., Lorentz, K. L., Soletti, L., Ramaswamy, A. K., Chung, T. K., Haskett, D. G., et al. (2020). Development of a semi-automated, bulk seeding device for large animal model implantation of tissue engineered vascular grafts. *Front. Bioeng. Biotechnol.* 8, 597847. doi:10.3389/fbioe.2020.597847

Cunnane, E. M., Weinbaum, J. S., O'Brien, F. J., and Vorp, D. A. (2018). Future perspectives on the role of stem cells and extracellular vesicles in vascular tissue regeneration. *Front. Cardiovasc Med.* 5, 86. doi:10.3389/fcvm.2018.00086

Dahan, N., Sarig, U., Bronshtein, T., Baruch, L., Karram, T., Hoffman, A., et al. (2017). Dynamic autologous reendothelialization of small-caliber arterial extracellular matrix: A preclinical large animal study. *Tissue Eng. Part A* 23 (1-2), 69–79. doi:10.1089/ten.TEA.2016.0126

de Almeida, P. E., Ransohoff, J. D., Nahid, A., and Wu, J. C. (2013). Immunogenicity of pluripotent stem cells and their derivatives. *Circ. Res.* 112 (3), 549–561. doi:10.1161/CIRCRESAHA.111.249243

Devine, R., Goudie, M. J., Singha, P., Schmiedt, C., Douglass, M., Brisbois, E. J., et al. (2020). Mimicking the endothelium: Dual action heparinized nitric oxide releasing surface. *ACS Appl. Mater Interfaces* 12 (18), 20158–20171. doi:10.1021/acsami.9b22277

Dhawan, S. S., Nanjundappa, R. P. A., Branch, J. R., Taylor, W. R., Quyyumi, A. A., Jo, H., et al. (2010). Shear stress and plaque development. *Expert Rev. Cardiovasc Ther.* 8 (4), 545–556. doi:10.1586/erc.10.28

Dimitrievska, S., Wang, J., Lin, T., Weyers, A., Bai, H., Qin, L., et al. (2020). Glycocalyx-like hydrogel coatings for small diameter vascular grafts. *Adv. Funct. Mater* 30 (23), 1908963. doi:10.1002/adfm.201908963

Ding, J., Liu, Y., Wang, F., and Bai, F. (2012). Impact of competitive flow on hemodynamics in coronary surgery: Numerical study of ITA-LAD model. *Comput. Math. Methods Med.* 2012, 1–7. doi:10.1155/2012/356187

Domínguez-Robles, J., Shen, T., Cornelius, V. A., Corduas, F., Mancuso, E., Donnelly, R. F., et al. (2021). Development of drug loaded cardiovascular prosthesis for thrombosis prevention using 3D printing. *Mater Sci. Eng. C Mater Biol. Appl.* 129, 112375. doi:10.1016/j.msec.2021.112375

Donadoni, F., Pichardo-Almarza, C., Homer-Vanniasinkam, S., Dardik, A., and Díaz-Zuccarini, V. (2020). Multiscale, patient-specific computational fluid dynamics models predict formation of neointimal hyperplasia in saphenous vein grafts. *J. Vasc. Surg. Cases Innov. Tech.* 6 (2), 292–306. doi:10.1016/j.jvscit.2019.09.009

Dou, J., Wang, Y., Jin, X., Li, P., Wang, L., Yuan, J., et al. (2020). PCL/sulfonated keratin mats for vascular tissue engineering scaffold with potential of catalytic nitric oxide generation. *Mater Sci. Eng. C Mater Biol. Appl.* 107, 110246. doi:10.1016/j.msec.2019.110246

Drews, J. D., Miyachi, H., and Shinoka, T. (2017). Tissue-engineered vascular grafts for congenital cardiac disease: Clinical experience and current status. *Trends Cardiovasc Med.* 27 (8), 521–531. doi:10.1016/j.tcm.2017.06.013

Drews, J. D., Pepper, V. K., Best, C. A., Szafron, J. M., Cheatham, J. P., Yates, A. R., et al. (2020). Spontaneous reversal of stenosis in tissue-engineered vascular grafts. *Sci. Transl. Med.* 12 (537), eaax6919. doi:10.1126/scitranslmed.aax6919

Dyer-Kindy, L. M., Heelan Gladden, A. A., Gralla, J., McCormick, N. D., Jenks, C., Cooper, J., et al. (2020). Relationship between bovine carotid artery grafts for hemodialysis access and human leukocyte antigen sensitization. *Hemodial. Int. Int. Symp. Home Hemodial.* 24 (1), 36–42. doi:10.1111/hdi.12784

Eilenberg, M., Enayati, M., Ehebruster, D., Grasl, C., Walter, I., Messner, B., et al. (2020). Long term evaluation of nanofibrous, bioabsorbable polycarbonate urethane grafts for small diameter vessel replacement in rodents. *Eur. J. Vasc. Endovasc. Surg.* 59 (4), 643–652. doi:10.1016/j.ejvs.2019.11.004

Enayati, M., Schneider, K. H., Almeria, C., Grasl, C., Kaun, C., Messner, B., et al. (2021). S-nitroso human serum albumin as a nitric oxide donor in drug-eluting vascular grafts: Biofunctionality and preclinical evaluation. *Acta Biomater.* 134, 276–288. doi:10.1016/j.actbio.2021.07.048

Fang, S., Ahlmann, A. H., Langhorn, L., Hussein, K., Sorensen, J. A., Guan, X., et al. (2021). Small diameter polycaprolactone vascular grafts are patent in sheep carotid bypass but require antithrombotic therapy. *Regen. Med.* 25, 117–130. doi:10.2217/rme-2020-0171

Fang, S., Ellman, D. G., and Andersen, D. C. (2021). Review: Tissue engineering of small-diameter vascular grafts and their *in vivo* evaluation in large animals and humans. *Cells* 10 (3), 713. doi:10.3390/cells10030713

Fathi-Karkan, S., Banimohamad-Shotorbani, B., Saghati, S., Rahbarghazi, R., and Davaran, S. (2022). A critical review of fibrous polyurethane-based vascular tissue engineering scaffolds. *J. Biol. Eng.* 16 (1), 6. doi:10.1186/s13036-022-00286-9

Fayon, A., Menu, P., and El Omar, R. (2021). Cellularized small-caliber tissue-engineered vascular grafts: Looking for the ultimate gold standard. *Npj Regen. Med.* 6 (1), 46–11. doi:10.1038/s41536-021-00155-x

Freeman, J., Chen, A., Weinberg, R. J., Okada, T., Chen, C., and Lin, P. H. (2018). Sustained thromboresistant bioactivity with reduced intimal hyperplasia of heparin-bonded polytetrafluoroethylene propaten graft in a chronic canine femoral artery bypass model. *Ann. Vasc. Surg.* 49, 295–303. doi:10.1016/j.avsg.2017.09.017

Fujita, S., Yamagishi, M., Kanda, K., Maeda, Y., Inoue, T., Yamanami, M., et al. (2020). Histology and mechanics of *in vivo* tissue-engineered vascular graft for children. *Ann. Thorac. Surg.* 110 (3), 1050–1054. doi:10.1016/j.athoracsur.2020.03.069

Fukunishi, T., Best, C. A., Ong, C. S., Groehl, T., Reinhardt, J., Yi, T., et al. (2018). Role of bone marrow mononuclear cell seeding for nanofiber vascular grafts. *Tissue Eng. Part A* 24 (1-2), 135–144. doi:10.1089/ten.TEA.2017.0044

Fukunishi, T., Best, C. A., Sugiura, T., Opfermann, J., Ong, C. S., Shinoka, T., et al. (2017). Preclinical study of patient-specific cell-free nanofiber tissue-engineered vascular grafts using 3-dimensional printing in a sheep model. *J. Thorac. Cardiovasc Surg.* 153 (4), 924–932. doi:10.1016/j.jtcvs.2016.10.066

Fukunishi, T., Best, C. A., Sugiura, T., Shoji, T., Yi, T., Udelsman, B., et al. (2016). Tissue-engineered small diameter arterial vascular grafts from cell-free nanofiber PCL/chitosan scaffolds in a sheep model. *PLOS ONE* 11 (7), e0158555. doi:10.1371/journal.pone.0158555

Fukunishi, T., Ong, C. S., He, Y. J., Inoue, T., Zhang, H., Steppan, J., et al. (2021). Fast-Degrading tissue-engineered vascular grafts lead to increased extracellular matrix cross-linking enzyme expression. *Tissue Eng. Part A* 27 (21-22), 1368–1375. doi:10.1089/ten.TEA.2020.0266

Fukunishi, T., Ong, C. S., Lui, C., Pitaktong, I., Smoot, C., Harris, J., et al. (2019). formation of neoarteries with optimal remodeling using rapidly degrading textile vascular grafts. *Tissue Eng. Part A* 25 (7-8), 632–641. doi:10.1089/ten.TEA.2018.0167

Fukunishi, T., Ong, C. S., Yesantharao, P., Best, C. A., Yi, T., Zhang, H., et al. (2020). Different degradation rates of nanofiber vascular grafts in small and large animal models. *J. Tissue Eng. Regen. Med.* 14 (2), 203–214. doi:10.1002/term.2977

Furdella, K. J., Higuchi, S., Behrangzade, A., Kim, K., Wagner, W. R., and Vande Geest, J. P. (2021). *In-vivo* assessment of a tissue engineered vascular graft computationally optimized for target vessel compliance. *Acta Biomater.* 123, 298–311. doi:10.1016/j.actbio.2020.12.058

Gage, S. M., and Lawson, J. H. (2017). Bioengineered hemodialysis access grafts. *J. Vasc. Access* 18, 56–63. doi:10.5301/jva.5000692

Gao, A., Hang, R., Li, W., Zhang, W., Li, P., Wang, G., et al. (2017). Linker-free covalent immobilization of heparin, SDF-1α, and CD47 on PTFE surface for antithrombogenicity, endothelialization and anti-inflammation. *Biomaterials* 140, 201–211. doi:10.1016/j.biomaterials.2017.06.023

Gaudino, M., Antoniades, C., Benedetto, U., Deb, S., Di Franco, A., Di Giammarco, G., et al. (2017). Mechanisms, consequences, and prevention of coronary graft failure. *Circulation* 136 (18), 1749–1764. doi:10.1161/CIRCULATIONAHA.117.027597

Gaudino, M., Niccoli, G., and Scalone, G. (2016). "Competitive flow and coronary artery bypass grafts," in *Coronary graft failure: State of the art*. Editors I. C. Țintoiu, M. J. Underwood, S. P. Cook, H. Kitabata, and A. Abbas (Germany: Springer International Publishing), 277–284. doi:10.1007/978-3-319-26515-5_25

Generali, M., Casanova, E. A., Kehl, D., Wanner, D., Hoerstrup, S. P., Cinelli, P., et al. (2019). Autologous endothelialized small-caliber vascular grafts engineered from blood-derived induced pluripotent stem cells. *Acta Biomater.* 97, 333–343. doi:10.1016/j.actbio.2019.07.032

Gentile, P., Sterodimas, A., Pizzicannella, J., Dionisi, L., De Fazio, D., Calabrese, C., et al. (2020). Systematic review: Allogenic use of stromal vascular fraction (SVF) and decellularized extracellular matrices (ECM) as advanced therapy medicinal products (ATMP) in tissue regeneration. *Int. J. Mol. Sci.* 21 (14), E4982. doi:10.3390/ijms21144982

Gong, W., Lei, D., Li, S., Huang, P., Qi, Q., Sun, Y., et al. (2016). Hybrid small-diameter vascular grafts: Anti-expansion effect of electrospun poly ε-caprolactone on heparin-coated decellularized matrices. *Biomaterials* 76, 359–370. doi:10.1016/j.biomaterials.2015.10.066

Gong, Z., and Niklason, L. E. (2008). Small-diameter human vessel wall engineered from bone marrow-derived mesenchymal stem cells (hMSCs). *FASEB J.* 22 (6), 1635–1648. doi:10.1096/fj.07-087924

Gupta, P., Chaudhuri, G. R., Janani, G., Agarwala, M., Ghosh, D., Nandi, S. K., et al. (2021). Functionalized silk vascular grafts with decellularized human wharton's jelly improves remodeling via immunomodulation in rabbit jugular vein. *Adv. Healthc. Mater* 10 (19), e2100750. doi:10.1002/adhm.202100750

Gupta, P., Lorentz, K. L., Haskett, D. G., Cunnane, E. M., Ramaswamy, A. K., Weinbaum, J. S., et al. (2020). Bioresorbable silk grafts for small diameter vascular tissue engineering applications: *In vitro* and *in vivo* functional analysis. *Acta Biomater.* 105, 146–158. doi:10.1016/j.actbio.2020.01.020

Gupta, P., and Mandal, B. B. (2021). Tissue-engineered vascular grafts: Emerging trends and technologies. *Adv. Funct. Mater* 31 (33), 2100027. doi:10.1002/adfm.202100027

Gutowski, P., Gage, S. M., Guziewicz, M., Ilzecki, M., Kazimierczak, A., Kirkton, R. D., et al. (2020). Arterial reconstruction with human bioengineered acellular blood vessels in patients with peripheral arterial disease. *J. Vasc. Surg.* 72 (4), 1247–1258. doi:10.1016/j.jvs.2019.11.056

Håkansson, J., Simsa, R., Bogestål, Y., Jenndahl, L., Gustafsson-Hedberg, T., Petronis, S., et al. (2021). Individualized tissue-engineered veins as vascular grafts: A proof of concept study in pig. *J. Tissue Eng. Regen. Med.* 15 (10), 818–830. doi:10.1002/term.3233

Halbert, R. J., Nicholson, G., Nordyke, R. J., Pilgrim, A., and Niklason, L. (2020). Patency of ePTFE arteriovenous graft placements in hemodialysis patients: Systematic literature review and meta-analysis. *Kidney360.* 1 (12), 1437–1446. doi:10.34067/KID.0003502020

Ham, H. O., Haller, C. A., Su, G., Dai, E., Patel, M. S., Liu, D. R., et al. (2021). A rechargeable anti-thrombotic coating for blood-contacting devices. *Biomaterials* 276, 121011. doi:10.1016/j.biomaterials.2021.121011

Hao, D., Fan, Y., Xiao, W., Liu, R., Pivetti, C., Walimbe, T., et al. (2020). Rapid endothelialization of small diameter vascular grafts by a bioactive integrin-binding ligand specifically targeting endothelial progenitor cells and endothelial cells. *Acta Biomater.* 108, 178–193. doi:10.1016/j.actbio.2020.03.005

Hao, D., Xiao, W., Liu, R., Kumar, P., Li, Y., Zhou, P., et al. (2017). Discovery and characterization of a potent and specific peptide ligand targeting endothelial progenitor cells and endothelial cells for tissue regeneration. *ACS Chem. Biol.* 12 (4), 1075–1086. doi:10.1021/acschembio.7b00118

Harris, L. J., Abdollahi, H., Zhang, P., McIlhenny, S., Tulenko, T. N., and DiMuzio, P. J. (2011). Differentiation of adult stem cells into smooth muscle for vascular tissue engineering. *J. Surg. Res.* 168 (2), 306–314. doi:10.1016/j.jss.2009.08.001

Harskamp, R. E., Alexander, J. H., Ferguson, T. B., Hager, R., Mack, M. J., Englum, B., et al. (2016). Frequency and predictors of internal mammary artery graft failure and subsequent clinical outcomes: Insights from the project of *ex-vivo* vein graft engineering via transfection (PREVENT) IV trial. *Circulation* 133 (2), 131–138. doi:10.1161/CIRCULATIONAHA.115.015549

Haskett, D. G., Saleh, K. S., Lorentz, K. L., Josowitz, A. D., Luketich, S. K., Weinbaum, J. S., et al. (2018). An exploratory study on the preparation and evaluation of a "same-day" adipose stem cell-based tissue-engineered vascular graft. *J. Thorac. Cardiovasc Surg.* 156 (5), 1814–1822. doi:10.1016/j.jtcvs.2018.05.120

Hatzibaloglou, A., Velissaris, I., Kaitzis, D., Grekas, D., Avdelidou, A., and Kiskinis, D. (2004). ProCol® vascular bioprosthesis for vascular access: Midterm results. *J. Vasc. Access* 5 (1), 16–18. doi:10.1177/112972980400500104

Heath, D. E. (2017). Promoting endothelialization of polymeric cardiovascular biomaterials. *Macromol. Chem. Phys.* 218 (8), 1600574. doi:10.1002/macp.201600574

Heidenhain, C., Veeravoorn, A., Vachkov, B., Weichert, W., Schmidmaier, G., Wildemann, B., et al. (2011). Fibroblast and vascular endothelial growth factor coating of decellularized vascular grafts stimulates undesired giant cells and graft encapsulation in a rat model. *Artif. Organs* 35 (1), E1–E10. doi:10.1111/j.1525-1594.2010.01072.x

Heng, J. W., Yazid, M. D., Abdul Rahman, M. R., and Sulaiman, N. (2021). Coatings in decellularized vascular scaffolds for the establishment of a functional endothelium: A scoping review of vascular graft refinement. *Front. Cardiovasc Med.* 8, 677588. doi:10.3389/fcvm.2021.677588

Herrmann, F. E. M., Lamm, P., Wellmann, P., Milz, S., Hagl, C., and Juchem, G. (2019). Autologous endothelialized vein allografts in coronary artery bypass surgery – long term results. *Biomaterials* 212, 87–97. doi:10.1016/j.biomaterials.2019.05.019

Hibino, N., McGillicuddy, E., Matsumura, G., Ichihara, Y., Naito, Y., Breuer, C., et al. (2010). Late-term results of tissue-engineered vascular grafts in humans. *J. Thorac. Cardiovasc Surg.* 139 (2), 431–436. doi:10.1016/j.jtcvs.2009.09.057

Hielscher, D., Kaebisch, C., Braun, B. J. V., Gray, K., and Tobiasch, E. (2018). Stem cell sources and graft material for vascular tissue engineering. *Stem Cell Rev. Rep.* 14 (5), 642–667. doi:10.1007/s12015-018-9825-x

Higashita, R., Miyazaki, M., Oi, M., and Ishikawa, N. (2022). First-in-human results of an in-body tissue architecture-induced tissue-engineered vascular graft "Biotube" for application in distal bypass for chronic limb-threatening ischemia. *J. Vasc. Surg. Cases Innov. Tech.* 8, 488–493. doi:10.1016/j.jvscit.2022.07.007

Hiob, M. A., She, S., Muiznieks, L. D., and Weiss, A. S. (2017). Biomaterials and modifications in the development of small-diameter vascular grafts. *ACS Biomater. Sci. Eng.* 3 (5), 712–723. doi:10.1021/acsbiomaterials.6b00220

Hu, S., Li, Z., Shen, D., Zhu, D., Huang, K., Su, T., et al. (2021). Exosome-eluting stents for vascular healing after ischaemic injury. *Nat. Biomed. Eng.* 5 (10), 1174–1188. doi:10.1038/s41551-021-00705-0

Huang, A. H., Balestrini, J. L., Udelsman, B. V., Zhou, K. C., Zhao, L., Ferruzzi, J., et al. (2016). Biaxial stretch improves elastic fiber maturation, collagen arrangement, and mechanical properties in engineered arteries. *Tissue Eng. Part C Methods* 22 (6), 524–533. doi:10.1089/ten.TEC.2015.0309

Huang, A. H., Lee, Y. U., Calle, E. A., Boyle, M., Starcher, B. C., Humphrey, J. D., et al. (2015). Design and use of a novel bioreactor for regeneration of biaxially stretched tissue-engineered vessels. *Tissue Eng. Part C Methods* 21 (8), 841–851. doi:10.1089/ten.TEC.2014.0287

Hutchin, P., Jacobs, J. R., Devin, J. B., Shaughnessy, S., and Roland, A. S. (1975). Bovine graft arteriovenous fistulas for maintenance hemodialysis. *Surg. Gynecol. Obstet.* 141 (2), 255–258.

Hytönen, J. P., Leppänen, O., Taavitsainen, J., Korpisalo, P., Laidinen, S., Alitalo, K., et al. (2019). Improved endothelialization of small-diameter ePTFE vascular grafts through growth factor therapy. *Vasc. Biol.* 1 (1), 1–9. doi:10.1530/VB-18-0001

Iglesias-Echevarria, M., Johnson, R., Rafuse, M., Ding, Y., and Tan, W. (2021). Vascular grafts with tailored stiffness and a ligand environment via multiarmed polymer sheath for expeditious regeneration. *ACS Appl. Bio Mater* 4 (1), 545–558. doi:10.1021/acsabm.0c01114

Issa Bhaloo, S., Wu, Y., Le Bras, A., Yu, B., Gu, W., Xie, Y., et al. (2018). Binding of dickkopf-3 to CXCR7 enhances vascular progenitor cell migration and degradable graft regeneration. *Circ. Res.* 123 (4), 451–466. doi:10.1161/CIRCRESAHA.118.312945

Itoh, M., Mukae, Y., Kitsuka, T., Arai, K., Nakamura, A., Uchihashi, K., et al. (2019). Development of an immunodeficient pig model allowing long-term accommodation of artificial human vascular tubes. *Nat. Commun.* 10 (1), 2244. doi:10.1038/s41467-019-10107-1

Jakimowicz, T., Przywara, S., Turek, J., Pilgrim, A., Macech, M., Zapotoczny, N., et al. (2022). Five year outcomes in patients with end stage renal disease who received a bioengineered human acellular vessel for dialysis access. *EJVES Vasc. Forum* 54, 58–63. doi:10.1016/j.ejvsvf.2022.01.003

Jiang, B., Suen, R., Wang, J. J., Zhang, Z. J., Wertheim, J. A., and Ameer, G. A. (2016). Mechanocompatible polymer-extracellular matrix composites for vascular tissue engineering. *Adv. Healthc. Mater* 5 (13), 1594–1605. doi:10.1002/adhm.201501003

Jiang, B., Suen, R., Wang, J. J., Zhang, Z. J., Wertheim, J. A., and Ameer, G. A. (2017). Vascular scaffolds with enhanced antioxidant activity inhibit graft calcification. *Biomaterials* 144, 166–175. doi:10.1016/j.biomaterials.2017.08.014

Jin, C., and Liu, Y. (2019). Influence of competitive flow caused by different stenosis on coronary artery bypass hemodynamics and PIV study. *Mol. Cell Biomech.* 16 (S1)–52. doi:10.32604/mcb.2019.05728

Jin, X., Lin, T., and Xu, Y. (2016). Stem cell therapy and immunological rejection in animal models. *Curr. Mol. Pharmacol.* 9 (4), 284–288. doi:10.2174/1874467208666150928153511

Ju, Y. M., Ahn, H., Arenas-Herrera, J., Kim, C., Abolbashari, M., Atala, A., et al. (2017). Electrospun vascular scaffold for cellularized small diameter blood vessels: A preclinical large animal study. *Acta Biomater.* 59, 58–67. doi:10.1016/j.actbio.2017.06.027

Julier, Z., Park, A. J., Briquez, P. S., and Martino, M. M. (2017). Promoting tissue regeneration by modulating the immune system. *Acta Biomater.* 53, 13–28. doi:10.1016/j.actbio.2017.01.056

Kato, N., Yamagishi, M., Kanda, K., Miyazaki, T., Maeda, Y., Yamanami, M., et al. (2016). First successful clinical application of the *in vivo* tissue-engineered autologous vascular graft. *Ann. Thorac. Surg.* 102 (4), 1387–1390. doi:10.1016/j.athoracsur.2016.06.095

Kennealey, P. T., Elias, N., Hertl, M., Ko, D. S., Saidi, R. F., Markmann, J. F., et al. (2011). A prospective, randomized comparison of bovine carotid artery and expanded polytetrafluoroethylene for permanent hemodialysis vascular access. *J. Vasc. Surg.* 53 (6), 1640–1648. doi:10.1016/j.jvs.2011.02.008

Keshavarzian, M., Meyer, C. A., and Hayenga, H. N. (2019). *In Silico*Tissue engineering: A coupled agent-based finite element approach. *Tissue Eng. Part C Methods* 25 (11), 641–654. doi:10.1089/ten.TEC.2019.0103

Khosravi, R., Ramachandra, A. B., Szafron, J. M., Schiavazzi, D. E., Breuer, C. K., and Humphrey, J. D. (2020). A computational bio-chemo-mechanical model of *in vivo* tissue-engineered vascular graft development. *Integr. Biol. Quant. Biosci. Nano Macro* 12 (3), 47–63. doi:10.1093/intbio/zyaa004

Kim, D., Chung, J. J., Jung, Y., and Kim, S. H. (2019). The effect of Substance P/Heparin conjugated PLCL polymer coating of bioinert ePTFE vascular grafts on the recruitment of both ECs and SMCs for accelerated regeneration. *Sci. Rep.* 9 (1), 17083. doi:10.1038/s41598-019-53514-6

Kimicata, M., Swamykumar, P., and Fisher, J. P. (2020). Extracellular matrix for small-diameter vascular grafts. *Tissue Eng. Part A* 26 (23-24), 1388–1401. doi:10.1089/ten.tea.2020.0201

Kirkton, R. D., Prichard, H. L., Santiago-Maysonet, M., Niklason, L. E., Lawson, J. H., and Dahl, S. L. M. (2018). Susceptibility of ePTFE vascular grafts and bioengineered human acellular vessels to infection. *J. Surg. Res.* 221, 143–151. doi:10.1016/j.jss.2017.08.035

Kirkton, R. D., Santiago-Maysonet, M., Lawson, J. H., Tente, W. E., Dahl, S. L. M., Niklason, L. E., et al. (2019). Bioengineered human acellular vessels recellularize and evolve into living blood vessels after human implantation. *Sci. Transl. Med.* 11 (485), eaau6934. doi:10.1126/scitranslmed.aau6934

Klinkert, P., Post, P. N., Breslau, P. J., and van Bockel, J. H. (2004). Saphenous vein versus PTFE for above-knee femoropopliteal bypass. A review of the literature. *Eur. J. Vasc. Endovasc. Surg.* 27 (4), 357–362. doi:10.1016/j.ejvs.2003.12.027

Kong, X., Kong, C., Wen, S., and Shi, J. (2019). The use of heparin, bFGF, and VEGF 145 grafted acellular vascular scaffold in small diameter vascular graft. *J. Biomed. Mater Res. B Appl. Biomater.* 107 (3), 672–679. doi:10.1002/jbm.b.34160

Koobatian, M. T., Row, S., Smith, R. J., Koenigsknecht, C., Andreadis, S. T., and Swartz, D. D. (2016). Successful endothelialization and remodeling of a cell-free small-diameter arterial graft in a large animal model. *Biomaterials* 76, 344–358. doi:10.1016/j.biomaterials.2015.10.020

Kosa, S. D., Al-Jaishi, A. A., Moist, L., and Lok, C. E. (2015). Preoperative vascular access evaluation for haemodialysis patients. *Cochrane Database Syst. Rev.* 9, CD007013. doi:10.1002/14651858.CD007013.pub2

Kostokis, I. D., and Loukopoulos, I. (2020). Comparison between bovine carotid artery graft and polytetrafluoroethylene graft for haemodialysis vascular access: A systemic review and meta-analysis. *J. Vasc. Surg.* 72 (5), 1814. doi:10.1016/j.jvs.2020.08.012

Krawiec, J. T., Liao, H. T., Kwan, L. L., D'Amore, A., Weinbaum, J. S., Rubin, J. P., et al. (2017). Evaluation of the stromal vascular fraction of adipose tissue as the basis for a stem cell-based tissue-engineered vascular graft. *J. Vasc. Surg.* 66 (3), 883–890. doi:10.1016/j.jvs.2016.09.034

Krawiec, J. T., Weinbaum, J. S., Liao, H. T., Ramaswamy, A. K., Pezzone, D. J., Josowitz, A. D., et al. (2016). *In Vivo*Functional evaluation of tissue-engineered vascular grafts fabricated using human adipose-derived stem cells from high cardiovascular risk populations. *Tissue Eng. Part A* 22 (9-10), 765–775. doi:10.1089/ten.TEA.2015.0379

Kristofik, N. J., Qin, L., Calabro, N. E., Dimitrievska, S., Li, G., Tellides, G., et al. (2017). Improving *in vivo* outcomes of decellularized vascular grafts via incorporation of a novel extracellular matrix. *Biomaterials* 141, 63–73. doi:10.1016/j.biomaterials.2017.06.025

Kurobe, H., Maxfield, M. W., Naito, Y., Cleary, M., Stacy, M. R., Solomon, D., et al. (2015). Comparison of a closed system to a standard open technique for preparing tissue-engineered vascular grafts. *Tissue Eng. Part C Methods* 21 (1), 88–93. doi:10.1089/ten.tec.2014.0160

Lawson, J. H., Glickman, M. H., Ilzecki, M., Jakimowicz, T., Jaroszynski, A., Peden, E. K., et al. (2016). Bioengineered human acellular vessels for dialysis access in patients with end-stage renal disease: Two phase 2 single-arm trials. *Lancet Lond Engl.* 387 (10032), 2026–2034. doi:10.1016/S0140-6736(16)00557-2

Lazarides, M. K., Georgiadis, G. S., Antoniou, G. A., and Staramos, D. N. (2007). A meta-analysis of dialysis access outcome in elderly patients. *J. Vasc. Surg.* 45 (2), 420–426. doi:10.1016/j.jvs.2006.10.035

Lee, K. S., Kayumov, M., Emechebe, G. A., Kim, D. W., Cho, H. J., Jeong, Y. J., et al. (2022). A comparative study of an anti-thrombotic small-diameter vascular graft with commercially available e-PTFE graft in a porcine carotid model. *Tissue Eng. Regen. Med.* 19 (3), 537–551. doi:10.1007/s13770-021-00422-4

Lee, Y. U., de Dios Ruiz-Rosado, J., Mahler, N., Best, C. A., Tara, S., Yi, T., et al. (2016). TGF-β receptor 1 inhibition prevents stenosis of tissue-engineered vascular grafts by reducing host mononuclear phagocyte activation. *FASEB J. Off. Publ. Fed. Am. Soc. Exp. Biol.* 30 (7), 2627–2636. doi:10.1096/fj.201500179R

Li, N., Rickel, A. P., Sanyour, H. J., and Hong, Z. (2019). Vessel graft fabricated by the on-site differentiation of human mesenchymal stem cells towards vascular cells on vascular extracellular matrix scaffold under mechanical stimulation in a rotary bioreactor. *J. Mater Chem. B* 7 (16), 2703–2713. doi:10.1039/c8tb03348j

Li, P., Wang, Y., Jin, X., Dou, J., Han, X., Wan, X., et al. (2020). Catalytic generation of nitric oxide from poly(ε-caprolactone)/phosphobetainized keratin mats for a vascular tissue engineering scaffold. *Langmuir ACS J. Surf. Colloids* 36 (16), 4396–4404. doi:10.1021/acs.langmuir.0c00579

Li, X., Ma, T., Sun, J., Shen, M., Xue, X., Chen, Y., et al. (2019). Harnessing the secretome of adipose-derived stem cells in the treatment of ischemic heart diseases. *Stem Cell Res. Ther.* 10, 196. doi:10.1186/s13287-019-1289-7

Li, X., Xu, J., Nicolescu, C. T., Marinelli, J. T., and Tien, J. (2017). Generation, endothelialization, and microsurgical suture anastomosis of strong 1-mm-Diameter collagen tubes. *Tissue Eng. Part A* 23 (7-8), 335–344. doi:10.1089/ten.tea.2016.0339

Lin, C. H., Hsia, K., Tsai, C. H., Ma, H., Lu, J. H., and Tsay, R. Y. (2019). Decellularized porcine coronary artery with adipose stem cells for vascular tissue engineering. *Biomed. Mater Bristol Engl.* 14 (4), 045014. doi:10.1088/1748-605X/ab2329

Lindsey, P., Echeverria, A., Cheung, M., Kfoury, E., Bechara, C. F., and Lin, P. H. (2018). Lower extremity bypass using bovine carotid artery graft (artegraft): An analysis of

124 cases with long-term results. *World J. Surg.* 42 (1), 295–301. doi:10.1007/s00268-017-4161-x

Liu, J. Y., Swartz, D. D., Peng, H. F., Gugino, S. F., Russell, J. A., and Andreadis, S. T. (2007). Functional tissue-engineered blood vessels from bone marrow progenitor cells. *Cardiovasc Res.* 75 (3), 618–628. doi:10.1016/j.cardiores.2007.04.018

Liu, R. H., Ong, C. S., Fukunishi, T., Ong, K., and Hibino, N. (2018). Review of vascular graft studies in large animal models. *Tissue Eng. Part B Rev.* 24 (2), 133–143. doi:10.1089/ten.teb.2017.0350

Liu, Y., Mahara, A., Kambe, Y., Hsu, Y. I., and Yamaoka, T. (2021). Endothelial cell adhesion and blood response to hemocompatible peptide 1 (HCP-1), REDV, and RGD peptide sequences with free N-terminal amino groups immobilized on a biomedical expanded polytetrafluoroethylene surface. *Biomater. Sci.* 9 (3), 1034–1043. doi:10.1039/d0bm01396j

Lok, C. E., Allon, M., Moist, L., Oliver, M. J., Shah, H., and Zimmerman, D. (2006). Risk equation determining unsuccessful cannulation events and failure to maturation in arteriovenous fistulas (REDUCE FTM I). *J. Am. Soc. Nephrol.* 17 (11), 3204–3212. doi:10.1681/ASN.2006030190

Lopera Higuita, M., Lopera Giraldo, J. F., Sarrafian, T. L., and Griffiths, L. G. (2021). Tissue engineered bovine saphenous vein extracellular matrix scaffolds produced via antigen removal achieve high *in vivo* patency rates. *Acta Biomater.* 134, 144–159. doi:10.1016/j.actbio.2021.06.034

Lorentz, K. L., Gupta, P., Shehabeldin, M. S., Cunnane, E. M., Ramaswamy, A. K., Verdelis, K., et al. (2021). CCL2 loaded microparticles promote acute patency in silk-based vascular grafts implanted in rat aortae. *Acta Biomater.* 135, 126–138. doi:10.1016/j.actbio.2021.08.049

Lu, D. Y., Chen, E. Y., Wong, D. J., Yamamoto, K., Protack, C. D., Williams, W. T., et al. (2014). Vein graft adaptation and fistula maturation in the arterial environment. *J. Surg. Res.* 188 (1), 162–173. doi:10.1016/j.jss.2014.01.042

Lu, S., Zhang, P., Sun, X., Gong, F., Yang, S., Shen, L., et al. (2013). Synthetic ePTFE grafts coated with an anti-CD133 antibody-functionalized heparin/collagen multilayer with rapid *in vivo* endothelialization properties. *ACS Appl. Mater Interfaces* 5 (15), 7360–7369. doi:10.1021/am401706w

Luo, J., Qin, L., Zhao, L., Gui, L., Ellis, M. W., Huang, Y., et al. (2020). Tissue-engineered vascular grafts with advanced mechanical strength from human iPSCs. *Cell Stem Cell* 26 (2), 251–261. doi:10.1016/j.stem.2019.12.012

Ma, X., He, Z., Li, L., Liu, G., Li, Q., Yang, D., et al. (2017). Development and *in vivo* validation of tissue-engineered, small-diameter vascular grafts from decellularized aortae of fetal pigs and canine vascular endothelial cells. *J. Cardiothorac. Surg.* 12 (1), 101. doi:10.1186/s13019-017-0661-x

Madden, R. L., Lipkowitz, G. S., Browne, B. J., and Kurbanov, A. (2004). Experience with cryopreserved cadaveric femoral vein allografts used for hemodialysis access. *Ann. Vasc. Surg.* 18 (4), 453–458. doi:10.1007/s10016-004-0055-0

Matsuzaki, Y., Miyamoto, S., Miyachi, H., Iwaki, R., Shoji, T., Blum, K., et al. (2021). Improvement of a novel small-diameter tissue-engineered arterial graft with heparin conjugation. *Ann. Thorac. Surg.* 111 (4), 1234–1241. doi:10.1016/j.athoracsur.2020.06.112

Maxfield, M. W., Stacy, M. R., Kurobe, H., Tara, S., Yi, T., Cleary, M. A., et al. (2017). Novel application and serial evaluation of tissue-engineered portal vein grafts in a murine model. *Regen. Med.* 12 (8), 929–938. doi:10.2217/rme-2017-0021

McAllister, T. N., Maruszewski, M., Garrido, S. A., Wystrychowski, W., Dusserre, N., Marini, A., et al. (2009). Effectiveness of haemodialysis access with an autologous tissue-engineered vascular graft: A multicentre cohort study. *Lancet Lond Engl.* 373 (9673), 1440–1446. doi:10.1016/S0140-6736(09)60248-8

Melchiorri, A. J., Bracaglia, L. G., Kimerer, L. K., Hibino, N., and Fisher, J. P. (2016). *In vitro* endothelialization of biodegradable vascular grafts via endothelial progenitor cell seeding and maturation in a tubular perfusion system bioreactor. *Tissue Eng. Part C Methods* 22 (7), 663–670. doi:10.1089/ten.TEC.2015.0562

Merola, J., Jane-Wit, D. D., and Pober, J. S. (2017). Recent advances in allograft vasculopathy. *Curr. Opin. Organ Transpl.* 22 (1), 1–7. doi:10.1097/MOT.0000000000000370

Miller, P. E., Tolwani, A., Luscy, C. P., Deierhoi, M. H., Bailey, R., Redden, D. T., et al. (1999). Predictors of adequacy of arteriovenous fistulas in hemodialysis patients. *Kidney Int.* 56 (1), 275–280. doi:10.1046/j.1523-1755.1999.00515.x

Mirhaidari, G. J. M., Barker, J. C., Zbinden, J. C., Santantonio, B. M., Chang, Y., Best, C. A., et al. (2020). Tissue engineered vascular graft recipient interleukin 10 status is critical for preventing thrombosis. *Adv. Healthc. Mater* 9 (24), e2001094. doi:10.1002/adhm.202001094

Misskey, J., Faulds, J., Sidhu, R., Baxter, K., Gagnon, J., and Hsiang, Y. (2018). An age-based comparison of fistula location, patency, and maturation for elderly renal failure patients. *J. Vasc. Surg.* 67 (5), 1491–1500. doi:10.1016/j.jvs.2017.08.080

Moist, L. M., Lok, C. E., Vachharajani, T. J., Xi, W., AlJaishi, A., Polkinghorne, K. R., et al. (2012). Optimal hemodialysis vascular access in the elderly patient. *Semin. Dial.* 25 (6), 640–648. doi:10.1111/sdi.12037

Mrówczyński, W., Mugnai, D., de Valence, S., Tille, J. C., Khabiri, E., Cikirikcioglu, M., et al. (2014). Porcine carotid artery replacement with biodegradable electrospun poly-e-caprolactone vascular prosthesis. *J. Vasc. Surg.* 59 (1), 210–219. doi:10.1016/j.jvs.2013.03.004

Munisso, M. C., and Yamaoka, T. (2020). Circulating endothelial progenitor cells in small-diameter artificial blood vessel. *J. Artif. Organs* 23 (1), 6–13. doi:10.1007/s10047-019-01114-6

Muniswami, D. M., Reddy, L. V. K., Amirtham, S. M., Babu, S., Raj, A. N., Sen, D., et al. (2020). Endothelial progenitor/stem cells in engineered vessels for vascular transplantation. *J. Mater Sci. Mater Med.* 31 (12), 119. doi:10.1007/s10856-020-06458-7

Nakatsuji, H., Yamagishi, M., Maeda, Y., Itatani, K., Fujita, S., Hongu, H., et al. (2021). Midterm results of pulmonary artery plasty with *in vivo* tissue-engineered vascular grafts. *Interact. Cardiovasc Thorac. Surg.* 32 (6), 956–959. doi:10.1093/icvts/ivab019

Nakayama, Y., Kaneko, Y., Okumura, N., and Terazawa, T. (2020). Initial 3-year results of first human use of an in-body tissue-engineered autologous "Biotube" vascular graft for hemodialysis. *J. Vasc. Access* 21 (1), 110–115. doi:10.1177/1129729819852550

Napoli, C., de Nigris, F., Williams-Ignarro, S., Pignalosa, O., Sica, V., and Ignarro, L. J. (2006). Nitric oxide and atherosclerosis: An update. *Nitric Oxide Biol. Chem.* 15 (4), 265–279. doi:10.1016/j.niox.2006.03.011

Ng, J., Bourantas Christos, V., Ryo, T., Ang, H. Y., Tenekecioglu, E., Serruys, P. W., et al. (2017). Local hemodynamic forces after stenting. *Arterioscler. Thromb. Vasc. Biol.* 37 (12), 2231–2242. doi:10.1161/ATVBAHA.117.309728

Nguyen, T. U., Shojaee, M., Bashur, C. A., and Kishore, V. (2018). Electrochemical fabrication of a biomimetic elastin-containing bi-layered scaffold for vascular tissue engineering. *Biofabrication* 11 (1), 015007. doi:10.1088/1758-5090/aaeab0

Nikfarjam, S., Rezaie, J., Zolbanin, N. M., and Jafari, R. (2020). Mesenchymal stem cell derived-exosomes: A modern approach in translational medicine. *J. Transl. Med.* 18 (1), 449. doi:10.1186/s12967-020-02622-3

Niklason, L. E., and Lawson, J. H. (2020). Bioengineered human blood vessels. *Science* 370 (6513), eaaw8682. doi:10.1126/science.aaw8682

Nordgaard, H., Swillens, A., Nordhaug, D., Kirkeby-Garstad, I., Van Loo, D., Vitale, N., et al. (2010). Impact of competitive flow on wall shear stress in coronary surgery: Computational fluid dynamics of a LIMA–lad model. *Cardiovasc Res.* 88 (3), 512–519. doi:10.1093/cvr/cvq210

Olausson, M., Patil, P. B., Kuna, V. K., Chougule, P., Hernandez, N., Methe, K., et al. (2012). Transplantation of an allogeneic vein bioengineered with autologous stem cells: A proof-of-concept study. *Lancet Lond Engl.* 380 (9838), 230–237. doi:10.1016/S0140-6736(12)60633-3

Ong, C. S., Fukunishi, T., Liu, R. H., Nelson, K., Zhang, H., Wieczorek, E., et al. (2017). Bilateral arteriovenous shunts as a method for evaluating tissue-engineered vascular grafts in large animal models. *Tissue Eng. Part C Methods* 23 (11), 728–735. doi:10.1089/ten.TEC.2017.0217

Owens, C. D., Gasper, W. J., Rahman, A. S., and Conte, M. S. (2015). Vein graft failure. *J. Vasc. Surg.* 61 (1), 203–216. doi:10.1016/j.jvs.2013.08.019

Pagel, M., and Beck-Sickinger, A. G. (2017). Multifunctional biomaterial coatings: Synthetic challenges and biological activity. *Biol. Chem.* 398 (1), 3–22. doi:10.1515/hsz-2016-0204

Pennel, T., Zilla, P., and Bezuidenhout, D. (2013). Differentiating transmural from transanastomotic prosthetic graft endothelialization through an isolation loop-graft model. *J. Vasc. Surg.* 58 (4), 1053–1061. doi:10.1016/j.jvs.2012.11.093

Peterson, W. J., Barker, J., and Allon, M. (2008). Disparities in fistula maturation persist despite preoperative vascular mapping. *Clin. J. Am. Soc. Nephrol.* 3 (2), 437–441. doi:10.2215/CJN.03480807

Petrus-Reurer, S., Romano, M., Howlett, S., Jones, J. L., Lombardi, G., and Saeb-Parsy, K. (2021). Immunological considerations and challenges for regenerative cellular therapies. *Commun. Biol.* 4 (1), 798. doi:10.1038/s42003-021-02237-4

Ponce, P. (2001). Vascular access for dialysis in the elderly. *Int. Urol. Nephrol.* 33 (3), 571–573. doi:10.1023/A:1019550307514

Poterucha, T. J., Libby, P., and Goldhaber, S. Z. (2017). More than an anticoagulant: Do heparins have direct anti-inflammatory effects? *Thromb. Haemost.* 117 (3), 437–444. doi:10.1160/TH16-08-0620

Qin, H., Jia, P., and Liu, H. (2016). Nursing strategies for patients with chronic renal failure undergoing maintenance hemodialysis treatment by arteriovenous fistula. *Iran. J. Public Health* 45 (10), 1270–1275.

Qiu, X., Lee, B. L. P., Ning, X., Murthy, N., Dong, N., and Li, S. (2017). End-point immobilization of heparin on plasma-treated surface of electrospun polycarbonate-urethane vascular graft. *Acta Biomater.* 51, 138–147. doi:10.1016/j.actbio.2017.01.012

Qiu, X., Lee, B. L. P., Wong, S. Y., Ding, X., Xu, K., Zhao, W., et al. (2021). Cellular remodeling of fibrotic conduit as vascular graft. *Biomaterials* 268, 120565. doi:10.1016/j.biomaterials.2020.120565

Radke, D., Jia, W., Sharma, D., Fena, K., Wang, G., Goldman, J., et al. (2018). Tissue engineering at the blood-contacting surface: A review of challenges and strategies in vascular graft development. *Adv. Healthc. Mater* 7 (15), e1701461. doi:10.1002/adhm.201701461

Ramachandra, A. B., Humphrey, J. D., and Marsden, A. L. (2017). Gradual loading ameliorates maladaptation in computational simulations of vein graft growth and remodelling. *J. R. Soc. Interface* 14 (130), 20160995. doi:10.1098/rsif.2016.0995

Ran, X., Ye, Z., Fu, M., Wang, Q., Wu, H., Lin, S., et al. (2019). Design, preparation, and performance of a novel bilayer tissue-engineered small-diameter vascular graft. *Macromol. Biosci.* 19 (3), e1800189. doi:10.1002/mabi.201800189

Reddy, M. A., Tak Park, J., and Natarajan, R. (2013). Epigenetic modifications in the pathogenesis of diabetic nephropathy. *Semin. Nephrol.* 33(4), 341–353. doi:10.1016/j.semnephrol.2013.05.006

Riolobos, L., Hirata, R. K., Turtle, C. J., Wang, P. R., Gornalusse, G. G., Zavajlevski, M., et al. (2013). HLA engineering of human pluripotent stem cells. *Mol. Ther.* 21 (6), 1232–1241. doi:10.1038/mt.2013.59

Robbin, M. L., Greene, T., Cheung, A. K., Allon, M., Berceli, S. A., Kaufman, J. S., et al. (2016). Arteriovenous fistula development in the first 6 Weeks after creation. *Radiology* 279 (2), 620–629. doi:10.1148/radiol.2015150385

Rodriguez-Soto, M. A., Suarez Vargas, N., Riveros, A., Camargo, C. M., Cruz, J. C., Sandoval, N., et al. (2021). Failure analysis of TEVG's I: Overcoming the initial stages of blood material interaction and stabilization of the immune response. *Cells* 10 (11), 3140. doi:10.3390/cells10113140

Roh, J. D., Sawh-Martinez, R., Brennan, M. P., Jay, S. M., Devine, L., Rao, D. A., et al. (2010). Tissue-engineered vascular grafts transform into mature blood vessels via an inflammation-mediated process of vascular remodeling. *Proc. Natl. Acad. Sci. U. S. A.* 107 (10), 4669–4674. doi:10.1073/pnas.0911465107

Rooijens, P. P. G. M., Burgmans, J. P. J., Yo, T. I., Hop, W., de Smet, A., van den Dorpel, M., et al. (2005). Autogenous radial-cephalic or prosthetic brachial-antecubital forearm loop avf in patients with compromised vessels? A randomized, multicenter study of the patency of primary hemodialysis access. *J. Vasc. Surg.* 42 (3), 481–487. doi:10.1016/j.jvs.2005.05.025

Rosa, S., Praça, C., Pitrez, P. R., Gouveia, P. J., Aranguren, X. L., Ricotti, L., et al. (2019). Functional characterization of iPSC-derived arterial- and venous-like endothelial cells. *Sci. Rep.* 9 (1), 3826. doi:10.1038/s41598-019-40417-9

Rothuizen, T. C., Damanik, F. F. R., Lavrijsen, T., Visser, M. J., Hamming, J. F., Lalai, R. A., et al. (2016). Development and evaluation of *in vivo* tissue engineered blood vessels in a porcine model. *Biomaterials* 75, 82–90. doi:10.1016/j.biomaterials.2015.10.023

Ruiz-Rosado, J. de D., Lee, Y. U., Mahler, N., Yi, T., Robledo-Avila, F., Martinez-Saucedo, D., et al. (2018). Angiotensin II receptor I blockade prevents stenosis of tissue engineered vascular grafts. *J. Fed. Am. Soc. Exp. Biol.* 15, 6822–6832. Published online June. doi:10.1096/fj.201800458

Sabik, J. F., Lytle, B. W., Blackstone, E. H., Khan, M., Houghtaling, P. L., and Cosgrove, D. M. (2003). Does competitive flow reduce internal thoracic artery graft patency? *Ann. Thorac. Surg.* 76 (5), 1490–1497. doi:10.1016/S0003-4975(03)01022-1

Sabik Joseph, F. (2016). Should coronary artery bypass grafting Be performed in patients with moderate stenosis of the left anterior descending coronary artery? *Circulation* 133 (2), 111–113. doi:10.1161/CIRCULATIONAHA.115.020084

Samson, R. H., Morales, R., Showalter, D. P., Lepore, M. R., and Nair, D. G. (2016). Heparin-bonded expanded polytetrafluoroethylene femoropopliteal bypass grafts outperform expanded polytetrafluoroethylene grafts without heparin in a long-term comparison. *J. Vasc. Surg.* 64 (3), 638–647. doi:10.1016/j.jvs.2016.03.414

Sánchez, P. F., Brey, E. M., and Briceño, J. C. (2018). Endothelialization mechanisms in vascular grafts. *J. Tissue Eng. Regen. Med.* 12 (11), 2164–2178. doi:10.1002/term.2747

Schinstock, C. A., Albright, R. C., Williams, A. W., Dillon, J. J., Bergstralh, E. J., Jenson, B. M., et al. (2011). Outcomes of arteriovenous fistula creation after the fistula first initiative. *Clin. J. Am. Soc. Nephrol.* 6 (8), 1996–2002. doi:10.2215/CJN.11251210

Schleimer, K., Jalaie, H., Afify, M., Woitok, A., Barbati, M. E., Hoeft, K., et al. (2018). Sheep models for evaluation of novel patch and prosthesis material in vascular surgery: Tips and tricks to avoid possible pitfalls. *Acta Vet. Scand.* 60, 42. doi:10.1186/s13028-018-0397-1

Schmidli, J., Savolainen, H., Heller, G., Widmer, M., Then-Schlagau, U., Baumgartner, I., et al. (2004). Bovine mesenteric vein graft (ProCol) in critical limb ischaemia with tissue loss and infection. *Eur. J. Vasc. Endovasc. Surg. Off. J. Eur. Soc. Vasc. Surg.* 27 (3), 251–253. doi:10.1016/j.ejvs.2003.12.001

Schneider, K. H., Enayati, M., Grasl, C., Walter, I., Budinsky, L., Zebic, G., et al. (2018). Acellular vascular matrix grafts from human placenta chorion: Impact of ECM preservation on graft characteristics, protein composition and *in vivo* performance. *Biomaterials* 177, 14–26. doi:10.1016/j.biomaterials.2018.05.045

Schwarz, E. L., Kelly, J. M., Blum, K. M., Hor, K. N., Yates, A. R., Zbinden, J. C., et al. (2021). Hemodynamic performance of tissue-engineered vascular grafts in Fontan patients. *NPJ Regen. Med.* 6 (1), 38. doi:10.1038/s41536-021-00148-w

Shafiq, M., Zhang, Q., Zhi, D., Wang, K., Kong, D., Kim, D. H., et al. (2018). *In situ* blood vessel regeneration using SP (substance P) and SDF (stromal cell–derived factor)-1α peptide eluting vascular grafts. *Arterioscler. Thromb. Vasc. Biol.* 38 (7), e117–e134. doi:10.1161/ATVBAHA.118.310934

Shi, J., Chen, S., Wang, L., Zhang, X., Gao, J., Jiang, L., et al. (2019). Rapid endothelialization and controlled smooth muscle regeneration by electrospun heparin-loaded polycaprolactone/gelatin hybrid vascular grafts. *J. Biomed. Mater. Res. B Appl. Biomater.* 107 (6), 2040–2049. doi:10.1002/jbm.b.34295

Shi, J., Zhang, X., Jiang, L., Zhang, L., Dong, Y., Midgley, A. C., et al. (2019). Regulation of the inflammatory response by vascular grafts modified with Aspirin-Triggered Resolvin D1 promotes blood vessel regeneration. *Acta Biomater.* 97, 360–373. doi:10.1016/j.actbio.2019.07.037

Shi, X., He, L., Zhang, S. M., and Luo, J. (2021). Human iPS cell-derived tissue engineered vascular graft: Recent advances and future directions. *Stem Cell Rev. Rep.* 17 (3), 862–877. doi:10.1007/s12015-020-10091-w

Shingarev, R., Maya, I. D., Barker-Finkel, J., and Allon, M. (2011). Arteriovenous graft placement in predialysis patients: A potential catheter-sparing strategy. *Am. J. Kidney Dis.* 58 (2), 243–247. doi:10.1053/j.ajkd.2011.01.026

Siddiqui, M. A., Ashraff, S., and Carline, T. (2017). Maturation of arteriovenous fistula: Analysis of key factors. *Kidney Res. Clin. Pract.* 36 (4), 318–328. doi:10.23876/j.krcp.2017.36.4.318

Skovrind, I., Harvald, E. B., Juul Belling, H., Jørgensen, C. D., Lindholt, J. S., and Andersen, D. C. (2019). Concise review: Patency of small-diameter tissue-engineered vascular grafts: A meta-analysis of preclinical trials. *Stem Cells Transl. Med.* 8 (7), 671–680. doi:10.1002/sctm.18-0287

Smith, R. J., Jr., Yi, T., Nasiri, B., Breuer, C. K., and Andreadis, S. T. (2019). Implantation of VEGF-functionalized cell-free vascular grafts: Regenerative and immunological response. *FASEB J.* 33 (4), 5089–5100. doi:10.1096/fj.201801856R

Smith, R. J., Nasiri, B., Kann, J., Yergeau, D., Bard, J. E., Swartz, D. D., et al. (2020). Endothelialization of arterial vascular grafts by circulating monocytes. *Nat. Commun.* 11 (1), 1622. doi:10.1038/s41467-020-15361-2

Song, H. H. G., Rumma, R. T., Ozaki, C. K., Edelman, E. R., and Chen, C. S. (2018). Vascular tissue engineering: Progress, challenges, and clinical promise. *Cell Stem Cell* 22 (3), 340–354. doi:10.1016/j.stem.2018.02.009

Sottiurai, V. S., Yao, J. S. T., Batson, R. C., Sue, S. L., Jones, R., and Nakamura, Y. A. (1989). Distal anastomotic intimal hyperplasia: Histopathologic character and biogenesis. *Ann. Vasc. Surg.* 3 (1), 26–33. doi:10.1016/S0890-5096(06)62381-9

Staramos, D. N., Lazarides, M. K., Tzilalis, V. D., Ekonomou, C. S., Simopoulos, C. E., and Dayantas, J. N. (2000). Patency of autologous and prosthetic arteriovenous fistulas in elderly patients. *Eur. J. Surg.* 166 (10), 777–781. doi:10.1080/110241500447407

Stegmayr, B., Willems, C., Groth, T., Martins, A., Neves, N. M., Mottaghy, K., et al. (2021). Arteriovenous access in hemodialysis: A multidisciplinary perspective for future solutions. *Int. J. Artif. Organs* 44 (1), 3–16. doi:10.1177/0391398820922231

Stowell, C. E. T., Li, X., Matsunaga, M. H., Cockreham, C. B., Kelly, K. M., Cheetham, J., et al. (2020). Resorbable vascular grafts show rapid cellularization and degradation in the ovine carotid. *J. Tissue Eng. Regen. Med.* 14 (11), 1673–1684. doi:10.1002/term.3128

Strang, A. C., Knetsch, M. L. W., Idu, M. M., Bisoendial, R. J., Kramer, G., Speijer, D., et al. (2014). Superior *in vivo* compatibility of hydrophilic polymer coated prosthetic vascular grafts. *J. Vasc. Access* 15 (2), 95–101. doi:10.5301/jva.5000166

Strijdom, H., Chamane, N., and Lochner, A. (2009). Nitric oxide in the cardiovascular system: A simple molecule with complex actions. *Cardiovasc J. Afr.* 20 (5), 303–310.

Strobel, H. A., Hookway, T. A., Piola, M., Fiore, G. B., Soncini, M., Alsberg, E., et al. (2018). Assembly of tissue-engineered blood vessels with spatially controlled heterogeneities. *Tissue Eng. Part A* 24 (19-20), 1492–1503. doi:10.1089/ten.tea.2017.0492

Sugimoto, K., Higashino, T., Kuwata, Y., Imanaka, K., Hirota, S., and Sugimura, K. (2003). Percutaneous transluminal angioplasty of malfunctioning brescia-cimino arteriovenous fistula: Analysis of factors adversely affecting long-term patency. *Eur. Radiol.* 13 (7), 1615–1619. doi:10.1007/s00330-002-1764-9

Sugiura, T., Matsumura, G., Miyamoto, S., Miyachi, H., Breuer, C. K., and Shinoka, T. (2018). Tissue-engineered vascular grafts in children with congenital heart disease: Intermediate term follow-up. *Semin. Thorac. Cardiovasc Surg.* 30 (2), 175–179. doi:10.1053/j.semtcvs.2018.02.002

Sugiura, T., Tara, S., Nakayama, H., Yi, T., Lee, Y. U., Shoji, T., et al. (2017). Fast-degrading bioresorbable arterial vascular graft with high cellular infiltration inhibits calcification of the graft. *J. Vasc. Surg.* 66 (1), 243–250. doi:10.1016/j.jvs.2016.05.096

Swartz, D. D., Russell, J. A., and Andreadis, S. T. (2005). Engineering of fibrin-based functional and implantable small-diameter blood vessels. *Am. J. Physiol. Heart Circ. Physiol.* 288 (3), H1451–H1460. doi:10.1152/ajpheart.00479.2004

Swillens, A., De Witte, M., Nordgaard, H., Lovstakken, L., Van Loo, D., Trachet, B., et al. (2012). Effect of the degree of LAD stenosis on "competitive flow" and flow field characteristics in LIMA-to-LAD bypass surgery. *Med. Biol. Eng. Comput.* 50 (8), 839–849. doi:10.1007/s11517-012-0927-3

Syedain, Z. H., Graham, M. L., Dunn, T. B., O'Brien, T., Johnson, S. L., Schumacher, R. J., et al. (2017). A completely biological "off-the-shelf" arteriovenous graft that recellularizes in baboons. *Sci. Transl. Med.* 9 (414), eaan4209. doi:10.1126/scitranslmed.aan4209

Syedain, Z. H., Maciver, R., and Tranquillo, R. T. (2020). Vascular grafts and valves that animate, made from decellularized biologically-engineered tissue tubes. *J. Cardiovasc Surg. (Torino)* 61 (5), 577–585. doi:10.23736/S0021-9509.20.11615-X

Syedain, Z. H., Meier, L. A., Bjork, J. W., Lee, A., and Tranquillo, R. T. (2011). Implantable arterial grafts from human fibroblasts and fibrin using a multi-graft pulsed flow-stretch bioreactor with noninvasive strength monitoring. *Biomaterials* 32 (3), 714–722. doi:10.1016/j.biomaterials.2010.09.019

Szafron, J. M., Khosravi, R., Reinhardt, J., Best, C. A., Bersi, M. R., Yi, T., et al. (2018). Immuno-driven and mechano-mediated neotissue formation in tissue

engineered vascular grafts. *Ann. Biomed. Eng.* 46 (11), 1938–1950. doi:10.1007/s10439-018-2086-7

Szafron, J. M., Ramachandra, A. B., Breuer, C. K., Marsden, A. L., and Humphrey, J. D. (2019). Optimization of tissue-engineered vascular graft design using computational modeling. *Tissue Eng. Part C Methods* 25 (10), 561–570. doi:10.1089/ten.tec.2019.0086

Talacua, H., Smits, A. I. P. M., Muylaert, D. E. P., van Rijswijk, J. W., Vink, A., Verhaar, M. C., et al. (2015). *In situ* tissue engineering of functional small-diameter blood vessels by host circulating cells only. *Tissue Eng. Part A* 21 (19-20), 2583–2594. doi:10.1089/ten.TEA.2015.0066

Tamimi, E. A., Ardila, D. C., Ensley, B. D., Kellar, R. S., and Vande Geest, J. P. (2019). Computationally optimizing the compliance of multilayered biomimetic tissue engineered vascular grafts. *J. Biomech. Eng.* 141 (6), 0610031–06100314. doi:10.1115/1.4042902

Tamma, R., Ruggieri, S., Annese, T., and Ribatti, D. (2020). "Vascular wall as source of stem cells able to differentiate into endothelial cells," in Cell Biology and translational medicine, volume 7: Stem Cells and therapy: Emerging approaches. *Advances in experimental medicine and biology*. Editor K. Turksen (Germany: Springer International Publishing), 29–36. doi:10.1007/5584_2019_421

Tan, R. P., Chan, A. H. P., Wei, S., Santos, M., Lee, B. S., Filipe, E. C., et al. (2019). Bioactive materials facilitating targeted local modulation of inflammation. *JACC Basic Transl. Sci.* 4 (1), 56–71. doi:10.1016/j.jacbts.2018.10.004

Tanaka, T., Abe, Y., Cheng, C. J., Tanaka, R., Naito, A., and Asakura, T. (2020). Development of small-diameter elastin-silk fibroin vascular grafts. *Front. Bioeng. Biotechnol.* 8, 622220. doi:10.3389/fbioe.2020.622220

Tang, D., Chen, S., Hou, D., Gao, J., Jiang, L., Shi, J., et al. (2018). Regulation of macrophage polarization and promotion of endothelialization by NO generating and PEG-YIGSR modified vascular graft. *Mater Sci. Eng. C Mater Biol. Appl.* 84, 1–11. doi:10.1016/j.msec.2017.11.005

Tang, Y., Zhou, Y., and Li, H. J. (2021). Advances in mesenchymal stem cell exosomes: A review. *Stem Cell Res. Ther.* 12 (1), 71. doi:10.1186/s13287-021-02138-7

Tesauro, M., Mauriello, A., Rovella, V., Annicchiarico-Petruzzelli, M., Cardillo, C., Melino, G., et al. (2017). Arterial ageing: From endothelial dysfunction to vascular calcification. *J. Intern Med.* 281 (5), 471–482. doi:10.1111/joim.12605

Thalla, P. K., Contreras-García, A., Fadlallah, H., Barrette, J., De Crescenzo, G., Merhi, Y., et al. (2012). A versatile star PEG grafting method for the generation of nonfouling and nonthrombogenic surfaces. *Biomed. Res. Int.* 2013, 1–12. doi:10.1155/2013/962376

Tinica, G., Chistol, R. O., Enache, M., Constantin, M. M. L., Ciocoiu, M., and Furnica, C. (2018). Long-term graft patency after coronary artery bypass grafting: Effects of morphological and pathophysiological factors. *Anatol. J. Cardiol.* 20 (5), 275–282. doi:10.14744/AnatolJCardiol.2018.51447

Tiwari, A., Cheng, K. S., Salacinski, H., Hamilton, G., and Seifalian, A. M. (2003). Improving the patency of vascular bypass grafts: The role of suture materials and surgical techniques on reducing anastomotic compliance mismatch. *Eur. J. Vasc. Endovasc. Surg.* 25 (4), 287–295. doi:10.1053/ejvs.2002.1810

Totorean, A. F., and Hudrea, I. C. (2019). "Local hemodynamics in coronary bypass in the presence of competitive flow and different diameter ratios between graft and host artery," in World Congress on medical Physics and biomedical engineering 2018. *IFMBE proceedings*. Editors L. Lhotska, L. Sukupova, I. Lacković, and G. S. Ibbott (Germany: Springer), 767–771. doi:10.1007/978-981-10-9035-6_141

Tseng, C. N., Karlöf, E., Chang, Y. T., Lengquist, M., Rotzius, P., Berggren, P. O., et al. (2014). Contribution of endothelial injury and inflammation in early phase to vein graft failure: The causal factors impact on the development of intimal hyperplasia in murine models. *PLOS ONE* 9 (6), e98904. doi:10.1371/journal.pone.0098904

Valencia-Rivero, K. T., Cruz, J. C., Wagner-Gutierrez, N., D'Amore, A., Miranda, M. C., Lopez, R., et al. (2019). Evaluation of microscopic Structure–Function relationships of PEGylated small intestinal submucosa vascular grafts for arteriovenous connection. *ACS Appl. Bio Mater* 2 (9), 3706–3721. doi:10.1021/acsabm.9b00158

van der Slegt, J., Steunenberg, S. L., Donker, J. M. W., Veen, E. J., Ho, G. H., de Groot, H. G., et al. (2014). The current position of precuffed expanded polytetrafluoroethylene bypass grafts in peripheral vascular surgery. *J. Vasc. Surg.* 60 (1), 120–128. doi:10.1016/j.jvs.2014.01.062

Vascular Access Society 2021. Guidelines | vascular access society. Accessed December 13, 2021. Available at: https://www.vascularaccesssociety.com/education/guidelines.

von Bornstädt, D., Wang, H., Paulsen, M. J., Goldstone, A. B., Eskandari, A., Thakore, A., et al. (2018). Rapid self-assembly of bioengineered cardiovascular bypass grafts from scaffold-stabilized, tubular bilevel cell sheets. *Circulation* 138 (19), 2130–2144. doi:10.1161/CIRCULATIONAHA.118.035231

Wang, D., Wang, X., Zhang, Z., Wang, L., Li, X., Xu, Y., et al. (2019). Programmed release of multimodal, cross-linked vascular endothelial growth factor and heparin layers on electrospun polycaprolactone vascular grafts. *ACS Appl. Mater Interfaces* 11 (35), 32533–32542. doi:10.1021/acsami.9b10621

Wang, D., Xu, Y., Wang, L., Wang, X., Ren, C., Zhang, B., et al. (2020). Expanded poly(tetrafluoroethylene) blood vessel grafts with embedded reactive oxygen species (ROS)-Responsive antithrombogenic drug for elimination of thrombosis. *ACS Appl. Mater Interfaces* 12 (26), 29844–29853. doi:10.1021/acsami.0c07868

Wang, J. N., Kan, C. D., Lin, S. H., Chang, K. C., Tsao, S., and Wong, T. W. (2021). Potential of autologous progenitor cells and decellularized porcine artery matrix in

construction of tissue-engineered vascular grafts. *Organogenesis* 17, 72–84. doi:10.1080/15476278.2021.1963603

Wang, L., Hu, J., Sorek, C. E., Chen, E. Y., Ma, P. X., and Yang, B. (2016). Fabrication of tissue-engineered vascular grafts with stem cells and stem cell-derived vascular cells. *Expert Opin. Biol. Ther.* 16 (3), 317–330. doi:10.1517/14712598.2016.1118460

Wang, T., Dong, N., Yan, H., Wong, S. Y., Zhao, W., Xu, K., et al. (2019). Regeneration of a neoartery through a completely autologous acellular conduit in a minipig model: A pilot study. *J. Transl. Med.* 17 (1), 24. doi:10.1186/s12967-018-1763-5

Wang, W., Liu, D., Li, D., Du, H., Zhang, J., You, Z., et al. (2019). Nanofibrous vascular scaffold prepared from miscible polymer blend with heparin/stromal cell-derived factor-1 alpha for enhancing anticoagulation and endothelialization. *Colloids Surf. B Biointerfaces* 181, 963–972. doi:10.1016/j.colsurfb.2019.06.065

Wang, Y., Chen, S., Pan, Y., Gao, J., Tang, D., Kong, D., et al. (2015). Rapid *in situ* endothelialization of a small diameter vascular graft with catalytic nitric oxide generation and promoted endothelial cell adhesion. *J. Mater Chem. B* 3 (47), 9212–9222. doi:10.1039/C5TB02080H

Washington, K. S., and Bashur, C. A. (2017). Delivery of antioxidant and anti-inflammatory agents for tissue engineered vascular grafts. *Front. Pharmacol.* 8, 659. doi:10.3389/fphar.2017.00659

Wen, M., Zhi, D., Wang, L., Cui, C., Huang, Z., Zhao, Y., et al. (2020). Local delivery of dual MicroRNAs in trilayered electrospun grafts for vascular regeneration. *ACS Appl. Mater Interfaces* 12 (6), 6863–6875. doi:10.1021/acsami.9b19452

Wissing, T. B., Bonito, V., Bouten, C. V. C., and Smits, A. I. P. M. (2017). Biomaterial-driven *in situ* cardiovascular tissue engineering—a multi-disciplinary perspective. *NPJ Regen. Med.* 2, 18. doi:10.1038/s41536-017-0023-2

Wu, D. J., van Dongen, K., Szymczyk, W., Besseling, P. J., Cardinaels, R. M., Marchioli, G., et al. (2020). Optimization of anti-kinking designs for vascular grafts based on supramolecular materials. *Front. Mater* 7, 220. doi:10.3389/fmats.2020.00220

Wu, P., Nakamura, N., Morita, H., Nam, K., Fujisato, T., Kimura, T., et al. (2019). A hybrid small-diameter tube fabricated from decellularized aortic intima-media and electrospun fiber for artificial small-diameter blood vessel. *J. Biomed. Mater Res. A* 107 (5), 1064–1070. doi:10.1002/jbm.a.36631

Wystrychowski, W., McAllister, T. N., Zagalski, K., Dusserre, N., Cierpka, L., and L'Heureux, N. (2014). First human use of an allogeneic tissue-engineered vascular graft for hemodialysis access. *J. Vasc. Surg.* 60 (5), 1353–1357. doi:10.1016/j.jvs.2013.08.018

Xing, Q., Qian, Z., Tahtinen, M., Yap, A. H., Yates, K., and Zhao, F. (2017). Aligned nanofibrous cell-derived extracellular matrix for anisotropic vascular graft construction. *Adv. Healthc. Mater* 6 (10), 1601333. doi:10.1002/adhm.20160133310.1002/adhm.201601333

Xu, Z., Gu, Y., Li, J., Feng, Z., Guo, L., Tong, Z., et al. (2018). Vascular remodeling process of heparin-conjugated poly(ε-caprolactone) scaffold in a rat abdominal aorta replacement model. *J. Vasc. Res.* 55 (6), 338–349. doi:10.1159/000494509

Yang, Y., Gao, P., Wang, J., Tu, Q., Bai, L., Xiong, K., et al. (2020). Endothelium-mimicking multifunctional coating modified cardiovascular stents via a stepwise metal-catechol-(amine) surface engineering strategy. *Research* 2020, 1–20. doi:10.34133/2020/9203906

Yang, Y., Lei, D., Zou, H., Huang, S., Yang, Q., Li, S., et al. (2019). Hybrid electrospun rapamycin-loaded small-diameter decellularized vascular grafts effectively inhibit intimal hyperplasia. *Acta Biomater.* 97, 321–332. doi:10.1016/j.actbio.2019.06.037

Yang, Z., Yang, Y., Xiong, K., Li, X., Qi, P., Tu, Q., et al. (2015). Nitric oxide producing coating mimicking endothelium function for multifunctional vascular stents. *Biomaterials* 63, 80–92. doi:10.1016/j.biomaterials.2015.06.016

Yi, S. W., Shin, Y. M., Lee, J. B., Park, J. Y., Kim, D., Baek, W., et al. (2021). Dilation-responsive microshape programing prevents vascular graft stenosis. *Small* 17 (18), 2007297. doi:10.1002/smll.202007297

Yu, L., Newton, E. R., Gillis, D. C., Sun, K., Cooley, B. C., Keith, A. N., et al. (2021). Coating small-diameter ePTFE vascular grafts with tunable poly(diol-co-citrate-co-ascorbate) elastomers to reduce neointimal hyperplasia. *Biomater. Sci.* 9 (15), 5160–5174. doi:10.1039/d1bm00101a

Yuan, H., Chen, C., Liu, Y., Lu, T., and Wu, Z. (2020). Strategies in cell-free tissue-engineered vascular grafts. *J. Biomed. Mater Res. A* 108 (3), 426–445. doi:10.1002/jbm.a.36825

Zamani, M., Khafaji, M., Naji, M., Vossoughi, M., Alemzadeh, I., and Haghighipour, N. (2017). A biomimetic heparinized composite silk-based vascular scaffold with sustained antithrombogenicity. *Sci. Rep.* 7 (1), 4455. doi:10.1038/s41598-017-04510-1

Zbinden, J. C., Blum, K. M., Berman, A. G., Ramachandra, A. B., Szafron, J. M., Kerr, K. E., et al. (2020). Effects of braiding parameters on tissue engineered vascular graft development. *Adv. Healthc. Mater* 9 (24), 2001093. doi:10.1002/adhm.202001093

Zeng, W., Wen, C., Wu, Y., Li, L., Zhou, Z., Mi, J., et al. (2012). The use of BDNF to enhance the patency rate of small-diameter tissue-engineered blood vessels through stem cell homing mechanisms. *Biomaterials* 33 (2), 473–484. doi:10.1016/j.biomaterials.2011.09.066

Zhang, F., and King, M. W. (2022). Immunomodulation strategies for the successful regeneration of a tissue-engineered vascular graft. *Adv. Healthc. Mater* 11 (12), 2200045. doi:10.1002/adhm.202200045

Zhang, P., Moudgill, N., Hager, E., Tarola, N., DiMatteo, C., McIlhenny, S., et al. (2011). Endothelial differentiation of adipose-derived stem cells from elderly patients with cardiovascular disease. *Stem Cells Dev.* 20 (6), 977–988. doi:10.1089/scd.2010.0152

Zhang, Q., Bosch-Rué, È., Pérez, R. A., and Truskey, G. A. (2021). Biofabrication of tissue engineering vascular systems. *Apl. Bioeng.* 5 (2), 021507. doi:10.1063/5.0039628

Zhang, X., Shi, J., Chen, S., Dong, Y., Zhang, L., Midgley, A. C., et al. (2019). Polycaprolactone/gelatin degradable vascular grafts simulating endothelium functions modified by nitric oxide generation. *Regen. Med.* 14 (12), 1089–1105. doi:10.2217/rme-2019-0015

Zhen, L., Creason, S. A., Simonovsky, F. I., Snyder, J. M., Lindhartsen, S. L., Mecwan, M. M., et al. (2021). Precision-porous polyurethane elastomers engineered for application in pro-healing vascular grafts: Synthesis, fabrication and detailed biocompatibility assessment. *Biomaterials* 279, 121174. doi:10.1016/j.biomaterials.2021.121174

Zhou, F., Jia, X., Yang, Y., Yang, Q., Gao, C., Hu, S., et al. (2016). Nanofiber-mediated microRNA-126 delivery to vascular endothelial cells for blood vessel regeneration. *Acta Biomater.* 43, 303–313. doi:10.1016/j.actbio.2016.07.048

Zhu, M., Wu, Y., Li, W., Dong, X., Chang, H., Wang, K., et al. (2018). Biodegradable and elastomeric vascular grafts enable vascular remodeling. *Biomaterials* 183, 306–318. doi:10.1016/j.biomaterials.2018.08.063

Zhu, T., Gu, H., Zhang, H., Wang, H., Xia, H., Mo, X., et al. (2021). Covalent grafting of PEG and heparin improves biological performance of electrospun vascular grafts for carotid artery replacement. *Acta Biomater.* 119, 211–224. doi:10.1016/j.actbio.2020.11.013

Zilla, P., Bezuidenhout, D., and Human, P. (2007). Prosthetic vascular grafts: Wrong models, wrong questions and no healing. *Biomaterials* 28 (34), 5009–5027. doi:10.1016/j.biomaterials.2007.07.017

Zilla, P., Deutsch, M., Bezuidenhout, D., Davies, N. H., and Pennel, T. (2020). Progressive reinvention or destination lost? Half a century of cardiovascular tissue engineering. *Front. Cardiovasc Med.* 7, 159. doi:10.3389/fcvm.2020.00159

Frontiers in Bioengineering and Biotechnology

Advances in the development and optimization strategies of the hemostatic biomaterials

Yayuan Guo[1], Nanqiong Cheng[1], Hongxiao Sun[1], Jianing Hou[1], Yuchen Zhang[1], Du Wang[1], Wei Zhang[1,2] and Zhuoyue Chen[1,2]*

[1]Faculty of Life Science, Northwest University, Xi'an, Shaanxi Province, China, [2]School of Medicine, Northwest University, Xi'an, Shaanxi Province, China

Most injuries are accompanied by acute bleeding. Hemostasis is necessary to relieve pain and reduce mortality in these accidents. In recent years, the traditional hemostatic materials, including inorganic, protein-based, polysaccharide-based and synthetic materials have been widely used in the clinic. The most prominent of these are biodegradable collagen sponges (Helistat®, United States), gelatin sponges (Ethicon®, SURGIFOAM®, United States), chitosan (AllaQuixTM, ChitoSAMTM, United States), cellulose (Tabotamp®, SURGICEL®, United States), and the newly investigated extracellular matrix gels, etc. Although these materials have excellent hemostatic properties, they also have their advantages and disadvantages. In this review, the performance characteristics, hemostatic effects, applications and hemostatic mechanisms of various biomaterials mentioned above are presented, followed by several strategies to improve hemostasis, including modification of single materials, blending of multiple materials, design of self-assembled peptides and their hybrid materials. Finally, the exploration of more novel hemostatic biomaterials and relative coagulation mechanisms will be essential for future research on hemostatic methods.

KEYWORDS

coagulation mechanism, hemostatic biomaterials, modified hemostatic biomaterials, hemostatic strategies, clinic application

Introduction

Uncontrollable bleeding caused by war, accident, trauma, and surgery procedures, is a major problem while performing surgery. Without timely and effective hemostasis, patients often have the risk of causing complications and even life-threatening situations. For instance, 50% of the deaths in the military were caused by excessive bleeding, 80% of which resulted from non-compressible injuries (Behrens, Sikorski et al., 2014). In addition, the drug-induced effects, congenital or disease-related diseases, like clotting factor deficiency and platelet dysfunction, may also cause excessive bleeding (Demetri 2000; Blajchman 2003). There are two traditional methods concerning hemostatic treatment of external injury or lesion: compression hemostasis and drug pro-coagulation hemostasis. Both of them are effective in stopping bleeding, but they have some disadvantages, such as compression hemostasis being only suitable for vascular bleeding, and drug hemostasis can just be used as auxiliary means. In the case of non-compressible hemorrhage, either whole blood or blood components (red blood cells, plasma and platelets) are transfused (Kauvar, Holcomb et al., 2006; Spinella, Perkins et al., 2007; Chandler, Roberts et al., 2012; Kaufman, Djulbegovic et al., 2015; Spitalnik, Triulzi et al., 2015; Etchill, Myers et al., 2017), and fibrinogen concentrate or recombinant clotting factor (Berrettini, Mariani et al., 2001; Roberts 2001; Fries and Martini

2010; Rahe-Meyer and Sorensen 2011; Levy and Goodnough 2015) is used in some specific patients. However, sources for whole blood and its components are limited. Apart from this, the blood has a short shelf- life, a high risk of pathological contamination or immunogenicity, and limited portability. Therefore, developing new hemostatic biomaterials which can rapid hemostasis is a critical issue to improve hemodynamic stability and avoid the side effects of blood transfusion.

Understanding the mechanism of blood coagulation is the premise for hemostatic biomaterial. The process of blood coagulation contains two steps (Yang, Liu et al., 2017). Firstly, vasoconstriction, platelets adhere and aggregate to form a hemostatic plug, achieving preliminary hemostasis. And then, the blood coagulation cascade initiates plasma coagulation, and the fibrin network reinforces platelet thrombosis to achieve effective hemostasis in the second phase. Thus, the key to successful hemostasis is consisted by two parts: one is coagulation cascade, the other is platelet activation. In the coagulation cascade, activation of coagulation factor X affects thrombin generation, which directly determines the blood clotting. Platelet activation affects the formation of a hemostatic plug, it also activates prothrombin to achieve blood clotting.

Until now, a large number of hemostatic materials have emerged in the market. For example, α-cyanoacrylate and gelatin, which stop the bleeding by physically sealing the wound or compressing the blood vessels. One type of hemostatic biomaterial that creates a nanometer or micron-sized pore size, such as zeolites, mesoporous silica, etc. (Ellis-Behnke, Liang et al., 2006; Laurenti, Zazeri et al., 2017), and biopolymer materials such as gelatin and starch, which accelerates the initiation of physiological hemostasis by concentrating certain components of the blood under physical or chemical action and accelerating the activation of coagulation factors to stop bleeding. There are also hemostatic biomaterials that directly activates coagulation factors or platelets to activate the coagulation cascade (Gorbet and Sefton 2004), such as chitosan, alginic acid, oxidized cellulose and fibrin glue. The chitosan adheres to the wound to activate platelets and complement system in the blood. The alginic acid activates clotting factors after reacting with sodium ions. The oxidized cellulose can activate a variety of coagulation factors and aggregate platelets after rapidly dissolving in the blood, and the fibrin glue can rapidly initiate the endogenous coagulation system.

However, some hemostatic biomaterials have the following risks: 1) red blood cells may hemolyze and release hemoglobin, leading to anemia or renal failure, 2) plasma components such as platelets, white blood cells and complements in the blood may be activated to cause blood coagulation and inflammatory reactions at the same time (Motlagh, Yang et al., 2006). Therefore, a qualified hemostatic biomaterial should have the following characteristics (Kommu, McArthur et al., 2015): 1) Good biocompatibility, non-toxic, no antigenicity and inflammation; 2) suitable elasticity, good gas permeability and water permeability; 3) low infection probability, good tissue compatibility, and rapid hemostasis. In this review, various hemostatic biomaterials are summarized, containing the characteristics and clotting mechanism, development and application of the hemostatic biomaterials, strategies for optimizing the hemostatic biomaterials.

The characteristic and application of the various hemostatic biomaterials

Naturally derived biomaterials

In ancient times, people used herbs, greasy material and also sand mediated animal hides as hemostatic remedies. With the advancement in biotechnology, natural polymers have been introduced as hemostatic agents, which are naturally derived biomaterials that have good biocompatibility, mainly including protein-based hemostatic biomaterials, carbohydrate-based hemostatic biomaterials and inorganic hemostatic biomaterials. Protein-based hemostatic biomaterials include fibrin glue, collagen and gelatin, and carbohydrate-based hemostatic biomaterials include cellulose-based hemostatic biomaterials, chitosan, polysaccharides, and calcium alginate fibers; inorganic hemostatic biomaterials mainly include zeolite, kaolin, montmorillonite, and so on (Table 1).

Inorganic hemostatic biomaterials

Zeolite (Yu, Shang et al., 2019), kaolin (Liang, Xu et al., 2018), montmorillonite (Li, Quan et al., 2016), etc. are all molecular sieve biomaterials, which have been applied to hemostasis. The zeolite has been approved by FDA as a topical hemostatic agent for clinical hemostasis. The main component of the first-generation Quikclot product is zeolite, which has an obvious exothermic effect of absorbing water when applied to the wound sites. Therefore, the research and development of early molecular sieve hemostatic materials are mainly focused on reducing its exothermic reaction, and developed the corresponding product, namely Quik Clot Sport Silver. Compared to other hemostats, they may cause more extensive blood loss due to failure to stop bleeding in a short time (Kheirabadi 2011; Pourshahrestani, Zeimaran et al., 2016). Moreover, long-term residual zeolite in the tissue may cause chronic inflammation. Hence, complete debridement should be conducted before wound closure. The researchers have been working on improving the hemostatic properties of zeolite by various methods and have found results. It was reported that mCHA-C (mesoporous zeolite CHA-cotton) has a better hemostatic effect by the mechanism that the gel particles induced on the cotton surface could be further developed to final fiber-bound CHA zeolite, or they self-assemble and crystalize into mesoporous CHA zeolitic crystals (Figure 1). Based on the biomaterials of montmorillonite and kaolin, the corresponding hemostatic products were developed, namely Wound stat and Combat Gauze. However, there are still many shortcomings, they cannot play a hemostatic role in arterial bleeding (Achneck, Sileshi et al., 2010; Granville-Chapman, Jacobs et al., 2011; Pourshahrestani, Zeimaran et al., 2016). Most importantly, all of these materials are less effective in coagulopathic patients, and can induce some problems, such as toxicity, tissue inflammation and embolization (Pourshahrestani, Zeimaran et al., 2016). Li, Quan et al. (2016) have developed a graphene-MMT composite sponge (GMCS) to solve these problems (Figure 2A). It was confirmed that it has good hemostasis through these aspects (Figure 2B): 1) fast-absorbing of plasma within the sponge; 2) concentrating blood on the sponge surface; 3) activating clotting factors by MMT; 4) accelerating the speed of blood clotting, totally resulting in an ultrafast hemostasis.

TABLE 1 The different types of biomaterials for hemostasis.

Types	Materials	Brand names	Characteristics	Application
Protein-based	Collagen	Avitene® Helitene®	Biodegradability, biocompatibility, cell adhesion, non-toxicity, and low antigenicity	It has a hemostasis in almost all operations, but cannot be applied to patients with thrombocytopenia
	Gelatin	Gelfoam® Surgifoam® Gelfilm® Gelita-spon®	Has no toxicity or antigenicity, has soft fiber, strong adsorption, and can adhere to the wound surface	It could be used in the treatment of various wounds and traumas, in particular, transfixed wounds from solid organs. But it cannot be used in confined spaces or near nerve structures owing to easily causing complications of compressive origin
	Fibrin glue	Tisseel TachoSil® Evicel® Crosseal®	Good hemostatic properties, adhesive properties and histocompatibility	It can be applied to extensive bleeding after clinical tumor removal, bleeding in parenchymal organs, and patients with abnormal blood coagulation. But not allowed to be applied to blood vessels bleeding
Polysaccharide	Cellulose	Surgicel® Original® NuKnit Fibrillar SNoW®	Soft and thin, good histocompatibility, antibacterial effect	It is suitable for packaging, application, stuffing and other operations, hemostasis for capillary, arterioles and venous bleeding, bone bleeding. But it is not suitable for the treatment of peripheral nerve-rich wounds and irregular lacerations
	Chitosan	HemCon Celox Rapid gauze	Good affinity with human cells, no rejection, good biocompatibility, biodegradation, and hemostatic effect	It can be used in patients with coagulopathy. But hemostasis in the wound of extensive bleeding is not very satisfactory
	Starch	MPH, Per Clot	Reduce bleeding and transfusion, minimize blood infection, reduce seroma formation, has no immune, allergic reactions, and toxic side effects	It has effective hemostasis, but cannot enter into the blood vessel, lest form an embolism
	Alginate	Algosteril	Hygroscopicity, gelation, good biocompatibility, and the ability to ignite and shield electromagnetics	It is suitable for filling the wound, especially the deep and wide surgical cavity after endoscopic surgery
Inorganic	Zeolite, kaolin, montmorillonite	Quikclot, Woundstat Combat Gauze	Stability, ease of use, no biological toxicity, and no disease transmission	They cannot achieve rapid hemostasis, and are less effective in arterial bleeding and coagulopathic patients
Synthetic polymer-based	Poly(ethyelene oxide)	CoSeal®	Has good biocompatibility, histocompatibility, low cytotoxicity, and great hemostasis	It has been widely used in surgical bleeding
	Poly(cyanoacrylates)	Dermabond® Omnex® Glubran®and Glubran2®	Non-toxic, non-carcinogenic, and has good histocompatibility and significant hemostasis	It can be widely used in anastomosis, wound hemostasis, wound adhesion, and tendon. But may lead to vascular embolization and release toxic substances
Self-assembling peptide	RADA-16	SAPB-T45K, Pura Stat, Pura Matrix	Programmable, good viscoelasticity and biocompatibility, low antigenicity, and low cost	It can achieve complete and rapid hemostasis in the fields of the brain, spinal cord, liver, femoral artery and skin wounds
	SPG-178 PSFCFKFGP KOD			It overcame the disadvantage of RADA, whose low pH is easy to cause tissue damage. And it could coagulate whole blood, minimize bleeding

In addition, both of protein-based and polysaccharide biomaterials have their own advantages on hemostasis. The researchers have developed a OBC/CS (oxidized bacterial nanocellulose/Chitosan) and OBC/COL/CS (oxidized bacterial nanocellulose/Collagen/Chitosan) sponge and confirmed the role of hemostasis in a rat liver trauma model (Yuan, Chen et al., 2020) (Figure 2C).

Protein-based hemostatic biomaterials

Fibrin glue

Currently, there is a wide variety of fibrin sealants on the market, most of which are composed of thrombin and purified human or bovine fibrinogen, factor XIII, to mimic the physiological coagulation process (Watrowski, et al., 2017). Absorbable fibrin glue consists of fibrinogen, thrombin, aprotinin and calcium chloride, which is the most effective and widely used fibrin sealant in hemostasis. Fibrin glue has some excellent properties, such as good hemostatic properties, adhesive properties and histocompatibility, which effectively reduces the amount of blood loss and blood transfusion during the operations. At present, fibrin glue has been applied to extensive bleeding of wounds after clinical tumor removal and bleeding in parenchymal organs such as liver and kidney. In addition, since it contains thrombin, fibrin glue can be applied to patients with abnormal blood coagulation. However, due to its adhesion and procoagulant effect, fibrin glue is not allowed to be applied to blood vessels bleeding in case the formation of blood clots blocks blood vessels. In addition,
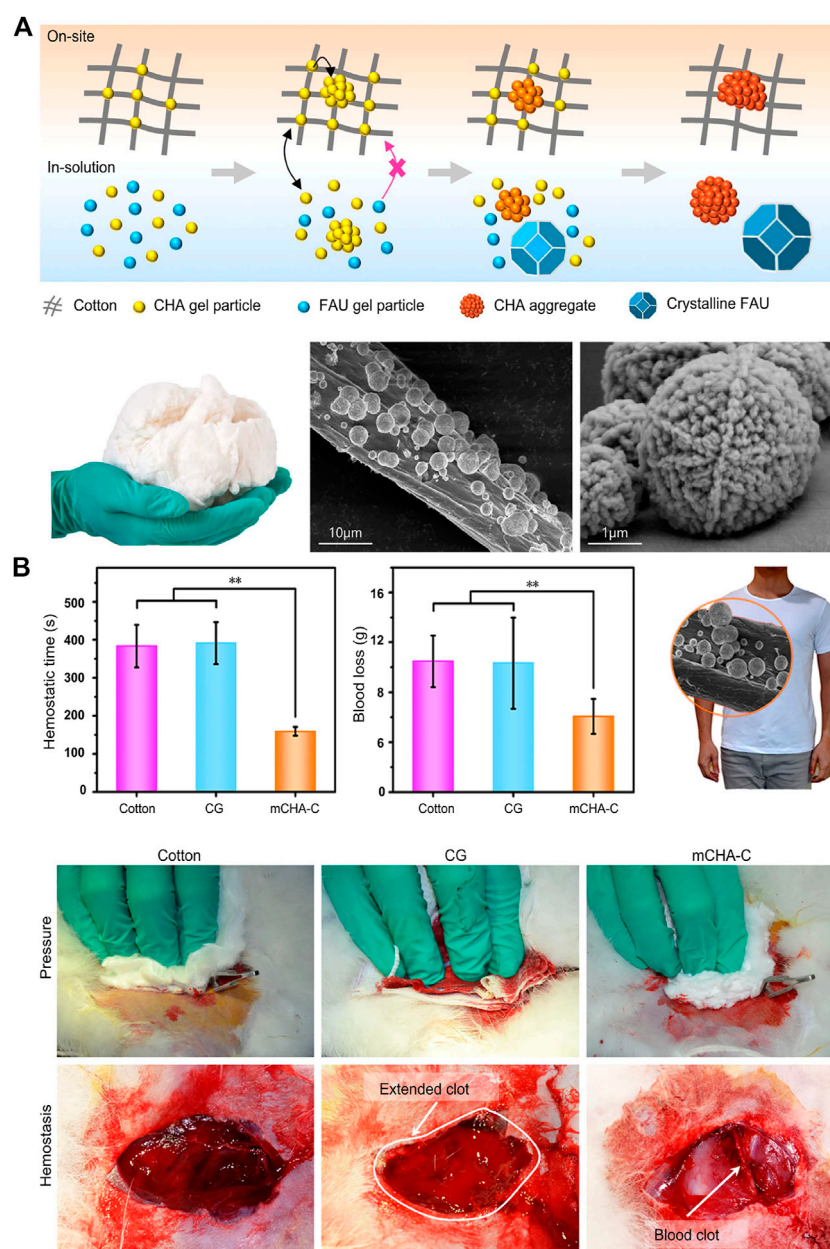
FIGURE 1
Inorganic biomaterials applied in hemostasis. **(A)** Upper:the schematic representation of formation process of on-site and in-solution products (Yu et al., 2019). Left: the photograph of mCHA-C. The SEM images of (Middle) mCHA-C, (Right) mCHA zeolite on cotton. **(B)** *In vivo* hemostatic capacity evaluation of hemostats. The quantitative analysis of hemostatic time (left) and blood loss (middle) in the rabbit femoral artery injury model. Right: Image of mCHA/T-shirt. The hemostasis was assessed upon manual pressure on the rabbit lethal femoral artery injury with cotton (left), CG (mid), or mCHA-C (right). Reproduced from (Yu et al., 2019) with permission from Copyright 2019 American Chemical Society.

due to its complicated procedure and inconvenient storage and transportation, fibrin glue is also not suitable for emergencies. Moreover, fibrin glue also has some disadvantages, such as the high cost, the potential for infecting human or animal hematogenous diseases (Valeri 2006), and the low efficiency of hemostasis for great vessels, limiting its application range.

Collagen

Collagen has some excellent performances, such as good biodegradability, biocompatibility, cell adhesion, non-toxicity, and low antigenicity (Hu, Yu et al., 2017). As a hemostatic biomaterial, collagen is always made into a porous or fibrous sponge which is beneficial for hemostasis of various wounds and the occurrence of hemostasis in almost all operations. A collagen sponge is especially applied to local bleeding where it is difficult to perform ligation during surgery, bleeding in fragile tissue or blood vessel-rich parts, and oozing of large areas in soft tissue. However, because the hemostasis of collagen requires the activation of platelets (Lewis, Kuntze et al., 2015), it cannot be applied to patients with thrombocytopenia, but it still has a good hemostasis effect on hemorrhage caused by
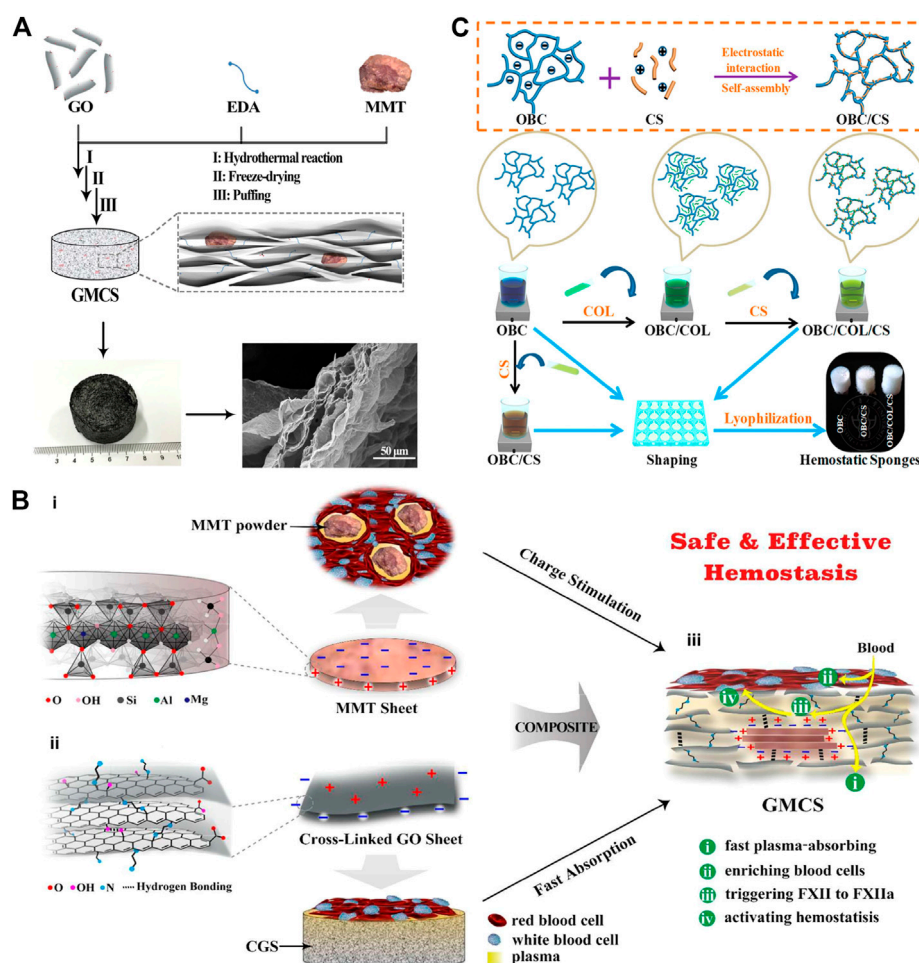
FIGURE 2
Naturally derived biomaterials are applied in hemostasis. **(A)** Schematic representation of the preparation route and the microstructure of the GMCS. The GMCS is firstly synthesized by hydrothermal reaction employing GO sheets, EDA linkers and MMT powders. Then, after freeze-drying and puffing treatments, the final product is obtained. The enlarged microstructure image shows MMT is fixed into the layered graphene. **(B)** Schematic representation of the GMCS construction and the potential synergy effect for hemostasis. (i) The MMT sheet possesses a permanent negative surface charge and a positive edge arising from the ordered and disordered crystal structure, respectively. Their powders can stimulate *in situ* clotting of blood with inward hydration and outward activating of blood coagulation. (ii) The cross-linked graphene sheet possesses a positive surface charge arising from EDA linkers and a permanent negative edge charge from inherent carboxyl groups. The resulted CGS can absorb plasma rapidly, increasing the concentration of hemocytes and platelets. (iii) MMT is fixed in the GMCS by the rich interactions, such as hydrogen bonding and electrostatic interactions. Reproduced from (Li et al., 2016) with permission from Copyright 2016 American Chemical Society. **(C)** Schematic diagram of the synthesis of OBC, OBC/CS, and OBC/COL/CS hemostatic sponges. Reproduced from (Yuan et al., 2020) with permission from Copyright 2019 American Chemical Society.

heparinization. Overall, collagen not only has the disadvantages of low mechanical strength, uncontrollable biodegradation rate, variability, potential pathogenic risk, etc. it is also a foreign protein, which increases the chance of infection and allergic reactions (Seyednejad, Imani et al., 2008). Excessive swelling can result in nerve compression and damage (Achneck, Sileshi et al., 2010). These shortcomings limit the use of collagen as a hemostatic biomaterial.

Gelatin

Gelatin-based biomaterial is not only absorbant by tissue cells, but also has no toxicity and antigenicity, and does not cause excessive scar tissue or cellular reactions. Hence, it could be used in the treatment of various wounds and traumas, in particular, transfixed wounds from solid organs. But it cannot be used in

confined spaces or near nerve structures owing to the fact that it could easily cause complications of compressive origin (Pereira, Bortoto et al., 2018). The gelatin sponges and gelatin fibers are most common in hemostasis. A gelatin sponge (GS) is a porous sponge that could absorb blood about 45 times heavier than itself (Piozzi, Reitano et al., 2018). Moreover, the porous structure of the gelatin foam is conducive to the aggregation and proliferation of fibroblasts, which then form new granulation tissue along the gelatin foam and rapidly fill the cavity and sinus tract. However, the gel formed by the gelatin sponge and the blood is soluble, so the above-mentioned hemostatic state and structure are easily broken. Moreover, it also has a poor traction ability on hemostatic components such as platelets and adhesion ability on the wound surface. Therefore, gelatin foam has a poor effect on hemostasis.

Polysaccharide hemostatic biomaterials

Cellulose

Oxidized cellulose (OC) and oxidized regenerated cellulose (ORC) are topical hemostatic biomaterials that have the appearance and texture of cotton yarns and are bioabsorbable. Both of them are soft and thin and have good histocompatibility, suitable for packaging, application, stuffing and other operations. When in close contact with the wound, the clotting components of the blood can be gathered around it, and hemostasis can be completed within 2–8 min. The soluble hemostatic gauze (Surgice1), which is often used in the clinic, is a regenerated oxidized fiber woven yarn, and belongs to the carboxymethylcellulose hemostatic material. Due to its slow dissolution, it is generally absorbed within 3–6 weeks, and is often used for bleeding on surgica1 wounds and sites where bleeding cannot be stopped, such as bone bleeding, etc. Moreover, it can play an effective role in hemostasis for capillary, arterioles and venous bleeding (Tam, Harkins et al., 2014). In addition, the Surgicel can lower the local pH of the wound to acidic, which has a certain antibacterial effect (Masci, Faillace et al., 2018).

However, the premise of using such hemostatic biomaterials is that the patient must have a complete coagulation function. In the absence of coagulation factors, the role of such hemostatic biomaterials in activating platelets is significantly weakened. Apart from this, Nagamatsu et al. (1997) found in the study of the formation of neuropathy that the highly acidic environment generated by oxidative cellulose can cause nerve injury through a diffuse chemical mechanism. The improved oxidized cellulose has a better hemostatic effect and fewer adverse reactions, but it is still not suitable for the treatment of peripheral nerve-rich wounds.

Chitosan

Chitosan is a primary derivative of chitin deacetylation and is a rare alkaline polysaccharide in nature. Chitosan has excellent properties, such as good affinity with human cells, no rejection, good biocompatibility, biodegradation, and has a hemostatic effect (Chan, Kim et al., 2016). It also has the following characteristics: 1) promote the secretion of hyaluronic acid and other glycosamines, 2) accelerate wound healing, 3) inhibit the growth of a variety of bacteria and fungi, 4) increase the mechanical properties of biomaterials, etc. (Pusateri, McCarthy et al., 2003). Therefore, a variety of medical materials such as chitosan-free gauze, chitosan-coated gauze and chitosan hemostatic sponges are used in clinical practice. The coagulation mechanism of chitosan is independent of blood clotting factors and platelets, so it can be used in patients with coagulopathy. However, due to the limited effect of hemostasis of chitosan, it is not very satisfactory in the wound with extensive bleeding. Therefore, the method of compounding other hemostatic agents, such as clotting factors and calcium chloride, are often used.

Starch

MPH (Microporous polysaccharide hemispheres) and Per Clot are hemostatic products of microporous polysaccharides prepared by extracting from plant starch and further processing. MPH containing no polypeptide or protein can not only rapidly dehydrate blood to form blood clots to prevent blood from oozing out, but also can be rapidly degraded and absorbed *in vivo*. At the same time, due to the low protein property of MPH, the local tissue response is weak, rarely causing foreign body reactions and reducing the risk of infection during use (Humphreys, Castle et al., 2008). As a hemostatic agent, the microporous polysaccharide has its own advantages: 1) effectively reduce the amount of bleeding and transfusion; 2) minimize the rate of blood-derived infection; 3) reduce seroma formation; 4) it has no immune, allergic reactions, and toxic side effects on wound healing (Egeli, Sevinç et al., 2012). Morover, these biomaterials cannot enter the blood vessel, lest form embolism.

Calcium alginate fiber

Calcium alginate fiber is a fibrillar-like polysaccharide, which is extracted from seaweed. It has the properties of hygroscopicity, gelation, good biocompatibility, and the ability to ignite and shield electromagnetics. Due to its excellent adhesion, it is suitable for filling the wound, especially the deep and wide surgical cavity after endoscopic surgery. Importantly, the formed gel material will not adhere to the operative cavity and is conducive to repairing nasal mucosa epithelium.

Synthetically derived hemostatic biomaterials

Synthetic hemostatic agents are typically made from cyanoacrylate, polyurethane, and polyethylene glycol. Because they have low immunogenicity and can customize their chemical properties to stimulate procoagulant mechanisms, they are widely used in various hemostasis operations. However, the toxic by-products from these hemostatic agents aggregate and degrade, causing local irritation and inflammation (Table 1).

Polymers-based hemostatic biomaterials

Poly(ethyelene glycol)

The polyethylene glycol (PEG), a synthetic polymer, is soluble in both aqueous and organic solvents, therefore it can interact with both the intra- and extra-cellular spaces, which provides an environment beneficial to cellular infiltration and growth (Harris 1992). It has been widely used in biomedical engineering, such as regeneration of nerves, articular cartilage and bladder tissue (Yamawaki, Taguchi et al., 2017).

There are some advantages, for example, completely no risk of infectious diseases, batch-batch stability, low price, and can be prepared in batches. In addition, a hemostatic liquid sealant made of the tetra-succinimidyl -derivatized PEG and tetra-thiol-derivatized PEG could stop bleeding by crosslinking with tissue and sealing the hemorrhagic spot (Overby and Feldman 2018). The commercial product, namely AdvaSeal®, was also developed by co-polymerizing poly(ethylene glycol) with poly(α-hydroxy acid) diacrylate. Moreover, the poly(ethyelene oxide) based hemostatic biomaterials have been widely used in surgical bleeding, such as Poly(alkylene oxides), e.g., poly(ethylene oxide) (PEO) and poly(propylene oxide) (PPO). For instance, Wang et al. and Wellisz et al. have reported that a PEO-PPO-PEO block copolymer-based waxy material, namely Ostene®, has an excellent effect on hemostasis in orthopedic surgeries (Hickman, Pawlowski et al., 2018).

Poly(cyanoacrylates)

Although α-cyanoacrylates have tissue toxicity at a low level, some of them have been widely used in the clinic, such as n-cyanoacrylate, n-butyl α-cyanoacrylate, n-octyl α-cyanoacrylate. And it is proven that
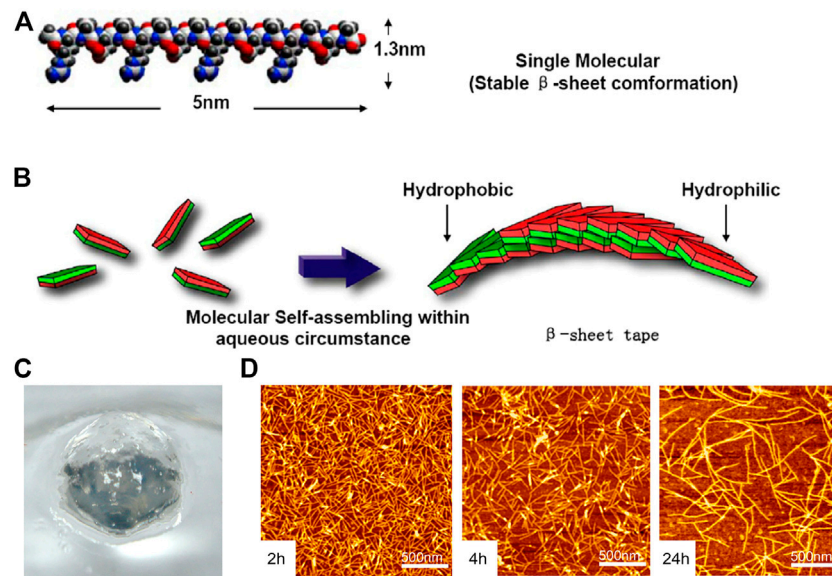
FIGURE 3
The RADA16 is applied in hemostasis. **(A)** Molecular model of the RADA16-1; **(B)** Molecular model of numerous RADA16-1 as they undergo self-assembly to form nanofibers with the hydrophobic alanine sandwiched inside and hydrophilic residues on the outside; **(C)** RADA16-1 gelatinized into hydrogel. Reproduced from (Wang et al., 2012) with permission from Copyright 2012. **(D)** AFM images of RADA16-I nanofibers at various points in time after sonication. Note the elongation and reassembly of the peptide nanofibers over time.

they are non-toxic, non-carcinogenic, and have good histocompatibility and significant hemostasis. It was reported that the Omnex® consisting of n-octyl α-cyanoacrylate and butyl lactoyl-2-cyanoacrylate could stop bleeding (Bhatia 2010). In addition, the Glubran® and Glubran2®, which are made of n-Butyl-2-cyanoacrylate and methacryloxysulpholane, have bacteriostatic and hemostatic properties (Montanaro, Arciola et al., 2000). For wounds with major artery bleeding, a tourniquet is first placed on proximal vein to temporarily stop bleeding, then the α-cyanoacrylate tissue glue is sprayed on the wound after wiping the blood. It is an ideal hemostatic method that has a high success rate of hemostasis and the side effects are minor (Fontenot, Rasmussen et al., 2005). At present, α-cyanoacrylate can be widely used in the anastomosis, wound hemostasis, wound adhesion, and tendon (de Azevedo, Marques et al., 2003; Lumsden and Heyman 2006). However, such hemostatic materials can lead to vascular embolization and release toxic substances such as cyanide and formaldehyde in the degradation process, which may induce inflammation and tissue necrosis around the injection site (Farooq and Wong 2005).

Self-assembling peptide as hemostatic biomaterials

Under physiological conditions, Self-assembled peptides can spontaneously and regularly form stable secondary structures through non-covalent bonds, then further stacked into nano-fiber to form a hydrogel scaffold structure with a water content of more than 99%. The self-assembled peptides have excellent performances, such as programmable, good viscoelasticity, good biocompatibility, low immunogenicity and low cost (Kondo, Nagasaka et al., 2014; Rad-Malekshahi, Lempsink et al., 2016; Gao, Xu et al., 2017). Moreover,

without the help of traditional hemostatic methods, such as pressure, cautery, vasoconstriction, coagulation and cross-linking agent, it can achieve complete and rapid hemostasis in the fields of the brain, spinal cord, liver, femoral artery and skin wounds (Fouani, Nikkhah et al., 2019).

RADA16-I (Ac-RADARADARADARAD-NH$_2$) is thoroughly studied and widely used as a self-assembling hemostatic biomaterial. The monomer of RADA16-1was ≈5 nm long, ≈1.3 nm wide, and ≈.8 nm thick in dimensions (Figure 3A). RADA16-1 samples can spontaneously assemble nanofibers ranging from a few hundred nanometers to a few microns in length (Figure 3B) and formed hydrogels that were achromatic color, hyaloid and can be fabricated into various geometric shapes (Figure 3C). The results of AFM (Wang et al., 2012) showed that RADA16-1 could form long self-assembled nanofibers ranging with hundred nanometers in a stable and repeatable manner (Figure 3D). Masuhara, Fujii et al. (2012) confirmed the hemostatic effect of RADA16-I by rabbit abdominal aortic puncture bleeding model, and also tested the safety of intravenous injection of lower concentration hydrogel. It has a 3D structure similar to ECM (extracellular matrix), which facilitates cell adhesion, proliferation and differentiation (Guo, Wang et al., 2011; Mie, Oomuro et al., 2013; Gao, Xu et al., 2017), and the European-certified commercial product which contains this biomaterial named Pura Stat is applied in clinical hemostasis. It was reported that RADA not only prevented traumatic bleeding in the brain, spinal cord, femoral artery and liver (Ellis-Behnke and Schneider 2011), but could also rapidly achieve hemostasis in both heparinized and non-heparinized animals, solving a series of problems caused by the use of anticoagulant drugs in surgical intraoperative and postoperative bleeding (Csukas, Urbanics et al., 2015).

FIGURE 4
The hemostatic biomaterials with different mechanisms.
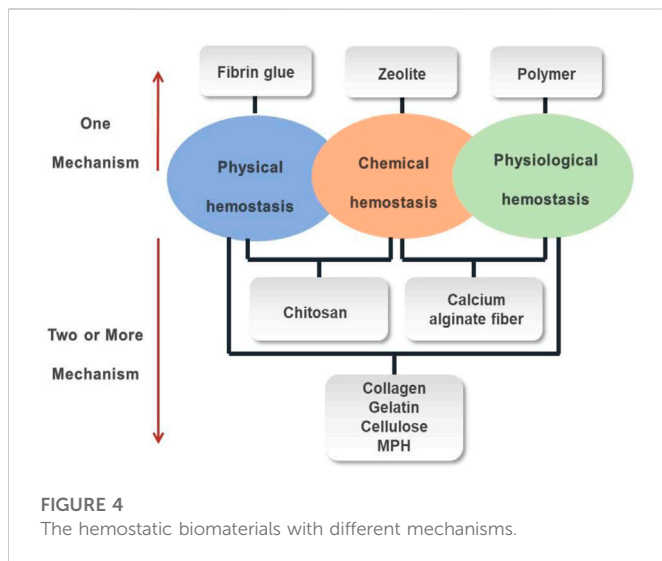
Komatsu, Nagai et al. (2014) designed a neutral (pH = 6.5–7.5) self-assembled peptide hydrogel namely SPG-178 (RLDLRLALRLDLR), which could achieve rapid hemostasis in the left hepatic lobe. Ruan, Zhang et al. (2009) designed an amphiphilic self-assembled short peptide (PSFCFKFGP), which was mainly self-assembled as a spherical polymer at a high concentration and then passed through the nanofiber body to form a hydrogel with a water content of more than 99%. And the results of the comparative experiment on hemostasis showed that the hemostatic time of the 1% short peptide hydrogel group was shorter than the gauze group and chitosan group. Kumar, Taylor et al. (2014) designed a mimetic peptide of collagen named KOD ((PKG)4(P-Hyp-G)4(D-Hyp-G)4), consisting of 36 amino acids. The KOD can self-assemble into three helical nanofibers to further form nanofiber hydrogels, which have been shown to coagulate whole blood, minimize bleeding, and significantly activate platelets.

The self-assembled peptides have some hemostatic properties: 1) when contacting with electrolytes in body fluids, self-assembled peptides begin to self-assemble and form a reticular hydrogel structure with a pore size of 50–200 nm, which can quickly fill and match irregular wounds, then form a nanofiber barrier to prevent the exudation of cells and body fluids. 2) High-concentration short peptides can self-assemble more nanofibers, better facilitating blood coagulation. Moreover, ions and charges can accelerate the self-assembly of short peptides into nanofibers in the blood containing red blood cells (Luo, Wang et al., 2011). 3) The self-assembled peptide hydrogel is a colorless and transparent biological scaffold, which could clearly observe the hemostasis inside the wound. 4) The elastic modulus of self-assembled peptide hydrogel is either too high or too low to achieve the best hemostatic effect. Only when the short peptide hydrogel closely fits the wound can it better withstand the vascular pulse and exert the maximum hemostatic effect. 5) The degradation products of self-assembling peptide hydrogels are natural L amino acids that can be absorbed by surrounding tissues for repair. Therefore, one of the hot topics is to develop a variety of self-assembling peptides with antimicrobial properties and hemostatic effects.

The mechanism of the hemostatic biomaterials

There are three hemostatic mechanisms when the most functional hemostatic biomaterials are exposed to blood (Figure 4). 1) Physical hemostasis: the biomaterial absorbs water in the blood, causing the viscosity and concentration of the blood to increase, thereby slowing down blood flow; or the biomaterial swells after absorbing water to cover the wound surface and stopping the bleeding. 2) Chemical hemostasis: the presence of negative ions can quickly bind or aggregate red blood cells and platelets, thereby releasing blood coagulation-related factors to accelerate blood coagulation. 3) physiological hemostasis: the biomaterial can rapidly activate coagulation delivering factors II, V, VII, X, and XII, which activates the endogenous coagulation system and forms insoluble fibrin polymer with thrombin to achieve hemostasis.

Some hemostatic biomaterials achieved the purpose of hemostasis through a mechanism, such as zeolite, fibrin glue and polymer. The hemostatic mechanism of zeolite is to concentrate platelets and clotting factors through the rapid absorption of water at the bleeding site, while the heat generated by water absorption enhances the rate and ability of aggregation of platelets, significantly improving the survival rate of patients with large areas and severe trauma. The fact that zeolite does not contain any biological components has some advantages, such as stability, ease of use, no biological toxicity and no disease transmission (Li, Cao et al., 2013). The hemostatic mechanism of fibrin glue is that thrombin cleaves the fibrinogen into fibrin, which causes blood coagulation, while aprotinin inhibits the dissolution of blood clots, making blood clots more stable on the wound, thereby achieving hemostasis. This polymer hemostat achieved the purpose of hemostasis through a tamponade mechanical effect, not a biochemical augmentation of coagulation mechanisms. They do not have a hemostatic effect by themselves, but could achieve hemostasis through physical closure, mechanical barriers, and wound closure.

In addition, the hemostatic biomaterials achieved the purpose of hemostasis by more than one mechanism, such as collagen, gelatin. Collagen mainly has a hemostatic function through the following three aspects: 1) activating partial coagulation factors to produce thrombin which cleaves fibrinogen into fibrin (Skopinska-Wisniewska, Sionkowska et al., 2009), 2) aggregating platelets to form a thrombus, preventing bleeding, 3) adhering to the wound and mechanically compressing the damaged blood vessel to serve as a packing effect. The gelatin, as a physical matrix, affects clot initiation. When it is in contact with blood, the gelatin would swell and induce a buffering effect. The hemostatic mechanism of a gelatin sponge is relatively simple, that is, it provides an attachment surface for platelets and stimulates the release of platelet factors. Gelatin fiber (GF) is a non-woven hemostatic biomaterial made from a gelatin sponge and extracts of a maple leaf, which can promote platelet adhesion and aggregation, and then accelerate hemostasis. Furthermore, the gelatin fiber has a dense network structure with uneven loose space inside, which enlarges the contact area with blood, so that the platelets are more likely to adhere and accumulate on the fibers, which is conducive to the formation of white thrombus and then achieve rapid hemostasis. Because gelatin fiber has strong adsorption, and can adhere to the wound surface, it has a more obvious hemostatic effect than a gelatin sponge in the deep part of the body.

The Polysaccharide hemostatic biomaterials achieved the purpose of hemostasis by different mechanismsm, such as cellulose, chitosan, MPH and calcium alginate fiber. Both oxidized cellulose and oxidized regenerated cellulose achieve the purpose of hemostasis in two aspects: on the one hand, a viscous gel block is formed by combining an acidic carboxyl group with Fe^{3+} in hemoglobin, to seal the damaged capillaries and stop bleeding; on the other hand, it activates the body's coagulation mechanism by adhering and accumulating platelets, to accelerate blood clotting. It was (Bano, Arshad et al., 2017) reported that positively charged molecules in chitosan could combine with negatively charged tangible components in blood, such as red blood cells, white blood cells and platelets, to form cell emboli or thrombus to play a role in blood coagulation. Particularly, due to the hydrophilicity of the amino group in the chitosan, more fibrinogen is adsorbed, thereby promoting the formation of a thrombus. The mechanism of MPH includes two aspects. One is that when the biomaterial is placed on the bleeding wound, the particles quickly absorb the water in the blood to concentrate the components in the blood such as platelets, red blood cells, and clotting factors (Thongrong, Kasemsiri et al., 2013), to form a gelatinous mixture, which plays a role on the instant hemostasis. Another is that the biomaterial accelerates the activation of endogenous clotting factors and forms a strong topical clot, shortening the clotting time (Ersoy, Kaynak et al., 2007). The calcium alginate fiber has been reported to have great hemostasis (Aydin, Tuncal et al., 2015). When the calcium alginate fiber is in contact with the sodium salt in the blood and wound secretion, it can absorb 15–20 times of blood than its weight and is converted into a gel substance, and simultaneously releases calcium ions to stop bleeding.

Hemostatic strategies in biomaterials

Optimization of the single hemostatic biomaterial

Various hemostatic materials have been emerging in recent years, but it is still a great challenge to achieve hemostasis in surgery. Different types of hemostatic biomaterials has their own shortcomings, which affects the efficacy of hemostasis. For instance, although the fibrin sealants could effectively enhance blood coagulation, they still have a potential risk of spreading viral infections. The acidic nature of cellulose products may have a side effect on the surrounding tissue and wound healing. The collagen-based hemostatic agents are easy to cause allergic reactions, as well as nerve compression and damage, resulting from excessive swelling. Inorganic hemostats may elicit a foreign-body response due to their poor biodegradability. Thus, many researchers are now committed to the optimization of biomaterial properties. The optimum methods for a hemostatic biomaterial are that 1) could change the mechanical properties by cross-linking technology, etc., to make the biomaterial more suitable for hemostatic application; 2) could optimize the nucleic sequence of certain protein by genetic engineering technology and recombinantly expressed to obtain a novel protein, which possesses new excellent properties and could overcome the inherent shortcomings of the biomaterial.

Modification of the biomaterial by crosslinking

It is necessary to modify the material intrinsically to overcome some shortcomings of the material. Taking collagen as an example, although collagen-based hemostatic biomaterials have great advantages. The disadvantage of the simple collagen limits its hemostatic application, such as poor mechanical properties, uncontrollability of biodegradation rate, variability, etc. Nowadays, cross-linking techniques are commonly used to change the physical properties of collagen. The method of physical cross-linking is simple, and has low cytotoxicity, mainly including hot-dry cross-linking (DHT) and ultraviolet cross-linking.

However, compared with physical cross-linking, chemical cross-linking has a better control of structure and could improve some properties of collagen, such as tensile strength, flexibility, mechanical properties, biodegradation rate and thermal stability. The main chemical cross-linking agents include aldehydes, dicarboxylic acids, genipin, carbodiimide, citric acid derivatives, chitosan and polyvinyl alcohol. After modifying the tilapia skin collagen sponge through chemical cross-linking methods (Verissimo, et al., 2010; Xie, Yi et al., 2018), the sponge has shown more excellent performances, such as mechanical properties, the elongation at break, and the collagenase degradation. Thus, it was an ideal medical hemostatic material with biocompatibility. It was reported that the collagen-cotton meshed by chemically modifying soluble collagen with aldehydes improved the hydrophilicity of collagen and its hemostatic performance. Chen, Zhang et al. (2016) designed the amphiphilic short peptide called I3QGK, which combines the self-assembly process of short peptides with the catalysis of transglutaminase (TGase), and was applied to hemostasis. It could form the hydrogel with good mechanical properties, and can effectively stop bleeding by gelatinizing blood and promoting platelet adhesion. The development of cross-linking technology is also very important. Although chemical cross-linkers can form strong bonds, most of them are cytotoxic. Therefore, the quality and biocompatibility of collagen hemostatic sponge prepared with chemical cross-linkers are often unsatisfactory. At present, the method of enzyme cross-linking, which has a milder condition and good biocompatibility, is commonly used in the fabrication of hemostatic biomaterials.

Genetic engineering for optimizing biomaterials

The cross-linking techniques can change certain properties of biomaterials to make them more suitable for hemostasis, but they cannot eliminate all the disadvantages of biomaterials. For example, since natural collagen is mostly extracted from animals, it has the potential of pathogenic transmission and the disadvantage of batch-batch instability. However, the proteins expressed by genetic recombination can overcome the above shortcomings, and can also realize large-scale production of proteins at a low price. Therefore, based on optimizing the nucleic acid sequence of natural collagen, human-like collagen (Fan, Luo et al., 2005) was obtained through genetic recombination technology, which has good biocompatibility and biodegradability. Based on the above, a new styptic sponge was prepared by cross-linking human-like collagen with glutamine transaminase and a two-step freezing method (Jiang, Wang et al.,

TABLE 2 The summary of composite hemostatic biomaterials.

Types	Major components	Advantages	References
Sponges	Collagen/chitosan/calcium pyrophosphate	It not only enhances the hemostatic effect, but also solves the problem of cavity filling in surgery	Yan, Cheng et al. (2017)
	Chitosan/gelatin	It has good biodegradability, no cytotoxicity, effective bacteriostasis, and could promote cell proliferation	Lan, Lu et al. (2015)
	Silk fibroin/gelatin	It significantly reduces the wound area and promotes wound healing, the formation of skin and collagen	Harrison and Spada (2018)
Films	Silk fibroin/polylactide (1:2)	As a hemostatic material for chronic wound	Shahverdi, Hajimiri et al. (2014)
	Chitosan/Ga_2O_3-containing mesoporous bioactive glass	It could promote cell proliferation, and has excellent antibacterial activity, high hemostatic efficacy	Ostomel, Shi et al. (2006), Dai, Yuan et al. (2009), Salinas, Shruti et al. (2011), Shruti, Salinas et al. (2013), Shruti, Salinas et al. (2013)
Hydrogels	Poly(vinyl alcohol)/human-like collagen/carboxymethyl chitosan	It has excellent swelling ratios, bacterial barrier activity, moisture vapor permeability, hemostasis activity and biocompatibility	Pan, Fan et al. (2017)
	Dihydroxyacetone (pDHA)/methoxypoly(ethylene glycol) (MPEG)	It eliminates the major problem of the insolubility of pDHA, and has some advantages, such as short residence time *in vivo*, low inflammation, and the risk of infection	Henderson, Kadouch et al. (2010)
	GelMA/HA-NB	The GelMA/HA-NB matrix hydrogel could adhere to the wet wound tissue and seal the hemostatic site through UV light irradiation	Yang, Zhang et al. (2016) and Hong, Zhou et al. (2019)
	SLac/bactretase	The SLac in itself provides a physical barrier to bleeding wounds. And SLac loaded with bactretase produced a kind of drug-loaded hydrogel (SB50), which enhanced the role of coagulation	Kumar, Wickremasinghe et al. (2015)
Fibers	Chitosan/recombinant batroxobin	It has a synergetic effect on blood coagulation	Seon, Lee et al. (2018)
	Chitosan/geltain	It has high porosity, rapid blood absorption, and yields synergistic effects in hemostatic function and wound repair	Gu, Park et al. (2016)
Particles	Chitosan/poly(vinyl alcohol)	It effectively reduces thromboembolic formation in stopping bleeding from femoral artery	Chen, Liu et al. (2017)
	Chitosan/Kaolin clay	It has high amount of pores, no adverse effects, and the synergetic combination mechanisms	Sun, Tang et al. (2017)
	A mesoporous silica sphere doped with calcium-silver	It has good degradability and antibacterial properties	Dai, Yuan et al. (2009)
liquid	tetra-succinimidyl-derivatized poly(ethylene glycol)/tetra-thiol-derivatized poly(ethylene glycol)	stop bleeding by cross-linking with tissue and sealing the hemorrhagic spot	Overby and Feldman (2018)
	Gelatin based bovine collagen/microgranules/glutaraldehyde/human thrombin	It is superior to Gelfoam-thrombin in cardiac surgeries, and has reduced bleeding when used in open nephrectomies and laparoscopy	Reuthebuch, Lachat et al. (2000) and Oz, Rondinone et al. (2003)
	ABS/(Lauryl -VVAGK-Am)	It has an excellent hemostatic effect in partial nephrectomy	Huri, Dogantekin et al. (2016)
Powder	Hydroxyethylcellulose/EGF (CEGP-003)	It appears to have effective treatment in peptic ulcers and ESD- or EMR-induced bleeding	Bang, Lee et al. (2018)

2017), which has good biocompatibility and a significant hemostatic effect in the ear artery model and liver injury model.

Creation of the composite hemostatic biomaterials

For certain biomaterials, it is possible to strengthen the properties of biomaterial through cross-linking technology or genetic recombination technology in order to stop the bleeding more effectively. Based on this assumption, it may be better to combine two or more kinds of biomaterials to strengthen advantages and avoid disadvantages, and thus achieve the purpose of more rapid and effective hemostasis (Table 2).

The Yan, Cheng et al. (2017) designed a novel collagen sponge combined with chitosan/calcium pyrophosphate for hemostasis. It has dual hemostatic effects: on the one hand, collagen adsorbs platelets and activates blood coagulation factors, and compresses small blood vessels to stop bleeding; on the other hand, the hemostatic mechanism of chitosan is that it promotes the aggregation of red blood cells to form a red thrombus. Furthermore, it not only enhances the hemostatic effect, but also solves the problem of cavity filling

during in surgery. The pH of the gelatin matrix is neutral, so it is used in conjunction with other hemostatic agents, such as biomaterials that blend chitosan with gelatin. These biomaterials have the advantages of the chitosan, such as good biodegradability, biocompatibility, antibacterial and film-forming properties, as well as the advantages of gelatin, such as low antigenicity, etc. The Guangqian Lan, Lu et al. (2015) prepared a kind of composite containing chitosan and gelatin for hemostasis by cross-linked with tannins and then freeze-dried under a vacuum. A double-layer hemostatic biomaterial (Harrison and Spada 2018), which was fabricated by combining silk fibroin and gelatin, has been reported. The silk fibroin fabric was used as a non-adhesive layer to contact the wound, while the bioactive layer of the silk fibroin/gelatin sponge could significantly reduce the wound area, promote wound healing and the formation of skin and collagen. Shahverdi, Hajimiri et al. (2014) optimized the electrostatic spinning process for a mixture of silk fibroin/polylactide (1:2) to make the mixed membrane as a hemostatic biomaterial for a chronic wound. Due to the unique features of mesoporous bioactive glasses (MBGs), such as high porosity, highly ordered mesoporous channel structure, huge surface area and pore volume (Ostomel, Shi et al., 2006; Dai, Yuan et al., 2009; Salinas, Shruti et al., 2011; Shruti, Salinas et al., 2013; Shruti, Salinas et al., 2013), it has excellent hemostatic property, as shown by enhancing capability of platelet aggregation, thrombus formation, and blood coagulation activation. Based on the above, some researchers also reported (Pourshahrestani, Zeimaran et al., 2017) that a 1% Ga-MBG/chitosan (Ga-MBG/CHT) composite scaffold has a rapid hemostatic effect. The researchers (Pan, Fan et al., 2017) have prepared a novel hemostatic biomaterial through simply repeated freeze-thawing of the mixed solution including poly(vinyl alcohol), human-like collagen and carboxymethyl chitosan, which showed a great hemostasis effect. The potential of poly(dihydroxyacetone) (pDHA) in hemostatic application is limited owing to its insolubility in all aqueous and almost all organic solvents. It was reported (Henderson, Kadouch et al., 2010) recently that a kind of block copolymer made of PEG and pDHA could be an effective and rapidly resorbable hemostatic agent, which has some advantages over other hemostats, such as short residence time *in vivo*, low inflammation and the risk of infection. It was reported (Seon, Lee et al., 2018) that an efficacious hemostatic agent made of chitosan-based non-woven dressing with recombinant batroxobin (rBat), which has a synergetic effect on blood coagulation. In addition, some researchers found (Gu, Park et al., 2016) that sonicated chitosan-geltain nanofiber mats with high porosity yield a synergistic effect in some ways, including hemostatic function and wound repair. Dai, Yuan et al. (2009) prepared hemostatic biomaterials doped with calcium-silver mesoporous silica spheres, and the results showed that the calcium ions in the biomaterials improved hemostatic properties. Poly(vinyl alcohol) (PVA) was conducive to increasing the swelling degree of the spheres and the enhanced hemostatic effect. To take full advantage of the PVA and chitosan, the Chitosan-PVA spheres (Chen, Liu et al., 2017) were prepared through electrospraying and ionotropic gelation, which effectively reduced thromboembolic formation in stopping the bleeding from the femoral artery. Sun, Tang et al. (2017) fabricated porous chitosan/kaolin composite microspheres (CSMS-K), whose hemostatic performance was superior to chitosan porous microspheres (CSMS) that it formed larger blood clots than CSMS and Celox within the same time period. The hemostat called FloSeal®, which is a gelatin matrix based on bovine collagen containing micro granules, crosslinked

with glutaraldehyde and human thrombin solution that is mixed at the time of use (Reuthebuch, Lachat et al., 2000; Oz, Rondinone et al., 2003), is superior to Gelfoam-thrombin in cardiac surgeries and has reduced bleeding when used in open nephrectomies and laparoscopy (Guzzo, Pollock et al., 2009). In addition, Kumar, Wickremasinghe et al. (2015) also designed a self-assembled short peptide nanofiber hydrogel SLac (KSLSLRGSLSLS LKGRGDS), which in itself provides a physical barrier to bleeding wounds. Batroxobin is a serine protease derived from snake venom, which can significantly reduce fibrinogen and thrombolysis. SLac loaded with bactretase produced a kind of drug-loaded hydrogel named SB50, which enhanced the role of coagulation. Huri, Dogantekin et al. (2016) mixed ABS hemostatic agent with amphiphilic short peptide (Lauryl -VVAGK-Am) 1:1 to obtain a kind of nano hemostatic agent, which played an excellent hemostatic role in partial nephrectomy.

Design and fusion of self-assembling peptides

Due to its stable gelatinization, self-assembled short peptide RADA has attracted much attention as a novel hemostatic biomaterial. However, its low pH (3.0–4.0) is easy to cause tissue damage, and the biological activity is unsatisfactory. Because of this, the researchers not only designed various types of self-assembled short peptides, but also fused other peptides or proteins with RADA to obtain new hemostatic biomaterials. It provides methods and ideas for designing and fabricating more hemostatic biomaterials.

RADA16-based fusion peptides have been gradually applied in the field of biomedicine, since RADA16-based fusion peptides have acquired new functions while maintaining the original functions of RADA16. Researchers have designed more excellent RADA16-derived hemostatic biomaterials by selecting different functional sequences from natural active peptides and linking them to RADA16. The short peptide GRGDS mediates cell adhesion by binding to a variety of integrins. The functional sequence YIGSR, which appears in the β1 chain of laminin-1, shows a strong ability for cell adhesion, migration and formation of the endothelial tube (Nomizu, Kim et al., 1995; Chada, Mather et al., 2006). Thus, Cheng, Wu et al. (2013) designed two novel self-assembled short peptides, namely RADA16-GRGDS and RADA16-YIGSR, by linking the functional sequence GRGDS and YIGSR respectively based on the RADA16 self-assembled short peptide.

Most of these functional peptides are small fragment functional motifs of the active protein. Therefore, there are some insurmountable shortcomings (Wang, Wang et al., 2019): 1) With the decrease in the number of functional sequence amino acids, the function of the active protein was greatly reduced. Therefore, it is difficult for small fragment functional motifs to give full play to the function of active proteins. 2) The peptides fused with RADA16 are all chemically synthesized, and the cost of synthesizing and purifying the polypeptide is relatively high. 3) The genetic engineering fermentation is the preferred method for obtaining drug proteins at a low cost. Due to the relatively low molecular weight and poor stability of RADA16 and fusion peptides, it is difficult to obtain the ideal concentration level even if they are over-expressed in host cells by genetic engineering. Therefore, the stability of the expression product is usually improved by fusing RADA-16 with other proteins. Yang, Wei et al. (2018) fused the RADA16 gene to the 3′ end of the open reading frame (ORF) encoding an elastin-like peptide (ELP) by genetic recombination to construct new hemostatic

biomaterials: 36ELP-RADA, 60ELP-RADA and 96ELP-RADA. In particular, the 96ELP-RADA sponge film showed a good hemostatic effect. Our group constructed a new hemostatic sponge of HLC-RADA by fusing human-like collagen with RADA16, then lyophilizing the fusion protein, which showed effective hemostasis in a hemostatic model of rabbit liver.

Flexibility of biomaterials for hemostatic applications

A variety of hemostatic products play an important role in the field of clinical hemostatic application by virtue of their unique advantages. However, the application of these hemostatic biomaterials is often limited by many factors, such as the amount of bleeding, bleeding sites, and different hemostatic effects of the biomaterials, etc. In the face of multiple bleeding conditions, a biomaterial can be made into various forms including granules, solution, powder, hydrogel, film, fiber, and porous sponge, and customized into different product types, such as gauze, spray, and injectable hydrogel. Take chitosan for an example, a high-viscosity chitosan solution can be injected into blood vessels, not only to block blood vessels and prevent blood flow to capillaries, but of little to avoid infection. Chitosan powder can be combined with gauze or made into a spray, which is suitable for emergency treatment with large-area skin damage but small blood loss (Muzzarelli, Morganti et al., 2007). Chitosan fiber not only has good cell compatibility and cell adhesion (Pillai, Paul et al., 2009), but also contributes to the regeneration of skin tissue and the inhibition of scar formation. Chitosan porous materials mainly include porous microspheres, porous fibers, porous sponges, or a combination of the above several types of hemostatic materials (Huang, Sun et al., 2015), the porous structure of which facilitates the discharge of secretion from the wound and tissue healing. Chitosan hydrogel can achieve better and more effective contact with the wound, and provide a moist environment to promote wound healing (Ono, Ishihara et al., 2001). Mi, Shyu et al. (2001) prepared a novel asymmetric chitosan film consisting of a surface with a macroporous sponge-like sub-layer, which can control water loss, has excellent oxygen permeability, and promotes fluid excretion. Meanwhile, due to the presence of a dense cortex and inherent antimicrobial properties of deacetylated chitosan, it can inhibit the invasion of exogenous microorganisms. Furthermore, it has a better hemostatic effect and can accelerate wound healing.

In addition, some researchers have reported that some hemostatic biomaterials could convert from, or strengthen the role of a certain type biomaterials to better facilitate hemostasis, when coming in contact with a bleeding wound. For example, it was reported that CEGP-003 (Bang, Lee et al., 2018) is a mixture of EGF and hydroxyethylcellulose. Considering the Hydroxyethylcellulose with good adhesion and hygroscopicity properties (Lee, Park et al., 2000) could change powder into the adhesive hydrogel, which is beneficial to seal the bleeding site by forming a stable mechanical barrier, it has the potential for the treatment of UGIB (upper gastrointestinal bleeding) and oozing lesions resulted from endoscopic resection. Moreover, a novel matrix hemostatic hydrogel (Hong, Zhou et al., 2019) prepared consisted of methacrylated gelatin (GelMA) and *N*-(2-aminoethyl)-4-(4-(hydroxym ethyl)-2- meth oxy-5-nitrosophenoxy) butanamide (NB) linked to the glycosam inoglycan hyaluronic acid (HA-NB), whose

composition is similar to the extracellular matrix (ECM). It not only has the advantage of high absorption of gelatin, but also makes full use of the advantages of HA-NB polymer matrices that has excellent tissue fusion and integration, which help the hydrogel rapid gelling and bond with the tissue surface through UV light irradiation (Yang, Zhang et al., 2016) to seal bleeding sites in arteries and cardiac walls.

Discussion

Traumas and excessive bleeding are major potential factors for coagulopathy, including persistent hypothermia, metabolic acidosis, and inability to form clots and initiate clotting mechanisms. In this case, the assistance of external force is required to effectively stop bleeding in a short amount of time, so as not to cause other side effects or even life-threatening situations. For this reason, researchers have been studying new hemostatic biomaterials and products to further improve their hemostatic properties in order to meet the hemostatic needs of patients with different bleeding wounds.

In recent years, a variety of hemostatic biological materials and products have been developed, mainly divided into natural biological materials and synthetic biological materials. Some of these biomaterials have only absorptive and passive interactions, while others with active biological interactions promote hemostatic mechanisms. Absorptive and passively interactive biomaterials do not contain any specific components that enhance hemostasis or protect organisms from bacterial infection, but merely serve the purpose of hemostasis by covering wounds and absorbing blood and exudates. For example, oxidized regenerated cellulose (ORC) gauze and starch-based microspheres could seal the wound by absorbing the fluid from the blood to concentrate the effective components (Cheng, He et al., 2016). In this process, the biomaterials improved the hemostasis by promoting the formation of the fibrin clot, which has nothing to do with the clotting cascade. On the other hand, bioactive materials and dressings are systems that adhere to bleeding tissue, primarily through themselves or embedded components to promote hemostasis and prevent infection. It was reported that the negatively charged surface of alginate can induce coagulation initiating *via* the auto-activation of coagulation factor XII (Sperling, Fischer et al., 2009), while the positively charged surface on the chitosan can adhere to platelets *via* charge interaction.

Although all commercial hemostatic products conform to the basic criteria for hemostatic biomaterials, their different hemostatic mechanisms affect the choice and application of hemostatic biomaterials in bleeding patients. In particular, the hemostatic biomaterials that are dependent on the presence of platelet, cannot be applied to bleeding patients with platelet deficiency or dysfunction. In comparison, other hemostatic biomaterials that can activate certain coagulation cascade components independent of platelet presence, are used to stop bleeding in those patients. In addition, different bleeding sites in the body have different requirements for the manner of hemostasis and the form of hemostatic biomaterials. The most common bleeding sites can be divided into compressible hemostasis and non-compressible hemostasis. For it, one of the common methods is to prepare hemostatic biomaterials in different forms, such as spray, powder, solution, hydrogel, etc., making them widely used in hemostasis. When using a hemostatic biomaterial to stop bleeding, the limitations in application should be taken into consideration to avoid side effects. For example, some hemostatic

biomaterials cannot be injected intravenously in case they cause vascular embolization.

In addition, hemostatic biomaterials also have a series of problems such as biosafety, hemostatic effect and high cost, which limit their wide application. To prepare hemostatic biomaterials that can meet the needs of patients with hemorrhage, it is necessary to modify the properties of the materials. For example, polysaccharide is natural molecule with advantages such as abundant sources, diversity of size and charge, no immune responses, as well as biodegradability (Swierczewska, Han et al., 2016). Particularly, polysaccharide-based biomaterials that can be easily prepared and modified by chemical or physical methods (Basu, Kunduru et al., 2015). On this basis, the biomaterial can be modified to overcome its original shortcomings and obtain new properties. At present, the commonly used technologies for improving biomaterials include crosslinking technology and gene recombination technology. For instance, the poor mechanical properties of collagen and gelatin can be improved by the cross-linking technology to adapt to hemodynamics and adhere to the tissues. It is vital important to choose a biocompatible, non-toxic cross-linking agent to cross-link the biomaterials in case of inflammation or side effects. On the other hand, the human-like collagen developed through genetic engineering technology not only overcame the disadvantages of the potential risk of the pathogen, and the instabilities between batches, but also possessed good hemostatic performance and the advantages of low cost and large-scale production.

Finally, it is difficult for a single biomaterial to meet all hemostatic requirements in the clinic and the development of hemostatic biomaterials. Because of these difficulties, two main strategies occur. One is to combine two or more hemostatic biomaterials to simultaneously obtain the multifunctional biomaterials. The other is to develop new hemostatic polypeptides or proteins with good biocompatibility and hemostatic effect through gene recombinant technology. It is worth mentioning that self-assembling peptides and their derivatives have attracted more and more attention in the field of hemostasis under their unique advantages. The design and development of self-assembling hemostatic peptides mainly include four aspects: 1) design a peptide matrix scaffold that helps red blood cells aggregation, blood coagulation, and has stronger viscous and compressive capacity. 2) Screen out novel peptides with specific self-assembly properties and hemostasis by the combinatorial chemical library and combined peptide library. 3) Fabricate a multifunctional hemostatic material capable of promoting blood coagulation, cell proliferation, and tissue regeneration by integrating the biological activity sequences such as coagulant procoagulant motifs, cell adhesion motifs and protein-protein interaction motifs into peptides. 4) Blend the synthetic peptides and other hemostatic agents including internal hemostatic drugs, topical hemostatic agents, etc., making them have higher tensile strength, hardness and hemostatic effect. The last but not least, some researchers have focused on developing a hemostatic sealant that has similar components to ECM, and are directed at finding an optimum system that mimics, enhances and even amplifies the clotting mechanism.

Author contributions

YG: Investigation, data curation, writing-original draft. NC and JH: Data curation, HS: Writing-original draft, YZ, DW, and WZ: Data curation, ZC: Supervision, funding acquisition, writing-review and editing.

Acknowledgments

Conflict of interest

The authors declare that the research was conducted in the absence of any commercial or financial relationships that could be construed as a potential conflict of interest.

Publisher's note

All claims expressed in this article are solely those of the authors and do not necessarily represent those of their affiliated organizations, or those of the publisher, the editors and the reviewers. Any product that may be evaluated in this article, or claim that may be made by its manufacturer, is not guaranteed or endorsed by the publisher.

References

Achneck, H. E., Sileshi, B., Jamiolkowski, R. M., Albala, D. M., Shapiro, M. L., and Lawson, J. H. (2010). A comprehensive review of topical hemostatic agents: Efficacy and recommendations for use. *Ann. Surg.* 251 (2), 217–228. doi:10.1097/SLA.0b013e3181c3bcca

Aydin, O., Tuncal, S., Kilicoglu, B., Onalan, A. K., Gonultas, M. A., Ozer, H., et al. (2015). Effects of Ankaferd Blood Stopper and calcium alginate in experimental model of hepatic parenchymal bleeding. *Bratisl. Lek. Listy* 116 (2), 128–131. doi:10.4149/bll_2015_025

Bang, B. W., Lee, D. H., Kim, H. K., Kwon, K. S., Shin, Y. W., Hong, S. J., et al. (2018). CEGP-003 spray has a similar hemostatic effect to epinephrine injection in cases of acute upper gastrointestinal bleeding. *Dig. Dis. Sci.* 63 (11), 3026–3032. doi:10.1007/s10620-018-5208-z

Bano, I., Arshad, M., Yasin, T., Ghauri, M. A., and Younus, M. (2017). Chitosan: A potential biopolymer for wound management. *Int. J. Biol. Macromol.* 102, 380–383. doi:10.1016/j.ijbiomac.2017.04.047

Basu, A., Kunduru, K. R., Abtew, E., and Domb, A. J. (2015). Polysaccharide-based conjugates for biomedical applications. *Bioconjug Chem.* 26 (8), 1396–1412. doi:10.1021/acs.bioconjchem.5b00242

Behrens, A. M., Sikorski, M. J., and Kofinas, P. (2014). Hemostatic strategies for traumatic and surgical bleeding. *J. Biomed. Mater. Res. Part A* 102 (11), 4182–4194. doi:10.1002/jbm.a.35052

Berrettini, M., Mariani, G., Schiavoni, M., Rocino, A., Di Paolantonio, T., Longo, G., et al. (2001). Pharmacokinetic evaluation of recombinant, activated factor VII in patients with inherited factor VII deficiency. *Haematologica* 86 (6), 640–645.

Bhatia, S. K. (2010). *Traumatic InjuriesChapter 10Traumatic injuries*. New York, NY, USA: Biomaterials for Clinical ApplicationsSpringer, 213–258.

Blajchman, M. A. (2003). Substitutes and alternatives to platelet transfusions in thrombocytopenic patients. *J. Thromb. Haemost.* 1 (7), 1637–1641. doi:10.1046/j.1538-7836.2003.00332.x

Chada, D., Mather, T., and Nollert, M. U. (2006). The synergy site of fibronectin is required for strong interaction with the platelet integrin αIIbβ3. *Ann. Biomed. Eng.* 34 (10), 1542–1552. doi:10.1007/s10439-006-9161-1

Chan, L. W., Kim, C. H., Wang, X., Pun, S. H., White, N. J., and Kim, T. H. (2016). PolySTAT-modified chitosan gauzes for improved hemostasis in external hemorrhage. *Acta Biomater.* 31, 178–185. doi:10.1016/j.actbio.2015.11.017

Chandler, M. H., Roberts, M., Sawyer, M., and Myers, G. (2012). The US military experience with fresh whole blood during the conflicts in Iraq and Afghanistan. *Semin. Cardiothorac. Vasc. Anesth.* 16 (3), 153–159. doi:10.1177/1089253212452344

Chen, C., Zhang, Y., Fei, R., Cao, C., Wang, M., Wang, J., et al. (2016). Hydrogelation of the short self-assembling peptide I3QGK regulated by transglutaminase and use for rapid hemostasis. *ACS Appl. Mater Interfaces* 8 (28), 17833–17841. doi:10.1021/acsami.6b04939

Chen, Q., Liu, Y., Wang, T., Wu, J., Zhai, X., Li, Y., et al. (2017). Chitosan–PVA monodisperse millimeter-sized spheres prepared by electrospraying reduce the thromboembolic risk in hemorrhage control. *J. Mater. Chem. B* 5 (20), 3686–3696. doi:10.1039/C7TB00032D

Cheng, T. Y., Wu, H. C., Huang, M. Y., Chang, W. H., Lee, C. H., and Wang, T. W. (2013). Self-assembling functionalized nanopeptides for immediate hemostasis and accelerative liver tissue regeneration. *Nanoscale* 5 (7), 2734–2744. doi:10.1039/c3nr33710c

Cheng, W., He, J., Chen, M., Li, D., Li, H., Chen, L., et al. (2016). Preparation, functional characterization and hemostatic mechanism discussion for oxidized microcrystalline cellulose and its composites. *Fibers Polym.* 17 (8), 1277–1286. doi:10.1007/s12221-016-6279-0

Csukas, D., Urbanics, R., Moritz, A., and Ellis-Behnke, R. (2015). AC5 Surgical Hemostat™ as an effective hemostatic agent in an anticoagulated rat liver punch biopsy model. *Nanomedicine Nanotechnol. Biol. Med.* 11 (8), 2025–2031. doi:10.1016/j.nano.2015.01.001

Dai, C., Yuan, Y., Liu, C., Wei, J., Hong, H., Li, X., et al. (2009). Degradable, antibacterial silver exchanged mesoporous silica spheres for hemorrhage control. *Biomaterials* 30 (29), 5364–5375. doi:10.1016/j.biomaterials.2009.06.052

de Azevedo, C. L., Marques, M. M., and Bombana, A. C. (2003). Cytotoxic effects of cyanoacrylates used as retrograde filling materials: An *in vitro* analysis. *Pesqui. Odontol. Bras.* 17 (2), 113–118. doi:10.1590/s1517-74912003000200003

Demetri, G. D. (2000). Pharmacologic treatment options in patients with thrombocytopenia. *Semin. Hematol.* 37 (24), 11–18. doi:10.1016/s0037-1963(00)90048-9

Egeli, T., Sevinç, A. İ., Bora, S., Yakut, M. C., Cevizci, T., Canda, T., et al. (2012). Microporous polysaccharide hemospheres and seroma formation after mastectomy and axillary dissection in rats. *Balkan Med. J.* 29 (2), 179–183. doi:10.5152/balkanmedj.2012.005

Ellis-Behnke, R. G., Liang, Y. X., Tay, D. K., Kau, P. W., Schneider, G. E., Zhang, S., et al. (2006). Nano hemostat solution: Immediate hemostasis at the nanoscale. *Nanomedicine* 2 (4), 207–215. doi:10.1016/j.nano.2006.08.001

Ellis-Behnke, R. G., and Schneider, G. E. (2011). Peptide amphiphiles and porous biodegradable scaffolds for tissue regeneration in the brain and spinal cord. *Methods Mol. Biol.* 726, 259–281. doi:10.1007/978-1-61779-052-2_17

Ersoy, G., Kaynak, M. F., Yilmaz, O., Rodoplu, U., Maltepe, F., and Gokmen, N. (2007). Hemostatic effects of microporous polysaccharide hemosphere in a rat model with severe femoral artery bleeding. *Adv. Ther.* 24 (3), 485–492. doi:10.1007/bf02848770

Etchill, E. W., Myers, S. P., Raval, J. S., Hassoune, A., SenGupta, A., and Neal, M. D. (2017). Platelet transfusion in critical care and surgery: Evidence-based review of contemporary practice and future directions. *Shock* 47 (5), 537–549. doi:10.1097/shk.0000000000000794

Fan, D. D., Luo, Y., Mi, Y., Ma, X. X., and Shang, L. (2005). Characteristics of fed-batch cultures of recombinant *Escherichia coli* containing human-like collagen cDNA at different specific growth rates. *Biotechnol. Lett.* 27 (12), 865–870. doi:10.1007/s10529-005-6720-8

Farooq, F. T., and Wong, R. C. K. (2005). Injection sclerotherapy for the management of esophageal and gastric varices. *Tech. Gastrointest. Endosc.* 7 (1), 8–17. doi:10.1016/j.tgie.2004.10.003

Fontenot, J. D., Rasmussen, J. P., Gavin, M. A., and Rudensky, A. Y. (2005). A function for interleukin 2 in Foxp3-expressing regulatory T cells. *Nat. Immunol.* 6 (11), 1142–1151. doi:10.1038/ni1263

Fouani, M. H., Nikkhah, M., and Mowla, J. (2019). Straightforward and cost-effective production of RADA-16I peptide in *Escherichia coli*. *Iran. J. Biotechnol.* 17 (2), 1–7. doi:10.21859/ijb.2125

Fries, D., and Martini, W. Z. (2010). Role of fibrinogen in trauma-induced coagulopathy. *Br. J. Anaesth.* 105 (2), 116–121. doi:10.1093/bja/aeq161

Gao, X. R., Xu, H. J., Wang, L. F., Liu, C. B., and Yu, F. (2017). Mesenchymal stem cell transplantation carried in SVVYGLR modified self-assembling peptide promoted cardiac repair and angiogenesis after myocardial infarction. *Biochem. Biophys. Res. Commun.* 491 (1), 112–118. doi:10.1016/j.bbrc.2017.07.056

Gorbet, M. B., and Sefton, M. V. (2004). Biomaterial-associated thrombosis: Roles of coagulation factors, complement, platelets and leukocytes. *Biomaterials* 25 (26), 5681–5703. doi:10.1016/j.biomaterials.2004.01.023

Granville-Chapman, J., Jacobs, N., and Midwinter, M. J. (2011). Pre-hospital haemostatic dressings: A systematic review. *Injury* 42 (5), 447–459. doi:10.1016/j.injury.2010.09.037

Gu, B. K., Park, S. J., Kim, M. S., Lee, Y. J., Kim, J. I., and Kim, C. H. (2016). Gelatin blending and sonication of chitosan nanofiber mats produce synergistic effects on hemostatic functions. *Int. J. Biol. Macromol.* 82, 89–96. doi:10.1016/j.ijbiomac.2015.10.009

Guo, H. D., Wang, H. J., Tan, Y. Z., and Wu, J. H. (2011). Transplantation of marrow-derived cardiac stem cells carried in fibrin improves cardiac function after myocardial infarction. *Tissue Eng. Part A* 17 (1-2), 45–58. doi:10.1089/ten.TEA.2010.0124

Guzzo, T. J., Pollock, R. A., Forney, A., Aggarwal, P., Matlaga, B. R., and Allaf, M. E. (2009). Safety and efficacy of a surgeon-prepared gelatin hemostatic agent compared with FloSeal for hemostasis in laparoscopic partial nephrectomy. *J. Endourol.* 23 (2), 279–282. doi:10.1089/end.2008.0535

Harris, J. M. (1992). Introduction to biotechnical and biomedical applications of poly(ethylene glycol), *Chem. Topics in Applied Chemistry.*, 8 1–14. doi:10.1007/978-1-4899-0703-5_1

Harrison, I. P., and Spada, F. (2018). Hydrogels for atopic dermatitis and wound management: A superior drug delivery vehicle. *Pharmaceutics* 10 (2), 71. doi:10.3390/pharmaceutics10020071

Henderson, P. W., Kadouch, D. J., Singh, S. P., Zawaneh, P. N., Weiser, J., Yazdi, S., et al. (2010). A rapidly resorbable hemostatic biomaterial based on dihydroxyacetone. *J. Biomed. Mater Res. A* 93 (2), 776–782. doi:10.1002/jbm.a.32586

Hickman, D. A., Pawlowski, C. L., Sekhon, U. D. S., Marks, J., and Gupta, A. S. (2018). Biomaterials and advanced technologies for hemostatic management of bleeding. *Adv. Mater* 30 (4), 1700859. doi:10.1002/adma.201700859

Hong, Y., Zhou, F., Hua, Y., Zhang, X., Ni, C., Pan, D., et al. (2019). A strongly adhesive hemostatic hydrogel for the repair of arterial and heart bleeds. *Nat. Commun.* 10 (1), 2060. doi:10.1038/s41467-019-10004-7

Hu, Y., Yu, X., Dan, W., Yin, T., You, J., and Xiong, S. (2017). Preparation, characterization and biomedical applications of collagen based hydrogels. *J. Funct. Mater.*5 9733–9743. doi:10.1021/acsomega.9b04080

Huang, X., Sun, Y., Nie, J., Lu, W., Yang, L., Zhang, Z., et al. (2015). Using absorbable chitosan hemostatic sponges as a promising surgical dressing. *Int. J. Biol. Macromol.* 75, 322–329. doi:10.1016/j.ijbiomac.2015.01.049

Humphreys, M. R., Castle, E. P., Andrews, P. E., Gettman, M. T., and Ereth, M. H. (2008). Microporous polysaccharide hemospheres for management of laparoscopic trocar injury to the spleen. *Am. J. Surg.* 195 (1), 99–103. doi:10.1016/j.amjsurg.2007.03.006

Huri, E., Dogantekin, E., Hayran, M., Malkan, U. Y., Ergun, M., Firat, A., et al. (2016). Ultrastructural analyses of the novel chimeric hemostatic agent generated via nanotechnology, ABS nanohemostat, at the renal tissue level. *Springerplus* 5 (1), 1931. doi:10.1186/s40064-016-3625-z

Jiang, X., Wang, Y., Fan, D., Zhu, C., Liu, L., and Duan, Z. (2017). A novel human-like collagen hemostatic sponge with uniform morphology, good biodegradability and biocompatibility. *J. Biomater. Appl.* 31 (8), 1099–1107. doi:10.1177/0885328216687663

Kaufman, R. M., Djulbegovic, B., Gernsheimer, T., Kleinman, S., Tinmouth, A. T., Capocelli, K. E., et al. (2015). Platelet transfusion: A clinical practice guideline from the AABB. *Ann. Intern Med.* 162 (3), 205–213. doi:10.7326/m14-1589

Kauvar, D. S., Holcomb, J. B., Norris, G. C., and Hess, J. R. (2006). Fresh whole blood transfusion: A controversial military practice. *J. Trauma* 61 (1), 181–184. doi:10.1097/01.ta.0000222671.84335.64

Kheirabadi, B. (2011). Evaluation of topical hemostatic agents for combat wound treatment. *US Army Med Dep J* 2, 25–37.

Komatsu, S., Nagai, Y., Naruse, K., and Kimata, Y. (2014). The neutral self-assembling peptide hydrogel SPG-178 as a topical hemostatic agent. *PLoS One* 9 (7), e102778. doi:10.1371/journal.pone.0102778

Kommu, S. S., McArthur, R., Emara, A. M., Reddy, U. D., Anderson, C. J., Barber, N. J., et al. (2015). Current status of hemostatic agents and sealants in urologic surgical practice. *Rev. urology* 17 (3), 150–159. doi:10.3909/riu0673

Kondo, Y., Nagasaka, T., Kobayashi, S., Kobayashi, N., and Fujiwara, T. (2014). Management of peritoneal effusion by sealing with a self-assembling nanofiber polypeptide following pelvic surgery. *Hepatogastroenterology* 61 (130), 349–353. doi:10.5754/hge121000

Kumar, V. A., Taylor, N. L., Jalan, A. A., Hwang, L. K., Wang, B. K., and Hartgerink, J. D. (2014). A nanostructured synthetic collagen mimic for hemostasis. *Biomacromolecules* 15 (4), 1484–1490. doi:10.1021/bm500091e

Kumar, V. A., Wickremasinghe, N. C., Shi, S., and Hartgerink, J. D. (2015). Nanofibrous snake venom hemostat. *ACS Biomater. Sci. Eng.* 1 (12), 1300–1305. doi:10.1021/acsbiomaterials.5b00356

Lan, G., Lu, B., Wang, T., Wang, L., Chen, J., Yu, K., et al. (2015). Chitosan/gelatin composite sponge is an absorbable surgical hemostatic agent. *Colloids Surfaces B Biointerfaces* 136, 1026–1034. doi:10.1016/j.colsurfb.2015.10.039

Laurenti, J. B., Zazeri, G., Povinelli, A. P. R., de Godoy, M. F., Braile, D. M., da Rocha, T. ó. R. F., et al. (2017). Enhanced pro-coagulant hemostatic agents based on nanometric zeolites. *Microporous Mesoporous Mater.* 239, 263–271. doi:10.1016/j.micromeso.2016.10.020

Lee, J. W., Park, J. H., and Robinson, J. R. (2000), 89. 2: CO, 850–866. doi:10.1002/1520-6017(200007)89:7<850:AID-JPS2>3.0Bioadhesive-based dosage forms: The next generation, *J. Pharm. Sci.*

Levy, J. H., and Goodnough, L. T. (2015). How I use fibrinogen replacement therapy in acquired bleeding. *Blood* 125 (9), 1387–1393. doi:10.1182/blood-2014-08-552000

Lewis, K. M., Kuntze, C. E., and Gulle, H. (2015). Control of bleeding in surgical procedures: Critical appraisal of HEMOPATCH (sealing hemostat). *N.Z.)* 9, 1–10. doi:10.2147/MDER.S90591

Li, G., Quan, K., Liang, Y., Li, T., Yuan, Q., Tao, L., et al. (2016). Graphene-montmorillonite composite sponge for safe and effective hemostasis. *ACS Appl. Mater Interfaces* 8 (51), 35071–35080. doi:10.1021/acsami.6b13302

Li, J., Cao, W., Lv, X. X., Jiang, L., Li, Y. J., Li, W. Z., et al. (2013). Zeolite-based hemostat QuikClot releases calcium into blood and promotes blood coagulation *in vitro*. *Acta Pharmacol. Sin.* 34 (3), 367–372. doi:10.1038/aps.2012.159

Liang, Y., Xu, C., Li, G., Liu, T., Liang, J. F., and Wang, X. (2018). Graphene-kaolin composite sponge for rapid and riskless hemostasis. *Colloids Surf. B Biointerfaces* 169, 168–175. doi:10.1016/j.colsurfb.2018.05.016

Lumsden, A. B., and Heyman, E. R. (2006). Prospective randomized study evaluating an absorbable cyanoacrylate for use in vascular reconstructions. *J. Vasc. Surg.* 44 (5), 1002–1009.e1. doi:10.1016/j.jvs.2006.06.039

Luo, Z., Wang, S., and Zhang, S. (2011). Fabrication of self-assembling D-form peptide nanofiber scaffold d-EAK16 for rapid hemostasis. *Biomaterials* 32 (8), 2013–2020. doi:10.1016/j.biomaterials.2010.11.049

Masci, E., Faillace, G., and Longoni, M. (2018). Use of oxidized regenerated cellulose to achieve hemostasis during laparoscopic cholecystectomy: A retrospective cohort analysis. *BMC Res. Notes* 11 (1), 239. doi:10.1186/s13104-018-3344-3

Masuhara, H., Fujii, T., Watanabe, Y., Koyama, N., and Tokuhiro, K. (2012). Novel infectious agent-free hemostatic material (TDM-621) in cardiovascular surgery. *Ann. Thorac. Cardiovasc Surg.* 18 (5), 444–451. doi:10.5761/atcs.oa.12.01977

Mi, F. L., Shyu, S. S., Wu, Y. B., Lee, S. T., Shyong, J. Y., and Huang, R. N. (2001). Fabrication and characterization of a sponge-like asymmetric chitosan membrane as a wound dressing. *Biomaterials* 22 (2), 165–173. doi:10.1016/s0142-9612(00)00167-8

Mie, M., Oomuro, M., and Kobatake, E. (2013). Hydrogel scaffolds composed of genetically synthesized self-assembling peptides for three-dimensional cell culture. *Polym. J.* 45 (5), 504–508. doi:10.1038/pj.2012.216

Montanaro, L., Arciola, C. R., Cenni, E., Ciapetti, G., Savioli, F., Filippini, F., et al. (2000). Cytotoxicity, blood compatibility and antimicrobial activity of two cyanoacrylate glues for surgical use. *Biomaterials* 22 (1), 59–66. doi:10.1016/S0142-9612(00)00163-0

Motlagh, D., Yang, J., Lui, K. Y., Webb, A. R., and Ameer, G. A. (2006). Hemocompatibility evaluation of poly(glycerol-sebacate) *in vitro* for vascular tissue engineering. *Biomaterials* 27 (24), 4315–4324. doi:10.1016/j.biomaterials.2006.04.010

Muzzarelli, R. A. A., Morganti, P., Morganti, G., Palombo, P., Palombo, M., Biagini, G., et al. (2007). Chitin nanofibrils/chitosan glycolate composites as wound medicaments. *Carbohydr. Polym.* 70 (3), 274–284. doi:10.1016/j.carbpol.2007.04.008

Nagamatsu, M., Podratz, J., Windebank, A. J., and Low, P. A. (1997). Acidity is involved in the development of neuropathy caused by oxidized cellulose. *J. Neurol. Sci.* 146 (2), 97–102. doi:10.1016/s0022-510x(96)00295-x

Nomizu, M., Kim, W. H., Yamamura, K., Utani, A., Song, S. Y., Otaka, A., et al. (1995). Identification of cell binding sites in the laminin alpha 1 chain carboxyl-terminal globular domain by systematic screening of synthetic peptides. *J. Biol. Chem.* 270 (35), 20583–20590. doi:10.1074/jbc.270.35.20583

Ono, K., Ishihara, M., Ozeki, Y., Deguchi, H., Sato, M., Saito, Y., et al. (2001). Experimental evaluation of photocrosslinkable chitosan as a biologic adhesive with surgical applications. *Surgery* 130 (5), 844–850. doi:10.1067/msy.2001.117197

Ostomel, T. A., Shi, Q., Tsung, C. K., Liang, H., and Stucky, G. D. (2006). Spherical bioactive glass with enhanced rates of hydroxyapatite deposition and hemostatic activity. *Small* 2 (11), 1261–1265. doi:10.1002/smll.200600177

Overby, R. J., and Feldman, D. S. (2018). Influence of poly(ethylene glycol) end groups on poly(ethylene glycol)-albumin system properties as a potential degradable tissue scaffold. *J. Funct. Biomater.* 10 (1), 1. doi:10.3390/jfb10010001

Oz, M. C., Rondinone, J. F., and Shargill, N. S. (2003). FloSeal matrix: New generation topical hemostatic sealant. *J. Card. Surg.* 18 (6), 486–493. doi:10.1046/j.0886-0440.2003.00302.x

Pan, H., Fan, D., Cao, W., Zhu, C., Duan, Z., Fu, R., et al. (2017). Preparation and characterization of breathable hemostatic hydrogel dressings and determination of their effects on full-thickness defects. *Polymers* 9 (12), 727. doi:10.3390/polym9120727

Pereira, B. M., Bortoto, J. B., and Fraga, G. P. (2018)., 45. *Rev. do Colégio Bras. Cir.*Agentes hemostáticos tópicos em cirurgia: Revisão e perspectivas,doi:10.1590/0100-6991e-20181900

Pillai, C. K. S., Paul, W., and Sharma, C. P. (2009). Chitin and chitosan polymers: Chemistry, solubility and fiber formation. *Prog. Polym. Sci.* 34 (7), 641–678. doi:10.1016/j.progpolymsci.2009.04.001

Piozzi, G. N., Reitano, E., Panizzo, V., Rubino, B., Bona, D., Tringali, D., et al. (2018). Practical suggestions for prevention of complications arising from oxidized cellulose retention: A case report and review of the literature. *Am. J. Case Rep.* 19, 812–819. doi:10.12659/ajcr.910060

Pourshahrestani, S., Zeimaran, E., Djordjevic, I., Kadri, N. A., and Towler, M. R. (2016). Inorganic hemostats: The state-of-the-art and recent advances. *Mater Sci. Eng. C Mater Biol. Appl.* 58, 1255–1268. doi:10.1016/j.msec.2015.09.008

Pourshahrestani, S., Zeimaran, E., Kadri, N. A., Gargiulo, N., Jindal, H. M., Naveen, S. V., et al. (2017). Potency and cytotoxicity of a novel gallium-containing mesoporous bioactive glass/chitosan composite scaffold as hemostatic agents. *ACS Appl. Mater Interfaces* 9 (37), 31381–31392. doi:10.1021/acsami.7b07769

Pusateri, A. E., McCarthy, S. J., Gregory, K. W., Harris, R. A., Cardenas, L., McManus, A. T., et al. (2003). Effect of a chitosan-based hemostatic dressing on blood loss and survival in a model of severe venous hemorrhage and hepatic injury in swine. *J. Trauma* 54 (1), 177–182. doi:10.1097/00005373-200301000-00023

Rad-Malekshahi, M., Lempsink, L., Amidi, M., Hennink, W. E., and Mastrobattista, E. (2016). Biomedical applications of self-assembling peptides. *Bioconjug Chem.* 27 (1), 3–18. doi:10.1021/acs.bioconjchem.5b00487

Rahe-Meyer, N., and Sorensen, B. (2011). For: Fibrinogen concentrate for management of bleeding. *J. Thromb. Haemost.* 9 (1), 1–5. doi:10.1111/j.1538-7836.2010.04099.x

Reuthebuch, O., Lachat, M. L., Vogt, P., Schurr, U., and Turina, M. (2000). FloSeal®: Ein neuartiges Hämostyptikum in der peripheren Gefäßchirurgie. *Vasa* 29 (3), 204–206. doi:10.1024/0301-1526.29.3.204

Roberts, H. R. (2001). Recombinant factor VIIa (Novoseven) and the safety of treatment. *Semin. Hematol.* 38 (412), 48–50. doi:10.1016/s0037-1963(01)90148-9

Ruan, L., Zhang, H., Luo, H., Liu, J., Tang, F., Shi, Y. K., et al. (2009). Designed amphiphilic peptide forms stable nanoweb, slowly releases encapsulated hydrophobic drug, and accelerates animal hemostasis. *Proc. Natl. Acad. Sci. U. S. A.* 106 (13), 5105–5110. doi:10.1073/pnas.0900026106

Salinas, A. J., Shruti, S., Malavasi, G., Menabue, L., and Vallet-Regí, M. (2011). Substitutions of cerium, gallium and zinc in ordered mesoporous bioactive glasses. *Acta Biomater.* 7 (9), 3452–3458. doi:10.1016/j.actbio.2011.05.033

Seon, G. M., Lee, M. H., Kwon, B.-J., Kim, M. S., Koo, M.-A., Seomun, Y., et al. (2018). Recombinant batroxobin-coated nonwoven chitosan as hemostatic dressing for initial hemorrhage control. *Int. J. Biol. Macromol.* 113, 757–763. doi:10.1016/j.ijbiomac.2018.03.017

Seyednejad, H., Imani, M., Jamieson, T., and Seifalian, A. M. (2008). Topical haemostatic agents. *Br. J. Surg.* 95 (10), 1197–1225. doi:10.1002/bjs.6357

Shahverdi, S., Hajimiri, M., Esfandiari, M. A., Larijani, B., Atyabi, F., Rajabiani, A., et al. (2014). Fabrication and structure analysis of poly(lactide-co-glycolic acid)/silk fibroin hybrid scaffold for wound dressing applications. *Int. J. Pharm.* 473 (1), 345–355. doi:10.1016/j.ijpharm.2014.07.021

Shruti, S., Salinas, A. J., Ferrari, E., Malavasi, G., Lusvardi, G., Doadrio, A. L., et al. (2013). Curcumin release from cerium, gallium and zinc containing mesoporous bioactive glasses. *Microporous Mesoporous Mater.* 180, 92–101. doi:10.1016/j.micromeso.2013.06.014

Shruti, S., Salinas, A. J., Lusvardi, G., Malavasi, G., Menabue, L., and Vallet-Regi, M. (2013). Mesoporous bioactive scaffolds prepared with cerium-gallium- and zinc-containing glasses. *Acta Biomater.* 9 (1), 4836–4844. doi:10.1016/j.actbio.2012.09.024

Skopinska-Wisniewska, J., Sionkowska, A., Kaminska, A., Kaznica, A., Jachimiak, R., and Drewa, T. (2009). Surface characterization of collagen/elastin based biomaterials for tissue regeneration. *Appl. Surf. Sci.* 255 (19), 8286–8292. doi:10.1016/j.apsusc.2009.05.127

Sperling, C., Fischer, M., Maitz, M. F., and Werner, C. (2009). Blood coagulation on biomaterials requires the combination of distinct activation processes. *Biomaterials* 30 (27), 4447–4456. doi:10.1016/j.biomaterials.2009.05.044

Spinella, P. C., Perkins, J. G., Grathwohl, K. W., Repine, T., Beekley, A. C., Sebesta, J., et al. (2007). Risks associated with fresh whole blood and red blood cell transfusions in a combat support hospital. *Crit. Care Med.* 35 (11), 2576–2581. doi:10.1097/01.Ccm.0000285996.65226.A9

Spitalnik, S. L., Triulzi, D., Devine, D. V., Dzik, W. H., Eder, A. F., Gernsheimer, T., et al. (2015). 2015 proceedings of the national heart, lung, and blood institute's state of the science in transfusion medicine symposium. *Transfusion* 55 (9), 2282–2290. doi:10.1111/trf.13250

Sun, X., Tang, Z., Pan, M., Wang, Z., Yang, H., and Liu, H. (2017). Chitosan/kaolin composite porous microspheres with high hemostatic efficacy. *Carbohydr. Polym.* 177, 135–143. doi:10.1016/j.carbpol.2017.08.131

Swierczewska, M., Han, H. S., Kim, K., Park, J. H., and Lee, S. (2016). Polysaccharide-based nanoparticles for theranostic nanomedicine. *Adv. Drug Deliv. Rev.* 99 (Pt A), 70–84. doi:10.1016/j.addr.2015.11.015

Tam, T., Harkins, G., Dykes, T., Gockley, A., and Davies, M. (2014). Oxidized regenerated cellulose resembling vaginal cuff abscess. *Jsls* 18 (2), 353–356. doi:10.4293/108680813x13693422518597

Thongrong, C., Kasemsiri, P., Carrau, R. L., and Bergese, S. D. (2013). Control of bleeding in endoscopic skull base surgery: Current concepts to improve hemostasis. *ISRN Surg.* 2013, 1–11. doi:10.1155/2013/191543

Valeri, C. R. (2006). Letters to the editor. *J. Trauma* 61 (1), 240–241. doi:10.1097/01.ta.0000224109.60301.a8

Verissimo, D. M., Leitao, R. F., Ribeiro, R. A., Figueiro, S. D., Sombra, A. S., Goes, J. C., et al. (2010). Polyanionic collagen membranes for guided tissue regeneration: Effect of progressive glutaraldehyde cross-linking on biocompatibility and degradation. *Acta Biomater.* 6 (10), 4011–4018. doi:10.1016/j.actbio.2010.04.012

Wang, R., Wang, Z., Guo, Y., Li, H., and Chen, Z. (2019). Design of a RADA16-based self-assembling peptide nanofiber scaffold for biomedical applications. *J. Biomater. Sci. Polym. Ed.* 30 (9), 713–736. doi:10.1080/09205063.2019.1605868

Wang, T., Zhong, X., Wang, S., Lv, F., and Zhao, X. (2012). Molecular mechanisms of RADA16-1 peptide on fast stop bleeding in rat models. *Int. J. Mol. Sci.* 13 (11), 15279–15290. doi:10.3390/ijms131115279

Watrowski, R., Jager, C., and Forster, J. (2017). Improvement of perioperative outcomes in major gynecological and gynecologic-oncological surgery with hemostatic gelatin-thrombin matrix. *Vivo* 31 (2), 251–258. doi:10.21873/invivo.11053

Xie, Y., Yi, Z. X., Wang, J. X., Hou, T. G., and Jiang, Q. (2018). Carboxymethyl konjac glucomannan - crosslinked chitosan sponges for wound dressing. *Int. J. Biol. Macromol.* 112, 1225–1233. doi:10.1016/j.ijbiomac.2018.02.075

Yamawaki, I., Taguchi, Y., Komasa, S., Tanaka, A., and Umeda, M. (2017). Effects of glucose concentration on osteogenic differentiation of type II diabetes mellitus rat bone marrow-derived mesenchymal stromal cells on a nano-scale modified titanium. *J. Periodontal Res.* 52 (4), 761–771. doi:10.1111/jre.12446

Yan, T., Cheng, F., Wei, X., Huang, Y., and He, J. (2017). Biodegradable collagen sponge reinforced with chitosan/calcium pyrophosphate nanoflowers for rapid hemostasis. *Carbohydr. Polym.* 170, 271–280. doi:10.1016/j.carbpol.2017.04.080

Yang, S., Wei, S., Mao, Y., Zheng, H., Feng, J., Cui, J., et al. (2018). Novel hemostatic biomolecules based on elastin-like polypeptides and the self-assembling peptide RADA-16. *BMC Biotechnol.* 18 (1), 12. doi:10.1186/s12896-018-0422-5

Yang, X., Liu, W., Li, N., Wang, M., Liang, B., Ullah, I., et al. (2017). Design and development of polysaccharide hemostatic materials and their hemostatic mechanism. *Biomaterials Sci.* 5 (12), 2357–2368. doi:10.1039/C7BM00554G

Yang, Y., Zhang, J., Liu, Z., Lin, Q., Liu, X., Bao, C., et al. (2016). Tissue-integratable and biocompatible photogelation by the imine crosslinking reaction. *Adv. Mater* 28 (14), 2724–2730. doi:10.1002/adma.201505336

Yu, L., Shang, X., Chen, H., Xiao, L., Zhu, Y., and Fan, J. (2019). A tightly-bonded and flexible mesoporous zeolite-cotton hybrid hemostat. *Nat. Commun.* 10 (1), 1932. doi:10.1038/s41467-019-09849-9

Yuan, H., Chen, L., and Hong, F. F. (2020). A biodegradable antibacterial nanocomposite based on oxidized bacterial nanocellulose for rapid hemostasis and wound healing. *ACS Appl. Mater. Interfaces* 12 (3), 3382–3392. doi:10.1021/acsami.9b17732

Check for updates

Comparative analysis of the cardiomyocyte differentiation potential of induced pluripotent stem cells reprogrammed from human atrial or ventricular fibroblasts

Lu Wang[1], Thanh Nguyen[1], Manuel Rosa-Garrido[1], Yang Zhou[1], David C. Cleveland[1,2,3] and Jianyi Zhang[1,4]*

[1]Department of Biomedical Engineering, School of Medicine, School of Engineering, University of Alabama at Birmingham, Birmingham, AL, United States , [2]Department of Surgery, University of Alabama at Birmingham, Birmingham, AL, United States, [3]Children's Hospital of Alabama, Birmingham, AL, United States, [4]Department of Medicine, Division of Cardiovascular Disease, School of Medicine, University of Alabama at Birmingham, Birmingham, AL, United States

Background: We had shown that cardiomyocytes (CMs) were more efficiently differentiated from human induced pluripotent stem cells (hiPSCs) when the hiPSCs were reprogrammed from cardiac fibroblasts rather than dermal fibroblasts or blood mononuclear cells. Here, we continued to investigate the relationship between somatic-cell lineage and hiPSC-CM production by comparing the yield and functional properties of CMs differentiated from iPSCs reprogrammed from human atrial or ventricular cardiac fibroblasts (^{A}iPSC or ^{V}iPSC, respectively).

Methods: Atrial and ventricular heart tissues were obtained from the same patient, reprogrammed into ^{A}iPSCs or ^{V}iPSCs, and then differentiated into CMs (^{A}iPSC-CMs or ^{V}iPSC-CMs, respectively) *via* established protocols.

Results: The time-course of expression for pluripotency genes (OCT4, NANOG, and SOX2), the early mesodermal marker Brachyury, the cardiac mesodermal markers MESP1 and Gata4, and the cardiovascular progenitor-cell transcription factor NKX2.5 were broadly similar in ^{A}iPSC-CMs and ^{V}iPSC-CMs during the differentiation protocol. Flow-cytometry analyses of cardiac troponin T expression also indicated that purity of the two differentiated hiPSC-CM populations (^{A}iPSC-CMs: 88.23% $\pm$ 4.69%, ^{V}iPSC-CMs: 90.25% $\pm$ 4.99%) was equivalent. While the field-potential durations were significantly longer in ^{V}iPSC-CMs than in ^{A}iPSC-CMs, measurements of action potential duration, beat period, spike amplitude, conduction velocity, and peak calcium-transient amplitude did not differ significantly between the two hiPSC-CM populations. Yet, our cardiac-origin iPSC-CM showed higher ADP and conduction velocity than previously reported iPSC-CM derived from non-cardiac tissues. Transcriptomic data comparing iPSC and iPSC-CMs showed similar gene expression profiles between ^{A}iPSC-CMs and ^{V}iPSC-CMs with significant differences when compared to iPSC-CM derived from other tissues. This analysis also pointed to several genes involved in electrophysiology processes responsible for the physiological differences observed between cardiac and non-cardiac-derived cardiomyocytes.

Conclusion: [A]iPSC and [V]iPSC were differentiated into CMs with equal efficiency. Detected differences in electrophysiological properties, calcium handling activity, and transcription profiles between cardiac and non-cardiac derived cardiomyocytes demonstrated that 1) tissue of origin matters to generate a better-featured iPSC-CMs, 2) the sublocation within the cardiac tissue has marginal effects on the differentiation process.

Introduction

Despite the ongoing refinement of treatments for managing cardiovascular disease, long-term improvement is limited because adult mammals' hearts cannot regenerate damaged myocardial tissue (Zhang et al., 2018). Whole-heart transplantation surgery remains the only proven option for treating patients who have entered the final stages of heart disease, but the availability of donated hearts is limited (Wang et al., 2021). Thus, researchers continue to develop strategies for repopulating the myocardial scar with exogenously administered cells; cardiomyocytes (CMs)—the fundamental contractile units of the heart—cannot be expanded in culture, so studies with human CMs generally cannot be conducted with cells obtained from primary sources.

The scarcity of CMs for therapeutic applications, as well as mechanistic studies and drug testing, was alleviated by the development of induced pluripotent stem cells (iPSCs), (Takahashi and Yamanaka, 2006), which are reprogrammed from cells of somatic tissues and, like embryonic stem cells (ESCs), can self-replicate indefinitely and be differentiated into cells of any lineage (Park et al., 2008a; Ebert et al., 2009; Soldner et al., 2009; Chen et al., 2018). iPSCs are typically generated *via* overexpression of four pluripotency factors (Oct3/4, Sox2, c-Myc, and klf4) (Takahashi and Yamanaka, 2006) and can be reprogrammed from a wide variety of cell types (Aasen et al., 2008; Aoi et al., 2008; Hanna et al., 2008; Kim et al., 2008; Stadtfeld et al., 2008; Utikal et al., 2009; Polo et al., 2010; Sanchez-Freire et al., 2014). Reprogrammed cells retain some of the epigenetic characteristics associated with their somatic-cell lineage, and this "epigenetic memory" appears to influence both the yield and functional properties of iPSC-derived cells (Kim et al., 2011; Rizzi et al., 2012; Meraviglia et al., 2016). We had shown that CMs were more efficiently differentiated from human iPSCs (hiPSCs) when the hiPSCs were reprogrammed from cardiac fibroblasts ([hCF]iPSCs) rather than dermal fibroblasts ([hDF]iPSCs) or umbilical cord blood mononuclear cells ([hUCB]iPSCs). [hCF]iPSCs -derived CMs also have a more cardiac-like Ca^{2+} handling profile, (Zhang et al., 2015), suggesting that hiPSCs may be more suitable for generating hiPSC-CMs if they are reprogrammed from cardiac, rather than non-cardiac lineage cells. The experiments described in this report continue to interrogate the relationship between the somatic-cell lineage of hiPSCs and hiPSC-CM production by comparing the yield and functional properties of CMs differentiated from hiPSCs reprogrammed from atrial cardiac fibroblasts or ventricular cardiac fibroblasts ([A]iPSC-CM or [V]iPSC-CM, respectively).

Materials and methods

All protocols in this study were approved by the Institutional Review Board (IRB) for Human Use at the University of Alabama, Birmingham.

Isolation and characterization of cardiac fibroblasts

Cardiac ventricular and atrial tissue specimens were obtained with informed consent from a 15-day-old patient with d-TGA (dextro-Transposition of the Great Arteries) severe pulmonary outflow obstruction who underwent open chest surgery; then, cardiac fibroblasts were isolated as described previously (Park et al., 2008b). Briefly, tissue specimens were cut into small pieces, placed in a 6-well plate containing hFib media (DMEM containing 10% FBS, 2 mM L-GIn, 50 U ml^{-1} penicillin and 50 mg mL^{-1} streptomycin), and covered with a cover slip. The culture medium was changed every three days for 2 weeks, and fibroblast outgrowth was observed after 10 days of culture. Fibroblast identification was confirmed *via* immunofluorescence staining for vimentin and TE-7 expression (Gao et al., 2018).

Immunofluorescence staining

Immunofluorescence staining was performed as previously described (Wang and Zhang, 2022). Briefly, cells were fixed in 4% paraformaldehyde (PFA) for 15 min at room temperature, permeabilized with 90% acetone for 3 min, and then blocked with 10% donkey serum for 20 min. The fixed cells were incubated with primary antibodies (Supplementary Table S1) overnight at 4°C and with corresponding fluorescently conjugated secondary antibodies at room temperature for 2 h; then, the cells were mounted with mounting medium containing 4,6-diamidino-2-phenyl- indole (DAPI) (Vector Laboratories; H-1200) and imaged with a confocal microscope.

iPSC reprogramming

iPSC reprogramming was performed with a CytoTune™-iPS 2.0 Sendai Reprogramming Kit as directed by the manufacturer's instructions. Briefly, cells (passage 2) were transduced with CytoTune™-iPS 2.0 Sendai reprogramming vectors and then transferred to feeder cells in fibroblast medium (DMEM

supplemented with 10% FBS, 1% MEM Non-Essential Amino Acids Solution, and 0.1% 2-mercaptoethanol). Putative hiPSC colonies were identified *via* Tra1-60 live staining, transferred into Matrigel-coated wells containing mTeSR medium, and expanded without feeder cells.

iPSC characterization

OCT4, Nanog, SSEA4, and SOX2 expression in reprogrammed iPSCs was evaluated *via* immunofluorescence staining. The absence of residual Sendai virus was confirmed after 10 passages by qRT-PCR with a primer for SeV amplification as previously described; (Grossmann et al., 2021); RNA from passage 0 iPSCs and from somatic fibroblasts served as the positive and negative controls, respectively. The absence of *mycoplasma* was confirmed at passage 12 with a LookOut *Mycoplasma* PCR Detection Kit (Sigma-Aldrich—Merck) as directed by the manufacturer's instructions. The PCR products were loaded on a 1% agarose gel containing SYBR Safe DNA Gel Stain (Invitrogen, S33102) and visualized with a ChemiDoc MP Imaging System (Bio-Rad).

Teratoma formation

The teratoma formation assay was performed as described previously (Nelakanti et al., 2015). Briefly, ~1×10^6 iPSCs were collected with Accutase, suspended in 50 µL Matrigel, and slowly injected into the gastrocnemius muscle of NOD/SCID Gamma mice. Teratomas were monitored and surgically removed 6–8 weeks after injection, fixed with 4% formaldehyde, and embedded in paraffin. The preserved samples were sectioned and stained with hematoxylin and eosin at the Pathology Core Research Laboratory in the Department of Pathology, University of Alabama, Birmingham.

Karyotype analysis

Karyotype analysis was conducted in the Cytogenetics Lab at the WiCell Research Institute (Madison, WI). Metaphases were analyzed for each sample by using a brightfield microscope after G-banding. Chromosome identification and karyotype descriptions were made according to the International System for Human Cytogenetic Nomenclature (McGowan-Jordan, 2016). Short tandem repeat (STR) analysis was performed in the Histocompatibility/Molecular Diagnostics laboratory at the University of Wisconsin Hospital and Clinics (Madison, WI).

Cardiomyocyte differentiation from [A]iPSC and [V]iPSC

[A]iPSC and [V]iPSC were differentiated into cardiomyocytes (CMs) as previously described (Lian et al., 2013). Briefly, [A]iPSC and [V]iPSC were maintained with mTeSR™ Plus (Stem Cell Technologies) cell media in GelTrex-coated (Thermo Fisher Scientific) plate until meeting 80% confluency. Cardiomyocyte differentiation was induced by culturing iPSCs with CHIR99021 for 24 h in RPMI 1640 medium and B27 without insulin (B27-) media. Cells were then

recovered for 48 h in RPMI 1640 medium and B27- media, and cultured with IWR-1 for 48 h in RPMI 1640 medium and B27-media. Beating cardiomyocytes typically appeared nine days after differentiation initiation.

Quantitative real-time polymerase chain reaction (qRT-PCR)

Total RNA was extracted using RNeasy mini kits (Qiagen, United States) as directed by the manufacturer's instructions and quantified *via* Nanodrop. cDNA was synthesized with SuperScriptTM II Reverse Transcriptase (Thermo Scientific, United States), and qRT-PCR was performed on a QuantStudio three real-time PCR system (Eppendorf, United States) with appropriate primers (Supplementary Table S2) and the Power Up SYBR Green PCR Mix (Thermo Fisher Scientific). Measurements were determined *via* the $2^{-\Delta\Delta CT}$ method and normalized to the abundance of glyceraldehyde phosphate dehydrogenase (GAPDH) RNA.

Flow cytometry

Purity of differentiated hiPSC-CMs was determined *via* flow cytometry analysis as previously described (Gao et al., 2020). Briefly, iPSC-CMs were trypsinized into single cells, fixed with fixation and permeabilization solution (51-2090KZ) for 30 min at 4°C, and blocked in Human BD Fc Block (564219) at room temperature for 10 min. Cells were then incubated with primary antibodies and isotype control antibodies at room temperature for 40 min, incubated with corresponding fluorescently conjugated secondary antibodies for 30 min, and resuspended in wash buffer (554723). Flow cytometry was performed with an LSR Fortessa instrument (BD Biosciences, United States).

Multi-electrode array (MEA) analysis

hiPSC-CM action and field potentials were assessed with a MaestroEdge multi-electrode array system as previously described (Wickramasinghe et al., 2022). Briefly, cells were plated on 24-well CytoView MRA plates (Axion BioSystems) coated with GelTrex at a density of 4×10^4 cells per well. One week later, the plates were equilibrated for 10 min, data were recorded using the Axion Integrated Studio (AxIS) software and finally analyzed using the Cardiac Analysis Tool (Axion Biosystems, Atlanta, GA, United States).

Ca²⁺ transient analysis

Ca^{2+} transients were measured as previously described (Gao et al., 2020). Briefly, hiPSC-CMs were plated as individual cells on cover glasses (25×25 mm) coated with Geltrex and incubated with Fura-2 AM (0.5 µM, Invitrogen, United States) for 10 min in Tyrode's solution. Cells were then stimulated at 1 Hz and 2 Hz, and the ratio of fluorescence emitted at 340 and 380 nm was determined with a Ca^{2+} recording system and analyzed using IonWizard (IonOptix, United States) software.

Generating the bulk-RNA sequencing data

[A]iPSC, [V]iPSC, [A]iPSC-CM, and [V]iPSC-CM RNA sequencing was performed by Novogene—Advancing Genomics using Illumina NovaSeq 6,000 platforms. RNA quality control was achieved by removing reads containing adapters, having more than 10% of undetermined bases, and low-quality reads. Less than 2% of these reads were removed in all samples. Reads were mapped to human GRCh38 reference genome (Nurk et al., 2022) using STAR pipeline (Dobin et al., 2013); the unique mapping rate was above 94% in all samples (Supplementary Table S3). Then, for each gene, the count of transcripts for each sample was recorded.

Collecting iPSC-CM bulk-RNA sequencing reported in the literature

The phrase "hiPSC derived cardiomyocyte" was used to search for iPSC-CM sequencing data in Gene Expression Omnibus database (https://www.ncbi.nlm.nih.gov/geo/); this query yields 69 data sources. Publications associated with these data sources were manually read to select data sets that 1) had the same cardiomyocyte differentiation (from iPSC) protocol as ours, without further chemical or genetic modification treatment; 2) iPSC-CMs were harvested 30 days or later after differentiation; 3) reported iPSC-CM electrophysiology; 4) have the iPSC-CM bulk-RNA sequencing data generated by Illumina platforms; and 5) the transcript raw count format (required for DeSeq2 gene expression normalization) was available. Two datasets (Zhao et al., 2017; Garay et al., 2022) were selected to be analyzed with [A]iPSC, [V]iPSC, [A]iPSC-CM, and [V]iPSC-CM RNA sequencing data, which were summarized in Supplementary Table S4. Dataset (Garay et al., 2022) contains iPSC-CM derived from skin tissue after 90 days of differentiation from skin ([S−D90]iPSC-CM) and kidney tissue ([K−D90]iPSC-CM). Dataset (Zhao et al., 2017) contains iPSC derived from the dermal fibroblast (skin) tissue ([S]iPSC) and iPSC-CM after 30 days of differentiation ([S−D30]iPSC-CM).

Bulk-RNA gene expression analysis

The raw transcript counts (35,794 genes) in each sample (24 samples) were normalized by Deseq2 (Love et al., 2014). After normalization, the sample pairwise similarities were calculated using all samples' expression data; then, the samples were clustered by applying hierarchical clustering (clustergram) (Frank, 2016; clustergram, 2022) on these similarities. Also, the normalized expression was embedded and visualized by Uniform Manifold Approximation (UMAP) toolkit (Leland McInnes and James, 2018; Uniform, 2021).

The expression fold-change was calculated for each gene to select differentially expressed genes (DEG) in two-group comparison. Due to low sample size (n = 3), the non-parametric Wilcoxon Ranksum test was implemented and applied as in (Bian et al., 2021) for statistical analysis. Genes with fold-change magnitude of two and above (>2 or < 0.5), average per-sample expression of 100 and above, and p-value < 0.05 were selected as DEGs.

Gene ontology analysis

The list of DEG, computed in bulk-RNA data analysis, was input into The Database for Annotation, Visualization and Integrated Discovery (DAVID) (Huang et al., 2009). DAVID resulted in a list of gene ontologies and signaling pathways enriched by the input DEG. Only, gene ontologies and signaling pathways with a False Discovery Rate of 0.05 and below were retained for statistical significance. The enrichment score was computed as the log-base-10 of the enrichment p-value, which was resulted from DAVID.

Statistical analysis

Data were presented as mean ± SEM. Significance was determined *via* the Student's t-test for comparisons between two groups and *via* one-way analysis of variance for comparisons among three or more groups. A p value of <0.05 was considered statistically significant.

For RNA sequencing data, due to the small sample size, non-parametric Wilcoxon-Ranksum test was applied for comparison between two groups, and non-parametric Kruskal–Wallis test was used for comparison among three or more groups. When a large number of genes were tested in the Deseq2 protocol, the Benjamini and Hochberg method was applied to adjust the p-values (false-positive correction). A p-value of < 0.05 was considered statistically significant.
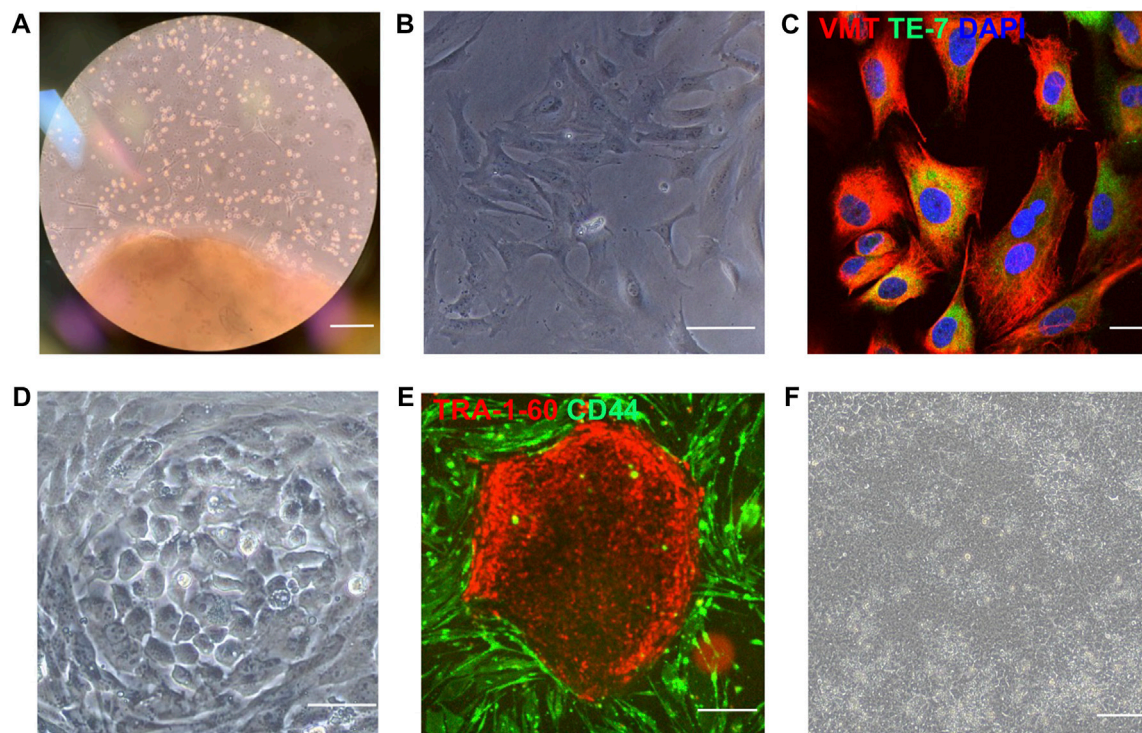
Results

Characterization of iPSCs reprogrammed from human atrial and ventricular fibroblasts

Both atrial and ventricular heart tissues were obtained from the same male newborn infant patient during open-chest surgery for d-TGA and cut into small pieces to induce fibroblast outgrowth (Figure 1A); then, atrial and ventricular fibroblasts were collected, expanded for two weeks (Figure 1B), and stained for the expression of vimentin and TE-7 to confirm fibroblast identity (Figure 1C). Fibroblasts were reprogrammed into [A]iPSC and [V]iPSC *via* transfection with non-integrating Sendai virus vectors coding for expression of the human variants of Oct3/4, Sox2, Klf4, and c-Myc. Two weeks later, colonies with an ESC-like morphology (Figure 1D) expressing the pluripotent/stem-cell marker Tra1-60 (Figure 1E) were mechanically isolated and expanded. The morphologies of the [A]iPSC and [V]iPSC lineages were indistinguishable (Figure 1F). Both [A]iPSC and [V]iPSC expressed the pluripotency genes OCT4, Nanog, SSEA4, and SOX2 (Figure 2A) and generated cells from all three germ layers when evaluated *via* teratoma formation assay (Figure 2B). Similar results for [A]iPSC see Supplementary Figure S1. Sendai virus (Figure 2C) and *mycoplasma* (Figure 2D) were undetectable after 10 and 12 passages, respectively, and the cells' karyotypes were normal (Figure 2E). (Grossmann et al., 2021)

CM differentiation potential of [A]iPSC and [V]iPSC

mRNA assessments of the expression of pluripotency genes (OCT4, NANOG, and SOX2; Figure 3A), the early mesodermal
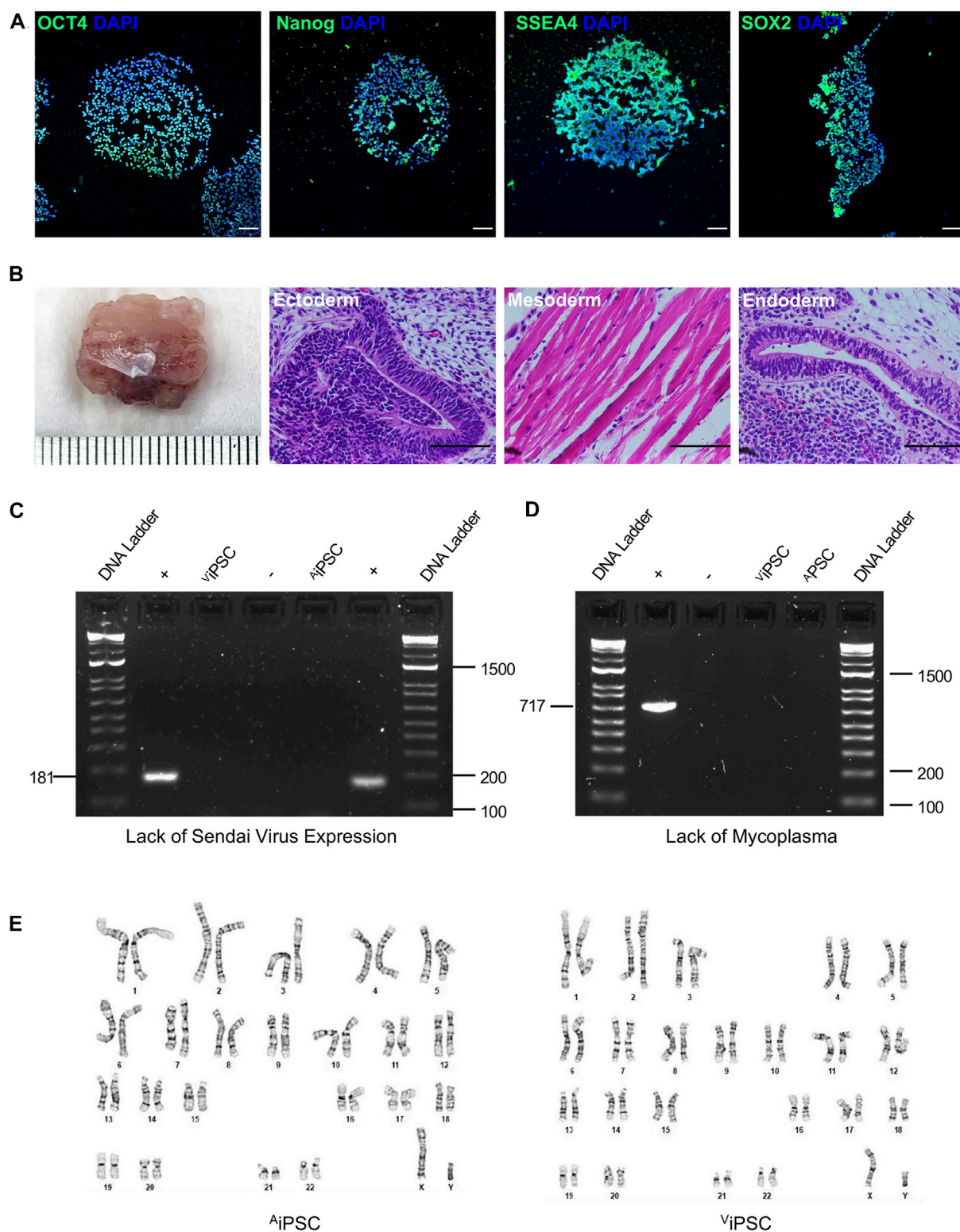
FIGURE 1
iPSCs were reprogrammed from human atrial and ventricular fibroblasts. **(A)** Cardiac tissue was obtained from the atrium and ventricle of a male newborn infant patient who underwent open-chest surgery for d-TGA and cultured to induce fibroblast outgrowth. **(B)** Isolated fibroblasts (bar = 100 μm) were **(C)** evaluated for expression of the fibroblast-specific markers vimentin (VMT) and TE-7 *via* immunofluorescence staining (bar = 20 μm) and then reprogrammed **(D)** into ᴬiPSC and ⱽiPSC *via* transfection with Sendai virus coding for OCT4, SOX2, KLF4, and C-MYC (bar = 100 μm). **(E)** Three weeks after transduction, putative hiPSCs were identified *via* live immunofluorescent staining for CD44 and the pluripotency marker Tra1-60 (bar = 200 μm) and **(F)** imaged for morphological assessments (bar = 100 μm). Representative images of cultured ventricular tissue (Panel A), ventricular fibroblasts **(B–C)**, and ⱽiPSC **(D–F)** are displayed.

marker Brachyury (Figure 3B), the cardiac mesodermal markers MESP1 (Figure 3C) and Gata4 (Figure 3D), and the cardiovascular progenitor-cell transcription factor NKX2.5 (Figure 3E) were conducted before the ᴬiPSC and ⱽiPSC were differentiated into hiPSC-CMs (Day 0), three and six days after the differentiation protocol (Lian et al., 2012) was initiated (D-Day 3 and D-Day 6), and 3 and 12 days after the cells began beating (B-Day 3 and B-Day 12). Measurements in both hiPSC lineages indicated that pluripotency gene expression declined from Day 0 to D-Day 6. At the same time, the abundance of Brachyury and Gata4 mRNA peaked on D-Day 3 and B-Day 3, respectively, and NKX2.5 expression progressively increased from D-Day 6 through B-Day 12. However, whereas measures of MESP1 abundance gradually increased through B-Day 3 in ⱽiPSC, MESP1 expression in ᴬiPSC peaked, and was significantly greater than in ⱽiPSC, on D-Day 3. Nevertheless, when the expression of cardiac troponin T (cTnT) (Figure 3F) was evaluated *via* immunofluorescence, the proportions of positively stained ᴬiPSC-CM and ⱽiPSC-CM populations were similar (Figure 3G) on B-Day 12, indicating that the differentiation protocol was equally efficient for both hiPSC lines.

Functional properties of ᴬiPSC-CM and ⱽiPSC-CM

Electrophysiological properties of ᴬiPSC-CM and ⱽiPSC-CM were characterized *via* action potential (Figure 4A) and field potential (Figure 4E) recordings acquired 30 days after the differentiation protocol was initiated. Action potential durations to 30% (APD_{30}, Figure 4B), 60% (APD_{60}, Figure 4C), and 90% (APD_{90}, Figure 4D) recovery, as well as measurements of beat period (Figure 4F), spike amplitude (Figure 4G), and conduction velocity (Figure 4H) were nearly identical in ᴬiPSC-CM and ⱽiPSC-CM. Field-potential durations (Figure 4I) were detected to be significantly longer in ⱽiPSC-CM. Calcium transients tended to have higher peak amplitudes in ᴬiPSC-CM than in ⱽiPSC-CM when the cells were paced at 1 or 2 Hz (Figures 4J,K), but the differences between groups did not reach statistical significance.

On the other hand, Table 1 shows that our ᴬiPSC-CM and ⱽiPSC-CM APD_{90} (measured at 1 Hz) were within the range of the iPSC-CM derived from the reported skin, kidney, and peripheral blood tissues. Meanwhile, ᴬiPSC-CM/ⱽiPSC-CM had significantly higher conduction velocity (Table 2) than iPSC-CM derived from other tissues.

FIGURE 2
[A]iPSC and [V]iPSC were pluripotent with normal karyotypes. **(A)** Expression of the pluripotency markers OCT4, Nanog, SSEA4, and Sox2 was evaluated *via* immunofluorescence staining in [A]iPSC and [V]iPSC. Nuclei were counterstained with DAPI (representative images of [V]iPSC; bar = 100 μm) **(B)** [A]iPSC and [V]iPSC were subcutaneously transplanted into immunodeficient mice and grew to form teratomas over the ensuing 8 weeks; then, the teratoma was excised, sectioned, stained with hematoxylin and eosin, and examined for the presence of all three developmental germ layers: ectoderm (i.e., neural epithelium), mesoderm (i.e., striated muscle), and endoderm (i.e., gut-like epithelium) (representative images for [V]iPSC teratomas; bar = 100 μm). **(C)** Loss of the Sendai virus vector was confirmed by electrophoresis of RT-PCR products at passage 10. **(D)** The absence of *mycoplasma* contamination was confirmed at passage 12 by electrophoresis of RT-PCR products from the culture supernatant. **(E)** Karyotype analyses were performed to confirm correct chromosomal number and structure of the selected cells.
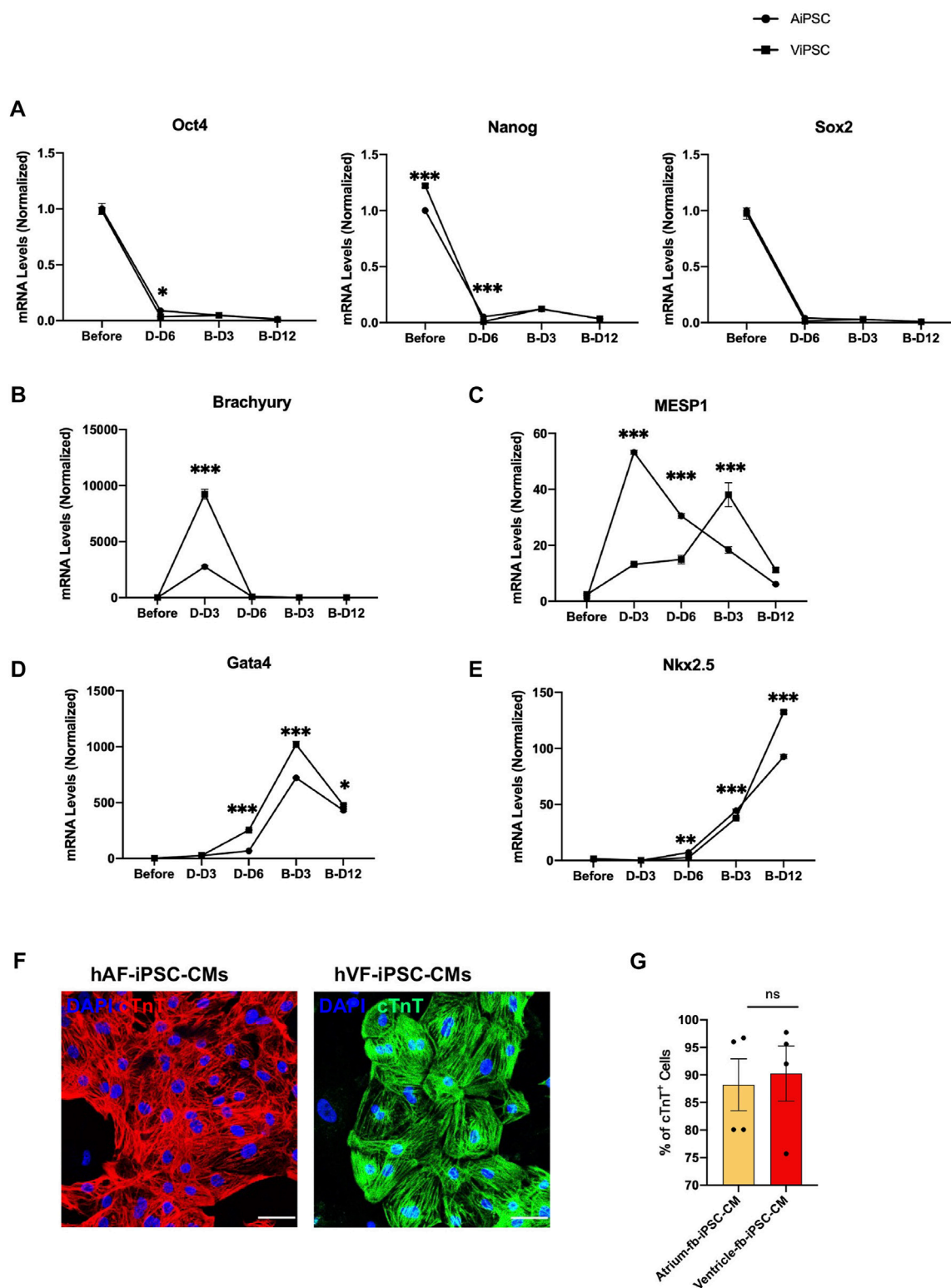
FIGURE 3
Differentiation of [A]iPSC and [V]iPSC into CMs was equally efficient. [A]iPSC and [V]iPSC were differentiated into [A]iPSC-CM and [V]iPSC-CM *via* established protocols. The abundance of mRNA for **(A)** the pluripotency genes Oct4, Nanog, and Sox2; **(B)** the early mesoderm marker Brachyury, **(C)** the early cardiac-mesoderm marker Mesp1; and the cardiac-cell markers **(D)** Gata4 and **(E)** Nkx2.5 was evaluated before differentiation, 3 days (D-D3) and 6 days (D-D6) after differentiation was initiated, and 3 days (B-D3) and 12 days (B-D12) after beating was observed. Measurements were performed *via* qRT-PCR and normalized to the abundance of glyceraldehyde phosphate dehydrogenase mRNA **(F)** [A]iPSC-CM and [V]iPSC-CM were immunofluorescently stained for the expression of cardiac troponin T (cTnT); bar = 50 μm. **(G)** The purity of the [A]iPSC-CM and [V]iPSC-CM was quantified *via* flow cytometry analyses of cTnT-expressing cells on B-Day 12. $*p < 0.05$, $**p < 0.01$, $***p < 0.001$.
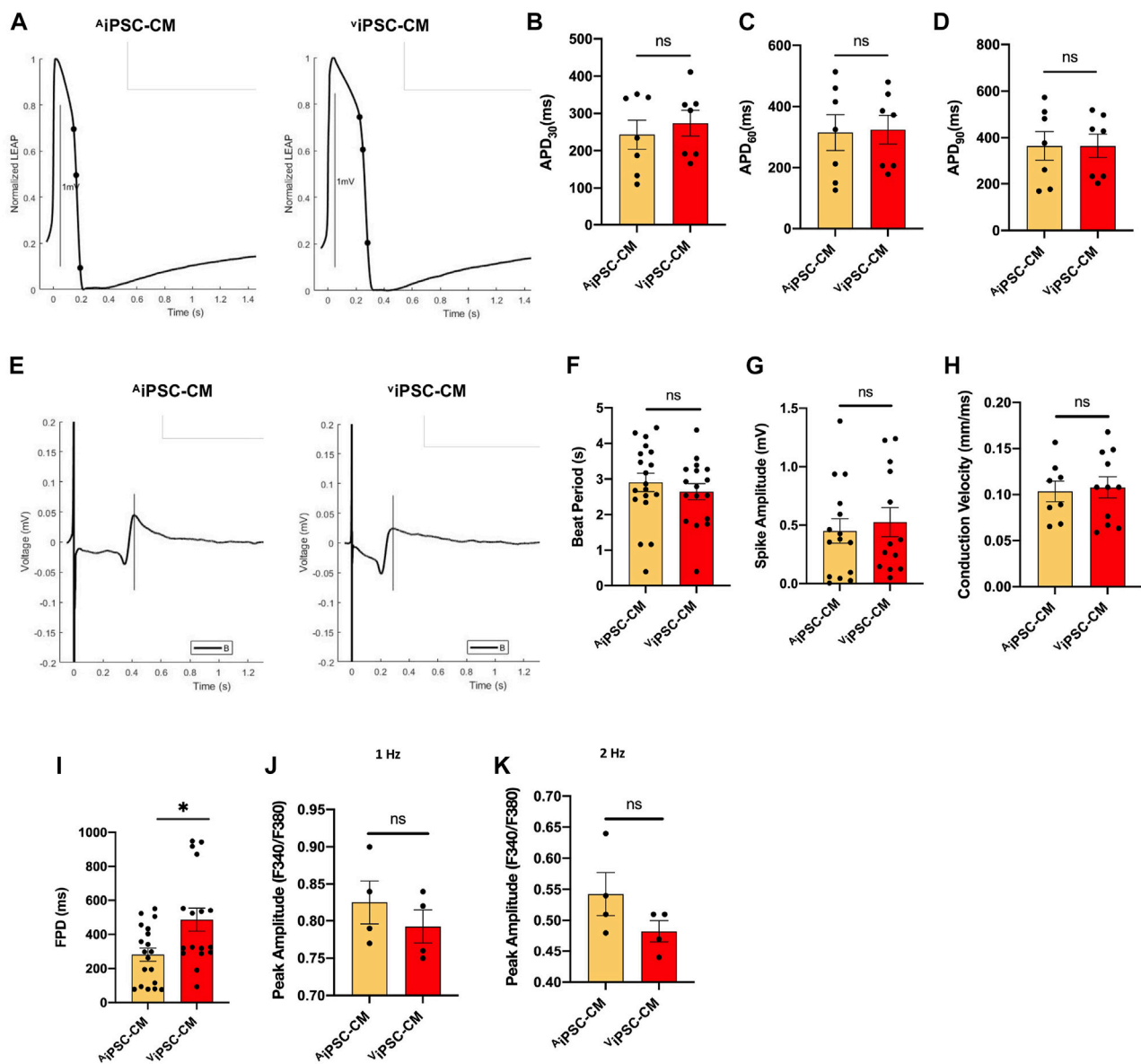
FIGURE 4
Electrophysiological properties of ^{A}iPSC-CM and ^{V}iPSC-CM were similar. **(A)** Representative action-potential and **(E)** field-potential recording are displayed for ^{A}iPSC-CM and ^{V}iPSC-CM. **(B–D)** Action potential durations to 30% (APD_{30}), 60% (APD_{60}), and 90% (APD_{90}) recovery were calculated for ^{A}iPSC-CM and ^{V}iPSC-CM. **(F–I)** Field potential recordings were used to calculate **(F)** beat period, **(G)** spike amplitude, **(H)** conduction velocity, and **(I)** field-potential duration (FPD) for ^{A}iPSC-CM and ^{V}iPSC-CM. **(J,K)** Peak Ca^{2+} transient amplitudes were calculated from Fura-2 AM dye fluorescence recordings in ^{A}iPSC-CM and ^{V}iPSC-CM while the cells were paced at 1 Hz and 2 Hz *$p < 0.05$.

Transcriptional heterogeneity among iPSC and iPSC-CM samples

RNA-seq experiments were performed to compare the transcriptional profiles of iPSC and derived cardiomyocytes from this study (^{A}iPSC-CM, ^{V}iPSC-CM) and two works where iPSC were generated and differentiated to cardiomyocytes using skin (^{SD30}iPSC-CM, $^{S–D90}$iPSC-CM) and kidney fibroblast ($^{K–D90}$iPSC-CM) (Zhao et al., 2017; Garay et al., 2022). Uniform Manifold Approximation and Projection (UMAP) analysis of the data showed clear separation of cardiomyocytes and their original induced pluripotent stem cells, suggesting that the differentiation process

was successful in all cases (Figure 5A). Transcriptional analysis comparing derived cardiomyocytes and iPSC identified 4,970 differentiated expressed genes between both groups (Figure 5B). When focused on this difference, a significant upregulation of genes belonging to the calcium signaling, Actin, Myosin, and Troponin in cardiomyocytes was detected in iPSC-CM. iPSC samples also showed upregulation of genes related to signaling pathways regulating stem cell pluripotency and cell differentiation (Figure 5C). Comparison between ^{A}iPSC-CM/^{V}iPSC-CM (derived from cardiac tissue), $^{S–D30}$iPSC-CM/$^{S–D90}$iPSC-CM (derived from skin tissue) and $^{K–D90}$iPSC-CM (derived from kidney) revealed minor transcriptional differences between cardiomyocytes derived

TABLE 1 Comparison of ADP$_{90}$ (in ms) between [A]iPSC-CM/[V]iPSC-CM and other reported iPSC-CM derived from skin, kidney, and peripheral blood tissues. The numbers were written in mean (standard deviation) format.

Cell line	Tissue origin	ADP$_{90}$, in ms
[A]iPSC-CM	Cardiac	390 (200)
[V]iPSC-CM	Cardiac	390 (190)
Lan et al. (2020)	Skin	200 (20) (*)
Poulin et al. (2021)	Skin	400 (50)
Guo et al. (2019)	Skin	378.9 (17.2)
Garay et al. (2022) ([S−D90]iPSC-CM and [K−D90]iPSC-CM)	Skin (dermal fibroblast)/Kidney (HEK293 cell)	176 (7)
Lam et al. (2020)	Peripheral blood	290 (40) (**)
Wang et al. (2022)	Peripheral blood	400 (50) (***)

(*): The precise numbers in Lan et al. (2020) are not reported. The table numbers were estimated from Lan et al. (2020) Figure 1.
(**): The precise numbers in Lam et al. (2020) are not reported. The table numbers were estimated from Lam et al. (2020) Figure 6.
(***): The precise numbers in Wang et al. (2022) are not reported. The table numbers were estimated from Wang et al. (2022) Figure 4.

TABLE 2 Comparison of conduction velocity (in cm/s) between [A]iPSC-CM/[V]iPSC-CM and other reported iPSC-CM derived from skin, kidney, and peripheral blood tissues. The numbers were written in mean (standard deviation) format.

Cell line	Tissue origin	Conduction velocity
[A]iPSC-CM	Cardiac	10.3 (0.5)
[V]iPSC-CM	Cardiac	10.7 (0.5)
Poulin et al. (2021)	Skin	9.1 (0.7)
Zhao et al. (2017) ([S−D30]iPSC-CM)	Skin	7.9 (0.2) (*)
Garay et al. (2022) ([S−D90]iPSC-CM and [K−D90]iPSC-CM)	Skin (dermal fibroblast)/Kidney (HEK293 cell)	4.5 (4)
Lam et al. (2020)	Peripheral blood	6 (2) (**)
Riedel et al. (2014)	Peripheral blood	4.8 (0.6) (***)
Ong et al. (2017)	Peripheral blood	4.3 (0.2) (****)

(*): The precise numbers in Zhao et al. (2017) are not reported. The table numbers were estimated from Zhao et al. (2017) Supplementary Figure S2.
(**): The precise numbers in Lam et al. (2020) are not reported. The table numbers were estimated from Lam et al. (2020) Figure 6.
(***): The precise numbers in Riedel et al. (2014) are not reported. The table numbers were estimated from Riedel et al. (2014) Figure 5.
(****): The precise numbers in Ong et al. (2017) are not reported. The table numbers were estimated from Ong et al. (2017) Figure 5.

from heart tissue (124 genes differentially expressed) and moderated change when compared to those differentiated from skin or kidney (1,081 differentially expressed genes) (Figure 5B). A clustergram to study the pairwise similarity among the iPSC and iPSC-CM samples demonstrated that while the detected transcriptional changes are mild, these are enough to establish significant differences between heart and non-heart tissue differentiated cardiomyocytes. iPSC and derived cardiomyocytes form two very different clusters. When focusing only on derived cardiomyocytes, clear subclusters can be observed separating cardiac-tissue-derived cardiomyocytes ([A]iPSC-CM and [V]iPSC-CM) from [S−D30]iPSC-CM, [S−D90]iPSC-CM and [K−D90]iPSC-CM (Figure 5D). Gene ontology analysis of the 1081 DE genes (fold change >2 see method section) identified 44 terms, some of them related to heart function (Supplementary Table S5). Further analysis identified 12 genes (AKAP9, BIN1, CACNA1G, CACNB2, CAV1, DSP, GJA5, IRX3, NKX2-5, RANGRF, RYR2 and ISL1) involved in the electrical conduction system of the heart (Zhou et al., 2011) (Supplementary Figure S3), suggesting that the differential expression of these genes play a key role in explaining the distinct electrophysiological properties

detected between cardiac and non-cardiac differentiated cardiomyocytes (Tables 1,2). Further analysis between [A]iPSC-CM and [V]iPSC-CM samples revealed no significant difference in gene expression for atrial (HEY2 and MYL2), ventricular (MYL7 and NPPA), and pacemaker (HCN4, TBX3, and GJC1) cardiomyocyte markers (Supplementary Figure S4).

Discussion

We have shown that when hiPSCs were reprogrammed from cardiac fibroblasts ([hCF]iPSCs), dermal fibroblasts ([hDF]iPSCs), or umbilical cord blood mononuclear cells ([hUCB]iPSCs) and then differentiated into sheets of CMs, spontaneous beating was observed in ≥ 90% of all [hCF]iPSC-CM batches tested, but fell to as low as 20%-30% of [hDF]iPSCs-CM and [hUCB]iPSCs-CMs (Zhang et al., 2015). Notably, the fibroblasts used for [hCF]iPSCs generation were obtained from the atrium, and more than 200 genes are differentially expressed between atrial and ventricular fibroblasts (Burstein et al., 2008). Thus, we investigated whether the
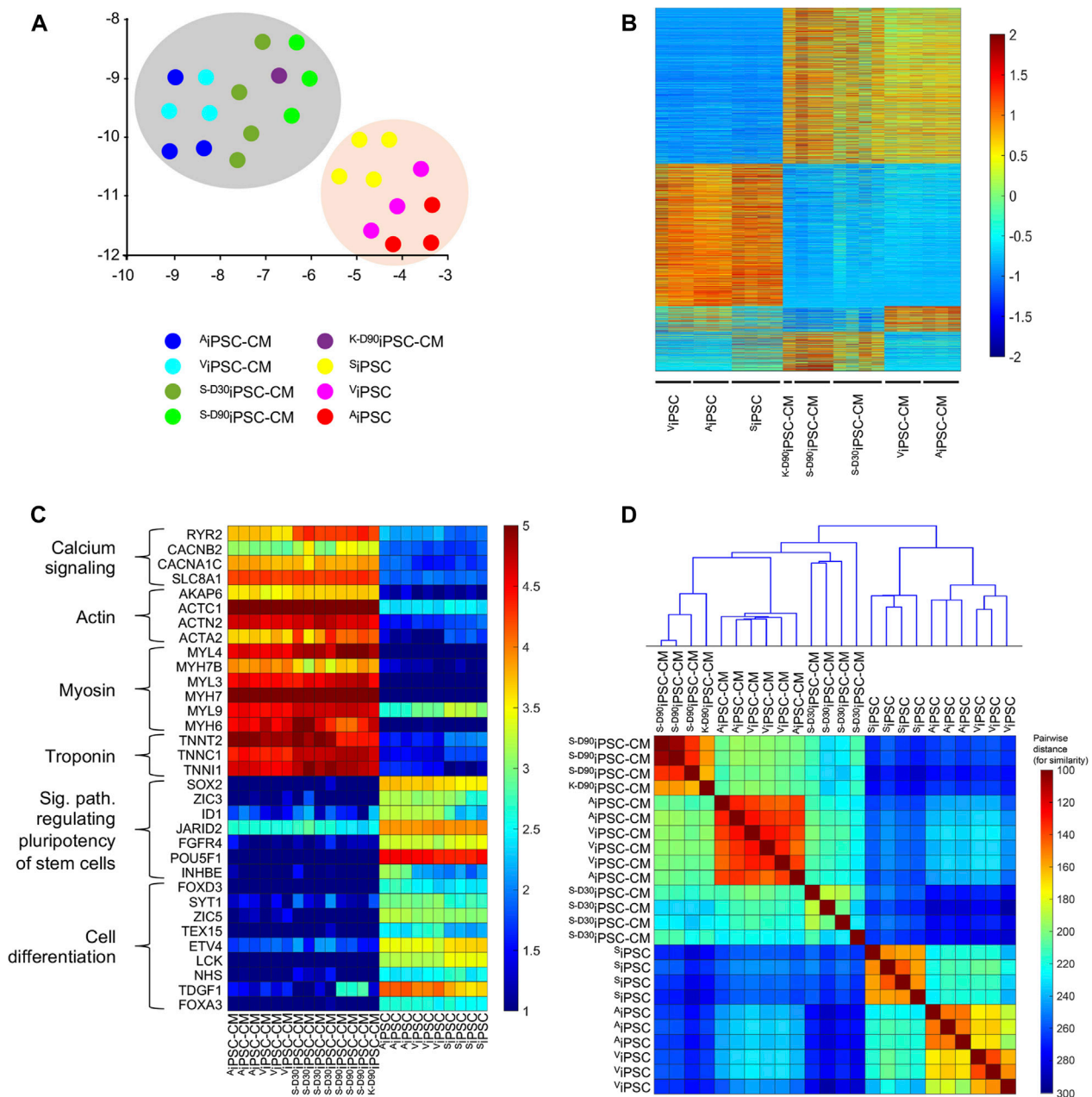
FIGURE 5

Transcriptional analysis of iPSC and iPSC-CM cell lines. **(A)** UMAP plot, where the entire gene expression (35,794 genes) was embedded and reduced to two dimensions. Note the difference in the transcriptional profile between iPSC-CM (grey shade) and iPSC (orange shade). **(B)** Heatmap of differentially expressed genes (*p*-value <0.05) when comparing iPSC to iPSC-CM and among iPSC-CM from different origins. While a high number of differentially expressed genes were detected when comparing iPSC and iPSC-CM samples (4,970), a mild number was observed between ^AiPSC-CM/^ViPSC-CM and other iPSC-CM samples and almost non-significative differences were identified after comparing ^AiPSC-CM and ^ViPSC-CM (124). The colors represent the z-score normalization (gene expression magnitude is ignored). Red color denotes upregulation of transcripts, while blue denotes downregulation of mRNA levels. **(C)** Heatmap of selected gene to show the efficiency of the iPSC-CM differentiation process. Calcium signaling, Actin, Myosin, Troponin, signaling pathway regulating stem cell pluripotency, and cell differentiation gene expression markers are differentially expressed among the iPSC-CM and iPSC cell lines. The colors represent the normalized expression *via* Deseq2 pathway to emphasize the expression magnitude of these genes. **(D)** Clustergram plot including a heatmap of pairwise Euclidian distance among the 24 studied samples and the cluster hierarchy among these. Note the small distance (high similarity) between ^AiPSC-CMs and ^ViPSC-CMs compared to the rest of the iPSC-CMs and iPSC.

transcriptional differences between atrial and ventricular fibroblasts may be accompanied by variations in the differentiation potential of hiPSCs reprogrammed from the two fibroblast subtypes. The results from our studies indicate that ^AiPSC-CM and ^ViPSC-CM can be differentiated into CMs with equal efficiency. Although field potential durations were significantly longer for ^ViPSC-CM than ^AiPSC-CM, measurements of action-potential duration, spike amplitude, conduction velocity, and calcium handling were

essentially indistinguishable. Thus, the CM differentiation potential of [A]iPSC and [V]iPSC appears not significantly different.

In this work, our generated iPSC-CM derived from cardiac fibroblast showed higher conduction velocity than previously reported iPSC-CM derived from the skin and peripheral blood tissues. However, comparing iPSCs derived from ventricular fibroblasts and atrial fibroblasts from the same donor showed no significant electrophysiological difference between iPSCs derived from ventricular fibroblasts and atrial fibroblasts, except in field potential duration. Also, we evaluated the gene expression of representative markers during cardiomyocyte differentiation and measured the purity of cardiomyocytes; the results demonstrated no significant difference.

This report examined gene expression profile differences among the iPSC-CM cell lines. Overall, the difference between [A]iPSC-CM and [V]iPSC-CM is minor compared to the difference between iPSC-CMs derived from different tissues. Regarding the cardiac conduction system, there are 13 DEG genes when comparing iPSC-CMs derived from other tissues; meanwhile, there are only 2 DEGs when comparing [A]iPSC-CM and [V]iPSC-CM. This trend coincides with the conduction velocity comparison reported in Table 2.

Fibroblasts were the first, (Takahashi and Yamanaka, 2006), and may still be the most common, somatic cells used to generate iPSCs, but the range of sources has expanded to encompass a wide variety of cell types, including cells from the blood, (Hanna et al., 2008), liver, and stomach; (Aoi et al., 2008); neural stem and progenitor cells; (Kim et al., 2008); keratinocytes; (Aasen et al., 2008); melanocytes; (Utikal et al., 2009); and even renal tubular cells obtained from urine (Zhou et al., 2011). However, the transcriptional heterogeneity of iPSCs generated from different cell types can be remarkably high; for example, more than 1,000 genes were differentially expressed (by > 2-fold) between iPSCs that had been reprogrammed from genetically matched mouse tail tip fibroblasts (TTFs) and splenic B cells (sBCs), or from genetically matched bone marrow–derived granulocytes (BMGs) and skeletal muscle precursors (SMPs) (Polo et al., 2010). Furthermore, although SMP-specific (Integrin B1) and BMG-specific (Lysozyme and Gr-1) marker expression were lower in SMP- and BMG-derived iPSCs, respectively, than in the corresponding lineages of somatic cells, SMP markers were more highly expressed in SMP-iPSCs than in BMG-iPSCs, BMG markers were more highly expressed in BMG-iPSCs than in SMP-iPSCs, and these differences in lineage-specific marker expression were accompanied by consistent changes in the presence of activating and suppressing acetylation and methylation markers in the genes' promoters.

Ample evidence suggests that epigenetic differences can impact both the efficiency of the differentiation procedure and the function of iPSC-derived cells (Kim et al., 2010; Polo et al., 2010; Kim et al., 2011). When iPSCs were reprogrammed from cardiac progenitor cells (CPC-iPSCs) or dermal fibroblasts (DF-iPSCs) and then differentiated into CMs, cTnT was more commonly expressed by CPC-iPSC-CMs, and spontaneous beating was observed in a more significant proportion of embryoid bodies composed of CPC-iPSC-CMs than in DF-iPSC-CM embryoid bodies; (Sanchez-Freire et al., 2014); beating cells also appeared at an earlier timepoint during the differentiation of CPC-iPSC-CMs, and the CPC-iPSC-CMs were more electrophysiologically

mature than DF-iPSC-CMs. (Pianezzi et al., 2020). Notably, when iPSCs that had been reprogrammed from fetal neural stem cells (fNSCs) or dermal fibroblasts were differentiated into neural progenitor cells (NPCs), and equal numbers of each iPSC-NPC population were mixed and injected into rodent brains, the engrafted iPSC-NPC population contained a more significant proportion of fNSC-iPSC-NPCs than DF-iPSC-NPCs ten weeks later, (Hargus et al., 2014), which suggests that the epigenetic memory of iPSCs may also have a role in engraftment. However, differences in CPC-iPSC- and DF-iPSC-CM yield were observed for iPSCs that had been passaged up to 30, but not >40 times before differentiation was initiated; (Sanchez-Freire et al., 2014); thus, epigenetic variations between iPSCs derived from different somatic-cell lineages may decline as the iPSCs undergo repeated mitotic events over an extended period. Also, our results do not contradict epigenetics memory heterogeneity in iPSC-CM. Instead, the results suggest that the epigenetics difference becomes so minor when iPSC-CM were generated from the fibroblast of the same tissue (cardiac) that the electrophysiological difference is negligible.

Overall, the effects of how "epigenetic memory" determines functional characteristics of iPSC-CMs depend on the similarity of the source of origin. Thus, while the epigenetic memory promotes important differences in the differentiation efficiency and function of iPSCs reprogrammed from cardiac and non-cardiac origins (Kim et al., 2010; Sanchez-Freire et al., 2014), this effect is weakened when iPSCs were derived from different sublocations of the same tissue (atrial and ventricular fibroblasts). Together these data suggest that epigenetic memory is a process that promotes major phenotypical differences as more divergent is the origin of the iPSCs.

The results presented in this report indicated that [A]iPSC and [V]iPSC can be differentiated into CMs with equal efficiency and that the electrophysiological properties and calcium handling activity of [A]iPSC-CM and [V]iPSC-CM are broadly similar. Thus, both [A]iPSC and [V]iPSC are suitable sources of hiPSC-CMs for investigations of regenerative cardiac therapy and other applications. Our data also demonstrate that iPSC-CMs generated from heart tissue develop better electrophysiological features than those obtained from skin or kidney tissue, suggesting that imprinting mechanisms established in the tissue of origin are retained during the reprogramming process and participate in mediating the expression profile of the newly differentiated cardiomyocytes. Despite the extended use and efficiency of the differentiation protocol used in this work (Lian et al., 2012), the fact that it generates a mixed population of cardiomyocytes may be considered a limitation of our work. Thus, it would be very interesting to compare our data with those obtained using a chamber-specific cardiomyocyte differentiation protocol in the future.

Data availability statement

The original contributions presented in the study are publicly available. The data presented in this study are deposited in the Gene Expression Omnibus (GEO) repository, accession number GSE221268. The article also partially reused the publicly available data from GEO database accession numbers GSE187308 and GSE94267.

Ethics statement

The studies involving human participants were reviewed and approved by Institutional Review Board (IRB) for Human Use at the University of Alabama, Birmingham. Written informed consent to participate in this study was provided by the participants' legal guardian/next of kin. The animal study was reviewed and approved by The Institutional Animal Care and Use Committee of the University of Alabama at Birmingham. Written informed consent was obtained from the individual(s), and minor(s)' legal guardian/next of kin, for the publication of any potentially identifiable images or data included in this article.

Author contributions

LW, YZ, and JZ designed the project. LW conducted all the experiments. LW, TN, and MRG analyzed data. LW and JZ wrote the manuscript. LW, TN, MRG, YZ, DC, and JZ revised the manuscript. JZ supervised the whole project. All the authors approved the submission and publication of the manuscript.

Funding

Conflict of interest

The authors declare that the research was conducted in the absence of any commercial or financial relationships that could be construed as a potential conflict of interest.

Publisher's note

Supplementary material

The Supplementary Material for this article can be found online at: https://www.frontiersin.org/articles/10.3389/fbioe.2023.1108340/full#supplementary-material

SUPPLEMENTARY FIGURE S1
Characterization of [A]iPSC. **(A)** Cardiac tissue was obtained from the atrium and ventricle of a male newborn infant patient who underwent open-chest surgery for d-TGA and cultured to induce fibroblast outgrowth. **(B)** Isolated fibroblasts (bar=100 μm) were **(C)** evaluated for expression of the fibroblast-specific markers vimentin (VMT) and TE-7 *via* immunofluorescence staining (bar=20 μm) and then reprogrammed **(D)** into [A]iPSC and [V]iPSC *via* transfection with Sendai virus coding for OCT4, SOX2, KLF4, and C-MYC (bar=100 μm). **(E)** Three weeks after transduction, putative hiPSCs were identified *via* live immunofluorescent staining for CD44 and the pluripotency marker Tra1-60 (bar=200 μm) and **(F)** imaged for morphological assessments (bar=100 μm). Representative images of cultured atrial tissue (Panel A), atrial fibroblasts (B−C), and [A]iPSC (D-F) are displayed. **(G)** Expression of the pluripotency markers OCT4, Nanog, SSEA4, and Sox2 was evaluated *via* immunofluorescence staining in [A]iPSC and [V]iPSC. Nuclei were counterstained with DAPI (representative images of [V]iPSC; bar=100 μm.) **(H)** [A]iPSC and [V]iPSC were subcutaneously transplanted into immunodeficient mice and grew to form teratomas over the ensuing 8 weeks; then, the teratoma was excised, sectioned, stained with hematoxylin and eosin, and examined for the presence of all three developmental germ layers: ectoderm (i.e., neural epithelium), mesoderm (i.e., striated muscle), and endoderm (i.e., gut-like epithelium) (representative images for [A]iPSC teratomas; bar=100 μm). **(I)** Representative figures for purity of [A]iPSC-CM and [V]iPSC-CM *via* flow cytometry analysis of cTnT-expression cell on B-Day 12.

SUPPLEMENTARY FIGURE S2
The enriched gene ontologies and KEGG pathways queried from the list of DEGs in: **(A)** comparison between cardiac-tissue-derived iPSC-CM ([A]iPSC-CM and [V]iPSC-CM) and skin-tissue-derived iPSC-CM ([S-D30]iPSC-CM and [S-D90]iPSC-CM); **(B)** comparison between [A]iPSC-CM and [V]iPSC-CM. The DEG was input into https://david.ncifcrf.gov, resulting in a list of enriched ontologies, pathways, and enrichment p-values. The enrichment score was calculated by taking the negative base10-logarithm of the enrichment p-value.

SUPPLEMENTARY FIGURE S3
The cardiac conduction DEGs gene expression among different iPSC-CM samples. This include AKAP9, BIN1, CACNA1G, CACNB2, CAV1, DSP, GJA5, IRX3, NKX2-5, RANGRF, RYR2, and ISL1.

SUPPLEMENTARY FIGURE S4
No significant difference in gene expression was observed between [A]iPSC-CM and [V]iPSC-CM samples for atrial, ventricular, pacemaker cardiomyocyte marker. **(A)** Atrium cardiomyocyte markers, including HEY2 and MYL2, expression between [A]iPSC-CM and [V]iPSC-CM samples. **(B)** Ventricular cardiomyocyte markers, including MYL7 and NPPA, expression between [A]iPSC-CM and [V]iPSC-CM samples. **(C)** Pacemaker cardiomyocyte markers, including HCN4, TBX3, and GJC1, expression between [A]iPSC-CM and [V]iPSC-CM samples.

References

Aasen, T., Raya, A., Barrero, M. J., Garreta, E., Consiglio, A., Gonzalez, F., et al. (2008). Efficient and rapid generation of induced pluripotent stem cells from human keratinocytes. *Nat. Biotechnol.* 26, 1276–1284. doi:10.1038/nbt.1503

Aoi, T., Yae, K., Nakagawa, M., Ichisaka, T., Okita, K., Takahashi, K., et al. (2008). Generation of pluripotent stem cells from adult mouse liver and stomach cells. *Science* 321, 699–702. doi:10.1126/science.1154884

Bian, W., Chen, W., Nguyen, T., Zhou, Y., and Zhang, J. (2021). miR-199a overexpression enhances the potency of human induced-pluripotent stem-cell-derived cardiomyocytes for myocardial repair. *Front. Pharmacol.* 12, 673621. doi:10.3389/fphar.2021.673621

Burstein, B., Libby, E., Calderone, A., and Nattel, S. (2008). Differential behaviors of atrial versus ventricular fibroblasts: A potential role for platelet-derived growth factor in atrial-ventricular remodeling differences. *Circulation* 117, 1630–1641. doi:10.1161/circulationaha.107.748053

Chen, H., Zhang, A., and Wu, J. C. (2018). Harnessing cell pluripotency for cardiovascular regenerative medicine. *Nat. Biomed. Eng.* 2, 392–398. doi:10.1038/s41551-018-0244-8

Clustergram (2021). *Natick*. Massachusetts: MathWorks, Inc. Available at: https://www.mathworks.com/help/bioinfo/ref/clustergram.html.

Dobin, A., Davis, C. A., Schlesinger, F., Drenkow, J., Zaleski, C., Jha, S., et al. (2013). Star: Ultrafast universal RNA-seq aligner. *Bioinformatics* 29, 15–21. doi:10.1093/bioinformatics/bts635

Ebert, A. D., Yu, J., Rose, F. F., Jr., Mattis, V. B., Lorson, C. L., Thomson, J. A., et al. (2009). Induced pluripotent stem cells from a spinal muscular atrophy patient. *Nature* 457, 277–280. doi:10.1038/nature07677

Frank, N. (2016). *Hierarchical clustering introduction to HPC with MPI for data science.* Springer, 195–211.

Gao, L., Wang, L., Wei, Y., Krishnamurthy, P., Walcott, G. P., Menasché, P., et al. (2020). Exosomes secreted by hiPSC-derived cardiac cells improve recovery from myocardial infarction in swine. *Sci. Transl. Med.* 12, eaay1318. doi:10.1126/scitranslmed.aay1318

Gao, L., Yang, L., Wang, L., Geng, Z., Wei, Y., Gourley, G., et al. (2018). Relationship between the efficacy of cardiac cell therapy and the inhibition of differentiation of human iPSC-derived nonmyocyte cardiac cells into myofibroblast-like cells. *Circulation Res.* 123, 1313–1325. doi:10.1161/circresaha.118.313094

Garay, B. I., Givens, S., Abreu, P., Liu, M., Yücel, D., Baik, J., et al. (2022). Dual inhibition of MAPK and PI3K/AKT pathways enhances maturation of human iPSC-derived cardiomyocytes. *Stem Cell Rep.* 17, 2005–2022. doi:10.1016/j.stemcr.2022.07.003

Grossmann, L., Yde Ohki, C. M., Döring, C., Hoffmann, P., Herms, S., Werling, A. M., et al. (2021). Generation of integration-free induced pluripotent stem cell lines from four pediatric ADHD patients. *Stem Cell Res.* 53, 102268. doi:10.1016/j.scr.2021.102268

Guo, F., Sun, Y., Wang, X., Wang, H., Wang, J., Gong, T., et al. (2019). Patient-specific and gene-corrected induced pluripotent stem cell-derived cardiomyocytes elucidate single-cell phenotype of short QT syndrome. *Circ. Res.* 124, 66–78. doi:10.1161/circresaha.118.313518

Hanna, J., Markoulaki, S., Schorderet, P., Carey, B. W., Beard, C., Wernig, M., et al. (2008). Direct reprogramming of terminally differentiated mature B lymphocytes to pluripotency. *Cell* 133, 365–464. doi:10.1016/j.cell.2008.07.013

Hargus, G., Ehrlich, M., Araúzo-Bravo, M. J., Hemmer, K., Hallmann, A. L., Reinhardt, P., et al. (2014). Origin-dependent neural cell identities in differentiated human iPSCs *in vitro* and after transplantation into the mouse brain. *Cell Rep.* 8, 1697–1703. doi:10.1016/j.celrep.2014.08.014

Huang, D. W., Sherman, B. T., and Lempicki, R. A. (2009). Systematic and integrative analysis of large gene lists using DAVID bioinformatics resources. *Nat. Protoc.* 4, 44–57. doi:10.1038/nprot.2008.211

Kim, J. B., Zaehres, H., Wu, G., Gentile, L., Ko, K., Sebastiano, V., et al. (2008). Pluripotent stem cells induced from adult neural stem cells by reprogramming with two factors. *Nature* 454, 646–650. doi:10.1038/nature07061

Kim, K., Doi, A., Wen, B., Ng, K., Zhao, R., Cahan, P., et al. (2010). Epigenetic memory in induced pluripotent stem cells. *Nature* 467, 285–290. doi:10.1038/nature09342

Kim, K., Zhao, R., Doi, A., Ng, K., Unternaehrer, J., Cahan, P., et al. (2011). Donor cell type can influence the epigenome and differentiation potential of human induced pluripotent stem cells. *Nat. Biotechnol.* 29, 1117–1119. doi:10.1038/nbt.2052

Lam, Y. Y., Keung, W., Chan, C. H., Geng, L., Wong, N., Brenière-Letuffe, D., et al. (2020). Single-cell transcriptomics of engineered cardiac tissues from patient-specific induced pluripotent stem cell-derived cardiomyocytes reveals abnormal developmental trajectory and intrinsic contractile defects in hypoplastic right heart syndrome. *J. Am. Heart Assoc.* 9, e016528. doi:10.1161/jaha.120.016528

Lan, H., Xu, Q., El-Battrawy, I., Zhong, R., Li, X., Lang, S., et al. (2020). Ionic mechanisms of disopyramide prolonging action potential duration in human-induced pluripotent stem cell-derived cardiomyocytes from a patient with short QT syndrome type 1. *Front. Pharmacol.* 11, 554422. doi:10.3389/fphar.2020.554422

Leland McInnes, J. H., and James, M. (2018). *Umap: Uniform manifold approximation and projection for dimension reduction.* arXiv preprint arXiv:180203426.

Lian, X., Hsiao, C., Wilson, G., Zhu, K., Hazeltine, L. B., Azarin, S. M., et al. (2012). Robust cardiomyocyte differentiation from human pluripotent stem cells *via* temporal modulation of canonical Wnt signaling. *Proc. Natl. Acad. Sci. U. S. A.* 109, E1848–E1857. doi:10.1073/pnas.1200250109

Lian, X., Zhang, J., Azarin, S. M., Zhu, K., Hazeltine, L. B., Bao, X., et al. (2013). Directed cardiomyocyte differentiation from human pluripotent stem cells by modulating Wnt/β-catenin signaling under fully defined conditions. *Nat. Protoc.* 8, 162–175. doi:10.1038/nprot.2012.150

Love, M. I., Huber, W., and Anders, S. (2014). Moderated estimation of fold change and dispersion for RNA-seq data with DESeq2. *Genome Biol.* 15, 550. doi:10.1186/s13059-014-0550-8

Meraviglia, V., Wen, J., Piacentini, L., Campostrini, G., Wang, C., Florio, M. C., et al. (2016). Higher cardiogenic potential of iPSCs derived from cardiac versus skin stromal cells. *Front. Biosci. (Landmark Ed.* 21, 719–743. doi:10.2741/4417

Nelakanti, R. V., Kooreman, N. G., and Wu, J. C. (2015). Teratoma formation: A tool for monitoring pluripotency in stem cell research. *Curr. Protoc. Stem Cell Biol.* 32, 4a.8.1–4A. doi:10.1002/9780470151808.sc04a08s32

Nurk, S., Koren, S., Rhie, A., Rautiainen, M., Bzikadze, A. V., Mikheenko, A., et al. (2022). The complete sequence of a human genome. *Science* 376, 44–53. doi:10.1126/science.abj6987

Ong, C. S., Fukunishi, T., Zhang, H., Huang, C. Y., Nashed, A., Blazeski, A., et al. (2017). Biomaterial-Free three-dimensional bioprinting of cardiac tissue using human induced pluripotent stem cell derived cardiomyocytes. *Sci. Rep.* 7, 4566. doi:10.1038/s41598-017-05018-4

Park, I-H., Lerou, P. H., Zhao, R., Huo, H., and Daley, G. Q. (2008). Generation of human-induced pluripotent stem cells. *Nat. Protoc.* 3, 1180–1186. doi:10.1038/nprot.2008.92

Park, I. H., Arora, N., Huo, H., Maherali, N., Ahfeldt, T., Shimamura, A., et al. (2008). Disease-specific induced pluripotent stem cells. *Cell* 134, 877–886. doi:10.1016/j.cell.2008.07.041

Pianezzi, E., Altomare, C., Bolis, S., Balbi, C., Torre, T., Rinaldi, A., et al. (2020). Role of somatic cell sources in the maturation degree of human induced pluripotent stem cell-derived cardiomyocytes. *Biochim. Biophys. Acta Mol. Cell Res.* 1867, 118538. doi:10.1016/j.bbamcr.2019.118538

Polo, J. M., Liu, S., Figueroa, M. E., Kulalert, W., Eminli, S., Tan, K. Y., et al. (2010). Cell type of origin influences the molecular and functional properties of mouse induced pluripotent stem cells. *Nat. Biotechnol.* 28, 848–855. doi:10.1038/nbt.1667

Poulin, H., Mercier, A., Djemai, M., Pouliot, V., Deschenes, I., Boutjdir, M., et al. (2021). iPSC-derived cardiomyocytes from patients with myotonic dystrophy type 1 have abnormal ion channel functions and slower conduction velocities. *Sci. Rep.* 11, 2500. doi:10.1038/s41598-021-82007-8

Riedel, M., Jou Chuanchau, J., Lai, S., Lux Robert, L., Moreno Alonso, P., Spitzer Kenneth, W., et al. (2014). Functional and pharmacological analysis of cardiomyocytes differentiated from human peripheral blood mononuclear-derived pluripotent stem cells. *Stem Cell Rep.* 3, 131–141. doi:10.1016/j.stemcr.2014.04.017

Rizzi, R., Di Pasquale, E., Portararo, P., Papait, R., Cattaneo, P., Latronico, M. V., et al. (2012). Post-natal cardiomyocytes can generate iPS cells with an enhanced capacity toward cardiomyogenic re-differentiation. *Cell Death Differ.* 19, 1162–1174. doi:10.1038/cdd.2011.205

Sanchez-Freire, V., Lee, A. S., Hu, S., Abilez, O. J., Liang, P., Lan, F., et al. (2014). Effect of human donor cell source on differentiation and function of cardiac induced pluripotent stem cells. *J. Am. Coll. Cardiol.* 64, 436–448. doi:10.1016/j.jacc.2014.04.056

Soldner, F., Hockemeyer, D., Beard, C., Gao, Q., Bell, G. W., Cook, E. G., et al. (2009). Parkinson's disease patient-derived induced pluripotent stem cells free of viral reprogramming factors. *Cell* 136, 964–977. doi:10.1016/j.cell.2009.02.013

Stadtfeld, M., Brennand, K., and Hochedlinger, K. (2008). Reprogramming of pancreatic beta cells into induced pluripotent stem cells. *Curr. Biol.* 18, 890–894. doi:10.1016/j.cub.2008.05.010

Takahashi, K., and Yamanaka, S. (2006). Induction of pluripotent stem cells from mouse embryonic and adult fibroblast cultures by defined factors. *Cell* 126, 663–676. doi:10.1016/j.cell.2006.07.024

Uniform, S. M. (2021). *Manifold approximation and projection.* UMAP.

Utikal, J., Maherali, N., Kulalert, W., and Hochedlinger, K. (2009). Sox2 is dispensable for the reprogramming of melanocytes and melanoma cells into induced pluripotent stem cells. *J. Cell Sci.* 122, 3502–3510. doi:10.1242/jcs.054783

Wang, F., Han, Y., Sang, W., Wang, L., Liang, X., Wang, L., et al. (2022). *In vitro* drug screening using iPSC-derived cardiomyocytes of a long QT-syndrome patient carrying KCNQ1 & TRPM4 dual mutation: An experimental personalized treatment. *Cells* 11, 2495. doi:10.3390/cells11162495

Wang, L., Serpooshan, V., and Zhang, J. (2021). Engineering human cardiac muscle patch constructs for prevention of post-infarction LV remodeling. *Front. Cardiovasc. Med.* 8, 621781. doi:10.3389/fcvm.2021.621781

Wang, L., and Zhang, J. (2022). Layer-by-layer fabrication of thicker and larger human cardiac muscle patches for cardiac repair in mice. *Front. Cardiovasc. Med.* 8, 800667. doi:10.3389/fcvm.2021.800667

Wickramasinghe, N. M., Sachs, D., Shewale, B., Gonzalez, D. M., Dhanan-Krishnan, P., Torre, D., et al. (2022). PPARdelta activation induces metabolic and contractile maturation of human pluripotent stem cell-derived cardiomyocytes. *Cell Stem Cell* 29, 559–576.e7. doi:10.1016/j.stem.2022.02.011

Zhang, J., Zhu, W., Radisic, M., and Vunjak-Novakovic, G. (2018). Can we engineer a human cardiac patch for therapy? *Circulation Res.* 123, 244–265. doi:10.1161/circresaha.118.311213

Zhang, L., Guo, J., Zhang, P., Xiong, Q., Wu, S. C., Xia, L., et al. (2015). Derivation and high engraftment of patient-specific cardiomyocyte sheet using induced pluripotent stem cells generated from adult cardiac fibroblast. *Circ. Heart Fail.* 8, 156–166. doi:10.1161/circheartfailure.114.001317

Zhao, M. T., Chen, H., Liu, Q., Shao, N. Y., Sayed, N., Wo, H. T., et al. (2017). Molecular and functional resemblance of differentiated cells derived from isogenic human iPSCs and SCNT-derived ESCs. *Proc. Natl. Acad. Sci. U. S. A.* 114, E11111–e11120. doi:10.1073/pnas.1708991114

Zhou, T., Benda, C., Duzinger, S., Huang, Y., Li, X., Li, Y., et al. (2011). Generation of induced pluripotent stem cells from urine. *J. Am. Soc. Nephrol.* 22, 1221–1228. doi:10.1681/asn.2011010106

Frontiers in Bioengineering and Biotechnology

Identifying molecular and functional similarities and differences between human primary cardiac valve interstitial cells and ventricular fibroblasts

Martha E. Floy[1†], Fathima Shabnam[1†], Sophie E. Givens[2], Vaidehi A. Patil[3], Yunfeng Ding[1], Grace Li[4], Sushmita Roy[5], Amish N. Raval[3,5], Eric G. Schmuck[5], Kristyn S. Masters[3], Brenda M. Ogle[2,6] and Sean P. Palecek[1]*

[1]Department of Chemical and Biological Engineering, University of Wisconsin-Madison, Madison, WI, United States, [2]Department of Biomedical Engineering, University of Minnesota, Minneapolis, MN, United States, [3]Department of Biomedical Engineering, University of Wisconsin-Madison, Madison, WI, United States, [4]Department of Chemical Engineering, University of Florida, Gainesville, FL, United States, [5]Department of Medicine, University of Wisconsin-Madison, Madison, WI, United States, [6]Stem Cell Institute, University of Minnesota, Minneapolis, MN, United States

Introduction: Fibroblasts are mesenchymal cells that predominantly produce and maintain the extracellular matrix (ECM) and are critical mediators of injury response. In the heart, valve interstitial cells (VICs) are a population of fibroblasts responsible for maintaining the structure and function of heart valves. These cells are regionally distinct from myocardial fibroblasts, including left ventricular cardiac fibroblasts (LVCFBs), which are located in the myocardium in close vicinity to cardiomyocytes. Here, we hypothesize these subpopulations of fibroblasts are transcriptionally and functionally distinct.

Methods: To compare these fibroblast subtypes, we collected patient-matched samples of human primary VICs and LVCFBs and performed bulk RNA sequencing, extracellular matrix profiling, and functional contraction and calcification assays.

Results: Here, we identified combined expression of *SUSD2* on a protein-level, and *MEOX2*, *EBF2* and *RHOU* at a transcript-level to be differentially expressed in VICs compared to LVCFBs and demonstrated that expression of these genes can be used to distinguish between the two subpopulations. We found both VICs and LVCFBs expressed similar activation and contraction potential *in vitro*, but VICs showed an increase in ALP activity when activated and higher expression in matricellular proteins, including cartilage oligomeric protein and alpha 2-Heremans-Schmid glycoprotein, both of which are reported to be linked to calcification, compared to LVCFBs.

Conclusion: These comparative transcriptomic, proteomic, and functional studies shed novel insight into the similarities and differences between valve interstitial cells and left ventricular cardiac fibroblasts and will aid in understanding region-

Abbreviations: ALP, alkaline phosphatase; CFB, cardiac fibroblast; ECM, extracellular matrix; hPSC, human pluripotent stem cell; LVCFB, left ventricular cardiac fibroblast; VIC, valve interstitial cell.

specific cardiac pathologies, distinguishing between primary subpopulations of fibroblasts, and generating region-specific stem-cell derived cardiac fibroblasts.

1 Introduction

Cardiac fibroblasts (CFBs) play a key role in cardiovascular diseases by contributing to inflammation and fibrotic scarring, and therefore are a potential therapeutic target. Many clinical cardiac pathologies occur in specific regions of the heart; for example, the majority of arrythmias occur in the atria (Sánchez et al., 2019), fibrosis mainly occurs in the left ventricle (Kanisicak et al., 2016), and mineralization occurs primarily in the heart valves and vasculature (Li et al., 2021). Hence, heterogeneity in CFBs from different regions of the heart likely contributes to regional clinical pathologies which may arise by patterning through developmental lineage progression and local environmental cues (Tallquist, 2020). However, it has been difficult to distinguish between lineage specification and local environmental specification using *in vivo* models.

In this study, we identify molecular and functional similarities and differences between valve interstitial cells (VICs) and left ventricular cardiac fibroblasts (LVCFBs). VICs are the interstitial cells located in all three layers of the heart valve (fibrosa, spongiosa, and ventricularis/atrialis), the surface of which is lined by valvular endothelial cells (Menon and Lincoln, 2018). This heterogenous CFB population is thought to play a key role in regulating ECM deposition of collagen, proteoglycans, and elastin during valve development and homeostasis (Aikawa et al., 2006; Liu et al., 2007). LVCFBs are located in the myocardium of the left ventricle and provide key support to endothelial cells and cardiomyocytes, heart muscle cells (Moore-Morris et al., 2014; Nicin et al., 2022). Lineage tracing studies using mouse Cre-based genetic tracing strategies have shown that VICs arise from both epicardial and endocardial cell progenitors with the composition varying between valves, with the majority of cells in the parietal and mural leaflets of the atrioventricular valves originating from epicardial cells and the majority of septal and aortic leaflets originating from endocardial cells (Wessels et al., 2012). In comparison, CFBs located in the heart wall are thought to be almost entirely derived from epicardial lineages (Moore-Morris et al., 2014). Despite a similar progenitor lineage, we hypothesize that LVCFBs and VICs have distinct transcriptional and functional differences that guide their specific roles in myocardium and valve tissues, respectively.

Here, we report molecular and functional differences *in vitro* between VICs and LVCFBs. This work identifies key similarities such as contraction potential, and differences such as increased calcification potential in LVCFBs compared to VICs. Furthermore, we analyzed differentially regulated genes and proteins between the two populations and identified marker genes and pathways as well as ECM proteins differentially regulated between VICs and LVCFBs. Characterizing the molecular and functional differences between these cells adds to our ability to distinguish between these subpopulations and increases understanding of the function of

these region-specific populations. For example, while calcification is typically observed in valves in clinical pathologies, our *in vitro* experiments indicate under similar culture conditions, LVCFBs exhibit higher calcification compared to VICs. Furthermore, while collagens and matricellular proteins such as periostin have been studied in VICs, we show that LVCFBs secrete a higher abundance of these proteins. Instead, clotting ECM proteins and some matricellular proteins such as cartilage oligomeric matrix protein and alpha-2-HS-glycoprotein were secreted at a higher abundance in VICs. The comparative findings in this paper may also be used for generating and identifying region-specific stem cell-derived cardiac fibroblasts to advance *in vitro* modeling of cardiac tissue and cell-based cardiac regenerative therapies.

2 Materials and methods

2.1 Donor approval

Human tissues were procured and used with local Institutional Review Board approval. Donor hearts ($n = 3$, 1 male, 2 female, ages 39, 33, and 34 years old respectively) were obtained from the University of Wisconsin Organ Procurement Organization, Madison, WI from brain dead patients undergoing routine organ and tissue donation for transplant. These hearts were considered healthy, but were unused for transplant. Hearts were harvested by aseptical excision followed by perfusion and storage in cold cardioplegia solution prior to transport on ice. Hearts were processed between 4–6 h post explant.

2.2 Primary cell isolation

To isolate left ventricular cardiac fibroblasts, epicardial fat was removed and 25–30 g of left ventricular free wall was minced and transferred into gentleMACS C tubes (Miltenyi Biotec). Then, 10 mL digestion medium (DMEM supplemented with 0.125 mg/mL Liberase TM (Roche)) was added to each tube. Samples were homogenized using gentleMACS Dissociator (Miltenyi Biotec) using a C-tube, and incubated at 37°C for 30 min under agitation. The process was repeated twice to ensure tissue dissociation. Heart samples were then run through a 200 μm filter and centrifuged at 1000 g for 20 min. The supernatant was aspirated, and the remaining cell pellet was suspended in 20 mL primary CFB maintenance medium (MCDB131 basal medium (Gibco) supplemented with 10% FBS (R&D Systems), 5 μg/mL insulin (Sigma-Aldrich), 1 ng/mL bFGF (R&D Systems), 0.01 mg/mL ciprofloxacin, and 2.5 μg/mL Amphotericin B) (Gibco) and plated into T75 flasks. 2 h later, non-adherent cells were removed by washing in DPBS. Finally, primary CFB maintenance medium

was replaced, and cells were cultured at 37°C, 5% CO$_2$, and 100% humidity.

To isolate valve interstitial cells, aortic valve leaflets were excised and washed in PBS (no Ca^{2+}, no Mg^{2+}). They were then incubated in a 2.5 mg/mL collagenase type II solution (Worthington) for 1 h. After incubation, valve leaflets were vortexed at the highest setting for 1 min to remove endothelial cells. The tissue was then further digested in a 1 mg/mL collagenase type II solution for 3 h and vortexed again for 2 min followed by pipetting with a 25 mL disposable pipette to release the valve interstitial cells. The cell suspension was centrifuged, and the resulting cell pellet was resuspended and plated.

2.3 Primary cell maintenance

Primary CFBs and VICs were maintained in primary CFB maintenance medium (MCDB131 basal medium supplemented with 10% FBS, 5 μg/mL insulin, 1 ng/mL bFGF, 0.01 mg/mL ciprofloxacin, and 2.5 μg/mL Amphotericin B) with medium changes every 2 days. These culture conditions have been demonstrated to maintain the native phenotype of healthy VICs (Porras et al., 2017). At 80% confluence, primary CFBs and VICs were passaged for up to six passages using Accutase or 1X TrypLE for 10 mins in the incubator at 37°C, 5% CO$_2$, and 100% humidity or until cells were singularized and then quenched with maintenance media, and centrifuged for 5 mins at 200 g.

2.4 Flow cytometry

Cells were singularized and fixed in 1% PFA for 15 min and stored in 90 (v/v)% methanol in water at −20°C until staining. Cells were then washed with 0.5% BSA in PBS (no Ca^{2+}, no Mg^{2+}) and stained with 100 μL of primary antibodies resuspended in 0.5% BSA with 0.1% Triton-X100 in PBS (no Ca^{2+}, no Mg^{2+}) in the ratio given in Supplementary Table S2. Samples were then incubated overnight at 4°C on a shaker. The following day, samples were washed with 0.5% BSA in PBS (no Ca^{2+}, no Mg^{2+}) and stained with 100 μL of secondary antibodies resuspended in 0.5% BSA with 0.1% Triton-X100 in PBS (no Ca^{2+}, no Mg^{2+}) at 1:1,000 according to Supplementary Table S2. Samples were then incubated for 30 min at room temperature, washed with 0.5% BSA in PBS (no Ca^{2+}, no Mg^{2+}), and analyzed on a BD Accuri C6 Plus cytometer. At least 10,000 events were collected per sample and analysis was performed using FlowJo software.

2.5 Immunocytochemistry and cell area analysis

Cells were fixed in 4% PFA for 15 min, and blocked using 0.5% BSA with 0.1% Triton-X100 in PBS (no Ca^{2+}, no Mg^{2+}) or 0.5% dry milk with 0.4% Triton-X100 in PBS (no Ca^{2+}, no Mg^{2+}) for 1 h at room temperature or overnight at 4°C. Then, cells were treated with primary antibody solution (see Supplementary Table S2) resuspended in 0.5% BSA with 0.1% Triton-X100 in PBS (no Ca^{2+}, no Mg^{2+}) or 0.5% dry milk with 0.4% Triton-X100 in PBS (no Ca^{2+}, no Mg^{2+}) and incubated overnight at 4°C. The following

day, samples were washed with PBS (no Ca^{2+}, no Mg^{2+}), treated with secondary antibody solution at 1:1,000 (see Supplementary Table S2, and incubated for 1 h at room temperature or overnight at 4°C. Finally, samples were washed with PBS (no Ca^{2+}, no Mg^{2+}), counterstained with 5 μg/mL Hoechst, and imaged using a Nikon Ti-2 inverted microscope. Image analysis was performed using ImageJ Fiji software to automatically threshold and tabulate cell attributes.

2.6 mRNA extractions

Cells were singularized in Accutase, quenched, and centrifuged for 5 min at 200 g. Cell pellets were snap frozen at −80°C until further extraction. Total mRNA was isolated using the Qiagen RNeasy mini kit and treated with DNase (Qiagen). mRNA was eluted using DNA/RNA free water and stored at −80°C until sequencing.

2.7 cDNA preparation and RT-qPCR analysis

Using the Ominiscript Reverse Transcriptase kit (Qiagen) and Oligo (dT)$_{20}$ Primers, 500 ng mRNA was reversed transcribed into cDNA. Real-time quantitative PCR with two technical replicates in 25 μL reactions using PowerUP Syber Master Mix were analyzed on an AriaMx Real-Time PCR System with an annealing temperature of 60°C. *RPL13A* was used as the housekeeper and analysis was performed using the ΔCt method. Primer sequences can be found in Supplementary Table S3.

2.8 Sequencing sample preparation and processing

Quantity and quality of RNA samples were first analyzed for the presence of 18 S and 28 S ribosomal RNA with A$_{260}$/A$_{280}$ ratio around 2.0 and A$_{260}$/A$_{230}$ ratios greater than 2.0. RNA was next quantified on an Agilent 2,100 Bioanalyzer using Qubit prior to library construction and sequencing. Sequencing libraries were constructed using the Illumina TruSeq Stranded mRNA kit and sequenced on an Illumina NovaSeq6000. Between 10 and 25 million reads were uniquely mapped per sample (Supplementary Material S2).

Raw FASTQ files were mapped to the human genome (hg38 + decoy) using STAR v2.5.3a (Dobin et al., 2013). Gene-level transcript abundances were calculated using featureCounts v2.0.3 (Liao et al., 2014). DESeq2 and all following commands were performed using R v4.1.3 (Love et al., 2014). DESeq2 was performed with a multi-factor design to account for the paired donor-matched samples. PCA plot was performed on variance-stabilized counts values, and differential gene lists were obtained with a threshold of p-adj<0.05. We also performed QuaternaryProd analysis using package v1.28.0 and gene ontology (GO) analysis using PANTHER with Reactome pathway database (Ashburner et al., 2000; Fakhry et al., 2016; Gene Ontology Consortium et al., 2021). Processed data including differential gene lists, transcripts per million (TPM) list, QuartneryProd and GO analysis are available in Supplementary Material S2.

We obtained count matrices for publicly available single cell sequencing datasets (GSE194180 and SCP498, Broad Institute) and selected the desired cells. UMAP and dot plots were prepared by the authors using the Seurat package version 4 (Hao et al., 2021).

2.9 Western blot analysis

Cell lysates were collected by treating cells with RIPA buffer in the presence of Halt Protease Inhibitor Cocktail (ThermoFisher). A BCA assay was used to determine the total protein concentration of cell lysates. Equal mass of protein was loaded on a 4%–12% tris-glycine gel under reducing conditions and transferred to nitrocellulose membranes. Membranes were blocked in tris-buffered saline +0.1% Tween20 (TBST) + 5 (wt/vol)% milk buffer for 1 h at room temperature. 15 mL of primary antibody solution (see Supplementary Table S2) were added to each membrane and incubated overnight at 4°C on a shaker. The following day, membranes were washed with TBST, incubated with secondary antibodies at 1:5,000 (see Supplementary Table S3) for 1 h at room temperature on a shaker, and washed again in TBST. Blots were then imaged on an LICOR Odyssey system, and bands were quantified using Image Studio 5.2.

2.10 Collagen gel contraction

Collagen gel contraction assays were performed with three wells per primary CFB line with a seeding density of 5×10^6 cells/mL in primary CFB maintenance medium according to manufacturer's instructions for the Cell Contraction Assay kit (CBA5020, Cell Biolabs). The gels were imaged after 24 h and gel area was quantified using ImageJ Fiji software.

2.11 Osteogenic induction

Cells were plated at 7,000 cells/cm^2 in a 6-well plate and cultured in primary CFB maintenance medium or αMEM (Gibco) with 10% FBS, 50 mg/L L-ascorbic acid 2-phosphate sesquimagnesium salt hydrate (Sigma-Aldrich), 10 mM β-glycerophosphate disodium salt hydrate (Chem Impex), 10 nM dexamethasone (Sigma-Aldrich), 0.01 mg/mL ciprofloxacin, and 2.5 μg/mL Amphotericin B) as has previously been used for osteoinduction (Masjedi et al., 2016; Pillai et al., 2017; Kostina et al., 2018). Medium was changed every 2 days for 4 weeks.

2.12 ALP activity assay

Lysate samples were normalized by total protein content using the BCA assay. Equal amounts of protein were used in the alkaline phosphatase diethanolamine activity kit (Sigma-Aldrich). Each well contained 190 μL reaction buffer, 0.4 μL p-nitrophenyl phosphate, and 10.5 μL sample lysate. Two technical replicates per sample were averaged and absorbance (405 nm) was measured on a Tecan M100 plate reader every 15 min while within the detection range of the plate reader.

2.13 Alizarin red staining and quantification

Cells were fixed in 4% paraformaldehyde for 15 min and washed with deionized water. Samples were stained with 0.5 mL/well (in a 6-well plate) of 40 mM Alizarin red for 30 min at room temperature on a rotary shaker. Samples were next washed four times with 1 mL/well DI water to remove excess stain, all liquid was removed from the wells, and they were imaged on an EVOS XL Core Imaging System. To quantify Alizarin red staining, samples were treated with 600 μL/well 10 (wt/vol)% cetylpyridinium chloride in 10 mM sodium phosphate at room temperature on a shaker for 1 h. Then, sample was diluted at 1:10 using deionized water, 150 μL was transferred into two wells of a 96-well plate (to account for variability in absorbance readings) and absorbance (560 nm) was measured on a Tecan M100 plate reader.

2.14 Von Kossa staining

Following Alizarin red staining and quantification, cells were washed with deionized water. Then, they were stained using a von Kossa staining kit (Abcam). Briefly, wells were incubated in 0.5 mL/well silver nitrate solution (5%) for 20 min with exposure to ultraviolet light. Wells were then washed three times with 2 mL/well deionized water. Cells were next incubated with 0.5 mL/well sodium thiosulfate solution (5%) for 2 min and washed three times with 2 mL/well deionized water. Lastly, cells were incubated with 0.5 mL/well Nuclear Fast Red solution for 5 min and washed with 2 mL/well deionized water three times prior to imaging on an EVOS XL Core Imaging System.

2.15 High-density culture and decellularization

High density fibroblast culture and decellularization protocols were performed as described previously (Floy et al., 2021). Fibroblasts were seeded at 7,000 cells/cm^2 in a 48-well plate and cultured for 16 days without passaging. At day 16, cells were washed with PBS (no Ca^{2+}, no Mg^{2+}) followed by washes using wash buffer 1 (100 mM Na$_2$HPO$_4$, 2 mM MgCl$_2$, 2 mM EDTA). Cells were then lysed in lysis buffer (8 mM Na$_2$HPO$_4$, 1% Triton X-100) and incubated at 37°C for 1 h. Following lysis, matrices were washed with wash buffer 2 (100 mM Na$_2$HPO$_4$, 300 mM KCl) and DI water. Plates were allowed to dry overnight in a biosafety cabinet and stored at −20°C prior to further sample processing.

2.16 High-density culture mass spectrometry sample preparation

Prior to trypsination, plates were removed from −20°C and allowed to reach room temperature for 20 min. Decellularized protein was dissolved in 75 μL of 6 M urea with 2.75 μL of 200 mM dithiothreitol (DTT) and incubated for 1 h at room temperature. Then, 15 μL of 200 mM iodoacetamide was added

to each well, contents were thoroughly mixed, and samples were incubated for 1 h at room temperature in the dark. An additional 15 µL of DTT was added to each well, contents were thoroughly mixed, and samples were incubated for 1 h at room temperature in the dark. Samples were then quenched with 340 µL of 1 mM calcium chloride and for the optimal trypsin activity sample pH was adjusted to 7.8–8.7 with sodium hydroxide. 5 µL of 1 µg/µL Trypisn Gold, Mass Spectrometry Grade (Promega) was added to the wells, and samples were incubated for 24 h at 37°C. The next day, the peptide solution was transferred from the well plate to Eppendorf LoBind microcentrifuge tubes, frozen at −80°C for at least 3 h, and lyophilized overnight.

Protein purification was performed using the ZipTip C18 protocol. Lyophilized samples were reconstituted in reconstitution solution (5:95 Acetonitrile [ACN]:H2O, 0.1% trifluoroacetic acid [TFA]) and pH was adjusted to be less than 3 using 10% TFA. ZipTipsC18 were hydrated by aspirating and expelling hydration solution (50:50 ACN:H2O, 0.1% TFA) from the ZipTipC18 twice followed by hydration using the wash solution twice (0.1% TFA in H2O). Samples were loaded into the ZipTipsC18 by aspirating and expelling the reconstituted sample from the ZipTipC18 six times. Then, samples were desalted by washing three times with wash solution (0.1% TFA in water). Purified proteins were eluted into an Eppendorf LoBind microcentrifuge tube containing elution solution (60:40 ACN:H2O, 0.1% TFA). Eluted samples were frozen, lyophilized, and stored at −80°C prior to further analysis.

2.17 Mass spectrometry data acquisition, processing, and analysis

Decellularized high-density fibroblast purified proteins were reconstituted and analyzed using 1D capillary mass spectrometry on the Thermo Orbitrap Velos. Raw mass spectrometry data were processed using Proteome Discoverer 2.5 Software human UniProt dabatase. Any proteins detected from cellular debris were excluded, and proteins with a sum of posterior error probability (PEP) score less than 2 were excluded to minimize false positive protein detection. Label-free quantification methods were used to determine the relative abundance of individual ECM proteins as well as the abundance ratio of each ECM protein using VICs as the numerator and LVCFBs as the denominator. A *p*-value for each abundance ratio was calculated to determine if the protein is either present in increased or decreased abundance in the VIC samples as compared to the LVCFBs.

2.18 Statistics and experimental replication

For primary cell experiments, three donors were identified (ages 33, 34 and 39) and left ventricular cardiac fibroblasts and VICs were isolated from the same hearts. Unless otherwise noted, experiments contained at least three technical replicates. Mean and standard deviation bars are plotted in gray in the figures. Statistics were performed in JMP Pro V15 using a paired Student's *t*-test, ANOVA, or ANOVA with Tukey's *post hoc* test.
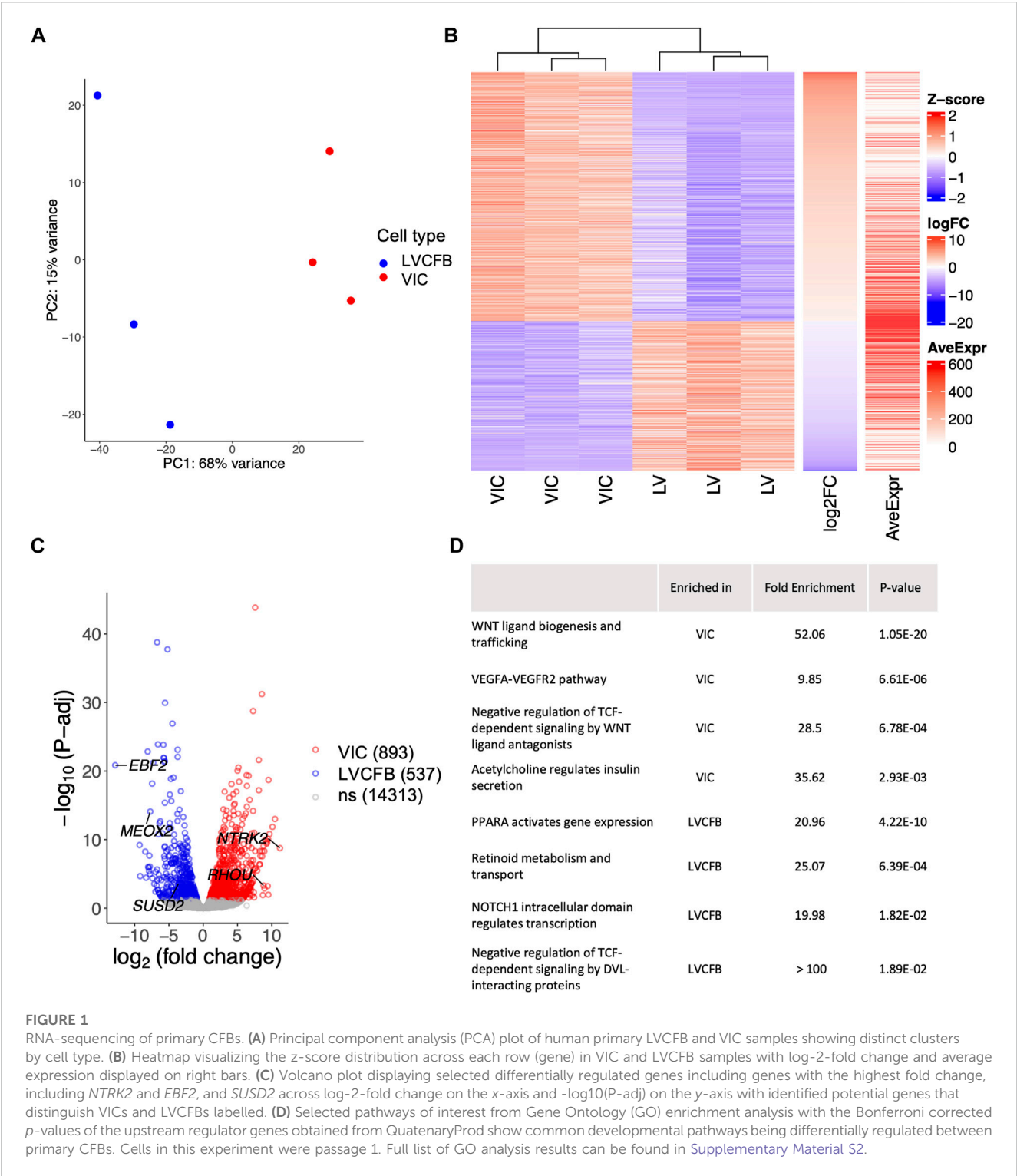
3 Results

3.1 Molecular characterization of primary CFBs reveals distinct CFB signatures

To investigate differences in fibroblast marker expression between VICs and LVCFBs, we isolated paired samples from 3 donors (Supplementary Table S1). We then verified expression of CFB surface and internal protein markers by flow cytometry and immunofluorescence staining. Flow cytometry results showed similar expression of CD90, fibronectin (FN), vimentin (VIM), and TE7 in both primary CFB populations (Supplementary Figure S1). Immunofluorescence staining also showed similar overall expression of fibroblast specific protein 1 (FSP1), TE7, VIM, collagen type 1 alpha 1 chain (COL1A1, and FN in both populations (Supplementary Figure S2). SUSD2 has been previously identified as enriched in left ventricular cardiac fibroblasts compared to dermal fibroblasts (Schmuck et al., 2021). Interestingly, SUSD2 protein expression was only observed in the LVCFBs while minimal expression was observed in the VICs by Western blotting, suggesting that these two populations have unique molecular signatures and SUSD2 can be used for distinguishing between the two CFB populations (Supplementary Figure S3).

In vitro, these two CFB populations had similar growth rates when cultured on uncoated tissue culture plastic in a low glucose maintenance medium (Supplementary Figure S4). To assess differences in morphology, we stained CFB filamentous actin with phalloidin and performed blinded image analysis on four well replicates per donor. We observed a larger cell area, perimeter, and increased circularity in the VICs compared to the LVCFBs (Supplementary Figure S4B–E). However, we observed a larger median forward scatter area in the LVCFBs compared to the VICs (Supplementary Figure S1) suggesting that the VICs exhibit a greater degree of spreading when plated than LVCFBs.

3.2 Bulk transcriptomics reveal differential genes between LVCFBs and VICs

To assess transcriptional differences between VICs and LVCFBs, we collected mRNA from paired donor samples and performed bulk RNA sequencing. Analysis of variance shows the two cell types clustered distinctly (Figure 1A). To identify the top differentially expressed genes driving this variance, we performed multi-factor DESeq2 to account for matched donor samples and added a threshold of p-adjusted<0.05, identifying 1,430 genes significantly differentially expressed between the VIC and LVCFB samples (Figure 1B). We then sorted the matrix by log-2-fold change and chose top genes that had high average expression and low variability in TPM values between donors to predict marker genes of each cell type (Figure 1C). Interestingly, we identified that Mesenchyme Homeobox 2 (*MEOX2*), a transcription factor that regulates transition from myofibroblasts to fibroblasts (Cunnington et al., 2014), and EBF Transcription Factor 2 (*EBF2*), a transcription factor highly expressed in the heart, were enriched in LVCFBs compared to VICs. We identified *NTRK2* and Ras Homolog Family Member U (*RHOU*) as enriched in VICs compared to LVCBs. *In vivo*, *RHOU* is expressed in the atrioventricular canal during heart development

FIGURE 1
RNA-sequencing of primary CFBs. **(A)** Principal component analysis (PCA) plot of human primary LVCFB and VIC samples showing distinct clusters by cell type. **(B)** Heatmap visualizing the z-score distribution across each row (gene) in VIC and LVCFB samples with log-2-fold change and average expression displayed on right bars. **(C)** Volcano plot displaying selected differentially regulated genes including genes with the highest fold change, including *NTRK2* and *EBF2*, and *SUSD2* across log-2-fold change on the *x*-axis and -log10(P-adj) on the *y*-axis with identified potential genes that distinguish VICs and LVCFBs labelled. **(D)** Selected pathways of interest from Gene Ontology (GO) enrichment analysis with the Bonferroni corrected *p*-values of the upstream regulator genes obtained from QuatenaryProd show common developmental pathways being differentially regulated between primary CFBs. Cells in this experiment were passage 1. Full list of GO analysis results can be found in Supplementary Material S2.

and loss of *RHOU* was shown to cause cardiac looping defects (Dickover et al., 2014).

These genes were validated using RT-qPCR (Supplementary Figure S3B) and we identified *MEOX2* and *EBF2* to be expressed at a greater level in LVCFBs than in VICs. Although the expression levels of *NTRK2* and Ras Homolog Family Member U (*RHOU*) were higher in VICs compared to LVCFBs, we did not

observe a statistically significant difference to demonstrate utility as a univariate marker. However, when the ΔCt values were analyzed using a multivariate correlation analysis (Supplementary Figure S3C), we observed that paired groups of two genes (*EBF2* and *RHOU*, or *MEOX2* and *RHOU*) were statistically significant, suggesting they can be used collectively for distinguishing between VIC and LVCFB subpopulations. To
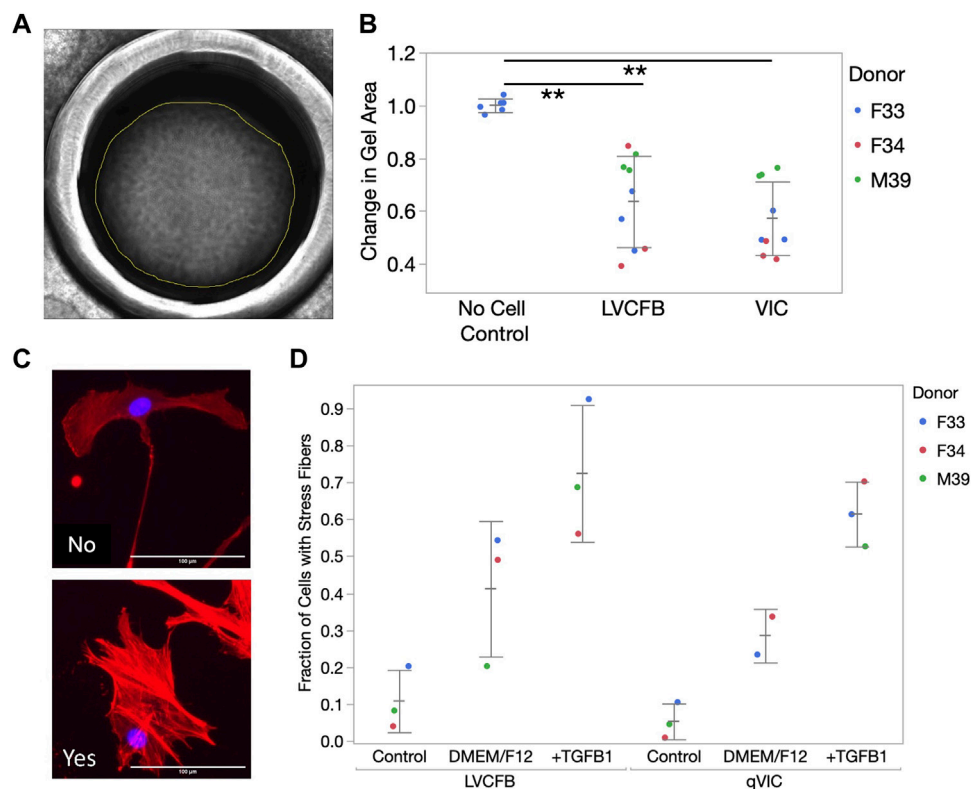
FIGURE 2
CFB contraction and stress activation. **(A)** CFB contractility was assayed through collagen gel contraction using passage 3 LVCFBs and VICs. Example brightfield image of collagen gel 24 h post-seeding. Gel area was analyzed using ImageJ. **(B)** Quantification of collagen gel contraction; gel areas with samples were normalized to an averaged area of control gels lacking cells at 24 h. Dots represent 3 wells and color represents donor. Statistics are a two-way ANOVA with Tukey's *post hoc* test where * is $p < 0.05$ and ** is $p < 0.01$. **(C)** Primary CFB stress activation potential measured by treatment of passage 4 cells with control primary CFB maintenance medium, DMEM/F12 medium, or DMEM/F12 medium supplemented with 10 ng/mL TGFβ1. Example images of cells stained for phalloidin (red) and Hoechst (blue) that were categorized as containing stress fibers (yes) or not containing stress fibers (no). Scale bar is 100 μm. **(D)** Quantification of fraction of cells containing stress fibers. Dots represent the percentage of cells for each sample with 20–750 cells per condition and color represents the donor. Statistics are a four-way ANOVA on donor, cell source, medium, and cell source cross medium. Statistically significant increase in percentage cells with filaments in different medium ($p < 0.05$) but no difference in stress activation potential was observed between LVCFBs and VICs ($p > 0.05$).

validate these marker genes, we assessed their expression in publicly available single cell and bulk RNA sequencing datasets that profiled VICs and LVCFBs (Supplementary Figure S5) (Zhang et al., 2019; Tucker et al., 2020; Floy et al., 2021; Decano et al., 2022; Wang et al., 2022). We found that VICs exhibit low expression ratios of *EBF2/RHOU* and *MEOX2/RHOU* compared to LVCFB. From the single nuclei RNA sequencing results, we observed heterogeneity in the expression levels of *EBF2/RHOU* and *MEOX2/RHOU* across the different myocardial fibroblast clusters (Supplementary Figure S5F), but these ratios were consistently higher than the VIC population expression, further supporting that these genes can be used as transcriptional markers between VICs and LVCFBs in human samples.

To explore pathways that regulate the differentially expressed genes in VICs and LVCFBs, we performed QuaternaryProd analysis to predict upstream regulators of the differentially expressed genes. We identified a list of upregulated and downregulated regulator genes in VICs compared to LVCFBs (Supplementary Material S2) and performed GO enrichment analysis. We list selected biological processes in Figure 1D

(full list available in Supplementary Material S2). Of note, key pathways involved in developmental regulation, including WNT, VEGF and NOTCH were identified.

3.3 Functional characterization of primary CFBs reveals distinct CFB signatures

3.3.1 FB activation and collagen contraction assays reveal similar activation and contraction potential in LVCFBs and VICs

We predicted that VICs and LVCFBs would have distinct functional properties, including contraction, activation, and mineralization potential due to their different niche environments *in vivo*. Contraction capability was assessed using a collagen gel assay. One day after seeding collagen gels in primary CFB maintenance medium, VIC and LVCFB-containing gels were smaller than no cell control gels, but there was no difference in contraction between gels seeded with the fibroblast populations (Figures 2A, B). To assess activation
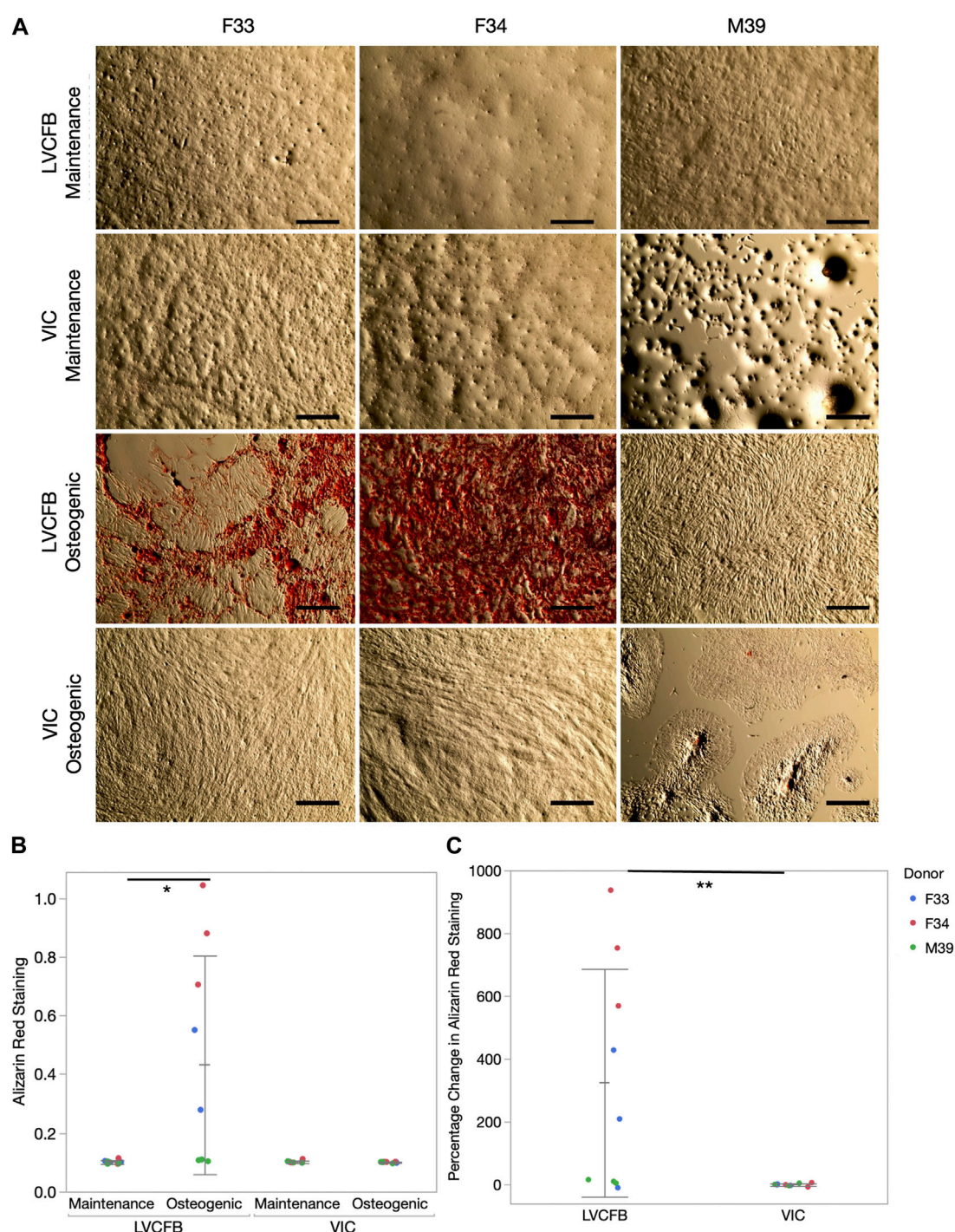
FIGURE 3
Alizarin red mineralization staining of primary CFBs. **(A)** Brightfield images of primary CFBs (passage 4) stained with Alizarin Red after 4 weeks of treatment with maintenance or osteogenic medium. Images shown are representative of three well replicates. Scale bar is 250 μm. **(B)** Quantification of Alizarin red staining by measuring absorbance at 560 nm. Dots represent three well replicates and donors are represented by color. Statistics are a two-way ANOVA on media controlling for donor where * is $p < 0.05$. **(C)** Percentage change in Alizarin Red staining comparing osteogenic to maintenance medium where dots represent three well replicates and donors are represented by color. Statistics are a two-way ANOVA on cell source controlling for donor where ** is $p < 0.01$.

potential, we treated CFBs with maintenance medium, DMEM/F12, or DMEM/F12 with 10 ng/mL TGFβ1 for 2 days and then stained with phalloidin to identify formation of actin stress

fibers. We acquired three images per well with four technical well replicates per given cell type from a donor. Using blinded image analysis, we classified whether each cell contained stress
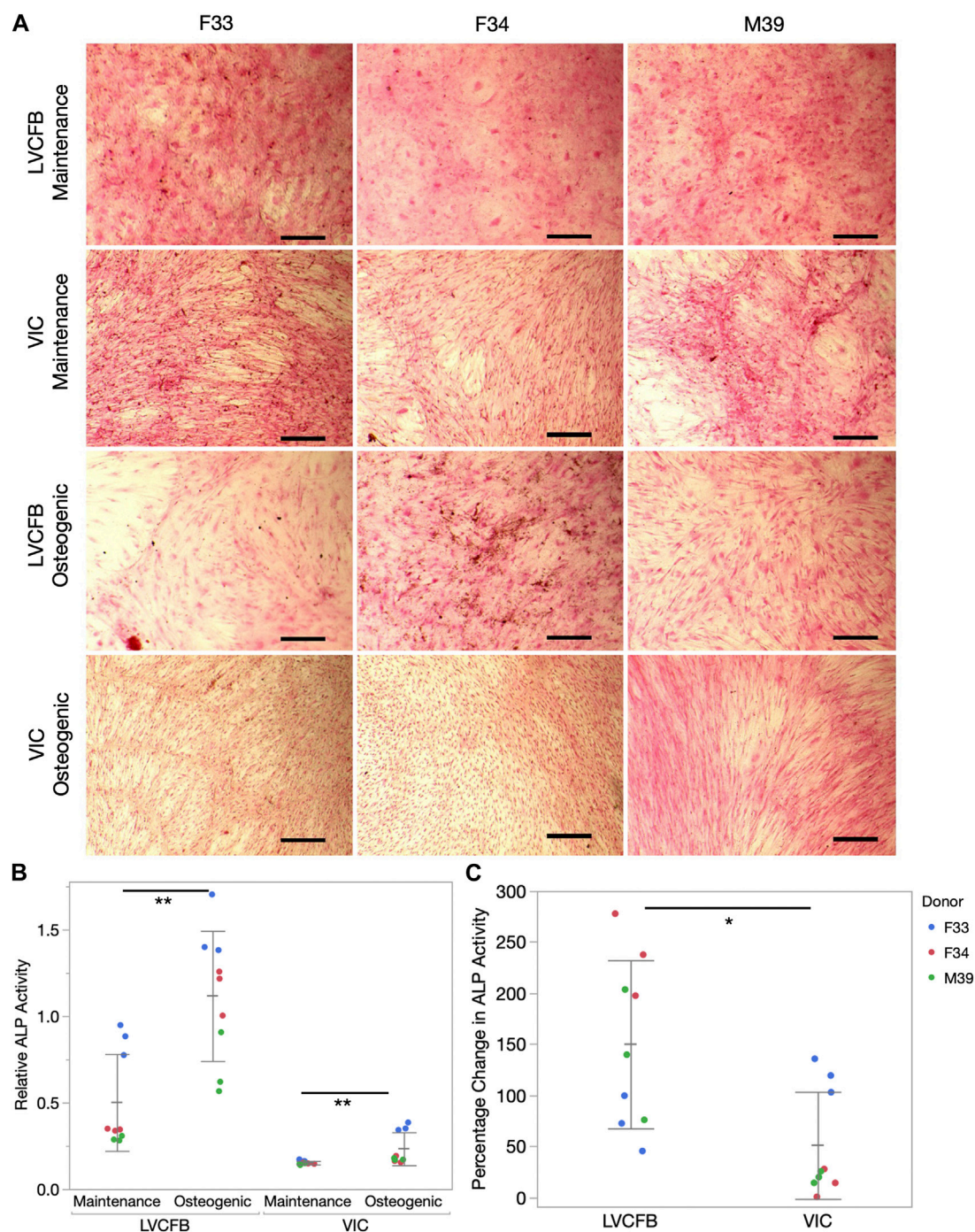
FIGURE 4
Calcification of primary CFBs. Primary CFBs (passage 4) were treated with maintenance or osteogenic medium for 4 weeks. **(A)** Von Kossa and Nuclear Fast Red Staining of primary CFBs. Calcium in mass deposits are black, calcium in dispersed deposits are gray, nuclei are red, and cytoplasm is light pink. Images are representative of three well replicates and scale bar is 100 μm. **(B)** Relative ALP activity in primary CFBs is quantified by measuring absorbance at 405 nm. Dots represent well replicates and color represents donor. Statistics are a two-way ANOVA for medium controlling for donor where * is $p < 0.05$ and ** is $p < 0.01$. **(C)** Percentage change in relative ALP activity between maintenance to osteogenic medium. Dots represent well replicates and color represents donor. Statistics are a two-way ANOVA for cell source controlling for donor where * is $p < 0.05$.

fibers and performed statistics on the averages for each donor. We observed increased stress fiber formation in DMEM/F12 compared to control maintenance medium and further increases upon addition of TGFβ1 in both cell types, however we did not observe a difference in

activation potential between the two CFB populations (Figures 2C, D). Overall, this suggests that LVCFBs and VICs have a similar contraction potential and activation response to stress conditions induced by DMEM/F12 and TGFβ1.

3.3.2 CFB mineralization reveals greater potential in LVCFBs compared to VICs under metastatic conditions

Pathologically, mineralization has been associated with valvular, coronary artery and conduction system disease, however recent studies have suggested that mineralization can also occur in the myocardium (Ahmed et al., 2020). CFBs isolated from human and mouse tissues have been shown to mineralize *in vitro* upon exposure to osteogenic medium, and *in vivo* mouse CFB calcification is thought to be regulated by the ENPP1-PPi-Pi axis (Pillai et al., 2017). Thus, we hypothesized that VICs and LVCFBs might have different mineralization potential *in vitro*.

We treated LVCFBs and VICs at approximately 80%–90% confluency with primary CFB maintenance medium or osteogenic medium containing ascorbic acid, β-glycerophosphate, and dexamethasone. After 4 weeks, we stained for Alizarin red to detect mineralization, stained for von Kossa to detect calcification, and performed an ALP activity assay. We observed increased Alizarin red staining in the LVCFB treated with osteogenic medium compared to primary CFB maintenance medium (Figures 3A, B). We observed large donor-to-donor variability with the male M39 LVCFBs having minimal Alizarin Red staining, but due to sample size, we cannot conclude if this is due to donor-to-donor differences or sex-related differences. Furthermore, no difference in Alizarin red staining was observed in the VICs between the two medium conditions. Additionally, the LVCFBs exhibited a greater percentage change in Alizarin red staining upon osteogenic medium treatment compared to the VICs (Figure 3C). Similarly, we observed some von Kossa staining in LVCFB treated with osteogenic medium with minimal staining in all other conditions including VICs (Figure 4A) suggesting that the LVCFBs demonstrated higher mineralization and calcification potential compared to VICs.

To further assess if VICs could respond to the osteogenic medium, we assayed for alkaline phosphatase (ALP) activity which is an early mineralization marker. We observed increased relative ALP activity in the LVCFBs and VICs after exposure to the osteogenic factors (Figure 4B) and a greater percentage change in ALP activity in the LVCFBs compared to the VICs (Figure 4C). This suggests that LVCFBs exhibited greater mineralization potential in this experimental model compared to VICs supporting our hypothesis that CFBs from different regions of the heart have distinct functional phenotypes.

3.3.3 CFB mineralization reveals greater potential in LVCFBs compared to VICs under dystrophic conditions

We hypothesized that the increase in LVCFB mineralization potential compared to VICs may indicate that VICs needed to undergo an intermediate stress activated state before calcification (metastatic calcification) whereas the LVCFBs may not need to be activated for higher mineralization (dystrophic calcification) (Cirka et al., 2017; Pillai et al., 2017; Li et al., 2021). To test this, we treated wells with or without activation medium containing 10 ng/mL TGFβ for 3 days before switching to osteogenic medium (Figure 5A). We confirmed cells were activated by observing higher α-SMA expression in both CFB subpopulations treated with activation media (Figures 5B, C).

Similar to data shown in Figures 4B, C, we found relative and percent ALP from control to be increased in metastatic conditions for both primary CFB populations (Figure 5D). Here, we observed a statistically significant increase in ALP activity for VICs when they were activated before treating with osteogenic factors compared to metastatic conditions. In comparison, there was no statistical difference between metastatic and dystrophic conditions for LVCFBs. This suggests that VICs are more sensitive to stress-activated dystrophic early calcification compared to LVCFBs.

3.3.4 Mass spectrometry of ECM reveals the distinct matrix composition of LVCFB and VICs is consistent with the cells' regional phenotypic function

Since LVCFB and VIC populations support different regions of the heart that have different structure and function, we hypothesized that these cell types would secrete different ECM profiles in concordance with their roles. To test this on a protein level, we cultured LVCFBs and VICs at a high density for 16 days. On day 16, we decellularized the matrices, harvested the ECM, and performed mass spectrometry to identify and analyze relative and secreted factors. Detected proteins were sorted into ten categories; remodeling, matricellular, linking, fibrillar, fibril associated, elastin and elastin associated, cytokines, clotting, basement membrane and apolipoproteins (Supplementary Material S3). The relative abundance ratio was used to determine whether each protein was more abundant (ratio > 2.0), of similar abundance (ratio from 0.5 to 2.0), or less abundant (ratio < 0.5) in VICs compared to LVCFBs (Figure 6A). Broadly, VICs had a lower deposition of linking, basement membrane proteins, and fibrillar collagens than LVCFBs. There was a slight increase in the abundance of proteins in the elastin and elastin-associated, clotting, and apolipoprotein categories in the VICs compared to the LVCFBs. Remodeling, matricellular and cytokine subclasses had various proteins that were differentially produced between both populations. Hierarchical clustering of the relative abundance of each protein for each donor determined that VIC and LVCFB matrices clustered distinctly from each other irrespective of donor (Figure 6B). Notably, the male VIC matrices and LVCFB matrices clustered distinctly from the female lines but additional donors would be needed to determine if these differences are due to sex-differences or donor related differences.

Of the 107 proteins detected, 32 had a VIC/LVCFB abundance ratio that was statistically decreased in abundance ($p < 0.05$) and only 6 were increased in abundance in the VICs, including alpha-2-antiplasmin, plasminogen, epidermal growth factor-like protein 7, cartilage oligomeric matrix protein, alpha-2-HS-glycoprotein, and inter-alpha-trypsin inhibitor heavy chain H4 (Figure 6C). This potentially indicates that fibroblasts that occupy the heart chamber play a larger role in ECM production and remodeling then valve fibroblasts in adulthood. The fibrillar collagens I and III, which are prevalent in the heart and play a role in maintaining the mechanical integrity of the ventricle were present in larger abundances in the LVCFB samples than the VIC samples
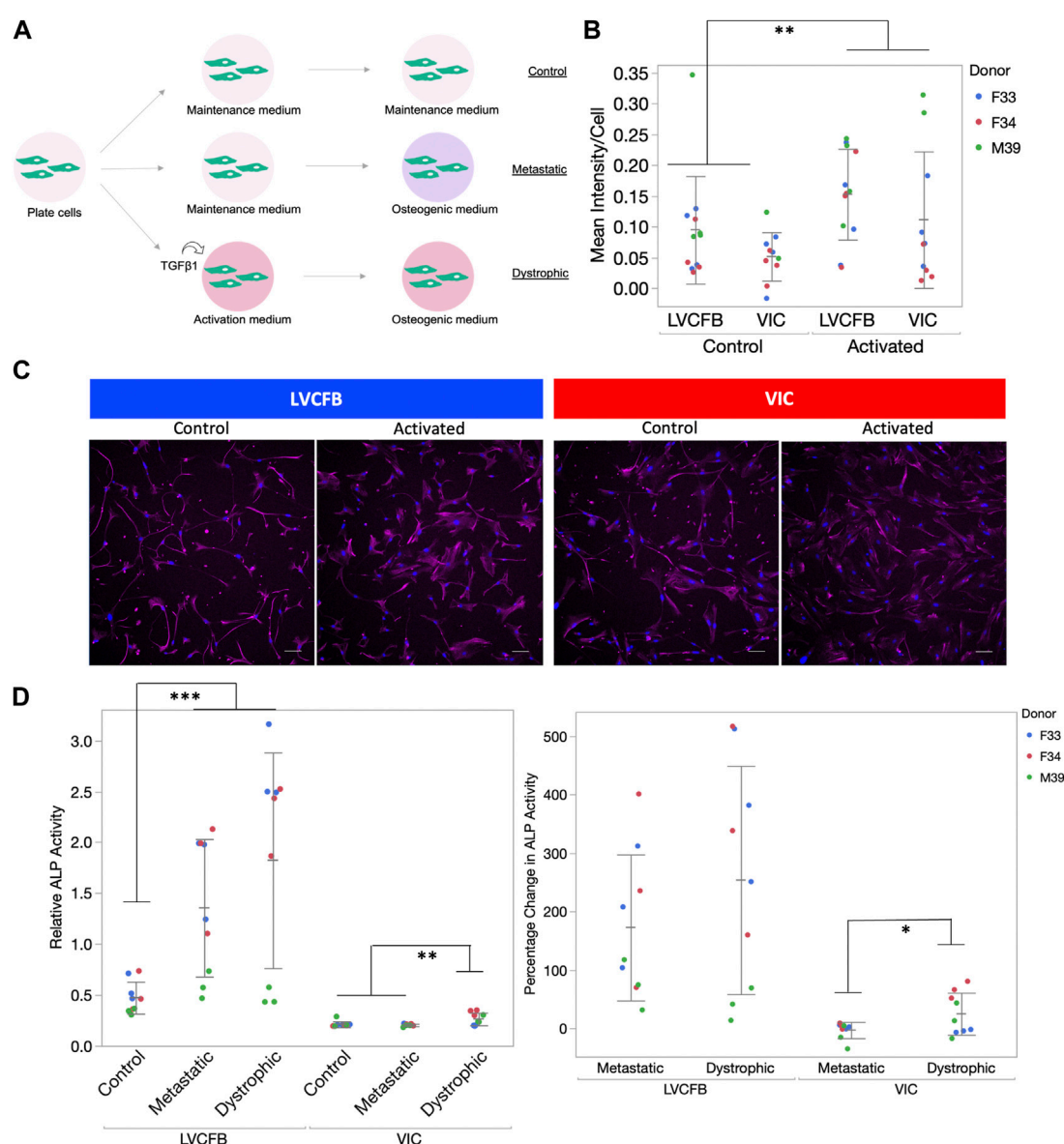
FIGURE 5
Calcification of primary CFBs post-activation. **(A)** Schematic showing experimental setup. Primary CFB samples (passages 5 and 6) were either pre-treated with activation medium or maintained in CFB maintenance medium prior to mineralization activation to mimic dystrophic and metastatic mineralization. **(B)** Quantification of αSMA immunocytochemistry (ICC) staining of cells after 3 days in activation medium. Graph is image αSMA mean intensity minus background normalized by number of nuclei. Dots represent well replicates and color represents donor. **(C)** Example ICC images used for quantification in B. Magenta is anti-αSMA antibody and blue is Hoechst stain. Scale bar is 100 μm. **(D)** Left: Relative ALP activity for primary CFBs upon activation. Dots represent well replicates and color represents donor. Right: Percentage change in relative ALP activity of metastatic and dystrophic compared to control. Dots represent well replicates and color represents donor. Statistics are a two-way ANOVA for cell source controlling for donor where * is $p < 0.05$, ** is $p < 0.01$, and ***is $p < 0.005$.

(Brower et al., 2006). Additionally, the key remodeling protein, lyse oxidase homolog 2, which is important in fibrillar collagen fibril formation was also significantly upregulated in LVCFB matrices compared to VIC matrices (Rodríguez and Martínez-González, 2019). Other notable differences include the increased presence of fibronectin and periostin ECM proteins in the LVCFBs compared to VICs; both proteins play important roles in heart development and injury response (George et al., 1993; Konstandin et al., 2013; Landry et al., 2017).

4 Discussion

CFBs play a crucial support role in the heart by producing and organizing extracellular matrix, secreting paracrine factors, interacting with other cell types, and responding to stress stimuli. Developmental lineages and differences in the local environmental niche are thought to lead to CFB specification resulting in molecular and functional phenotypical differences in different regions of the heart. Tissue level specification may be a driver in regional-specific
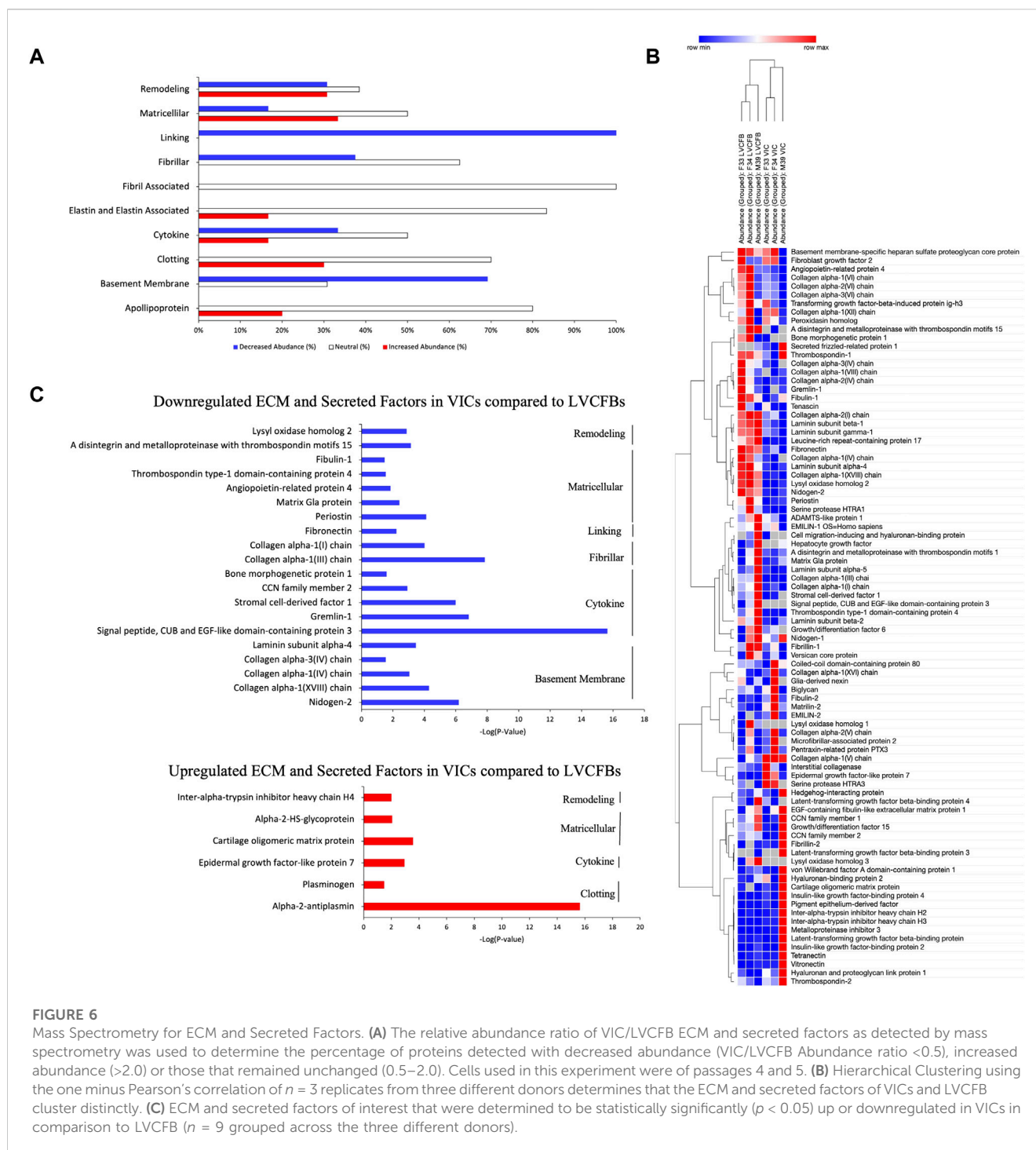
FIGURE 6
Mass Spectrometry for ECM and Secreted Factors. **(A)** The relative abundance ratio of VIC/LVCFB ECM and secreted factors as detected by mass spectrometry was used to determine the percentage of proteins detected with decreased abundance (VIC/LVCFB Abundance ratio <0.5), increased abundance (>2.0) or those that remained unchanged (0.5–2.0). Cells used in this experiment were of passages 4 and 5. **(B)** Hierarchical Clustering using the one minus Pearson's correlation of *n* = 3 replicates from three different donors determines that the ECM and secreted factors of VICs and LVCFB cluster distinctly. **(C)** ECM and secreted factors of interest that were determined to be statistically significantly (*p* < 0.05) up or downregulated in VICs in comparison to LVCFB (*n* = 9 grouped across the three different donors).

patient pathology and since some CFBs in the valve and most CFBs in the myocardium arise from epicardial lineages, learning the differences between regional tissues and developing protocols to specify cell types can shed light onto disease mechanism and help develop better therapeutics (Sun et al., 2013; Moore-Morris et al., 2014; Liu et al., 2018).

In this study, we compared molecular and functional attributes between three paired samples of human VICs and LVCFBs. We

identified that the VICs exhibited a larger cell area, perimeter, and circularity compared to the LVCFBs. We found that both populations stained positive for common cardiac fibroblasts markers and displayed similar stress fiber activation potential and collagen gel contraction, indicating that LVCFBs and VICs possess some similar attributes.

We identified that the LVCFBs expressed SUSD2, a novel cultured CFB marker (Schmuck et al., 2021), while the VICs did

not. Furthermore, from our bulk RNA-sequencing results, we identified a panel of genes, *RHOU*, *MEOX2*, and *EBF2* to distinguish between VICs and LVCFBs at a transcript-level. *MEOX2* is a transcription factor that decreases in expression during conversion of fibroblasts to myofibroblasts. Its lower expression in VICs compared to LVCFBs could indicate a difference in the susceptibility of VICs to myofibroblast activation. Not much is known about the role of *EBF2* in cardiac tissue development or homeostasis. *In vivo*, *RHOU* is expressed in the atrioventricular canal during heart development and loss of *RHOU* was shown to cause cardiac looping defects (Dickover et al., 2014). Furthermore, *RHOU* expression is regulated by Wnt1 (Tao et al., 2001) and Wnt2 signaling (Dickover et al., 2014) both of which were enriched upstream regulators in the VICs compared to LVCFBs. To further test these markers, we compared expression of these genes in publicly available bulk and single cell RNA sequencing datasets (Zhang et al., 2019; Tucker et al., 2020; Floy et al., 2021; Decano et al., 2022; Wang et al., 2022). We show our marker genes show similar trends in these datasets, as our calculated *EBF2/RHOU* and *MEOX2/RHOU* ratios are consistently low in the VIC datasets and high in the LVCFB datasets. These fold-level statistically significant differences in transcriptional expression show robust validation of these genes as a method to identify regional specification of these subpopulations.

Since assessment of these markers at the protein level would be useful in discriminating fibroblast populations, we attempted to validate expression of EBF2, RHOU2, and MEOX2 in both primary human LVCFBs and VICs, and in primary porcine tissue samples of the left ventricle and aortic valves *via* immunostaining and Western blotting. However, the antibodies we were able to obtain provided no signal in samples or positive controls, or exhibited high non-specific background (e.g., signal in negative controls or non-nuclear signal) It is possible that since these genes encode transcription factors, their low protein levels may not make them suitable targets for protein-level discrimination. Based on these results, we cannot currently validate the ability of proteins encoded by *EBF2*, *RHOU2*, and *MEOX2* to discriminate between LVCFs and VICs, but identification of proteins that can discriminate between fibroblast populations would facilitate analytic efforts to assess fibroblast identity and heterogeneity.

Since calcification is a significant problem in valve disease pathology, we were surprised to find LVCFBs exhibited higher mineralization and calcification potential compared to VICs. However, in a dystrophic condition, activated VICs displayed increased ALP activity compared to a metastatic condition, whereas LVCFBs displayed similar ALP activity regardless of an intermediate activated stressed state, indicating these fibroblast subpopulations may differ in mechanism of early calcification. Understanding the differences in calcification mechanism may provide an avenue for development of regional pathology specific anti-calcification drugs. To note here, we consider the VICs used in this study to be mostly quiescent as observed through morphology and low fraction of cells exhibiting stress fibers. Additionally, we used a medium formulation that has been shown to keep VICs cells in a quiescent phenotype (Porras et al., 2017). Cells in the calcification post-activation experiment expressed aSMA in the control condition which could indicate a stress response to a higher passage number. However, since there was a significant

difference in aSMA expression between control and activated conditions, we can conclude the VICs were responsive to activation stimuli.

We compared ECM protein synthesis between VICs and LVCFBs using mass spectrometry and found that VICs secreted less ECM proteins compared to ventricular CFBs. In fact, only 6 proteins were significantly increased in abundance in the VIC samples and they belonged to clotting, cytokine, matricellular and remodeling subclasses. While our mass spectrometry results included proteins reported to be found in valves such as collagen type I and III or periostin (Lockhart et al., 2011; Wiltz et al., 2013), we found that their abundance in LVCFB matrices was much greater than in VIC matrices. These give an insight into functional necessity as collagen fibers mainly function for tensile strength and flexibility, and since the left ventricle experiences the highest systolic pressure, this could explain the increased secretion by ventricular CFBs compared to valve CFBs (Wiltz et al., 2013). Similarly, periostin has been shown to promote cardiomyocyte proliferation after injury and this function is useful in the myocardium (Polizzotti et al., 2012). Cartilage oligomeric protein (COMP) and alpha 2-Heremans-Schmid glycoprotein (AHSG) were among the 6 VIC upregulated proteins. COMP has been reported to be expressed higher in calcific valve samples near calcific nodules in calcific aortic valve disease patients (Xu et al., 2021) and AHSG was shown to be an inhibitor of ectopic calcification (Schäfer et al., 2003). Furthermore, we also found some previously identified valve ECM proteins, including hyaluron-1 and fibrillin-2, to have a VIC/LVCFBs abundance ratio greater than 1, but these showed variability in magnitude between donor samples (*p*-values 0.25 and 0.77 respectively) (Lockhart et al., 2011; Wiltz et al., 2013).

Cellular sex is important to consider in basic cardiac research (Ventura-Clapier et al., 2017) and may play a key role in CFB specification. For example, porcine VICs have sex-dependent angiogenic secretion profiles (Nelson et al., 2021) and mice have sex-dependent fibrosis pathologies (Achkar et al., 2020). Furthermore, clinical differences in valve calcification between sexes have been reported and has been a recent interest in the field (Myasoedova et al., 2020; Aguado et al., 2022). We observed our 2 female donors clustered together in the mass spectrometry results regardless of cell type, but due to sample size limitations, we are unable to ascertain how sex differences affect ECM secretion in this study. Additional limitations of our study regarding donor samples include similar age and a history of hypertension. All three donors in this study were of similar young age (33, 34, and 39 years old) and while these patients were considered healthy, they had a previous history of hypertension. We need to consider that some findings of this study may differ with older donors or patients without hypertensive history. To test if these limitations affected the expression of identified marker genes, we first compared the *EBF2/RHOU* and *MEOX2/RHOU* ratios between cultured human fetal and adult ventricular CFBs from a publicly available RNA sequencing dataset (Floy et al., 2021) to assess the effect of developmental stage. Here, we noted no statistical differences between the fetal and adult groups suggesting these gene expression ratios are not age dependent (data not shown). To test if these gene expression ratios are dependent on a diseased state, we compared these ratios from a single cell study using ventricular and intraventricular septum cells from mice

undergoing sham and MI-induced surgery procedures (Farbehi et al., 2019). Here, we obtain four fibroblast clusters, and we found the *MEOX2/RHOU* and *EBF2/RHOU* TPM averages in a sham, 3 days post-surgery and 7 days post-surgery conditions were 4.2, 5, and 2.2 respectively for *MEOX2/RHOU* and 1.5, 2.2, and 0.8 respectively for *EBF2/RHOU* (data not shown). The dropouts in the single cell RNAseq datasets suggest low expression or insufficient sequencing depth, but this variability in expression ratios between days 3 and 7 post-surgery suggest these markers may be dependent on recovery processes following MI. However, this needs to be further studied.

Human pluripotent stem cells (hPSCs) provide an alternative to primary cells for *in vitro* modeling and *in vivo* cell therapy applications. Due to the small amount of tissue present in the valves, isolating human VICs can be difficult as living heart tissue is hard to obtain in adults and nearly impossible to obtain in early stages of development (Scott et al., 2021). Human VICs and LVCFBs have limited expansion capability and maintaining VICs in a quiescent state has previously been a major hurdle for the field (Latif et al., 2015; Porras et al., 2017). hPSC sources offer a greater potential for manipulation, improved consistency between experiments, recapitulation of early development and early onset of disease states. However, little is known about regional specificity of fibroblasts differentiated from hPSCs (Floy et al., 2021). Findings from this study could inform methods to generate human stem cell-derived VICs or LVCFBs.

We have previously reported a protocol to generate hPSC-derived epicardial cells and their subsequent differentiation to hPSC-derived cardiac fibroblasts (EpiC-CFBs) (Floy et al., 2021). In addition, we have characterized the differences between hPSC-derived epicardial and second heart field-derived fibroblasts (SHF-CFBs) (Floy et al., 2021). Fibroblasts generated from both protocols expressed characteristic fibroblast markers and had unique gene expression signatures, assessed by bulk RNAseq (dataset available at GSE168380) (Floy et al., 2021). When we compared TPM values of the differentially expressed genes between VICs and LVCFBs in the hPSC-CFBs against the primary ventricular CFBs collected in this dataset, we find that both hPSC-derived cell populations expressed significantly lower TPM values compared to adult ventricular CFBs for the two transcriptional LVCFB markers, *MEOX2* and *EBF2* and higher expression of *RHOU* on a transcript-level compared to adult ventricular CFBs, more consistent with primary VICs than LVCFBs. This transcript level difference could suggest that current hPSC-CFBs protocols generate cells that may be VIC-like. To test proteomics, we combined mass spectrometry data from the previous study Floy et al., 2021) and this one and compared the ratio of protein expression between primary and hPSC-derived CFBs. A limitation of this analysis is that culture conditions and experimental procedure between these two studies were different and this could impact this comparative analysis. We found proteomics did not reveal a bias of hPSC-derived CFB identity toward either primary cell type (Supplementary Material S4). This could indicate that both current protocols generate hPSC-derived CFBs that may lean toward VIC-like on a transcriptional basis, but further manipulation is required to make these cell region-specific.

Identifying fate specifying pathways is a critical step in generating region-specific cells. Here, identified upstream

regulators of the list of differentially expressed genes using QuartneryProd analysis with the GO database to identify differential pathways between VICs and LVCFBs. We identified various cardiac developmental pathways, including VEGF and WNT, which were enriched among the VIC upstream regulators, and the NOTCH pathway was enriched among the LVCFB upstream regulators. Multiple canonical and non-canonical Wnt pathways are involved in endothelial-to-mesenchymal (EndoMT) transition, proliferation of the endocardial cushion stage in development and in osteoblast differentiation (Alfieri et al., 2010). In adults, Wnt pathways are involved in regulating fibrosis and are quiescent until they are reactivated in various cardiac diseased conditions (Dawson et al., 2013). In the valves, Wnt upregulation has been shown to worsen pathogenesis of aortic valve stenosis (Khan et al., 2020). VEGF signaling is involved in EndoMT in the outflow tract regions and through VEGFR2 is involved in the maturation of atrioventricular cushions into leaflets (Stankunas et al., 2010). In adults, VEGF was shown to be involved in vascular homeostasis and to promote angiogenesis in myocardial infarcted rats (Lee et al., 2007; Lv et al., 2018), but little is understood about its role in adult valves apart from its significance in development. During valve formation, Notch signaling activates the epithelial-to-mesenchymal transition and mutations results in defective valves (MacGrogan et al., 2011). Furthermore, suppression of Notch signaling has been shown to increase calcific nodules in VIC cultures suggesting a homeostatic role in adulthood (Nisham and Srivastava, 2009). The Notch signaling pathway is also involved in fibrosis, cardiac hypertrophy, and regenerative process after injury (Nemir et al., 2014; Nistri et al., 2017). These critical pathways have been leveraged to generate valve endothelial cells and subsequently VICs from hPSCs in a previous study by treating cardiac progenitor cells with VEGF, TGFβ1, BMP4, and bFGF (Cheng et al., 2021) and may be promising to explore in generating a differentiation protocol from hPSC-derived epicardial cells to VICs.

In summary, CFB subtype specification highlights the diversity and complexity of cardiac cell subpopulations. By directly comparing CFBs isolated from the left ventricle and the aortic heart valve, we have identified key molecular and functional phenotypes which can be used to further understand regional disease pathology.

Data availability statement

The RNA sequencing data presented in the study are deposited in the Gene Expression Omnibus (GEO) repository, accession number GSE218251.

Author contributions

MF: Conceptualization, formal analysis, investigation, writing—original draft, writing—review and editing, visualization, project administration FS: Validation, formal analysis, investigation, writing–original draft, writing—review and editing, visualization SG: Conceptualization, formal analysis, investigation, writing–original draft, writing—review and editing, visualization VP: Resources, writing—review and editing YD: Investigation, visualization GL: Investigation, writing—review and editing SR: Resources,

writing—review and editing AR: Resources, writing—review and editing, funding acquisition ES: Resources, writing—review and editing, supervision, funding acquisition KM: Conceptualization, resources, writing—review and editing, supervision, funding acquisition BO: Conceptualization, writing—review and editing, supervision, funding acquisition SP: Conceptualization, writing—review and editing, funding acquisition.

Funding

Acknowledgments

Conflict of interest

MF and SP hold a provisional patent on the differentiation process of hPSCs to epicardial-derived CFBs. ES and AR are founders and hold equity ownership in Cellular Logistics Inc. AR. is a consultant in Blue Rock Therapeutics and Novo Nordisk, and received a research grant from BioCardia Inc.

The remaining authors declare that the research was conducted in the absence of any commercial or financial relationships that could be construed as a potential conflict of interest.

Publisher's note

All claims expressed in this article are solely those of the authors and do not necessarily represent those of their affiliated organizations, or those of the publisher, the editors and the reviewers. Any product that may be evaluated in this article, or claim that may be made by its manufacturer, is not guaranteed or endorsed by the publisher.

Supplementary material

The Supplementary Material for this article can be found online at: https://www.frontiersin.org/articles/10.3389/fbioe.2023.1102487/full#supplementary-material

SUPPLEMENTARY TABLE S1
Processed RNA sequencing results.

SUPPLEMENTARY TABLE S2
Mass spectrometry results of primary CFBs.

SUPPLEMENTARY TABLE S3
Mass spectrometry results comparing hPSC–derived and primary CFBs.

SUPPLEMENTARY PRESENTATION 1
Supplementary Figures and Tables.

References

Achkar, A., Saliba, Y., and Fares, N. (2020). Differential gender-dependent patterns of cardiac fibrosis and fibroblast phenotypes in aging mice. *Oxid. Med. Cell. Longev.* 2020, 8282157. doi:10.1155/2020/8282157

Aguado, B. A., Walker, C. J., Grim, J. C., Schroeder, M. E., Batan, D., Vogt, B. J., et al. (2022). Genes that escape X chromosome inactivation modulate sex differences in valve myofibroblasts. *Circulation* 145, 513–530. doi:10.1161/CIRCULATIONAHA.121.054108

Ahmed, T., Ahmad, M., and Mungee, S. (2020). "Cardiac calcifications," in *StatPearls* (Treasure Island, FL: StatPearls Publishing).

Aikawa, E., Whittaker, P., Farber, M., Mendelson, K., Padera, R. F., Aikawa, M., et al. (2006). Human semilunar cardiac valve remodeling by activated cells from fetus to adult: Implications for postnatal adaptation, pathology, and tissue engineering. *Circulation* 113, 1344–1352. doi:10.1161/CIRCULATIONAHA.105.591768

Alfieri, C. M., Cheek, J., Chakraborty, S., and Yutzey, K. E. (2010). Wnt signaling in heart valve development and osteogenic gene induction. *Dev. Biol.* 338, 127–135. doi:10.1016/j.ydbio.2009.11.030

Ashburner, M., Ball, C. A., Blake, J. A., Botstein, D., Butler, H., Cherry, J. M., et al. (2000). Gene ontology: Tool for the unification of biology. *Nat. Genet.* 25, 25–29. doi:10.1038/75556

Brower, G. L., Gardner, J. D., Forman, M. F., Murray, D. B., Voloshenyuk, T., Levick, S. P., et al. (2006). The relationship between myocardial extracellular matrix remodeling and ventricular function. *Eur. J. Cardio-Thoracic Surg.* 30, 604–610. doi:10.1016/j.ejcts.2006.07.006

Cheng, L., Xie, M., Qiao, W., Song, Y., Zhang, Y., Geng, Y., et al. (2021). Generation and characterization of cardiac valve endothelial-like cells from human pluripotent stem cells. *Commun. Biol.* 4, 1039. doi:10.1038/s42003-021-02571-7

Cirka, H. A., Uribe, J., Liang, V., Schoen, F. J., and Billiar, K. L. (2017). Reproducible *in vitro* model for dystrophic calcification of cardiac valvular interstitial cells: Insights into the mechanisms of calcific aortic valvular disease. *Lab. Chip* 17, 814–829. doi:10.1039/c6lc01226d

Coppiello, G., Collantes, M., Sirerol-Piquer, M. S., Vandenwijngaert, S., Schoors, S., Swinnen, M., et al. (2015). Meox2/Tcf15 heterodimers program the heart capillary endothelium for cardiac fatty acid uptake. *Circulation* 131, 815–826. doi:10.1161/CIRCULATIONAHA.114.013721

Cunnington, R. H., Northcott, J. M., Ghavami, S., Filomeno, K. L., Jahan, F., Kavosh, M. S., et al. (2014). The Ski-Zeb2-Meox2 pathway provides a novel mechanism for regulation of the cardiac myofibroblast phenotype. *J. Cell. Sci.* 127, 40–49. doi:10.1242/jcs.126722

Dawson, K., Aflaki, M., and Nattel, S. (2013). Role of the wnt-frizzled system in cardiac pathophysiology: A rapidly developing, poorly understood area with enormous potential. *J. Physiology* 591 (6), 1409–1432. doi:10.1113/jphysiol.2012.235382

Decano, J. L., Iwamoto, Y., Goto, S., Lee, J. Y., Matamalas, J. T., Halu, A., et al. (2022). A disease-driver population within interstitial cells of human calcific aortic valves identified via single-cell and proteomic profiling. *Cell. Rep.* 39, 110685. doi:10.1016/j.celrep.2022.110685

Dickover, M., Hegarty, J. M., Ly, K., Lopez, D., Yang, H., Zhang, R., et al. (2014). The atypical Rho GTPase, RhoU, regulates cell-adhesion molecules during cardiac morphogenesis. *Dev. Biol.* 389, 182–191. doi:10.1016/j.ydbio.2014.02.014

Dobin, A., Davis, C. A., Schlesinger, F., Drenkow, J., Zaleski, C., Jha, S., et al. (2013). Star: Ultrafast universal RNA-seq aligner. *Bioinformatics* 29, 15–21. doi:10.1093/bioinformatics/bts635

Gene Ontology ConsortiumDouglass, E., Good, B. M., Unni, D. R., Harris, N. L., Mungall, C. J., et al. (2021). The gene ontology resource: Enriching a GOld mine. *Nucleic Acids Res.* 49, D325–D334. doi:10.1093/nar/gkaa1113

Edgar, R., Domrachev, M., and Lash, A. E. (2002). Gene expression Omnibus: NCBI gene expression and hybridization array data repository. *Nucleic Acids Res.* 30, 207–210. doi:10.1093/nar/30.1.207

Fakhry, C. T., Choudhary, P., Gutteridge, A., Sidders, B., Chen, P., Ziemek, D., et al. (2016). Interpreting transcriptional changes using causal graphs: New methods and their practical utility on public networks. *BMC Bioinforma.* 17, 318. doi:10.1186/s12859-016-1181-8

Farbehi, N., Patrick, R., Dorison, A., Xaymardan, M., Janbandhu, V., Wystub-Lis, K., et al. (2019). Single-cell expression profiling reveals dynamic flux of cardiac stromal, vascular and immune cells in health and injury. *eLife* 8, e43882. doi:10.7554/eLife.43882

Floy, M. E., Givens, S. E., Matthys, O. B., Mateyka, T. D., Kerr, C. M., Steinberg, A. B., et al. (2021). Developmental lineage of human pluripotent stem cell-derived cardiac fibroblasts affects their functional phenotype. *FASEB J.* 35, e21799. doi:10.1096/fj.202100523R

George, E. L., Georges-Labouesse, E. N., Patel-King, R. S., Rayburn, H., and Hynes, R. O. (1993). Defects in mesoderm, neural tube and vascular development in mouse embryos lacking fibronectin. *Development* 119, 1079–1091. doi:10.1242/dev.119.4.1079

Hao, Y., Hao, S., Andersen-Nissen, E., Mauck, W. M., Zheng, S., Butler, A., et al. (2021). Integrated analysis of multimodal single-cell data. *Cell.* 184, 3573–3587.e29. doi:10.1016/j.cell.2021.04.048

Kanisicak, O., Khalil, H., Ivey, M. J., Karch, J., Maliken, B. D., Correll, R. N., et al. (2016). Genetic lineage tracing defines myofibroblast origin and function in the injured heart. *Nat. Commun.* 7, 12260. doi:10.1038/ncomms12260

Khan, K., Yu, B., Kiwan, C., Shalal, Y., Filimon, S., Cipro, M., et al. (2020). The role of wnt/β-catenin pathway mediators in aortic valve stenosis. *Front. Cell. Dev. Biol.* 8, 862. doi:10.3389/fcell.2020.00862

Konstandin, M. H., Toko, H., Gastelum, G. M., Quijada, P., De La Torre, A., Quintana, M., et al. (2013). Fibronectin is essential for reparative cardiac progenitor cell response after myocardial infarction. *Circulation Res.* 113, 115–125. doi:10.1161/CIRCRESAHA.113.301152

Kostina, A., Shishkova, A., Ignatieva, E., Irtyuga, O., Bogdanova, M., Levchuk, K., et al. (2018). Different Notch signaling in cells from calcified bicuspid and tricuspid aortic valves. *J. Mol. Cell. Cardiol.* 114, 211–219. doi:10.1016/j.yjmcc.2017.11.009

Landry, N. M., Cohen, S., and Dixon, I. M. C. (2017). Periostin in cardiovascular disease and development: A tale of two distinct roles. *Basic Res. Cardiol.* 113, 1. doi:10.1007/s00395-017-0659-5

Latif, N., Quillon, A., Sarathchandra, P., McCormack, A., Lozanoski, A., Yacoub, M. H., et al. (2015). Modulation of human valve interstitial cell phenotype and function using a fibroblast growth factor 2 formulation. *PLOS ONE* 10, e0127844. doi:10.1371/journal.pone.0127844

Lee, S., Chen, T. T., Barber, C. L., Jordan, M. C., Murdock, J., Desai, S., et al. (2007). Autocrine VEGF signaling is required for vascular homeostasis. *Cell.* 130 (4), 691–703. doi:10.1016/j.cell.2007.06.054

Li, W., Su, S., Chen, J., Ma, H., and Xiang, M. (2021). Emerging roles of fibroblasts in cardiovascular calcification. *J. Cell. Mol. Med.* 25, 1808–1816. doi:10.1111/jcmm.16150

Liao, D. (2009). Emerging roles of the EBF family of transcription factors in tumor suppression. *Mol. Cancer Res.* 7, 1893–1901. doi:10.1158/1541-7786.MCR-09-0229

Liao, Y., Smyth, G. K., and Shi, W. (2014). featureCounts: an efficient general purpose program for assigning sequence reads to genomic features. *Bioinformatics* 30, 923–930. doi:10.1093/bioinformatics/btt656

Liu, A. C., Joag, V. R., and Gotlieb, A. I. (2007). The emerging role of valve interstitial cell phenotypes in regulating heart valve pathobiology. *Am. J. Pathol.* 171, 1407–1418. doi:10.2353/ajpath.2007.070251

Liu, K., Yu, W., Tang, M., Tang, J., Liu, X., Liu, Q., et al. (2018). A dual genetic tracing system identifies diverse and dynamic origins of cardiac valve mesenchyme. *Development* 145, dev167775. doi:10.1242/dev.167775

Lockhart, M., Wirrig, E., Phelps, A., and Wessels, A. (2011). Extracellular matrix and heart development. *Birth Defects Res. A Clin. Mol. Teratol.* 91, 535–550. doi:10.1002/bdra.20810

Love, M. I., Huber, W., and Anders, S. (2014). Moderated estimation of fold change and dispersion for RNA-seq data with DESeq2. *Genome Biol.* 15, 550. doi:10.1186/s13059-014-0550-8

Lv, Y., Zhong, S., Tang, H., Luo, B., Chen, S. J., Chen, L., et al. (2018). VEGF-A and VEGF-B coordinate the arteriogenesis to repair the infarcted heart with vagus nerve stimulation. *Cell. Physiology Biochem.* 48 (2), 433–449. doi:10.1159/000491775

MacGrogan, D., Luna-Zurita, L., and de la Pompa, J. L. (2011). Notch signaling in cardiac valve development and disease. *Birth Defects Res. A Clin. Mol. Teratol.* 91, 449–459. doi:10.1002/bdra.20815

Masjedi, S., Amarnath, A., Baily, K. M., and Ferdous, Z. (2016). Comparison of calcification potential of valvular interstitial cells isolated from individual aortic valve cusps. *Cardiovasc. Pathol.* 25, 185–194. doi:10.1016/j.carpath.2015.12.002

Menon, V., and Lincoln, J. (2018). The genetic regulation of aortic valve development and calcific disease. *Front. Cardiovasc. Med.* 5, 162. doi:10.3389/fcvm.2018.00162

Moore-Morris, T., Guimarães-Camboa, N., Banerjee, I., Zambon, A. C., Kisseleva, T., Velayoudon, A., et al. (2014). Resident fibroblast lineages mediate

pressure overload-induced cardiac fibrosis. *J. Clin. Invest.* 124, 2921–2934. doi:10.1172/JCI74783

Myasoedova, V. A., Di Minno, A., Songia, P., Massaiu, I., Alfieri, V., Valerio, V., et al. (2020). Sex-specific differences in age-related aortic valve calcium load: A systematic review and meta-analysis. *Ageing Res. Rev.* 61, 101077. doi:10.1016/j.arr.2020.101077

Nelson, V., Patil, V., Simon, L. R., Schmidt, K., McCoy, C. M., and Masters, K. S. (2021). Angiogenic secretion profile of valvular interstitial cells varies with cellular sex and phenotype. *Front. Cardiovasc Med.* 8, 736303. doi:10.3389/fcvm.2021.736303

Nemir, M., Metrich, M., Plaisance, I., Lepore, M., Cruchet, S., Berthonneche, C., et al. (2014). The Notch pathway controls fibrotic and regenerative repair in the adult heart. *Eur. Heart J.* 35 (32), 2174–2185. doi:10.1093/eurheartj/ehs269

Nicin, L., Wagner, J. U. G., Luxán, G., and Dimmeler, S. (2022). Fibroblast-mediated intercellular crosstalk in the healthy and diseased heart. *FEBS Lett.* 596, 638–654. doi:10.1002/1873-3468.14234

Nigam, V., and Srivastava, D. (2009). Notch1 represses osteogenic pathways in aortic valve cells. *J. Mol. Cell. Cardiol.* 47 (6), 828–834. doi:10.1016/j.yjmcc.2009.08.008

Nistri, S., Sassoli, C., and Bani, D. (2017). Notch signaling in ischemic damage and fibrosis: Evidence and clues from the heart. *Front. Pharmacol.* 8, 187. doi:10.3389/fphar.2017.00187

Pillai, I. C. L., Li, S., Romay, M., Lam, L., Lu, Y., Huang, J., et al. (2017). Cardiac fibroblasts adopt osteogenic fates and can be targeted to attenuate pathological heart calcification. *Cell. Stem Cell.* 20, 218–232.e5. doi:10.1016/j.stem.2016.10.005

Polizzotti, B. D., Arab, S., and Kühn, B. (2012). Intrapericardial delivery of gelfoam enables the targeted delivery of periostin peptide after myocardial infarction by inducing fibrin clot formation. *PLoS One* 7, e36788. doi:10.1371/journal.pone.0036788

Porras, A. M., van Engeland, N. C. A., Marchbanks, E., McCormack, A., Bouten, C. V. C., Yacoub, M. H., et al. (2017). Robust generation of quiescent porcine valvular interstitial cell cultures. *J. Am. Heart Assoc.* 6, e005041. doi:10.1161/JAHA.116.005041

Rodríguez, C., and Martínez-González, J. (2019). The role of lysyl oxidase enzymes in cardiac function and remodeling. *Cells* 8, 1483. doi:10.3390/cells8121483

Sánchez, J., Gomez, J. F., Martinez-Mateu, L., Romero, L., Saiz, J., and Trenor, B. (2019). Heterogeneous effects of fibroblast-myocyte coupling in different regions of the human atria under conditions of atrial fibrillation. *Front. Physiol.* 10, 847. doi:10.3389/fphys.2019.00847

Schäfer, C., Heiss, A., Schwarz, A., Westenfeld, R., Ketteler, M., Floege, J., et al. (2003). The serum protein α₂–Heremans-Schmid glycoprotein/fetuin-A is a systemically acting inhibitor of ectopic calcification. *J. Clin. Invest.* 112, 357–366. doi:10.1172/JCI17202

Schmuck, E. G., Roy, S., Dhillon, A., Walker, S., Spinali, K., Colevas, S., et al. (2021). Cultured cardiac fibroblasts and myofibroblasts express Sushi Containing Domain 2 and assemble a unique fibronectin rich matrix. *Exp. Cell. Res.* 399, 112489. doi:10.1016/j.yexcr.2021.112489

Scott, A. J., Simon, L. R., Hutson, H. N., Porras, A. M., and Masters, K. S. (2021). Engineering the aortic valve extracellular matrix through stages of development, aging, and disease. *J. Mol. Cell. Cardiol.* 161, 1–8. doi:10.1016/j.yjmcc.2021.07.009

Stankunas, K., Ma, G. K., Kuhnert, F. J., Kuo, C. J., and Chang, C.-P. (2010). VEGF signaling has distinct spatiotemporal roles during heart valve development. *Dev. Biol.* 347, 325–336. doi:10.1016/j.ydbio.2010.08.030

Sun, W., Zhao, R., Yang, Y., Wang, H., Shao, Y., and Kong, X. (2013). Comparative study of human aortic and mitral valve interstitial cell gene expression and cellular function. *Genomics* 101, 326–335. doi:10.1016/j.ygeno.2013.03.004

Tallquist, M. D. (2020). Cardiac fibroblast diversity. *Annu. Rev. Physiol.* 82, 63–78. doi:10.1146/annurev-physiol-021119-034527

Tao, W., Pennica, D., Xu, L., Kalejta, R. F., and Levine, A. J. (2001). Wrch-1, a novel member of the Rho gene family that is regulated by Wnt-1. *Genes. Dev.* 15, 1796–1807. doi:10.1101/gad.894301

Tucker, N. R., Chaffin, M., Fleming, S. J., Hall, A. W., Parsons, V. A., Bedi, K. C., et al. (2020). Transcriptional and cellular diversity of the human heart. *Circulation* 142, 466–482. doi:10.1161/CIRCULATIONAHA.119.045401

Ventura-Clapier, R., Dworatzek, E., Seeland, U., Kararigas, G., Arnal, J.-F., Brunelleschi, S., et al. (2017). Sex in basic research: Concepts in the cardiovascular field. *Cardiovasc Res.* 113, 711–724. doi:10.1093/cvr/cvx066

Wang, S., Yu, H., Gao, J., Chen, J., He, P., Zhong, H., et al. (2022). PALMD regulates aortic valve calcification via altered glycolysis and NF-κB–mediated inflammation. *J. Biol. Chem.* 298, 101887. doi:10.1016/j.jbc.2022.101887

Wessels, A., van den Hoff, M. J. B., Adamo, R. F., Phelps, A. L., Lockhart, M. M., Sauls, K., et al. (2012). Epicardially derived fibroblasts preferentially contribute to the parietal leaflets of the atrioventricular valves in the murine heart. *Dev. Biol.* 366, 111–124. doi:10.1016/j.ydbio.2012.04.020

Wiltz, D., Arevalos, C. A., Balaoing, L. R., Blancas, A. A., Sapp, M. C., Zhang, X., et al. (2013). *Extracellular matrix organization, structure, and function*. London, UK: IntechOpen. doi:10.5772/52842

Xu, Y., Cao, Y., Liu, Y., Wang, J., Chen, G., Tao, Z., et al. (2021). Upregulation of cartilage oligomeric matrix protein and bone morphogenetic protein-2 may associate with calcific aortic valve disease. *Cardiol. Discov.* 1, 105–111. doi:10.1097/CD9.0000000000000015

Zhang, J., Tao, R., Campbell, K. F., Carvalho, J. L., Ruiz, E. C., Kim, G. C., et al. (2019). Functional cardiac fibroblasts derived from human pluripotent stem cells via second heart field progenitors. *Nat. Commun.* 10, 2238. doi:10.1038/s41467-019-09831-5

Plasma polymerized nanoparticles are a safe platform for direct delivery of growth factor therapy to the injured heart

Zoë E. Clayton[1,2]*[†], Miguel Santos[3,4†], Haisam Shah[1,2], Juntang Lu[5], Siqi Chen[1], Han Shi[1,2], Shaan Kanagalingam[1], Praveesuda L. Michael[3,4], Steven G. Wise[3,4] and James J. H. Chong[1,2,5]*

[1]Westmead Institute for Medical Research, Sydney, NSW, Australia, [2]Sydney Medical School, University of Sydney, Sydney, NSW, Australia, [3]School of Medical Sciences, Faculty of Health and Medicine, The University of Sydney, Sydney, NSW, Australia, [4]Charles Perkins Centre, The University of Sydney, Sydney, NSW, Australia, [5]Cardiology Department, Westmead Hospital, Sydney, NSW, Australia

Introduction: Heart failure due to myocardial infarction is a progressive and debilitating condition, affecting millions worldwide. Novel treatment strategies are desperately needed to minimise cardiomyocyte damage after myocardial infarction and to promote repair and regeneration of the injured heart muscle. Plasma polymerized nanoparticles (PPN) are a new class of nanocarriers which allow for a facile, one-step functionalization with molecular cargo.

Methods: Here, we conjugated platelet-derived growth factor AB (PDGF-AB) to PPN, engineering a stable nano-formulation, as demonstrated by optimal hydrodynamic parameters, including hydrodynamic size distribution, polydisperse index (PDI) and zeta potential, and further demonstrated safety and bioactivity *in vitro* and *in vivo*. We delivered PPN-PDGF-AB to human cardiac cells and directly to the injured rodent heart.

Results: We found no evidence of cytotoxicity after delivery of PPN or PPN-PDGFAB to cardiomyocytes *in vitro,* as determined through viability and mitochondrial membrane potential assays. We then measured contractile amplitude of human stem cell derived cardiomyocytes and found no detrimental effect of PPN on cardiomyocyte contractility. We also confirmed that PDGF-AB remains functional when bound to PPN, with PDGF receptor alpha positive human coronary artery vascular smooth muscle cells and cardiac fibroblasts demonstrating migratory and phenotypic responses to PPN-PDGF-AB in the same manner as to unbound PDGF-AB. In our rodent model of PPN-PDGF-AB treatment after myocardial infarction, we found a modest improvement in cardiac function in PPN-PDGF-AB treated hearts compared to those treated with PPN, although this was not accompanied by changes in infarct scar size, scar composition, or border zone vessel density.

Discussion: These results demonstrate safety and feasibility of the PPN platform for delivery of therapeutics directly to the myocardium. Future work will optimize PPN-PDGF-AB formulations for systemic delivery, including effective dosage and timing to enhance efficacy and bioavailability, and ultimately improve the therapeutic benefits of PDGF-AB in the treatment of heart failure cause by myocardial infarction.

1 Introduction

Heart failure caused by myocardial infarction is a debilitating condition with high morbidity and mortality. Acute myocardial infarction results in the loss of millions of highly specialised cardiomyocytes, which are unable to regenerate in any meaningful capacity and are instead replaced by non-contractile scar tissue. This leads to permanent and progressive impairment of the pump function of the heart. Despite substantial advances in cardiovascular drug and device therapy, heart transplantation remains the only cure for end-stage heart failure. There is an urgent unmet need for novel treatment strategies to minimise cardiomyocyte death after myocardial infarction and promote repair of the injured heart.

One such strategy is platelet derived growth factor (PDGF) therapy. PDGF is a potent stimulator of cell migration and proliferation, particularly in the context of new blood vessel formation (angiogenesis) and wound healing. There are four PDGF ligands (A, B, C, D), which function as dimers (AA, AB, BB, CC, DD). The heterodimer ligand, PDGF-AB, signals though both PDGF receptors, PDGFRα and PDGFRβ. PDGFRα is present on many cardiac cell types, including cardiac fibroblasts and vascular smooth muscle cells. Recently published research in preclinical models of myocardial infarction has shown that treatment with recombinant PDGF-AB protein (Asli et al., 2019; Thavapalachandran et al., 2020) and overexpression of the *Pdgf-a* gene via recombinant adeno-associated virus mediated gene transfer (Rashid et al., 2021) improves cardiac function after myocardial infarction via fibroblast and macrophage activation and enhanced angiogenesis in the infarct border zone, leading to improved scar alignment and mechanics.

These studies administered PDGF-AB via systemic infusion. However, previous studies have demonstrated that pretreatment with PDGF via direct intramyocardial delivery can also be effective in limiting cardiac damage after infarction (Edelberg et al., 2002; Xaymardan et al., 2004). As PDGF-AB is reported to have a short half-life in the circulation and is susceptible to degradation by proteases, we investigated a nanocarrier-mediated direct delivery method to extend the bioavailability of PDGF-AB during the critical post-infarct period, without the need for continuous systemic infusion (Cianciolo et al., 1999; Barrientos et al., 2008). Carbon-activated, plasma polymerized nanoparticles (PPN) are a high-throughput, low-cost strategy for localized delivery of bioactive cargo (Santos et al., 2018; Santos et al., 2019). PPN can effectively bind and deliver functional siRNAs and pharmaceuticals to target cancer cells (Michael et al., 2020). They have undergone comprehensive cytotoxicity testing in immortalized cell lines, endothelial cells, and smooth muscle cells, but have not been tested in cardiomyocytes nor delivered directly to the heart (Michael et al., 2021).

Here, we show that application of therapeutically relevant doses of PPN and PPN-PDGF-AB to cardiac cells, including primary and pluripotent stem cell derived cardiomyocytes, does not detrimentally affect their viability or function *in vitro*. We also demonstrate that PDGF-AB protein retains its functional efficacy while bound to PPN and establish the potential of PPN as a suitable platform to deliver growth factors and other therapeutic materials to the injured heart.

2 Methods

2.1 PPN-PDGFAB formulation

2.1.1 PPN synthesis

PPN were produced in a custom-built capacitively coupled radiofrequency (rf) plasma chamber as previously described (Santos et al., 2018). Briefly, an rf-driven (13.52 MHz) plasma discharge was created at a pressure of 110 mTorr, by ionization of a gaseous mixture comprising of argon, nitrogen, and acetylene. The flow rate of each gas was set constant and monitored by mass flow controllers throughout the process. The rf power was delivered by an rf power supply and coupled to the plasma via an automatic matching box to minimize reflected power. The plasma emission fingerprint was monitored *in-situ* via optical emission spectroscopy (OES) using an Ocean Optics HR4000 (Oceans Optics). The OES process is used for quality control purposes, by tracking the emission dynamics of selected molecular species, including molecular nitrogen excited states and ions, as well as CN molecular radicals.

2.1.2 PPN collection

The nanoparticles produced within the plasma bulk were collected in 24-well polystyrene plates (Corning) directly from the active plasma volume as previously described (Santos et al., 2019). Following synthesis, the plates were brought to atmospheric pressure and removed from the vacuum chamber for storage at room temperature and in ambient air for 48 h before resuspension in aqueous solution. Since PPN are produced in a dry plasma state, they can be stored in a dry state and only be resuspended in solution as needed before functionalization with molecular cargo. Here, PPN were dispersed in ultra-pure nuclease-free water (NFW) directly from the well plates, into 1.5 mL Eppendorf tubes. The concentration of PPN in solution was determined by UV/VIS spectroscopy as previously described (Michael et al., 2020), by measuring the optical density of PPN in solution at 500 nm.

2.1.3 PPN characterization

The hydrodynamic parameters of PPN, i.e., hydrodynamic size, polydisperse index (PDI) and zeta potential, were obtained using a Zetasizer Nano ZS (Malvern Instruments, Germany). Samples were measured at room temperature in disposable folded capillary cells (Malvern DTS1070) and data for each hydrodynamic parameter was acquired from the average of five independent acquisitions. The quality of the measurements was monitored in real time and the data was analyzed using standard procedures within the manufacturer's software (Malvern Instruments, Germany). The hydrodynamic size distribution was further confirmed in a higher resolution NanoSight NS300 laser light scattering system. Samples were introduced into

the analysis chamber and allowed to flow at a constant flow rate. The trajectories and Brownian motion of PPNs flowing through the chamber were continuously tracked for 60 s, using a nanoparticle tracking and analysis software (NanoSight NTA 3.0).

2.1.4 PPN–PDGFAB conjugation

Conjugation of PDGF-AB to PPN was performed in ultrapure NFW, by adding PDGF-AB (1 mg/mL) to PPN solutions (10^{10} PPN/mL) at a ratio of 5 µg PDGFAB/10^{10} PPN. The ratio between PDGFAB and PPN during the conjugation process ensures that PDGFAB is present in excess amount compared to what is theoretically necessary to fully decorate the surface of PPNs with a monolayer of PDGFAB molecules, i.e., 3.1 µg/10^{10} PPN. The PPN and PDGF-AB mixtures were incubated for 1 h at 4°C. Unbound PDGF-AB remaining in solution following conjugation was washed by centrifugation at 10,000 G for 5 min.

2.2 Cell culture

2.2.1 Neonatal rat ventricular myocytes

All NRVM collection procedures had ethical approval (Western Sydney Local Health District animal ethics protocol 4232) and were performed in accordance with the National Health and Medical Research Council (NHMRC) Code for the care and use of animals for scientific purposes.

NRVMs were obtained from neonatal hearts at postnatal day 3. The hearts were placed in trypsin and incubated at 4°C on a shaking platform overnight. The following morning, the hearts were further dissociated with repeat washes in 1 mg/mL collagenase in HBSS. The cells were collected, centrifuged, resuspended in M199 + 10% fetal bovine serum (FBS), and filtered using a 40 µm cell strainer. The cells were then pre-plated onto T150 flasks for 1 hour, to reduce fibroblast contamination of the NRVM cultures. NRVMs in suspension were then centrifuged, counted, resuspended in fresh M199 + 10% FBS and re-plated onto gelatin-coated 48 well plates for downstream assays.

2.2.2 Human coronary artery vascular smooth muscle cells

Primary HCASMCs were purchased from ATCC (Lot # 61646600). The cells were cultured on T25 and T75 flasks, in Smooth Muscle Cell Growth Medium-2 (SmGm-2, Lonza) at a seeding density of 2500–5,000 cells/cm². Media was replaced every 2–3 days. Replicates were sourced from 3 different donors and used for experiments between passage 3 and 5.

2.2.3 Human cardiac fibroblasts

Human cardiac fibroblasts were isolated from 3 donor heart samples provided by the Sydney Heart Bank. The cells were expanded in complete MEMα culture medium (Thermofisher Scientific) supplemented with 20% FBS, 4 mM L-glutamine, and 100U Penicillin/Streptomycin. The fibroblasts were cultured in T150 flasks and passaged when they reached approximately 80% confluence. Culture media was removed, and the cells were washed twice with PBS. Cells were detached with 2X trypsin-EDTA for 4 min at 37°C. Trypsin-EDTA was deactivated by adding double volume complete medium to trypsin-EDTA. The cell suspension

was transferred to a 50 mL falcon tube and centrifuged at 250 g for 5 min at room temperature to pellet cells and remove trypsin. Cells were resuspended in growth medium for reseeding.

2.2.4 Human pluripotent stem cell derived cardiomyocytes

Human embryonic pluripotent stem cells (HES3 NKX2.5$^{eGFP/w}$) were cultured in Geltrex (Thermofisher)-coated T75 flasks, in TeSR-E8 + Penicillin/Streptomycin (STEM CELL Technologies). For differentiation, ESCs were dissociated at 80% confluency and seeded onto Geltrex-coated 6 well plates at a density of 2.5×10^5 cells per well, in TeSR-E8 + Pen/Strep + 1 µM Y-27632 (Rock inhibitor). Media was replaced with fresh TeSR-E8 + Pen/Strep the following day.

Human induced pluripotent stem cells (SCVI8 - Stanford Cardiovascular Institute) were cultured on Matrigel (Corning) -coated 60 mm dishes, in mTeSR Plus (STEMCELL Technologies) complete media. For differentiation, iPSCs were dissociated at 80%–90% confluency and seeded onto Matrigel-coated 6 well plates at a density of 1.5×10^6 cells per well, in mTeSR Plus +1 µM Y-27632. Media was replaced with fresh mTeSR Plus the following day.

For both cell lines, cardiomyocyte differentiations commenced 2 days after replating, using an established small molecule protocol described by Lian et al. (2013). Briefly, the cells were incubated in RPMI 1640 + B27 minus insulin + Glutamax + Pen/Strep + 6 µM CHIR99021 for 24 h. Media was then changed to fresh RPMI 1640 + B27 minus insulin + Glutamax + Pen/Strep. On day 3 the cells were incubated with 5 µM Wnt signaling inhibitor, IWP-2. Media was changed to fresh RPMI 1640 + B27 minus insulin + Glutamax + Pen/Strep on day 5 and then to RPMI 1640 + B27 (with insulin) + Glutamax + Pen/Strep from day 7 onwards. PSC-CMs commenced beating on day 7–8, with robust spontaneous contractions observed from day 10 onwards.

2.3 *In Vitro* assays

2.3.1 DCFDA (2′,7′ −dichlorofluorescin diacetate) reactive oxygen species assay

After 14 days of differentiation, iPSC-CMs (SCVI8) were dissociated from 6 well plates with TryPLE and replated into Matrigel-coated wells of a 24 well plate. The cells incubated overnight in RPMI1640 + B27 + Glutamax + Penicillin/Streptomycin + 1 µM Y-27632 (Rock inhibitor) and media was changed to fresh RPMI1640 + B27 + Glutamax + Penicillin/Streptomycin the following day. Three days after replating, all wells had resumed beating and cells were treated with PPN or PPN-PDGFAB.

DCFDA cellular reactive oxygen species (ROS) assay (ab113851, Abcam) was performed on iPSC-CMs after 24 h incubation with 1×10^8 or 1×10^9 PPN or PPN-PDGFAB, according to the manufacturer's instructions for pretreatment of adherent cells and with volume modifications for the 24-well plate format. Four hours prior to the end of the incubation period, media was removed from 3 wells and the cells were treated with 55 µM TBHP positive control compound in 400 µL supplemented buffer. One hour before the end of the incubation period, media was removed from all other

wells and replaced with 400 μL supplemented buffer containing 20 μM DCFDA. DCFDA (20 μM) was also added to TBHP wells. The plate was incubated in the dark for 45 min, transferred to the microplate reader without washing, and fluorescence was read at 485/535 nm. The experiment included cell-only controls (no PPN/PPN-PDGFAB) and blank wells (no cells).

2.3.2 MTT (3-(4, 5-dimethylthiazol-2-yl)-2, 5-diphenyltetrazolium bromide) viability assay

For viability and mitochondrial activity assays, NRVMs were seeded onto gelatin-coated 48 well plates at a density of 1×10^5 cells/well and incubated for 24 h in. The following day, the cells were washed three times with PBS and incubated with fresh M199 + 10% FBS. On d2, the media was switched to M199 + 2% FBS and cells were incubated with PPN or PPN-PDGFAB at high (1×10^8 particles), medium (5×10^7 particles) or low (2.5×10^7 particles) doses, or PBS only control. MTT and TMRE assays were performed on d1, d4, d7, d14 and d21 post-treatment with PPN/PPN-PDGFAB. Each assay was performed using 3 different NRVM preps (n = 3 technical replicates per biological replicate, n = 3 biological replicates per time-point).

MTT was diluted in RPMI 1640 without phenol red, at a concentration of 5 mg/mL. The solution was filtered and added to the cells at a final concentration of 0.5 mg/mL. The cells were incubated at 37°C for 4 h in the dark and then washed twice with PBS. A solvent (500μL, 1:1 DMSO: Isopropanol) was added to each well to dissolve the formazan crystals. The absorbance of each well was measured using a microplate spectrophotometer at 570 nm. Each experiment included appropriate control and blank wells (solvent only).

2.3.3 Tetramethylrhodamine, ethyl ester mitochondrial membrane activity assay

TMRE mitochondrial membrane potential assays were performed using commercially available reagents (ab113852, Abcam, Cambridge, United Kingdom), per the manufacturer's instructions. The cells were washed with PBS and incubated in M199 + 2% FBS +500 nM TMRE for 25 min in the dark. The cells were then washed twice with 0.2% BSA in PBS and the fluorescence in each well was measured using a microplate spectrophotometer (Spectramax) at Ex/Em 549/575 nm. Each experiment included cells only (no TMRE) and FCCP inhibitor controls.

2.3.4 Boyden chamber migration assay

Human coronary artery vascular smooth muscle cells were seeded in Corning Transwell polycarbonate membrane cell culture inserts (8 μm pore size) at a density of 1.5×10^4 cells in 100 μL DMEM +10% FBS per insert. The transwells were inserted into 24 well plates containing 600 μL DMEM +10% FBS + either 10 ng/mL rhPDGF-AB, 1×10^8 NP3, or 2.5×10^7, 5×10^7, or 1×10^8 PPN-PDGF-AB. The cells were incubated overnight and on the following morning the membranes were washed with 1 mL PBS and fixed in 650 μL 70% ethanol for 30 min. The membranes were then scraped with a 1 mL syringe tip to remove non-migrated cells and washed with PBS. The membranes were cut away from the transwells using a scalpel blade, mounted on microscope slides with mounting media (Vectashield with DAPI (Vector Laboratories Inc.) to stain cell nuclei), and coverslipped. The

membranes were imaged on a fluorescent microscope (Olympus BX50), using the ×10 objective.

2.3.5 Myofibroblast differentiation

Human cardiac fibroblasts were reseeded onto 12 mm glass coverslips laid into 24 well plates once reaching approximately 80% confluence as described above. 2.5×10^4 cells were seeded onto the glass coverslips and cultured in complete MEMα culture medium overnight. Cells were then washed in PBS and cultured in serum starved MEMα culture medium supplemented with 4 mM L-glutamine and 100U Penicillin/Streptomycin. Media was replaced every 24 h with serum starved MEMα culture medium. At 72 h, cells were then treated with one of the following conditions, Serum Starved control, rhPDGF-AB (10 ng/ml), 1×10^9/ml PPN-PDGFAB, 1×10^9/ml PPN only. Media was replaced every 24 h with fresh media and growth factor/PPN for 72 h.

2.3.6 Immunocytochemistry

For myofibroblast differentiation of human cardiac fibroblasts, wells with glass coverslips were aspirated and cells were fixed in 10% neutral buffered formalin for 15 min, permeabilised in 0.1% Triton X-100/PBS for 10 min and blocked for 1 h in 10% normal goat serum (NGS)/0.01% Triton X-100/PBS. Primary antibodies (Table 1) were diluted in 10% NGS/0.01% Triton X-100/PBS and added to coverslips overnight at 4°C. The following morning, the cells were incubated for 1 h with secondary antibodies (Table 1) diluted in 10% NGS/0.01% Triton X-100/PBS, incubated with 1 μg/ml DAPI/PBS for 10 min. Glass cover slips were then mounted in 50% Glycerol/PBS and attached to glass slides.

2.3.7 Imaging and analysis

Cells were imaged for immunofluorescence at the Cell Imaging Facility at the Westmead Institute for Medical Research using the VS.120 Slide Scanner with ×20 objective and DAPI, FITC, Texas-Red, and Cy5 channels. 3 × 3mm areas of DAPI positive cells were imaged on each glass slide.

Immunocytochemistry images acquired from the VS. 120 were analysed using FIJI (ImageJ) software. Masks were generated through thresholding images equally. FIJI fill holes and watershed functions were used to acquire full DAPI positive nuclei and the 'analyze particles' function removed false negative signals that were not of consistent nuclei size. Masks were then layered using binary reconstruct plugin to acquire αSMA/Vimentin/αSMA + Vimentin only positive cells. Positive cell counts were acquired through the FIJI 'analyse particles' function.

2.3.8 Cardiomyocyte contraction analysis using Musclemotion

After 14 days of differentiation, PSC-CMs were dissociated from 6 well plates with TryPLE (Thermofisher) and replated onto Geltrex-coated wells of a 24 well plate. One well of the 6 well plate was replated evenly into 4 wells of the 24 well plate. The cells incubated overnight in RPMI1640 + B27 + Glutamax + Penicillin/Streptomycin + 1 μM Y-27632 (Rock inhibitor) and media was changed to RPMI1640 + B27 + Glutamax + Penicillin/Streptomycin the following day. Experiments commenced when all wells had resumed beating.

The cardiomyocytes were visualised using a light microscope (Olympus), under the ×40 objective. For Musclemotion analysis,

TABLE 1 Antibodies for flow cytometry and immunocytochemistry.

Target	Host	Clone	Vendor	Catalogue #
Anti-PDGFRα-BV786	Mouse	αR1	BD Biosciences	742,669
Anti-vimentin	Rabbit		Cell Signaling	5,741
Anti-smooth muscle alpha actin	Mouse		DAKO	M0851
Anti-sarcomeric alpha actinin	Rabbit		Abcam	68,167

20–40 s video recordings of spontaneous beating were taken on an iPhone 11, using a smartphone digiscoping adapter (Gosky Optics) attached to the microscope eyepiece. Immediately following baseline recordings, 1×10^9 PPN or 1×10^9 PPN-PDGFAB were added directly to the wells. Subsequent 20–40 s video recordings were taken at days 2, 4, and 7. Media changes were performed every third day as normal. All video recordings (.mov file format) were obtained at 60 frames per second and converted to.avi files using open-source software, FFMPEG. Contraction profiles were then generated using the MUSCLEMOTION plugin for ImageJ/FIJI as previously described by Sala et al. (Sala et al., 2018).

2.4 In Vivo

2.4.1 Left anterior descending artery ligation model of myocardial infarction

Male Sprague-Dawley rats were housed at constant room temperature and humidity, with *ad libitum* access to food and water, and a 12-h light/dark cycle. All animal *in vivo* procedures had ethics approval (Western Sydney Local Health District animal ethics protocol number 5166.10.20) and were performed in accordance with the National Health and Medical Research Council (NHMRC) Code for the care and use of animals for scientific purposes.

Rats aged 10–16 weeks were allocated to one of four treatment groups; Control, PDGF-AB, PPN, or PPN-PDGF-AB prior to experiments commencing. The rats were anaesthetized with isoflurane (5% in O_2) and ketamine (20 mg/kg, i.p.), intubated, ventilated and maintained on 2% isoflurane for the duration of the procedure. A left anterolateral thoracotomy was performed, and the ribs and lung retracted to expose the heart. The left anterior descending (LAD) coronary artery was ligated with a 5-0 prolene suture. Vessel occlusion was confirmed by blanching of the left ventricular (LV) anterior wall distal to the suture. The researcher performing ligation surgery was blinded to treatment group.

Immediately after ligation, a 31G needle was used for intramyocardial injection of a 50 μL solution containing one of four treatments: saline vehicle only, 100 ng recombinant PDGF-AB, 1×10^9 nanoparticles, or 1×10^9 nanoparticles with bound PDGF-AB. The dose of 1×10^9 PPN-PDGFAB is estimated to be equivalent to 310 ng of recombinant PDGF-AB. Our reasoning for opting for a higher (equivalent) dose of PPN-PDGFAB was to account for the assumption of full surface coverage of the nanoparticles and that as PPN and PPN-PDGFAB readily cross the plasma membrane we anticipated some degree of PPN-PDGFAB internalization by cardiac cells, which may reduce the availability of PDGF-AB to its surface

bound receptor. After delivery of injections, the chest wall, overlying muscle, and skin were sutured closed. The rats were treated with antibiotic (enrofloxacin 2.5 mg/kg s.c.) and pain relief (buprenorphine 0.05 mg/kg, s.c.).

2.4.2 Echocardiography

Transthoracic echocardiography was performed at baseline (prior to infarct), 3 days post-infarct and 14 days post-infarct, using a Philips Envisor C ultrasound and pediatric probe. M-mode measurements were taken in the parasternal short-axis view (pSAX - LV Mid). End systolic (LVESD) and end diastolic (LVEDD) diameters were measured for 3 consecutive cardiac cycles per view. Six separate views were recorded by two operators. Fractional shortening measurements reported represent the average of three measurements by one operator at each time-point. Final sample sizes for echocardiography analysis in each treatment group were n = 5 (PPN-PDGFAB), n = 6 (Control), or n = 7 (PPN and PDGFAB) biological replicates. Bland-Altman analysis was performed to measure inter-operator variability of echocardiography measurements (Donner et al., 2018; Bunting et al., 2019).

2.4.3 Histology and immunohistochemistry

Rat hearts were fixed in 10% neutral buffered formalin and then cut into two blocks, apex, and mid-ventricle, using a rodent heart matrix and microtome blades. The tissue was paraffin-embedded and cut into 4 μm sections. Sections were deparaffinized in xylene and hydrated by sequential incubation in 100%, 95%, 70%, 50% ethanol, and water. Sections from both blocks were stained with 0.1% Picrosirius Red +0.1% Fast Green to distinguish collagen infarct area from healthy myocardium. Infarct size was calculated as a percentage of the total LV area.

Adjacent sections from apex and mid-ventricle blocks were used for immunohistochemistry. Antigen retrieval was performed using heated sodium citrate buffer and the sections were washed in PBS +0.1% Tween 20, blocked with 5% goat serum in PBS +0.05% Tween-20, and stained with primary antibodies overnight at 4°C (Table 2). The following day, the sections were washed and incubated with secondary antibodies (Table 2), then washed and incubated with DAPI (1 μg/mL, Sigma-Aldrich/Merck). Coverslips were mounted with PBS: Glycerol.

2.4.4 Imaging and analysis

Immunofluorescence and brightfield microscopy were performed on an Olympus VS. 120 Slide Scanner (Olympus® Corporation, Tokyo, Japan), with the ×10 objective (for brightfield), ×20 objective (UPLSAPO ×20/NA 0.75, WD 0.6/CG

TABLE 2 Antibodies for immunohistochemistry.

Primary Antibodies				
Marker	Host	Dilution	Vendor	Product
Alpha smooth muscle actin	Mouse	1:200	Dako	M0851
Cardiac troponin T	Mouse	2.5ug/mL	DSHB	CT3
CD31	Rabbit	1:50	Abcam	ab28364
Collagen type I	Rabbit	1:150	Cell Signalling Technology	91,144
Collagen type III	Rabbit	1:300	Proteintech	22734-1-AP
Secondary Antibodies				
Alpha Fluor 488	Goat anti-mouse	1:500	ThermoFisher	A-11029
Alexa Fluor 594	Goat anti-rabbit	1:500	ThermoFisher	A-11012

Thickness 0.17 or the ×40 objective (UPLSAPO ×40/NA 0.95, WD 0.18/CG Thickness 0.11–0.23) for IHC. Images were acquired using Olympus VS-ASW 2.92 software and processed using Olympus VS-DESKTOP 2.9.

Researchers were blinded to treatment group during image analysis. Images for vessel analysis were prepared by selecting up to 10 fields of view (0.5 × 0.5 mm) from the infarct border zones and infarct scar core regions. Vessel density was measured by counting the number of CD31+/αSMA + vessels in each 0.25 mm² field of view and comparing the mean density between samples. All analyses were performed using FIJI software (ImageJ, U. S. National Institutes of Health, Bethesda, Maryland, United States of America). Collagen sub-type analysis was performed using the "color threshold" plugin to measure the area of target staining relative to the total area of the left ventricular myocardium.

2.5 Statistics

Data are presented as mean ± standard error of the mean (SEM). Normally distributed assay and histology measurements were analysed by ordinary one-way or two-way ANOVA with Tukey adjustment for multiple comparisons. Non-normally distributed assay and histology measurements were analysed by Kruskal–Wallis test by ranks with Dunn's adjustment for multiple comparisons. Fractional shortening measurements were analysed by two-way repeated measures ANOVA with Tukey adjustment for multiple comparisons. Echocardiography inter-operator variability (bias) was measured by Bland-Altman analysis. Statistical analyses were performed using GraphPad Prism software (version 9.4.1), with p values <0.05 considered statistically significant. Raw data files and full-size image files are available on request.

3 Results

### 3.1 Characterisation of PPN-PDGF-AB

We measured the hydrodynamic parameters of PPN, including size distribution, polydisperse index (PDI) and zeta potential in ultrapure nuclease-free water (NFW) using dynamic light scattering (DLS). The process yielded dispersions of pristine PPN with a mean hydrodynamic diameter (Figure 1A), polydisperse index (Figure 1B) and zeta potential (Figure 1C) of 187.9 nm ± 4.6 nm, 0.14 ± 0.05, and 33.2 mV ± 0.9 mV, respectively. Functionalization of PPN with PDGF-AB was performed in NFW by simply mixing PDGF-AB to PPN solutions, following incubation for 1 h at 4°C. The ratio between PDGF-AB molecules to PPN upon conjugation was optimized based on our previous work, which established a relationship between the molecular weight of the molecular cargo and the number of molecules necessary to achieve a full monolayer on the surface of each PPN. Based on the molecular weight of PDGF-AB (26.4 kDa), our model estimates a total of 7.04×10^3 PDGF-AB molecules in a single PPN, or $3.1\mu g/10^{10}$ PPN. Functionalization of PPN with PDGF-AB resulted in a stable formulation, as shown in Figure 1D by non-significant changes to median hydrodynamic size and PDI compared to pristine PPN. Measurements showed a decrease in the zeta potential of PPN-PDGF-AB (29.2 mV ± 0.6 mV) relative to unfunctionalized PPN ($p < 0.001$), indicating binding and retention of PDGF-AB on the surface of PPN.

3.2 PPN and PPN-PDGFAB is non-toxic to cardiac cells *in vitro*

Plasma polymerized nanoparticles readily crossed the cardiomyocyte membrane and formed intracellular aggregates observable by microscopy (Figure 2A). We sought to determine whether the presence of intracellular PPN is detrimental to cardiovascular cells, particularly non-dividing cardiomyocytes. We investigated for potential cytotoxic effects of PPN or PPN-PDGF-AB in cardiomyocytes and coronary artery vascular smooth muscle cells, using physiologically relevant doses of PPN/PPN-PDGF-AB. The PPN-PDGF-AB doses were chosen based on the surface area of the nanoparticles and the size of free rhPDGF-AB to approximate a dose of 50 ng/mL and lower and higher dose equivalents.

To detect signs of cellular stress, we performed a ROS assay on iPSC-CMs 24 h after continuous incubation with PPN or PPN-PDGFAB. The fluorogenic dye, DCFDA, is taken up by cells and oxidized by hydroxyl, peroxyl, and other ROS to the highly fluorescent compound, 2′, 7′ –dichlorofluorescein (DCF). DCF
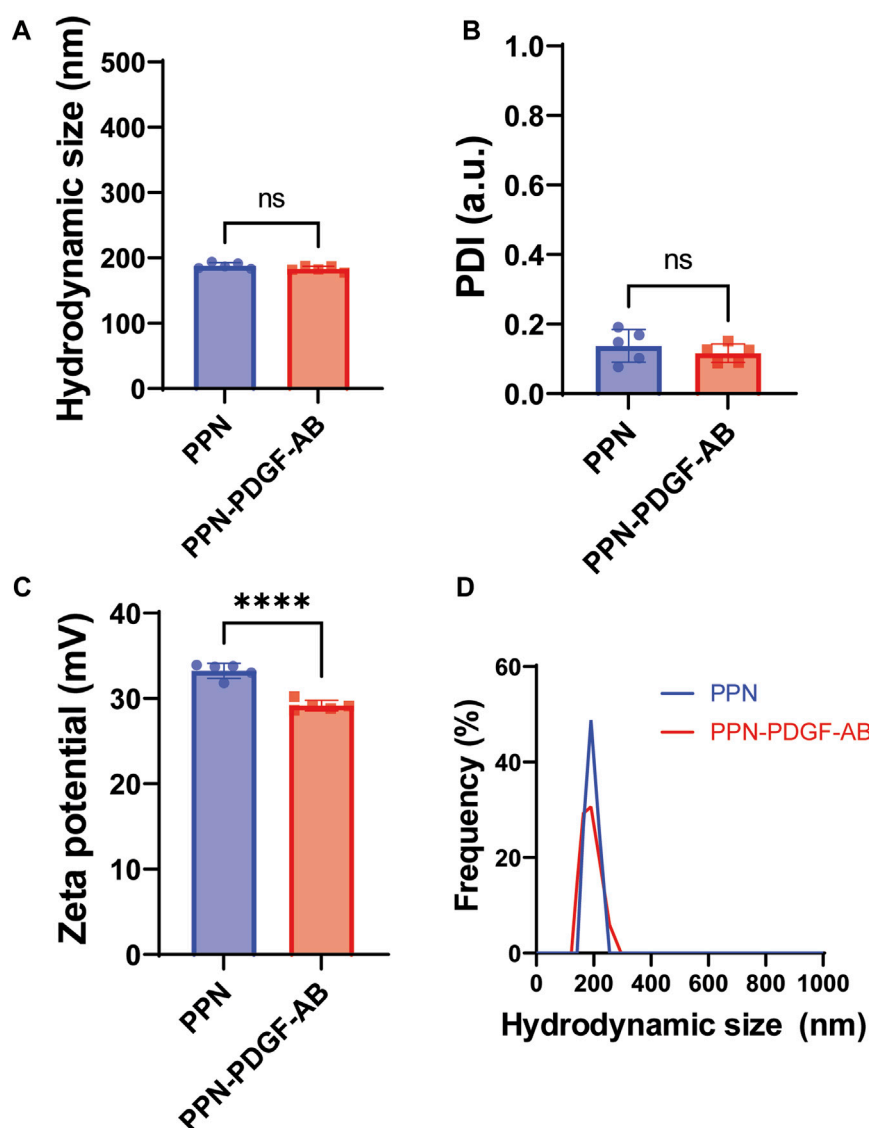
FIGURE 1
Hydrodynamic parameters of PPN-PDGF-AB formulation. Hydrodynamic size **(A)**, polydisperse index **(B)** and zeta potential **(C)** of pristine PPN and PDGF-AB functionalized PPN. Conjugation of PDGF-AB to PPN yielded stable nano-constructs as indicated by a low PDI and negligible change in hydrodynamic size compared to pristine PPN. The decrease in zeta potential of the PPN-PDGF-AB formulation compared to pristine PPN suggests binding and retention of PDGF-AB to PPN following conjugation. The resulting net surface charge of the nano-constructs allows for stabilization of the formulation via electrostatic repulsion. **(D)**. Hydrodynamic size distribution of PPN and PPN-PDGF-AB formulation in ultra-pure NFW is single-peaked, indicating the formation of monodisperse formulations without aggregation.

fluorescence levels were not significantly different between control wells and those treated with nanoparticles, therefore we found no evidence of increased ROS production by PPN or PPN-PDGFAB treated cardiomyocytes at this timepoint, despite the presence of abundant intracellular PPN aggregates (Figure 2B). We did observe a significant reduction in DCF fluorescence in cardiomyocytes treated with 1×10^8 PPN, compared to those treated with the TBHP positive control compound.

We used the MTT assay as a measure of cell viability. We found no effect of treatment with PPN or PPN-PDGFAB on NRVM or vascular smooth muscle cell viability at any of the doses or time-points tested (Figures 2C, D, Supplementary Figure S1). We then performed TMRE assays to detect changes in NVRM mitochondrial membrane potential

in response to PPN or PPN-PDGF-AB. TMRE, a positively charged fluorescent dye, is sequestered by active mitochondria due to the relative negative charge of the mitochondrial matrix. Stressed or dying mitochondria experience a breakdown of their membrane potential and therefore do not accumulate TMRE. We found no significant reduction in TMRE fluorescence in NRVMs at 1, 7, 14, or 21 days after incubation with PPN and PPN-PDGF-AB, compared to controls. An inhibitor of mitochondrial oxidative phosphorylation, FCCP, was used as a positive control and reduced TMRE fluorescence measurements by approximately 50% (Figures 2E, F).

To determine whether the presence of intracellular PPN detrimentally impacts cardiomyocyte contractile function, we recorded beating pluripotent stem cell derived cardiomyocytes
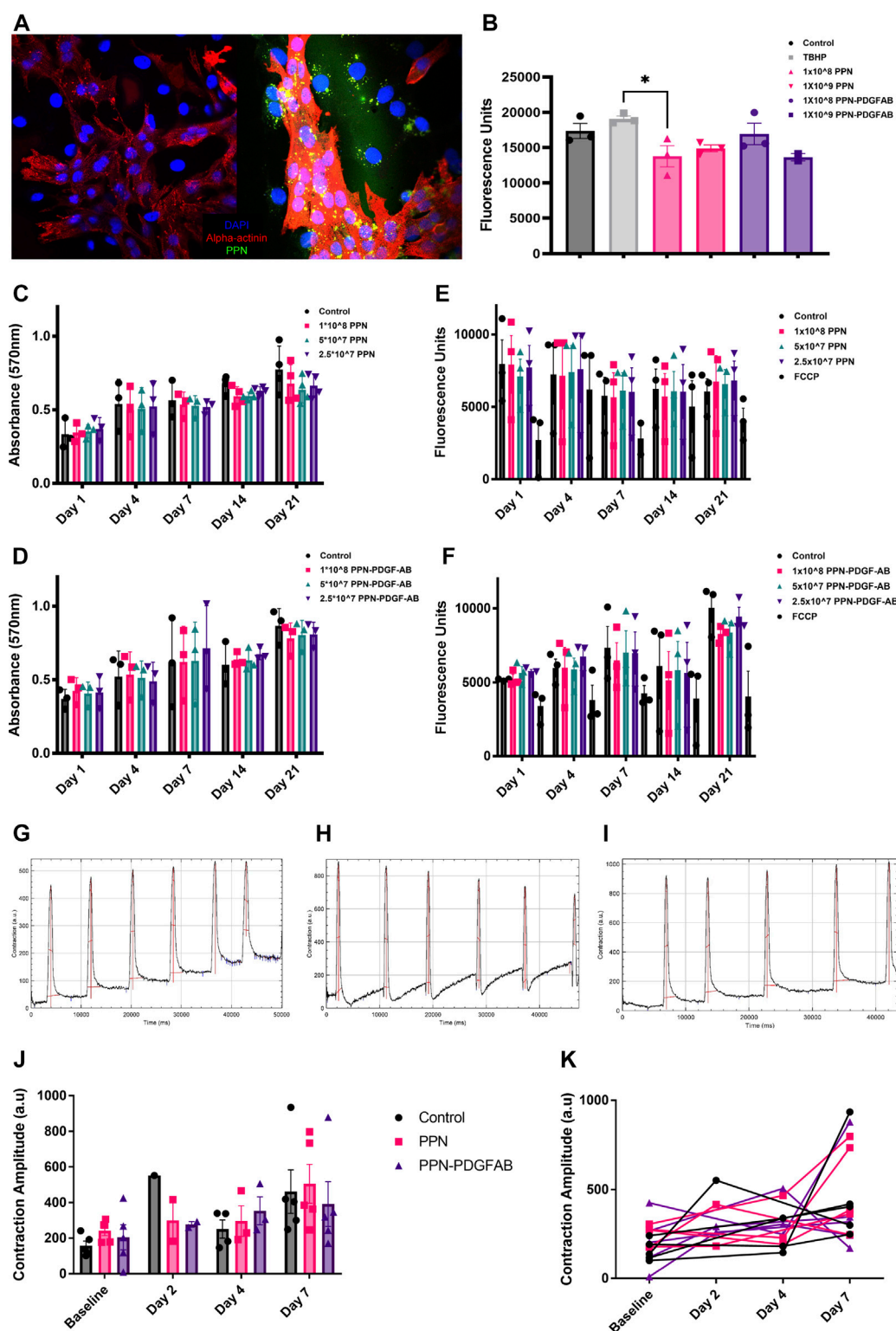
FIGURE 2
Intracellular presence of plasma polymerized nanoparticles is non-toxic to cardiomyocytes. **(A)**. Confocal images of NRVMs and NRVMs treated with PPN, showing intracellular PPN aggregates (green). **(B)**. Fluorescence intensity after 45 min incubation of DCFDA with pluripotent stem cell derived cardiomyocytes 24 h after treatment with PPN or PPN-PDGFAB. **(C, D)**. Optical density after 4h incubation of MTT with NRVMs 1-, 4-, 7-, 14- and 21-day after treatment with PPN **(C)** or PPN-PDGF-AB **(D)**. **(E, F)**. Mitochondrial membrane activity measured by TMRE fluorescence intensity in NRVMs 1-, 4-, 7, 14- and 21-day after treatment with PPN **(E)** or PPN-PDGF-AB **(F)**. **(G–I)**. Representative contraction amplitude traces from control **(G)** PPN treated **(H)** and PPN-PFGF-AB treated PSC-CMs, generated using the MUSCLEMOTION plugin for FIJI. **(J)**. Summary data showing mean contraction amplitude of PSC-CMs treated with PPN or PPN-PDGF at baseline and at 2-, 4- and 7-day post-treatment, in comparison to untreated controls. **(K)**. Individual well data showing contraction amplitude of PPN, and PPN-PDGF-AB, treated PSC-CMs over time, compared to untreated controls.
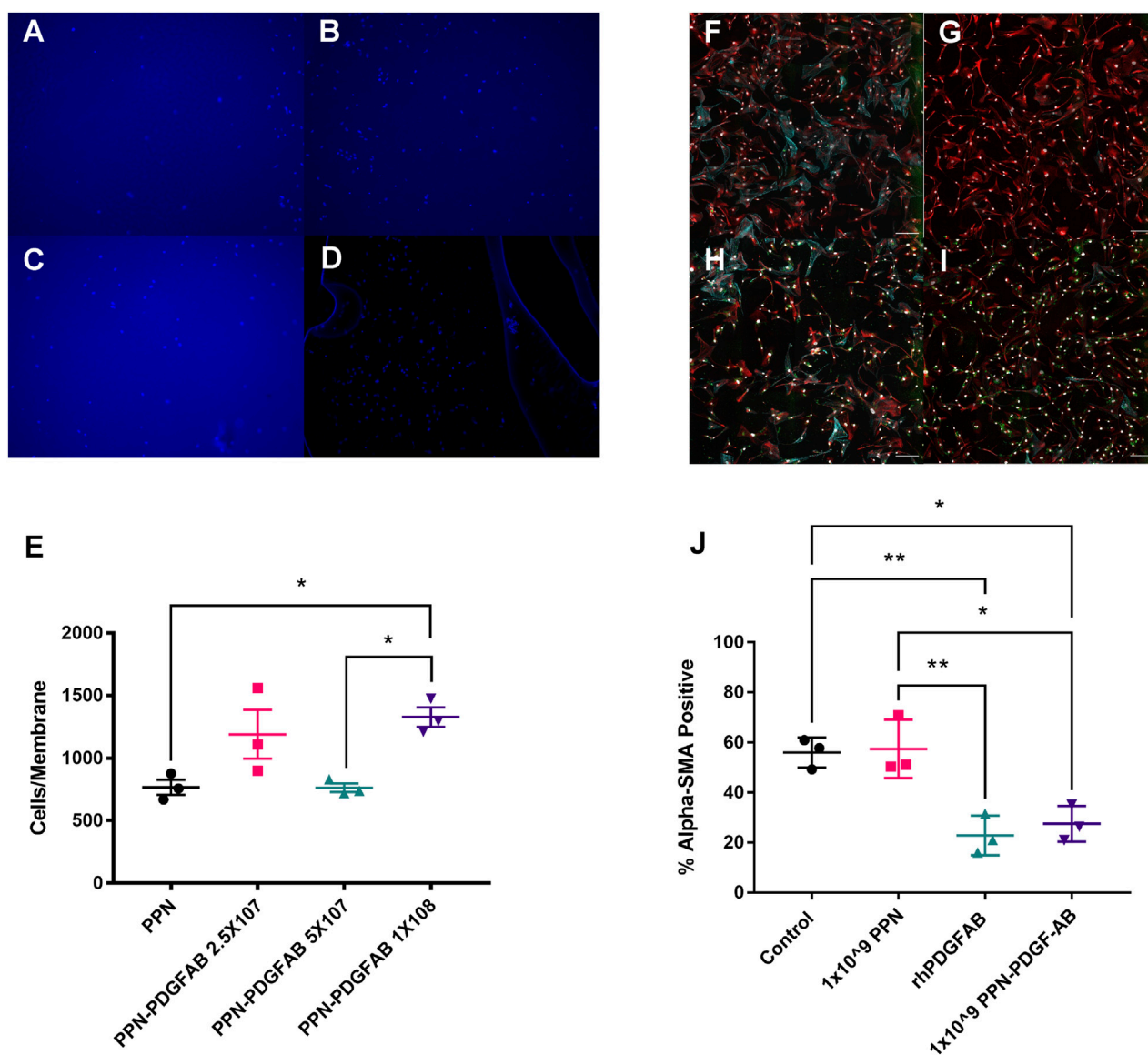
FIGURE 3
PDGF-AB remains functional when bound to plasma polymerized nanoparticles. (A–D). Transwell migration assays. Images of DAPI stained nuclei of HCASMCs that migrated through to the underside of the Boyden chamber membrane in wells that contained 1×10^8 PPN only (A) or 2.5×10^7 (B), 5×10^7 (C), or 1×10^8 (D) PPN-PDGF-AB. Scale bars: 50 μm (E). Quantitative analysis of transwell migration assays, showing increased migration of HCASMCs through membranes from wells containing 2.5×10^7 and 1×10^8 PPN-PDGF-AB, compared to PPN only. (F–I). Expression of alpha smooth muscle actin (α-SMA) by human cardiac fibroblasts. Representative images of serum-starved cardiac fibroblasts (F) taken post-treatment with rhPDGFAB (G), cargo-free PPN (H) and PPN-PDGF-AB (I). (J) Quantitative analysis shows PPN-PDGFAB reduces alpha-SMA expression by human cardiac fibroblasts to a similar extent as unbound rhPDGF-AB. Application of cargo-free PPN has no effect on α-SMA expression. Red-vimentin; teal—α-SMA; green—nanoparticle autofluorescence; white—DAPI. n = 3 biological replicates per group. Scale bars: 300 μm *$p < 0.05$, **$p < 0.01$.

(PSC-CMs) and used a FIJI plugin, MUSCLEMOTION, to measure contraction amplitude before and up to 7 days after application of 1×10^9 PPN or 1×10^9 PPN-PDGF-AB or PBS control. We found a significant effect of time in culture on cardiomyocyte contraction amplitude, which increased in all treatment groups over the 7-day period. There was no difference in mean contraction amplitude between control wells and PPN or PPN-PDGF-AB treated wells at baseline or at 4 days or 7 days post-treatment (Figures 2G–J). As there is inherent variability in PSC-CM contraction amplitude between wells, plotting repeated measurements for individual

wells confirmed that there is no decline in PPN treated cardiomyocytes' contractile activity relative to their own baseline (Figure 2K).

3.3 PDGF-AB remains functional when bound to PPN

We next sought to confirm that PDGF-AB protein remains functional when bound to PPN. PDGF is a known chemoattractant

for PDGFRα+ human vascular smooth muscle cells, so we used a boyden chamber migration assay to measure the cells' response to PPN-PDGF-AB (Figures 3A–D). A significantly increased number of cells migrated through the chamber membrane in wells containing media with PPN-PDGF-AB compared to those containing media with unbound PPN only (PPN 768 ± 60 vs. 1×10^8 PPN-PDGF-AB 1329 ± 78 nuclei) (Figure 3E).

Following a tissue injury such as myocardial infarction, fibroblasts undergo activation to myofibroblasts and contribute to fibrosis via deposition of extracellular matrix components, such as collagens and elastin. The most commonly used marker of activated (myo)fibroblasts is alpha smooth muscle actin (Ivey and Tallquist, 2016). PDGF isoforms play a complex role in fibroblast activation and ECM accumulation, with PDGF-AB having previously been shown to reduce the expression of alpha smooth muscle actin in cardiac fibroblasts (Hume et al., 2023). We performed immunocytochemistry staining for αSMA and vimentin on human cardiac fibroblasts treated with PPN and PPN-PDGFAB (Figures 3F–I). We found that the percentage of alpha smooth muscle actin positive cardiac fibroblasts was significantly reduced in CFs treated with PPN-PDGF-AB and free PDGF-AB, compared to CFs treated with control vehicle or the cargo-free PPN (Serum starved (control) 56.0% ± 3.5% vs. PPN 57.5% ± 6.7% vs. rhPDGF-AB 22.9% ± 4.6% vs. PPN-PDGF-AB 27.5% ± 4.1%) (Figure 3J).

3.4 PPN-PDGF-AB in a rodent model of myocardial infarction

After confirming PDGF-AB remains functional while bound to PPN, we sought to determine whether PPN-PDGF-AB is cardioprotective in a rat model of myocardial infarction. Twenty-nine animals underwent surgery for permanent ligation of the left anterior descending artery (LAD) to induce myocardial infarction. All received PPN-PDGF-AB (1×10^9 particles per dose) or equivalent doses of PPN, rhPDGF-AB, or saline control, injected into the infarct border regions immediately following reperfusion. Twenty-six animals recovered and reached the study endpoint at 14 days post-infarct. Three animals succumbed to large infarcts during surgery or during the 24-h period immediately following surgery.

To measure LV function, we performed transthoracic echocardiography at baseline, and at 3 days and 14 days post-infarction. At 3 days post-infarct, infarct burden was comparable between all treatment groups, as measured by fractional shortening. At 14- days post-infarct, rats treated with PPN-PDGF-AB had significantly improved fractional shortening compared to rats treated with PPN only (day 14 44.5% ± 2.4% for PPN-PDGF-AB vs. 29.4% ± 2.0% for PPN), attributable to preserved systolic function as measured by LVESD (Figures 4A,B, Supplementary Figure S2, Supplementary Table S1). Echocardiography analysis was performed by 2 operators, with good inter-operator agreement (Supplementary Figure S3). Two animals were excluded from analyses due to failure of infarct creation as determined by the absence of reduction in fractional shortening at day 3 and total absence of infarct scar at the apical and mid LV levels as measured by histology.

To investigate possible underlying mechanisms for the preservation of fractional shortening in PPN-PDGFAB treated hearts, we collected tissue for histology and immunohistochemistry analyses at day 14 post-

infarct. To determine if PPN-PDGF-AB treatment affected infarct scar size, we quantified scar as a percentage of the total LV area, using picrosirius red and fast green staining at the apex and mid-ventricle levels. We found that infarct scar sizes were not significantly different between groups at either level (Figures 4C, D, Supplementary Figures S4A–D, S5). Overall scar burden was higher at the apex, so we first focused on measuring scar composition and vessel density at this level.

We performed immunohistochemistry targeting collagen I and collagen III in adjacent tissue sections. We then quantified the ratio of collagen I to collagen III. At this timepoint (day 14 post-infarct) collagen III was the predominant collagen subtype present in all scars, however we found no differences in the ratio of type I to type III between the treatment groups (Figure 4E).

As PDGF-AB is known to be angiogenic during the proliferative stage of wound healing, we hypothesized that enhanced growth of new blood vessels may have salvaged at-risk myocardium in the infarct border regions. At the apical level, there were no significant differences in infarct core region or border zone vessel density (Figures 4F, G). We did observe a trend towards increased vessel density in the mid-LV border zone of PPN-PDGF-AB treated infarcts, compared to controls and a significantly increased vessel density in the mid-LV infarct core region of PDGFAB treated hearts compared to both Control and PPN-PDGFAB treated hearts (Border zone 50 ± 7 vessels per FOV for PPN-PDGF-AB vs.30 ± 4 vessels for Control, $p = 0.0797$; Infarct core 52 ± 7 vessels per FOV for PDGFAB vs. 24 ± 5 vessels for Control ($p = 0.0137$) and 30 ± 3 vessels for PPN-PDGFAB ($p = 0.0491$), Supplementary Figure S5).

4 Discussion

Preclinical evidence suggests PDGF-AB has therapeutic potential for repair and functional recovery of the acutely infarcted heart (Asli et al., 2019; Thavapalachandran et al., 2020). There is precedent for the use of PDGF clinically, with PDGF-BB products already available for the treatment of chronic wounds and periodontal defects (Smiell et al., 1999; Nevins et al., 2005). However, the pro-angiogenic and pro-proliferative effects of PDGF receptor signaling have been implicated in the progression of cancers and the development of atherosclerosis, organ fibrosis, and pulmonary hypertension (Bonner, 2004; Raines, 2004; Barst, 2005; Farooqi and Siddik, 2015). The potential for unwanted off-target effects of continuous systemic delivery of PDGF-AB combined with the prospect of increasing availability of PDGF-AB to the infarct and border zone region prompted us to investigate a nanocarrier-based method for localised delivery to cardiac cells.

Plasma polymerized nanoparticles (PPN) are a new class of nanocarriers which allow for a facile, one-step functionalization with molecular cargo. In contrast with conventional wet chemistry approaches, PPN are produced in a dry plasma medium via plasma polymerization (Santos et al., 2016) of a reactive gaseous mixture comprising of nitrogen, argon and acetylene (Santos et al., 2018). Activation of acetylene-containing mixtures in a rf discharge generates complex dusty plasmas, which are populated with high concentrations of electrostatically stabilized nanoparticles. Control over the formation, yield and physical-chemical properties of PPN (e.g., size, surface chemistry and charge) is achieved by selection of relevant input parameters, including system pressure, gas flow rates, pumping efficiency and input rf power.
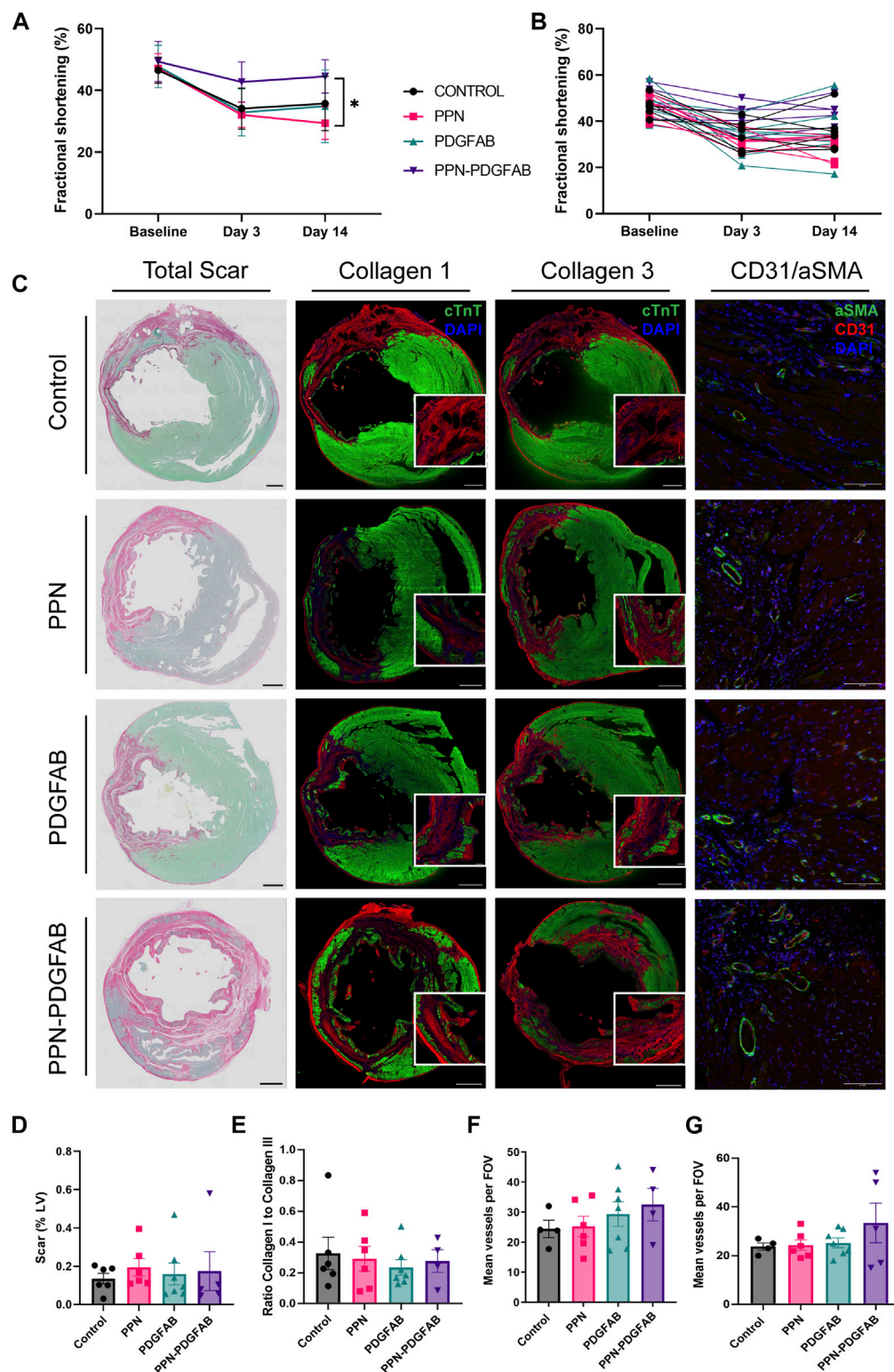
FIGURE 4
PPN-PDGFAB delivery after myocardial infarction preserves fractional shortening. **(A)**. Fractional shortening summary data and individual animal data **(B)** at each time point. Sample sizes were n = 5 (PPN-PDGFAB), n = 6 (Control), and n = 7 (PPN and PDGFAB) biological replicates. **(C)**. Representative images of total apical infarct scar, infarct collagen I, infarct collagen III, and CD31+/αSMA + vessels in the infarct border zone. Scale bars: 1 mm. Inset scale bars: 200μm **(D)**. Quantitative analysis of picrosirius red fast green stained sections, showing infarct scar size as a percentage of LV area at the apex. **(E)**. Ratio of infarct collagen I to collagen III at the apical level. **(F, G)**. CD31+/αSMA + vessel density at the apical infarct core and infarct border zone.

The extraction of PPN from the plasma medium is carried through exposure of a well-shape substrate (polystyrene well plates) to the dusty plasma, enabling high yield collection and further storage of PPN in their native dry state up until before the conjugation process with molecular cargo in solution (Santos et al., 2019).

Here, we selected plasma input parameters that yield pristine PPNs with a surface chemistry characterized by the presence of functional groups (e.g., amines and carboxylic acid). Dispersion of PPN in aqueous solution yields aggregation-free nano-formulations, stabilized by electrostatic repulsion due to protonation of amine functional groups. Immobilization of PDGF-AB to PPN was performed in a one-step mixing and incubation process in water. The stability of the resulting PPN-PDGF-AB formulations was demonstrated by unchanged hydrodynamic size and PDI compared to pristine PPN. The decrease in zeta potential of PPN-PDGF-AB relative to unfunctionalized PPN suggests changes to the ionic double layer upon binding, hence confirming immobilization and retention of PDGF-AB on the surface of PPN. The resulting net charge of the nano-constructs stabilized dispersion in solution, resulting in a monodisperse nano-population without aggregation.

PPN readily crossed the cell membrane and intracellular aggregates were still visible 3 weeks after delivery. Although PPN have been previously proven non-cytotoxic in multiple cell lines, cardiomyocytes present a unique environment due to their complex contractile machinery and their inability to dilute PPN aggregate build up through proliferation. Despite these additional considerations, we did not find evidence of cellular stress or cytotoxicity in PPN, or PPN-PDGF-AB treated cardiomyocytes. The MTT assay is a non-specific measure of viability and can be influenced by cell number, proliferation rate, MTT concentration, and incubation time (Ghasemi et al., 2021). We controlled for all factors except inherent variability in proliferation rate of non-myocytes and between HCASMCs from different donors. Nevertheless, we observed that biological replicates behaved similarly in their response to PPN and PPN-PDGF-AB.

We also measured cardiomyocyte mitochondrial membrane potential and contractile activity. It is common to see variability between PSC-CM differentiations and within PSC-CM differentiations recorded on different days. Unexpectedly, we observed reduced contractile amplitude at 7 days post-treatment in some wells treated with PPN-PDGF-AB, but not with PPN only. This suggests any inhibitory effect may be mediated via PDGF-AB rather than the nanoparticles themselves. Potentially, there is a stimulatory effect of PDGF-AB on stem cell derived PDGFRα+ non-myocytes present in the well, which influences the contractile properties of surrounding PSC-CMs (Huang et al., 2020).

The PDGF-A and PDGF-B chains contain highly conserved regions known to be crucial for receptor binding (Clements et al., 1991; Ostman et al., 1991; Fenstermaker et al., 1993). For the PDGF-AB heterodimer to remain functional while bound to PPN, these monomer binding sites must remain available to PDGF receptors. We confirmed that human PDGFRα+ vascular smooth muscle cells and cardiac fibroblasts respond to treatment with PPN-PDGFAB in the same manner as they do to free recombinant human PDGF-AB. We saw increased migration of coronary artery vascular smooth muscle cells in response to PPN-PDGF-AB, as well as a striking reduction in alpha smooth muscle actin expression in cardiac fibroblasts treated with recombinant human PDGF-AB protein and with PPN-PDGF-AB.

We observed a modest preservation of fractional shortening at day 14 in animals treated with PPN-PDGF-AB after permanent LAD ligation, compared to those treated with PPN only. However, this was not accompanied by significant changes in scar composition or peri-infarct vascularity. A single dose of PDGF-AB or PPN-PDGFAB direct to the myocardium post-infarct does not appear to be sufficient to induce cardiac repair. Given that pretreatment with PPN-PDGF-AB is the less clinically applicable scenario, an increased or repeat dosage of PPN-PDGF-AB post infarct may be required for robust efficacy of PDGF-AB in this model.

One limitation of this study is that the PPN-PDGFAB treatment was given immediately following infarct by permanent ligation, so we were not able to collect post-infarct baseline echocardiography measurements of LVEDV and LVESV. A second limitation relates to the difficulty in accurately determining equivalent doses of recombinant PDGF-AB protein and PPN-PDGF-AB. We calculated the surface area of the nanoparticles and the size of the PDGF-AB protein to estimate total PDGF-AB bound to PPN. It is also not possible to compare this direct intramyocardial dose to the dose received by the heart when PDGF-AB was delivered systemically in earlier studies (Asli et al., 2019; Thavapalachandran et al., 2020).

Had we observed a beneficial effect of PPN-PDGFAB over PDGFAB our next steps would be to investigate potential mechanisms, including increased PDGF-AB stability, bioavailability, or other paracrine effects of PPN-PDGFAB. As it stands, this work establishes the possibility of using PPN as a platform for delivery of bioactive compounds directly to the heart. From a translational perspective, minimally invasive PPN delivery methods such as catheter-based intracoronary delivery or endocardial injections will be superior to direct intramyocardial injections. Larger, longer-term studies to compare these methods will require the use of clinically relevant pig or non-human primate models and should evaluate PPN biodistribution and bioavailability to the heart. This is particularly pertinent for any systemic intravenous or even intracoronary delivery method given that PPN are readily taken up by other organs (Michael et al., 2021).

In summary, we have performed simple conjugation of PDGF-AB to plasma polymerised nanoparticles for direct administration of functional protein to cardiac cells *in vitro* and *in vivo*. Our results demonstrate safety and feasibility of the PPN platform for delivery of therapeutics directly to the myocardium for either cell surface or intracellular interactions. Future work will focus on optimizing PPN-PDGF-AB formulations and determining the most effective dosage and timing to deliver PDGF-AB systemically, ultimately to improve bioavailability and efficacy of PDGF-AB and accelerate recovery of patients with heart failure following myocardial infarction.

Data availability statement

The raw data supporting the conclusion of this article will be made available by the authors, without undue reservation.

Ethics statement

The animal study was reviewed and approved by the Western Sydney Local Health District Animal Ethics Committee.

Author contributions

ZC contributed to the conception and design of the work, data collection, analysis, and interpretation, and wrote the majority of the manuscript. MS contributed to the conception and design of the work, data collection, analysis, and interpretation, and wrote parts of the manuscript. HSha contributed to *in vivo* data collection, analysis, and interpretation. JL contributed to *in vivo* data collection. SC contributed to *in vivo* data analysis and interpretation. HShi contributed to *in vitro* data collection, analysis, and interpretation. SK contributed to *in vitro* data collection, analysis, and interpretation. PM contributed to *in vitro* data collection. SW contributed to the conception and design of the work, interpretation of the data, and revision of the manuscript. JC contributed to the conception and design of the work, interpretation of the data, and revision of the manuscript. All authors contributed to the article and approved the submitted version.

Funding

Acknowledgments

Conflict of interest

The authors declare that the research was conducted in the absence of any commercial or financial relationships that could be construed as a potential conflict of interest.

Publisher's note

All claims expressed in this article are solely those of the authors and do not necessarily represent those of their affiliated organizations, or those of the publisher, the editors and the reviewers. Any product that may be evaluated in this article, or claim that may be made by its manufacturer, is not guaranteed or endorsed by the publisher.

Supplementary material

The Supplementary Material for this article can be found online at: https://www.frontiersin.org/articles/10.3389/fbioe.2023.1127996/full#supplementary-material

References

Asli, N. S., Xaymardan, M., Patrick, R., Farbehi, N., Cornwell, J., Forte, E., et al. (2019). *PDGFRα signaling in cardiac fibroblasts modulates quiescence, metabolism and self-renewal, and promotes anatomical and functional repair*. New York: bioRxiv, 225979.

Barrientos, S., Stojadinovic, O., Golinko, M. S., Brem, H., and Tomic-Canic, M. (2008). Perspective article: Growth factors and cytokines in wound healing. *Wound Repair Regen.* 16 (5), 585–601. doi:10.1111/j.1524-475x.2008.00410.x

Barst, R. J. (2005). PDGF signaling in pulmonary arterial hypertension. *J. Clin. Invest.* 115 (10), 2691–2694. doi:10.1172/jci26593

Bonner, J. C. (2004). Regulation of PDGF and its receptors in fibrotic diseases. *Cytokine & Growth Factor Rev.* 15 (4), 255–273. doi:10.1016/j.cytogfr.2004.03.006

Bunting, K. V., Steeds, R. P., Slater, L. T., Rogers, J. K., Gkoutos, G. V., and Kotecha, D. (2019). A practical guide to assess the reproducibility of echocardiographic measurements. *J. Am. Soc. Echocardiogr.* 32 (12), 1505–1515. doi:10.1016/j.echo.2019.08.015

Cianciolo, G., Stefoni, S., Zanchelli, F., Iannelli, S., Colì, L., Borgnino, L. C., et al. (1999). PDGF-AB release during and after haemodialysis procedure. *Nephrol. Dial. Transplant.* 14 (10), 2413–2419. doi:10.1093/ndt/14.10.2413

Clements, J. M., Bawden, L. J., Bloxidge, R. E., Catlin, G., Cook, A. L., Craig, S., et al. (1991). Two PDGF-B chain residues, arginine 27 and isoleucine 30, mediate receptor binding and activation. *EMBO J.* 10 (13), 4113–4120. doi:10.1002/j.1460-2075.1991.tb04988.x

Donner, D. G., Kiriazis, H., Du, X-J., Marwick, T. H., and McMullen, J. R. (2018). Improving the quality of preclinical research echocardiography: Observations, training, and guidelines for measurement. *Am. J. Physiology-Heart Circulatory Physiology* 315 (1), H58–H70. doi:10.1152/ajpheart.00157.2018

Edelberg, J. M., Lee, S. H., Kaur, M., Tang, L., Feirt, N. M., McCabe, S., et al. (2002). Platelet-derived growth factor-AB limits the extent of myocardial infarction in a rat model. *Circulation* 105 (5), 608–613. doi:10.1161/hc0502.103672

Farooqi, A. A., and Siddik, Z. H. (2015). Platelet-derived growth factor (PDGF) signalling in cancer: Rapidly emerging signalling landscape. *Cell. Biochem. Funct.* 33 (5), 257–265. doi:10.1002/cbf.3120

Fenstermaker, R. A., Poptic, E., Bonfield, T. L., Knauss, T. C., Corsillo, L., Piskurich, J. F., et al. (1993). A cationic region of the platelet-derived growth factor (PDGF) A-chain (Arg159-Lys160-Lys161) is required for receptor binding and mitogenic activity of the PDGF-AA homodimer. *J. Biol. Chem.* 268 (14), 10482–10489. doi:10.1016/s0021-9258(18)82224-4

Ghasemi, M., Turnbull, T., Sebastian, S., and Kempson, I. (2021). The MTT assay: Utility, limitations, pitfalls, and interpretation in bulk and single-cell analysis. *Int. J. Mol. Sci.* 22 (23), 12827. doi:10.3390/ijms222312827

Huang, C. Y., Peres Moreno Maia-Joca, R., Ong, C. S., Wilson, I., DiSilvestre, D., Tomaselli, G. F., et al. (2020). Enhancement of human iPSC-derived cardiomyocyte maturation by chemical conditioning in a 3D environment. *J. Mol. Cell. Cardiol.* 138, 1–11. doi:10.1016/j.yjmcc.2019.10.001

Hume Robert, D., Deshmukh, T., Doan, T., Shim Woo, J., Kanagalingam, S., Tallapragada, V., et al. (2023). PDGF-AB reduces myofibroblast differentiation without increasing proliferation after myocardial infarction. *JACC Basic Transl. Sci.* 0 (0). doi:10.1016/j.jacbts.2022.11.006

Ivey, M. J., and Tallquist, M. D. (2016). Defining the cardiac fibroblast. *Circ. J.* 80 (11), 2269–2276. doi:10.1253/circj.cj-16-1003

Lian, X., Zhang, J., Azarin, S. M., Zhu, K., Hazeltine, L. B., Bao, X., et al. (2013). Directed cardiomyocyte differentiation from human pluripotent stem cells by modulating Wnt/β-catenin signaling under fully defined conditions. *Nat. Protoc.* 8 (1), 162–175. doi:10.1038/nprot.2012.150

Michael, P., Lam, Y. T., Filipe, E. C., Tan, R. P., Chan, A. H. P., Lee, B. S. L., et al. (2020). Plasma polymerized nanoparticles effectively deliver dual siRNA and drug therapy *in vivo*. *Sci. Rep.* 10 (1), 12836. doi:10.1038/s41598-020-69591-x

Michael, P. L., Lam, Y. T., Hung, J., Tan, R. P., Santos, M., and Wise, S. G. (2021). Comprehensive evaluation of the toxicity and biosafety of plasma polymerized nanoparticles. *Nanomaterials* 11 (5), 1176. doi:10.3390/nano11051176

Nevins, M., Giannobile, W. V., McGuire, M. K., Kao, R. T., Mellonig, J. T., Hinrichs, J. E., et al. (2005). Platelet-derived growth factor stimulates bone fill and rate of attachment level gain: Results of a large multicenter randomized controlled trial. *J. Periodontology* 76 (12), 2205–2215. doi:10.1902/jop.2005.76.12.2205

Ostman, A., Andersson, M., Hellman, U., and Heldin, C. H. (1991). Identification of three amino acids in the platelet-derived growth factor (PDGF) B-chain that are important for binding to the PDGF beta-receptor. *J. Biol. Chem.* 266 (16), 10073–10077. doi:10.1016/s0021-9258(18)99191-x

Raines, E. W. (2004). PDGF and cardiovascular disease. *Cytokine & Growth Factor Rev.* 15 (4), 237–254. doi:10.1016/j.cytogfr.2004.03.004

Rashid, F. N., Clayton, Z. E., Ogawa, M., Perdomo, J., Hume, R. D., Kizana, E., et al. (2021). Platelet derived growth factor-A (Pdgf-a) gene transfer modulates scar

composition and improves left ventricular function after myocardial infarction. *Int. J. Cardiol.* 341, 24–30. doi:10.1016/j.ijcard.2021.07.021

Sala, L., Meer, B. J., Tertoolen, L. G. J., Bakkers, J., Bellin, M., Davis, R. P., et al. (2018). Musclemotion: A versatile open software tool to quantify cardiomyocyte and cardiac muscle contraction *in vitro* and *in vivo*. *MUSCLEMOTION. Circulation Res.* 122 (3), e5–e16. doi:10.1161/CIRCRESAHA.117.312067

Santos, M., Filipe, E. C., Michael, P. L., Hung, J., Wise, S. G., and Bilek, M. M. M. (2016). Mechanically robust plasma-activated interfaces optimized for vascular stent applications. *ACS Appl. Mater. Interfaces* 8 (15), 9635–9650. doi:10.1021/acsami.6b01279

Santos, M., Michael, P. L., Filipe, E. C., Chan, A. H. P., Hung, J., Tan, R. P., et al. (2018). Plasma synthesis of carbon-based nanocarriers for linker-free immobilization of bioactive cargo. *ACS Appl. Nano Mater.* 1 (2), 580–594. doi:10.1021/acsanm.7b00086

Santos, M., Reeves, B., Michael, P., Tan, R., Wise, S. G., and Bilek, M. M. M. (2019). Substrate geometry modulates self-assembly and collection of plasma polymerized nanoparticles. *Commun. Phys.* 2 (1), 52. doi:10.1038/s42005-019-0153-5

Smiell, J. M., Wieman, T. J., Steed, D. L., Perry, B. H., Sampson, A. R., and Schwab, B. H. (1999). Efficacy and safety of becaplermin (recombinant human platelet-derived growth factor-BB) in patients with nonhealing, lower extremity diabetic ulcers: A combined analysis of four randomized studies. *Wound Repair Regen.* 7 (5), 335–346. doi:10.1046/j.1524-475x.1999.00335.x

Thavapalachandran, S., Grieve, S. M., Hume, R. D., Le, T. Y. L., Raguram, K., Hudson, J. E., et al. (2020). Platelet-derived growth factor-AB improves scar mechanics and vascularity after myocardial infarction. *Sci. Transl. Med.* 12 (524), eaay2140. doi:10.1126/scitranslmed.aay2140

Xaymardan, M., Zheng, J., Duignan, I., Chin, A., Holm, J. M., Ballard, V. L. T., et al. (2004). Senescent impairment in synergistic cytokine pathways that provide rapid cardioprotection in the rat heart. *J. Exp. Med.* 199 (6), 797–804. doi:10.1084/jem.20031639

Glossary

αSMA	alpha smooth muscle actin
CF	cardiac fibroblast
DCFDA	2′,7′–dichlorofluorescin diacetate
DLS	dynamic light scattering
DMEM	Dulbecco's modified eagle medium
ECM	extracellular matrix
FFCP	carbonyl cyanide 4-(trifluoromethoxy) phenylhydrazone
FOV	field of view
HCASMC	human coronary artery smooth muscle cell
LAD	left anterior descending (artery)
LV	left ventricle
LVESD	left ventricular end systolic diameter
LVEDD	left ventricular end diastolic diameter
MEMα	modified minimum essential medium
MI	myocardial infarction
MTT	3-(4,5-dimethylthiazol-2-yl)-2,5-diphenyltetrazolium bromide
NFW	nuclease free water
NGS	normal goat serum
NRVM	neonatal rat ventricular myocyte
OES	optical emission spectroscopy
PDGF-AB	platelet derived growth factor AB
PDGFR	platelet derived growth factor receptor
PDI	polydisperse index
PPN	plasma polymerized nanoparticles
pSAX	parasternal short axis
PSC-CM	pluripotent stem cell derived cardiomyocyte
RF	radiofrequency
rhPDGF-AB	recombinant human platelet derived growth factor AB
ROS	reactive oxygen species
RPMI	roswell park memorial institute
SCVI	Stanford cardiovascular institute
TBHP	Tert-butyl hydroperoxide
TMRE	Tetramethylrhodamine, ethyl ester
UV/VIS	ultraviolet-visible spectroscopy

Frontiers in Bioengineering and Biotechnology

Single-cell RNA sequencing analysis identifies one subpopulation of endothelial cells that proliferates and another that undergoes the endothelial–mesenchymal transition in regenerating pig hearts

Thanh Minh Nguyen[1], Xiaoxiao Geng[1], Yuhua Wei[1], Lei Ye[1], Daniel J. Garry[2] and Jianyi Zhang[1,3]*

[1]Department of Biomedical Engineering, University of Alabama at Birmingham, Birmingham, AL, United States, [2]Department of Medicine, School of Medicine, University of Minnesota, Minneapolis, MN, United States, [3]Department of Medicine, Cardiovascular Diseases, University of Alabama at Birmingham, Birmingham, AL, United States

Background: In our previous work, we demonstrated that when newborn pigs undergo apical resection (AR) on postnatal day 1 (P1), the animals' hearts were completely recover from a myocardial infarction (MI) that occurs on postnatal day 28 (P28); single-nucleus RNA sequencing (snRNAseq) data suggested that this recovery was achieved by regeneration of pig cardiomyocyte subpopulations in response to MI. However, coronary vasculature also has a key role in promoting cardiac repair.

Method: Thus, in this report, we used autoencoder algorithms to analyze snRNAseq data from endothelial cells (ECs) in the hearts of the same animals.

Main results: Our results identified five EC clusters, three composed of vascular ECs (VEC1-3) and two containing lymphatic ECs (LEC1-2). Cells from VEC1 expressed elevated levels of each of five cell-cyclespecific markers (Aurora Kinase B [AURKB], Marker of Proliferation Ki-67 [MKI67], Inner Centromere Protein [INCENP], Survivin [BIRC5], and Borealin [CDCA8]), as well as a number of transcription factors that promote EC proliferation, while (VEC3 was enriched for genes that regulate intercellular junctions, participate in transforming growth factor β (TGFβ), bone morphogenic protein (BMP) signaling, and promote the endothelial mesenchymal transition (EndMT). The remaining VEC2 did not appear to participate directly in the angiogenic response to MI, but trajectory analyses indicated that it may serve as a reservoir for the generation of VEC1 and VEC3 ECs in response to MI. Notably, only the VEC3 cluster was more populous in regenerating (i.e., $AR_{P1}MI_{P28}$) than non-regenerating (i.e., MI_{P28}) hearts during the 1-week period after MI induction, which suggests that further investigation of the VEC3 cluster could identify new targets for improving myocardial recovery after MI. Histological analysis of KI67 and EndMT marker PDGFRA demonstrated that while the expression of proliferation of endothelial cells was not significantly

different, expression of EndMT markers was significantly higher among endothelial cells of $AR_{P1}MI_{P28}$ hearts compared to MI_{P28} hearts, which were consistent with snRNAseq analysis of clusters VEC1 and VEC3. Furthermore, upregulated secrete genes by VEC3 may promote cardiomyocyte proliferation via the Pi3k-Akt and ERBB signaling pathways, which directly contribute to cardiac muscle regeneration.

Conclusion: In regenerative heart, endothelial cells may express EndMT markers, and this process could contribute to regeneration via a endothelial-cardiomyocyte crosstalk that supports cardiomyocyte proliferation.

1 Introduction

Adult mammal hearts, especially the cardiomyocytes, cannot regenerate (Laflamme and Murry, 2011; Steinhauser and Lee, 2011); after being damaged by an acute injury, such as myocardial infarction (MI), a large amount of cardiomyocytes die (Chiong et al., 2011). Although the adult and juvenile hearts may undergo remodeling (Sutton and Sharpe, 2000) to attempt repairing the damage, cardiomyocytes undergo pathological hypertrophy instead of proliferation, leading to further decrease of heart function, left ventricle dilation, and heart failure (McMullen and Jennings, 2007). No approach to reverse the post-MI pathological remodeling has been found; therefore, treatments of MI are only temporary, such as strengthening the heartbeat and increasing blood flow to the heart (Lu et al., 2015); and heart failure still frequently occurs (McMullen and Jennings, 2007). On the other hand, 4 weeks after MI was induced in postnatal (P) day 1, mammal hearts recovered completely by P30 with no decline in cardiac function and negligible myocardial scarring (Porrello et al., 2011; Ye et al., 2018; Zhu et al., 2018; Zhao et al., 2020); in these cases, cardiomyocytes robustly proliferated instead of becoming hypertrophic. Therefore, studying how neonatal hearts undergo 'regenerative' remodeling instead of 'failure' remodeling is important to find better treatment for MI and heart failure. Furthermore, We demonstrated that when apical resection (AR) surgery is performed in pig hearts on P1 (AR_{P1}), cardiomyocytes proliferated in response to MI induction on P28 (MI_{P28}), and the animals fully recovered with no evidence of scar formation and also no decline in heart function by P56 (Zhao et al., 2020; Nakada et al., 2022). Thus, we established a model where the juvenile hearts perform a 'regenerative' remodel to repair MI damage. Although inducing AR_{P1} may not be a therapeutic solution to prevent heart failure in mammals, this 'juvenile' regenerative model is more mature than the neonatal P1; therefore, understanding how different the cardiac cell types' regeneratively' respond to MI in this model may lead to better approaches for treating MI in adult hearts. The single nuclei RNA sequencing data (snRNAseq), which encompassed the gene expression of not only cardiomyocyte but also other cardiac cell types, were generated from these $AR_{P1}MI_{P28}$ regenerative hearts, the age-match naïve hearts (including embryonic day 80, postnatal P1, P28, and P56), and age-match non-regenerative hearts (MI_{P28} only) (Nakada et al., 2022). The cardiomyocyte

snRNAseq data were analyzed in (Nguyen et al., 2022; Nguyen et al., 2023a) via our Autoencoder, and ten cardiomyocyte subpopulations were identified, one of which was present only in cardiomyocytes from AR_{P1} hearts on P28 and appeared to proliferate in response to MI (Nguyen et al., 2022); the subpopulation upregulated T-box transcription factors 5, 20 (TBX5 and TBX20), and erb-b2 receptor tyrosine kinase 4 (ERBB4), which were known to promote mouse cardiomyocyte proliferation (Bersell et al., 2009; Maitra et al., 2009; Chakraborty and Yutzey, 2012; Chakraborty et al., 2013; Misra et al., 2014; Xiang et al., 2016).

On the other hand, how the endothelial cells responded to MI in regenerative hearts was poorly studied. The primary function of the coronary vasculature is to deliver oxygen and nutrients to myocardial cells while removing waste products. The transport and transfer of these materials are facilitated by the endothelium. Thus, regeneration of the vessels that are damaged by MI is essential for minimizing the loss of pre-existing cardiac cells and promoting cardiac repair (Khurana et al., 2005; Ingason et al., 2018; Singh et al., 2022). The endothelial cells (ECs) that line the coronary vasculature are highly specialized for each vessel category (arteries, veins, capillaries, and lymph vessels) and for different segments within each category (Becker et al., 2023). Even adjacent ECs within the same vessel can display substantial phenotypic differences, and this heterogeneity is further exacerbated by myocardial injury. For the experiments described in this report, we used the Autoencoder to analyze snRNAseq data from ECs in the same animal hearts, and because ECs in the coronary vasculature rarely proliferate in healthy hearts but are robustly proliferative in response to injury (Potente et al., 2011), we focused our analyses on the angiogenic response to MI by restricting our cluster analysis to only the 1,646 genes included under the ontology term "cell cycle" in the Gene Ontology Resource (Gene Ontology Annotations, 2022). Our main hypothesis is whether EC subpopulations that highly expressed cell-cycle markers appeared in the regenerative heart data. Understanding through which molecules the EC increased proliferating, thus improving angiogenesis, may lead to new approaches in enhancing the vascular functions following MI. Also, we examined the potential mechanism of how EC subpopulations may crosstalk with signaling pathways in cardiomyocytes and promote cardiomyocyte proliferation, which is another contribution to deciphering heart regeneration.
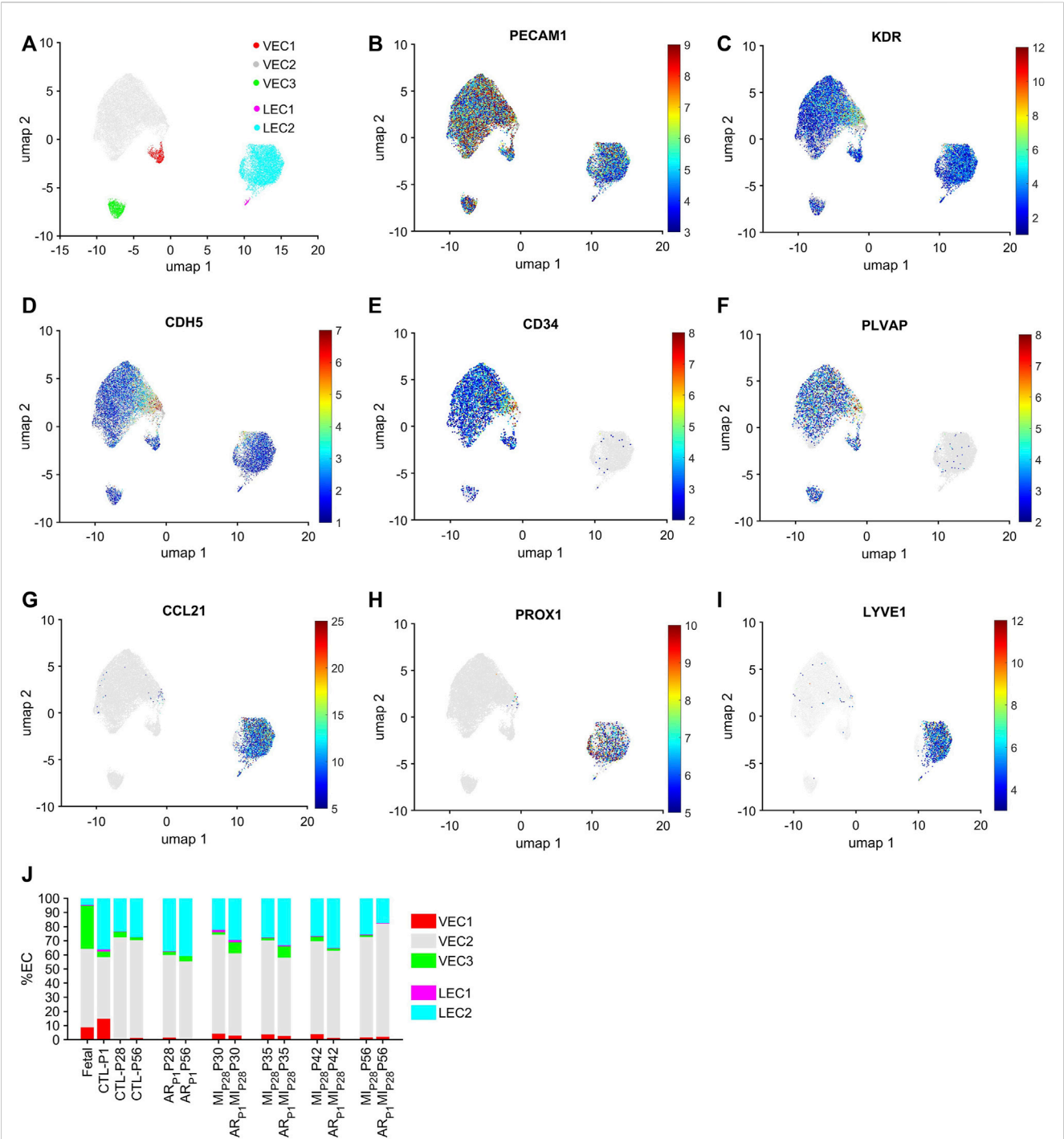
FIGURE 1
Cell-cycle specific Autoencoding defined five EC clusters in pig snRNAseq data. **(A)** Data for the expression of cell-cycle genes was extracted from the pig EC snRNAseq dataset, processed via an AI-based Autoencoder, and visualized in 2 dimensions (2D) via UMAP; the locations of each cluster are displayed. Cells that express the EC-specific markers **(B)** PECAM1, **(C)** KDR, and **(D)** CDH5; the VEC-specific markers **(E)** CD34 and **(F)** PLVAP; and the LEC-specific markers **(G)** CCL21, **(H)** PROX1 and **(I)** LYVE1 are displayed across the 2D cell-cycle−specific UMAP with the magnitude of expression represented as a color-coded heatmap; gray ECs did not express the corresponding molecule. **(J)** The proportion of ECs from each cluster is displayed for each injury group and time point.
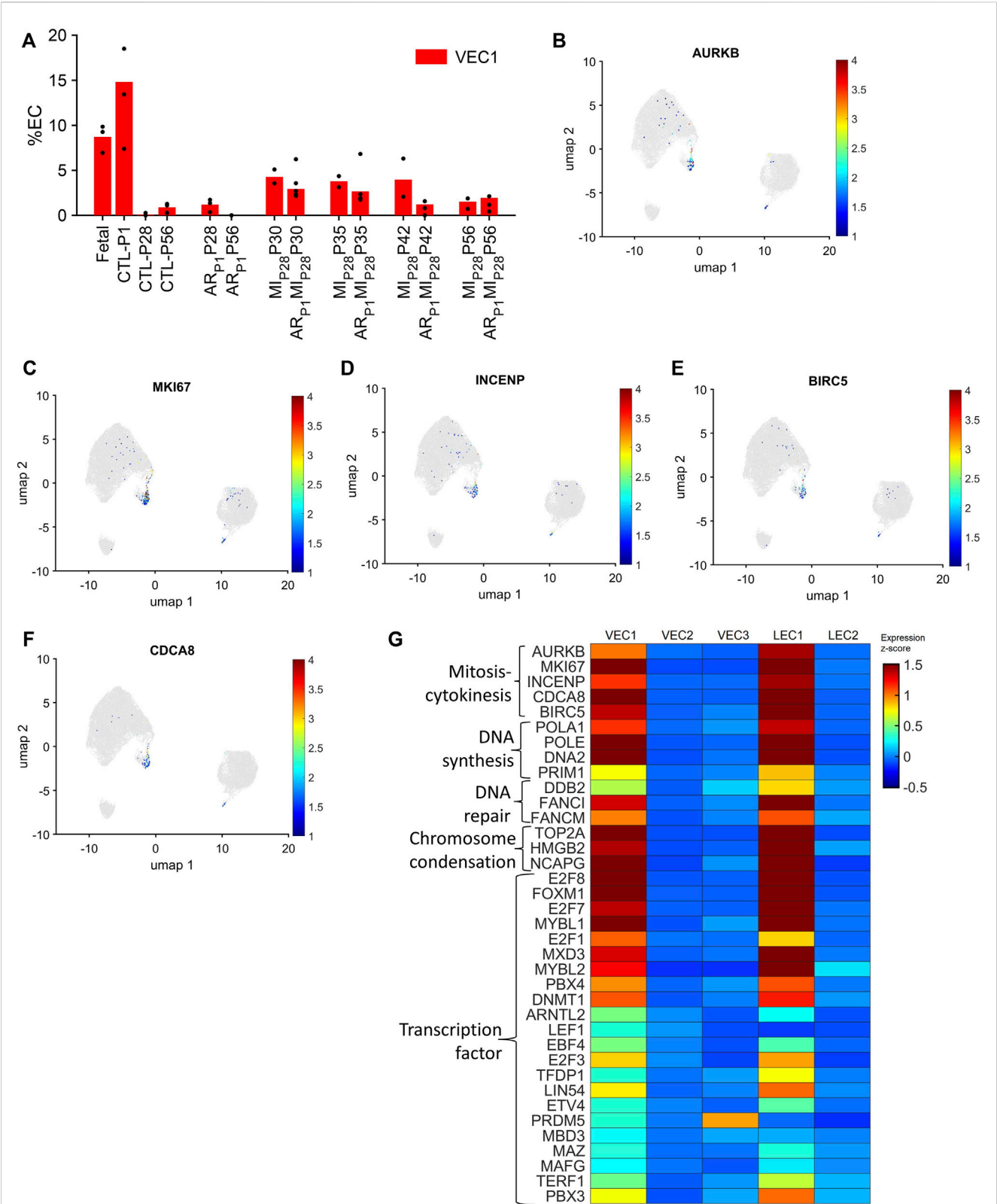
FIGURE 2
The VEC1 cluster is enriched for the expression of cell-cycle−related genes. **(A)** Data for VEC1 from Figure 1I is displayed with the *y*-axis rescaled for clarity. Cells that express the mitosis and cytokinesis markers **(B)** AURKB, **(C)** MKI67, **(D)** INCENP, **(E)** BIRC5, and **(F)** CDCA8 are displayed across the 2D cell-cycle−specific UMAP with the magnitude of expression represented as a color-coded heatmap; gray ECs did not express the corresponding molecule. **(G)** The abundance of expression for genes that are involved in mitosis and cytokinesis, DNA synthesis, DNA repair, and chromosome condensation, and for cell-cycle−regulating transcription factors is displayed for each cluster as a color-coded heat map (normalized by Seurat and converted to z-score).

TABLE 1 Summary of upregulated transcription factors in VEC1.

Transcription factor	Proportion of expressing cells (%)	Fold-change	p-value	References
E2F8	23.49	55.63	2.44×10^{-157}	Weijts et al. (2012)
FOXM1	22.11	42.54	4.58×10^{-132}	Zhao et al. (2006)
E2F7	15.89	27.14	1.57×10^{-89}	Weijts et al. (2012)
MYBL1	29.88	17.78	1.28×10^{-146}	Zhu et al. (2022)
E2F1	13.47	16.20	4.25×10^{-63}	Qin et al. (2006)
MXD3	21.07	14.89	4.56×10^{-89}	Diebold et al. (2019)
MYBL2	30.22	9.13	3.65×10^{-102}	
PBX4	19.34	8.35	1.60×10^{-55}	Martinou et al. (2022)
DNMT1	42.49	5.07	9.34×10^{-96}	Zhang et al. (2016)
ARNTL2	13.99	3.84	4.37×10^{-25}	
LEF1	10.19	3.09	1.59×10^{-12}	Planutiene et al. (2011)
EBF4	20.55	3.08	8.00×10^{-32}	
E2F3	51.47	3.08	6.77×10^{-82}	Zhou et al. (2013)
TFDP1	11.40	2.92	2.75×10^{-18}	
LIN54	49.91	2.87	3.05×10^{-72}	
ETV4	11.74	2.76	2.51×10^{-17}	Harel et al. (2021)
PRDM5	16.75	2.32	2.38×10^{-18}	
MBD3	10.19	2.26	2.34×10^{-13}	Yan et al. (2022)
MAZ	14.85	2.22	1.16×10^{-16}	Smits et al. (2012)
MAFG	11.74	2.07	3.31×10^{-13}	
TERF1	43.70	2.01	4.83×10^{-37}	
PBX3	80.66	2.01	2.43×10^{-62}	Chen et al. (2020), Wu et al. (2020)

Results are summarized as the proportion of VEC1 ECs that express the transcription factor, the fold-change in expression relative to expression in non-VEC1 ECs, and the p-value (Fisher's Exact test).

2 Results

2.1 Cell-cycle-specific AI autoencoding and cluster analysis of pig snRNAseq data identified five EC clusters

Pigs underwent AR_{P1}, MI_{P28}, $AR_{P1}MI_{P28}$, or neither surgical procedure (CTL). Subsequent experiments confirmed that pigs in the $AR_{P1}MI_{P28}$ group, but not MI_{P28} animals, completely regenerated the myocardial tissue that was damaged by MI (Zhao et al., 2020; Nakada et al., 2022). snRNAseq was performed with myocardial tissue collected from MI_{P28} and $AR_{P1}MI_{P28}$ animals on P30, P35, P42, and P56; from AR_{P1} and CTL animals on P28 and P56; from CTL animals on P1, and from fetal pigs.

The cell-cycle-specific Autoencoder (CSA) and clustering pipeline visualized five EC clusters (Figure 1A), each of which expressed elevated levels of the EC-specific surface markers Platelet And Endothelial Cell Adhesion Molecule 1 (PECAM1) (Newman, 1994), Kinase Insert Domain Receptor (KDR) (Terman et al., 1992), and vascular endothelial cadherin (CDH5) (Wu et al., 2021) (Figures 1B–D; Supplementary Figure S1). Three of the clusters were enriched for

expression of the vascular-EC (VEC) markers CD34 (Fina et al., 1990) and Plasmalemma Vesicle Associated Protein (PLVAP) (Denzer et al., 2023) (Figures 1E, F), while the other two expressed high levels of the lymphatic-EC (LEC) markers C-C Motif Chemokine Ligand 21 (CCL21) (Johnson and Jackson, 2010), Prospero Homeobox 1 (PROX1) (Wigle et al., 2002), and Lymphatic Vessel Endothelial Hyaluronan Receptor 1 (LYVE1) (Banerji et al., 1999) (Figures 1G–I). Thus, the CSA appeared to separate the global cardiac EC population into three clusters of vascular ECs (VEC1-3) and two clusters of lymphatic ECs (LEC1-2).

Each EC cluster contained cells from multiple experimental groups and time points (Supplementary Figure S2), confirming that our results were not compromised by sampling bias. Further, we verified that the results were not compromised by batch effects. VEC1-3 collectively comprised >95% of ECs in fetal hearts and 59%–81% of ECs in hearts from all nonfetal animal groups (Figure 1J), whereas LEC1-2 included the remaining <5% of ECs in fetal hearts and 19%–41% of ECs in nonfetal hearts. The majority of VECs were clustered in VEC2, regardless of animal groups or time points, with the highest proportions of VEC1 and VEC3 ECs observed in CTL hearts on P1 and in fetal hearts, respectively. Nearly all LECs were clustered in LEC2.
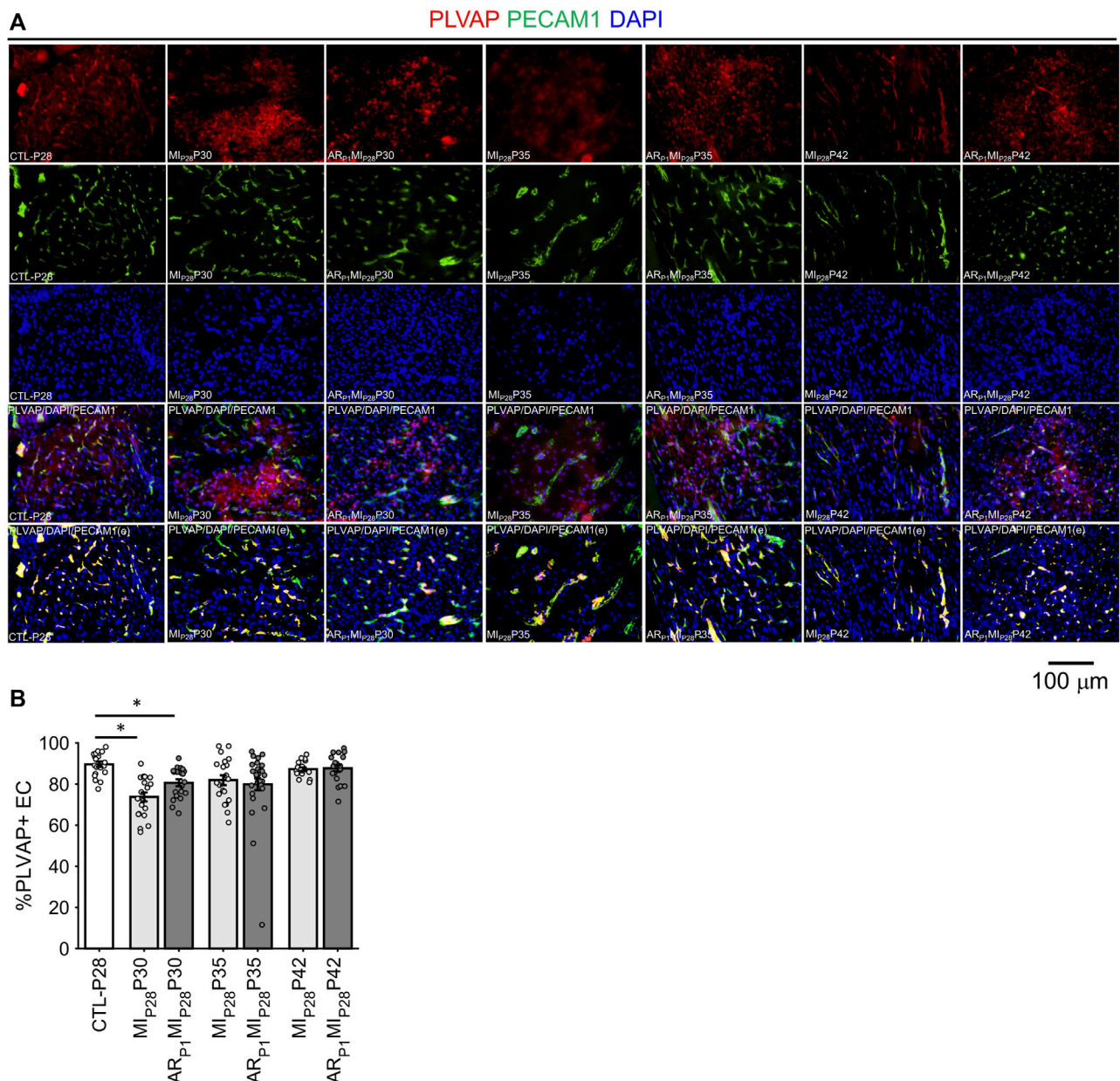
FIGURE 3
Fluorescence immunostaining analysis to assess ing the percentage of PLVAP + endothelial cells (VEC marker) in all animal group. **(A)** Representative images; the number of endothelial cells, marked by the DAPI blue fluorescence overlapping with EC marker PECAM1 green fluorescence, was counted; then, PLVAP red fluorescence and green fluorescence was amplified by 2x; red the signal not overlapping with green was removed before merging with DAPI (PLVAP/DAPI/PECAM(e) channel) to enhance PLVAP + EC visualization and counting. **(B)** Percentage of PLVAP + EC in all animal groups; the horizontal bar and the star (*) indicates non-parametric Wilcoxon's ranksum test between two sample groups. *: p-value < 0.05.

2.2 VEC1 was enriched for the expression of genes involved in cell-cycle activity and proliferation

VEC1 ECs comprised 8.7% of ECs in fetal hearts and 14.8% of ECs in CTL hearts on P1, they declined to nearly undetectable levels in CTL hearts on P28, and then expanded to include 3.5%–4.2% of ECs in MI_{P28} hearts from P30-P42 and in $AR_{P1}MI_{P28}$ hearts on P30-P35 (Figure 2A). VEC1 was also the only VEC cluster to express elevated levels of each of five markers for mitosis and cytokinesis (Aurora Kinase B [AURKB], marker of proliferation Ki-67 [MKI67], Inner Centromere Protein [INCENP], Survivin [BIRC5], and Borealin [CDCA8]) (Li et al., 1998; Vader et al., 2006); Figures 2B–G; Supplementary Figure S3) and was enriched for the expression of genes associated with DNA synthesis and repair (Gene Ontology Annotations, 2023b), chromosome condensation (Gene Ontology Annotations, 2023c), and the gene ontology terms DNA replication ($p = 3.86 \times 10^{-8}$), mitotic spindle organization ($p = 8.71 \times 10^{-7}$), and mitotic cytokinesis ($p = 2.42 \times 10^{-6}$) (Figure 2G; Supplementary Tables S1A, B), as well as numerous transcription
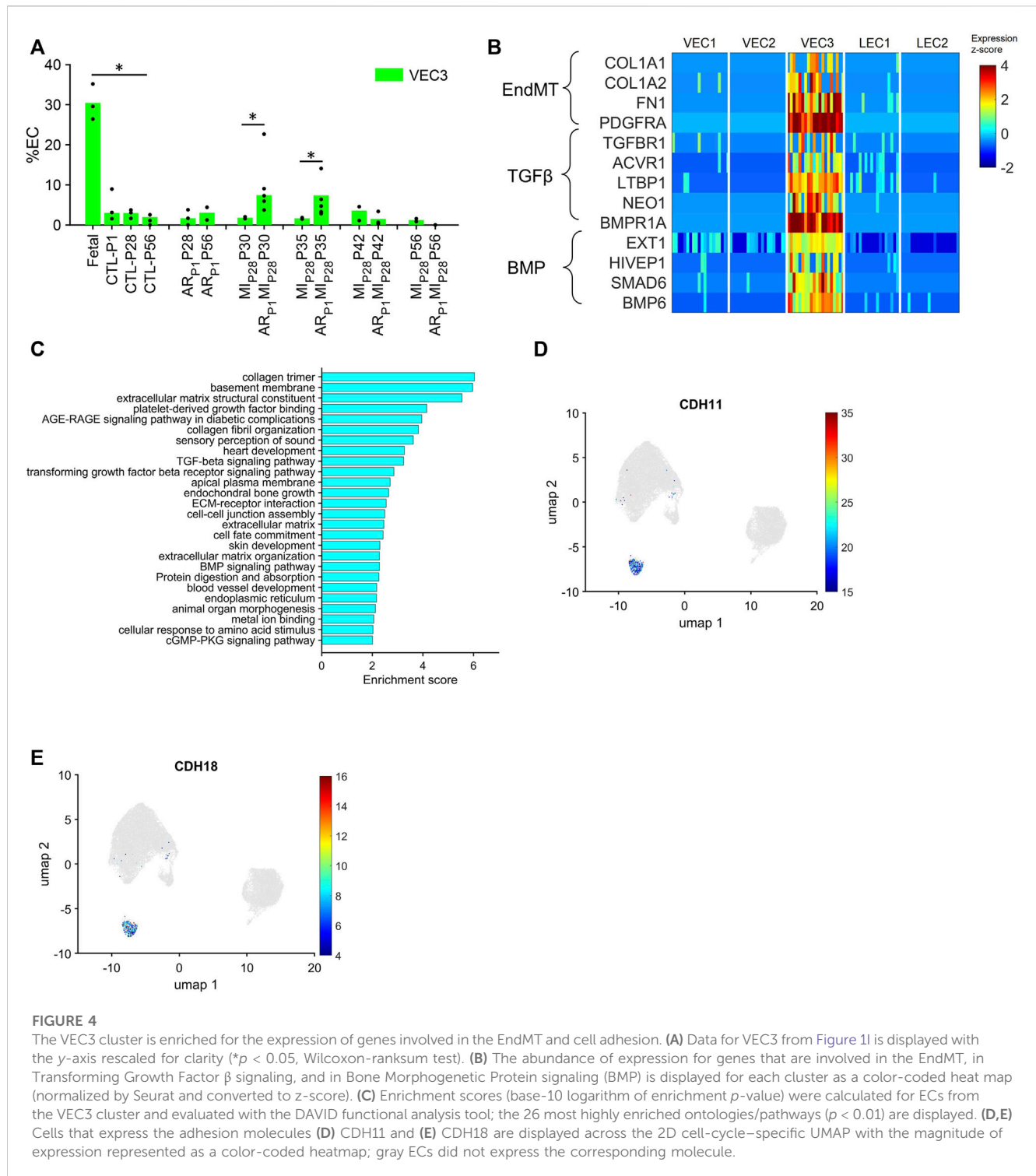
FIGURE 4
The VEC3 cluster is enriched for the expression of genes involved in the EndMT and cell adhesion. **(A)** Data for VEC3 from Figure 1I is displayed with the *y*-axis rescaled for clarity (*$p < 0.05$, Wilcoxon-ranksum test). **(B)** The abundance of expression for genes that are involved in the EndMT, in Transforming Growth Factor β signaling, and in Bone Morphogenetic Protein signaling (BMP) is displayed for each cluster as a color-coded heat map (normalized by Seurat and converted to z-score). **(C)** Enrichment scores (base-10 logarithm of enrichment *p*-value) were calculated for ECs from the VEC3 cluster and evaluated with the DAVID functional analysis tool; the 26 most highly enriched ontologies/pathways (*$p < 0.01$) are displayed. **(D,E)** Cells that express the adhesion molecules **(D)** CDH11 and **(E)** CDH18 are displayed across the 2D cell-cycle−specific UMAP with the magnitude of expression represented as a color-coded heatmap; gray ECs did not express the corresponding molecule.

factors that have been linked to increases in EC proliferation and angiogenesis (Figure 2G; Table 1). Collectively, these observations are consistent with previous reports that the coronary vasculature undergoes a period of rapid growth and remodeling shortly after birth (Tian et al., 2014; Tan and Lewandowski, 2020) and suggest that a small proportion of cardiac ECs revert to a more proliferative phenotype in response to MI on P28.

Notably, although LEC1 ECs were exceptionally rare (<1.5%) in hearts from all groups and time points, they were most abundant in

CTL hearts on P1 and in MI_{P28} and $AR_{P1}MI_{P28}$ hearts on P30 (Figure 1I; Supplementary Figure S4), and were enriched for many of the same mitosis/cytokinesis markers, gene ontology terms, and transcription factors that were upregulated in VEC1 ECs (Figure 2G), which suggests that expansion of the LEC1 cluster may have a role in the inflammatory response (Prabhu and Frangogiannis, 2016) and/or contribute to the re-uptake of interstitial fluid after MI. Also, Immunohistological staining of VEC clusters' markers (PLVAP + PECAM1) (Figure 3) showed
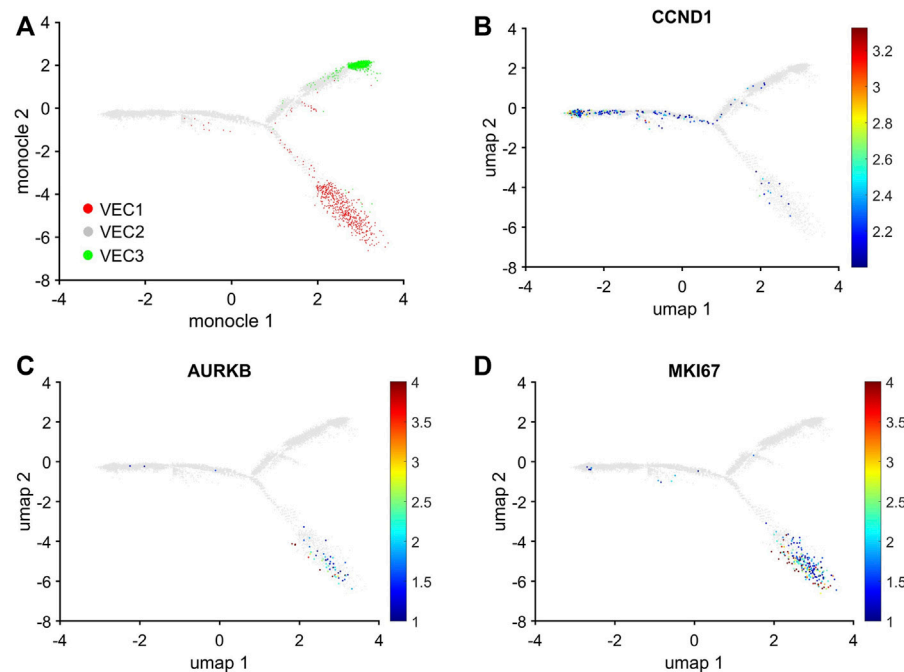
FIGURE 5
Trajectory analysis of pig EC snRNAseq data identified pathways between VEC2 and VEC1 or VEC3, but not between VEC1 and VEC3. Trajectory analysis of cell-cycle gene expression in VEC1, VEC2, and VEC3 ECs was performed via Monocle. **(A)** The positions of cells from each of the three VEC clusters is displayed across the trajectory. ECs that express **(B)** CCND1, which regulates the G1/S phase transition, and the proliferation markers **(C)** AURKB and **(D)** MKI67 are displayed across the 2D cell-cycle−specific UMAP with the magnitude of expression represented as a color-coded heatmap; gray ECs did not express the corresponding molecule.

that on P30, the percentage of PLVAP + ECs significantly decreased, compared to CTL-P28 level as the baseline, following MI_{P28} in both regenerative ($p = 3.382 \times 10^{-4}$) and non-regenerative heart ($p = 3.4995 \times 10^{-6}$); then, these percentage returned to the baseline level on P42. Since the percentages of VEC and LEC clusters were complemented, this result also suggested an increase of LEC between 2 and 7 days after MI_{P28}. This LEC expansion was also suggested by an increase of cycling LEC1 cluster found in the snRNAseq analysis. Besides, trajectory analysis of LEC clusters (Supplementary Figure S4) also showed continuous paths from LEC2 to LEC1; the ordered was from cell-cycle G1/S phase marker Cylin D1 (CCND1) through S-phase marker CCNE2, M-phase marker CCNB2, to proliferation marker MKI67.

2.3 VEC3 was enriched for the expression of genes involved in cell adhesion, the regulation of intercellular junctions, and the endothelial-mesenchymal transition (EndMT)

Although VEC1 ECs became more common in pig hearts after MI was induced on P28, they tended to be *less* common (though not significantly) in $AR_{P1}MI_{P28}$ hearts than in MI_{P28} hearts from P30-P42 and, consequently, are unlikely to contribute to the enhanced regenerative potential observed in the hearts of $AR_{P1}MI_{P28}$ pigs. Conversely, the VEC3 cluster was

significantly *more* prominent in fetal (30.46%) than CTL hearts (3.9%–2.0% from P1-P56; $p < 0.05$ at each time point) and in $AR_{P1}MI_{P28}$ hearts than in MI_{P28} hearts on P30 ($AR_{P1}MI_{P28}$: 6.33%, MI_{P28}: 1.6%; $p < 0.05$) and P35 ($AR_{P1}MI_{P28}$: 6.86%, MI_{P28}: 1.8%; $p < 0.05$) (Figure 4A), but was *not* enriched for the expression of mitosis/cytokinesis markers (Figure 2G; Supplementary Table S2A). Instead, VEC3 ECs expressed elevated levels of genes associated with the EndMT, with the Transforming Growth Factor β (TGFβ) and Bone Morphogenetic Protein (BMP) (Figure 4B; Supplementary Table S2B) pathways (Huang et al., 2022; Gene Ontology Annotations, 2023a; KEGG, 2023), and with ontology terms that are associated with the upregulation of blood-vessel development (Figure 4C; Supplementary Table S2B). Notably, both TGFβ and BMP signaling regulate the EndMT, and although the EndMT appears to contribute to the formation of a number of pathological vascular abnormalities (Huang et al., 2022), all three processes are crucial for embryonic cardiovascular development (Gordon and Blobe, 2008; Morrell et al., 2016; Kovacic et al., 2019). Furthermore, VEC3 ECs expressed elevated levels of Plakophilin 2 (PKP2, fold-change: 24.62, p-value: 5.74×10^{-247}), which regulates the assembly of intercellular junctions (Bass-Zubek et al., 2008), as well as the adhesion molecules Cadherin 11 (CDH11) and Cadherin 18 (CDH18) (Figures 4D, E; Supplementary Figure S5), while expression of the junctional proteins KDR and CDH5 (Giannotta et al., 2013) was somewhat lower in VEC3 than in VEC1 ECs (Supplementary Figure S1).
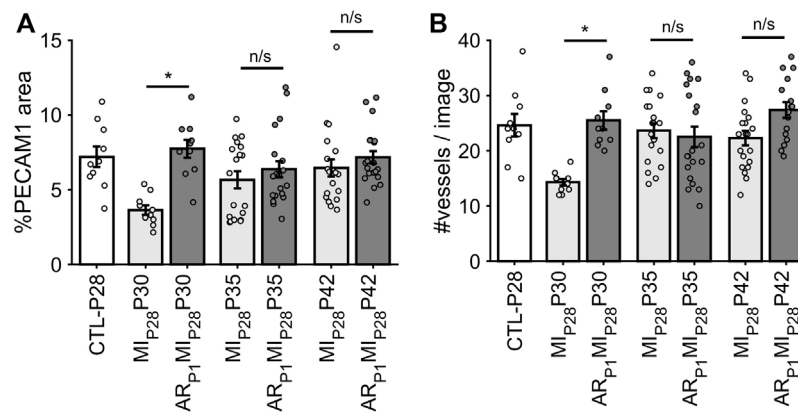
FIGURE 6
Estimating vessel density in each animal group via fluorescence immunostaining. **(A)** For each image, the percentage of pixel having PECAM1 green fluorescence was counted. **(B)** For each image, the number of vessels was manually counted. The horizontal bar and the star (*) indicates non-parametric Wilcoxon's ranksum test between two sample groups. *: p-value <0.05; ns: p-value ≥ 0.05.

2.4 Trajectory analysis linked VEC2 to VEC1 and VEC3, but there was no direct pathway between VEC1 and VEC3

The uniqueness of the VEC1 and VEC3 clusters was also evidenced by the results from Monocle pseudotime trajectory analysis (Qiu et al., 2017) of cell-cycle snRNAseq data for cells in all three VEC clusters. The analysis produced a branched structure with the tips of two branches each composed almost exclusively of VEC1 or VEC3 ECs and the third branch, as well as the region where all three branches converged, occupied by primarily VEC2 ECs (Figure 5A). Furthermore, the distribution of cells expressing Cyclin D1 (CCND1), which regulates the G1/S phase transition, and the proliferation markers AURKB and MKI67 traced a pathway between VEC2 and VEC1, but not between VEC2 and VEC3 or VEC3 and VEC1 (Figures 5B–D). Collectively, these observations indicated that VEC2 ECs could transform into either VEC1 or VEC3 ECs, but there was no direct transformational pathway between the VEC1 and VEC3 clusters, and identified a trajectory from VEC2 to VEC1 that recapitulated the onset and progression of cell-cycle activity and proliferation.
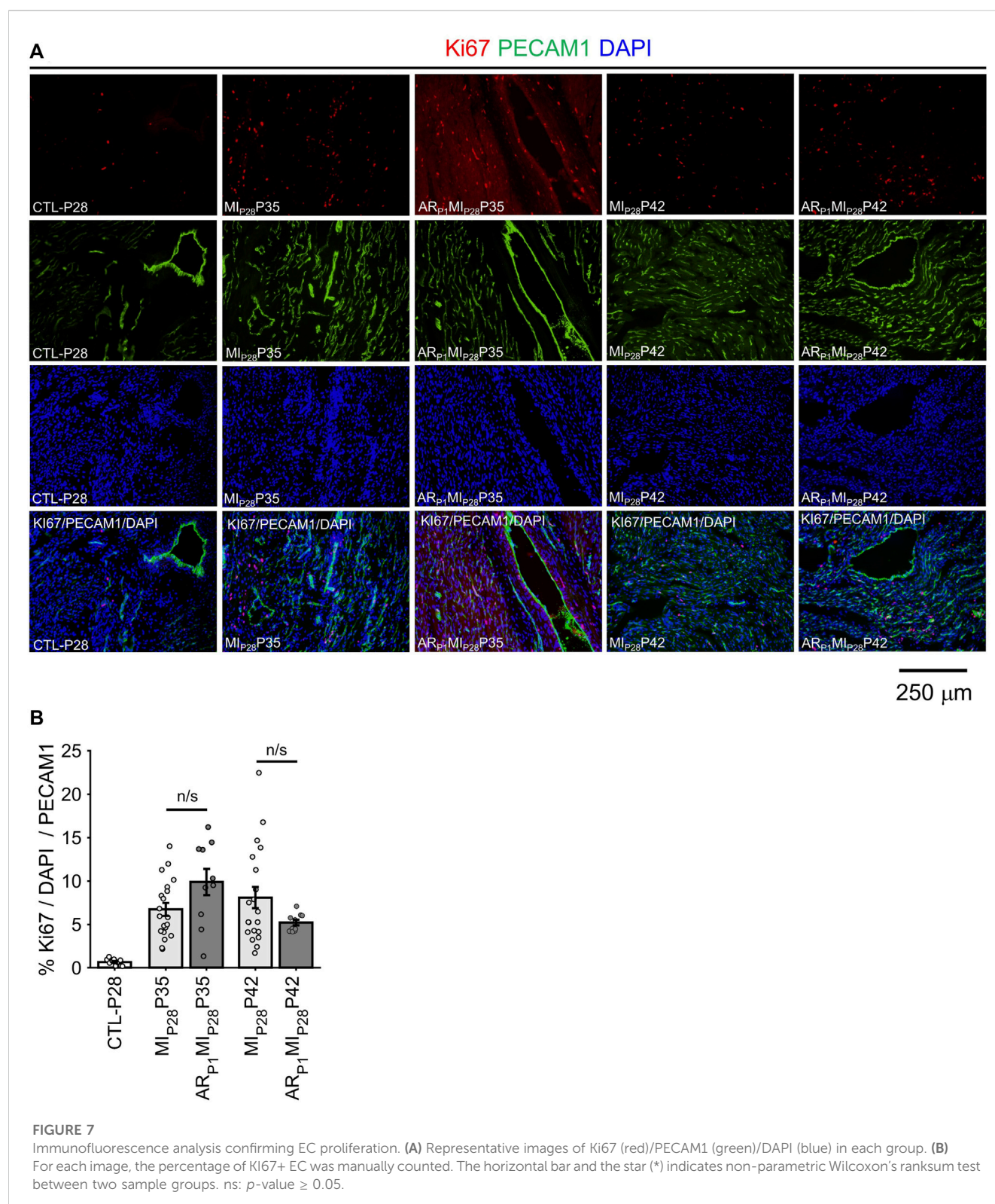
2.5 Angiogenesis (vessel density and proliferation marker)

Following MI_{P28}, the vessel density, quantified by the percentage of image PECAM1 area and by the manual counting of vessels in each image (Figure 6), significantly decreased on P30 in non-regenerative hearts; then, on P35 and P42, their vessel densities recovered to the level of CTL-P28 hearts. Meanwhile, in regenerative hearts, the vessel densities did not significantly change, remaining similar to CTL-P28. On the other hand, Marker of Proliferation

Ki67 immunofluorescence analysis (Figure 7) showed that seven to 14 days following the MI_{P28} injury, endothelial cells in both regenerative and non-regenerative hearts actively proliferate. Before the injury, less than 1% of EC expressed Ki67. Then, on day 7 and 14 after MI_{P28}, the percentages of Ki67+ EC increased to, and remained between 6% and 8% in the non-regenerative hearts ($MI_{P28}P35$ and $MI_{P28}P42$, respectively); meanwhile, in the regenerative hearts, % Ki67+ EC increased to 9.88% on P35, then decreased to 5.20% on P42. The difference of Ki67+ EC between the two groups was insignificant at these time points ($p = 0.062$ and $p = 0.467$, respectively), and was consistent with the snRNAseq analysis. Then, we compared the expression of Vascular Endothelial Growth Factor A (VEGFA) and Vascular Endothelial Growth Factor B (VEGFB), which are known as the driver genes in angiogenesis involved in wound healing (Johnson and Wilgus, 2014), in the whole-heart snRNAseq data. Supplementary Figure S6 showed that it was unclear whether these two genes expressions were consistently higher in the regenerative (or on-regenerative) groups. This observation may explain why we did not observe significant angiogenesis between the regenerative and non-regenerative hearts.

2.6 VEC3 markers PDGFRA are highly expressed in ECs of regenerative hearts up to 7 days following MI_{P28} injury

In Figure 8, the expression of EndMT marker PDGFRA in EC was represented by the intensity of red fluorescence overlapping with green (EC marker PECAM1) fluorescence. A small number (~1.5%) of EC in the CTL-P28 hearts were VEC3; therefore, the PDGFRA expression in CTL-P28 EC was used as the baseline. Then, following MI_{P28} injury, PDGFRA expression in the non-regenerative hearts EC sharply decreased on P30, then gradually increased on P35 and P42; however, the

FIGURE 7
Immunofluorescence analysis confirming EC proliferation. **(A)** Representative images of Ki67 (red)/PECAM1 (green)/DAPI (blue) in each group. **(B)** For each image, the percentage of KI67+ EC was manually counted. The horizontal bar and the star (*) indicates non-parametric Wilcoxon's ranksum test between two sample groups. ns: p-value ≥ 0.05.

increased expression did not reach beyond the baseline level. Meanwhile, PDGFRA expression sharply increased in the regenerative heart on P30 ($p = 7.69 \times 10^{-4}$) and P35 ($p = 4.71 \times 10^{-5}$), then reverted to the baseline level on P42. These trends were consistent with the snRNAseq analysis.

Also, surprisingly, PDGFRA immunofluorescence analysis showed that non-endothelial cells surrounding PDGFRA + EC also expressed PDGFRA; these cells could be cardiac fibroblasts and cardiomyocytes, as reported in (Bloomekatz et al., 2017; Yao et al., 2022).
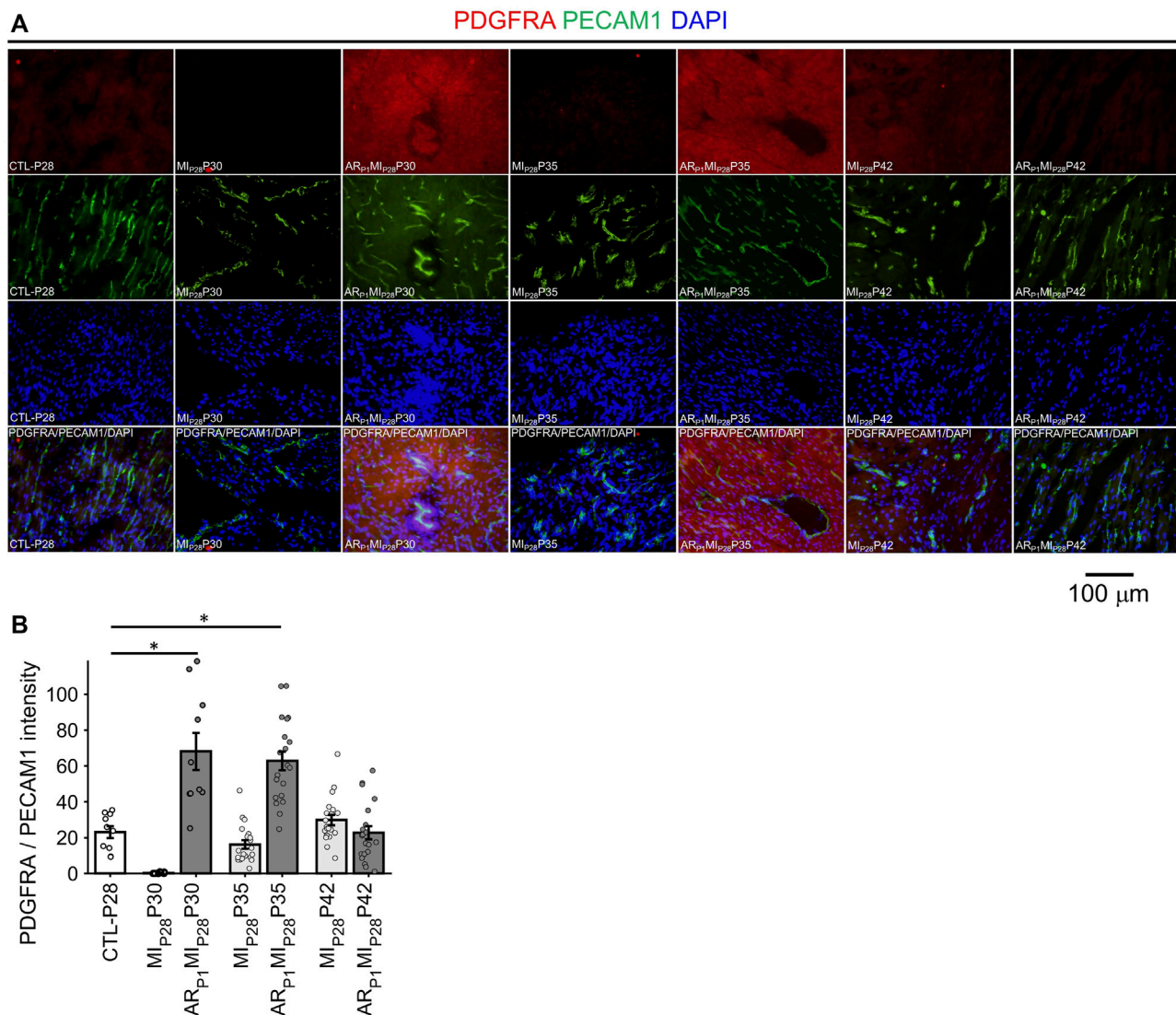
FIGURE 8
Fluorescence immunostaining analysis to confirm PDGFRA (EndMT marker) expression in endothelial cells. **(A)** Representative images of PDGFRA (red)/PECAM1 (green)/DAPI (blue) in each group. **(B)** The expression of PDGFRA was represented by the average PDGFRA red light intensity that are overlapped with EC marker green regions. The horizontal bar and the star (*) indicates non-parametric Wilcoxon's ranksum test between two sample groups. *: p-value < 0.05.

2.7 VEC3 upregulated genes encoding secretable proteins that may promote cardiomyocyte proliferation and heart regeneration via Pi3k-Akt, Hippo/YAP, and ERBB4 signaling pathways

Our previous works demonstrated the upregulation of Hippo/YAP signaling pathway in regenerative pig hearts that underwent myocardial infarction on P1 (Zhang et al., 2020), as well as ERBB4 in $AR_{P1}P28$ hearts (Nguyen et al., 2022) at the protein level. Also, Pi3k-Akt signaling pathway was found enriched in $AR_{P1}MI_{P28}$ cardiomyocytes (Nakada et al., 2022; Nguyen et al., 2023b). Therefore, we examined whether the VEC3 cluster may have genes that interact with these pathways (Figure 9A). Thirty genes encoding secretable

proteins were found upregulated in VEC3; among them, Fibronectin 1 [FN1] (Wang et al., 2013), Neuregulin 1 [NRG1] (Bersell et al., 2009; Gemberling et al., 2015), Versican [VCAM] (Feng et al., 2023), and Periostin [POSTN] (Kuhn et al., 2007) were known to promote cardiomyocyte proliferation in zebrafish, mice, and rat. We also queried the protein-protein interactions between these 30 genes and their receptors linked to Pi3k-Akt, Hippo/YAP, and ERBB4 signaling pathways in the Biological General Repository for Interaction Datasets (BioGrid) (Oughtred et al., 2021). Figure 9B shows that POSTN, FN1, and VCAM interact with Integrin Alpha 1 [ITGA1] and Integrin Beta 1 [ITGB1], which are receptors of the Pi3k-Akt signaling pathway (Feng et al., 2023). Also, Fibrillin 2 [FBN2], which was upregulated in VEC3, interact with Insulin Receptor [INSR] of Pi3k-Akt signaling pathway.
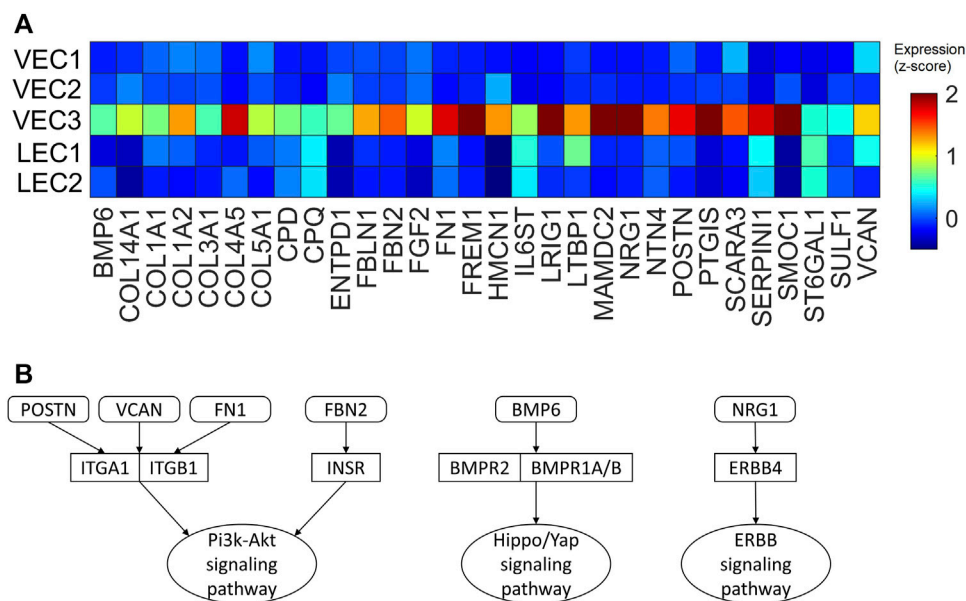
FIGURE 9
Upregulated genes encoding secretable proteins in cluster VEC3 interact with receptors of signaling pathways enriched in the regenerative hearts. **(A)** Heatmap of 30 genes encoding secretable proteins that exclusively upregulated (fold-change >2) in cluster VEC3; here, the expression is scaled by z-score and reflected in the heatmap color. **(B)** Protein-protein interactions, which were queried from BioGrid database, between the genes and their receptors of Pi3k-Akt, Hippo/YAP, and ERRB4 signaling pathways; round rectangle: genes; rectangle: signaling pathway receptors; oval: downstream signaling pathway.

Furthermore, NRG1 interacts with ERBB4, and Bone Morphogenetic Protein 6 [BMP6] interacts with receptors Bone Morphogenetic Protein Receptor Type 1A/B and Type 2 [BMPR1A/B, BMPR2] of the Hippo/Yap signaling pathway. Overall, these secret protein-receptor interactions suggested that VEC3 cluster may promote cardiomyocyte proliferation and overall regeneration.

3 Discussion

ECs comprise an exceptionally heterogeneous population of cells with unique features and functions that are specialized for each organ, for each vascular category (i.e., arteries, veins, capillaries, lymph vessels) within an organ, and for each segment within a vessel (Becker et al., 2023). The rate of EC turnover is believed to be low in most healthy organs, but the cells rapidly proliferate in response to injury (Potente et al., 2011). Thus, as we sought to characterize how different subpopulations of ECs participate in the angiogenic response to MI, we analyzed snRNAseq data from ECs that were collected during previous studies in our neonatal pig cardiac double-injury ($AR_{P1}MI_{P28}$) model via our cell-cycle–specific AI Autoencoder. Our analysis distributed the cells into five EC clusters, three containing VECs and two containing LECs.

Of the three VEC clusters, only one (VEC1) was enriched for cell-cycle activity, while another (VEC3) highly expressed genes involved in cell adhesion, in the regulation of intercellular junctions, in the EndMT, and in TGFβ/BMP signaling, which regulates the EndMT (Piera-Velazquez and Jimenez, 2019). Notably, angiogenesis is initiated by vessel sprouting (Sun et al., 2016), which begins with the loss of

junctions between ECs and may be accompanied by onset of the EndMT in tip cells (Gerhardt et al., 2003); then, ECs located in the stalk of the sprout proliferate to lengthen and expand the endothelial tube (Marcelo et al., 2013). Thus, our observations suggest that VEC3 ECs may function as EC tip cells, while the VEC1 cluster could be composed primarily of stalk ECs. Furthermore, while ECs of the VEC2 cluster did not appear to be directly involved in angiogenesis, our trajectory analyses identified pathways linking VEC2 to both VEC1 and VEC3, which suggests that the VEC2 cluster contains a reservoir of ECs that can transform into tip (VEC3) or stalk (VEC1) ECs during angiogenesis. This observation is consistent with reports (Tian et al., 2015) that proliferating ECs are generated primarily from pre-existing ECs rather than another source, but we did not find a trajectory between VEC1 and VEC3, so the onset of EC cell-cycle activity does not appear to be driven by the EndMT. Notably, LEC1 ECs were enriched for many of the same mitosis/ cytokinesis markers, gene ontology terms, and transcription factors that were upregulated in VEC1 ECs, which suggests that they also proliferate in response to MI and, consequently, may limit cardiac edema by increasing the uptake of interstitial fluid, but their precise role during recovery from myocardial injury has yet to be investigated.

The EndMT has been linked to increases in fibrosis (Fan et al., 2023), and recent studies in mice suggest that the acquisition of a mesenchymal-like phenotype in ECs after MI can lead to vascular abnormalities in newly formed vessels that block the efficient delivery of oxygen and other nutrients to the myocardium (Huang et al., 2022). These reports may appear to conflict with our observation that VEC3 ECs, which expressed elevated levels of EndMT genes, were the only EC subpopulation that was enriched in regenerating hearts. However, this discrepancy may be at least partially explained by

differences in the prevalence and/or persistence of the mesenchymal-like phenotype: whereas the VEC3 cluster never contained more than ~7.5% of ECs in nonfetal pig hearts and was expanded for just 1 week after MI induction in $AR_{P1}MI_{P28}$ pigs, the proportion of ECs that expressed mesenchymal genes in infarcted mouse hearts (Huang et al., 2022) increased from 1%–3% to 20%–70% during the first week after MI induction, and 5%–20% of them continued to express at least some mesenchymal genes for 3–8 weeks afterward. On the other hand, EC acquiring the EndMT markers may enhance their ability to proliferate, migrate, and dissociate (Huang et al., 2022). Our vessel density analysis showed that 2 days following MI_{P28} injury, the regenerative heart vessel density, where the VEC3 cluster strongly presented, quickly reached the CTL-P28 level; meanwhile, the non-regenerative heart, with a very small amount of VEC3, vessel density did not. VEC3 may promote cardiomyocyte proliferation and overall heart generation by secreting pro-proliferative proteins.

In conclusion, our analyses of cardiac snRNAseq data collected from fetal pigs and pigs that underwent AR_{P1}, MI_{P28}, both AR_{P1} and MI_{P28}, or neither experimental injury identified three clusters of VECs and two LEC clusters. Cells from just one of the VEC clusters (VEC1) appeared to proliferate in response to MI induction, and a second VEC cluster (VEC3) was enriched for the expression of genes that regulate intercellular junctions, participate in TGFβ/BMP signaling and promote the EndMT, while the remaining VEC cluster (VEC2) appeared to provide a reservoir of ECs that transformed into VEC1 or VEC3 ECs after MI. Notably, although the roles of TGFβ/BMP signaling and the EndMT have been well-studied in cardiac development, their involvement in cardiac regeneration is not well understood. Thus, more in-depth studies of the VEC3 cluster could identify new targets for improving the regeneration of infarcted hearts.

4 Methods

4.1 snRNAseq datasets

The pig snRNAseq dataset was obtained from the Gene Expression Omnibus database (accession number GSE185289). The complete dataset included 250,700 cells and was processed as described previously (Nakada et al., 2022; Nguyen et al., 2022; Nguyen et al., 2023b). The number of pig hearts for each group was summarized in Supplementary Table S3. The data were normalized with Seurat v.4 (Hao et al., 2021); then, expression data for 14,753 genes with at least 1,000 unique molecular identifiers were embedded into 10 dimensions with an Autoencoder. The results were visualized via Uniform Manifold Approximation (UMAP), and clustering was performed with the UMAP density-based clustering (dbscan) algorithm (McInnes et al., 2018; Meehan, 2021). Cells in clusters that specifically expressed the EC markers PECAM1 and KDR were considered ECs. A total of 29,826 ECs were identified.

4.2 Animal heart tissues

Frozen tissues, from which the snRNAseq datasets (Nakada et al., 2022; Nguyen et al., 2022; Nguyen et al., 2023b) were generated, were cut into 1 cm thick sections, embedded in

optimal cutting temperature compound, and preserved in −80℃ freezers. All experimental protocols were approved by The Institutional Animal Care and Use Committee (IACUC) of the University of Alabama, Birmingham, and performed in accordance with the National Institutes of Health Guide for the Care and Use of Laboratory Animals (NIH publication No 85-23).

4.3 Cell-cycle-specific analyses

4.3.1 Autoencoder and clustering

EC data was extracted from the full pig dataset, and then snRNAseq data for the 1,646 genes associated with the Gene Ontology term "cell cycle" (GO:0007049) (Gene Ontology Annotations, 2022) were reprocessed via AI Autoencoding and cluster analysis. This cell-cycle-specific Autoencoder was composed of three layers: an input layer of 1,646 nodes (i.e., the snRNA expression data for each of the 1,646 cell-cycle genes), a hidden (embedded) layer of 10 nodes, and an output layer of 1,646 nodes. The input layer was alternately embedded into the hidden layer and expanded to form the output layer, and the similarity of the input and output layers was optimized by minimizing the following equation:

$$E = \frac{1}{N}\sum_{i}^{N}\sum_{j}^{N}\left(x_i - y_j\right)^2 + 0.001\|W\|^2 + Q \qquad (1)$$

where N represents the number of ECs, x_i represents the cell-cycle–specific gene expression for an EC from the input layer, y_j represents the cell-cycle–specific gene expression for an EC from the output layer, $\|W\|^2$ represents the regularization of autoencoder weights, and Q represents the sparsity parameters (trainAutoencoder, 2021). Visualization and clustering were performed with the UMAP toolkit (McInnes et al., 2018; Meehan, 2021), and clusters of proliferating ECs were defined by co-enrichment for the expression of five proliferation markers (AURKB, MKI67, INCENP, CDCNA8, and BIRC5). We also conducted independent analysis using the entire genome (Supplementary Note S1) and other clustering parameters (Supplementary Note S2) to confirmed that the cell-cycle-specific approach did not miss any specific EC subpopulations.

4.3.2 Trajectory analysis

Cell-cycle–specific trajectory and pseudotime analysis were performed by processing snRNAseq data for the 1,646 cell-cycle–specific genes with the Monocle (v.3) toolkit (Trapnell et al., 2014; Qiu et al., 2017), and pseudotime order was determined by the localization of Cyclin D1, AURKB, and MKI67 expression.

4.4 Identification of cluster-specific genes

Upregulated genes for each EC cluster were identified according to the following criteria: 1) a cluster p-value (Fisher's Exact test (Fisher, 1922)) of less than 10^{-6}, 2) expression by more than 25% of cells in the cluster, and 3) mean expression at least 2-fold greater than among ECs in other clusters. For transcription factors, which

are typically expressed in low abundance, criteria for upregulation were modified to 1) a cluster p-value of $<10^{-6}$, 2) expression by >10% of cluster cells, and 3) mean expression >2-fold greater than among cells in other clusters. The list of transcription factors was obtained from the Transcriptional Regulatory Relationships Unraveled by Sentence-based Text mining database (TRRUST) (Han et al., 2018) version 2, and the set of upregulated genes for each cluster was analyzed with the DAVID functional annotation tool (Huang da et al., 2009); only terms present in the Gene Ontology (Huntley et al., 2015) and KEGG (Kanehisa et al., 2017) categories were selected. To avoid false positives caused by multihypothesis testing, the selected results were required to have a Benjamini-adjusted (Li and Barber, 2019) $p < 0.05$.

4.5 Immunohistochemistry studies

The immunofluorescence analyses were conducted similar to our previous work in (Nakada et al., 2022). Briefly, samples were cut into transverse sections (thickness: 10 μm), embedded into slides, washed in PBS, and fixed in 4% paraformaldehyde for 20 min at room temperature. Then, the slides were permeabilized at 4°C, 0.1% triton-x for 10 min, and then blocked with Ultra-V block for 7 min. Samples were incubated with mouse anti- PECAM1 at 1:100 (MCA1738, BioRad, United States) or rabbit anti Ki67 (1: 100 dilution, ab15580, Abcam, United States), or rabbit antiPDGFRA (1:100 dilution, AF0241, Affinity, United States), or rabbit anti-PLVAP (1:100 dilution, AF0241, Affinity), in PBS containing 10% goat serum (10% PBS)for overnight at 4°C. On the next day, donkey anti-mouse IgG conjugated with FITC at 1: 200 dilution and donkey anti-rabbit IgG conjugated with Cy3 at 1; 200 dilution were added for 1 h at room temperature Then, samples were washed after 1:1000 DAPI solution was added for 1 min, mounted in vectorshieldand cover slide for imaging.

The slides were put into an Olympus IX83 microscope to capture images. The image frame size was 1360-width × 1024-height pixels. Exposure time for PECAM1 fluorescence (green) was initially set to 2.8 s, and could be case-by-case adjusted between 2.6 and 3.2 s. Exposure time for Ki67 and PLVAP fluorescence (red) was initially set to 1.2s, and could be adjusted between 0.9 and 1.4 s. Exposure time for PDGFRA fluorescence (red) was always set to 1.2s. DAPI (blue) exposure time was between 12 and 18 μs. Z-stack parameter was set to 0 for all images and channels. For each slide, ten image sets were captured; each image set include three channels: red, green, and blue; then, the three-channels were put together by Matlab to create a 'merge' RGB-color image.

Three-channel images (green: PECAM1; red: either Ki67, PDGFRA, or PLVAP; blue: DAPI) were processed using Matlab as in (Nguyen et al., 2022). Multi-thresholding segmentation method (Otsu, 1979) (Matlab multithresh function) was applied to extract image fluorescence regions. The vessel density was computed as the percentage of image area with green fluorescence. EC nuclei were recognized as the DAPI (blue) blocks overlapping with green regions; EC proliferating cells were recognized as the Ki67 red block overlapping with green regions; and EC proliferation marker was computed by the ratio between EC proliferating cells and EC DAPI. EC PDGFRA expression was assessed by the average red intensity overlapping with green

fluorescence. For PLVAP + EC analysis, the PECAM1 and PLVAP fluorescence intensity was amplified by 2x before merging into one 3D image channel, PLVAP signal that were not overlapping with PECAM1 was removed for enhanced visualization (PLVAP/DAPI/PECAM1(e) images); then, the number of PLVAP + ECs was manually counted. Statistical comparison among the groups was completed using non-parametric Wilcoxon's Ranksum test. A p-value < 0.05 indicates statistical significance.

Data availability statement

The original contributions presented in the study are included in the article/Supplementary Material; the analytic program is provided at https://github.com/thamnguy/Cardiac-endothelial-cell; further inquiries can be directed to the corresponding author.

Ethics statement

The animal study was approved by the Institutional Animal Care and Use Committee (IACUC) of the University of Alabama, Birmingham, and performed in accordance with the National Institutes of Health Guide for the Care and Use of Laboratory Animals (NIH publication No. 85-23). The study was conducted in accordance with the local legislation and institutional requirements.

Author contributions

TN: Formal Analysis, Methodology, Investigation, Writing–original draft, XG: Investigation, Writing–review and editing, YW: Investigation, Writing–review and editing, LY: Methodology, Writing–review and editing, DG: Conceptualization, Writing–review and editing. JZ: Conceptualization, Funding acquisition, Supervision, Writing–review and editing.

Funding

Conflict of interest

The authors declare that the research was conducted in the absence of any commercial or financial relationships that could be construed as a potential conflict of interest.

The reviewer AQ declared a past co-authorship with the author JZ to the handling editor.

The author(s) declared that they were an editorial board member of Frontiers, at the time of submission. This had no impact on the peer review process and the final decision.

Publisher's note

All claims expressed in this article are solely those of the authors and do not necessarily represent those of their affiliated organizations, or those of the publisher, the editors and the reviewers. Any product that may be evaluated in this article, or claim that may be made by its manufacturer, is not guaranteed or endorsed by the publisher.

Supplementary material

The Supplementary Material for this article can be found online at: https://www.frontiersin.org/articles/10.3389/fbioe.2023.1257669/full#supplementary-material

SUPPLEMENTARY TABLE S1
Summary of upregulated genes, pathways, and biological processes in VEC1. **(A)** Gene expression is summarized as the proportion of VEC1 ECs that express the gene, the fold-change in gene expression relative to expression

in non-VEC1 ECs, and the *p*-value (Fisher's Exact test). **(B)** Expression of genes in **(A)** was processed with the DAVID toolkit (https://david.ncifcrf.gov/) to identify pathways and biological processes that were enriched in VEC1; the enrichment *p*-value was corrected to control for false-discoveries.

SUPPLEMENTAL TABLE S2
Summary of upregulated genes, pathways, and biological processes in VEC3. **(A)** Gene expression is summarized as the proportion of VEC3 ECs that express the gene, the fold-change in gene expression relative to expression in non-VEC3 ECs, and the *p*-value (Fisher's Exact test). **(B)** Expression of genes in **(A)** was processed with the DAVID toolkit (https://david.ncifcrf.gov/) to identify pathways and biological processes that were enriched in VEC3; the enrichment *p*-value was corrected to control for false-discoveries.

SUPPLEMENTAL TABLE S3
Sample size *n* (number of pig hearts) per each sample group in our study. The first column indicates the animal group (injury & timepoints), including n. The second column indicates the heart identification. The third and fourth columns indicate whether the heart underwent apical resection on P1 and/or myocardial infarction on P28. The last column indicates the age (day) when the heart tissues were harvested.

References

Banerji, S., Ni, J., Wang, S. X., Clasper, S., Su, J., Tammi, R., et al. (1999). LYVE-1, a new homologue of the CD44 glycoprotein, is a lymph-specific receptor for hyaluronan. *J. Cell. Biol.* 144, 789–801. doi:10.1083/jcb.144.4.789

Bass-Zubek, A. E., Hobbs, R. P., Amargo, E. V., Garcia, N. J., Hsieh, S. N., Chen, X., et al. (2008). Plakophilin 2: a critical scaffold for PKC alpha that regulates intercellular junction assembly. *J. Cell. Biol.* 181, 605–613. doi:10.1083/jcb.200712133

Becker, L. M., Chen, S. H., Rodor, J., de Rooij, L., Baker, A. H., and Carmeliet, P. (2023). Deciphering endothelial heterogeneity in health and disease at single-cell resolution: progress and perspectives. *Cardiovasc Res.* 119, 6–27. doi:10.1093/cvr/cvac018

Bersell, K., Arab, S., Haring, B., and Kuhn, B. (2009). Neuregulin1/ErbB4 signaling induces cardiomyocyte proliferation and repair of heart injury. *Cell.* 138, 257–270. doi:10.1016/j.cell.2009.04.060

Bloomekatz, J., Singh, R., Prall, O. W., Dunn, A. C., Vaughan, M., Loo, C. S., et al. (2017). Platelet-derived growth factor (PDGF) signaling directs cardiomyocyte movement toward the midline during heart tube assembly. *Elife* 6, e21172. doi:10.7554/elife.21172

Chakraborty, S., Sengupta, A., and Yutzey, K. E. (2013). Tbx20 promotes cardiomyocyte proliferation and persistence of fetal characteristics in adult mouse hearts. *J. Mol. Cell. Cardiol.* 62, 203–213. doi:10.1016/j.yjmcc.2013.05.018

Chakraborty, S., and Yutzey, K. E. (2012). Tbx20 regulation of cardiac cell proliferation and lineage specialization during embryonic and fetal development *in vivo*. *Dev. Biol.* 363, 234–246. doi:10.1016/j.ydbio.2011.12.034

Chen, Q., Yu, W. Y., Zhang, H. H., Zhang, S. Z., Fang, J., Wu, F., et al. (2020). PBX3 promotes tumor growth and angiogenesis via activation of at1r/VEGFR2 pathway in papillary thyroid carcinoma. *Biomed. Res. Int.* 2020, 1–10. doi:10.1155/2020/8954513

Chiong, M., Wang, Z. V., Pedrozo, Z., Cao, D. J., Troncoso, R., Ibacache, M., et al. (2011). Cardiomyocyte death: mechanisms and translational implications. *Cell. Death Dis.* 2, e244. doi:10.1038/cddis.2011.130

Denzer, L., Muranyi, W., Schroten, H., and Schwerk, C. (2023). The role of PLVAP in endothelial cells. *Cell. Tissue Res.* 392, 393–412. doi:10.1007/s00441-023-03741-1

Diebold, L. P., Gil, H. J., Gao, P., Martinez, C. A., Weinberg, S. E., and Chandel, N. S. (2019). Mitochondrial complex III is necessary for endothelial cell proliferation during angiogenesis. *Nat. Metab.* 1, 158–171. doi:10.1038/s42255-018-0011-x

Fan, M., Yang, K., Wang, X., Chen, L., Gill, P. S., Ha, T., et al. (2023). Lactate promotes endothelial-to-mesenchymal transition via Snail1 lactylation after myocardial infarction. *Sci. Adv.* 9, eadc9465. doi:10.1126/sciadv.adc9465

Feng, J., Li, Y., Li, Y., Yin, Q., Li, H., Li, J., et al. (2023). Versican promotes cardiomyocyte proliferation and cardiac repair. *Circulation*. doi:10.1161/circulationaha.123.066298

Fina, L., Molgaard, H. V., Robertson, D., Bradley, N. J., Monaghan, P., Delia, D., et al. (1990). Expression of the CD34 gene in vascular endothelial cells. *Blood* 75, 2417–2426. doi:10.1182/blood.v75.12.2417.bloodjournal75122417

Fisher, R. A. (1922). On the interpretation of χ 2 from contingency tables, and the calculation of P. *J. R. Stat. Soc.* 85, 87–94. doi:10.2307/2340521

Gemberling, M., Karra, R., Dickson, A. L., and Poss, K. D. (2015). Nrg1 is an injury-induced cardiomyocyte mitogen for the endogenous heart regeneration program in zebrafish. *Elife* 4, e05871. doi:10.7554/elife.05871

Gene Ontology Annotations (2022). *Cell cycle*. China: Mouse Genome Informatics.

Gene Ontology Annotations (2023a). BMP signaling pathway. *Mouse Genome Inf.*

Gene Ontology Annotations (2023b). *DNA repair, mouse genome informatics*.

Gene Ontology Annotations (2023c). Mitotic chromosome condensation. *Mouse Genome Inf.*

Gerhardt, H., Golding, M., Fruttiger, M., Ruhrberg, C., Lundkvist, A., Abramsson, A., et al. (2003). VEGF guides angiogenic sprouting utilizing endothelial tip cell filopodia. *J. Cell. Biol.* 161, 1163–1177. doi:10.1083/jcb.200302047

Giannotta, M., Trani, M., and Dejana, E. (2013). VE-cadherin and endothelial adherens junctions: active guardians of vascular integrity. *Dev. Cell.* 26, 441–454. doi:10.1016/j.devcel.2013.08.020

Gordon, K. J., and Blobe, G. C. (2008). Role of transforming growth factor-beta superfamily signaling pathways in human disease. *Biochim. Biophys. Acta* 1782, 197–228. doi:10.1016/j.bbadis.2008.01.006

Han, H., Cho, J. W., Lee, S., Yun, A., Kim, H., Bae, D., et al. (2018). TRRUST v2: an expanded reference database of human and mouse transcriptional regulatory interactions. *Nucleic Acids Res.* 46, D380–D386. doi:10.1093/nar/gkx1013

Hao, Y., Hao, S., Andersen-Nissen, E., Mauck, W. M., 3rd, Zheng, S., Butler, A., et al. (2021). Integrated analysis of multimodal single-cell data. *Cell.* 184, 3573–3587 e29. doi:10.1016/j.cell.2021.04.048

Harel, S., Sanchez, V., Moamer, A., Sanchez-Galan, J. E., Abid Hussein, M. N., Mayaki, D., et al. (2021). ETS1, ELK1, and ETV4 transcription factors regulate angiopoietin-1 signaling and the angiogenic response in endothelial cells. *Front. Physiol.* 12, 683651. doi:10.3389/fphys.2021.683651

Huang, M., Yang, F., Zhang, D., Lin, M., Duan, H., El-Mayta, R., et al. (2022). Endothelial plasticity drives aberrant vascularization and impedes cardiac repair after myocardial infarction. *Nat. Cardiovasc Res.* 1, 372–388. doi:10.1038/s44161-022-00047-3

Huang da, W., Sherman, B. T., and Lempicki, R. A. (2009). Systematic and integrative analysis of large gene lists using DAVID bioinformatics resources. *Nat. Protoc.* 4, 44–57. doi:10.1038/nprot.2008.211

Huntley, R. P., Sawford, T., Mutowo-Meullenet, P., Shypitsyna, A., Bonilla, C., Martin, M. J., et al. (2015). The Goa database: gene Ontology annotation updates for 2015. *Nucleic Acids Res.* 43, D1057–D1063. doi:10.1093/nar/gku1113

Ingason, A. B., Goldstone, A. B., Paulsen, M. J., Thakore, A. D., Truong, V. N., Edwards, B. B., et al. (2018). Angiogenesis precedes cardiomyocyte migration in regenerating mammalian hearts. *J. Thorac. Cardiovasc Surg.* 155, 1118–1127 e1. doi:10.1016/j.jtcvs.2017.08.127

Johnson, K. E., and Wilgus, T. A. (2014). Vascular endothelial growth factor and angiogenesis in the regulation of cutaneous wound repair. *Adv. Wound Care (New Rochelle)* 3, 647–661. doi:10.1089/wound.2013.0517

Johnson, L. A., and Jackson, D. G. (2010). Inflammation-induced secretion of CCL21 in lymphatic endothelium is a key regulator of integrin-mediated dendritic cell transmigration. *Int. Immunol.* 22, 839–849. doi:10.1093/intimm/dxq435

Kanehisa, M., Furumichi, M., Tanabe, M., Sato, Y., and Morishima, K. (2017). KEGG: new perspectives on genomes, pathways, diseases and drugs. *Nucleic Acids Res.* 45, D353–D361. doi:10.1093/nar/gkw1092

KEGG (2023). *TGF-beta signaling pathway - Sus scrofa (pig).* Kyoto University.

Khurana, R., Simons, M., Martin, J. F., and Zachary, I. C. (2005). Role of angiogenesis in cardiovascular disease: a critical appraisal. *Circulation* 112, 1813–1824. doi:10.1161/circulationaha.105.535294

Kovacic, J. C., Dimmeler, S., Harvey, R. P., Finkel, T., Aikawa, E., Krenning, G., et al. (2019). Endothelial to mesenchymal transition in cardiovascular disease: JACC state-of-the-art review. *J. Am. Coll. Cardiol.* 73, 190–209. doi:10.1016/j.jacc.2018.09.089

Kuhn, B., del Monte, F., Hajjar, R. J., Chang, Y. S., Lebeche, D., Arab, S., et al. (2007). Periostin induces proliferation of differentiated cardiomyocytes and promotes cardiac repair. *Nat. Med.* 13, 962–969. doi:10.1038/nm1619

Laflamme, M. A., and Murry, C. E. (2011). Heart regeneration. *Nature* 473, 326–335. doi:10.1038/nature10147

Li, A., and Barber, R. F. (2019). Multiple testing with the structure-adaptive Benjamini–Hochberg algorithm. *J. R. Stat. Soc. Ser. B Stat. Methodol.* 81, 45–74. doi:10.1111/rssb.12298

Li, F., Ambrosini, G., Chu, E. Y., Plescia, J., Tognin, S., Marchisio, P. C., et al. (1998). Control of apoptosis and mitotic spindle checkpoint by survivin. *Nature* 396, 580–584. doi:10.1038/25141

Lu, L., Liu, M., Sun, R., Zheng, Y., and Zhang, P. (2015). Myocardial infarction: symptoms and treatments. *Cell. Biochem. Biophys.* 72, 865–867. doi:10.1007/s12013-015-0553-4

Maitra, M., Schluterman, M. K., Nichols, H. A., Richardson, J. A., Lo, C. W., Srivastava, D., et al. (2009). Interaction of Gata4 and Gata6 with Tbx5 is critical for normal cardiac development. *Dev. Biol.* 326, 368–377. doi:10.1016/j.ydbio.2008.11.004

Marcelo, K. L., Goldie, L. C., and Hirschi, K. K. (2013). Regulation of endothelial cell differentiation and specification. *Circ. Res.* 112, 1272–1287. doi:10.1161/circresaha.113.300506

Martinou, E. G., Moller-Levet, C. S., and Angelidi, A. M. (2022). PBX4 functions as a potential novel oncopromoter in colorectal cancer: a comprehensive analysis of the PBX gene family. *Am. J. Cancer Res.* 12, 585–600.

McInnes, L., Healy, J., and Melville, J., UMAP: Uniform manifold approximation and projection for dimension reduction. arXiv preprint arXiv:1802.03426 (2018).

McMullen, J. R., and Jennings, G. L. (2007). Differences between pathological and physiological cardiac hypertrophy: novel therapeutic strategies to treat heart failure. *Clin. Exp. Pharmacol. Physiol.* 34, 255–262. doi:10.1111/j.1440-1681.2007.04585.x

Meehan, S. (2021). *Uniform Manifold approximation and projection.* USA: UMAP.

Misra, C., Chang, S. W., Basu, M., Huang, N., and Garg, V. (2014). Disruption of myocardial Gata4 and Tbx5 results in defects in cardiomyocyte proliferation and atrioventricular septation. *Hum. Mol. Genet.* 23, 5025–5035. doi:10.1093/hmg/ddu215

Morrell, N. W., Bloch, D. B., ten Dijke, P., Goumans, M. J., Hata, A., Smith, J., et al. (2016). Targeting BMP signalling in cardiovascular disease and anaemia. *Nat. Rev. Cardiol.* 13, 106–120. doi:10.1038/nrcardio.2015.156

Nakada, Y., Zhou, Y., Gong, W., Zhang, E. Y., Skie, E., Nguyen, T., et al. (2022). Single nucleus transcriptomics: apical resection in newborn pigs extends the time window of cardiomyocyte proliferation and myocardial regeneration. *Circulation* 145, 1744–1747. doi:10.1161/circulationaha.121.056995

Newman, P. J. (1994). The role of PECAM-1 in vascular cell biology[a]. *Ann. N. Y. Acad. Sci.* 714, 165–174. doi:10.1111/j.1749-6632.1994.tb12041.x

Nguyen, T., Wei, Y., Nakada, Y., Chen, J. Y., Zhou, Y., Walcott, G., et al. (2023a). Analysis of cardiac single-cell RNA-sequencing data can be improved by the use of artificial-intelligence-based tools. *Sci. Rep.* 13, 6821. doi:10.1038/s41598-023-32293-1

Nguyen, T., Wei, Y., Nakada, Y., Chen, J. Y., Zhou, Y., Walcott, G., et al. (2023b). Analysis of cardiac single-cell RNA-sequencing data can be improved by the use of artificial-intelligence-based tools. *Sci. Rep.* 13, 6821. doi:10.1038/s41598-023-32293-1

Nguyen, T., Wei, Y., Nakada, Y., Zhou, Y., and Zhang, J. (2022). Cardiomyocyte cell-cycle regulation in neonatal large mammals: single nucleus RNA-sequencing data analysis via an artificial-intelligence-based pipeline. *Front. Bioeng. Biotechnol.* 10, 914450. doi:10.3389/fbioe.2022.914450

Otsu, N. (1979). A threshold selection method from gray-level histograms. *IEEE Trans. Syst. Man, Cybern.* 9, 62–66. doi:10.1109/tsmc.1979.4310076

Oughtred, R., Rust, J., Chang, C., Breitkreutz, B. J., Stark, C., Willems, A., et al. (2021). The BioGRID database: a comprehensive biomedical resource of curated protein, genetic, and chemical interactions. *Protein Sci.* 30, 187–200. doi:10.1002/pro.3978

Piera-Velazquez, S., and Jimenez, S. A. (2019). Endothelial to mesenchymal transition: role in physiology and in the pathogenesis of human diseases. *Physiol. Rev.* 99, 1281–1324. doi:10.1152/physrev.00021.2018

Planutiene, M., Planutis, K., and Holcombe, R. F. (2011). Lymphoid enhancer-binding factor 1, a representative of vertebrate-specific Lef1/Tcf1 sub-family, is a Wnt-beta-catenin pathway target gene in human endothelial cells which regulates matrix metalloproteinase-2 expression and promotes endothelial cell invasion. *Vasc. Cell.* 3, 28. doi:10.1186/2045-824x-3-28

Porrello, E. R., Mahmoud, A. I., Simpson, E., Hill, J. A., Richardson, J. A., Olson, E. N., et al. (2011). Transient regenerative potential of the neonatal mouse heart. *Science* 331, 1078–1080. doi:10.1126/science.1200708

Potente, M., Gerhardt, H., and Carmeliet, P. (2011). Basic and therapeutic aspects of angiogenesis. *Cell.* 146, 873–887. doi:10.1016/j.cell.2011.08.039

Prabhu, S. D., and Frangogiannis, N. G. (2016). The biological basis for cardiac repair after myocardial infarction: from inflammation to fibrosis. *Circ. Res.* 119, 91–112. doi:10.1161/circresaha.116.303577

Qin, G., Kishore, R., Dolan, C. M., Silver, M., Wecker, A., Luedemann, C. N., et al. (2006). Cell cycle regulator E2F1 modulates angiogenesis via p53-dependent transcriptional control of VEGF. *Proc. Natl. Acad. Sci. U. S. A.* 103, 11015–11020. doi:10.1073/pnas.0509533103

Qiu, X., Mao, Q., Tang, Y., Wang, L., Chawla, R., Pliner, H. A., et al. (2017). Reversed graph embedding resolves complex single-cell trajectories. *Nat. Methods* 14, 979–982. doi:10.1038/nmeth.4402

Singh, S., Prakash, S., and Gupta, S. K. (2022). Angiogenesis: a critical determinant for cardiac regeneration. *Mol. Ther. Nucleic Acids* 29, 88–89. doi:10.1016/j.omtn.2022.06.007

Smits, M., Wurdinger, T., van het Hof, B., Drexhage, J. A., Geerts, D., Wesseling, P., et al. (2012). Myc-associated zinc finger protein (MAZ) is regulated by miR-125b and mediates VEGF-induced angiogenesis in glioblastoma. *FASEB J.* 26, 2639–2647. doi:10.1096/fj.11-202820

Steinhauser, M. L., and Lee, R. T. (2011). Regeneration of the heart. *EMBO Mol. Med.* 3, 701–712. doi:10.1002/emmm.201100175

Sun, X., Altalhi, W., and Nunes, S. S. (2016). Vascularization strategies of engineered tissues and their application in cardiac regeneration. *Adv. Drug Deliv. Rev.* 96, 183–194. doi:10.1016/j.addr.2015.06.001

Sutton, M. G., and Sharpe, N. (2000). Left ventricular remodeling after myocardial infarction: pathophysiology and therapy. *Circulation* 101, 2981–2988. doi:10.1161/01.cir.101.25.2981

Tan, C. M. J., and Lewandowski, A. J. (2020). The transitional heart: from early embryonic and fetal development to neonatal life. *Fetal Diagn Ther.* 47, 373–386. doi:10.1159/000501906

Terman, B. I., Dougher-Vermazen, M., Carrion, M. E., Dimitrov, D., Armellino, D. C., Gospodarowicz, D., et al. (1992). Identification of the KDR tyrosine kinase as a receptor for vascular endothelial cell growth factor. *Biochem. Biophys. Res. Commun.* 187, 1579–1586. doi:10.1016/0006-291x(92)90483-2

Tian, X., Hu, T., Zhang, H., He, L., Huang, X., Liu, Q., et al. (2014). *De novo* formation of a distinct coronary vascular population in neonatal heart. *Science* 345, 90–94. doi:10.1126/science.1251487

Tian, X., Pu, W. T., and Zhou, B. (2015). Cellular origin and developmental program of coronary angiogenesis. *Circ. Res.* 116, 515–530. doi:10.1161/circresaha.116.305097

trainAutoencoder (2021). *trainAutoencoder, Mathworks.* USA: Inc.

Trapnell, C., Cacchiarelli, D., Grimsby, J., Pokharel, P., Li, S., Morse, M., et al. (2014). The dynamics and regulators of cell fate decisions are revealed by pseudotemporal ordering of single cells. *Nat. Biotechnol.* 32, 381–386. doi:10.1038/nbt.2859

Vader, G., Medema, R. H., and Lens, S. M. (2006). The chromosomal passenger complex: guiding Aurora-B through mitosis. *J. Cell. Biol.* 173, 833–837. doi:10.1083/jcb.200604032

Wang, J., Karra, R., Dickson, A. L., and Poss, K. D. (2013). Fibronectin is deposited by injury-activated epicardial cells and is necessary for zebrafish heart regeneration. *Dev. Biol.* 382, 427–435. doi:10.1016/j.ydbio.2013.08.012

Weijts, B. G., Bakker, W. J., Cornelissen, P. W., Liang, K. H., Schaftenaar, F. H., Westendorp, B., et al. (2012). E2F7 and E2F8 promote angiogenesis through transcriptional activation of VEGFA in cooperation with HIF1. *EMBO J.* 31, 3871–3884. doi:10.1038/emboj.2012.231

Wigle, J. T., Harvey, N., Detmar, M., Lagutina, I., Grosveld, G., Gunn, M. D., et al. (2002). An essential role for Prox1 in the induction of the lymphatic endothelial cell phenotype. *EMBO J.* 21, 1505–1513. doi:10.1093/emboj/21.7.1505

Wu, J., Meng, X., Jia, Y., Chai, J., Wang, J., Xue, X., et al. (2020). Long non-coding RNA HNF1A-AS1 upregulates OTX1 to enhance angiogenesis in colon cancer via the binding of transcription factor PBX3. *Exp. Cell. Res.* 393, 112025. doi:10.1016/j.yexcr.2020.112025

Wu, X., Reboll, M. R., Korf-Klingebiel, M., and Wollert, K. C. (2021). Angiogenesis after acute myocardial infarction. *Cardiovasc Res.* 117, 1257–1273. doi:10.1093/cvr/cvaa287

Xiang, F. L., Guo, M., and Yutzey, K. E. (2016). Overexpression of Tbx20 in adult cardiomyocytes promotes proliferation and improves cardiac function after myocardial infarction. *Circulation* 133, 1081–1092. doi:10.1161/circulationaha.115.019357

Yan, W., Han, Q., Gong, L., Zhan, X., Li, W., Guo, Z., et al. (2022). MBD3 promotes hepatocellular carcinoma progression and metastasis through negative regulation of tumour suppressor TFPI2. *Br. J. Cancer* 127, 612–623. doi:10.1038/s41416-022-01831-5

Yao, L., Rathnakar, B. H., Kwon, H. R., Sakashita, H., Kim, J. H., Rackley, A., et al. (2022). Temporal control of PDGFRα regulates the fibroblast-to-myofibroblast transition in wound healing. *Cell. Rep.* 40, 111192. doi:10.1016/j.celrep.2022.111192

Ye, L., D'Agostino, G., Loo, S. J., Wang, C. X., Su, L. P., Tan, S. H., et al. (2018). Early regenerative capacity in the porcine heart. *Circulation* 138, 2798–2808. doi:10.1161/circulationaha.117.031542

Zhang, E., Nguyen, T., Zhao, M., Dang, S. D. H., Chen, J. Y., Bian, W., et al. (2020). Identifying the key regulators that promote cell-cycle activity in the hearts of early neonatal pigs after myocardial injury. *PLoS One* 15, e0232963. doi:10.1371/journal.pone.0232963

Zhang, R., Wang, N., Zhang, L. N., Huang, N., Song, T. F., Li, Z. Z., et al. (2016). Knockdown of DNMT1 and DNMT3a promotes the angiogenesis of human mesenchymal stem cells leading to arterial specific differentiation. *Stem Cells* 34, 1273–1283. doi:10.1002/stem.2288

Zhao, M., Zhang, E., Wei, Y., Zhou, Y., Walcott, G. P., and Zhang, J. (2020). Apical resection prolongs the cell cycle activity and promotes myocardial regeneration after left ventricular injury in neonatal pig. *Circulation* 142, 913–916. doi:10.1161/circulationaha.119.044619

Zhao, Y. Y., Gao, X. P., Zhao, Y. D., Mirza, M. K., Frey, R. S., Kalinichenko, V. V., et al. (2006). Endothelial cell-restricted disruption of FoxM1 impairs endothelial repair following LPS-induced vascular injury. *J. Clin. Investig.* 116, 2333–2343. doi:10.1172/jci27154

Zhou, J., Cheng, M., Wu, M., Boriboun, C., Jujo, K., Xu, S., et al. (2013). Contrasting roles of E2F2 and E2F3 in endothelial cell growth and ischemic angiogenesis. *J. Mol. Cell. Cardiol.* 60, 68–71. doi:10.1016/j.yjmcc.2013.04.009

Zhu, J., Wu, Y., Yu, Y., Li, Y., Shen, J., and Zhang, R. (2022). MYBL1 induces transcriptional activation of ANGPT2 to promote tumor angiogenesis and confer sorafenib resistance in human hepatocellular carcinoma. *Cell. Death Dis.* 13, 727. doi:10.1038/s41419-022-05180-2

Zhu, W., Zhang, E., Zhao, M., Chong, Z., Fan, C., Tang, Y., et al. (2018). Regenerative potential of neonatal porcine hearts. *Circulation* 138, 2809–2816. doi:10.1161/circulationaha.118.034886

Frontiers in
Bioengineering and Biotechnology

Accelerates the development of therapies, devices, and technologies to improve our lives

A multidisciplinary journal that accelerates the development of biological therapies, devices, processes and technologies to improve our lives by bridging the gap between discoveries and their application.

Discover the latest Research Topics

See more →

Frontiers

Avenue du Tribunal-Fédéral 34
1005 Lausanne, Switzerland
frontiersin.org

Contact us

+41 (0)21 510 17 00
frontiersin.org/about/contact

Frontiers in
Bioengineering
and Biotechnology

frontiers | Research Topics